PONTIFICIA UNIVERSIDAD CATOLICA DE CHILE
FACULTAD DE FISICA
DEPARTAMENTO DE ASTRONOMIA Y ASTROFISICA

RESOLVED STELLAR POPULATIONS IN THE NEARBY GALAXIES NGC 5128 AND WLM

Por
MARINA REJKUBA

Tesis de doctorado presentada al Departamento de Astronomía y Astrofísica
de la Facultad de Física de la Pontificia Universidad Católica de Chile,
como uno de los requisitos para optar al
título de Doctor en Ciencias Exactas mención Física

Profesor guía: Prof. Dante Minniti
Profesor co-guía: Dr. David Silva
Profesores correctores: Prof. Alejandro Clocchiatti, Prof. Maximo Bañados

June, 2002
Santiago, Chile

For Anto

Acknowledgements

I am very grateful to many people whose support and guidance gave me a chance to complete this thesis. Most of all I would like to thank my supervisors, Dante Minniti, from Pontificia Universidad Católica de Chile, and David Silva, from European Southern Observatory in Garching, Germany. Dante introduced me to the study of stellar populations and galactic astronomy. He was always there supporting me and leading me in the right direction even though much of my research was conducted on the other side of the Ocean. Dave always had the best advice and his support and encouragement helped to get through my student years in Garching very smoothly. I was very lucky to have two such great advisors. I am indebted to Laura Greggio and Manuella Zoccali who spent a lot of time with me helping with the construction of the color-magnitude diagram simulator and teaching me about the stellar evolution. I would like to thank Father George Coyne who helped with a good advice, pointing me in the right direction and giving me a chance to choose my way to Chile.

I am indebted to many ESO astronomers who took the data presented in this thesis in service mode. Without them this work would not be the same. Juan Veliz, Kevin McGuire and Antonello Piemonte helped a lot with Unix support.

My office mates, Julio Chaname in Santiago and Joel Vernet, Elena Pancino and Maren Hempel in Garching often helped with numerous details. Sometimes in discussions they would suggest where and how to look for the solution of the problem. It was great to have their company which made every day life in the office lively.

Several people influenced my research through discussions. In particular I benefited a lot from Frederic Courbin, Michael Hilker, George Hau, Andres Meza, Leopoldo Infante, Alejandro Clocchiati, Markus Kissler-Patig, Tom Richtler, Thomas Puzia, Bob Fosbury, Peter Stetson, Carme Gallart, Maria Rosa Cioni, Martino Romaniello, Bill Harris, Steve Zepf, Dough Geisler, Albert Zijlstra, Tim Bedding, Leo Girardi and Helmut Jerjen among others.

George Hau was the best flatmate Antonello and I could have in the first two years in Santiago. I am highly indebted to him for letting me stay in his flat on my visits to Santiago and in the last months while I was finishing the writing of the thesis. He also helped a lot polishing my english and being a good friend. I would also like to thank Vanessa Hill and Jacopo Farinato for sharing their appartments with me and for helping me to settle in Garching.

I gratefully acknowledge funding from Pontificia Universidad Católica through "Ayudante becario" and "Instructor becario" studentships and two year funding from ESO studentship programme as well as from Fondecyt 1990440 and FONDAP Center for Astrophysics. I am also grateful for the financial support from the organizing comitees that enabled me to attend several meetings and conferences: Princeton/PUC workshop on "Ω" in Pucon in 1999, joint CTIO/ESO/LCO workshop "Stars, Gas and Dust in Galaxies: Exploring the Links" in La Serena in 2000, IAU Symposium 207 "Extragalactic Star Clusters" in Pucon in 2001 and the Euroconference "Evolution of galaxies. II-Basic building blocks" held in Reunion Island in 2001.

My stay in Chile thaught me that distance counts. I would like to thank my family for their continuous support and to friends "back home", Vanja Margetić, Ticijana Ban and Melita Tadić, for staying in touch and close even though we saw each other rarely. The possibility to come back to Europe, through ESO studentship programme, helped. I could go again skiing with my sister and friends in Austria and swimming at the Adriatic Coast. But above all, I would like to thank my husband, Antonello Piemonte, for his love and support, for staying with me through good and bad times, for waiting for me and following me around the world and for showing me which are the most important things in the life!

Contents

List of Figures

List of Tables

Summary

We have investigated stellar populations of two nearby galaxies representative of the two extremes of the Hubble sequence: the Local Group dwarf irregular WLM and the nearest giant elliptical NGC 5128 (Centaurus A). The analysis of their color-magnitude diagrams (CMDs) and the comparison with the simulated star formation histories is used to infer the basic parameters like distance, reddening, metallicity and ages of the stars.

Deep STIS *CL* and *LP*-band images taken with the Hubble Space Telescope were used to identify a horizontal branch population in WLM. An empirical calibration of the STIS non-standard photometric bands to the ground based Johnson-Cousins VI system has been derived. From the V-band magnitude of the horizontal branch, adopting $\mathrm{E(V-I)} = 0.03$, a distance modulus of $(m-M)_0 = 24.95 \pm 0.13$ ($D = 978 \pm 60$ kpc) was measured to WLM. The horizontal branch, extending blueward from the red giant clump, is an unambiguous signature of an old population, implying an early formation of this isolated dwarf galaxy. Finding of an old metal-poor halo in an isolated dwarf irregular constrains dwarf galaxy formation scenarios, excluding those in which dwarf galaxies form recently.

NGC 5128 presents a complex mix of stellar populations. VLT with FORS1 and ISAAC was used to obtain deep U, V and K-band images in two halo fields at ~ 14 (Field 1) and ~ 9 kpc (Field 2) from the center of the galaxy. In them we have discovered 71 globular clusters, based on their non-stellar profiles. A deep globular cluster luminosity function (GCLF) was constructed and compared to the GCLF of the spiral galaxies M31 and Milky Way. Their mutual similarity suggests that GCLF is unique and independent of Hubble type of its host galaxy. Bimodal color distribution of globular clusters is indicative of multiple populations in this galaxy.

In the optical UV CMDs of Field 1, which coincides with the location of the north-eastern diffuse stellar shell, recent star formation is observed. The comparison of the observed and synthetic CMDs suggests that the star formation started at least 100 Myr ago and is still on-going or at most has stopped some 2 Myr ago. Its fuel is provided by the large HI gas cloud in the vicinity of the field, most probably acquired during the last merger episode. This gas fuels low level star formation in the halo (SFR$\sim 0.007\ \mathrm{M_\odot\ yr^{-1}}$). The most remarkable feature about this star formation is, however, its alignment with the radio and X-ray structure of the host galaxy.

Additional UV images from Magellan I telescope at Las Campanas Observatory show that the collimated star formation extends for more than 10 kpc along the direction of the X-ray and radio jet. This highly collimated star formation is present only in the north-eastern halo of the galaxy, suggesting an interaction of the jet with the gas clouds deposited during the last accretion event as the preferred triggering mechanism. The triggering of the star formation in the gas clouds in the halo of the galaxy by the jet supports the alignment effect observed in high redshift radio galaxies. It also suggests that radio galaxies should have higher than normal star formation rates.

The underlying stellar population of the halo of NGC 5128 is predominantly old with a broad metallicity distribution. The deep K-band luminosity function of Field 1 shows a clear break at the location of the red giant branch (RGB) tip. Its magnitude was used to determine a distance modulus of $\mathrm{(m-M)_0} = 27.97 \pm 0.10$. The RGB tip is less sharp in Field 2 due to a much wider spread in metallicity combined with larger number of blends. The peak metallicity of halo stars is at least $\mathrm{[M/H]} = -0.3$ dex, implying that it could not formed by late accretion of small satellite galaxies.

The presence of an extended giant branch reaching $\mathrm{M_{bol}} = -5$ suggests the existence of a significant intermediate-age population in the halo of this galaxy. The large majority of stars brighter than the RGB tip belong to the asymptotic giant branch (AGB) population in NGC 5128 with numerous long period Mira and semiregular variables. This is the first variable star catalogue in a giant elliptical galaxy. We also present the first Mira period-luminosity relation outside the Local Group. It is used to determine the distance of NGC 5128. We derive the distance modulus of 28.01 ± 0.07, adopting the LMC distance modulus of 18.50. The straight mean of RGB tip and LPV distances yields distance modulus to NGC 5128 of 27.99 ± 0.12 ($D = 3.96 \pm 0.22$ Mpc).

Resumen

Hemos investigado las poblaciones estelares de dos galaxias cercanas representativas de los dos extremos de la sequencia de Hubble: la galaxia enana irregular del Grupo Local WLM y la galaxia elíptica más cercana NGC 5128 (Centaurus A). El análisis de sus diagramas color-magnitud (CMD) y la comparación con las historias de formación estelar simuladas han sido usadas para obtener parametros básicos como la distancia, enrojecimiento, metalicidad y la edad de las estrellas.

Las imágenes profundas en bandas CL y LP, tomadas por el Telescopio Espacial Hubble con STIS, se usaron para identificar las estrellas de rama horizontal en WLM. Se hizo una calibración empírica de las bandas fotométricas no-estandards de STIS al sistema estandard VI de Johnson-Cousins. Utilizando la magnitud V de la rama horizontal, y adoptando un enrojecimiento de $\mathrm{E(V-I)} = 0.03$, medimos el módulo de distancia hasta WLM de $(m-M)_0 = 24.95 \pm 0.13$ ($D = 978 \pm 60$ kpc). La rama horizontal, la cual se extiende hacia el azul desde la posición de las estrellas del red clump, es un indicador seguro de la presencia de una población vieja, y implica que esta galaxia aislada se formó temprano. La detección de un halo viejo y pobre en los metales en una galaxia aislada irregular enana restringe los escenarios para la formación de las galaxias enanas, excluyendo los que predicen una formación más reciente de estas galaxias.

NGC 5128 presenta una compleja mezcla de las poblaciones estelares. Se usó VLT con FORS1 y ISAAC para obtener imágenes profundas en las bandas U, V y K de dos campos en el halo a ~ 14 kpc (Campo 1) y ~ 9 kpc (Campo 2) desde el centro de la galaxia. En esos campos se descubieron 71 cúmulos globulares por sus perfiles no-estelares. Se construyó una función de luminosidad para los cúmulos globulares (GCLF) y esa fue comparada con las GCLF de las galaxias espirales M31, y la Vía Láctea. Su similitud mutua sugiere que la GCLF es única y independiente del tipo de galaxia.

En los diagramas color-magnitud ópticos en bandas U y V del Campo 1, el cual conicide con la ubicación de la cáscara de estrellas difusa en el noroeste de la galaxia, se presenta una formación estelar reciente. La comparación de los diagramas observados y sintéticos sugiere que la formación estelar empezó por lo menos hace 100 Myr y que sigue activa o almenos habría terminado hace ~ 2 Myr. Su combustible proviene de la nube de hidrógeno neutro que se encuentra en la vecindad de campo y que ha sido depositado allí durante el último episodio de colisión. Este gas alimenta un bajo nivel de formación estelar en el halo (SFR~ 0.007 $\mathrm{M}_\odot$ yr^{-1}). La característica más notable acerca de esta formación de estrellas es, sin embargo, su alineamiento con la estructura de los jets observados en rayos-X y en radio.

Imágenes adicionales en bandas U y V del telescopio Magellan I de Observatorio de Las Campanas muestran que la formación estelar colimada se extiende por más de 10 kpc a lo largo de la dirección de los jets. Esta formación estelar tan fuertemente alineada con los jets se presenta solamente en la parte noroeste de la galaxia, sugiriendo que ha sido provocada por la interacción del jet con las nubes de gas depositadas en la última órbita de la galaxia satelite. La formación de las estrellas en las nubes de gas en el halo de la galaxia debido al jet sostiene el efecto de la alineación observado en galaxias con emissión radio a alto redshift. Esto sugiere también que radio galaxias deben tener una formación estelar más fuerte que las galaxias normales.

La majoría de las estrellas en el halo de NGC 5128 es predominantemente vieja y con una distribución ancha de metalicidad. La función de luminosidad profunda en banda K de Campo 1 muestra un cambio de pendiente muy fuerte en la ubicación de terminar de la rama de gigantes rojas (TRGB). Se usó su magnitud para determinar el módulo de distancia de $(\mathrm{m}-\mathrm{M})_0 = 27.97 \pm 0.10$. TRGB no es tan obvio en Campo 2 debido a una distribución más ancha en la metalicidad combinada con un número más grande de superposiciones. La metalicidad mas probable de las estrellas de halo es por lo menos de $[\mathrm{M/H}] = -0.3$ dex, implicando que no se pudo crear por el canibalismo de galaxias satélites pequeñas.

La presencia de una rama de gigantes extendida, alcanzando $\mathrm{M_{bol}} = -5$, sugiere la presencia de una población de edad intermedia significativa. La mayoría de las estrellas más brillantes que el TRGB pertenece a la población de

rama de gigantes asint'oticas (AGB) en NGC 5128, incluyendo numerosas variables con largo período (LPV) como variables semiregulares y Mira. Este es el primer catalogo de las estrellas variables en una galaxia eliptica. Variables Mira han sido usadas para determinar la distancia hacia NGC 5128 usando su relación período-luminosidad calibrada usando las paralajes de Hipparcos. Derivamos el módulo de distancia de 28.01 ± 0.07, adoptando el módulo de distancia la Gran Nube de Magallanes de 18.50. El promedio simple de las distancias obtenindas por la magnitud de RGBT y las LPV es 27.99 ± 0.12 ($D = 3.96 \pm 0.22$ Mpc).

Chapter 1

Introduction

The subject of this dissertation is the resolved stellar populations in two nearby galaxies at two extremes of the Hubble sequence: the dwarf Irregular (dIrr) galaxy, WLM, and the giant elliptical (gE) galaxy, NGC 5128. The aim is to study the properties of the stars in these two galaxies in order to establish the main parameters like distance, reddening, metallicity and formation epoch of these galaxies and to test galaxy formation and evolution scenarios. This introductory chapter starts with a short historical overview of stellar populations research. It is followed with a brief description of stellar evolution and the various evolutionary phases in color-magnitude diagrams. In the next section the importance of the two galaxies, WLM and NGC 5128, for stellar population studies is described and then the objectives of the thesis are stated. The known properties of WLM are summarized in section 1.6 and those of NGC 5128 in section 1.7. The organization of the thesis and a description of its chapters is presented at the end of this chapter.

1.1 Historical overview

The development and confirmation of the theory of stellar structure and evolution is one of the great achievements of the science in the last century. Stars are the building blocks of galaxies. In their interiors essentially all the elements found in the nature, except hydrogen and other primordial elements, are produced. Just as stars are the building blocks of galaxies, on much larger scale, galaxies are the building blocks of the universe. They come in a variety of types, ranging from elliptical, to spiral and irregular systems (Hubble 1926). While many stars belonging to our own galaxy, the Milky Way (MW), are visible to the naked eye during the night, due to their great distances galaxies are much fainter and more difficult to study. This is why the study of properties of individual stars was predominant in the last centuries. The study of extragalactic systems had to wait for the development of telescopes and photography.

The first ideas about their existence and the first observations of galaxies date from around the 18^{th} century. Kant (1724–1804) proposed the idea that we live in a galaxy, that was made of a large number of stars and that had a limited extent. He assumed that it is similar to other diffuse and faint nebulae, which he named *"island universes"*.

The early investigations of the structure and size of our own Galaxy were mainly based on the technique of star counting. The first maps and the models derived from them were very crude and often incorrect due to false assumptions about the stellar density, stellar absolute magnitudes and absorption by gas and dust. For example, William Herschel (1785) and Johannes C. Kapteyn (1851–1922; 1922) independently made maps of our galaxy where they placed the Sun near its center.

Extensive catalogues were made not only of stars in our Galaxy, but also of nebulae in order to investigate their nature. Among the most famous catalogues are the Messier catalogue (Charles Messier 1730–1817), which contains 110 objects visible from the northern hemisphere, and the catalogue of nebulae made by William Herschel, his sister Caroline and his son, Sir John Herschel covering the whole sky containing more than 5000 nebulae. Their catalogue was steadily updated with new discoveries over the course of the 19^{th} century until The New General Catalogue was published by J. L. E. Dreyer (1852–1926) with 7840 objects (Dreyer 1888). Two supplements to this list were published as the Index Catalogue (Dreyer 1895, 1908). Today many objects are still referred to by their NGC and IC numbers.

However, not everybody believed that the fuzzy nebulae were distant and independent systems. Harlow Shapley

(1885-1972) used variable stars to estimate distances to globular clusters. In a series of papers published between 1915 and 1920, he demonstrated that the Sun is not in the center of the Galaxy and that most of the stars lay in a plane around which an extended halo of globular clusters is found. His model of the Galaxy is much closer to the model accepted today, but the dimensions of Shapley's galaxy were too large and he could not accept the existence of even larger distances required for other galaxies. His viewpoint is well described in the introduction to his 12^{th} paper in the series (1919):

> The adoption of such an arrangement of sidereal objects leaves us with no evidence of a plurality of stellar "universes." Even the remotest of recorded globular clusters do not seem to be independent organizations. The hypothesis that spiral nebulae are separate galactic systems now meets with further difficulties. So long as the high velocities of nebulae were unapproached by the motions of other objects and the maximum luminosity attainable by stars was beyond estimate, and so long as the diameter of the galactic system was thought to be only a thousand light-years or so, we had a fairly plausible case for the "island universe" hypothesis. But now we must consider radial velocities of several hundred kilometers a second as quite possible for objects in our own system; we must assume a moderate upper limit of luminosity, perhaps even for the most massive of novae; and any external "universe" must now be compared with a galactic system probably more than three hundred thousand light-years in diameter. As seen from the center of the galactic system, globular clusters would be distributed in the sky much as the spirals are when observed from the earth.

The contrasting opinions about the "island universes" lead to a famous debate between Harlow Shapley and Heber D. Curtis (1872–1932) in 1920 at the National Academy of Sciences in Washington (Trimble 1995). Curtis defended a smaller model of the Galaxy, similar to Kapteyn's, and argued in favour of the existence of other "universes". The question of the existence of separate, external galaxies or "island universes" was resolved with a contribution of Edwin Hubble (1889–1953) at the winter 1924–1925 meeting of AAAS announcing the discovery of Cepheid variables in several nebulae with apparent brightnesses that placed these nebulae well beyond the limits of even the Shapley's Milky Way. According to Trimble (1995) this result did not immediately get much attention. However, with the publication of the Cepheid distance to a dwarf irregular galaxy NGC 6822 (Hubble 1925), the existence of the extragalactic systems similar to our galaxy and Magellanic Clouds started to be generally accepted.

Hubble was one of the most important investigators in the following research of extragalactic nebulae. In 1926 he published the classification scheme for extragalactic nebulae that is still in use. He divided the extragalactic nebulae into elliptical, spiral and irregular ones. Parallel to the sequence of spiral are barred spiral galaxies. He also defined subgroups for elliptical and spiral nebulae. It is actually due to this classification that we call elliptical galaxies early and spiral late type. However, it is often not known that in the original paper Hubble warned against the temporal connotations of adjectives "early" and "late" (Hubble 1926):

> It should be borne in mind, however, that the basis of the classification is descriptive and entirely independent of any theory.
>
> ...
>
> "Early" and "late", in spite of their temporal connotations, appear to be the most convenient adjectives available for describing relative position in sequence. ...... Terms which apply to series in general are available, however, and of these "early" and "late" are the most suitable. They can be assumed to express a progression from simple to complex forms.

In spite of these warnings the adjectives "early" and "late" type were used later to denote that elliptical galaxies were old and spirals younger and a significant effort was spent to explain the Hubble classification as an evolutionary scheme. The early studies of the stellar populations in galaxies contributed to this issue when it was established that early type or elliptical galaxies and bulges contain mainly old and disks of spirals or late type galaxies young blue stars.

1.2 Definition of Stellar Populations

In fall 1942 and 1943, Baade used the 100-inch Mt. Wilson telescope with red-sensitive photographic plates to resolve individual stars in the central regions of M31 and its two companions M32 and NGC 205. On the basis of these observations and comparing to the stellar populations in the solar neighbourhood, he introduced the idea of two stellar populations, Population I and Population II, distinguished by age, kinematics and chemical composition (Baade 1944). Characteristic of Population I group are young blue stars identified with the gas-rich disk of our Galaxy; they are traced by the open clusters and slow-moving stars in our solar neighbourhood. The stars belonging to Population II are identified with spheroidal systems, centers of spiral galaxies, globular clusters and high-velocity stars on more elongated and inclined orbits; these stars are old and their light is dominated by red giants. Baade (1944) notes that these same two types of stars were recognized in our own galaxy by Oort as early as 1926 through the study of their kinematic properties. He pointed out the difference between classical Cepheids belonging to Population I and so called short-period Cepheids found in Population II systems (RR Lyrae), which was important in the later determination of extragalactic distance scale.

Traditionally since Baade's work, only two main stellar populations were considered: Population I was young and metal-rich, like the stars in the solar neighbourhood and the Hyades open cluster, and Population II was older (age $> 10^{10}$ yr) and more metal-poor ([Fe/H] < -1 dex) by an order of magnitude like halo globular clusters. However, in the last several decades more data became available and with them galaxies containing mixture of Population I and Population II stars were found. For example it is nowadays generally accepted that the bulge of our own Galaxy and most ellipticals contain majority of stars that are old (characteristic of Population II stars; e.g. Renzini 1994) and metal-rich (characteristic of Population I; e.g. Minniti 1993, McWilliam & Rich 1994).

1.3 Hertzsprung-Russell and color-magnitude diagrams

The understanding of stellar structure and evolution is fundamental for our understanding of galaxy formation and evolution. The theory of stellar structure has been extensively covered by Iben (1967, 1974) and Chiosi, Bressan & Bertelli (1992) among others. Here a brief overview of stellar evolution and the main features in observational color-magnitude diagrams are given.

Ejnar Hertzsprung and Henry Norris Russell realized almost simultaneously that stars can be separated into two groups, dwarfs and giants, in a plot of spectral type against apparent magnitude. The first such plot, nowadays called the Hertzsprung-Russell (HR) diagram was published by Hertzsprung in 1911. Today HR diagram is mostly used as a diagram of temperature ($T_{\rm eff}$) against luminosity $\log(L/L_\odot)$ by theoreticians. Its observational counterpart, referred to as color-magnitude diagram (CMD) is usually a plot of color (difference of two magnitudes in different bands) against magnitude. The color of a star is a measurement of the slope of its spectral energy distribution and is thus directly related to the stellar effective temperature, and magnitude is a measure of the stellar luminosity.

Astronomy in the last century was mainly concerned with interpretation of the color-magnitude diagrams in the framework of the stellar evolution. Many observational studies contributed to the development of the theoretical models which can now successfully interpret almost all features in color-magnitude diagrams. While it is impossible to list here all the works that contributed to the development of the stellar evolution theory, most of the results can be found in studies by Castellani et al. (1969), Demarque & Gisler (1975), Iben (1982), Iben & Renzini (1983, 1984), Vandenberg & Bell (1985), Renzini & Fusi Pecci (1988), Bell (1992), Chiosi et al. (1992), Renzini et al. (1992), Chaboyer et al. (1995), Castellani et al. (1999), Cassisi et al. (1999), Maeder (2001) and Salaris et al. (2002) among many others.

The stars in the CMD lie along distinctive sequences. Most of the stars lie along the main sequence (MS), which crosses the CMD in diagonal from lower right where faint, cool and red M dwarfs lie, to luminous, hot and blue O stars in the upper left corner. Stars that lie on the MS burn hydrogen into helium in their cores. This is the longest phase in their lives, ranging from $\sim 10^6$ to $\sim 15 \times 10^9$ yr for highest to lowest mass stars. After the exhaustion of the hydrogen in the core, stars leave the MS, their luminosity increases and the rest of the evolution is much more rapid. The evolutionary timescales and evolutionary paths are very different for high and low mass

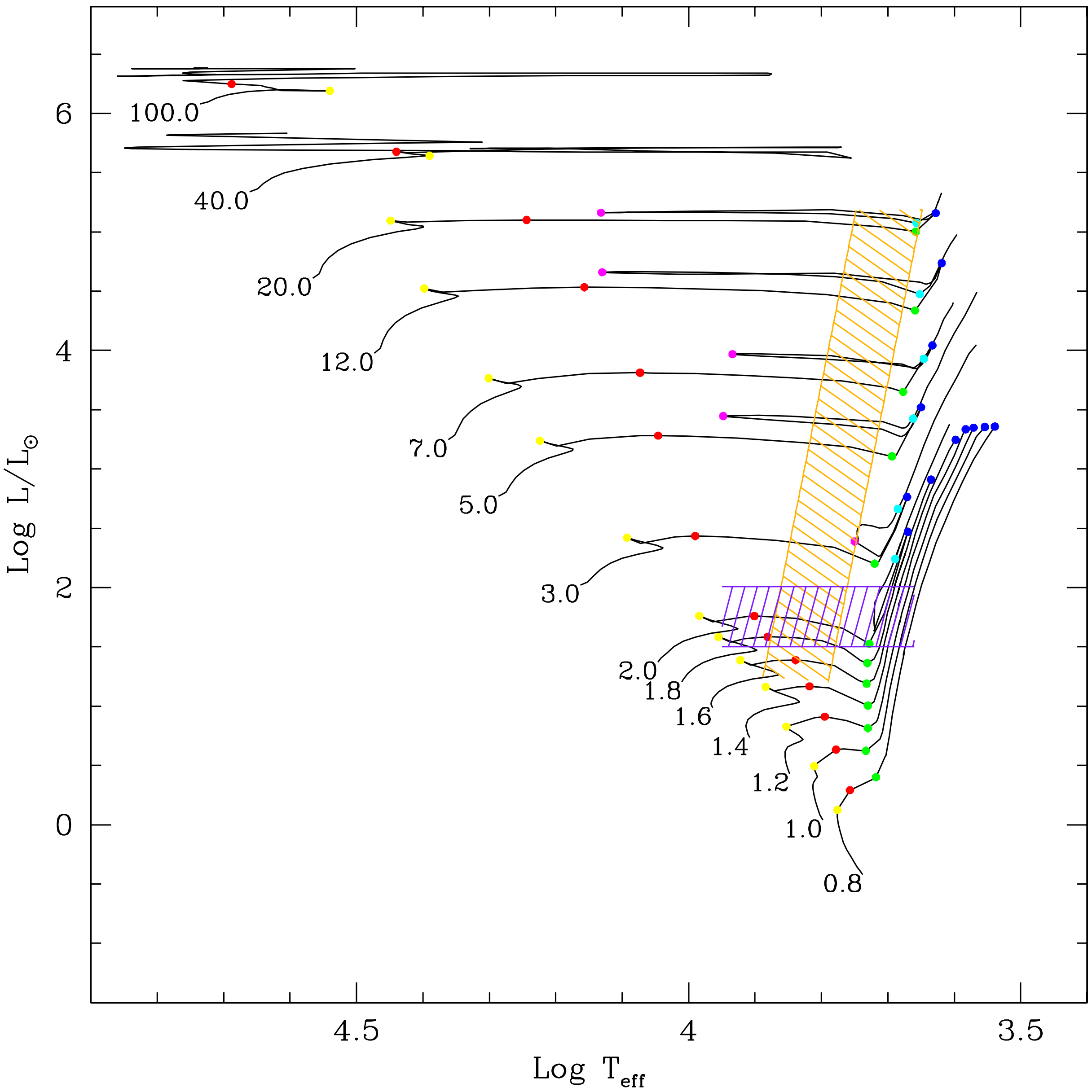

Figure 1.1: Padova group evolutionary tracks for Z=0.004 stars with masses in ranging from 0.8 to 100 M$_\odot$ (Fagotto et al. 1994). The points on each track indicate main evolutionary phases: end of core-H burning or turn-off point, slow H-shell burning on SGB, base of RGB, tip of RGB (He flash for low mass stars), core-He burning and AGB. For clarity evolutionary tracks of low mass stars (M<2 M$_\odot$) on the horizontal branch have been omitted; these tracks end at the tip of the RGB. The locations of the instability strip (hashed area vertically crossing the HRD) where the pulsating variable stars are found and the horizontal branch (horizontal hashed strip) are indicated.

stars. Figure 1.1 shows the evolution of stars of various masses in the HR diagram as they move off the main sequence.

After leaving the MS, high mass stars ($M \gtrsim 9M_{\odot}$) ignite He and expand, moving horizontally to the red part of the CMD. They cross the instability strip within which the stellar structure is unstable and causes pulsations. In this strip Cepheid variables are found among higher mass stars and RR Lyr variables among low mass stars. After the evolution from blue to red supergiants in so called blue loops, when the nuclear burning proceeds until their cores consist of iron-peak nuclei, the high mass stars end their lives as core-collapse SNe (type II) and leave a neutron star or a black hole as a remnant. The most massive stars ($M \gtrsim 20 - 40M_{\odot}$) probably become type Ib SNe. The lifetime of these stars range from several 10^6 to $\sim 10^7$ years.

Stars with masses in the range $M_{\rm up} \geq M/M_{\odot} \geq M_{\rm HeF}$, called intermediate mass stars, ignite He quiescently. $M_{\rm up}$ is the limiting mass for the formation of a C-O degenerate core and it is $\sim 5 - 9M_{\odot}$ depending on stellar models and metallicity. $M_{\rm HeF} = 1.85 - 2.2M_{\odot}$ is the limiting mass for the helium flash, explosive ignition of He in the core that defines the maximum luminosity reached on the red giant branch (RGB) for the stars of lower mass. Following helium exhaustion in the core there is the asymptotic giant branch (AGB) phase (see below). The lifetimes of intermediate mass stars range from several 10^7 to 10^9 years. These stars die as C-O white dwarfs (WDs) if they are not in binary systems, otherwise they can give rise to type I SNe.

For the low mass stars ($0.5 \leq M/M_{\odot} \leq M_{\rm HeF}$) the evolution on the RGB is joined to the MS by the subgiant branch (SGB), a short phase when the stars burn H into He in the shell rather than in their cores, but they still have not developed fully convective envelopes. Stars move almost vertically towards higher luminosities on the RGB burning H in the shell having fully convective envelopes. After the explosive ignition of He, the helium flash at the tip of the RGB, low mass stars burn He in their cores on the horizontal branch (HB). The color of the HB strongly depends on metallicity being almost attached to the RGB for solar metallicity and extending horizontally to the blue for lower metallicities, but its luminosity is fixed by the characteristic mass of He ($\sim 0.45M_{\odot}$) accumulated in the core, at which He flash occurs. Metal-poor populations intersect the instability strip on the HB giving rise to RR Lyrae variables.

After the exhaustion of the He in the core, the stars ascend the AGB that runs parallel on the blue side of RGB. The AGB phase is one of the least well known phases of stellar evolution. It is complex due to very rapid changes in the composition and stellar structure and heavy mass loss through stellar winds. While moving up the AGB, stars are subject to changes in chemical composition and a strong mass loss in the form of a stellar wind. The convection and mixing of the material in the envelope may bring the material processed in the shells to the stellar surface changing the M giant into a carbon star. At the end of their AGB life-time they enter a thermally pulsating phase and essentially all the stars that pass through that phase are long period variables.

Soon after reaching the top of the AGB the envelope is ejected in the last thermal pulse exposing the blue core of the star and causing an extremely rapid leftward displacement in the CMD. The hot core shines on the ejected material producing a planetary nebula (PN). The final locus of low mass stars is on the white-dwarf cooling sequence in the lower left corner of the CMD. The lifetimes of low mass stars is from several 10^9 years up to several Hubble times ($\sim 15 \times 10^9$ year).

1.4 Why study stellar populations in WLM and NGC 5128?

One of the main characteristics of galaxies along the Hubble sequence is the wide range of ages in their stellar content and star formation activity. This variation in stellar content is part of the basis of the Hubble classification itself (Hubble 1926), and understanding its physical nature and origins is fundamental to understand the formation and evolution of galaxies (Sandage 1986). The current knowledge of star formation histories of galaxies along the Hubble sequence is summarized by Kennicutt (1998).

Thanks to improvements in telescope sizes, detector sensitivity, field of view and of spatial resolution, compared with a decade ago, there has been a rapid progress in our understanding of galaxy formation and evolution. Now it is no longer necessary to rely on the integrated photometric or spectroscopic properties of nearby galaxies, but we can directly observe their constituent stars. The predictions of population synthesis based on the integrated light of star clusters (e.g. Bica 1988) and galaxies (e.g. Bruzual & Charlot 1993, Gonzalez & Gorgas 1995) can now be tested directly for nearby galaxies (nearby means $d < 10$ Mpc). The work of extragalactic population synthesis is now being applied to more distant systems, at intermediate and high redshifts (e.g. Pello et al. 1998, Vazdekis & Arimoto 1999), but it is anchored on the detailed knowledge that we acquire by resolving nearby galaxies into stars.

Stellar evolution theory provides predictions, based on relatively well understood physics (Iben & Renzini 1983, Renzini et al. 1992 Chiosi, Bertelli & Bressan 1992), of features expected in color-magnitude diagrams for different age and metallicity stellar populations (Renzini & Fusi Pecci 1988, Aparicio 1998, Gallart 1998). There are a number of indicators of varying star formation rates at different times which can be combined to obtain an accurate picture of the entire star formation history of a galaxy. Observations of the present stellar content and simulations of star formation histories of nearby galaxies allow us to take a leap to early times in order to predict what nearby galaxies looked like at intermediate and high redshifts (Aparicio 1998, Tolstoy 1999).

The galaxies we see today in and around our Local Group have been forming and evolving for a significant fraction of the age of the Universe. Since there are no evidences that our region of space might be in some way peculiar, the manner in which the Local Group and other nearby galaxies have formed and evolved must be fairly representative of these processes in general (Tolstoy 1999). A projection of the nearby galaxies to the Galactic plane is shown in figure 1.2.

In the Local Group all the objects except the two large spiral galaxies, the MW and M31, are dwarf galaxies. There are two major groups of dwarf galaxies: dwarf spheroidal (dSph) galaxies which have very low gas content (or no gas at all) and negligible present day star formation rates and dwarf irregular (dIrr) galaxies which, on the contrary, are usually associated with HI gas clouds and present varying degrees of recent star formation (Mateo 1998). In general, the low metallicity and large gas content in dIrr galaxies would suggest a late star formation in these systems (e.g. Searle & Sargent 1972, Broadhurst et al. 1988, Salzer et al. 1991, Babul & Rees 1992, Izotov & Thuan 1999). On the other side, in bottom-up cosmological scenarios they are the first self-gravitating systems to form and thus could be important contributors in the build-up of larger systems (e.g. Searle & Zinn 1978, Dekel & Silk 1986). It is important to establish the redshift of the first star formation activity in these galaxies because many galaxy evolution models predict rapid enrichment of the intergalactic medium as the low-mass halos (in which dwarf galaxies reside) collapse in the early universe (e.g. Cole et al. 2000, Efstathiou 2000).

Various scenarios have been proposed for the formation and evolution of elliptical galaxies. The two extremes are represented by the early monolithic collapse of a gas cloud or an early merging of lumps of gas where dissipation plays a fundamental role (e.g. Larson 1974, Arimoto & Yoshii 1987, Matteucci & Tornambè 1987), similar to the MW formation scenario proposed by Eggen, Lyden-Bell & Sandage (1962), as opposed to merging of earlier formed stellar systems accompanied with a possible star formation burst during the major merger (e.g. Toomre & Toomre 1972, Schweizer 1996, Kauffmann 1996).

The main goal of this thesis project is to test galaxy formation scenarios by studying the old stellar populations in nearby galaxies. The adopted approach consists in a detailed study of two characteristic objects representing major groups of Hubble sequence:

1. WLM, a Local Group dwarf irregular galaxy representing the most numerous group of galaxies in the Universe
2. NGC 5128, the nearest giant elliptical and a recent merger, representing the group of luminous galaxies that can be seen at large distances.

1.5 Objectives of the dissertation

The specific objectives of this work are to give the explanation and interpretation of the following questions:

- What are the metallicities and ages of the oldest stars in WLM dwarf irregular galaxy?
- What are the metallicities and ages of the stars in the halo and in the shells of a giant elliptical NGC 5128?
- What are the properties of globular clusters in the halo of NGC 5128?
- What were the ages and metal abundances of the stellar populations of the cannibalized satellite of NGC 5128?

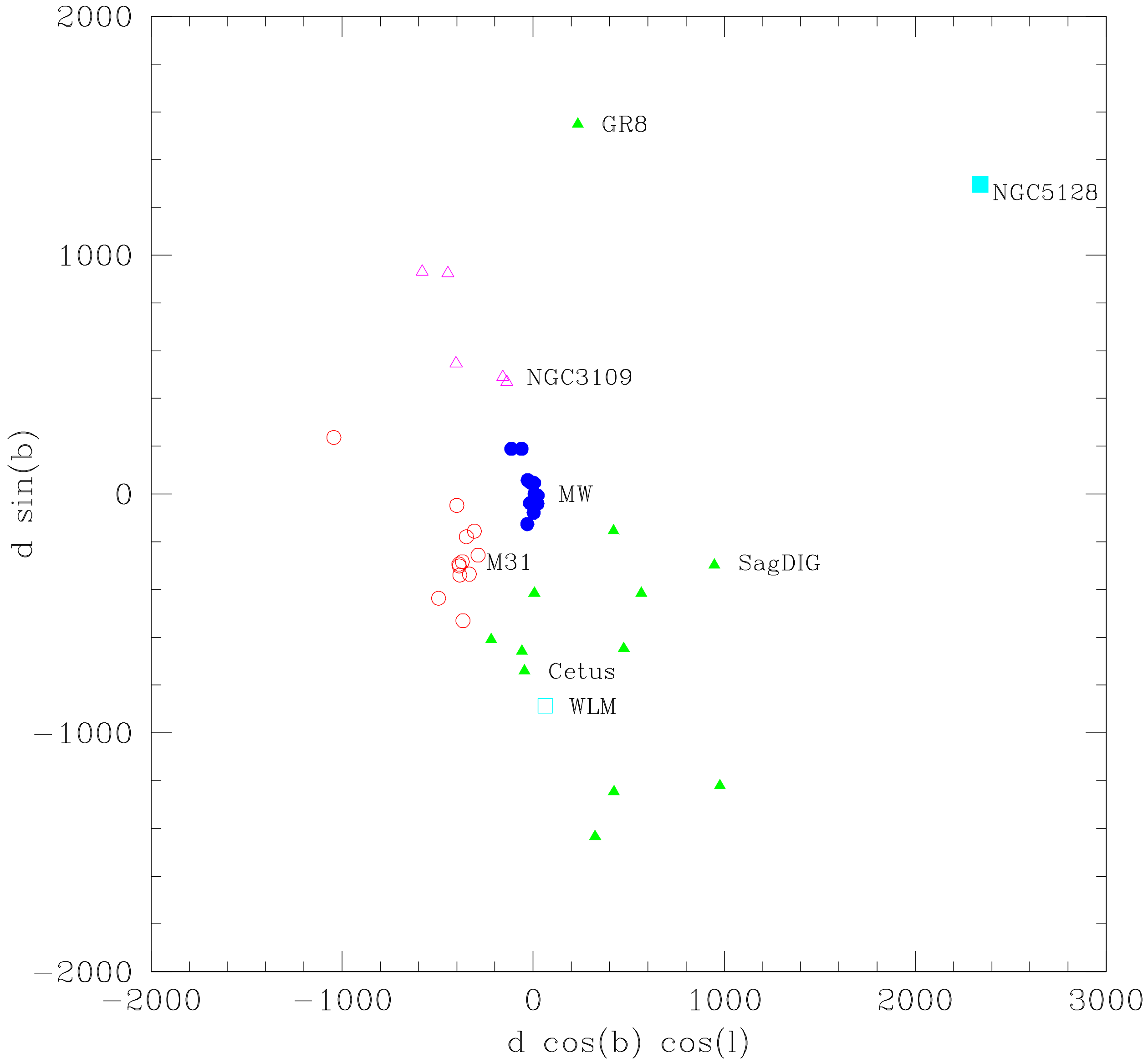

Figure 1.2: Local Group galaxies and NGC 5128 projected to the plane perpendicular to the galactic plane. Distance information has been taken from Mateo (1998), Whiting et al. (1999) and Israel (1998). Members of various subgroups are coded: Milky Way subgroup: filled dots; M31 subgroup: open circles; isolated dwarf galaxies (members of the Local Group): filled triangles; small subgroup of dwarf galaxies around NGC3109 (open triangles) is sparse in this projection. The location of WLM (open square) and its nearest neighbour Cetus dwarf galaxy are labeled. Clearly NGC5128 (filled square) is outside but near the Local Group. It is the main galaxy of the Centaurus Group.

This two galaxies will be the groundwork that will allow us to study other selected galaxies in the future.

1.6 WLM - an isolated dwarf irregular galaxy

The best studied galaxies are the local ones, those contained within the Local Group. While the total light and the total mass are dominated by the two large spirals, M31 and the Milky Way, dwarf galaxies are by far the most numerous members of the Local Group (Mateo 1998). Their large number is not specific only to the Local Group; the high specific frequency of low luminosity systems in groups and clusters is in fact very common (e.g. Sandage & Binggeli 1984, Ferguson 1989) and they are considered to be the most numerous type of galaxies in the Universe as a whole (Mateo 1998). They play an important role in the formation of galaxies, as they can build-up more massive galaxies through mergers and accretion. The hierarchical scenarios of galaxy formation, such as a Universe dominated by cold dark matter, predict that dwarf galaxies are likely to be the first structures to form, arising from 1σ fluctuations in the density distribution of the primeval Universe and that they would merge afterwards to form larger galaxies (e.g. White & Rees 1978, Dekel & Silk 1986, Kauffmann, Guideroni & White 1994, Kauffmann & Charlot 1998). The surviving dwarf galaxies provide a fossil record of the early formation and evolutionary conditions of their parent clusters.

The Im IV-V galaxy WLM (DDO 221) is an isolated dwarf irregular located at the edge of the Local Group (van den Bergh 1994) some ~0.9 Mpc away from us (Minniti & Zijlstra 1997). It has been discovered by Wolf (1909) and then again by Lundmark and Melotte (1926), hence getting its name Wolf-Lundmark-Melotte, subsequently abbreviated into WLM. The early studies of this galaxy are described by Sandage & Carlson (1985) who presented a color-magnitude diagram for the brightest stars in the galaxy and identified 15 short period ($P < 10$ days) Cepheids. The Cepheids were used to derive the distance modulus of $(m-M)_{AB} = 24.93$ by Sandage & Carlson (1985) and were later reanalyzed by Feast & Walker (1987) and by Lee et al. (1993). Feast & Walker give distance modulus value of $(m-M)_{pg} = 24.7$ using only Cepheids, while Lee et al. derive $(m-M)_0 = 24.92$ using Cepheids and $(m-M)_0 = 24.81$ from the I-band magnitude of the tip of the RGB. The latter method was also used by Minniti & Zijlstra (1997) who obtained the distance modulus of $(m-M)_0 = 24.75$.

Ferraro et al. (1989) presented the first CCD photometry of WLM. In their work for the first time the comparison of the observed and synthetic CMDs was used to derive the star formation history of a dwarf irregular galaxy. They noted that the recent star formation in WLM was localized, showing large differences between different regions, while an underlying population of at least 10^9 yr was present throughout the galaxy. Minniti & Zijlstra (1996, 1997) concluded that the star formation in this galaxy started at least 10 Gyr ago and established the presence of an extended, slightly flattened halo consisting of Population II, metal poor ([Fe/H]=–1.45 dex) and old stars. They showed that the color gradient found earlier by Ables & Ables (1977) was due to a stellar population gradient.

Only one globular cluster in WLM was discovered by Humason et al. (1956). Further searches for other globular clusters in this galaxy yielded negative results (Ables & Ables 1977, Minniti & Zijlstra 1997), which is interesting given the high brightness of its only globular cluster. The absolute magnitude of the globular cluster is $M_V = -8.8$, brighter than the mean absolute magnitude of globular clusters in our Galaxy ($M_V = -7.1$; Harris 1996). No other Local Group dwarf irregular galaxy fainter than $M_V = -16$ has a globular cluster. Hodge et al. (1999) resolved the globular cluster using Wide Field Planetary Camera 2 (WFPC2) at Hubble Space Telescope (HST) and presented its CMD. From it they obtain the best fitting metallicity of [Fe/H] = -1.52 dex and an age of 14.8 ± 0.6 Gyr, similar to normal old halo globulars in our Galaxy.

Most recently Dolphin (2000) constructed deep CMDs using the WFPC2 at HST and derived the star formation history of WLM. He concluded that about half of the stars were formed in this galaxy in an early burst that started ~ 13 Gyr ago, during which the metallicity increased from [Fe/H] ~ -2.2 to -1.3 dex. A summary of the parameters for WLM collected from the literature is given in table 1.1 and a 20 square arcmin image is shown in figure 1.3.

It is of particular interest to study the old stellar populations of WLM and hence establish its formation epoch and put it in the context of dwarf galaxy formation scenarios, because most probably it has remained isolated during its evolution (Peebles 1995). Its nearest companion is the recently discovered Local Group member, dwarf irregular galaxy Cetus (Whiting, Irwing & Hau 1999), at the distance of ~ 100 kpc (see also Figure 1.2). Thus

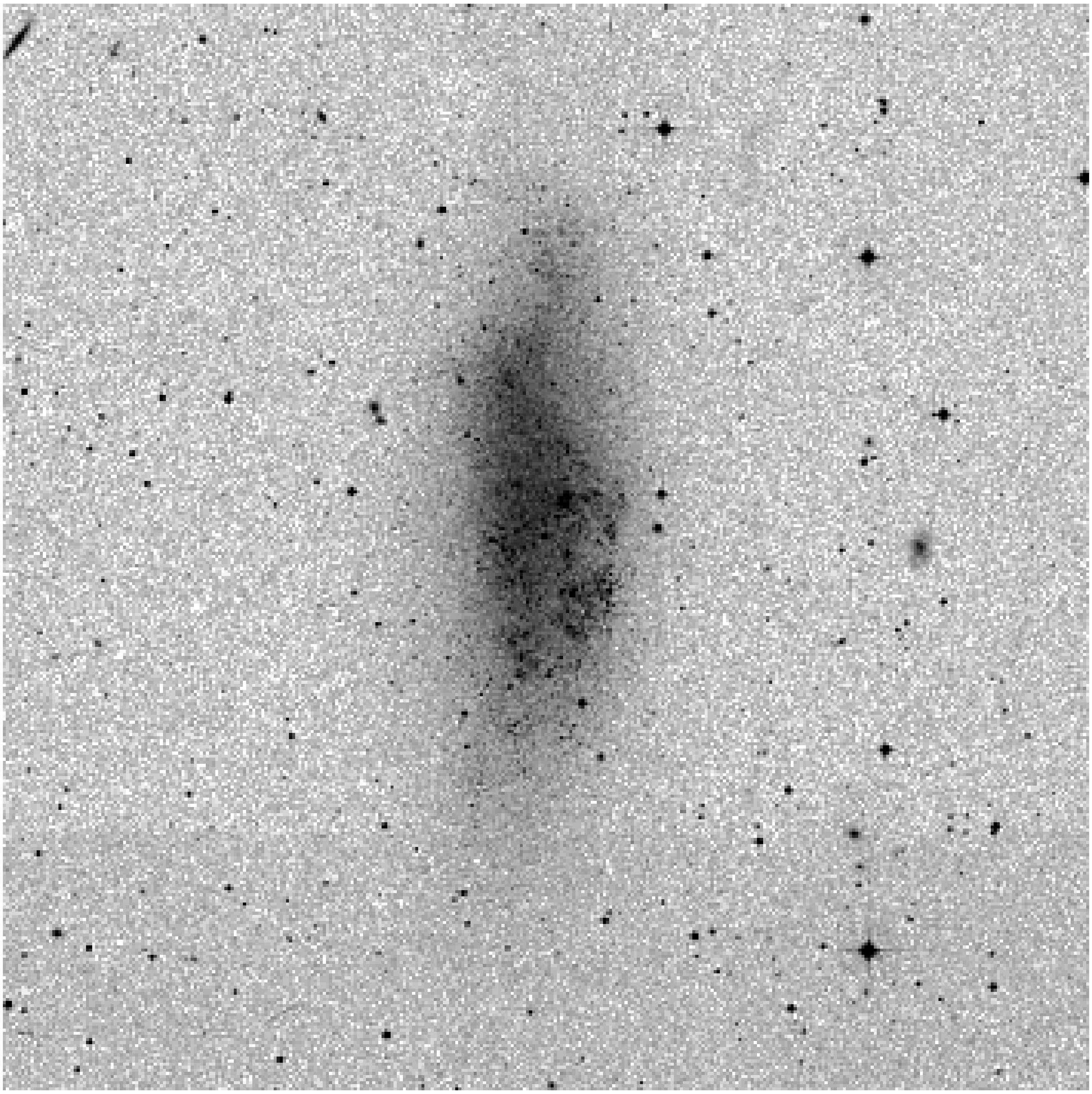

Figure 1.3: WLM dwarf irregular galaxy image from the Digitized Sky Survey. The field of view is $20' \times 20'$. North is up and east to the left. This galaxy can be seen with a moderate size telescope during the winter season in the Southern Hemisphere.

Table 1.1: Summary of parameters for WLM and NGC 5128 (for references see Minniti & Zijlstra 1997, Mateo 1998, Israel 1998 and Harris et al. 1999).

Parameter	WLM Value	NGC 5128 Value
α_{2000}	00 01 58.0	13 25 26.4
δ_{2000}	-15 27 50	-43 01 06
l	75.85	309.51
b	-73.63	+19.42
Distance modulus	24.75 ± 0.10	27.8 ± 0.15
Distance	0.9 Mpc	3.6 Mpc
Type	Irr IV-V	gE
M_{HI}	$60 \times 10^6\,\mathrm{M}_\odot$	$8.3 \times 10^8\,\mathrm{M}_\odot$
M_{Total}	$150 \times 10^6\,\mathrm{M}_\odot$	$4 \times 10^{11}\,\mathrm{M}_\odot$
V_r	$-127\,\mathrm{km/s}$	$543\,\mathrm{km/s}$
V_T	10.42	6.98
$(B-V)_T$	0.62	0.98
$E(B-V)$	0.02	0.11
N_{globs}	1	> 1500
$[Fe/H]_{globs}$	-1.52 ± 0.08	$-0.6 \leq [Fe/H] \leq +0.1$
$\langle [Fe/H]_{halo} \rangle$	-1.45	-0.41

WLM is an ideal representative of dwarf irregular galaxies. The hypothesis like the presence of old and young stellar populations, the presence of dark matter dominated halos and the questions about the chemical enrichment and star formation history can be explored by studying its stellar content with photometric and spectroscopic techniques.

1.7 NGC 5128 - survivor of a recent merger

What is missing entirely from the Local Group is the important giant elliptical galaxy class. The closest one is NGC 5128 (Centaurus A), the dominant galaxy in the Centaurus group at a distance of $\sim$ 3.6 Mpc (Tonry & Schechter 1990, Hui et al. 1995, Soria et al. 1996, Harris et al. 1999). It is also the closest high-luminosity AGN, closest and one of the largest radio galaxies. Comprehensive reviews on this galaxy have been written by Ebneter & Balick (1983) and Israel (1998).

NGC 5128 was discovered by James Dunlop on August 4, 1826 (Dunlop 482, Dunlop 1828). Later it was very little studied until the second part of the 20^{th} century. In 1949 the nebula NGC 5128 was identified with the prominent radio source Centaurus A by Bolton et al. Commenting on its unusual optical appearance, Baade & Minkowski (1954) suggested that the nebula actually represented a merger of an elliptical and spiral galaxy:

> The curvature of the outer parts of the spiral system and the irregular distribution of absorbing clouds outside the main absorption bands clearly indicate tidal distortion of the E nebula. The two nebulae thus are not merely optically superimposed but form a close pair in a state of strong gravitational interaction, perhaps actually in collision.

However, the merger scenario was ignored for a number of years until numerous other indications were found.

Being crossed by a prominent dust band, the center of the galaxy is invisible in the optical wavelengths. The dust lane has been identified with a highly inclined disk (Dufour et al. 1979) with which young stars and HII regions are associated (Graham 1979, Unger et al. 2000, Wild & Eckart 2000). In mid-infrared and submilimeter wavelengths the dust emission in the center is remarkably similar to a small barred spiral galaxy (Mirabel et al. 1999). Mirabel

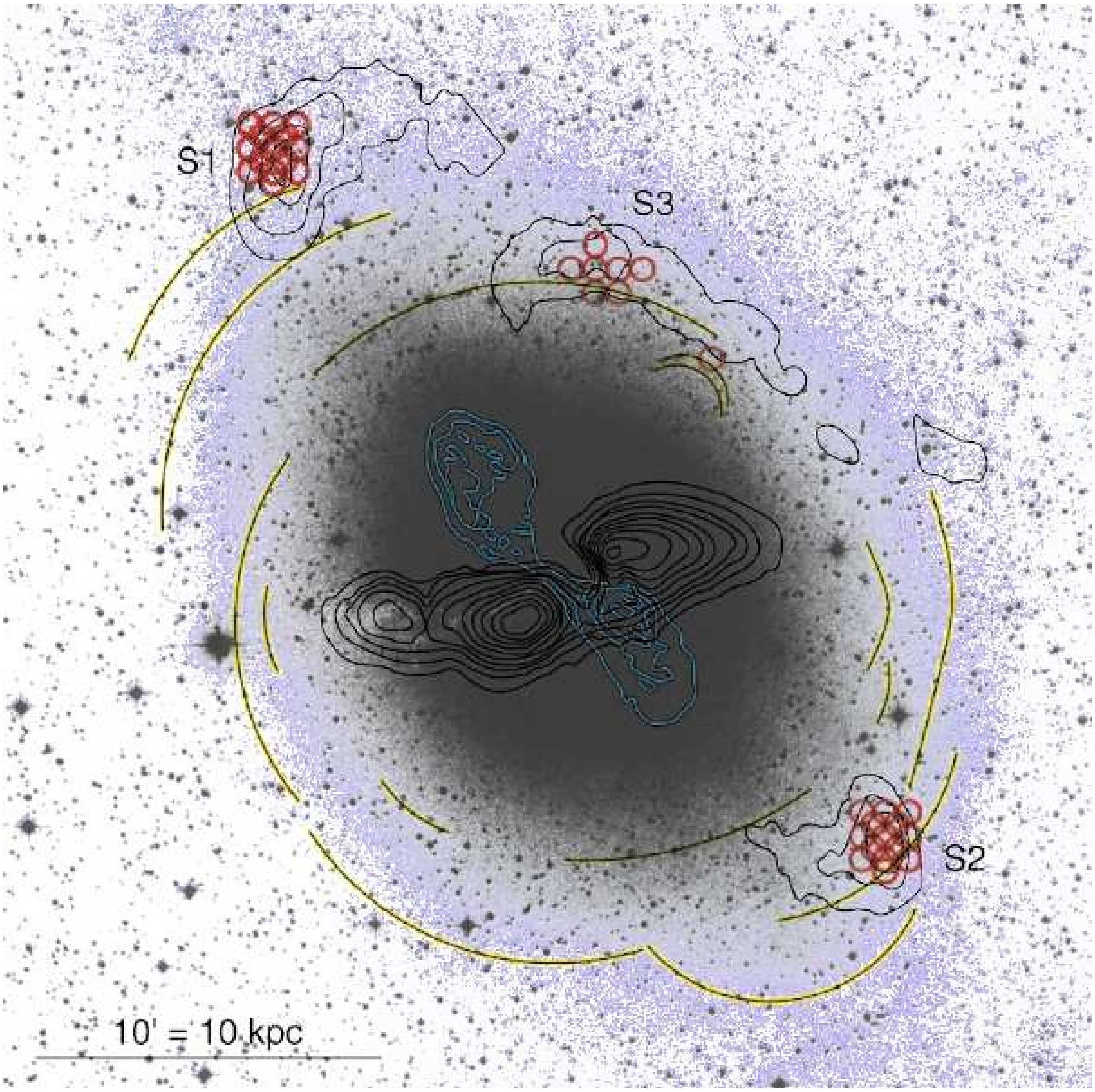

Figure 1.4: This image of NGC 5128 has been taken from Charmandaris et al. (2000). North is up and east to the left. A wide dust lane crosses the center. Grey contours extending from the center in the north-east and in south-west direction are the inner 6cm radio continuum lobes (Clarke et al. 1992). The locations of the stellar shells are indicated with solid lines (Malin et al. 1983). Black contours associated with the shells and in the center of the galaxy indicate HI gas detected by Schiminovich et al. (1994). The molecular CO gas has been detected close at S1 and S2 positions (circles) by Charmandaris et al. (2000). This galaxy can be seen with a small telescope during between January and July in the Southern Hemisphere.

et al. suggested that the bar structure in the center might help funneling the gas toward the central active galactic nucleus (AGN) which powers the radio and X-ray jets (Cooper et al. 1965, Feigelson et al. 1981, Kraft et al. 2000, Schreier et al. 1981, Clarke et al. 1992). Most recently dynamical studies of the ionized and molecular gas in the center have revealed the presence of a supermassive black hole with $M_{BH} = 2 \times 10^8 M_\odot$ (Marconi et al. 2001).

The signs of merger are not only confined to the central parts of the galaxy. In 1983 Malin et al. discovered a system of interleaving shells surrounding the galaxy using the photographic plates. Dynamical models suggest that the stellar shells are formed by phase wrapping or spatial-wrapping of the tidal debris from an accreted smaller galaxy (Quinn 1984, Hernquist & Quinn 1989) or in a merger between comparable-mass galaxies (Hernquist & Spergel 1992). A different origin was proposed by Thomson & Wright (1990), that the shell material originates from the *primary* galaxy representing density waves formed in a close encounter, but not a merger. Associated with shells in NGC 5128, but slightly off-set from them some $4 \times 10^8 M_\odot$ of HI gas were detected by Schiminovich et al. (1994). More recently Charmandaris et al. (2000) have found molecular CO gas close to the north-east and south-west diffuse shells (see Fig. 1.4). In the north-east region optical filaments (Blanco et al. 1975, Dufour & van den Bergh 1978) and young blue supergiants (Graham 1998, Fasset & Graham 2000, Mould et al. 2000, Rejkuba et al. 2001b - Chapter 4) are present.

Furthermore, the studies of the globular cluster system of NGC 5128 have revealed a number of intermediate-age clusters in the central 3 kpc of the galaxy (Minniti et al. 1996) and a bimodal metallicity distribution of globular clusters (Zepf & Ashman 1993, Rejkuba 2001 - see Chapter 3). Hui et al. (1995) has shown that the metal-poor population of clusters rotate with velocity significantly larger than the metal-rich population in agreement with the Ashman & Zepf (1992) model of a spiral-spiral merger.

Because mergers and accretions of the type now going on in NGC 5128 are recognised as normal episodes in the histories of large galaxies in hierarchical galaxy formation scenarios, it is not unreasonable to expect that we can learn a great deal about elliptical galaxy evolution by studying the stellar populations of NGC 5128. Fortunately, it is now possible to resolve NGC 5128 into stars thanks to HST and VLT.

HST with WFPC2 was used to resolve the halo of Centaurus A into stars for the first time in 1996 (Soria et al. 1996). Soria et al. measured the I magnitude of the tip of the RGB and used it to determine the distance to the galaxy ($D = 3.6 \pm 0.2$ Mpc), but their CMD was not deep enough to investigate fully the metallicity distribution of the stars. Subsequently Harris et al. (1999) and Harris & Harris (2000) obtained deeper VI CMDs of two different halo fields in order to study the metallicity distribution of the old stellar population, while Mould et al. (2000) imaged the young stars associated with outer optical filaments in the north-eastern part of the halo.

NICMOS on HST was used to resolve the stars in the near-IR (Marleau et al. 2000) in the same field as the optical study of Soria et al. (1996; ~9kpc south of the center of the galaxy). In these two studies, a small intermediate-age population of $\sim$ 5Gyr has been found, comprising up to $\sim$ 10% of the total stellar population in the halo. On the other hand, there are almost no intermediate-age stars in the field further out in the halo, at $\sim$ 20 kpc from the galaxy center (Harris et al. 1999) nor at $\sim$ 31 kpc (Harris & Harris 2000). The comparison of the two results may indicate the presence of a gradient in the stellar population in the halo, as suggested by Marleau et al. (2000). However, the use of V and I-bands (by Soria et al. and Harris et al.) in which intermediate-age AGB giants get only up to 0.5 mag brighter than the older first ascent giants (RGB) and even more the small field of view of HST limits such conclusions. Hence the presence of the intermediate-age population in this giant elliptical galaxy remains an open question, which is addressed in chapters 4, 6 and 7.

Another open question is the source of the ionization for the line-emitting gas observed in the north-eastern halo. Beamed photoionization from the active nucleus is the interpretation proposed by Morganti et al. (1991, 1992), while the shock induced ionization is prefered by Sutherland et al. (1993). Recently young blue supergiants have been detected in the area where the outer filaments are located (Graham 1998, Fassett & Graham 2000, Mould et al. 2000). In chapter 5 we investigate the stellar populations associated with the outer and inner filaments and their role in the ionization of the surrounding gas.

The vicinity of NGC 5128 provides a unique testing ground for stellar population models and for theories of giant galaxy formation. It is also the only giant elliptical galaxy in which a direct comparison between the age and metallicity distributions of stars and globular clusters can be made.

1.8 Outline of the thesis

In chapter 2 we describe the photometry of WLM obtained with the European Southern Observatory (ESO) New Technology Telescope (NTT) in La Silla Observatory using EMMI imaging spectrograph and with Space Telescope Imaging Spectrograph (STIS) at HST. We derive an empirical calibration of the STIS photometric system to the standard ground based VI filters. The analysis of the color-magnitude diagrams and the basic parameters for the dwarf irregular galaxy WLM are presented.

Chapter 3 presents optical and near-IR photometry of globular clusters in the halo of NGC 5128. The deep globular cluster luminosity function (GCLF) is constructed and compared with the GCLFs of the Milky Way and M31. Color and metallicity distributions of the globular cluster system of NGC 5128 are also investigated.

The optical and near-IR photometry of the two fields observed with the ESO Very Large Telescope (VLT) in the halo of NGC 5128 are presented in chapter 4. The optical UV and optical-near-IR VK CMDs are constructed and used to investigate stellar populations in the two fields. The north-eastern, shell field, at the distance of ~ 14 kpc from the nucleus, has a conspicuous young population of stars, while the second, halo field, which overlaps with the HST field studied by Soria et al. (1996) and Marleau et al. (2000), has dominant old stellar populations. The presence of an intermediate-age population and population gradients are then investigated. The stars in the diffuse shell are resolved and compared to the rest of the halo.

In chapter 5 the association of the young stars, optical filaments, radio and x-ray features is investigated in more details. Additional observations along the direction of the radio jet were acquired at Magellan I telescope in the Las Campanas Observatory. A simple scenario that explains the observed properties of stars and ionized gas is given.

Chapter 6 presents the first detection of long period variables in the halo of a giant elliptical NGC 5128. We constructed the lightcurves and measured statistical properties of long period variables (LPVs) in two fields observed with VLT. Distance to NGC 5128 is determined via the RGB tip detection and Mira PL relation.

In chapter 7 we construct synthetic CMDs and luminosity functions and compare them with the observed ones for NGC 5128 in order to derive a star formation history for the galaxy.

Finally, in the last chapter the main results from previous chapters are summarized in a common picture and possible future work is discussed.

Chapter 2

Deep HST+STIS color-magnitude diagrams of the dwarf irregular galaxy WLM: detection of the horizontal branch[1,2]

Abstract

We have obtained V and I-band photometry for 1886 stars down to I = 27 and V = 28 in the field of the dwarf irregular galaxy WLM, using deep STIS *CL* and *LP*-band images taken in the parallel mode with the Hubble Space Telescope. The photometry is used to study the horizontal branch identified in WLM. The horizontal branch, extending blueward from the red giant clump, is an unambiguous signature of an old population. We demonstrate that it is possible to reach the horizontal branch of an old population at a distance of $\simeq 1$ Mpc using STIS, with relatively short exposure times. From the VI color–magnitude diagram we obtain an accurate distance modulus $(\mathrm{m}-\mathrm{M})_0 = 24.95 \pm 0.13$ for WLM by using the V-magnitude of the horizontal branch, and by adopting $\mathrm{E(V-I)} = 0.03$. The implications are: 1) WLM formed stars at high redshift, and 2) the old population of WLM can be representative of a protogalactic fragment, related to those accreted to form the Milky Way halo.

2.1 Introduction

In 1997 February, the second Space Shuttle servicing mission to the Hubble Space Telescope (HST) installed the Space Telescope Imaging Spectrograph (STIS). This spectrograph can be used in direct imaging mode providing very deep high-resolution images. The two optical wideband choices on STIS are a clear aperture (*CL*) and a longpass ($\lambda > 5500$ Å) filter (*LP*). Based on these two wide bands, Gregg & Minniti (1997) defined an effective shortpass filter (SP), thus establishing a two color photometric system. They suggested that these unusually wide bandpasses of STIS offer the possibility to reach much fainter limiting magnitudes with respect to the other HST imaging instruments like the Wide Field Planetary Camera 2 (WFPC2). STIS reaches ~ 1.5 mag fainter than WFPC2 for a given integration time. This advantage of STIS over WFPC2 is due to three factors: (i) much broader passbands; (ii) the higher quantum efficiency and (iii) the lower readout noise of STIS's CCD.

By using spectrophotometric stellar libraries, Gregg & Minniti (1997) argued that it is possible to convert the STIS magnitudes and $(SP - LP)$ color to the standard photometric systems. They derived preliminary transformations to the VI Kron–Cousins wideband system. These transformations were based upon preflight specifications of the instrument and had to be empirically calibrated. Such an empirical calibration is possible for the data collected during the STIS Parallel Survey (see, e.g., Gardner et al. 1998).

The STIS Parallel Survey data contain observations of the dwarf irregular galaxy DDO221 (= WLM) located at the edge of the Local Group (Sandage & Carlson 1985, van den Bergh 1994). In a photometric study of this galaxy,

[1]Based on observations obtained with the NASA-ESA Hubble Space Telescope, and with the ESO NTT telescope at La Silla Observatory.

[2]Based on Rejkuba, M., Minniti, D., Gregg, M.D., Zijlstra, A.A., Alonso M.V. & Goudfrooij, P., 2000, AJ 120, 810

Minniti & Zijlstra (1996, 1997) presented VI photometry obtained with the NTT at La Silla Observatory. There is an overlap between the STIS field of WLM and the NTT field, enabling us to establish the empirical calibrations of the STIS photometric system. Based on this calibration, we construct a VI color–magnitude diagram (CMD) that is much deeper than those of any other Local Group galaxy studied so far with a comparable amount of exposure time (see Section 2.2), reaching V $\sim$ 28 and I $\sim$ 27. The analysis of the CMD provides us with the fundamental properties of WLM's stellar populations, such as, metallicities, reddening, age and distance (Lee 1993, Minniti and Zijlstra 1996, Dolphin 2000). These properties are essential for establishing the formation history and evolution of WLM, a typical dwarf irregular galaxy that is representative of the most numerous group of galaxies in the Universe (Dekel & Silk 1986). The importance of WLM is stressed by the fact that it is located far from any other large spiral member of the Local Group, and therefore most probably has remained isolated over the Hubble time (Peebles 1995). The nearest galaxy to WLM is the recently discovered Cetus dSph, at a distance of $\sim$ 175 kpc (Whiting et al. 1999). Having remained isolated, WLM carries the unperturbed imprint of its formation and evolution in its stellar content.

The observations, data reductions, and photometry of WLM, and the resulting color–magnitude diagrams are given in Section 2. An empirical calibration of the STIS photometric system is given in section 2.3. Fundamental parameters of WLM (metallicity, age and distance) are redetermined in Section 3. The conclusions and implications of this work are summarized in Section 4.

2.2 The data

2.2.1 Ground-based photometry

The ground-based observations of WLM were obtained during the night of 1995 September 5 as part of a long term program monitoring the variable stars in several galaxies (Zijlstra, Minniti & Brewer 1997). We used the red arm (RILD mode) of the ESO Multi-Mode Instrument (EMMI) on the New Technology Telescope (NTT) at La Silla Observatory, operated remotely from the ESO headquarters in Garching, Germany. We used the 2048×2048 Tek CCD with a scale of $0''.268$ pix^{-1}. The weather was photometric, with seeing varying from $0''.5$ to $1''.0$.

The observations of WLM were secured with the V and Cousins I filters. They consist of pairs of frames with exposure times of 900 sec in I (airmass 1.1), and 1800 sec in V (airmass 1.1). These frames, covering an area of $9' \times 9'$, are centered on the galaxy. Figure 2.1 shows a portion, covering only $1' \times 1'$, of the NTT+EMMI images.

The reductions of the CCD frames were carried out by following standard procedures, using the package CCDRED within the IRAF environment. The pairs of images observed through each filter were combined. The final FWHM of stellar images were 0.8 and 0.7 arcsec in V and I respectively.

A total of 5 standards were observed during the night in order to calibrate our photometry. The photometric transformations to the standard system were done following the procedure described by Minniti & Zijlstra (1997). These transformations reproduce, with an rms of 0.016 in V and 0.031 in I, the magnitudes of the standard stars.

The photometric measurements were performed within the IRAF environment using DAOPHOT II, an improved version of the original DAOPHOT package developed by Stetson (1987). In particular, DAOPHOT II can accommodate a spatially varying point-spread function across the field. All stars in the field of WLM that were more than 4σ above the background in the V and I frames were located, and their magnitudes measured by fitting a Moffat point-spread function. The resulting NTT limiting magnitudes (4σ) were V = 24, and I = 23.5.

2.2.2 STIS photometry

The STIS images were acquired through the HST parallel program 7912 in September 1998. The center of the observed field was $\alpha_{2000} = 00^{\rm h}02^{\rm m}03.19^{\rm s}$, $\delta_{2000} = -15^\circ 23' 57''.5$, at the N-E edge of WLM's disk. The LP-band image covers $28'' \times 50''$, and the CL-band image covers $50'' \times 50''$, but only the overlap region has been used. Four images with a total exposure time of 1680 seconds were combined to obtain the final CL-band image, and four images with a total exposure time of 2665 seconds were combined to obtain the final LP-band image. Cosmic rays were identified and eliminated in this process.

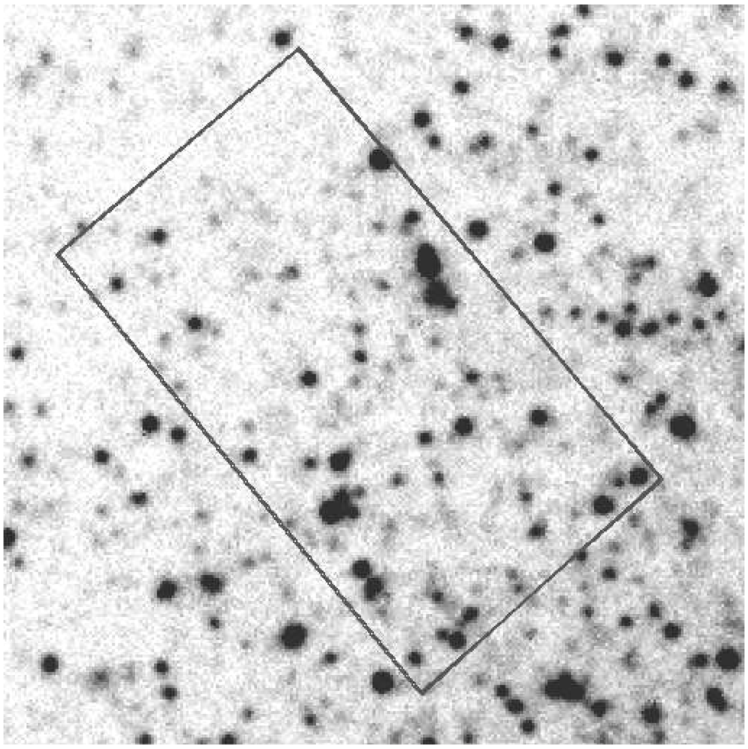

Figure 2.1: NTT V-band image of WLM, covering 1×1 arcmin^2. North is up and East is to the left. At the distance of WLM, $1' = 0.26$ kpc. The point sources in this image have FWHM = $0\farcs8$. The box indicates the location of the $50'' \times 28''$ STIS field.

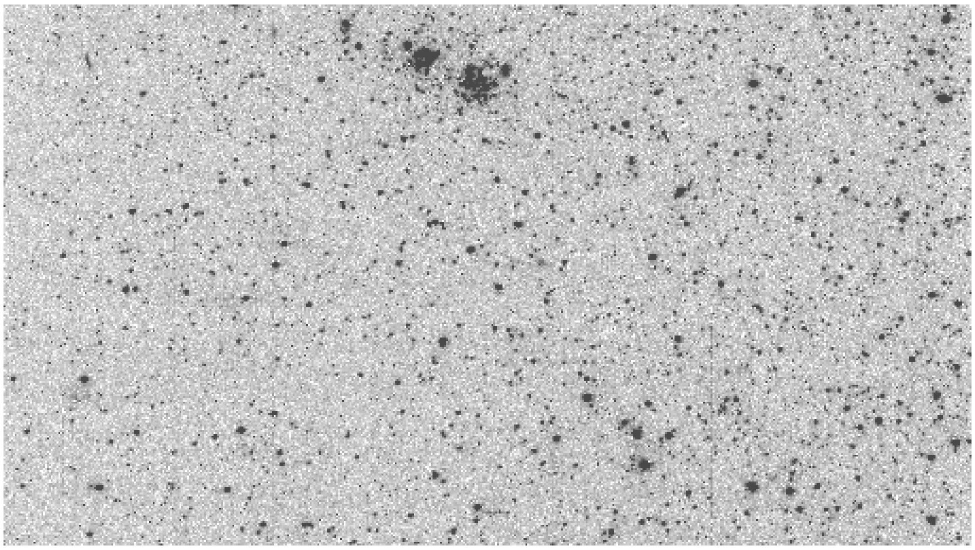

Figure 2.2: STIS image of the WLM field with the *LP* filter, covering $50'' \times 28''$. The point sources in this image have FWHM = $0\farcs1$.

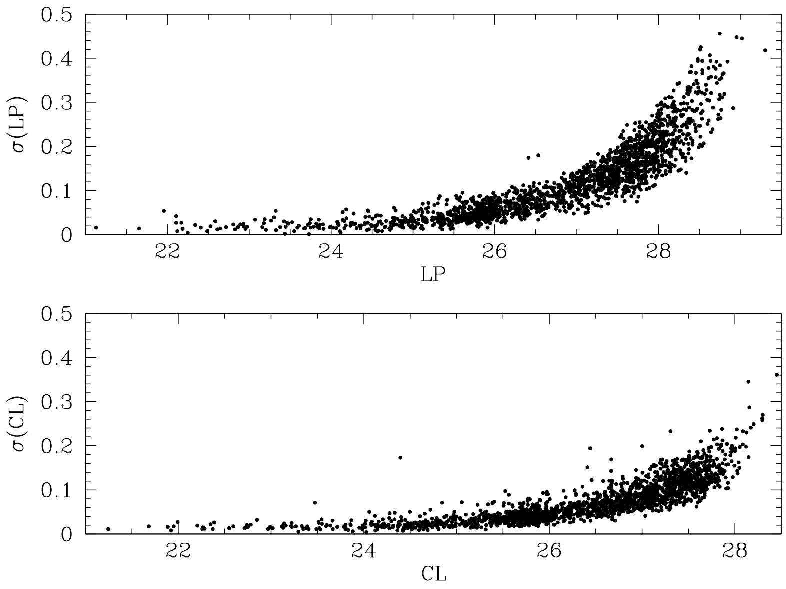

Figure 2.3: Photometric errors as a function of instrumental LP (top) and CL-band (bottom) magnitudes.

In the $28'' \times 50''$ STIS images we detect 1886 point sources, reaching more than 3 magnitudes fainter than the faintest stars seen in the NTT images. In particular, some of the single sources in the NTT images are resolved into multiple sources by STIS. Objects containing bad pixels were eliminated from our final photometry list.

Figure 2.2 shows the STIS LP-band image, with the orientation indicated in Figure 2.1. This parallel observation with STIS falls at the edge of the WLM disk, and is expected to include disk and halo stars.

The photometry was performed with DAOPHOT II package in IRAF. For the zero-point calibration we followed instructions in the "HST Data Handbook" (1997). Using the values of the inverse sensitivity (PHOTFLAM) and HST zero-point (PHOTZPT) keywords in the headers of the images, zero-points of 26.067 and 26.518 were calculated for LP and CL respectively. The aperture corrections applied to the magnitudes measured through apertures of 2 pixels in diameter were -0.575 for LP and -0.484 for CL.

The STIS CCD suffers from imperfect Charge Transfer Efficiency (CTE), as reported by Gilliland, Goudfrooij & Kimble (1999). We have used their formulation of the CTE to estimate its effect on our photometry. It turns out that, except for very faint stars that are near our detection threshold (V $\gtrsim 27.5$) and near the bottom of the CCD, the effect on our magnitudes is below 0.01 mag, which is negligible for our purposes. Figure 2.3 shows the photometric errors as function of instrumental CL and LP magnitudes.

We note that since the galaxy/star ratio increases rapidly at faint magnitudes (Tyson 1988), the background galaxy contamination also has to be taken into account. Using the number counts in the STIS field of the Hubble Deep Field South image (Gardner et al. 2000), we estimate that in the field ~ 85 galaxies are present between CL magnitudes of 26 and 28. Most of the galaxies are resolved on our STIS images and are discarded by our choice of the "sharpness" parameter in the DAOPHOT II routines. Only a few fainter and very compact galaxies may be confused with stars, but these do not have a significant impact on the present work.

Figure 4 shows the CL *vs* $CL-LP$, and LP *vs* $CL-LP$ instrumental color-magnitude diagrams for a total of 1886 stars with centroids matched in CL and LP frames to better than 1.0 pixels ($0\farcs05$), and which satisfy stringent criteria of photometric quality ($\sigma \leq 0.5$, $\chi \leq 2$, and sharpness ≥ -1). The sharpness criterion eliminates galaxies as well as possible star clusters at the distance of WLM (see Sect. 3.1). The filled circles in Figure 2.4 represent the stars in common with the NTT images (41 in total) that are used for the empirical calibration of the STIS photometry.

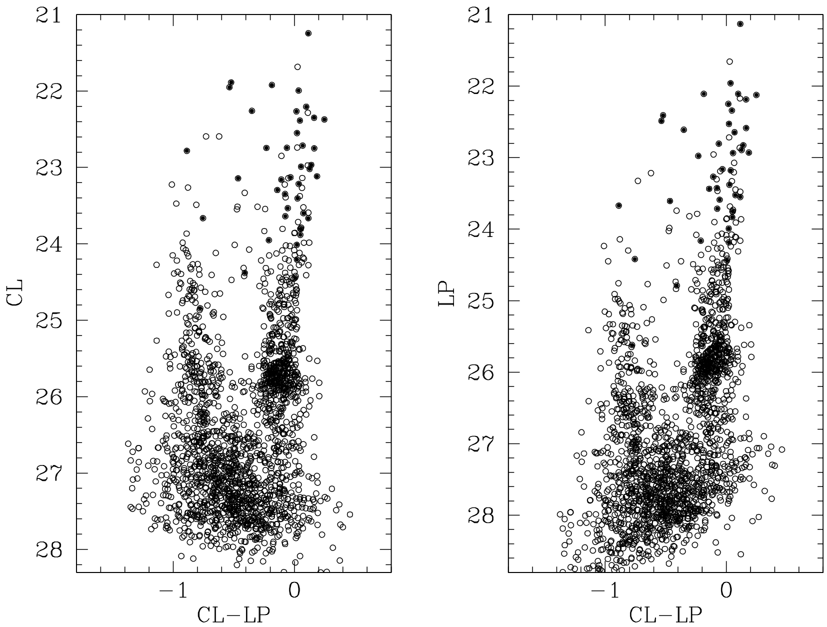

Figure 2.4: Color-magnitude diagrams of the WLM field in the STIS photometric system. The filled circles show the stars in common with the NTT data, which are used to calibrate the STIS photometric system.

2.2.3 Empirical calibration of the STIS photometric system

After STIS became operational in space, a significantly lower throughput of the CCD+LP system has been observed (e.g. Gardner et al. 2000). Although it is still possible to define the effective short bandpass by subtracting, from the CL flux, the LP flux scaled by 1.31, we use here only the CL and LP bandpasses for calibration. This simplifies the estimation of the uncertainties in the final photometry.

The photometry of the 41 STIS stars in common with the NTT observations is listed in Table 1. Respectively, columns 2 and 3 give the x and y positions of the stars on the NTT chip, columns 4 and 5 give V and I magnitudes of these stars, columns 6, 7, 8 and 9 give x and y positions of the stars on the STIS chip and their CL and LP magnitudes. For some of these stars careful inspection of the STIS images showed crowding, i.e. more than 2-3 stars with different magnitudes at the position of one NTT "star". These were not used for the calibration and are flagged with two asterisks in the last column of Table 1. Two more calibrators were rejected because of their marginal detection in the NTT image which carries a big magnitude error (flagged with one asterisk in Table 1).

The remaining 33 stars were used to transform CL into V magnitude, and LP into I magnitude. Figure 2.5 shows the comparison of the photometry. The relationships are approximately linear, as expected within the color range $-0.8 < \mathrm{V} - \mathrm{I} < 2.0$ under consideration (Gregg & Minniti 1997). Using a least square fit the following transformation equations were obtained:

$$(V - I) = 1.76(\pm 0.13) \times (CL - LP) + 1.18(\pm 0.03) \tag{2.1}$$

$$(V - CL) = 0.26(\pm 0.19) \times (CL - LP) + 0.01(\pm 0.04) \tag{2.2}$$

$$(I - LP) = -0.51(\pm 0.14) \times (CL - LP) - 1.17(\pm 0.03) \tag{2.3}$$

The scatter about the mean relations is significant: $\sigma_{\mathrm{rms}} = 0.16$, 0.24 and 0.17 for the first, second and third equation respectively. This is largely due to the NTT photometric errors at faint magnitudes ($\sigma_V > 0.08$ for $\mathrm{V} > 22.5$, $\sigma_I > 0.10$ for $\mathrm{I} > 22$; Minniti & Zijlstra 1997), and the small number of acceptable calibrators in the

Table 2.1: NTT VI vs. STIS CL-LP photometry: positions and magnitudes of the 41 stars in common in both the NTT and STIS fields.

#	$x(NTT)$	$y(NTT)$	V	I	$x(STIS)$	$y(STIS)$	CL	LP
1	816.9	1937.9	22.59	21.51	81.998	169.736	22.71	22.65
2	803.1	1922.3	23.16	21.69	96.888	59.512	23.17	22.93
3	829.3	1908.6	22.97	21.44	241.726	118.313	22.75	22.59
4	823.5	1887.3	23.68	22.59	305.413	21.158	24.21	24.19**
5	890.6	1941.2	24.12	22.65	322.588	475.961	23.67	23.55
6	901.8	1944.4	21.95	21.76	347.604	532.426	22.26	22.61
7	892.4	1921.4	23.36	22.42	406.552	414.659	23.53	23.59
8	883.7	1906.3	23.40	22.26	438.210	329.957	23.80	23.75
9	867.5	1890.2	22.32	21.23	446.591	208.103	22.27	22.25
10	910.5	1920.0	21.25	21.16	474.453	476.121	24.84	25.62**
11	884.3	1897.6	23.35	21.78	474.557	301.366	23.02	22.89
12	847.5	1864.3	22.99	21.67	481.419	39.644	22.99	22.94
13	914.7	1915.4	21.53	21.54	509.622	484.332	21.95	22.49**
14	894.2	1893.9	23.81	23.03	523.888	326.995	23.14	23.61**
15	909.5	1902.4	23.75	22.68	542.293	418.119	23.30	23.44
16	867.5	1861.7	22.80	22.00	561.449	109.459	22.75	22.98
17	880.4	1864.7	23.60	22.43	592.676	170.379	23.88	23.83
18	877.4	1862.0	22.92	20.82	593.314	150.726	22.37	22.12
19	910.9	1888.1	25.14	23.03	605.225	377.214	24.44	24.44**
20	878.5	1850.4	21.76	21.50	642.896	115.016	21.89	22.41
21	874.8	1845.3	21.41	19.95	651.276	82.676	21.25	21.13
22	882.0	1845.2	23.08	21.62	676.151	111.879	22.97	22.83
23	931.0	1890.3	23.89	22.94	687.633	452.606	24.01	23.99
24	919.5	1874.3	22.36	20.91	688.662	361.977	22.35	22.19
25	876.0	1835.1	24.25	22.80	696.083	53.898	23.64	23.71*
26	910.7	1856.6	23.71	22.38	729.336	266.375	23.41	23.38
27	885.0	1826.5	22.00	20.77	761.784	59.269	21.99	21.96
28	889.1	1820.5	22.33	21.11	799.237	55.663	22.39	22.34
29	892.2	1811.9	23.71	22.72	847.889	38.486	23.95	24.16
30	940.1	1850.3	23.25	22.04	855.515	362.924	23.13	23.16
31	908.3	1822.4	22.90	22.99	857.748	140.250	22.78	23.67
32	910.5	1816.7	23.10	22.01	889.823	127.514	23.22	23.18
33	914.0	1813.2	23.73	23.20	910.690	126.506	24.38	24.79**
34	943.6	1838.4	23.13	21.83	914.359	331.962	23.60	23.52
35	971.3	1855.4	22.96	22.10	943.155	503.628	23.16	23.27
36	921.7	1811.2	22.74	21.77	948.750	153.724	22.74	22.81
37	965.9	1847.5	21.56	20.84	956.147	455.374	21.92	22.11
38	977.9	1857.3	22.48	21.14	958.390	536.273	22.55	22.53
39	917.1	1802.4	22.45	20.99	968.605	105.047	22.21	22.11
40	928.8	1812.6	23.74	24.24	969.604	182.020	23.66	24.42*
41	937.8	1819.4	23.28	22.35	971.038	247.251	23.35	23.43

$*$ marginal detection in the NTT image

$**$ multiple sources in the STIS image

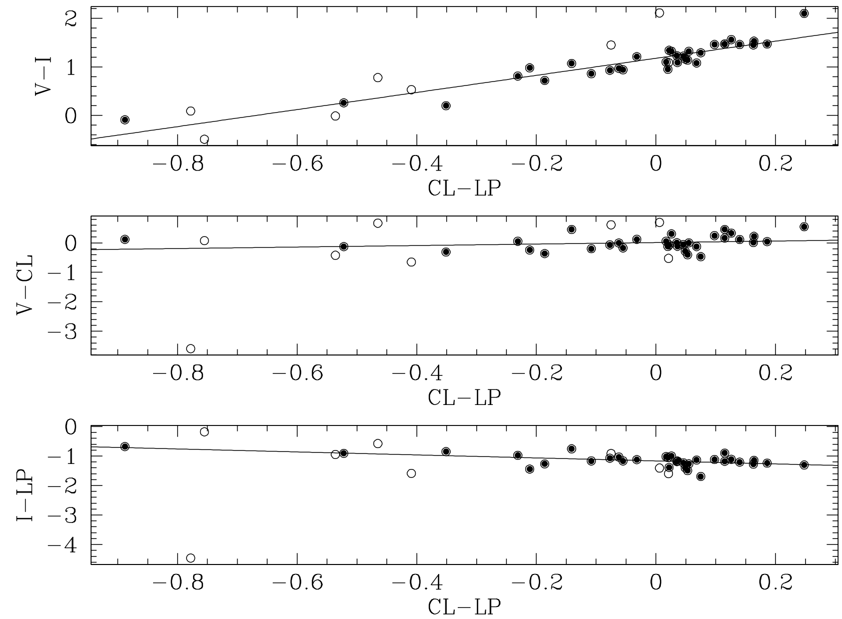

Figure 2.5: Empirical calibration of the STIS photometric system (CL, LP and SP-bands) into the V and I-bands. Only the 33 stars (filled circles) out of the total 41 (open and filled circles), found in both NTT and STIS fields, were used for the calibration.

blue part of the color range, $-0.8 < \mathrm{V} - \mathrm{I} < -0.4$. There is also an inherent scatter because of the differences in widths and central wavelengths between CL (λ_c = 5851.5 Å) and V (λ_c = 5426 Å) as well as between LP (λ_c = 7228.5 Å) and I (λ_c = 7985 Å) filters. This scatter will depend on abundances, temperature and surface gravities, but because of the homogeneity of our comparison stars,almost all being red giants or supergiants, we estimate that it is smaller than the scatter induced by the NTT photometric errors. The complete photometry list, given in Table 2, will appear only in the electronic edition. The table contains x and y positions of each star on the chip, CL and LP magnitudes with their respective uncertainties as well V and I magnitudes calibrated using the calibration equations (1)–(3). The uncertainties given for V and I magnitudes come from the errors in CL and LP photometry and from the transformations.

Our calibration equations are only preliminary and valid for a limited color range ($-0.8 < (\mathrm{V} - \mathrm{I}) < 2$). Since essentially all our comparison stars are red giants or supergiants, the transformation may be different for dwarfs

Table 2.2: The complete photometry list.*

x	y	CL	σ(CL)	LP	σ(LP)	V	σ(V)	I	σ(I)
1.338	376.277	26.594	0.054	27.400	0.106	26.40	0.19	26.64	0.21
5.169	97.329	27.412	0.092	27.479	0.143	27.41	0.14	26.35	0.24
6.707	504.232	26.415	0.059	26.428	0.047	26.42	0.08	25.27	0.10
7.505	500.302	27.658	0.109	28.046	0.156	27.57	0.19	27.08	0.27
8.480	553.033	27.345	0.099	27.189	0.123	27.40	0.15	25.94	0.22

The complete version of this table can be found in the electronic version of the AJ publication. The table printed here contains only a sample.

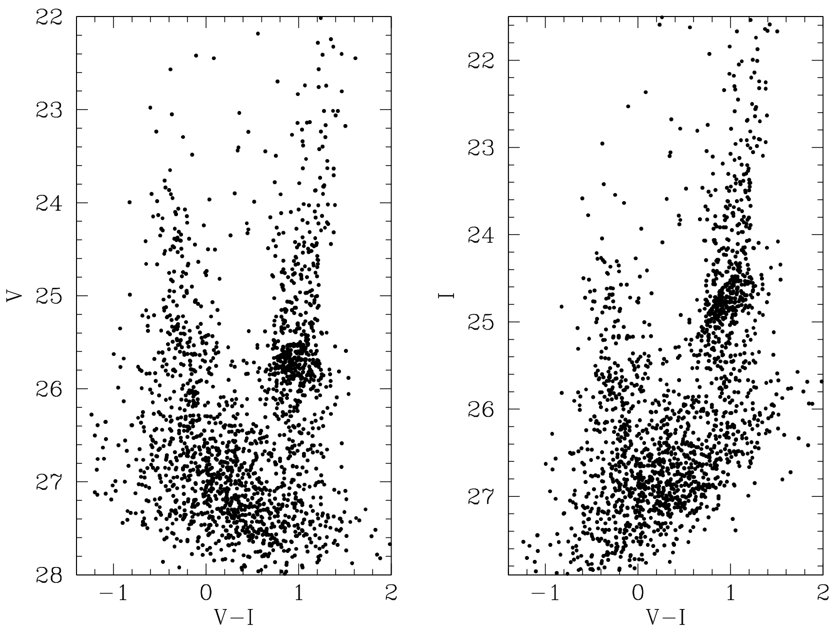

Figure 2.6: Final calibrated VI color-magnitude diagrams of the WLM STIS field.

(Gregg & Minniti 1997). The complete calibration of the STIS photometry to the standard photometric system, as well as a more quantitative analysis of the influence of different physical parameters (i.e. temperature, abundances, surface gravity) on the transformation, will be published elsewhere (Goudfrooij et al. in preparation).

2.3 Fundamental parameters of WLM

Figure 2.6 shows the final calibrated V *vs* V − I and I *vs* V − I color-magnitude diagrams. These diagrams are typical for a disk + halo population in WLM. The main features are a red giant branch (RGB), a blue main sequence with mean color $V - I = -0.2$, a prominent red giant clump at $I = 24.68 \pm 0.05$ and $V - I = 0.9$, and a horizontal branch (see also Fig. 2.4). The horizontal branch (HB) is extended, and can be traced to $V \simeq 26$, and $V - I \simeq 0$.

Using the deep color-magnitude diagram of Figure 2.6 we can redetermine fundamental WLM parameters such as distance, metallicity and age. It is beyond the scope of this paper to determine the detailed star formation history in the field.

2.3.1 The distance

Recent Hipparcos observations accurately measured the absolute magnitudes of the old and metal-poor blue HB stars of the Milky Way halo. For these stars, Hipparcos gives $M_V = 0.7$ for $[Fe/H] = -1.5$ (de Boer 1999). This metallicity is typical for the WLM halo, allowing one to obtain an accurate distance to this galaxy by comparing directly the V-band magnitude of the HB.

We created V-band luminosity functions and derivatives, with different magnitude bins and with different bin starting points, for stars with color $0.0 < V - I < 0.55$, in order to exclude contamination by the red giant clump. In this color range there is still small contamination by the reddest stars of the main sequence. We tried also other different color ranges and different binning procedures, but the results were unchanged. The V-band magnitudes of

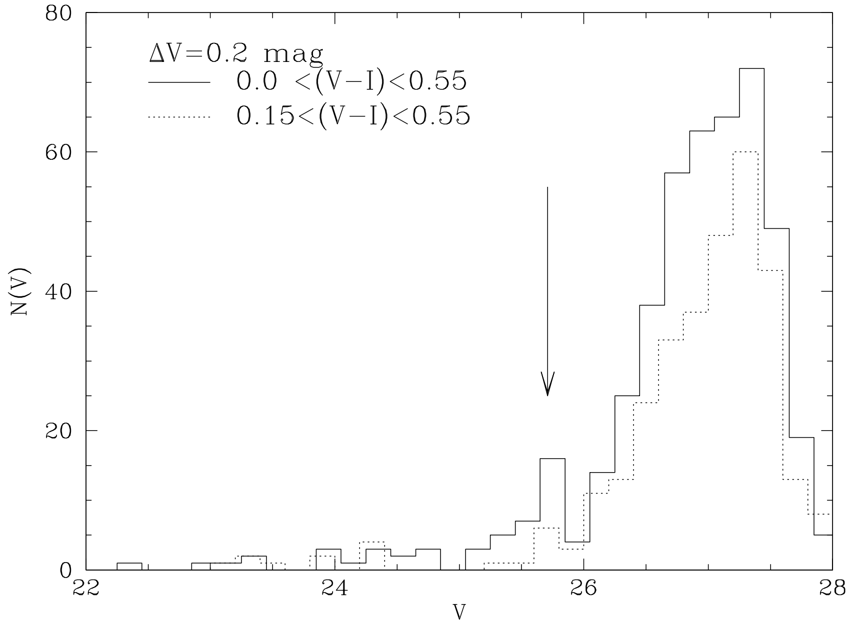

Figure 2.7: Two typical V-band luminosity functions for the magnitude bin of 0.2 mag and two different color ranges, $0.00 < \mathrm{V} - \mathrm{I} < 0.55$ (solid line) and $0.15 < \mathrm{V} - \mathrm{I} < 0.55$ (dotted line). The arrow indicates the position of the horizontal branch.

the HB, calculated from individual luminosity function derivatives, were averaged to obtain the mean V magnitude of the HB: $\mathrm{m_V^{HB}} = 25.71 \pm 0.09$. Two examples of typical luminosity functions created for a bin size of 0.2 mag are given in Figure 2.7. A luminosity function for the color range $0.0 < \mathrm{V} - \mathrm{I} < 0.55$ is plotted with the solid line, while the dotted line is used for the one covering $0.15 < \mathrm{V} - \mathrm{I} < 0.55$. The arrow indicates the average V magnitude of the blue HB (which is a 3σ detection here) obtained from many different luminosity function derivatives. The strength of the HB feature in the luminosity function shows that it is indeed extended beyond the red giant clump. In such an extended HB we expect to have some RR Lyrae stars which can widen the feature in the CMD, although unfortunately we do not have temporal sampling to find them.

If we adopt $\mathrm{E_{V-I}} = 0.03$ from Minniti & Zijlstra (1997), the distance modulus turns out to be $(\mathrm{m} - \mathrm{M})_0 = 24.95 \pm 0.09$, including only our statistical error. However, the final conservative distance error we adopt is $\sigma = 0.13$, in order to account for any systematic error in the Hipparcos results. Using the magnitude of the tip of the red giant branch (RGBT), Lee et al. (1993) measured a distance modulus of $(\mathrm{m} - \mathrm{M})_0 = 24.81 \pm 0.15$, and Minniti & Zijlstra (1997) measured $(\mathrm{m} - \mathrm{M})_0 = 24.75 \pm 0.10$. The Cepheid distance modulus measured by Lee et al. (1993), based on a distance modulus to LMC of $(\mathrm{m} - \mathrm{M})_0^{\mathrm{LMC}} = 18.5$, is $(\mathrm{m} - \mathrm{M})_0 = 24.92 \pm 0.21$. The present distance modulus to WLM measured using the HB stars blueward of the red giant clump, $(\mathrm{m} - \mathrm{M})_0 = 24.95$, is within 1σ of the former and 2σ of the latter RGBT distances mentioned above, and is very close to the Cepheid distance. It is also in good agreement with $(\mathrm{m} - \mathrm{M})_0 = 24.88 \pm 0.09$, the distance modulus determined from WFPC2 HST data by fitting the entire color-magnitude diagram (Dolphin 2000). Therefore, we conclude that for $\mathrm{E_{V-I}} = 0.03$, the distance modulus to WLM is $(\mathrm{m} - \mathrm{M})_0 = 24.95 \pm 0.13$. This translates to a distance of $\mathrm{D} = 0.98 \pm 0.06$ Mpc, within 1σ of $\mathrm{D_{WLM}} = 0.94$ Mpc listed by van den Bergh (1994).

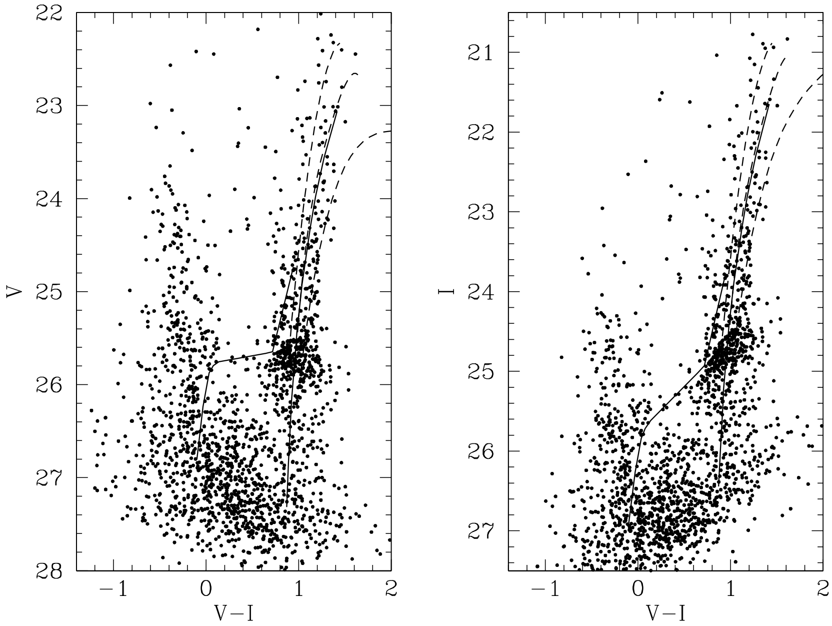

Figure 2.8: Comparison of the WLM VI color-magnitude diagram with that of the galactic globular clusters M5 (solid line; Johnson & Bolte 1998) and the RGBs of M15, NGC 6752 and 47 Tuc (dashed lines; Da Costa & Armandroff 1990).

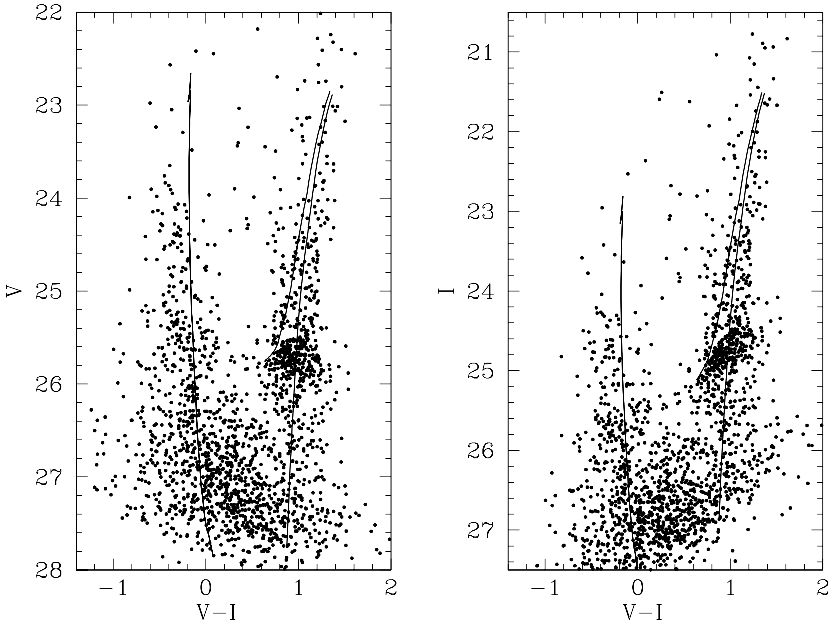

Figure 2.9: Comparison of the WLM VI color-magnitude diagram with the Padova isochrones (Girardi et al. 2000). Isochrones for $Z = 0.001$ and $\log t = 7.80$ and 10.20 are plotted over the data.

2.3.2 The metal abundances

The metallicity of the old and metal-poor populations such as those found in the halo around WLM, can be derived from the $V - I$ color of their RGB. Using the calibration of Lee (1993), Minniti & Zijlstra (1997) obtained $[Fe/H] = -1.45 \pm 0.2$. The full line on Figure 2.8 compares the location of the RGB, AGB and HB of the globular cluster M5 (Johnson & Bolte 1998) with the WLM photometry. The globular cluster fiducial lines were brought to the distance of WLM (see Sec. 3.1) adopting the distance modulus of 14.35 and the reddening of E(B-V)=0.03 for M5. The metallicity of M5 in Zinn & West (1984) is $[Fe/H]_{M5} = -1.40$. The mean color of the RGB from the STIS color-magnitude diagrams is similar to that obtained with the NTT data, and to the fiducial RGB sequence of M5, therefore confirming the metallicity determined by Minniti & Zijlstra (1997).

The RGB in our CMD appears wider than that of Dolphin's (2000) CMDs. These are different fields, and the effect can be due to a) different metallicities, b) different ages, c) bigger errors in the STIS V-I colors, d) differential reddening, or e) a combination of the above. The CMDs clearly show the presence of young main sequence stars as well as old horizontal branch stars in this field. For comparison, we show the effects of old populations of different metallicities in Figure 2.8, where the dashed lines are the RGB fiducials for Galactic globular clusters M15, NGC 6752 and 47 Tuc (Da Costa & Armandroff 1990), from left to right respectively. These globular clusters span a wide range in metallicities, from -2.17 dex to -0.71 dex. Note that there are stars more metal poor than the mean metallicity, as well as the absence of metal-rich stars.

By fitting the theoretical isochrones Hodge et al. (1999) find a metallicity of $[Fe/H] = -1.52 \pm 0.08$ for the only globular cluster detected in WLM, in good agreement with the metallicity obtained for the outer field giant stars by Minniti & Zijlstra (1997).

2.3.3 The ages

Blue HB stars, like RR Lyrae stars, are unambiguous indicators of old populations with age $> 10^{10}$ yr (Da Costa 1994, Hodge 1989, Olszewski 1994, Grebel 1998, Mateo 1998). The detection of a blue horizontal branch in WLM confirms the presence of ancient stars. Based on the HB morphology, we predict the existence of RR Lyrae variables in this galaxy.

Figure 2.9 shows the photometry of the field compared with the most recent Padova isochrones. There is a good agreement with the isochrones of Girardi et al. (2000) for $Z = 0.001$, $Y = 0.23$, and $\log t = 10.20$ and 7.80. These indicate a mixture of an old and young population, characteristic of the halo and disk respectively, as expected for a field situated at the very edge of the WLM disk.

By comparing with theoretical isochrones and luminosity functions Sandquist et al. (1996) measure an absolute age for M5 of 13.5 ± 1 Gyr or 11 ± 1 Gyr, for $[Fe/H]_{M5} = -1.40$ or $[Fe/H]_{M5} = -1.17$ respectively. The good agreement of our photometry and the fiducial sequence of M5 (Figure 2.8) is another strong argument in favor of the presence of an old stellar population with age$> 10^{10}$ yr in the halo of WLM.

Hodge et al. (1999) obtain an absolute age of 14.8 ± 0.6 Gyr for the only globular cluster detected in WLM. The age and metallicity of this globular cluster is similar to normal old halo globulars in our Galaxy. This confirms again the presence of an old and metal-poor population in WLM similar to the one in the Milky Way halo and to the populations found in the halos of the other spirals of the Local Group (Mould & Kristian 1986).

Following its early phase of star formation, a galaxy like WLM could have been accreted to form the Milky Way halo. It would have given its stellar content to the halo, which today we observe to be of similar age and metallicity as the oldest stars in WLM (see also the comparison between WLM and M5 Galactic globular cluster in Figure 2.8). The remaining gas from a WLM-like galaxy would have sunk down to the bottom of the potential well and contribute to the gas used to form stars in the disk of the Milky Way. Because of this, WLM can be considered as an example of a surviving protogalactic fragment, related to those that built up the Milky Way halo (Minniti & Zijlstra 1996).

2.4 Conclusions and implications

We have obtained deep STIS *CL* and *LP*-band photometry for 1886 stars in the field of the dwarf irregular galaxy WLM, located at the edge of the Local Group.

We have calibrated the STIS photometric system empirically onto the V and I-band system using our previous observations with the NTT telescope (Minniti & Zijlstra 1997). The VI color-magnitude diagram of a field located in the transition region between WLM's disk and halo shows a prominent RGB, a blue main sequence, a red clump, and an extended HB. The presented CMD was obtained with HST+STIS over less than 2 orbits, and revealed the presence of a HB in this distant Local Group galaxy. These results prove that it is now possible to reach the blue horizontal branch out to D $\simeq$ 1 Mpc using STIS with relatively short exposure times ($\lesssim$ 1 orbit), allowing the study of the horizontal branches throughout the Local Group.

We have obtained an accurate distance modulus for WLM of $(\mathrm{m-M})_0 = 24.95 \pm 0.13$, based on the magnitude of the horizontal branch. This value agrees well with recent distance determinations using the RGB tip and Cepheids.

Our main result is, however, the detection of a horizontal branch that extends blueward from the red giant clump, an unambiguous indicator of the presence of an old population (age$> 10^{10}$ yr) in WLM. It is likely to be associated with the halo of the galaxy, which is found to be an extended metal-poor component by Minniti & Zijlstra (1996). The old age measured for the globular cluster of this galaxy by Hodge et al. (1999) favors such an interpretation.

Kinematics of individual stars is needed to compare the disk population with the halo population to check if the latter is kinematically hotter (with higher velocity dispersion and lower rotational velocity).

There are two major implications of these results:

1) WLM formed stars more than 10 Gyr ago. Various cosmological models give different redshifts for the same lookback time (Carroll, Press & Turner 1992). For example, according to the model of a flat universe with a plausible matter ($\Omega_M = 0.1$) and without the cosmological constant ($\Omega_\Lambda = 0$), WLM formed stars at $z > 4$, while according to the cosmological model of a flat universe with $\Omega_M = 0.1$ and $\Omega_\Lambda = 0.9$, WLM formed stars at $z > 1$. Star formation in this galaxy was not inhibited at early times by photoionization by UV sources such as QSOs and AGNs. This does not favor scenarios where dwarf galaxies form recently (e.g. Babul & Rees 1992).

2) The old population found in the WLM halo is similar to that of the old and metal-poor halos of the spiral galaxies in the Local Group. Having remained isolated throughout its lifetime, WLM can now be considered as a good example of a surviving protogalactic fragment, related to those that built up the Milky Way halo.

Chapter 3

Deep VLT search for globular clusters in NGC 5128: color-magnitude diagrams and globular cluster luminosity function[1,2]

Abstract

At the distance of NGC 5128 (3.6±0.2 Mpc) it is possible to resolve globular clusters with high resolution imaging from the ground, thus allowing the globular cluster candidate selection primarily through their morphological properties. We report the discovery of 71 globular clusters in NGC 5128 on VLT UT1+FORS1 images, including the faintest members ($M_V \sim -5$) known to date in this galaxy as well as 5 previously known clusters. U- and V-band photometry has been measured for all the candidates and the luminosity function, spanning $-10.1 < M_V < -4.9$ and $-9.3 < M_U < -3.3$, constructed. These are the deepest globular cluster luminosity functions in an elliptical galaxy determined so far. The Kolmogorov-Smirnov statistics show that the difference between the globular cluster luminosity functions of NGC 5128 and the MW is not larger than the difference between the ones of M31 and the MW. The $(U-V)_0$ color histogram shows a bimodal distribution. For 23 globular clusters we obtained K-band images with SOFI at the NTT in La Silla. Their positions in the (U−V) vs. (V−K) color-color diagram indicate that they are indeed old globular clusters. Assuming that the globular clusters in NGC 5128 span a similar age range as the ones in the Milky Way and adopting a linear fit between the metallicity and $(U-V)_0$ color, the metal–rich clusters peak at [Fe/H]= −0.6 dex and the metal–poor ones peak at [Fe/H]= −1.7 dex.

3.1 Introduction

Globular Clusters are among the oldest objects in the Universe. Moreover, they are intrinsically luminous and found around almost all galaxies in which searches have been made. There are growing evidences for globular cluster formation during major star formation episodes (Schweizer 1997; Larsen & Richtler 1999). This makes them useful tracers of the formation and the evolution of galaxies (Harris 1991, 2000, Kissler-Patig et al. 1998, van den Bergh 2000a).

The globular cluster luminosity function (GCLF) of a galaxy is the relative number of its globular clusters per luminosity (or magnitude) interval. It is usually unimodal and nearly symmetric with a peak at a characteristic (turn–over) magnitude. Empirically it was found that turn–over magnitudes for galaxies at the same distance (e.g. in the same galaxy cluster) differ by < 0.1, which makes the GCLF a good standard candle (Harris 1991; Jacoby et al. 1992). However, the full calibration of the GCLF is incomplete. The essential problem is that the galaxies at large distances, for which the GCLF method is mostly used, are giant ellipticals in which globular clusters are found in largest numbers and in which there are usually fewer problems with extinction, whilst the primary calibration

[1]Based on observations collected at the European Southern Observatory, Paranal, Chile, within the Observing Programme 63.N-0229, and at La Silla Observatory, Chile.

[2]Based on Rejkuba M., 2001, A&A 369, 812

of the standard candle M_V^0 rests on the MW and M31, which are spiral galaxies. In fact, evidence that GCLFs depend on Hubble type and environment has been claimed (Fleming et al. 1995), but the former is probably due to differences in mean metallicity of the globular clusters and the latter was never reliably demonstrated (Kissler-Patig 2000).

There is strong observational evidence that most luminous giant ellipticals have a bimodal globular cluster metallicity distribution (Gebhardt & Kissler-Patig 1999; Kundu 1999). The globular cluster specific frequencies (the number of clusters normalized to the galaxy luminosity; Harris & van den Bergh 1981) are typically higher in ellipticals than in spirals (Harris 1991, 2000). To explain the high number of globular clusters and the presence of several populations indicated by the bimodal metallicity distributions, different globular cluster formation mechanisms have been proposed (e.g. Ashman & Zepf 1992, Côté et al. 1998, Forbes et al. 1997). The number, chemical abundance and spatial distribution of a globular cluster system (GCS) put strong constraints on the formation of its parent galaxy.

At the distance of 3.6 Mpc (Soria et al. 1996, Harris et al. 1999) NGC 5128 is the closest giant elliptical galaxy. The first globular cluster in NGC 5128 was discovered by Graham & Phillips (1980). Its brightness was high with $V = 17.2 \pm 0.1$ mag, which corresponds to $M_V = -10.6$ mag. Subsequent investigation of photographic plates (van den Bergh et al. 1981, Hesser et al. 1984, 1986) revealed a rich GCS in this galaxy. The estimated number of globular clusters in NGC 5128 is N$\sim$1700 (Harris et al. 1984) compared with N$\sim$150 for the MW.

On the basis of the near IR colors for a magnitude–limited sample of 12 globular clusters, Frogel (1980, 1984) found one third of the sample to be super metal rich (above solar metallicity) and luminous. However, the Washington photometry of 62 spectroscopically confirmed clusters (Harris et al. 1992) as well as a spectrophotometry for 5 clusters (Jablonka et al. 1996) showed less extreme metallicity. Harris et al. (1992) found a large spread in metallicities with a mean of $[\mathrm{Fe/H}]_{C-T_1} = -0.8 \pm 0.2$ dex. They also find evidence for a weak spatial metallicity gradient, but state that the same could be produced by unknown reddening effects. Zepf & Ashman (1993), using the same photometric data, suggest that the metallicity distribution of globular clusters in NGC 5128 is bimodal, with the higher metallicity peak at [Fe/H]=+0.25 dex, and proposed that this was due to the formation of a second population of globular clusters in a previous merger which created NGC 5128.

Several photometric studies in the inner regions of NGC 5128 have been conducted, with the aim of constraining the dependence of globular cluster metallicity on galactocentric radius and of finding super-metal-rich clusters (Minniti et al. 1996; Holland et al. 1999). These studies suggest the existence of radial gradients and bimodal distribution in globular cluster metallicity. However, their conclusions are limited due to the restricted samples, possible reddening within NGC 5128 that is especially severe in the central parts around the prominent dust lane, and possible contamination by stars within NGC 5128 as well as background galaxies.

In this paper, we present a sample of globular clusters from two fields in the halo of NGC 5128. Deep images combined with high resolving power of the VLT and the proximity of NGC 5128 allow the identification of globular clusters primarily on the basis of their non-stellar profiles. Constructing the GCLF for a statistically significant number of clusters that span the whole range of magnitudes, we pursue the question of the uniqueness of GCLF in elliptical galaxies.

This paper is organized as follows. The data, the photometric calibrations and completeness tests are described in Sect. 3.2. In Sect. 3.3 the color–magnitude diagram for the NGC 5128 globular clusters is compared to the ones of the MW and M31. The luminosity function is presented in Sect. 3.4 and the color distribution in Sect. 3.5. In the latter, the mean abundances are determined for the metal-poor and metal-rich populations. The results are summarized in Sect. 3.6.

3.2 The data

3.2.1 Observations and data reduction

We used the VLT Antu (UT1)+FORS1 (FOcal Reducer/low dispersion Spectrograph) to obtain the Bessel U- and V-band photometry of globular clusters and stars in two different fields in NGC 5128. The field of view was $6'.8 \times 6'.8$ and the pixel scale $0''.2$/pixel. The FORS1 detector is a 2048×2048 CCD with 24μm pixels.

Table 3.1: Journal of Observations

Field #	$\alpha_{(2000)}$ (h min sec)	$\delta_{(2000)}$ (° ′ ″)	Date dd/mm/yy	Telescope & Instrument	Exposure (sec)	FILTER	Airmass	Seeing ″
1	13 26 23.5	-42 52 00	12/Jul/1999	Antu+FORS1	2×900	U	1.536	0.52
1	13 26 23.5	-42 52 00	12/Jul/1999	Antu+FORS1	2×900	V	1.768	0.54
2	13 25 24.0	-43 10 00	11/Jul/1999	Antu+FORS1	2×900	U	1.283	0.53
2	13 25 24.0	-43 10 00	11/Jul/1999	Antu+FORS1	2×900	V	1.196	0.44
2	13 25 24.0	-43 09 04	20/Feb/2000	NTT+SOFI	45×6×10	K_s	1.055	0.56
1	13 26 48.1	-42 46 00	28/Feb/2000	2.2m+WFI	3×210	V	1.117	1.00
2	13 26 48.1	-43 16 01	28/Feb/2000	2.2m+WFI	3×210	V	1.037	0.81
2	13 24 07.6	-43 15 58	29/Feb/2000	2.2m+WFI	3×210	V	1.057	1.12

Field 1 was centered on the prominent N-E shell $\sim 14'$ away from the center of the galaxy, while Field 2 was chosen to overlap with Soria et al. (1996) HST observations at a distance of $\sim 9'$ from the center of the galaxy. Observations were carried out on the 11th and 12th of July 1999 in service mode. Pairs of images of 15 min exposure time were taken per field in each filter. The journal of observations is given in Tab. 3.1.

In addition to VLT data, we obtained a 45 min long exposure of Field 2 in K_s using SOFI at the New Technology Telescope (NTT) at the ESO/La Silla Observatory. The field of view of SOFI is $4\farcm94 \times 4\farcm94$ and the pixel scale $0\farcs292$/pixel. This field is smaller than the one of FORS1 and so only about 40% of objects in one field have K_s-band magnitudes.

Both fields were also observed with the Wide Field Imager (WFI) at the 2.2m telescope on La Silla. The data from WFI observations are used here to assess the V-band magnitude of some of the brightest cluster candidates that were saturated on V-band FORS1 images. We calibrated the WFI photometry by comparing magnitudes of globular clusters well exposed (but not saturated) on VLT and WFI images in order to determine the zero point of WFI observations.

For optical data (VLT and 2.2m images), the standard image processing, including the overscan and bias subtraction and the flat-field correction, was performed within the IRAF[1] environment. The pairs of exposures in each filter were registered using the *imalign* task and averaged to obtain the final images. Cosmic rays were rejected in this process using the *crreject* algorithm within the *imcombine* task in IRAF. Bad pixels were masked out.

The standard procedure in reducing infrared (IR) data consists of sky subtraction, flat-field correction, registering and combining the images. Good sky subtraction in a crowded field like that of a galactic halo is particularly important. For that step we used the DIMSUM package (Stanford et al. 1995) within IRAF. In DIMSUM the sky subtraction is made in two passes. In the first one a median sky is computed for each image from 6 temporarily closest frames. The shifts between the sky subtracted frames are then computed and all the images stacked together using a rejection algorithm to remove cosmic rays. An object mask is computed for the coadded image and then shifted back in order to create object masks for the individual frames. In the second pass, the sky subtraction is made using the object masks to avoid overestimation of the sky level. These masks are also used to check that the bright object cores were not removed as cosmic rays in the previous pass. After the mask-pass sky subtraction, the frames are registered with *imalign* and combined with *imcombine* task in IRAF.

3.2.2 Cluster identification and photometry

NGC 5128 is close enough that its globular clusters can be distinguished from stars on the basis of their slightly non-stellar appearance on high resolution ground-based images taken in excellent seeing conditions. At the distance of NGC 5128 (3.6 Mpc) a typical MW globular cluster with a mean King core radius of $r_c = 2.3$ pc had, on the

[1] IRAF is distributed by the National Optical Astronomy Observatories, which is operated by the Association of Universities for Research in Astronomy, Inc., under contract with the National Science Foundation

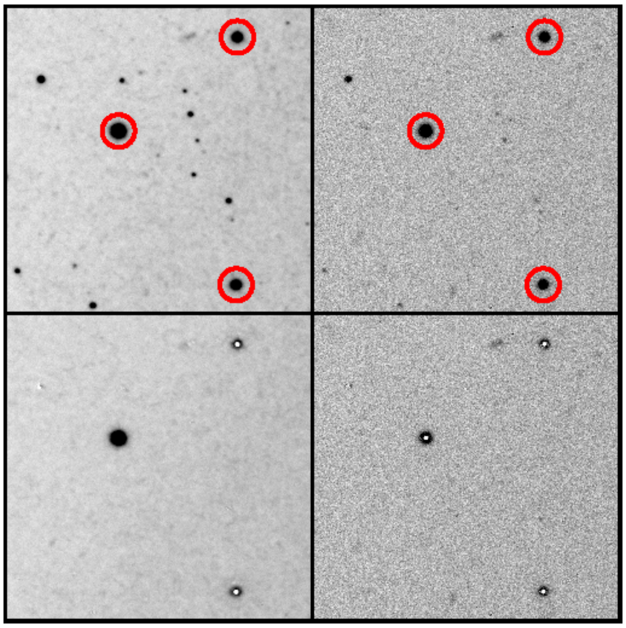

Figure 3.1: Residual image of a $51'' \times 51''$ portion of Field 2. On the left panels the V-band image (top) and its residual image (bottom) and on the right panels the corresponding U-band images are shown. Three globular cluster candidates are circled. The left-most globular cluster is slightly overexposed in the V-band image. Its classification as a globular cluster follows from the U-band residuals.

best seeing VLT images, a FWHM of 2.6 pix, which is $\sim$ 0.4 pix bigger than the stellar FWHM. The excellent seeing, especially on the V-band images of Field 2, allowed us to identify globular cluster candidates with r_c as small as 1.7 pc, corresponding to observed FWHM of 2.4 pix (see f2.GC-6 in Tab. 3.4), purely on the basis of their non-stellar appearance through the following procedure within IRAF: (i) first the *daofind* algorithm was run in order to detect all the stars and clusters in the image; (ii) photometry through a 3 pixels aperture was performed on all the objects; (iii) relatively bright, isolated, stellar objects were used to create the PSF, which was then fitted to all the objects, subtracted and the residual images created. DAOPHOT II (Stetson 1987) permits creation of the variable PSF, which was necessary for the U-band images that showed fixed pattern residuals upon subtraction of the non-variable PSF. In order to create a variable PSF we used 35 stars per image.

Because of their slightly larger FWHM and non-stellar PSF, globular clusters were easily detected on residual images created by subtracting the objects fitted with a stellar PSF. This subtraction was performed using the *allstar* task. Globular cluster residuals were oversubtracted in the center and undersubtracted in the wings (Fig. 3.1). Images were visually inspected and the residuals in the U- and V-band images compared. This was necessary to discard obvious galaxies from the candidate list.

After visual inspection of the residual images, 50 and 81 objects in Field 1 and 2, respectively, were retained as candidates for globular clusters. Good globular cluster candidates, the ones that have round ring-like residuals, are listed in Tab. 3.3. Other extended objects for which the visual distinction was not very clear, some of them being blended stars or round galaxies, but some of which might be globular clusters as well, are listed in Tab. 3.4. The Sextractor programme (Bertin & Arnouts 1996) was used to measure precise coordinates, FWHM (f_U and f_V columns in Tab. 3.3 and 3.4) and ellipticities (ϵ_V and ϵ_U columns) for these objects.

We performed aperture photometry within IRAF for all the objects. Since the fields were quite crowded, stellar objects had to be removed in order to obtain more precise photometry of globular clusters. To do so, we first subtracted all the stars (this time excluding the globular cluster candidates from the aperture photometry list)

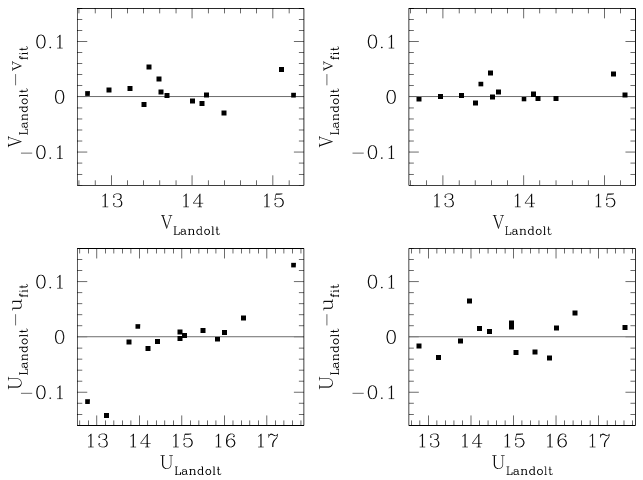

Figure 3.2: Photometric calibration of Landolt (1992) stars during the nights of observations in U and V filters. Left panels: the scatter for the calibration without the color term; right panels: the scatter for the calibration with the color term.

from the original images using the *allstar* task. Aperture photometry of globular cluster candidates was then measured through circular apertures of 16, 20 and 25 pixel radii. In some cases a bright saturated star or another globular cluster candidate was found near the cluster, or the latter was located near the edge of the image and thus only a 3 pix aperture magnitude was used. The 3 pix magnitudes were later extrapolated to 25 pix magnitude values using an aperture correction calculated as a median correction for more isolated globular clusters. The error in magnitude for these clusters is larger and hard to quantify, since the aperture correction depends on the concentration and compactness of the cluster. The positions and magnitudes of globular clusters are presented in Tab. 3.3 and Tab. 3.4. The clusters with magnitudes measured through a smaller aperture and later corrected are flagged with “b” (near the bright star or another globular cluster) or “e” (near the edge of the image).

3.2.3 Photometric calibration

For the photometric calibration of the VLT images, a total of 14 stars in 4 different Landolt (1992) fields, spanning the color range $-1.321 < (U - V) < 4.162$, were observed during the two nights. The following transformations were calculated:

$$\begin{aligned} u_{inst} &= U - 24.262(\pm 0.089) + 0.379(\pm 0.068) * X \\ &\quad -0.042(\pm 0.007) * (U - V) \end{aligned} \tag{3.1}$$

$$v_{inst} = V - 27.348(\pm 0.042) + 0.213(\pm 0.034) * X \tag{3.2}$$

where X is the mean airmass of the observations, u_{inst} and v_{inst} are the instrumental magnitudes and U and V magnitudes from the Landolt (1992) catalogue. The one sigma scatter around the mean was 0.031 mag for the U band and 0.023 mag for the V band (Fig. 3.2 left panel). Adding the color term (U−V) in the transformations slightly reduces the scatter in the V-band to 0.017 mag (Fig. 3.2 right panel). However, the calibration equation without the color term for the V-band was prefered, since the data in that filter go much deeper and U magnitudes for some objects could not be measured accurately enough.

SOFI images were calibrated using 6 standards from the Persson et al. (1998) list observed during the night and spanning an airmass range from 1.1 to 3.4. Each standard star was observed at 5 different positions on the

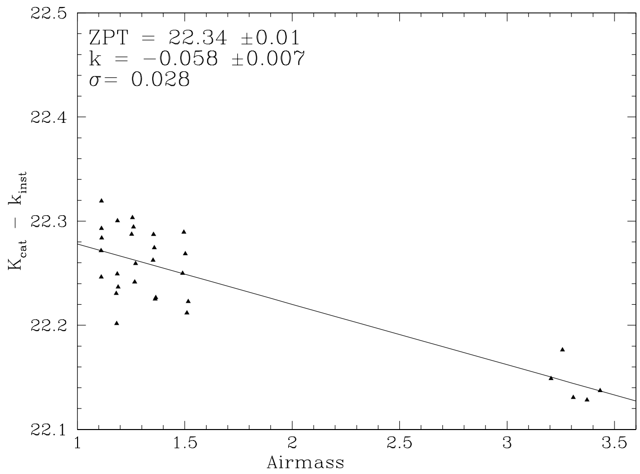

Figure 3.3: Photometric calibration of Persson et al. (1998) stars in K_s filter.

IR-array. In this way total of 30 independent measurements was obtained. The least square fit (Fig. 3.3) yielded the following calibration equation:

$$k_{s,inst} = K_s - 22.34(\pm 0.01) + 0.058(\pm 0.007) * X \tag{3.3}$$

3.2.4 Completeness

We made completeness tests for detection of stars on the U- and V-band images. Using the IRAF task *addstar* within the DAOPHOT package we added 400 stars each time to each of the U- and V-band images, all stars having the same magnitude and uniformly distributed over the whole field. The photometry was re-computed in the same way as for the original images. Repeating the procedure for stars added in 0.5 mag bins, the completeness and the accuracy of photometry were measured. The 90% completeness for stellar sources is reached at magnitude 25 in the V-band and 23.5 in U-band. The completeness drops to 50% at V$\sim$ 26 and U$\sim$ 24.5. More detailed results of completeness tests will be presented in the forthcoming paper where the stellar photometry of NGC 5128 is analyzed (Rejkuba et al. 2001b, Chapter 4).

Globular clusters have larger profiles than stellar PSFs, their selection is based mainly on the recognition of a "globular-like" residual on a subtracted image and thus their identification as such is more subjective. In order to check the completeness level of globular cluster detections, we made similar simulations as for the stars. The fainter globular clusters, that are of interest in simulation, are not resolved and thus we just treat them as stars. To add a correct, typical globular cluster profile, the best cluster candidates' model profiles were used to create simulated images. In order to investigate the dependence of detection on core radius, simulations with different typical profiles were made. Two sets of simulations were done using the profiles of clusters with small core radii, f1.GC-17 and f2.GC-4, to add objects, while in the other two sets much less concentrated clusters f1.GC-10 and f2.GC-36 were used. At each pass 100 clusters were added, distributed uniformly all with the same magnitude. The completeness of the globular cluster detection was measured for each half magnitude.

The detection depends quite significantly on core radius in the sense that more small r_c clusters are lost at faint end. The incompleteness magnitude is defined as magnitude where more than 50% of the added clusters are not detected as such (they are actually all detected, but their residuals are not recognized as globular cluster-like, because they are lost in noise). It sets in at V$\sim$22.7 mag for clusters like f1.GC-17 and f2.GC-4, but most of the larger clusters, like f1.GC-10 and f2.GC-36 can still be detected at 90% level at magnitude V=23. The incompleteness for clusters with large r_c sets in at magnitude V=23.5. In the simulations clusters could be detected with magnitudes as

Table 3.2: Comparison with the data from literature.

ID1	ID2	B_{pg}	V_{pg}	V_{Wash}	V_{WFI}	(U−V)
f1.GC-13	C36	19.04	18.24	18.27	18.39	0.91
f1.GC-16	C37	19.24	18.17	18.46	18.47	1.33
f1.GC-23	C38	19.00	···	···	18.40	1.16
f2.GC-26	C15	19.76	18.62	···	18.58	1.40
f2.GC-81	C12	18.82	17.74	17.79	18.01	1.47

faint as V=24. However, at those magnitude limits it is almost impossible to distinguish globular cluster residuals from galaxies.

From the simulations we conclude that clusters fainter than $V \sim 23$ mag would probably not be detected. MW clusters corresponding to these magnitudes are Pal 1, Pal 13, Terzan 1, E 3 and AM 4. However, at magnitude $V = 22.0$ ($\sim$ 2 magnitudes past the GCLF peak) more than 90% of the clusters are detected.

3.2.5 Comparison with published data

The most recent studies of the GCS in NGC 5128 (Holland et al. 1999, Alonso & Minniti 1997) have investigated the central regions of the galaxy away from the fields studied here. The only photometry of globular clusters found in common with the data presented here is the photographic plate measurements of five clusters in Hesser et al. (1986, 1984) and the Washington photometry of the three of these 5 clusters in Harris et al. (1992). The clusters in common are C36, C37, C38, C12 and C15 (numbering from Hesser et al. 1984, 1986). While in the Hesser et al. papers only the $\langle B \rangle$ magnitude is given, Harris et al. (1992) report also photographic V-band magnitudes as well as Washington photometry for C12, C36 and C37. In order to compare the Washington photometry with Bessell V magnitudes, we used the transformation equation (Harris et al. 1992): $V = T_1 + 0.66(M - T_1)$.

The clusters in common are among the brightest ones and in this study their magnitudes were measured on 2.2m+WFI images. The comparison between the data from the literature and our measurements is given in Tab. 3.2. In columns 1 and 2 the identification of the objects in common is given, B_{pg} magnitudes are from Hesser et al. (1984, 1986), V_{pg} and V_{Wash} are photographic magnitudes and the V-band brightness derived from Washington photometry. The last two columns present our measurements. There is a good agreement between the V-band magnitude derived from the Washington photometry and our measurements. The largest difference is for cluster C12 (f2.GC-81), which we measured 0.2 magnitudes fainter, probably due to the vicinity of a bad column on the WFI chip.

3.2.6 Selection of globular clusters

Typical Galactic globular clusters have mean King core radii $r_c = 2.3 \pm 3.6$pc, mean tidal radii $r_t = 45.1 \pm 32.4$pc and mean ellipticities $\epsilon = 0.07 \pm 0.01$ (June 1999 update of Harris 1996 catalogue; White & Shawl 1987).

Holland et al. (1999) used HST WFPC2 data to find globular clusters in the central parts of NGC 5128 and measured their structural parameters. They did not find any significant difference between the MW and NGC 5128 globular clusters' King core radii (r_c), tidal radii (r_t) and half-mass radii (r_h). They also found no trend in r_c, r_t or r_h with galactocentric distance, contrary to what one may expect due to stronger tidal forces closer to the galactic center. However, they measured higher mean ellipticities for their globular cluster candidates with respect to the MW globular clusters. Their samples are restricted only to the brighter clusters in NGC 5128, corresponding to the absolute magnitude $M_V = -6.4$. For comparison, the present sample reaches almost 2 magnitudes deeper.

We measured the FWHM and ellipticity for all the objects in Tab. 3.3 and 3.4 using the Sextractor programme (Bertin & Arnouts 1996). U-band images had variable PSF across the frame and the objects were, in some places, elongated, thus showing higher ellipticity than in the V-band images.

The FWHM *vs.* ellipticity for all the objects in Fields 1 and 2 is plotted in Fig. 3.4. The upper panel shows the

Table 3.3: Coordinates, photometry, FWHM (f_V and f_U), ellipticities (ϵ_V and ϵ_U) and projected galactocentric distance of globular cluster candidates.

name	alpha (2000)	delta (2000)	V mag	σ_V mag	U mag	σ_U mag	K_s mag	$\sigma_{K}s$ mag	f_V pix	f_U pix	ϵ_V	ϵ_U	R kpc	c
f1.GC-1	13:26:26.32	-42:48:55.8	19.58	0.00	20.49	0.04	···	···	8.70	7.40	0.21	0.24	17.07	
f1.GC-2	13:26:29.01	-42:49:44.7	20.77	0.03	23.26	0.30	···	···	4.11	4.34	0.05	0.3	16.79	
f1.GC-3	13:26:26.99	-42:49:50.4	22.41	0.04	24.5:	0.4	···	···	5.17	···	0.11	···	16.45	u
f1.GC-4	13:26:28.13	-42:51:29.5	21.02	0.03	24.17	0.31	···	···	4.09	3.49:	0.04	0.4:	15.41	u,n
f1.GC-5	13:26:33.52	-42:51:00.6	19.52	0.05	21.11	0.03	···	···	3.32	3.46	0.05	0.04	16.53	b
f1.GC-6	13:26:40.76	-42:50:18.2	21.10	0.10	24.1:	0.4	···	···	4.23	···	0.11	···	18.07	u,b,n
f1.GC-7	13:26:21.10	-42:48:41.4	19.59	0.00	21.32	0.04	···	···	4.61	4.77	0.06	0.09	16.62	
f1.GC-8	13:26:19.88	-42:49:11.5	20.27	0.10	19.44	0.05	···	···	3.80	3.84	0.15	0.27	16.06	b,n
f1.GC-9	13:26:21.36	-42:49:59.6	20.79	0.01	21.69	0.05	···	···	3.45	3.63	0.07	0.09	15.60	
f1.GC-10	13:26:14.80	-42:50:09.1	20.80	0.01	21.74	0.09	···	···	5.07	5.33	0.23	0.32	14.67	
f1.GC-11	13:26:09.76	-42:50:29.9	20.30	0.09	21.47	0.07	···	···	4.33	4.66	0.03	0.20	13.80	b
f1.GC-12	13:26:08.77	-42:51:28.5	19.70	0.05	21.15	0.07	···	···	4.30	4.86	0.16	0.14	12.87	
f1.GC-13	13:26:07.80	-42:52:00.3	18.39	0.10	19.30	0.01	···	···	···	3.45	···	0.19	12.31	v
f1.GC-14	13:26:09.45	-42:53:17.4	19.93	0.05	20.85	0.02	···	···	4.01	4.22	0.05	0.21	11.52	b
f1.GC-15	13:26:08.96	-42:53:42.4	19.44	0.01	20.93	0.06	···	···	4.49	5.32	0.09	0.08	11.14	
f1.GC-16	13:26:10.65	-42:53:42.4	18.47	0.10	19.80	0.02	···	···	···	3.58	···	0.19	11.37	v
f1.GC-17	13:26:22.03	-42:53:45.0	19.58	0.01	20.36	0.03	···	···	3.42	3.49	0.08	0.15	13.02	
f1.GC-18	13:26:22.04	-42:54:25.9	19.67	0.01	20.45	0.04	···	···	3.44	3.58	0.07	0.15	12.61	
f1.GC-19	13:26:05.27	-42:54:58.1	18.75	0.10	19.52	0.01	···	···	···	3.29	···	0.12	9.72	v
f1.GC-20	13:26:05.45	-42:55:22.4	21.51	0.05	23.33	0.10	···	···	5.52	4.29:	0.06	0.5:	9.47	u,e
f1.GC-21	13:26:10.60	-42:55:00.0	21.65	0.03	23.72	0.28	···	···	4.16	3.89:	0.07	0.4:	10.48	u
f1.GC-22	13:26:15.95	-42:55:00.5	18.09	0.10	18.95	0.01	···	···	···	3.34	···	0.17	11.30	v
f1.GC-23	13:26:23.81	-42:54:00.5	18.40	0.10	19.56	0.01	···	···	···	3.32	···	0.17	13.14	v
f1.GC-24	13:26:28.87	-42:52:35.9	19.33	0.00	20.17	0.02	···	···	3.73	3.84	0.12	0.11	14.8	
f1.GC-34	13:26:09.76	-42:53:16.8	21.27	0.10	23.22	0.30	···	···	4.45	5.63	0.09	0.32	11.57	b
f1.GC-38	13:26:20.06	-42:55:22.8	21.84	0.10	23.54	0.30	···	···	5.29	4.49:	0.13	0.46:	11.75	u,e
f2.GC-1	13:25:42.07	-43:12:44.2	23.10	0.07	24.9:	0.4	···	···	3.79	···	0.03	···	12.43	u
f2.GC-2	13:25:41.92	-43:10:40.7	19.52	0.10	20.40	0.03	···	···	···	3.61	···	0.14	10.33	v
f2.GC-3	13:25:40.82	-43:08:15.1	20.10	0.10	20.62	0.03	···	···	···	3.56	···	0.13	7.84	v
f2.GC-4	13:25:40.46	-43:07:16.9	19.77	0.01	21.13	0.06	···	···	2.81	3.59	0.05	0.08	6.87	
f2.GC-7	13:25:39.04	-43:12:56.7	22.41	0.05	25.8:	0.4	···	···	3.45	···	0.13	···	12.53	u,n
f2.GC-8	13:25:38.97	-43:10:40.9	21.55	0.02	23.27	0.14	···	···	3.62	5.95	0.07	0.08	10.20	
f2.GC-9	13:25:38.10	-43:13:01.2	20.59	0.01	21.66	0.07	···	···	3.07	4.00	0.06	0.13	12.57	
f2.GC-10	13:25:37.58	-43:12:32.3	23.16	0.10	23.90	0.20	···	···	3.15	3.68	0.15	0.38	12.06	u
f2.GC-11	13:25:36.65	-43:12:49.9	22.30	0.04	26.0:	0.4	···	···	3.49	···	0.05	···	12.34	u,n
f2.GC-13	13:25:35.84	-43:07:27.2	20.96	0.02	22.60	0.10	···	···	2.66	3.32	0.07	0.13	6.77	
f2.GC-14	13:25:35.82	-43:07:15.3	22.08	0.02	22.70	0.10	···	···	2.85	4.17	0.06	0.16	6.57	
f2.GC-15	13:25:35.55	-43:08:36.1	20.83	0.01	21.99	0.07	18.29	0.10	2.88	3.72	0.06	0.05	7.94	
f2.GC-17	13:25:34.01	-43:10:44.6	20.48	0.10	21.43	0.05	17.60	0.10	2.73	3.50	0.08	0.05	10.10	b
f2.GC-18	13:25:33.58	-43:07:18.5	21.44	0.04	22.41	0.09	17.96	0.19	2.85	4.02	0.05	0.12	6.54	
f2.GC-20	13:25:33.07	-43:07:00.6	21.26	0.04	22.84	0.04	17.68	0.09	3.18	4.62	0.07	0.18	6.21	b
f2.GC-21	13:25:33.03	-43:09:20.8	20.84	0.01	21.54	0.05	18.18	0.11	2.86	3.70	0.04	0.09	8.63	
f2.GC-22	13:25:32.76	-43:11:51.1	21.13	0.04	25.4:	0.5	···	···	3.26	···	0.05	···	11.23	u,n
f2.GC-23	13:25:32.71	-43:07:01.6	18.80	0.10	20.03	0.02	15.60	0.03	···	3.50	···	0.16	6.22	v,b
f2.GC-24	13:25:32.25	-43:07:16.5	20.12	0.01	20.95	0.04	17.71	0.08	2.83	3.56	0.05	0.08	6.46	
f2.GC-26	13:25:30.35	-43:11:48.4	18.58	0.10	19.98	0.02	···	···	···	3.88	···	0.19	11.15	v
f2.GC-28	13:25:30.10	-43:06:54.0	21.49	0.03	22.56	0.16	17.05	0.08	3.49	4.35	0.13	0.08	6.02	
f2.GC-29	13:25:29.68	-43:11:41.7	19.76	0.10	20.62	0.04	···	···	···	3.61	···	0.15	11.03	v

Table 3.3: continuation.

name	alpha (2000)	delta (2000)	V mag	σ_V mag	U mag	σ_U mag	K_s mag	$\sigma_K s$ mag	f_V pix	f_U pix	ϵ_V	ϵ_U	R kpc	c
f2.GC-31	13:25:29.38	-43:07:41.1	20.66	0.02	21.47	0.08	18.24	0.12	2.97	3.74	0.09	0.13	6.84	
f2.GC-34	13:25:28.06	-43:06:46.3	22.40	0.09	23.12	0.17	···	···	3.17	3.68	0.02	0.15	5.87	
f2.GC-35	13:25:26.75	-43:09:39.7	19.54	0.00	20.44	0.03	17.00	0.05	3.40	4.01	0.10	0.12	8.90	
f2.GC-36	13:25:26.68	-43:08:52.7	19.72	0.01	20.57	0.03	17.12	0.06	4.50	5.13	0.09	0.08	8.08	
f2.GC-40	13:25:24.32	-43:07:58.5	19.59	0.10	20.58	0.04	16.72	0.04	···	3.75	···	0.16	7.15	v
f2.GC-41	13:25:22.61	-43:07:37.6	21.43	0.04	23.29	0.19	17.65	0.09	3.85	5.36	0.08	0.16	6.83	
f2.GC-43	13:25:21.26	-43:10:03.0	21.41	0.02	21.78	0.10	17.62	0.12	4.91	5.48	0.12	0.13	9.38	
f2.GC-46	13:25:20.63	-43:06:35.6	20.27	0.20	21.50	0.20	···	···	3.11	3.73	0.07	0.07	5.83	e
f2.GC-47	13:25:19.90	-43:07:43.5	20.22	0.01	21.78	0.05	16.75	0.04	3.25	4.04	0.05	0.15	7.02	
f2.GC-48	13:25:19.42	-43:11:51.0	21.09	0.02	21.63	0.09	···	···	3.99	4.89	0.21	0.13	11.29	
f2.GC-49	13:25:18.79	-43:07:11.1	22.21	0.23	23.59	0.15	18.88	0.28	5.07	···	0.16	···	6,52	b,u
f2.GC-50	13:25:18.79	-43:10:53.7	22.61	0.08	24.4:	0.3	18.39	0.11	3.31	···	0.06	···	10.32	u
f2.GC-52	13:25:17.84	-43:13:21.4	21.94	0.12	22.44	0.08	···	···	4.45	6.57	0.19	0.31	12.90	
f2.GC-53	13:25:17.28	-43:08:38.6	19.87	0.10	20.69	0.03	16.61	0.08	3.11	3.50	0.07	0.12	8.07	b
f2.GC-54	13:25:16.91	-43:09:27.4	19.48	0.10	20.41	0.03	16.55	0.05	···	3.67	···	0.10	8.91	v
f2.GC-57	13:25:15.19	-43:08:38.8	20.86	0.02	22.10	0.05	17.58	0.08	2.86	3.72	0.07	0.14	8.18	
f2.GC-59	13:25:13.82	-43:07:32.3	20.61	0.02	22.04	0.11	17.43	0.07	3.09	4.01	0.05	0.08	7.17	b
f2.GC-60	13:25:12.90	-43:06:39.2	20.50	0.05	23.52	0.16	···	···	2.51	4.30	0.04	0.01	6.39	n
f2.GC-61	13:25:12.85	-43:07:58.9	18.23	0.10	19.64	0.01	15.12	0.02	···	3.46	···	0.14	7.67	v
f2.GC-63	13:25:12.76	-43:10:42.7	20.75	0.02	22.39	0.19	17.77	0.08	4.45	5.95	0.09	0.19	10.38	
f2.GC-65	13:25:10.39	-43:08:11.1	22.74	0.09	23.73	0.25	···	···	3.00	5.23:	0.07	0.43:	8.04	u
f2.GC-66	13:25:10.11	-43:06:41.7	21.05	0.02	23.43	0.15	···	···	2.50	4.79:	0.01	0.20	6.68	
f2.GC-69	13:25:09.07	-43:10:01.4	19.87	0.01	21.23	0.04	···	···	2.78	3.64	0.10	0.07	9.92	
f2.GC-70	13:25:08.92	-43:08:53.3	20.30	0.01	21.33	0.05	···	···	3.67	4.51	0.06	0.06	8.83	
f2.GC-71	13:25:08.78	-43:09:09.1	19.42	0.10	20.43	0.03	···	···	···	3.88	···	0.12	9.09	v
f2.GC-74	13:25:07.48	-43:12:28.6	20.43	0.01	21.40	0.07	···	···	2.89	4.18	0.12	0.19	12.44	
f2.GC-75	13:25:07.41	-43:07:34.8	21.83	0.04	23.36	0.17	···	···	4.10	5.80	0.13	0.40	7.74	u
f2.GC-76	13:25:07.31	-43:08:29.3	20.67	0.01	21.80	0.07	···	···	3.78	4.28	0.02	0.15	8.58	
f2.GC-79	13:25:05.88	-43:12:02.2	22.70	0.07	23.97	0.37	···	···	3.19	5.25:	0.11	0.46:	12.11	u
f2.GC-81	13:25:05.70	-43:10:30.2	18.01	0.20	19.48	0.01	···	···	···	3.83	···	0.11	10.63	v

comment:
- b = near bright (saturated) star
- e = near edge of the field
- u = marginal or no detection
- v = object saturated in V; V mag from WFI data
- n = object does not satisfy all the criteria for globular cluster classification

Table 3.4: Same as Tab. 3.3, but for other extended objects, some of which might as well be globular clusters.

name	alpha (2000)	delta (2000)	V mag	σ_V mag	U mag	σ_U mag	K_s mag	$\sigma_K s$ mag	f_V pix	f_U pix	ϵ_V	ϵ_U	R kpc	c
f1.GC-25	13:26:28.27	-42:50:03.9	20.43	0.10	19.68	0.10	···	···	4.65	4.42	0.29	0.32	16.45	
f1.GC-26	13:26:25.48	-42:51:07.5	21.15	0.11	21.23	0.04	···	···	7.63	9.06	0.39	0.33	15.3	
f1.GC-27	13:26:30.45	-42:52:10.8	18.33	0.10	19.19	0.01	···	···	···	3.62	···	0.31	15.3	v
f1.GC-28	13:26:14.46	-42:49:34.1	20.20	0.05	24.13	0.30	···	···	4.85	···	0.18	···	15.12	u
f1.GC-29	13:26:07.23	-42:51:38.1	17.09	0.10	18.92	0.01	···	···	···	2.84	···	0.11	12.55	v

Table 3.4: continuation.

name	alpha (2000)	delta (2000)	V mag	σ_V mag	U mag	σ_U mag	K_s mag	$\sigma_K s$ mag	f_V pix	f_U pix	ϵ_V	ϵ_U	R kpc	c
f1.GC-30	13:26:16.36	-42:54:28.5	21.37	0.02	21.84	0.10	···	···	6.05	7.33	0.38	0.55	11.69	
f1.GC-31	13:26:17.40	-42:54:14.5	19.24	0.10	19.76	0.02	···	···	···	2.99	0.10	···	12.00	v
f1.GC-32	13:26:06.37	-42:53:54.4	20.74	0.04	21.20	0.03	···	···	2.83	3.26	0.08	0.23	10.64	
f1.GC-33	13:26:04.74	-42:54:00.6	22.90	0.10	22.91	0.20	···	···	4.53	5.51	0.14	0.38	10.35	u,e
f1.GC-35	13:26:07.81	-42:55:05.6	19.95	0.00	21.19	0.04	···	···	2.80	3.15	0.08	0.18	10.00	
f1.GC-36	13:26:11.89	-42:54:51.8	16.95	0.10	19.35	0.01	···	···	···	3.10	···	0.21	10.76	v
f1.GC-37	13:26:14.14	-42:54:37.6	20.91	0.02	21.09	0.04	···	···	5.41	6.56	0.25	0.32	11.26	
f1.GC-39	13:26:26.66	-42:55:19.3	17.01	0.10	19.49	0.01	···	···	···	2.93	···	0.21	12.88	v
f1.GC-40	13:26:09.63	-42:54:26.2	22.32	0.05	23.22	0.23	···	···	4.15	4.11	0.11	0.09	10.71	
f1.GC-41	13:26:07.05	-42:52:37.5	17.14	0.10	18.07	0.01	···	···	···	2.98	···	0.17	11.72	v
f1.GC-42	13:26:05.18	-42:52:34.0	16.59	0.10	17.94	0.00	···	···	···	3.10	···	0.18	11.55	v
f1.GC-43	13:26:06.78	-42:52:43.2	17.62	0.10	18.30	0.01	···	···	···	2.97	···	0.15	11.61	v
f1.GC-44	13:26:11.93	-42:53:02.9	18.65	0.10	19.25	0.01	···	···	···	2.94	···	0.14	12.03	v
f1.GC-45	13:26:07.65	-42:54:28.3	17.76	0.10	19.16	0.01	···	···	···	3.04	···	0.20	10.41	v
f1.GC-46	13:26:07.22	-42:54:20.7	17.43	0.10	18.24	0.00	···	···	···	3.16	···	0.22	10.43	v
f1.GC-47	13:26:06.43	-42:54:21.3	18.88	0.10	20.26	0.02	···	···	···	3.10	···	0.22	10.32	v
f1.GC-48	13:26:06.19	-42:54:30.3	18.54	0.10	19.25	0.01	···	···	···	3.08	···	0.20	10.18	v
f1.GC-49	13:26:10.13	-42:54:56.4	19.89	0.10	21.16	0.05	···	···	···	3.27	···	0.22	10.45	v
f1.GC-50	13:26:14.97	-42:55:21.4	17.57	0.10	18.26	0.15	···	···	···	3.08	···	0.23	10.94	v
f2.GC-5	13:25:40.13	-43:10:13.3	21.96	0.03	26.3:	0.5	···	···	4.12	···	0.23	···	9.78	u
f2.GC-6	13:25:39.11	-43:12:11.6	21.34	0.02	23.11	0.11	···	···	2.40	3.78	0.04	0.14	11.76	
f2.GC-12	13:25:36.39	-43:08:02.7	21.47	0.07	22.35	0.16	···	···	4.98	5.32	0.29	0.32	7.40	
f2.GC-16	13:25:34.40	-43:12:04.2	23.58	0.13	23.58	0.21	···	···	3.95	5.24	0.16	0.46	11.49	u
f2.GC-19	13:25:33.25	-43:10:19.6	22.67	0.06	24.6:	0.5	17.75	0.11	4.01	···	0.17	···	9.65	u
f2.GC-25	13:25:31.09	-43:10:27.6	21.13	0.02	24.34	0.24	17.00	0.10	3.54	4.01	0.10	0.09	9.75	u
f2.GC-27	13:25:30.30	-43:11:26.6	21.90	0.03	24.04	0.30	···	···	4.84	···	0.09	···	10.77	u
f2.GC-30	13:25:29.42	-43:09:21.9	22.36	0.06	24.60	0.26	20.03	0.47	3.58	···	0.03	···	8.59	u
f2.GC-32	13:25:29.00	-43:12:50.9	22.44	0.05	23.67	0.19	···	···	6.74	3.40:	0.43	0.39	12.23	
f2.GC-33	13:25:28.26	-43:06:40.0	22.31	0.06	24.71	0.27	···	···	4.26	···	0.04	···	5.76	u
f2.GC-37	13:25:24.77	-43:06:54.8	22.36	0.09	24.07	0.26	17.84	0.18	4.36	···	0.17	···	6.04	u
f2.GC-38	13:25:24.66	-43:11:50.6	21.95	0.03	23.48	0.38	···	···	4.06	6.91:	0.10	0.49	11.19	u
f2.GC-39	13:25:24.61	-43:08:15.2	22.97	0.11	26.1:	0.6	16.90	0.07	4.16	···	0.26	···	7.44	u
f2.GC-42	13:25:21.46	-43:11:43.8	20.80	0.20	21.80	0.08	···	···	6.46	7.17	0.42	0.45	11.12	
f2.GC-44	13:25:21.24	-43:06:57.0	20.70	0.01	24.66	0.32	16.92	0.08	2.42	4.31	0.03	0.21	6.17	
f2.GC-45	13:25:21.03	-43:08:31.9	21.83	0.04	21.98	0.07	18.14	0.08	5.72	5.57	0.29	0.25	7.81	
f2.GC-51	13:25:18.00	-43:06:57.6	22.09	0.05	23.07	0.11	17.86	0.10	4.23	5.19	0.39	0.31	6.33	
f2.GC-55	13:25:16.76	-43:13:13.5	19.38	0.00	21.16	0.05	···	···	3.65	4.98	0.08	0.26	12.79	
f2.GC-56	13:25:16.72	-43:13:18.4	20.63	0.20	22.19	0.10	···	···	3.98	5.62	0.26	0.14	12.88	
f2.GC-58	13:25:14.84	-43:11:00.3	22.81	0.09	22.95	0.16	18.22	0.10	4.58	6.75	0.33	0.41	10.58	
f2.GC-62	13:25:12.81	-43:12:00.7	21.51	0.05	25.8:	0.5:	···	···	5.55	···	0.35	···	11.70	u
f2.GC-64	13:25:12.17	-43:08:48.7	21.31	0.10	23.43	0.20	17.30	0.09	6.31	···	0.15	···	8.52	u
f2.GC-67	13:25:09.32	-43:09:58.4	22.88	0.10	23.99	0.12	···	···	5.15	···	0.15	···	9.85	u
f2.GC-68	13:25:09.06	-43:13:18.4	20.44	0.01	22.00	0.09	···	···	7.25	8.77	0.46	0.27	13.19	
f2.GC-72	13:25:08.11	-43:10:37.4	21.00	0.03	21.51	0.07	···	···	6.21	6.69	0.36	0.19	10.57	
f2.GC-73	13:25:08.03	-43:09:51.8	22.99	0.12	23.88	0.17	···	···	5.32	···	0.16	···	9.84	u
f2.GC-77	13:25:06.66	-43:08:57.9	21.16	0.03	23.41	0.19	···	···	5.73	4.25	0.18	0.29	9.09	u
f2.GC-78	13:25:06.11	-43:06:51.9	22.06	0.05	24.4:	0.5	···	···	3.39	···	0.08	···	7.23	u
f2.GC-80	13:25:05.72	-43:06:50.9	20.96	0.02	23.91	0.40	···	···	2.52	4.51	0.08	0.18	7.26	

comment: b = near bright (saturated) star
e = near edge of the field
u = marginal or no detection
v = object saturated in V; V mag is from WFI data

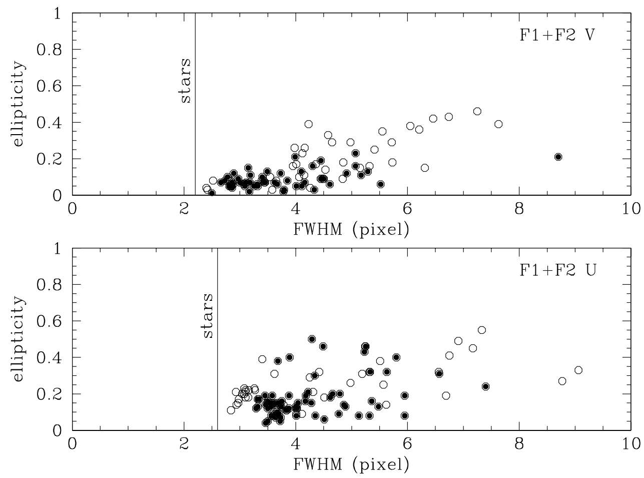

Figure 3.4: FWHM *vs.* ellipticity: objects retained as good globular cluster candidates after the visual inspection of the residual images of Field 1 and 2 are plotted with filled circles. Empty circles are used for other extended objects.

results obtained from the V-band, the lower panel the ones obtained from the U-band. The vertical line indicates the mean FWHM for stars. The objects from Tab. 3.4, some of which might as well be blended stars or galaxies are plotted as open symbols, while the filled dots were used for objects from Tab. 3.3 (i.e. good candidates). Objects that were slightly saturated on the V-band VLT images are shown only in the U-band diagram (lower panel). Due to the poorer seeing conditions during the observations with the 2.2m telescope, their profiles are more similar to the stellar profiles on the WFI images.

In order to classify an object as a globular cluster all of the following criteria were imposed:

1. non-stellar PSF that leaves ring-like residuals on subtracted images (Fig. 3.1);

2. FWHM>mean stellar FWHM and ellipticity(V)<0.4 (Fig. 3.4)

3. $0 < (U - V)_0 < 2.5$ (Fig. 3.6)

The selection of objects with ellipticity measured on the V-band images smaller than 0.4 excludes galaxies from the sample. The color range in the last criterion corresponds to the observed range of the $(U-V)_0$ colors for the MW and M31 globular clusters. This range does not include the reddest M31 clusters (Fig. 3.6) because they were corrected only for the foreground average extinction towards M31 and thus might still be reddened. The cutoff at $(U-V)_0 = 2.5$ takes into account the bulk of M31 clusters around $V_0 \sim 21$. The objects that did not pass all of the above criteria were flagged with "n" in Tab. 3.3.

3.3 Color-magnitude and color-color diagrams

The UV color-magnitude diagram (CMD) for all the objects is presented in Fig. 3.5. As before, the objects retained as good candidates after visual inspection of the images are plotted as filled symbols and the rest as open symbols. The objects from Field 1 are plotted as diamonds, the ones from Field 2 as triangles. Vertical lines indicate the color range within which the MW and majority of M31 globular clusters are located. Note that several open symbols are found in the same area of the CMD as globular clusters. Spectroscopic observations are necessary to assess the real nature of these objects.

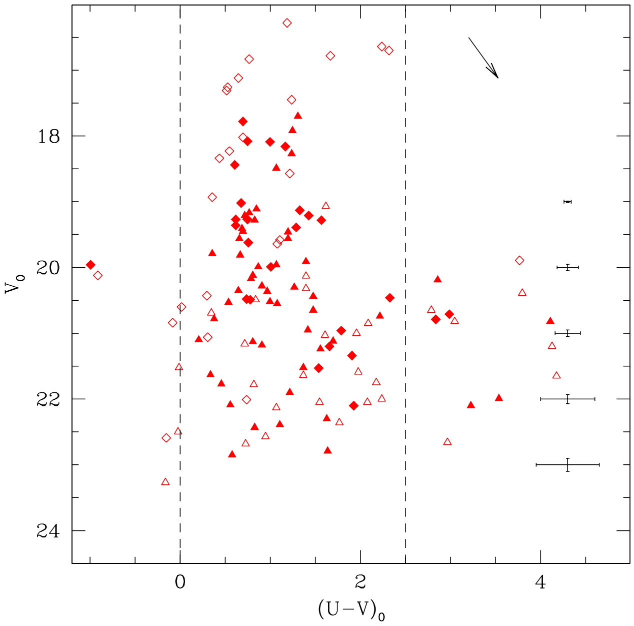

Figure 3.5: Color-Magnitude Diagram for all non-stellar objects found in Field 1 (diamonds) and in Field 2 (triangles). Objects retained as good globular cluster candidates after the visual inspection of images are plotted as filled symbols and the rest as open ones.

The object at $(U-V)_0 = -0.99$ and $V_0 = 19.96$ (f1.GC-8) is located very close to the area where a large number of bright young blue stars were found (Rejkuba et al. 2001a). It might be a young object, precursor of a globular cluster, similar to the ones found in other merging galaxies (e.g. Whitmore et al. 1999), as well as to some clusters found in the central regions of NGC 5128 (Holland et al. 1999).

There is a number of objects brighter than $V < 17.5$ that were all identified in Field 1. Probably these are bright stars blended with some faint companions. They all appear saturated in the V-band VLT images and were found in the lower right corner (south-west) of Field 1 on U-band images. Their FWHM, that was larger than stellar, is probably an artifact due to the distortion of the PSF in that part of the chip.

Figure 3.6 shows the CMD for all NGC 5128 globular clusters (filled circles) that satisfy all the selection criteria. This CMD is compared with the ones of the MW (stars) and M31 (squares) globular clusters. Globular clusters populate a similar region of the CMD in the three galaxies. Data for the MW clusters were taken from the web page of W. Harris (1996). M31 clusters are from the catalogue of Barmby et al. (2000). We did not take into account globular clusters with colors bluer than B−V= 0.55, as they might be younger objects (Barmby et al. 2000). The magnitudes were corrected for the mean reddening towards M31 (E(B−V) = 0.08). For the globular cluster candidates in NGC 5128 a mean foreground reddening of E(B−V) = 0.1 (Burstein & Heiles 1982; Schlegel et al. 1998) was used. The reddening vector plotted in the upper right corner corresponds to E(B−V) = 0.2.

By constraining the colors to be within the range of the reddest MW and bluest M31 globular cluster colors (cf. the third selection criterion) we exclude distant compact galaxies (Barrientos 2000). The total number of *bona fide* globular cluster candidates is 71, with 23 in Field 1 and 48 in Field 2. Only those are taken into account in the further analysis.

K_s band magnitudes were measured on SOFI images for 23 of the *bona fide* globular cluster candidates and 10 of the extended objects, some of which might also be globular clusters. The U−V color is strongly dependent on both metallicity and age (Buzzoni 1995; Kurth et al. 1999; Maraston 1998). Adding the K-band magnitude

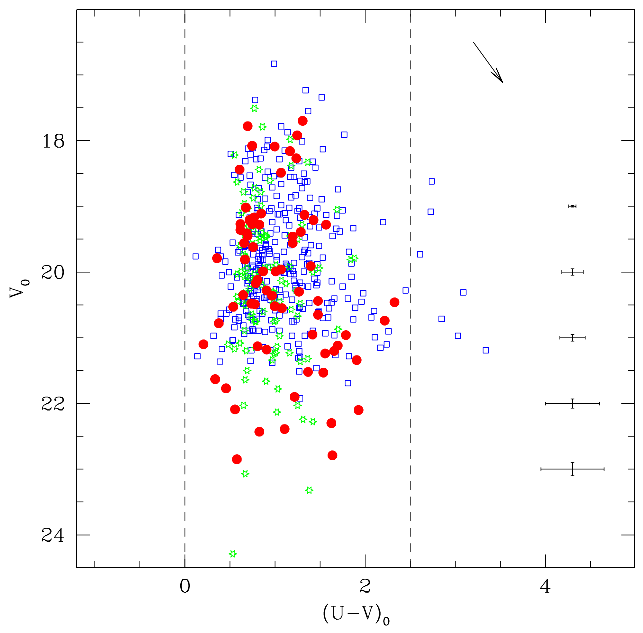

Figure 3.6: Color-magnitude diagrams for globular clusters in NGC 5128 (filled circles) compared to the MW (stars) and M31 globular clusters (open squares).

information it is possible to disentangle the young from the old objects. The color-color plot is shown in Fig. 3.7. Filled dots are used to denote globular cluster candidates that satisfied all of the classification criteria. The lines are isochrones of evolutionary synthesis models of simple stellar populations (SSP) calculated for a Salpeter IMF and a range of metallicities from Z=0.0001 to 0.05 (see caption for the exact metallicities plotted for each model). The four different models displayed on panels (a), (b), (c) and (d) are from Kurth et al. (1999), Bruzual & Charlot (2001), Maraston (2001) and Worthey (1994), respectively. The ages are indicated with numbers denoting Gyr next to the lines. Unfortunately the models do not allow one to discriminate between ages in the range of 5-20 Gyr. However, it is comforting to see that almost all the objects are concentrated towards the isochrones in excess of 1 Gyr. This is additional evidence that they are indeed globular clusters. A spread of metallicities of more than 1.5 dex is also evident.

In Fig. 3.7 most of the clusters lie slightly to the right and below the model lines. There are two possible explanations. First, a difference with the SSP models, particularly significant in U-V and B-V colors, has already been pointed out by Barmby & Huchra (2000). They suggested U fluxes from the stellar libraries, systematic problems with modeling HB color and observational errors as possible causes of this offset. Second, in the data presented here additional offset may arise from the difference between the Bessel and Johnson U-band transmission curves (Bessell 1995).

3.4 Luminosity function

The V-band GCLF for NGC 5128 is compared to the ones of the MW and M31 in Fig. 3.8. The actual shape of the luminosity function depends on the size of the bins and on the bin-centers. Statistically it is possible to compare them independently of binning using the Kolmogorov-Smirnov (KS) test. In Fig. 3.9 the cumulative distribution functions for the three GCLFs are shown. The thick line is used for NGC 5128, thin line for the MW and dotted line for M31. Absolute magnitudes for NGC 5128 globular clusters were calculated using the distance modulus

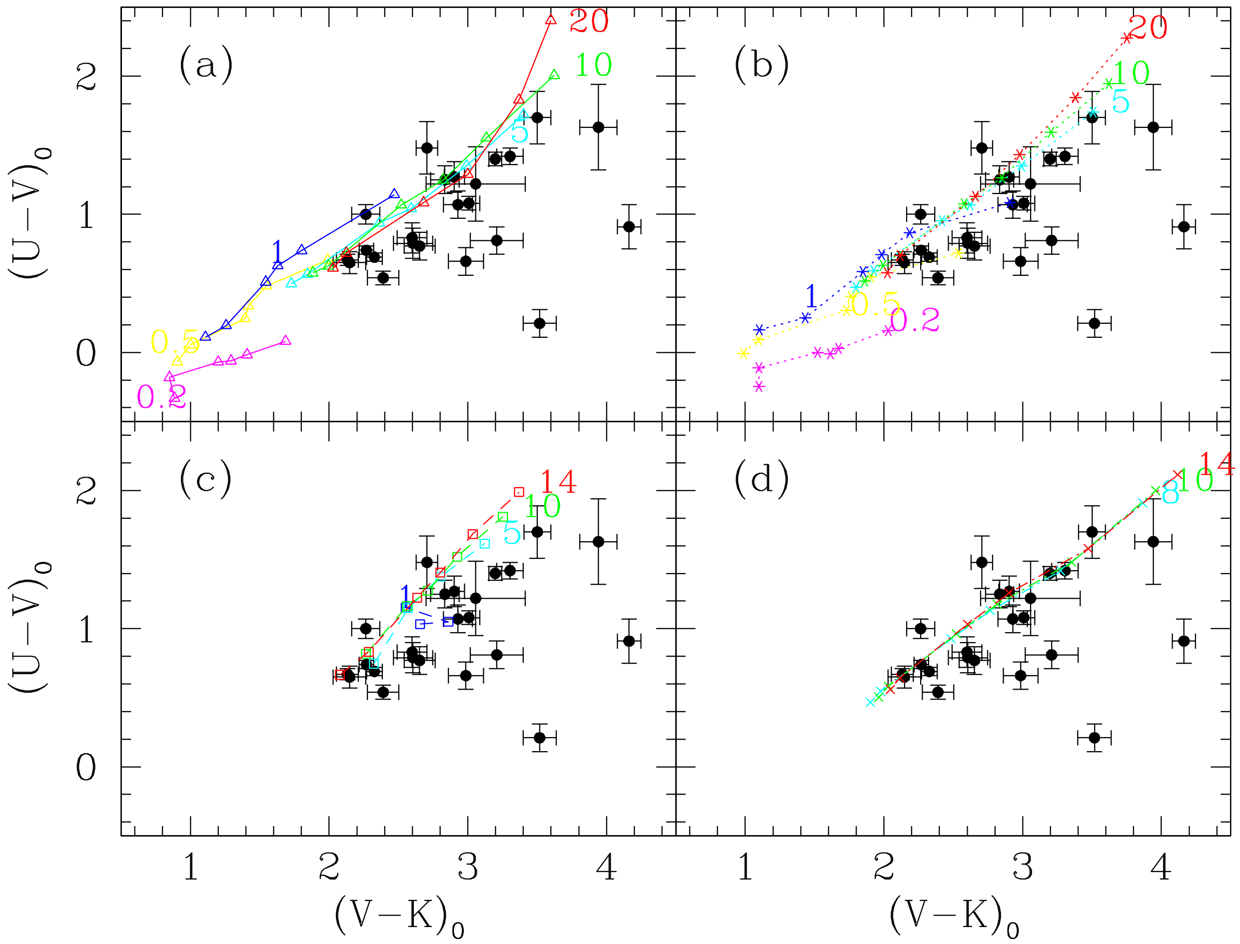

Figure 3.7: Color-color diagram for globular clusters in NGC 5128 (filled circles). The lines are the isochrones of SSP models. The number next to each isochrone indicate the age in Gyr. Each isochrone is plotted for a range of metallicities and for a Salpeter IMF. The four different models are from: (a) Kurth et al. (1999) for Z=0.0001, 0.0004, 0.008, 0.004, 0.02 and 0.05; (b) Bruzual & Charlot (2001) for the same range of age and Z as the previous model; (c) Maraston (2001) for [Fe/H]= −2.25 (only 14 Gyr isochrone), −1.35, −0.55, −0.33, 0.00 and 0.35 dex; and (d) Worthey (1994) for Z=0.0002, 0.0004, 0.008, 0.004, 0.02 and 0.05.

value of $(m-M)_0 = 27.8$ (Soria et al. 1996) and reddening value of $E(B-V) = 0.1$.

The KS statistic measures the maximum value of the absolute difference between two cumulative distribution functions from which a probability that the two distributions are drawn from a common distribution can be calculated. The probability that the GCLF of NGC 5128 matches the one of the MW is 89%, comparable to the probability that M31 GCLF matches the MW one (85%). The difference is slightly bigger in the U-band distributions (Fig. 3.9 right panel), but it is also probable that the three luminosity functions are essentially similar for the three galaxies. We conclude that the NGC 5128 GCLF is as similar (or as different) to the MW GCLF as the M31 one.

Usually the GCLF is fitted with a gaussian or t_5 distribution function in order to determine its peak magnitude. It should be noted, however, that the reasonably complete luminosity functions are known only for the two spiral galaxies, the MW and M31. Both of these GCLFs appear to depart from the gaussian distribution (Ashman et al. 1995), while there is no complete GCLF for any elliptical galaxy. The dependence of the turn–over magnitude on the detection of the faint end of GCLF is discussed in Ashman et al. (1995). The determination of the turn–over magnitude for NGC 5128 is left for a subsequent paper where the complete analysis of WFI data is going to be presented.

The detection of the faint end of the GCLF in an elliptical galaxy is also important from the dynamical point of view. The faint globular clusters are typically also the less massive ones and their presence in the deep potential of a giant elliptical puts strong constraints on the potential itself as well as on the effects of tidal forces in the halo. Unfortunately the faintest globular clusters, corresponding to the MW Pal 1, AM 4, Terzan 1, Pal 13 are probably not detectable on FORS1 images (see Sect. 3.2.4).

The processes that destroy globular clusters can be divided into internal, like two-body relaxation and mass loss during stellar evolution, and external. The external processes depend greatly on environment and therefore on the position of the clusters in the galaxy. While tidal shocks preferentially destroy less dense clusters, dynamical friction brings more massive clusters very close to galactic centre. Both of these external processes are much stronger in the inner part of the galaxy. According to theoretical simulations (Vesperini 2000, Ostriker & Gnedin 1997) in a galaxy like NGC 5128, with the total mass of $\sim 4 \times 10^{11}$ $M_\odot$ (Israel 1998) and $R_e = 5.24$ kpc (Dufour et al. 1979), a strong disruption and mass loss are efficient only within a galactocentric distance of $1 - 2$ R_e, while at larger radii most of the mass loss is due to effects of stellar evolution. Field 1 is located at $2 - 3.5$ R_e and Field 2 at $1.2 - 2.3$ R_e. While the dynamical effects may still be important for Field 2 clusters, they are probably completely negligible for clusters in the outer field. It is not possible to quantify these effects by simple comparison of the two subsamples, because of the small number statistics.

3.5 Color and metallicity distributions

The $(U-V)_0$ color histogram for 71 globular clusters in NGC 5128 indicates a bimodal distribution (Fig. 3.10). Note that the $(U-V)_0$ color distribution of the MW globular clusters does not show bimodality while the one of M31 does. The $(U-V)_0$ color distribution of the MW globular clusters is in fact biased due to lack of U-magnitude and higher reddening values (only clusters with $E(B-V) < 0.5$ are plotted) of bulge (more metal-rich and redder) cluster. The blue peaks of the MW, M31 and NGC 5128 globular cluster color distributions coincide. The blue cutoff in the three galaxies is quite sharp and is driven principally by the colors of blue horizontal branch stars. The red side of the color distribution is much broader. In M31 it can be partially driven by differential reddening inside the host spiral galaxy, because the colors for M31 clusters presented here were corrected only for the mean foreground reddening of $E(B-V)=0.08$. Examination of the stellar $(U-V)$ *vs.* $(V-K)$ diagram in the two fields in NGC 5128 indicates that the amount of reddening does not vary much in the halo of this giant elliptical (Rejkuba et al. 2001b, Chapter 4). Harris et al. (1992) and Holland et al. (1999) also found more red (metal-rich) clusters in their NGC 5128 data.

The color distribution of the MW globular clusters in Fig. 3.10, being dominated by halo clusters, is representative of the GCS of our Galaxy as if observed from outside. The NGC 5128 clusters in Harris et al. (1992) and in this work belong as well to the halo population. The differences in the color (metallicity) distribution of clusters and stars in the halo of a spiral, like MW and a gE like NGC 5128, are reflected in Fig. 3.10 with a much larger

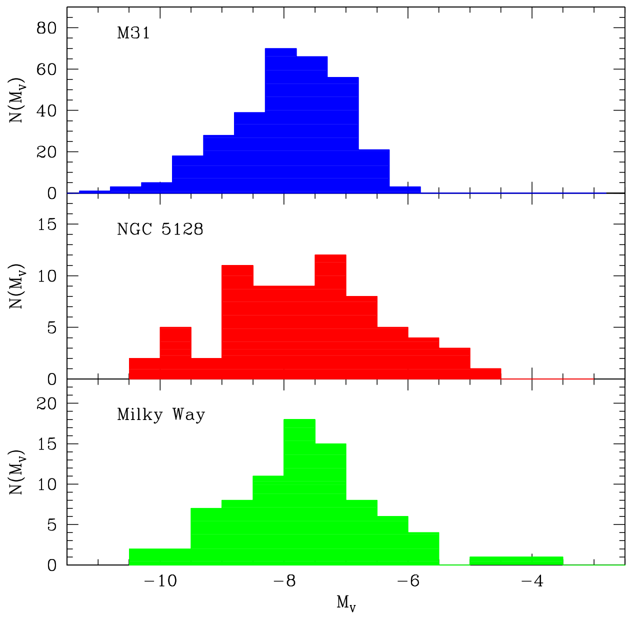

Figure 3.8: From top to bottom: V-band GCLF for M31, NGC 5128 and MW.

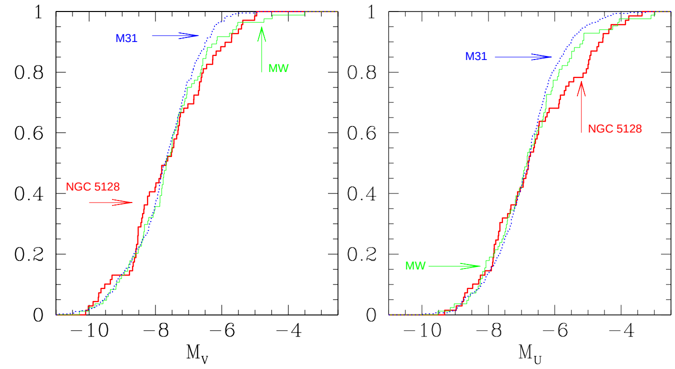

Figure 3.9: Kolmogorov-Smirnov statistic: The cumulative distribution function for NGC 5128 (thick line) is constructed from the V-band GCLF (left panel) and U-band GCLF (right panel) and compared with the ones of the MW (thin line) and M31 (dotted line).

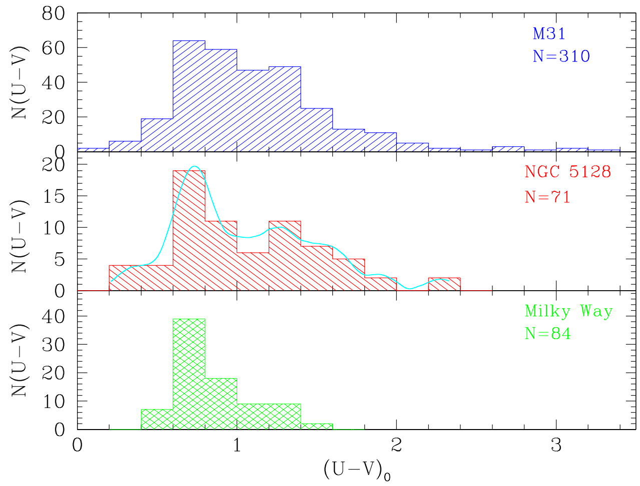

Figure 3.10: The color distribution for M31, NGC 5128 and the MW. The line overplotted on the NGC 5128 histogram is the best nonparametric kernel estimate (Silverman 1986) of the color distribution.

metallicity spread in gE galaxy.

The line overplotted on the color distribution of NGC 5128 is the best nonparametric kernel estimate (Silverman 1986) of the color distribution used to measure accurately the blue and the red peaks of the distribution. The blue and red peaks are measured at $(U-V)_0 = 0.73 \pm 0.01$ and 1.28 ± 0.01, respectively.

From the color-color diagram (Fig. 3.7) it is obvious that the globular clusters in NGC 5128 are older than 1 Gyr. Unfortunately, the models do not allow one to better constrain the ages (Fig. 3.7; see also Barmby & Huchra 2000). Assuming that the globular clusters in NGC 5128 have similar ages as the MW ones, one can use the Galactic globular clusters to calibrate the metallicity scale. It is known that for the very low and very high metallicities the color-metallicity relation cannot be expressed by a simple linear function, but extrapolation from lower metallicities towards the higher ones by using the higher polynomial fit might lead to unphysical results. Thus we prefered to make a linear fit with gaussian errors in $\sigma(Fe/H) = 0.1$ in order to calibrate the metallicity as a function of intrinsic $(U-V)_0$ color. Only MW globular clusters from W. Harris (1996) web list with $E(B-V) < 0.5$ (equivalent to $E(U-V) < 0.82$; Rieke & Lebofsky 1985) were used in the fit. The following color-metallicity relation is based on the Zinn & West (1984) scale and is valid only for the range of metallicities observed in the MW globular clusters (Fig. 3.11):

$$[Fe/H] = -2.93(\pm 0.07) + 1.79(\pm 0.07) \times (U - V)_0 \tag{3.4}$$

In the Fig. 3.11 linear $(U-V)_0$ *vs.* [Fe/H] color-metallicity relation (Eq. 3.4; full line) is plotted along with the evolutionary synthesis models of simple stellar populations (short dashed lines) from Kurth et al. (1999). Using the empirical linear calibration and the SSP models we calculate the metallicity of the two peaks in the color-distribution. The blue and the red peak correspond to [Fe/H]$= -1.7$ dex and [Fe/H]$= -0.6$ dex using the linear relation (Eq. 3.4) and to [Fe/H]$= -1.7$ dex and [Fe/H]$= -0.5$ dex using the models.

Although it is not obvious from the $(U-V)_0$ color distribution, but rather from the spectroscopically measured [Fe/H] distribution, the metallicity distribution of MW globular clusters is bimodal with the metal-poor and metal-rich peaks at -1.6 and -0.6 dex respectively (Harris 2000). These values are practically the same as the ones derived here for globular clusters in NGC 5128 from the $(U-V)_0$ colors. On the other hand, on the basis of Washington photometry of 62 globular clusters in NGC 5128, Harris et al. (1992) conclude that *"in both the range and distribution of abundance, the NGC 5128 GCS is clearly different from the Galactic GCS and quite similar to that of the large elliptical NGC 1399"*. They measured a mean metallicity of $\langle [\mathrm{Fe/H}]_{C-T_1} \rangle = -0.8 \pm 0.2$ dex, substantially more metal-rich than the mean value for the MW GCS. They, however, mention that the values

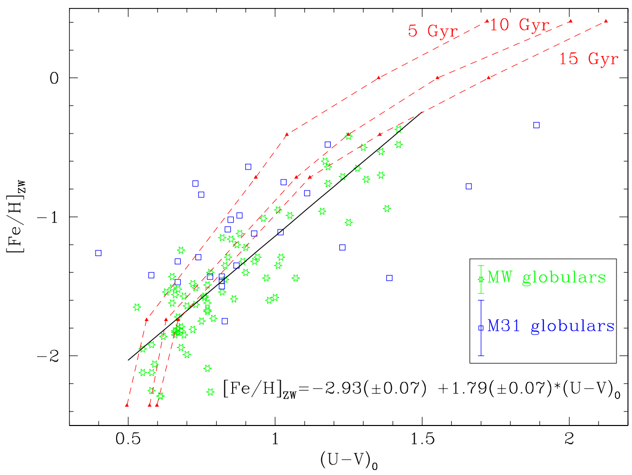

Figure 3.11: The $(\mathrm{U}-\mathrm{V})_0$ *vs.* [Fe/H] color-metallicity linear relation (full line) derived from the MW globular clusters with E(B−V)< 0.5 (stars). The M31 clusters with spectroscopic metallicities and accurate (U-V) colors plotted for comparison (squares) were not used for the fit. Typical errors in measured metallicities are plotted on in the box. Short dashed lines are the SSP models from Kurth et al. (1999) for ages of 5, 10 and 15 Gyrs, from blue to left, respectively. Each model spans metallicities from Z=0.0001 to 0.05.

exceeding [Fe/H]~ -0.25 are extrapolated, a fact that is also true in the metallicity calibration from $(\mathrm{U}-\mathrm{V})_0$ color distribution. The extrapolation leads to large errors and a possible overestimation of abundances of the metal-rich clusters. Because of this we do not report here the metallicities of individual clusters.

Note also that we restricted the $(\mathrm{U}-\mathrm{V})_0$ color to be within the range observed in MW and bulk of the M31 globular clusters. In this way the sample was selected to be as clean as possible from the very compact and red galaxies. It is not surprising that the clusters with supra-solar abundances are not present, reducing the mean abundance of the sample. However, relaxing the red color cut and adding the 6 "good" globular cluster candidates redder than $(\mathrm{U}-\mathrm{V})_0 = 2.5$ (filled symbols in Fig. 3.5) the mean of the color distribution shifts from $\langle(\mathrm{U}-\mathrm{V})_0\rangle = 1.05 \pm 0.45$ to $\langle(\mathrm{U}-\mathrm{V})_0\rangle = 1.22 \pm 0.75$, corresponding to mean metallicities of $\langle[\mathrm{Fe/H}]\rangle = -1.1 \pm 0.1$ dex and $\langle[\mathrm{Fe/H}]\rangle = -0.7 \pm 0.2$ dex, respectively. The latter value is very similar to the mean metallicity derived from Washington photometry by Harris et al. (1992). In order to assess the real nature of the objects redder than $(\mathrm{U}-\mathrm{V})_0 = 2.5$ spectroscopic observations are necessary.

3.6 Conclusions

The main results and their implications presented in this work are the following:

1. On the basis of high resolution ground-based images, taken with VLT and FORS1, we identified 71 *bona fide* globular clusters in the halo of the nearest giant elliptical galaxy NGC 5128. Only 5 of these clusters were previously known.

2. In a UV color-magnitude diagram for the complete sample of 71 clusters and a UVK color-color diagram for a subsample of 23 clusters, the objects span a similar magnitude and color range as the globular clusters in the MW and M31. Note, however, that there is no cluster corresponding to ω Cen, the brightest MW cluster, in these two fields. The position of 23 objects in the $(\mathrm{U}-\mathrm{V})_0$ *vs.* $(\mathrm{V}-\mathrm{K})_0$ color-color diagram is consistent with their classification as old globular clusters.

3. The GCLFs spanning $-10.1 < M_V < -4.9$ and $-9.3 < M_U < -3.3$ have been constructed. These are the deepest GCLFs of an elliptical galaxy made so far. Kolmogorov-Smirnov statistics show that the difference between the GCLFs of NGC 5128 and MW is not larger than the difference between the GCLFs of M31 and MW. Similarity of the GCLFs of an elliptical with respect to the spiral galaxy had never been tested at the faint end before.

4. The presence of faint globular clusters in the halo of NGC 5128 puts constraints on the effectiveness of the tidal forces in the deep elliptical galaxy potential. The dynamical effects may be important for clusters that are found within ~ 2 R_e from the galactic center. Unfortunately, the selection of globular clusters from VLT images is not sensitive to the most compact and the faintest clusters, similar to ones like Pal 1, Pal 13, AM 4 and Terzan 1 in our Galaxy, while the less dense ones start to be confused with background galaxies at faint magnitudes.

5. The $(U-V)_0$ color histogram of 71 clusters indicates a bimodal distribution, supporting the Zepf & Ashman (1993) suggestion. Assuming that the clusters in NGC 5128 and in the MW span a similar age interval, and adopting the linear fit between the $(U-V)_0$ color and metallicity, we derived the [Fe/H] of the red and blue peaks of the bimodal distribution to be -1.7 dex and -0.6 dex, respectively. Using the SSP models from Kurth et al. (1999), instead of the linear fit, the results do not change significantly, giving values of -1.7 dex and -0.5 dex for the metal-poor and metal-rich peaks, respectively. This is different from the Harris et al. (1992) and Zepf & Ashman (1993) result, but is partially due to the adopted color cut of $(U-V)_0 < 2.5$ in selecting globular clusters and to small number statistics, since both samples have $< 10\%$ of the total cluster population. Relaxing the red color cut the mean color of the distribution corresponds to mean metallicity of [Fe/H] $= -0.7$ dex, very similar to Harris et al. (1992) result. The true nature of the redder objects has to be assessed through spectroscopy.

Chapter 4

Stellar populations in NGC 5128 with the VLT: evidence for recent star formation[1,2]

Abstract

We resolve stars of the nearest giant elliptical galaxy NGC 5128 using VLT with FORS1 and ISAAC. We construct deep U, V and K_s color-magnitude and color-color diagrams in two different halo fields (in the halo and in the north-eastern diffuse shell). In the outer, shell field, at ~ 14 kpc from the center of the galaxy, there is a significant recent star formation with stars as young as 10 Myr, approximately aligned with the prominent radio and x-ray jet from the nucleus of the host AGN. Ionized gas filaments are evident in ultraviolet images near the area where neutral HI and CO molecular gas was previously observed. The underlying stellar population of the halo of the giant elliptical is predominantly old with a very broad metallicity distribution. The presence of an extended giant branch reaching $M_{\rm bol} = -5$ mag suggests the existence of a significant intermediate-age AGB population in the halo of this galaxy.

4.1 Introduction

Galaxies show a wide range of star formation activity and a large range of metallicities and ages in their stellar populations. Understanding the physical nature and origins of their stars is fundamental to understanding the formation and evolution of galaxies. The current knowledge of star formation histories of galaxies along the Hubble sequence is summarized by Kennicutt (1998). This knowledge is mainly based on the integrated photometric and spectroscopic studies through the predictions of population synthesis of the integrated light of star clusters (Bica 1988) and galaxies (Bruzual & Charlot 1993, Maraston 1998). The predictions of population synthesis can now be tested directly not only for globular clusters (e.g. Vazdekis et al. 2001), but also for nearby galaxies.

Stellar evolution theory provides predictions of the features expected in color-magnitude diagrams (CMDs) for stellar populations with different ages and metallicities (Renzini & Fusi Pecci 1988, Chiosi et al. 1992, Gallart 1998, Aparicio 1998, Tolstoy 1999). Coupled with the improvements in telescope sizes, detector sensitivity, field of view and spatial resolution, compared with those a decade ago, the direct observations of the stellar content of nearby galaxies is becoming one of the most active areas of extragalactic research.

In the Local Group, indicators of the old stellar populations such as old main sequence turn-offs or at least the horizontal branch magnitudes are within reach of available instrumentation (e.g. Hurley-Keller et al. 1998, Gallart et al. 1999, Held et al. 2000, Rejkuba et al. 2000, Chapter 2). The recent results on the studies of the Local Group galaxies have been summarized by Mateo (1998), van den Bergh (1999, 2000b) and Grebel (2000).

The Local Group contains galaxies representative of almost all the classes, except the important giant elliptical class of galaxies. The closest giant elliptical is NGC 5128, the dominant galaxy in the Centaurus group at distance

[1]Based on observations collected at the European Southern Observatory, Paranal, Chile, within the Observing Programmes 63.N-0229 and 65.N-0164, and in part on observations collected by the NASA/ESA Hubble Space Telescope, which is operated by AURA, Inc., under NASA contract NAS5–26555.

[2]Based on Rejkuba, M., Minniti, D., Silva, D.R., Bedding, T.R., 2001, A&A 379, 781

of 3.6 ± 0.3 Mpc (Harris et al. 1999, Soria et al. 1996, Hui et al. 1995, Tonry & Schechter 1990). It has been extensively studied over the last 50 years (for an exhaustive review see Israel 1998).

Its popularity is not only due to its brightness, but also to its many unusual features: (i) there is a prominent dust band containing young stars and HII regions (Unger et al. 2000, Wild & Eckart 2000, Graham 1979); (ii) there is an active nucleus with a radio and x-ray jet, radio lobes and optical filaments (Cooper et al. 1965, Feigelson et al. 1981, Kraft et al. 2000, Schreier et al. 1981, Clarke et al. 1992, Blanco et al. 1975, Dufour & van den Bergh 1978); (iii) Malin et al. (1983) discovered a large number of faint narrow shells of stars surrounding the galaxy; (iv) Schiminovich et al. (1994) detected 4×10^8 $M_\odot$ of HI gas associated with the stellar shells, but slightly displaced outside the shells; and (v) most recently, molecular CO gas has been found associated with the HI gas and the stellar shells (Charmandaris et al. 2000). All of these are clear indications of a recent interaction with a gas–rich galaxy.

The high resolution and sensitivity of WFPC2 on the Hubble Space Telescope (HST) enabled the first studies of the resolved old stellar populations in the halo of NGC 5128 (Soria et al. 1996, Harris et al. 1999, Harris & Harris 2000, Mould et al. 2000). NICMOS on HST was used to resolve the stars in the near IR (Marleau et al. 2000) in the same field as the optical study of Soria et al. (1996; ~9kpc south of the center of the galaxy). In these two studies, a small intermediate-age population of $\sim$ 5Gyr has been found, comprising up to $\sim$ 10% of the total stellar population in the halo. On the other hand, there are almost no intermediate–age stars in the field further out in the halo, at $\sim$ 20 kpc from the galaxy center (Harris et al. 1999) nor at $\sim$ 31 kpc (Harris & Harris 2000). The comparison of the two results may indicate the presence of a gradient in the stellar population in the halo, as suggested by Marleau et al. (2000). However, the small field of view of HST puts serious limitations to the conclusions in the cases where the strong gradients in galaxy populations exist (see, for example, the case of Local Group dwarf galaxies like Leo I (Gallart et al. 1999, Held et al. 2000) or WLM (Minniti & Zijlstra 1996, 1997)).

We present here a wide wavelength range photometry of the resolved stellar populations in NGC 5128 obtained from the ground with Very Large Telescope (VLT) in U, V and K_s band. The deep and high-resolution VLT imaging, coupled with the much larger field of view than HST, enables us to address the questions of the gradients in stellar populations in the halo of this giant elliptical galaxy. The proximity of NGC 5128 provides an unusual opportunity for a direct study of shell stars. We use infrared-optical colour-magnitude diagrams of the shell to study the ages and metallicities of the stars belonging to the cannibalized galaxy.

4.2 The data

The observations were carried out with the ESO Very Large Telescope (VLT) at Paranal Observatory, Chile. They consist of optical (Bessel U- and V-band) and near-IR (K_s-band) images. We observed two fields in the halo of NGC 5128. Field 1 ($\alpha_{2000} = 13^h26^m23.5^s$, $\delta_{2000} = -42°52'00''$; Fig. 4.1) was centered on the prominent N-E shell, $\sim 14'$ away from the center of the galaxy. Field 2 ($\alpha_{2000} = 13^h25^m26^s$, $\delta_{2000} = -43°10'00''$; Fig. 4.2) was chosen to overlap with the HST field of Soria et al. (1996) and lies at a distance of $\sim 9'$ from the center of the galaxy. The optical data were obtained on 1999 July 11 and 12, while the K_s-band images cover several epochs and will be used to search for long-period variable stars. All of the observations were secured in the service mode. Calibration data, bias, dark and flat-field images as well as photometric standards from Landolt (in optical; 1992) and Persson et al. (IR; 1998) catalogues, were supplied by the ESO calibration plan. The observations are summarized in Table 4.1.

4.2.1 Optical observations and data reduction

Two 15-minute exposures in both U and V were acquired for each of the two fields in NGC 5128 using FORS1 (FOcal Reducer and low dispersion Spectrograph) on VLT Unit Telescope 1 (Antu). The FORS1 detector is a 2048×2048 Tektronix CCD, thinned and anti-reflection coated. The pixel size is 24×24 μm. The field of view is $6\farcm8 \times 6\farcm8$ and the scale is $0\farcs2$/pixel.

For service observations in direct-imaging mode, the FORS1 CCD is read out in four-port read-out mode. We used the ESO pipeline reductions which are based on MIDAS package specially developed to reduce images with 4

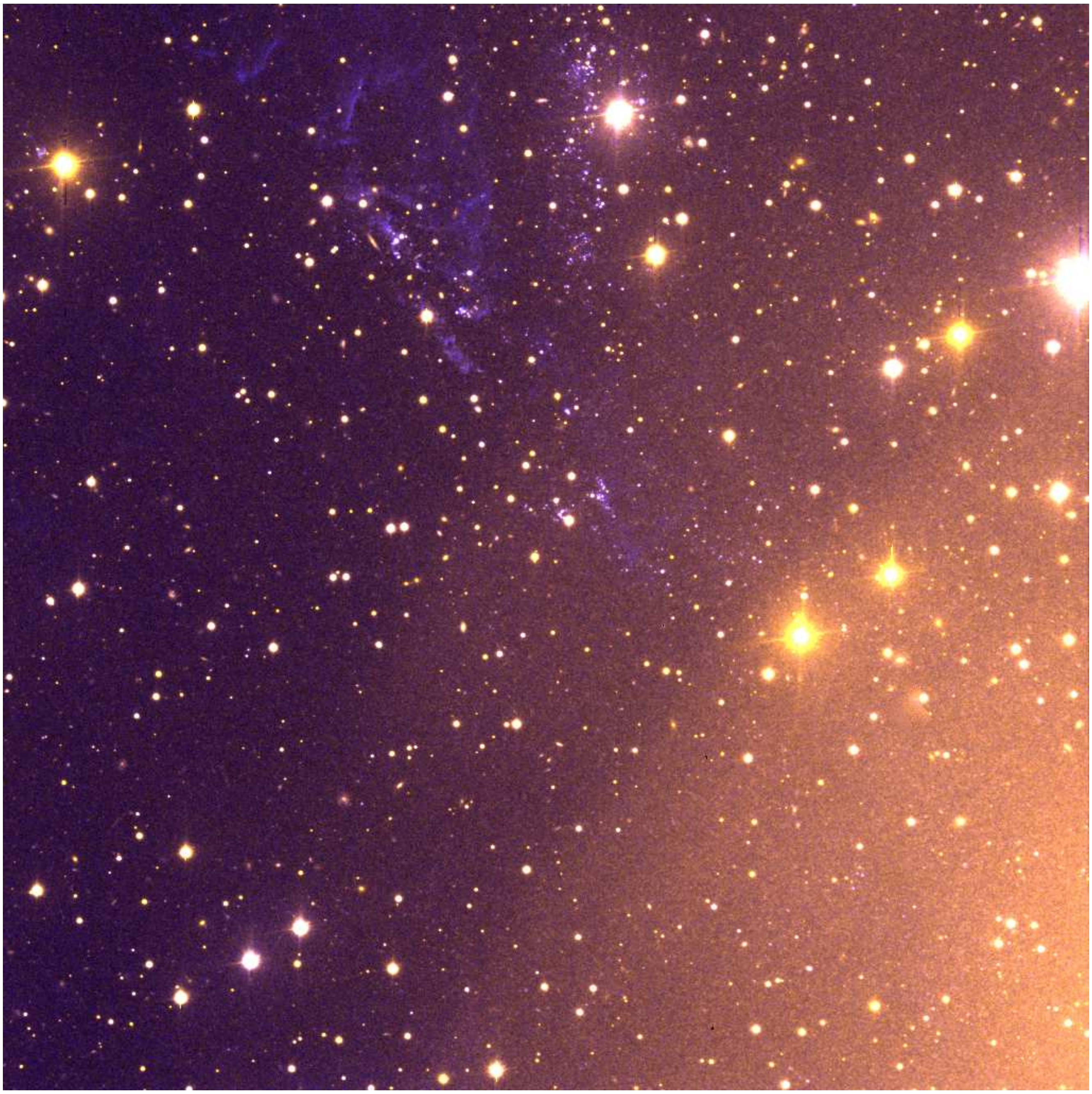

Figure 4.1: Combined U- and V- band image of Field 1, taken at the VLT (UT1+FORS1). The field of view is $6\overset{\prime}{.}8 \times 6\overset{\prime}{.}8$. North is at the top and east to the left.

Figure 4.2: Combined U- and V- band image of Field 2, taken at the VLT (UT1+FORS1). The field of view is $6'.8 \times 6'.8$. North is at the top and east to the left.

Table 4.1: Journal of observations

Field #	$\alpha_{(2000)}$ (h min sec)	$\delta_{(2000)}$ (° ′ ″)	Date dd/mm/yyyy	Telescope & Instrument	Exposure (sec)	FILTER	Airmass	Seeing ″	Epoch
1	13 26 23.5	−42 52 00	12/07/1999	Antu+FORS1	2×900	U	1.54	0.52	
1	13 26 23.5	−42 52 00	12/07/1999	Antu+FORS1	2×900	V	1.77	0.54	
1	13 26 23.5	−42 52 00	08/04/1999	Antu+ISAAC	10×36×10	K_s	1.15	0.41	A
1	13 26 23.5	−42 52 00	07/05/1999	Antu+ISAAC	10×36×10	K_s	1.05	0.40	B
1	13 26 23.5	−42 52 00	28/05/1999	Antu+ISAAC	10×36×10	K_s	1.14	0.51	C
1	13 26 23.5	−42 52 00	15/04/2000	Antu+ISAAC	65×6×10	K_s	1.09	0.35	D
1	13 26 23.5	−42 52 00	10/05/2000	Antu+ISAAC	65×6×10	K_s	1.22	0.43	E
1	13 26 23.5	−42 52 00	07/06/2000	Antu+ISAAC	65×6×10	K_s	1.13	0.60	F
1	13 26 23.5	−42 52 00	08/07/2000	Antu+ISAAC	65×6×10	K_s	1.15	0.31	G
2	13 25 24.0	−43 10 00	11/07/1999	Antu+FORS1	2×900	U	1.28	0.53	
2	13 25 24.0	−43 10 00	11/07/1999	Antu+FORS1	2×900	V	1.20	0.44	
2	13 25 24.0	−43 10 00	08/04/1999	Antu+ISAAC	10×36×10	K_s	1.05	0.36	A
2	13 25 24.0	−43 10 00	07/05/1999	Antu+ISAAC	10×36×10	K_s	1.10	0.39	B
2	13 25 24.0	−43 10 00	29/05/1999	Antu+ISAAC	10×36×10	K_s	1.06	0.44	C
2	13 25 24.0	−43 10 00	15/04/2000	Antu+ISAAC	65×6×10	K_s	1.09	0.40	D
2	13 25 24.0	−43 10 00	12/05/2000	Antu+ISAAC	51×6×10	K_s	1.22	0.51	Eb
2	13 25 24.0	−43 10 00	19/05/2000	Antu+ISAAC	20×6×10	K_s	1.22	0.44	Ec
2	13 25 24.0	−43 10 00	07/06/2000	Antu+ISAAC	41×6×10	K_s	1.13	0.57	Fa
2	13 25 24.0	−43 10 00	09/06/2000	Antu+ISAAC	30×6×10	K_s	1.13	0.40	Fb
2	13 25 24.0	−43 10 00	08/07/2000	Antu+ISAAC	65×6×10	K_s	1.15	0.40	G
2	13 25 24.0	−43 09 04	20/02/2000	NTT+SOFI	45×10×6	K_s	1.04	0.55	
2	13 25 24.3	−43 09 58	27/06/1998	HST+NIC3	256	F222M			

different amplifiers. With it the overscan for each amplifier was subtracted individually and after the subtraction of bias the images were corrected for the flat-field.

4.2.2 Near-IR observations and data reduction

For the near-IR K_s-band observations we used ISAAC, also on Antu. In this wavelength domain (0.9–2.5 μm) the detector is a 1024×1024 Hawaii Rockwell array. The field of view is $2'.5 \times 2'.5$ and the scale is $0''.147$/pixel. A series of 10-second exposures were taken at each epoch, usually in groups of six, with the number of repeats depending on weather conditions and any technical problems. The total exposure time for each epoch is given in Table 4.1.

An additional K_s-band observation of Field 2, with a total on-target exposure time of 45 minutes, was acquired with the SOFI instrument at the ESO 3.5-m New Technology Telescope (NTT) at La Silla Observatory, Chile. The field of view of SOFI is $4'.94 \times 4'.94$ and the scale is $0''.292$/pixel.

We also obtained observations with the NIC3 array on HST, using the F222M filter, which is similar to (although narrower than) the standard K filter. The NIC3 field of view is $51''.2 \times 51''.2$, much smaller than the one of ISAAC.

The standard procedure in reducing IR data consists of (i) dark subtraction, (ii) flat-field correction, (iii) sky subtraction, (iv) registering and combining the images. We did not use the ESO pipeline reduction product. Good sky subtraction in a crowded field like that of a galactic halo is particularly important. For that step we used the DIMSUM package (Stanford et al. 1995) within IRAF[1]. In DIMSUM the sky subtraction is made in two passes. In the first, a median sky is computed for each image from the six frames that are closest in time. The shifts between the sky-subtracted frames are then computed and all the images stacked together using a rejection algorithm to

[1]IRAF is distributed by the National Optical Astronomy Observatories, which is operated by the Association of Universities for Research in Astronomy, Inc., under contract with the National Science Foundation

remove cosmic rays. An object mask is computed for the coadded image and then shifted back in order to create object masks for the individual frames. In the second pass, the sky subtraction is made using the object masks to avoid overestimation of the sky level. These masks are also used to check that the bright object cores were not removed as cosmic rays in the previous pass. After the mask-pass sky subtraction, all frames belonging to single epoch are registered with *imalign* and combined with *imcombine* task in IRAF.

4.3 The photometry

4.3.1 Data analysis

The photometric reduction of the combined U-, V- and K_s-band images was performed using the DAOPHOT II programme (Stetson 1987, 1994). First, we located all the objects that were $> 3\sigma$ above the background on individual images. More than 50 relatively bright, not saturated, isolated, stellar objects were chosen to create the variable PSF for each image. ALLSTAR fitting of the PSF to all the objects produced the object lists that were matched with DAOMATCH and DAOMASTER, where only objects with good photometry in at least two frames were kept. The final photometric catalogue was obtained with ALLFRAME which uses as input information photometry lists from ALLSTAR and fits the PSF to all frames (in U, V and K-band) simultaneously. Again, only the objects detected in at least 2 images were kept. Using the information on the location of stars in all bands simultaneously improved our photometry, which is deeper by $\sim$ 1 mag with respect to ALLSTAR photometry. Moreover, the treatment of close companions, in particular the ones that have different colors, is much better with ALLFRAME.

NGC 5128 is close enough that its globular clusters appear slightly resolved, in the sense of having a larger FWHM and non-stellar PSF (Minniti et al. 1996, Rejkuba 2001, Chapter 3). Restricting the sharpness and goodness of the fit parameters to $-0.7 <$SHARP< 0.7, we rejected most of the galaxies, star clusters and other extended objects as well as remaining blemishes and cosmic rays from the final photometry list. Also stars with large photometric uncertainties in one or more filters ($\sigma \geq 0.5$ mag) were rejected. Finally the images were visually checked and a few remaining extended background objects (e.g. partially resolved star forming region in a background spiral galaxy) were discarded. With this selection our final U, V photometry catalogue contains 1581 and 1944 stars in Fields 1 and 2, respectively, while the V, K catalogue contains 5172 and 8005 stars and the numbers of stars with good photometry in U, V and K-band are 508 and 663 in Fields 1 and 2, respectively.

4.3.2 The photometric calibration

For the photometric calibration of the optical images, standard stars from the catalogue of Landolt (1992) were used. We checked the photometric quality of the two nights separately and since both were photometric, with almost identical zeropoints, we combined the standard stars for the two nights. Using a total of 14 stars in 4 different fields, spanning the color range $-1.321 < (U-V) < 4.162$, we derived the following calibration transformations:

$$\begin{aligned} u_{\mathrm{inst}} &= U - 24.262(\pm 0.089) + 0.379(\pm 0.068) * X \\ &\quad -0.042(\pm 0.007) * (U-V) \end{aligned} \tag{4.1}$$

$$v_{\mathrm{inst}} = V - 27.348(\pm 0.042) + 0.213(\pm 0.034) * X \tag{4.2}$$

where X is the mean airmass of the observations, u_{inst} and v_{inst} are instrumental magnitudes and U and V magnitudes from the Landolt (1992) catalogue. The one-sigma scatter around the mean was 0.031 mag for the U band and 0.023 mag for the V band (Fig. 4.3, left panel). Adding the color term $(U-V)$ in the transformations slightly reduces the scatter in the V-band to 0.017 mag (Fig. 4.3, right panel). However, the calibration equation without the color term for the V-band was preferred, since the scientific data in that filter go much deeper and U magnitudes for some objects could not be measured accurately enough.

Observations at our reference K_s-band epoch (G in Table 4.1) were taken in photometric conditions. During the same night, July 8 2000, three standard stars from the list of Persson et al. (1998) were observed. Each standard

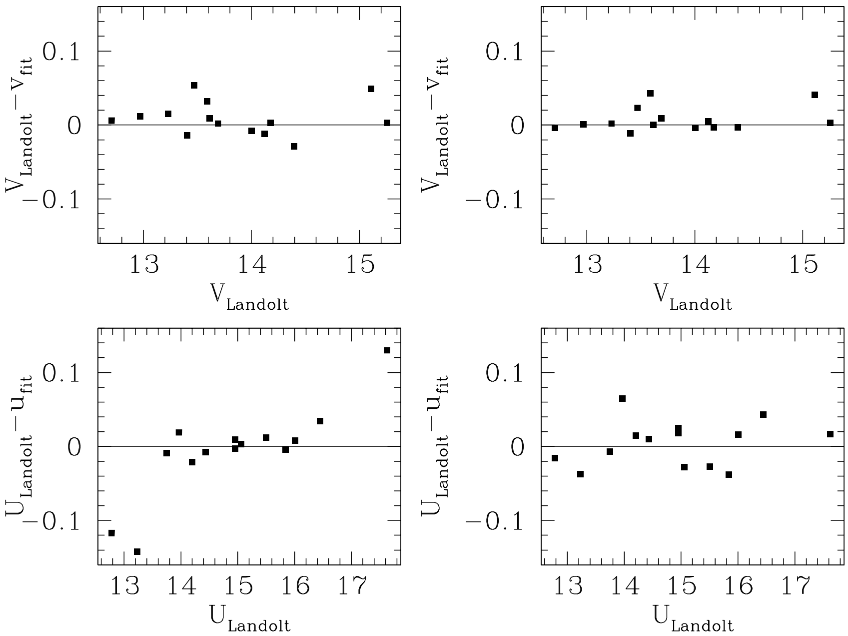

Figure 4.3: Photometric calibration of Landolt (1992) stars during the nights of observations in U and V filters. Left panels: the scatter for the calibration without the color term; right panels: the scatter for the calibration with the color term.

star was observed at 5 different positions on the IR-array. In this way, a total of 15 independent measurements were obtained. However, the number of measurements with different airmass was only 3, so that we preferred to adopt the mean extinction coefficients measured on Paranal for K_s - band of 0.05 mag/airmass. The derived zeropoint of the G-epoch observations is 24.23 ± 0.04. The following calibration equation was applied to our data:

$$k_{s,\mathrm{inst}} = K_s - 24.23(\pm 0.04) + 0.05 * X \tag{4.3}$$

where X is the airmass of observations, $k_{s,\mathrm{inst}}$ is the instrumental magnitude and K_s is the calibrated magnitude. The photometry of all other K-band epochs were measured with respect to the reference epoch.

4.3.3 Completeness and contamination

We made extensive tests to measure completeness and magnitude uncertainties as a function of magnitude and radial distance from the center of the galaxy. The completeness for the U, V and K_s-band photometry has been calculated using the ADDSTAR programme within DAOPHOT. We made twenty artificial star experiments, adding each time ~ 3000 stars to the first frame. The stars were added on a regular grid separated by $2 \times R_{PSF} + 1$ pixels in order not to alter crowding (where R_{PSF} is the PSF radius used for fitting the image with the worst seeing) and having magnitudes randomly distributed in the observed range. The position of the first star in the list was chosen randomly, so that over 20 different experiments the added stars were uniformly distributed over the whole field. After the appropriate coordinate shifts were applied and magnitudes changed to instrumental system taking into account the observed magnitudes and colors, the same stars from the first frame were added also to all other frames. Their photometry was recomputed in the same way as for the original images. The stellar PSF obtained from the field stars for the respective image was used in the simulations. Incompleteness in Field 1, defined by a recovery rate of 50% from the artificial-star experiment, sets in around magnitude 25 in the U-band (but depends strongly on $U - V$ color; see Fig. 4.4) and 22.5 in K_s-band (Fig. 4.5). The corresponding numbers for Field 2 are

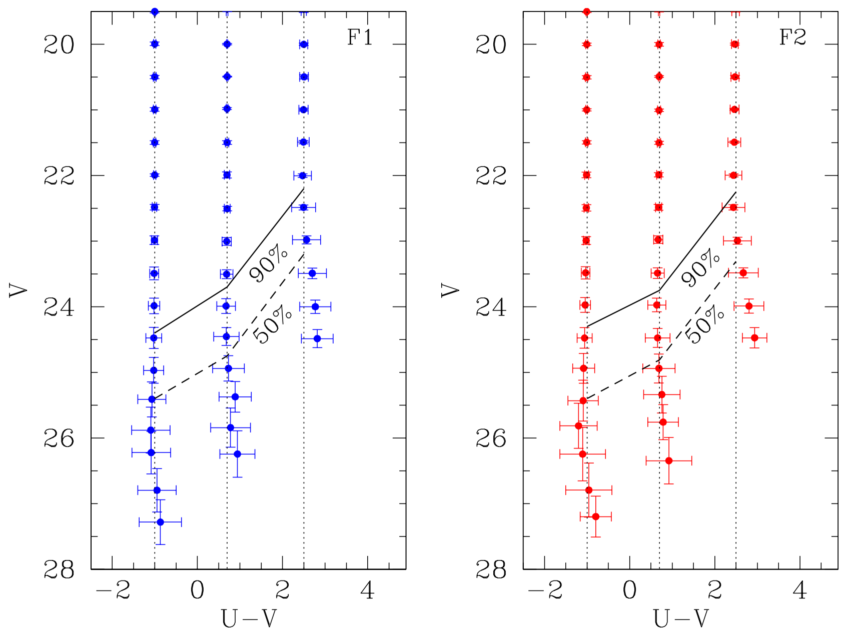

Figure 4.4: Completeness and photometric uncertainties as a function of magnitude and color. The thin vertical dotted lines indicate the value of input $U - V$ colors. The full line defines the 90% completeness limit and the dashed line is for 50% completeness limit.

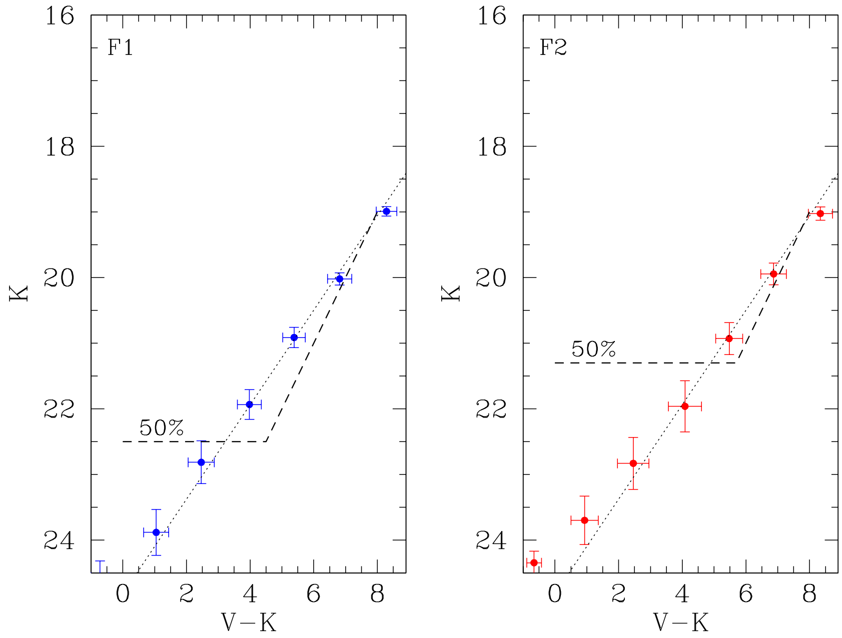

Figure 4.5: The completeness and photometric uncertainties as a function of magnitude and color. The thin dotted line indicate the value of input $V - K$ colors. The dashed line defines the 50% completeness limit.

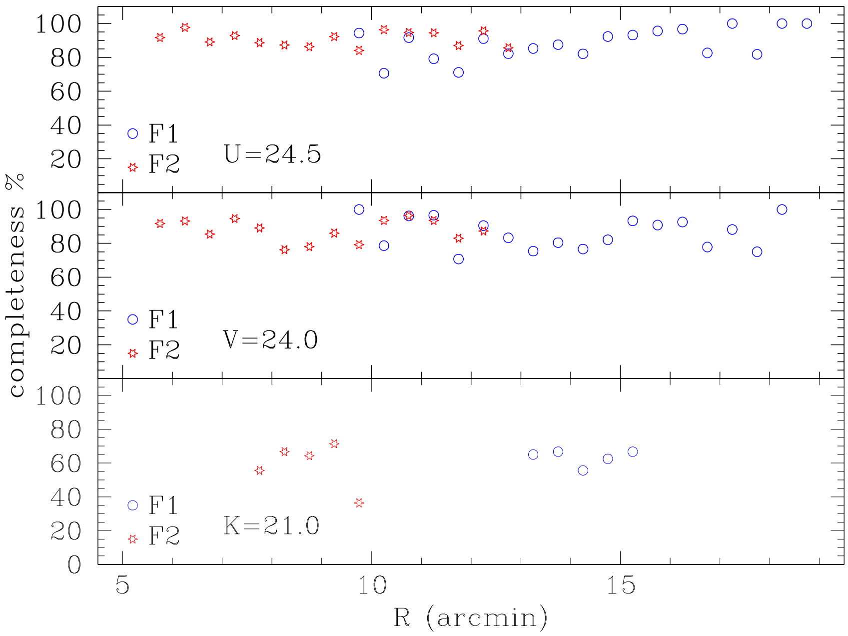

Figure 4.6: The completeness as function of radial distance from the center of NGC 5128 calculated around 90% completeness limit for U- and V-band (for $(U-V)=0.7$) and around 65% for K_s-band.

25 for U-band and 21.3 for K_s-band. The difference at K_s-band between the two fields is due to (1) better seeing in Field 1 ($FWHM = 2.1$ pix vs. 2.7 pix) and (2) higher surface brightness in Field 2.

Dependence of the completeness on radial distance from the center of the galaxy ($\alpha_{2000} = 13^{\mathrm{h}}25^{\mathrm{m}}26\overset{\mathrm{s}}{.}4$, $\delta_{2000} = -43°01'05\overset{''}{.}1$) was calculated for the magnitude bin around 90% level of completeness in U- and V-band (Fig. 4.6) and around 65% of completeness in K_s-band. There is no significant spatial variation of completeness in our data.

To assess the accuracy of our photometry, we calculated the difference between the input and recovered magnitudes for each magnitude bin (Fig. 4.4, 4.5). Our photometry is reliable down to the incompleteness limit and blending is not seriously affecting our data (see the discussion in Sec. 4.4.2). For magnitudes fainter than the 50% completeness limit, the measured values are systematically brighter, because of the bias towards brighter fluctuations and blending due to crowding. The colors of the recovered stars with magnitudes fainter than the 50% completeness limits are redder than the input colors in the UV CMDs (Fig. 4.4), due to the larger incompleteness in the U- than in the V-band. In the VK CMDs the colors of the recovered stars range from slightly redder than the input color for the very red stars, due to the dominant incompleteness in the V-band, to bluer for the faintest and bluest stars, due to the dominant incompleteness in the K-band (Fig. 4.5). We did not correct our data for this systematic shift, because magnitudes fainter than the 50% completeness limit will not be used in further analysis.

Contamination by foreground Galactic stars and unresolved background galaxies is important because of the low Galactic latitude of our fields ($b = 19\overset{\circ}{.}5$) and the very deep photometric limits observed. We used the Besançon group model of stellar population synthesis of the Galaxy available through the Web[2] (Robin & Creze 1986, Robin et al. 1996) to simulate the total number and optical magnitude and color distribution of Galactic foreground stars in our fields. The simulated catalogue has 1827 stars in the FORS1 field ($6\overset{'}{.}8 \times 6\overset{'}{.}8$) in the magnitude interval $18 < V < 30$. In order to get a realistic estimate for the number of stars that would be observed in our fields, the correction for completeness is necessary. Therefore, we added the stars from the simulated catalogue (with magnitudes scaled to correspond to instrumental magnitudes) to our images and re-measured their magnitudes.

[2] http://www.obs-besancon.fr/www/modele/modele_ang.html

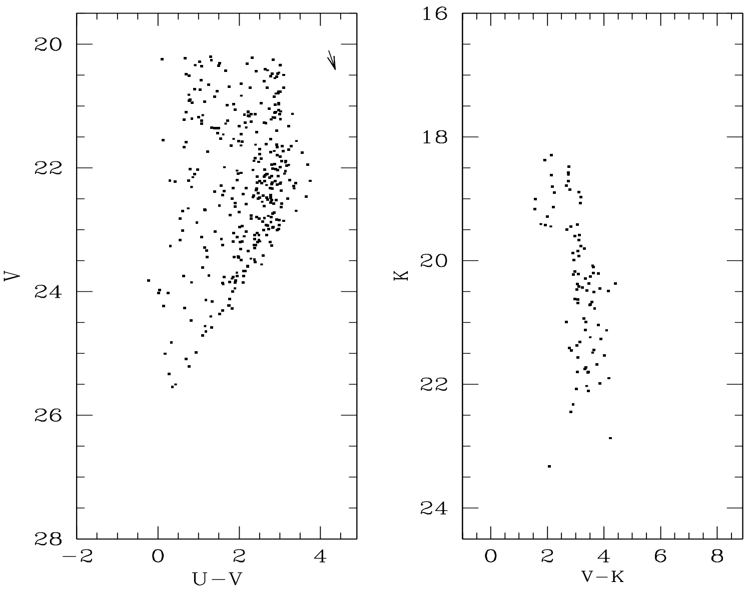

Figure 4.7: UV (left) and VK (right) color-magnitude diagrams for foreground Galactic stars simulated using the Besançon group model. The correction for completeness and realistic photometric uncertainties have been applied by adding the simulated stars to our Field 2 images and re-measuring them. The reddening vector $E(B-V) = 0.1$ is plotted in the upper right corner.

In this way, realistic photometric uncertainties were applied and the number of stars recovered in two fields was corrected for completeness. A total of 340 and 350 stars with U- and V-band photometry satisfying profile fitting and photometric uncertainty selection criteria were measured in Field 1 and 2, respectively. Most of the foreground stars have $0 < U - V < 3$ (Fig. 4.7). All of the stars in the red part of the Field 2 CMD brighter than $V \sim 22$ are expected to be foreground stars (see Sect. 4.4.1). In order to adjust for the expected number of Galactic stars we normalized the models to the observed number of reddest stars in Field 2. Thus the total number of foreground stars was increased by 31% in both fields.

The Galaxy model simulation supplies not only the colors of the simulated stars, but also their metallicities, ages, spectral types and luminosity classes. Using all these data and the Kurucz (1998) model atmospheres[3], we derived the foreground contamination in the K-band. After correction for completeness, the expected number of foreground stars in ISAAC images is 112 and 91 in the VK CMD of Field 1 and 2, respectively. All of the foreground stars have $1.0 < V - K < 4.5$ (Fig. 4.7 right panel).

The measured number of compact background galaxies on the FORS1 images, taken in similar observing conditions, is $\lesssim 400$ in magnitude range $V = 20 - 25$ mag for the selection of sharpness parameter $-1 < sharp < 1$ (Jerjen & Rejkuba 2001). Our tighter selection criteria ($-0.7 < sharp < 0.7$) eliminated most of them. In the smaller field of view of ISAAC, the predicted number of background galaxies is ~ 330 in the interval of magnitudes $16 < K_s < 23$ and ~ 180 between $16 < K_s < 22$ (Saracco et al. 2001). Most of the background galaxies are resolved and rejected by sharp and magnitude uncertainty parameter requirements on our photometry. Only few compact galaxies might contaminate the sample.

Table 4.2: Comparison with Fasset & Graham (FG) photometry; the numbers of stars in the first column are from FG

#	V_{FG}	$(B-V)_{\mathrm{FG}}$	$(U-B)_{\mathrm{FG}}$	V_{FORS1}	U_{FORS1}
1	19.94	+0.23	−0.54	19.987	19.498
4[a]	21.07	+0.12	−1.26	20.871	19.711
5[b]	21.19	+0.04	−1.26	20.925	19.717
7[c]	21.51	−0.07	−0.34	...	20.291
10	21.65	+0.04	−1.16	20.986	20.440
12	21.72	+0.21	−0.20	21.722	21.580
13	21.75	+0.11	−0.84	21.667	20.600
15	21.86	+0.09	−0.61	21.885	21.099
16	21.94	−0.05	−0.92	21.978	20.862
17	21.95	+0.34	−0.82	21.963	21.391
18[d]	22.01	+0.30	−0.84	...	...
20	22.10	+0.07	−0.82	22.150	21.144
21	22.12	−0.08	−1.00	22.127	20.942
26	22.25	+0.08	−0.98	22.323	21.234
27	22.35	−0.03	−0.91	22.331	21.295
28	22.40	−0.05	−0.87	22.412	21.323
30	22.51	+0.20	−0.56	22.631	22.032
32	22.53	+0.13	−0.50	22.579	22.217
33	22.54	+0.07	−0.76	22.623	21.528
35	22.55	+0.11	−0.55	22.503	21.968
36	22.58	−0.08	−0.88	22.606	21.535
37	22.58	+0.02	−1.06	22.777	21.549
39	22.69	−0.12	−0.82	22.706	21.585
42	22.82	+0.00	−1.02	22.856	21.646
46	22.89	+0.31	−0.12	22.919	23.260
47	22.90	−0.05	−1.00	22.934	21.737
48	22.96	+0.08	−0.74	23.051	22.149
50	22.99	−0.04	−0.81	23.134	22.027

[a] f1.GC-8 (Rejkuba 2001)
[b] f1.GC-25 (Rejkuba 2001)
[c] saturated in FORS1 V image
[d] extended in FORS1 images

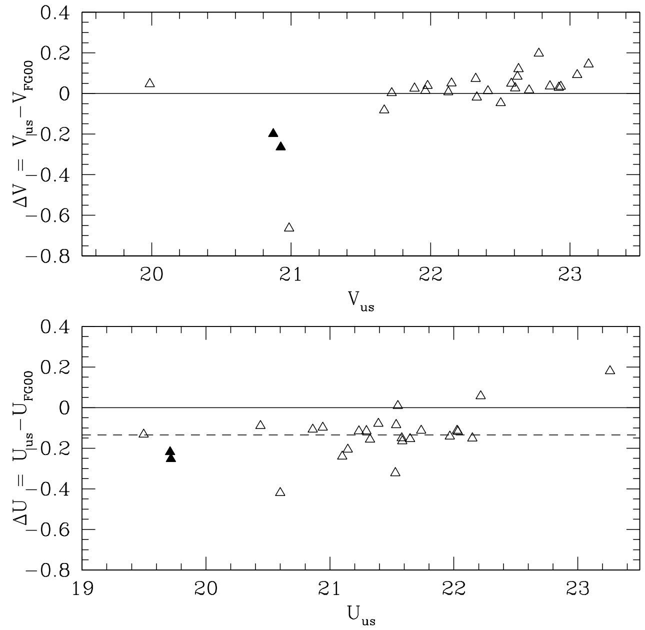

Figure 4.8: Comparison of our photometry with that of Fasset & Graham (2000) for 26 bright blue stars in common. In the upper panned the comparison of V band magnitudes is presented and in the lower panel U-band magnitudes are compared. The two extended objects (#4 and #5 in Tab. 4.2) noted by Rejkuba (2001, Chapter 3) are plotted with filled symbols. The mean offset of -0.13 mag in U-band is indicated with the dashed line.

4.3.4 Comparison with published data

Several recent studies of resolved stellar populations in NGC 5128 exist in the literature, all but one made with HST in F606W (V) and F814W (I) or F110W (J) and F160W (H) photometric bands, which are not very sensitive to the recent star formation. Our Field 2 is centered on the field of Soria et al. (1996), which was also observed in the near-IR (F110W and F160W filters) by Marleau et al. (2000), but the direct comparison is not possible due to different photometric bands used.

The only possible direct comparison is for our Field 1 photometry, which partially overlaps with the HST photometry of Mould et al. (2000) and the ground based photometry of Fasset & Graham (2000). The last authors observed a wider field than ours in U, B and V Glass filters, but due to smaller telescope aperture (2.5m), their photometry is much shallower. The HST photometry is deeper, but covers a much smaller area. The mean difference between V magnitudes of Fasset & Graham and Mould et al. photometry is -0.13 ± 0.07 mag, in the sense of HST photometry having a systematically fainter zero point (Fasset & Graham 2000). Comparison of 26 stars in common between our data and that of Fasset & Graham for the brightest blue stars (their Table 3) is presented in Fig. 4.8. The mean difference for all 26 stars is negligible for V-band photometry, but it amounts to 0.13 mag in U-band. From Fig. 4.8 a systematic trend with the magnitude is apparent in V and U band. Excluding the star #10 (see Tab. 4.2), which has HST V magnitude of 21.04 (thus close to our value; star R4 in Table 1 of Mould et al.), and extended sources #4, #5 (see Rejkuba 2001; filled triangles in Fig. 4.8) and #18, these trends can be represented by the following equations:

$$V_{\mathrm{FORS1}} - V_{\mathrm{FG}} = 0.030 \times V_{\mathrm{FORS1}} - 0.65 \tag{4.4}$$

$$U_{\mathrm{FORS1}} - U_{\mathrm{FG}} = 0.089 \times U_{\mathrm{FORS1}} - 2.05 \tag{4.5}$$

[3] http://cfaku5.harvard.edu/grids.html

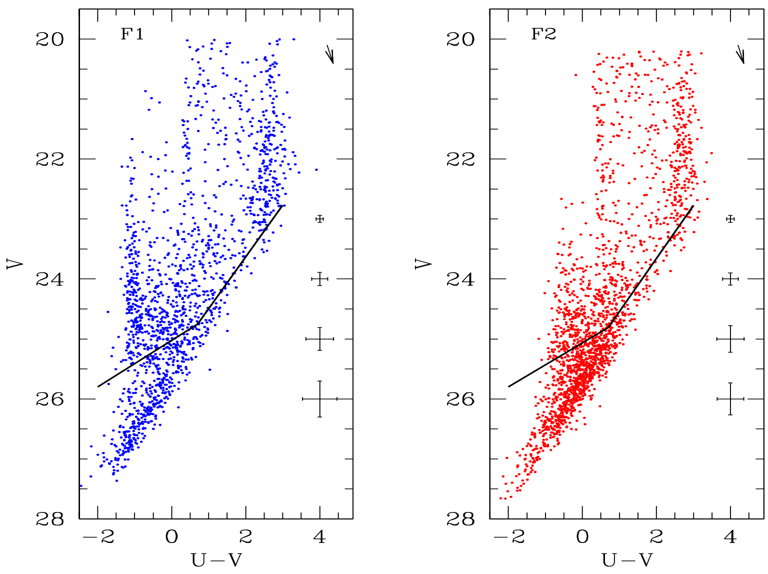

Figure 4.9: UV color-magnitude diagram for Field 1 (left) and Field 2 (right). The arrow represents the reddening vector of $E(B-V)=0.1$. Typical photometry uncertainties are plotted on the right side. The solid line indicates the 50% completeness.

with rms equal to 0.055 for V and 0.096 for U. At least part of this difference may be due to different filters used (Bessell 1995). Fasset & Graham further neglected the color term in their calibration due to insufficient color coverage of their standards, while we found that the color term is important for our U-band calibration.

4.4 The color-magnitude diagrams

4.4.1 Optical CMDs

Optical CMDs probe young and intermediate age populations. Theoretically, the U and V light is dominated by young main sequence stars (Buzzoni 1995).

Figure 4.9 shows $(U-V)-V$ color-magnitude diagrams for stars in both observed halo fields of NGC 5128. Due to better seeing the saturation magnitude of the V-band is ~ 0.3 mag fainter for Field 2. Most of the stars redder than $(U-V)\sim 0$ belong to our own Galaxy (see Fig. 4.7). The most important characteristic of the UV CMD of Field 1 is the upper main sequence, visible as the blue plume at $(U-V)\sim -1$ mag. By contrast, there are no such young massive stars in Field 2.

The Besançon Galaxy model (see previous section) was used to "clean" the CMDs of foreground star contamination. In Fig. 4.10 we show UV CMDs after the subtraction of foreground stars. Overplotted are isochrones from Bertelli et al. (1994) for $Z=0.004$ and for log(age)=7.0, 7.3, 7.5 for Field 1 and log(age)=7.0, 7.5 and 7.8 for Field 2. The isochrones were shifted to the distance of NGC 5128, assuming a distance modulus of $(m-M)=27.8$ and reddening of $E(B-V)=0.11$ mag (Schlegel et al. 1998). The difference between the two diagrams is striking: the blue main sequence containing stars as young as $\sim$ 10 Myr that is present in Field 1 is completely absent from the CMD of Field 2. Well separated from the main sequence in Field 1 is the sequence of blue core-helium burning (BHeB) stars at $(U-V)\sim 0.5$. The width of the gap and the tightness of the main sequence indicate low differential extinction in the field. In Field 2, the stars with $0.5<(U-V)<2.8$ and brighter than $V\lesssim 22.5$

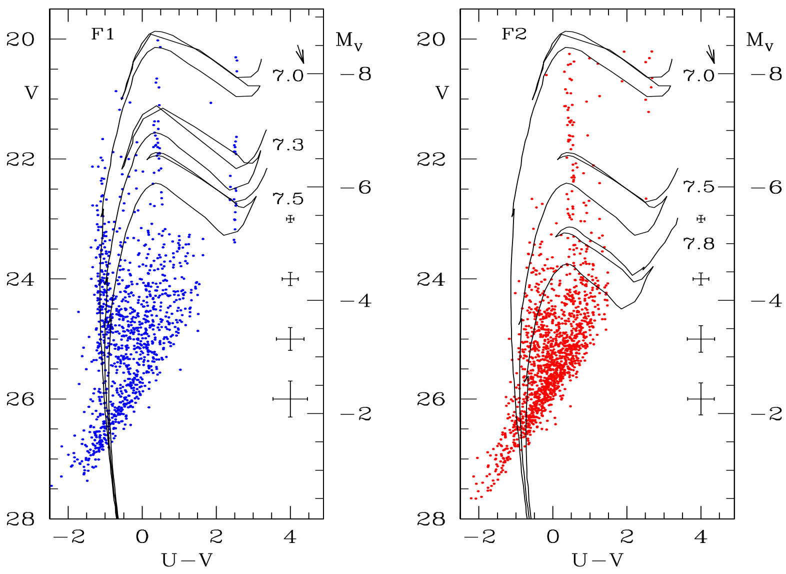

Figure 4.10: CMDs with foreground stars statistically subtracted. Overplotted are isochrones from Bertelli et al. (1994) for $Z = 0.004$ with log(age) indicated with the number on the right side. The size of the reddening vector corresponds to $E(B - V) = 0.1$ mag.

have no corresponding main sequence stars and thus cannot be young stars migrating from blue to red during their core-He burning phase, as is the case for most of the objects in Field 1 with colors $0.5 < (U - V) < 2.5$. These stars in Field 2 are most probably the remaining foreground contamination, indicating that the foreground contamination may affect the numbers of blue and red HeB stars in Field 1 (see next paragraph). Only a few stars are lying along the isochrone of log(age) = 7.5 (Fig. 4.10), while most of them are consistent with much older ages. We conclude that there are no stars younger than ~ 40 Myr in Field 2.

Note that isochrones for metallicities higher than $Z = 0.004$ extend on the red supergiant edge to redder values of $U - V$ than the reddest stars in Field 1 and thus do not fit well our observations. The ratio of blue to red supergiants strongly depends on metallicity (Langer & Maeder 1995, Maeder & Meynet 2001) and in principle could be used to constrain the metallicity of the youngest population in NGC 5128. Counting the number of blue and red supergiants for stars more massive than $\sim 12\ M_\odot$, we find their ratio to be $B/R < 0.7-0.8$ (although with high uncertainty due to the possible foreground contamination), in good agreement with the observed B/R value in SMC cluster NGC 300 (see discussion by Langer & Maeder 1995). The metallicity of $Z = 0.004$ (corresponding to [Fe/H]$= -0.7$ dex) is appropriate for the SMC. However, since the B/R value depends also on other parameters such as stellar mass, rotation and degree of overshooting (Maeder & Meynet 2001), a more detailed comparison with models and the determination of the metallicity of this youngest stellar population in NGC 5128 is warranted (Rejkuba et al., Chapter 7).

The low metallicity implied by the fit of the isochrones on UV CMDs probably reflects the metallicity of the gas left in the halo of NGC 5128 by the accreted satellite. Atomic H I (Schiminovich et al. 1994) and molecular CO gas (Charmandaris et al. 2000) present in Field 1 are slightly offset from the position of the diffuse stellar shell, the obvious remnant from the accreted galaxy.

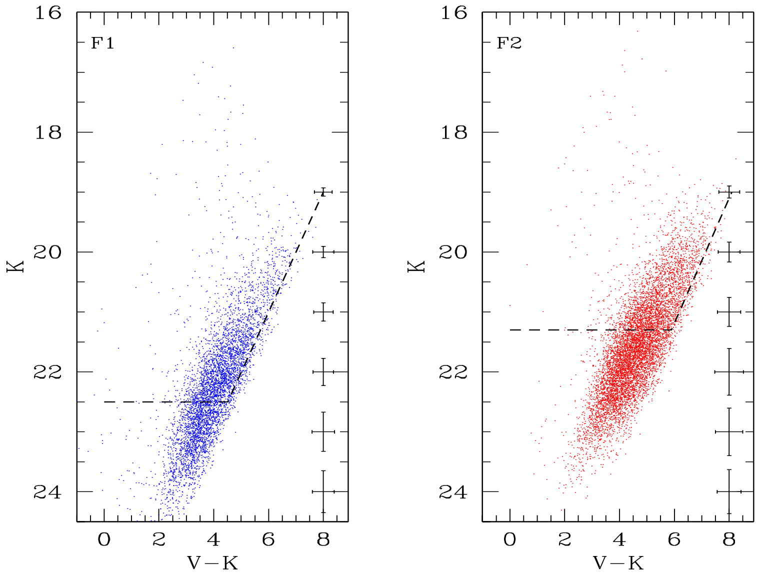

Figure 4.11: VK color-magnitude diagram for Field 1 (left) and Field 2 (right). The dashed line identifies the 50% completeness level.

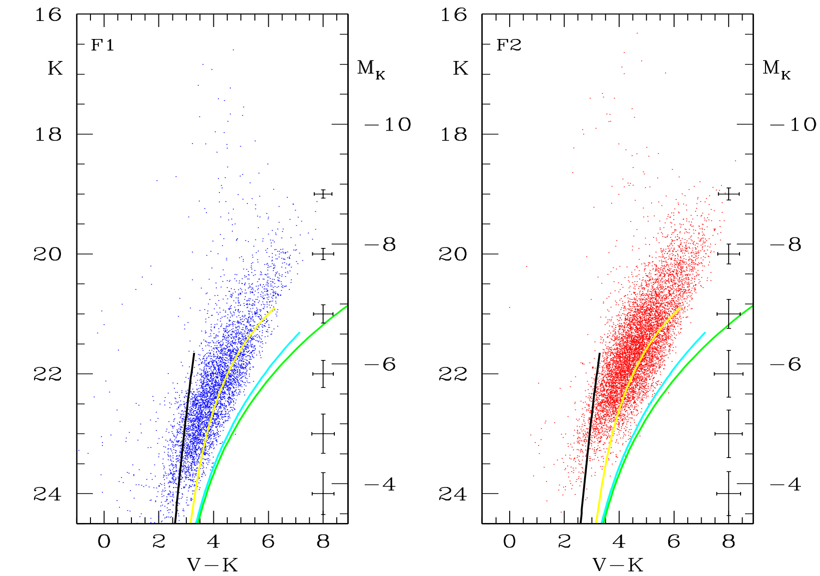

Figure 4.12: VK CMDs with foreground stars statistically subtracted. Overplotted are fiducial RGB sequences of Galactic globular clusters (from left to right): M15, 47 Tuc, NGC 6553 and NGC 6528, from Ferraro et al. (2000).

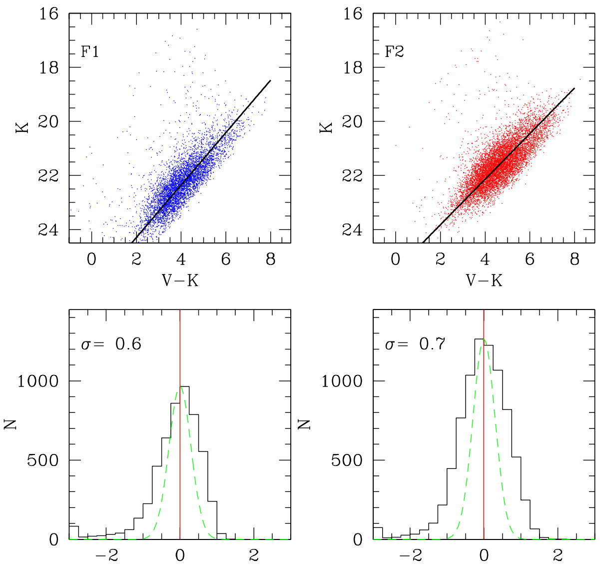

Figure 4.13: The histogram of the observed color distribution along the RGB (lower panels) is plotted accounting for the actual slope of the RGB (thick line in upper panels) in Field 1 (left) and 2 (right). The 1σ spread in color of the RGB is indicated in the upper left corner. Overplotted with the dashed line is a Gaussian with the $\sigma = 0.3$, typical of the distribution from the photometry errors.

4.4.2 Optical–near IR CMDs

Optical-near IR CMDs probe old and intermediate-age stellar populations. Theoretically, more than two thirds of the light in K-band is dominated by cool stars on the red giant branch (RGB) and asymptotic giant branch (AGB), and by red dwarfs (Buzzoni 1995). The red dwarfs are too faint to be detected at the distance of NGC 5128, and thus our VK CMDs are entirely dominated by RGB and AGB stars (Fig. 4.11).

In Fig. 4.12 we show VK CMDs of Fields 1 and 2 after the statistical subtraction of foreground stars. Overlaid are fiducial RGB sequences of Galactic globular clusters (from left to right: M15, 47 Tuc, NGC 6553 and NGC 6528; Ferraro et al. 2000) spanning a large range of metallicities ($-2.17 \leq$[Fe/H]≤ -0.23 dex). As before, we used a distance modulus of 27.8 and reddening corresponding to $E(B-V) = 0.1$ ($E(V-K) = 0.274$ and $A_K = 0.0347$; Rieke & Lebofsky 1985) to adjust the magnitudes and colors of RGB fiducials to those of NGC 5128. Obviously, most of the stars in Fig. 4.12 belong to the RGB. The right edge of the RGB is quite sharp, with most of the stars being more metal-poor than 47 Tuc ([Fe/H]$= -0.71$ dex) and none appearing to be as metal-rich as NGC 6553 ([Fe/H]$= -0.29$ dex). However, the latter is due to incompleteness in V-band photometry.

Figure 4.13 illustrates the actual color distribution, which accounts for the slope of the RGB, compared with the distribution expected from the errors. The spread in color of the RGB is larger than the photometric uncertainties (Fig. 4.13), indicating the presence of spread in metallicity and/or age. The most metal-poor stars have metallicities of -2 dex if their ages correspond to those of Galactic globular clusters. The population we probe with VK photometry is more metal-poor than -0.7 dex. Our V-band images are not deep enough to detect more metal rich giants. Walsh et al. (1999) measured the mean oxygen abundance of five planetary nebulae in NGC 5128 to be [O/H]$= -0.5 \pm 0.3$ dex, consistent with the presence of the large population of stars with metallicities below solar, as we observe in the VK CMDs.

There are 1830 stars in Field 1 and 1197 in Field 2 which have good K-band photometry ($\sigma_K < 0.5$, $-0.7 <$ *sharp* < 0.7 and $\chi < 2.0$) above the respective K-band completeness limits, but which have not been detected in

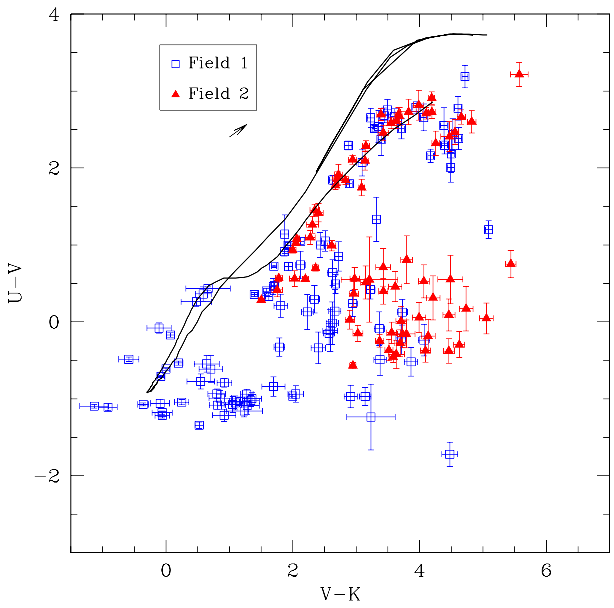

Figure 4.14: Color-color diagram for the objects matched in U, V and K_s frames that had ALLFRAME photometry uncertainties < 0.5 mag and magnitudes brighter than the 50% completeness limits in all bands. Field 1 objects are plotted with open squares and Field 2 with filled triangles. Overplotted is the Padova isochrone (Bertelli et al. 1994) for the solar metallicity and log(age)=7.0 yr that indicates the locus of the foreground stellar sequence. Reddening vector has dimensions corresponding to $E(B-V) = 0.1$.

optical bands. They are uniformly distributed over the whole ISAAC images. The large number of very red stars with good photometry in K_s and no counterpart in V-band suggests that stars more metal-rich than [Fe/H]$= -0.7$ dex are present, as expected for a luminous giant elliptical galaxy. This is in good agreement with the results of Harris et al. (1999) and Harris & Harris (2000).

4.5 The color-color diagram

Fig. 4.14 shows the color-color diagram for the objects detected in U-, V- and K-band in Field 1 (open squares) and Field 2 (filled triangles) that had ALLFRAME photometry uncertainties < 0.5 mag and magnitudes brighter than the 50% completeness limits in all bands. The error-bars plotted are the ones given by ALLFRAME. A total of 99 objects in Field 1 and 90 in Field 2 satisfy these criteria. Most of them are located along the stellar sequence that crosses the color-color diagram in diagonal. Matching the UV and VK catalogues after the statistical subtraction of the foreground contamination, the stellar sequence disappears and only 54 and 44 objects with good photometry in all three filters are left in Field 1 and 2, respectively.

We use the color-color diagram presented in Fig. 4.14 to measure the reddening and the contamination by background galaxies.

4.5.1 Reddening

The objects crossing the color-color diagram in diagonal from top right to bottom left belong to the Milky Way. The quality of the fit of the stellar sequence with isochrones depends on the age of the isochrone with respect to stars. Because the foreground Milky Way stars span a range of ages, isochrones of different ages fit different parts

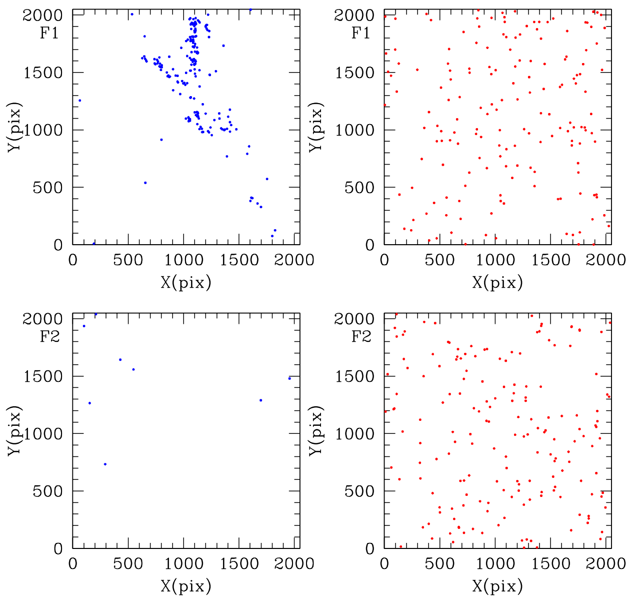

Figure 4.15: The spatial distribution of the bluest $(U-V) < -0.75$ (left panels) and the reddest $(U-V) > 2$ (right panels) stars in Field 1 (top panels) and 2 (bottom panels) for stars with magnitudes above the 50% completeness limit ($V < 25$ and $U < 25$). The north is up and east is to the left.

of the stellar sequence. As an example, in order to guide the eye we overplotted the stellar loci of solar metallicity stars and log(age)=7.0 yr (Bertelli et al. 1994). The tight stellar sequence in the $U-V$ vs. $V-K$ color-color diagram shows that the foreground reddening in the two fields is the same. Its magnitude was measured by fitting the theoretical isochrones and it amounts to $E(B-V) = 0.15 \pm 0.05$ mag. This is in excellent agreement with the Schlegel et al. (1998) extinction maps and the reddening determined by Fasset & Graham (2000), who used UBV color-color diagrams to measure a value of $E(B-V) = 0.14 \pm 0.02$ mag.

4.5.2 Star-galaxy separation

Using the color-color plots it is possible to distinguish the foreground dwarf stars from the most compact unresolved galaxies. Galaxies are located in the lower right part of the diagram in Fig. 4.14. The resolved galaxies are not plotted here since they got rejected by our selection of shape parameters in FIND and ALLFRAME. Note that the group of objects with $-0.5 < (V-K) < 2$ are the young stars detected in Field 1.

4.6 Jet aligned star formation in the halo

The chains of bright blue compact objects and optical filaments, first noticed by Blanco et al. (1975), were recognized as young blue supergiants and OB associations by Graham & Price (1981) and Graham (1998). Our Field 1, situated ~ 14 kpc away from the center of the galaxy and coinciding with the NE radio lobe, contains part of this "string of blue knots and filaments."

In Fig. 4.15 we show the spatial distribution of the bluest (left) and the reddest (right) stars in both our fields. The red stars, belonging to the foreground Galactic population, are uniformly distributed in both fields. Field 2 has almost no very young blue stars, while the majority of the young population in Field 1 is aligned with the jet direction coming from the nucleus of the galaxy. The vertical structure to the right of the jet is located at the leftmost edge of a large HI cloud found by Schiminovich et al. (1994). In the northern part of this field, a CO molecular cloud was recently discovered by Charmandaris et al. (2000).

Mould et al. (2000), Graham (1998) and Fasset & Graham (2000) report on the presence of the collimated star formation in the halo of NGC 5128. They favor the scenario in which a past interaction between the radio jet (Morganti et al. 1999) and the HI cloud complex (Schiminovich et al. 1994) is responsible for the star formation.

Finding active star formation far out in the halo of an elliptical galaxy is unusual. Understanding the triggering mechanism and the origin of the star formation, as well as the nature of the underlying ionized gas (Graham 1998, Morganti et al. 1991, 1992), is important for explaining the filamentary emission and jet-aligned structures observed in other galaxies (e.g., in NGC 1275: Lazareff et al. 1989, Sabra et al. 2000; in M87: Gavazzi et al. 2000; and in other more distant radio sources: Rees 1989, Best et al. 1996, De Breuck et al. 1999).

The alignment of the luminous blue stars with the radio axis of NGC 5128 (Fig. 4.15) may shed some light on the debated issue of the observed alignment of the radio and optical structures in high-z radio galaxies (Rees 1989, Best et al. 1996). One of the proposed alignment models is based on the assumption that the action of the jets tunneling through a galactic medium affects the gas via shock heating, thereby inducing vigorous star formation (Begelman & Cioffi 1989, Rees 1989, Daly 1990). In particular, as Rees (1989) discussed in detail, the stars form from the cool-phase gas (with $T \leq 10^4$ K) in clouds massive or dense enough to be Jeans-unstable.

This mechanism may work well for massive high-z radio galaxies, in which most of the baryonic mass would still be gaseous. In the present day giant ellipticals, on the other hand, little gas is usually left to support strong star formation. However, probably due to previous accretion of a gas rich galaxy, NGC 5128 has substantial cool, dense clouds of molecular CO and atomic HI gas in its halo (Schiminovich et al. 1994, Charmandaris et al. 2000). We note that these clouds could form the clumpy ISM/IGM necessary for the 'bursting bubble' model proposed by Morganti et al. (1999).

We have shown clear evidence for blue stars as young as 10×10^6 yr (Fig. 4.10). We also see underlying emission, particularly in our U-band images, which probably comes from the [OII] 3727 emission line. High-resolution spectra with good signal-to-noise are needed to decide whether this emission is due to gas being photoionized by the newly formed stars or being photoionized by particles coming directly from the nucleus.

Other low-redshift galaxies also show filamentary ionized gas structures in their halos. In the case of M87 (Gavazzi et al. 2000), the filament of ionized gas in the NE part of the halo coincides with the Eastern radio-lobe, in much the same way as in the much closer NGC 5128. It would be interesting to search for young stars associated with that filament too.

4.7 Intermediate age population

In contrast with the conclusions of HST studies (Harris et al. 1999, Harris & Harris 2000) of stellar populations in NGC 5128, we detect not only old population II stars, but also a significant number of stars with magnitudes brighter than the tip of RGB ($M_K^{\rm Tip} = -0.64(\pm0.12)[{\rm M/H}] - 6.93(\pm0.14)$; Ferraro et al. 2000).

We took bolometric corrections from Bessell & Wood (1984) and the empirical fit of $(V-K)$ vs. $T_{\rm eff}$ from Bessell, Castelli & Plez (1998) to transform our K–$(V-K)$ CMDs to the theoretical plane (Fig. 4.16). Overplotted on the H-R diagrams are the Padova tracks from Girardi et al. (2000) for the first-ascent giant branch stars with masses M=0.6, 0.8, 1.2 and 1.6 $M_\odot$ and metallicities $Z = 0.004$ (full lines) and $Z = 0.008$ (dashed lines). The sharp cut-off on the right side of the H-R diagrams is due to incompleteness in V-band.

In discussing the H-R diagram, we should consider blending. According to theoretical predictions (Renzini 1998), at the fiducial galactocentric distances of 9, 12.8 and 17.9 kpc, the number of blends consisting of 2 stars belonging to the tip of RGB is $\sim$ 1300, 300 and 55 stars (per $2.2' \times 2.2'$; i.e. field of view of ISAAC), respectively. In this calculation, the B-band surface brightness measurements from Mathieu, Dejonghe & Hui (1996) were used. Obviously, the inner most regions of the galaxy, at the distance < 10 kpc from the nucleus are too crowded to give accurate photometry for RGB stars and most of the stars above the tip of RGB.

We attempted to use the NIC3 HST images overlapping with our Field 2 (galactocentric distance $R_{gc} \sim 9$ kpc) data to improve the resolution. However, we found out that many faint stars visible on ISAAC images are completely within the noise of NIC3 data. The resolution of our ISAAC data in the best seeing is as good as that

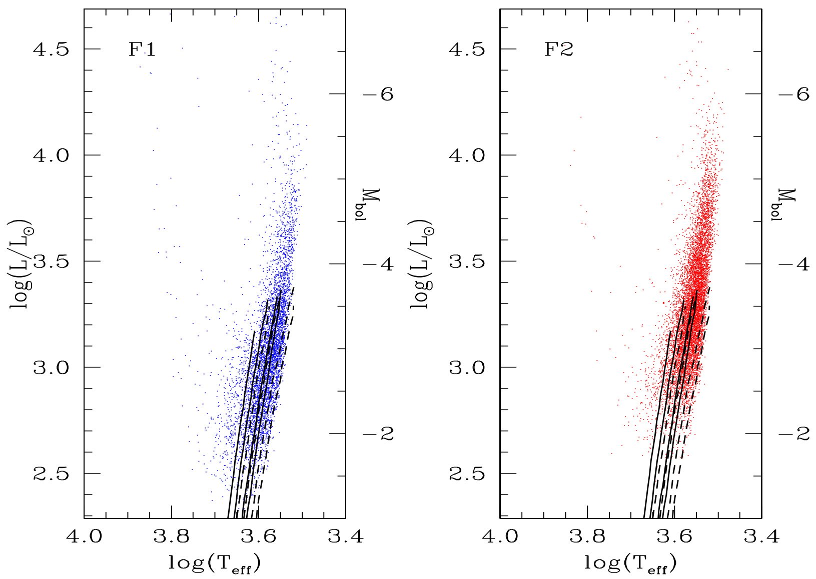

Figure 4.16: The HR diagram for old and intermediate stellar populations in Field 1 and 2. Overplotted are evolutionary tracks from Padova (Girardi et al. 2000) for stars with masses M=0.6, 0.8, 1.2 and 1.6 M$_\odot$ and $Z = 0.004$ (full line) and $Z = 0.008$ (dashed line).

of NICMOS images, with the advantage of having much better S/N and a more stable PSF. The confirmation of the number of AGB stars in Field 2 can be obtained only through the analysis of the LPVs (Rejkuba et al., Chapter 6).

In Field 1 ($R_{gc} \sim 14$ kpc), our outer shell field, crowding is not that severe. The expected number of two-star blends at the RGB tip in this field ranges from 300–50, as the surface brightness drops across the field. The total number of such blends is therefore less than $\sim$ 200 in the most pessimistic calculation. On the other hand, the number of stars above the tip of RGB ($M_{\rm bol} \sim -3.7$; Girardi et al. 2000) is 768. Subtracting the number of possible blends and allowing for a few of the brightest and bluest stars ($\sim$ 30 stars with $M_K < 9$) to be the remaining foreground contamination, there are still more than 500 stars whose position in the H-R diagram and CMD is consistent with an intermediate-age AGB population.

In the inner halo field, Field 2, the number of stars above the tip of RGB is 2844. After subtracting the number of expected blends ($\lesssim 1500$), the number of AGB stars is 2.5 times larger than in Field 1. This confirms the presence of gradients in the intermediate-age population within the halo of NGC 5128, as suggested by Marleau et al. (2000).

The intermediate-age AGB population could have easily been missed in V and I-band HST studies due to small field of view and small (< 0.5 mag) optical magnitude difference between the tip of the RGB and the tip of AGB. The AGB stars are up to $\sim$ 2 magnitudes brighter in M_K and $M_{\rm bol}$ than RGB stars and thus are easily detectable in near-IR. Thanks to this, Marleau et al. (2000) could detect some AGB stars in the much smaller NICMOS field.

The brightest stars in M32, in the Galactic bulge and the bulge of M31 have similar brightnesses, reaching $M_{\rm bol} = -5.5$ (Freedman 1992, Elston & Silva 1992, Frogel & Whitford 1987, Rich & Mould 1991). Due to this similarity, Davidge & van den Bergh (2001) suggested that the tip of AGB could be used as standard candle for determination of distances. In Fig. 4.17 we present the K_s-band and bolometric magnitude luminosity functions. The tip of the AGB is observed at bolometric magnitude of -5 in both fields (in spite of the crowding in Field 2), consistent with the adopted distance modulus for NGC 5128. Most of the stars brighter than this magnitude (as

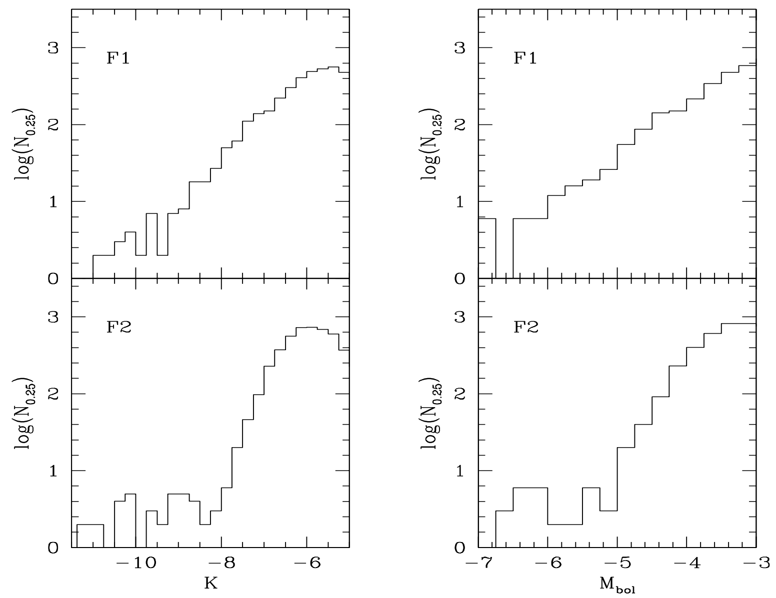

Figure 4.17: K-band (left) and bolometric magnitude luminosity functions (right) for stars redder than $(V-K_s) > 2$ in Fields 1 and 2.

well as stars brighter than $M_K = -9$; see left panels in Fig. 4.17) probably belong to our Galaxy.

4.8 The shell

In our deep V-band image of Field 1, the prominent NE shell is easily recognizable as the region with higher surface brightness, and also with higher density of stellar objects. All the stars that are spatially coincident with the shell on the V-band image are shown in Fig. 4.18. In the left two panels we plot the UV CMD of all stars coincident with the position of the diffuse shell (middle panel), while the corresponding VK CMD is on the right. The much smaller field of view of ISAAC is centered on the shell so that the shell stars cover most of the image. Note that projected on the shell is the stream of blue, young objects that are aligned with the jet direction. Excluding the stars that are coincident with the star forming area (lower panels), the stellar population belonging to the shell is very similar to the one observed in the halo of NGC 5128, i.e., our Field 2 population (Fig. 4.9, 4.11). As in the rest of the galaxy there is a significant spread in metallicity.

The presence of stellar shells or ripples around early-type galaxies is usually explained as evidence of the accretion and later merging of a smaller companion galaxy. The simulations of the stellar component in the merging galaxies have shown that the shells are created as a result of phase-wrapping or of spatial-wrapping of the tidal debris (Quinn 1984; Hernquist & Quinn 1989). The companion galaxies may contain different stellar populations with respect to the giant elliptical (e.g. most dwarf galaxies have much lower metallicity than giants Mateo 1998).

Here for the first time we obtained the magnitudes and colors of stars belonging to a shell. They are surprisingly similar to the rest of the halo stars in NGC 5128. However, due to incompleteness of our V-band photometry, we cannot probe the most metal rich part of the halo of NGC 5128. Very high resolution and deeper observations of the shell stars are possible with the Advanced Camera for Surveys at Hubble Space Telescope. In order to be able to better separate the stars that genuinely belong to shells from the "normal" halo stars in NGC 5128 and confirm the present result a more quantitative comparison between the stellar populations in our two fields is necessary (Rejkuba et al., Chapter 7).

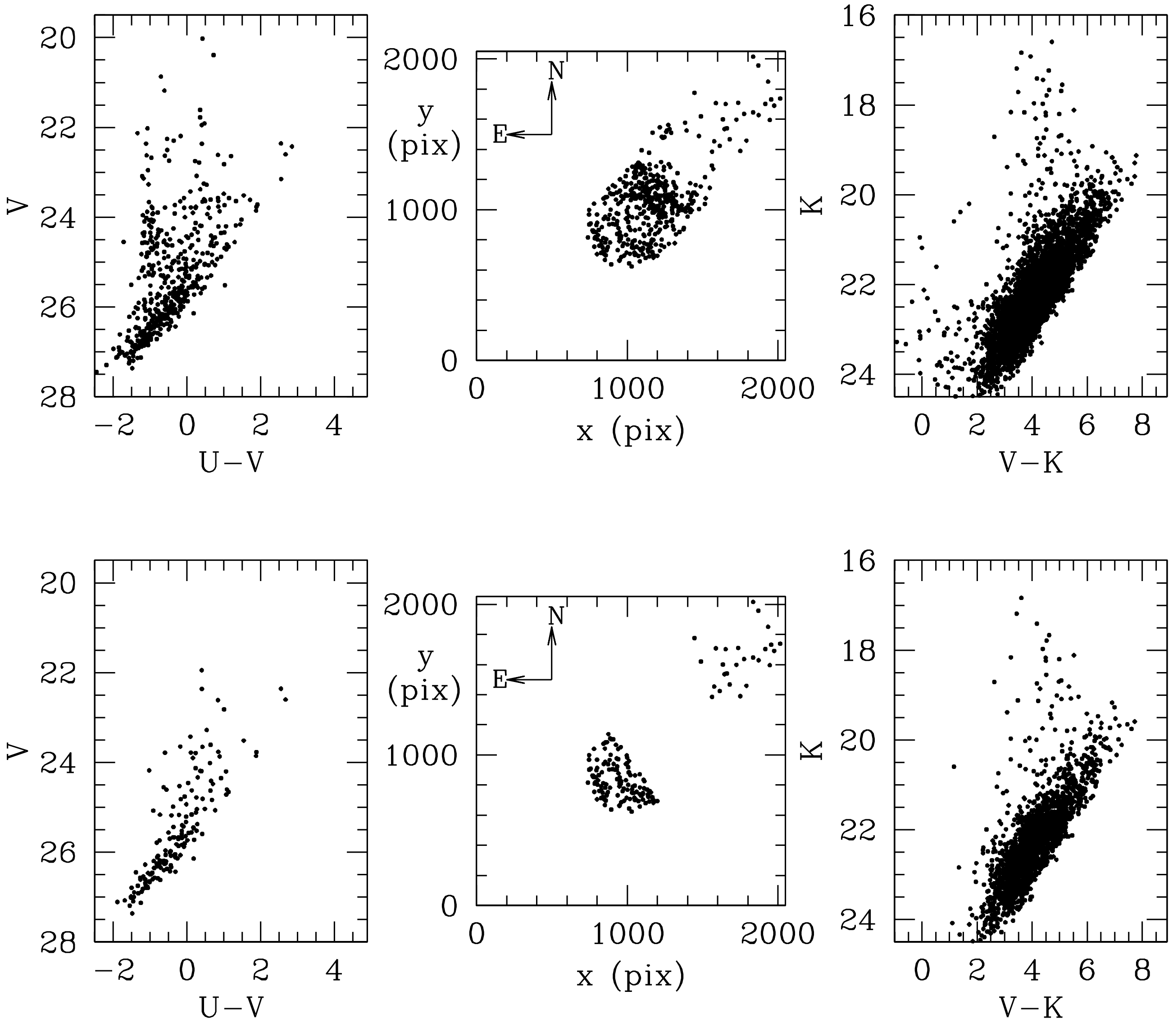

Figure 4.18: The color-magnitude diagrams for the stars located at the position of the diffuse NE shell.

4.9 Summary

Using the VLT with FORS1 and ISAAC, we have resolved stars in the halo and in the diffuse north-eastern shell of the closest giant elliptical galaxy, NGC 5128. With the U, V and K_s-band photometry we probe different stellar populations. The U filter, in particular, is sensitive to the youngest stars. It has revealed the striking difference in the star formation history between the the inner halo field (Field 2) and outer halo field (Field 1), the latter coinciding with the diffuse shell that is presumably the signature of a recent merger.

In Field 1, stars as young as 10 Myr are present, while there are no stars younger than at least 40 Myr in Field 2. Thanks to the high quality of our UV photometry, we also detect the gap between the main sequence and the blue core-helium burning supergiants. The foreground and background contamination has been corrected using the Besançon Galaxy model and our own color-color diagram.

The recent star formation in Field 1 is approximately aligned with the direction of the jet coming from the center of AGN. However, there is also a chain of young blue stars offset from the jet direction that is aligned with the edge of the molecular clouds. The presence of the atomic and molecular gas (Schiminovich et al. 1994, Charmandaris et al. 2000) and their association with the diffuse stellar shell is compatible with the dynamical scenario of phase-wrapping following the merger of a smaller gas-rich galaxy with NGC 5128 (Quinn 1984). In this scenario, the interaction of the material coming from the AGN in the center of the galaxy with the material left from the merger stimulated the star formation in the halo, ~ 15 kpc away from the galactic centre. The metallicity of the newly formed stars gives an upper limit on the abundance of the gas of the accreted satellite with value of $Z = 0.004$, a value typical of the SMC.

While the UV CMDs probed the youngest stellar populations, the combination of optical and near-IR filters is most sensitive to old and intermediate-age populations. In our VK CMDs we observe a very wide and extended giant branch. The width indicates the presence of Population II stars with metallicities ranging from -2 to -0.7 dex. Unfortunately, our V-band images are not deep enough to detect more metal rich stars, but the large number of stars detected on K-band images without a counterpart in V-band suggests an even redder and more metal-rich RGB population, in agreement with the previous HST studies (Soria et al. 1996, Harris et al. 1999, Harris & Harris 2000).

In contrast with the previous two studies, we find a very extended giant branch up to $M_{\rm bol} = -5$, which reveals the presence of the intermediate-age AGB population. Our extensive crowding experiments and theoretical predictions of the amount of blending (Renzini 1998) demonstrate that blending due to crowding is not significant enough to mimic this population in the outer field (Field 1). In the inner field, the extent and the properties of the AGB population will be assessed through the study of the long period variables that have been detected in both fields (Rejkuba et al., Chapter 6).

Chapter 5

The radio/optical alignment and the recent star formation associated with ionized filaments in the halo of NGC 5128 (Centaurus A)[1,2]

Abstract

We used the direct CCD camera at the Magellan I telescope at Las Campanas Observatory and FORS1 at Antu VLT at ESO Paranal Observatory to image fields centered on the inner and outer optical filaments in the halo of NGC 5128. In the V vs. $U-V$ color-magnitude diagrams we have identified young blue supergiants associated with these line-emitting filaments located between the inner radio lobe and the northern middle lobe. Around the outer filament stars as young as 10 Myr were detected. They are principally aligned with the direction of the radio jet, but a vertical north-east alignment along the edge of the HI cloud is also present. Young stars in the inner filament field are found inside the bright knots of photoionized gas and are strongly aligned in the direction towards the center of the galaxy at the same position angle as the inner radio jet. Fitting the Padova isochrones on UV color-magnitude diagrams we find that the blue stars around the inner filaments have ages similar to the ones around the outer filaments $\sim 10-15$ Myr and the same abundance of Z=0.004. The presence of young blue supergiants clearly shows that the bright blue knots in the north-eastern halo of NGC 5128 are associations of young stars with photoionized gas. The temperature of the brightest stars is T$\sim 12000-16000$ K, insufficient to account alone for the high excitation lines observed in the surrounding ionized gas. Thus the optical emission jet is principally seen due to its alignment with the radio structure of the AGN. The highly collimated star formation is present only in the north eastern halo of the galaxy, suggesting the interaction of the jet with the gas clouds deposited during the last accretion event as the preferred triggering mechanism. From these observations we infer a lower limit for the age of the NGC 5128 jet of 10^7 yr. The triggering of the star formation in the dense clouds in the halo of the galaxy by the jet supports the alignment effect observed in high redshift radio galaxies. It also suggests that radio galaxies should have higher than normal star formation rates.

5.1 Introduction

NGC 5128, the nearest giant elliptical galaxy (Israel 1998), was associated with the strong radio source Centaurus A by Bolton et al. (1949). In the optical, the galaxy has an elliptical light distribution crossed in the center by a strong warped dust lane. The diffuse optical extensions were first discovered by Johnson (1963) and subsequently the rich system of shells around the elliptical galaxy was detected by Malin et al. (1983). Blanco et al. (1975) and Peterson et al. (1975) discovered the optical jet or filaments in NGC 5128. The origin and the nature of the

[1]Based on observations collected at the European Southern Observatory, Paranal, Chile, within the Observing Programme 63.N-0229, and on observations collected by Magellan I telescope at Las Campanas Observatory, Chile.

[2]Based on Rejkuba, M., Minniti, D., Courbin, F. & Silva, D.R., 2002, ApJ 564, 688

emission-line filaments have been hotly debated (Dufour & van den Bergh 1978, Graham & Price 1981, Graham 1983, Morganti et al. 1991, Sutherland et al. 1993 and Morganti et al. 1999).

The origin of diffuse shells (Malin et al. 1983) can be explained with phase wrapping of stars from an accreted disk galaxy (Quinn 1984). Rejkuba et al. (2001b, Chapter 4) discussed the stellar populations in the prominent diffuse north-eastern shell and in the halo of NGC 5128. The 'outer filament' situated at $13\overset{'}{.}6$ from the centre extends for $\sim 8'$ in the direction of position angle 22° (Blanco et al. 1975) overlaping partially with the diffuse stellar shell. While the stellar populations in the shell are similar to the rest of the halo of the giant elliptical, the stars close to the emission-line filament are predominantly young (see also Mould et al. 2000, Fassett & Graham 2000).

The 'inner filament' is located at the distance of $7\overset{'}{.}8$ from the nucleus and extends outward over $\sim 2'$ at a position angle 55° (Blanco et al. 1975). It consists of three bright knots, identified as A, B and C by Blanco et al. (1975) and two more diffuse structures, E and F (Morganti et al. 1991). Here we report the detection of a young stellar population associated with the optical emission-line inner ($r \sim 8'$) and outer ($r \sim 14'$) filaments in the north-eastern halo of NGC 5128. Throughout the paper we adopt distance modulus to NGC 5128 of 27.8 (Soria et al. 1996, Harris et al. 1999) that corresponds to a distance $D = 3.6$ Mpc. At this distance, $1'$ on the sky translates to 1.047 kpc in the galaxy.

5.2 The data

We used FORS1 at VLT Antu to image the outer field because it is less crowded and the filaments cover a larger area than in the inner field. On the contrary in the inner field Magellan I was necessary because despite of having a smaller area it gives higher resolution for the crowded field.

The field with the inner filaments ($\alpha_{2000} = 13^h26^m05.9^s$, $\delta_{2000} = -42°56'35''$) was imaged with the Magellan I (Walter Baade) Telescope, one of the twin 6.5 m Magellan telescopes at Cerro Manqui at the Las Campanas Observatory. The observations were taken on 22 February 2001, during the first Chilean run on the new telescope and one of the first 10 nights of scientific operations. The instrument was the direct CCD camera Tektronix 2048×2048 with gain of 2 e^-/DN. At the f/11 focus of Magellan I the pixel scale is $0\overset{''}{.}069$/pixel with a total field size of $2\overset{'}{.}36^2$. The small pixel scale and the extraordinary good and stable seeing of $0\overset{''}{.}31 - 0\overset{''}{.}38$ during the whole night enabled us to obtain well sampled point spread function (PSF) images with almost no crowding problems deep in the halo of NGC 5128. The observations consist of 3×1800s, $2 \times 900 + 30$s and 2×300s$+ 4 \times 900$s exposures in Harris U-, V- and I-bands[1], respectively. The color composite image of the field can be found at the following URL http://www.lco.cl/magellan_lco/publicity/science_images/cena.html.

The standard stars from the Landolt (1992) catalogue in two different fields were observed at four different airmasses on 22 and 23 February 2001 with the identical instrumental setup. Additional photometric standards in these fields were defined by Stetson (2000) in the V and I bands, making the total number of useful standard stars observed 15, 50 and 48 in U, V and I, respectively. The following calibration equations reproduce the calibrated magnitudes with one-sigma scatter around the mean of 0.08, 0.024 and 0.031 for U, V and the I band, respectively.

$$\begin{aligned} u_{\text{inst}} &= U - 24.771(\pm 0.168) + 0.36(\pm 0.15) * X \\ &\quad -0.064(\pm 0.011) * (U - V) \end{aligned} \tag{5.1}$$

$$\begin{aligned} v_{\text{inst}} &= V - 26.756(\pm 0.005) + 0.15(\pm 0.05) * X \\ &\quad +0.045(\pm 0.004) * (V - I) \end{aligned} \tag{5.2}$$

$$\begin{aligned} i_{\text{inst}} &= I - 26.390(\pm 0.008) + 0.06(\pm 0.03) * X \\ &\quad -0.068(\pm 0.007) * (V - I) \end{aligned} \tag{5.3}$$

The observations of the field that contains outer filaments ($\alpha_{2000} = 13^h26^m23.5^s$, $\delta_{2000} = -42°52'00''$) were carried out in the service mode with FORS1 instrument on the 8.2m ESO Very Large Telescope (VLT) Antu at

[1] The exact names of filters were LC-3012, LC-3014 and LC-3011. For the filter transmission curves see http://www.lco.cl/lco/instruments/manuals/direct_ccd/filters/.

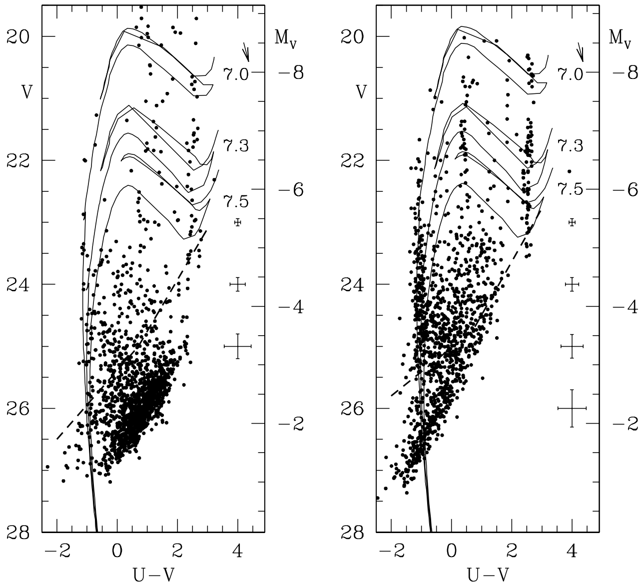

Figure 5.1: UV color-magnitude diagram for the inner filaments field (left) and the outer filament field (right). The foreground stellar contamination was statistically subtracted. The arrow represents the reddening vector of E(B−V)=0.1. Typical photometry errors are plotted on the right side. The dashed line indicates 50% completeness limit. Full lines are isochrones from Bertelli et al. (1994) for Z=0.004. The logarithm of ages in years is indicated on the right edge of each isochrone.

Paranal, on July 11^{th} and 12^{th} 1999. They consist of pairs of 15-min optical (Bessel U- and V-band) exposures taken in photometric conditions with seeing ranging from 0.″45 to 0.″55. The FORS1 detector has pixel scale of 0.″2/pixel and the field of view 6.′8 × 6.′8. A detailed description of these data and their reduction is given in Rejkuba et al. (2001b, Chapter 4).

The photometric measurements of the outer filament images were described in Rejkuba et al. (2001b; Field 1). The photometry in the inner filament field followed a similar procedure. The stars were identified on the median combined image with the FIND algorithm that is part of the DAOPHOT II programme (Stetson 1987). The PSF magnitudes were measured on all individual frames simultaneously with ALLFRAME (Stetson 1994). Restricting the PSF fitting parameters sharpness and chi we rejected bad pixels and extended objects like galaxies and globular clusters (Rejkuba 2001, Chapter 3) from the final photometry list. Only the stars with good photometry ($\sigma_{mag} <$ 0.5) in at least two images were kept. The final photometric catalogue of of the inner filament field contains 1612, 8003 and 7683 stars with good photometry in the U, V and I bands, respectively.

5.3 The color-magnitude and color-color diagrams

In Fig. 5.1 we compare the UV color-magnitude diagrams of the inner and outer filament fields. The much larger field of VLT than Magellan I and the more extended star formation region in the outer field accounts for higher number of blue stars with colors $(U - V) \sim -1$. In both fields there is a young blue main sequence extending to magnitudes of $M_V \sim -7$. We "cleaned" the CMDs from foreground contamination using the Besançon group model of stellar populations in the Galaxy (Robin & Creze 1986, Robin et al. 1996). Some of the stars in the red part $(U - V > 0)$ of the CMD are most probably still the remaining Galactic foreground stars, but in that area of

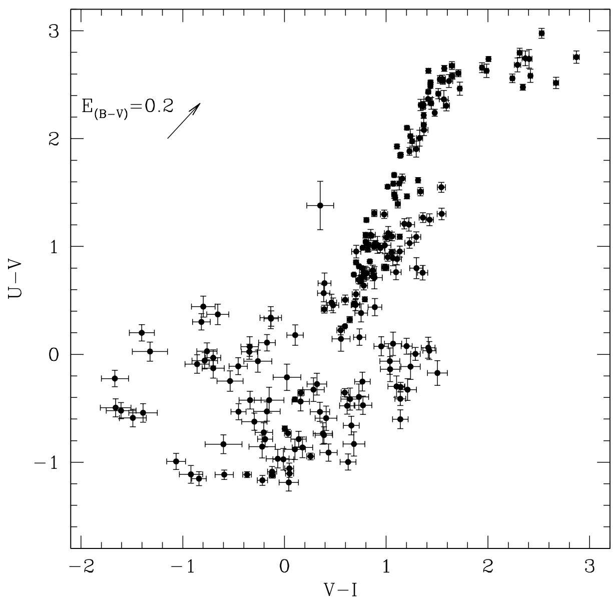

Figure 5.2: Color-color diagram for the point sources matched in U, V and I frames of the inner filament field that had ALLFRAME photometry errors < 0.5 mag and magnitudes brighter than 50% completeness limits in all bands.

the CMD supergiants on their blue–red excursions are also located (see also Rejkuba et al. 2001b, Chapter 4).

The width of the blue to red supergiant loops in the red part constrains the abundance, while the brightness of the main sequence stars constrains the age of the population. In order to determine an upper limit for the temperature and ionizing fluxes of the stars we assumed the age and abundance from the isochrone fitting. The best fit from the available set of Padova isochrones (Bertelli et al. 1994) is obtained for Z=0.004 and the log(age) ≥ 7.0 yr. The brightest stars in both fields are lying along the 10^7 yr old isochrone. Assuming then that the brightest stars have Z=0.004 and log(age)=7.0-7.1 yr, the temperature of the most luminous stars is between $\sim$ 12000 and 16000 K.

The comparison with another halo field in the southern region of the galaxy (Field 2 in Rejkuba et al. 2001b, Chapter 4) indicates that the young population is confined to the regions aligned with the optical filaments.

The (U-V) vs. (V-I) color-color diagram for all the stars in the inner filament field with photometric errors < 0.5 mag and magnitudes brighter than 50% completeness limits in all bands is presented in Fig. 5.2. The foreground stars have not been subtracted. They form the sequence that crosses the diagram from upper right towards lower left corner. The objects in the lower left part of the color-color diagram are young supergiants in NGC 5128. The spread is due to possible differential reddening and spread in ages of the young stars. Most galaxies have $0 < (U-V) < 4$ and $0.25 < (V-I) < 1.25$ (Rodighiero et al. 2000), so only few of them at higher redshift may contribute to the spread in the bluest part of the color-color diagram. The isolated point to the left of the stellar sequence at $(U-V) = 1.4$ and $(V-I) = 0.4$ is most probably a galaxy. Absence of other points with similar colors indicate a good selection criteria and low contamination by background galaxies in our stellar photometry.

The reddening value inferred from the isochrone fitting to the stellar sequence is $E(B-V) = 0.10 \pm 0.05$ in good agreement with the values from the literature (Schlegel et al. 1998, Fassett & Graham 2000, Rejkuba et al. 2001b, Chapter 4). The width of the young blue sequence is somewhat larger in the inner than in the outer filament field. This may indicate the presence of the small differential reddening amounting at most to $E(B-V) = 0.07$. However, a possible spread in ages of young stars and the photometric errors at fainter magnitudes complicate the interpretation.

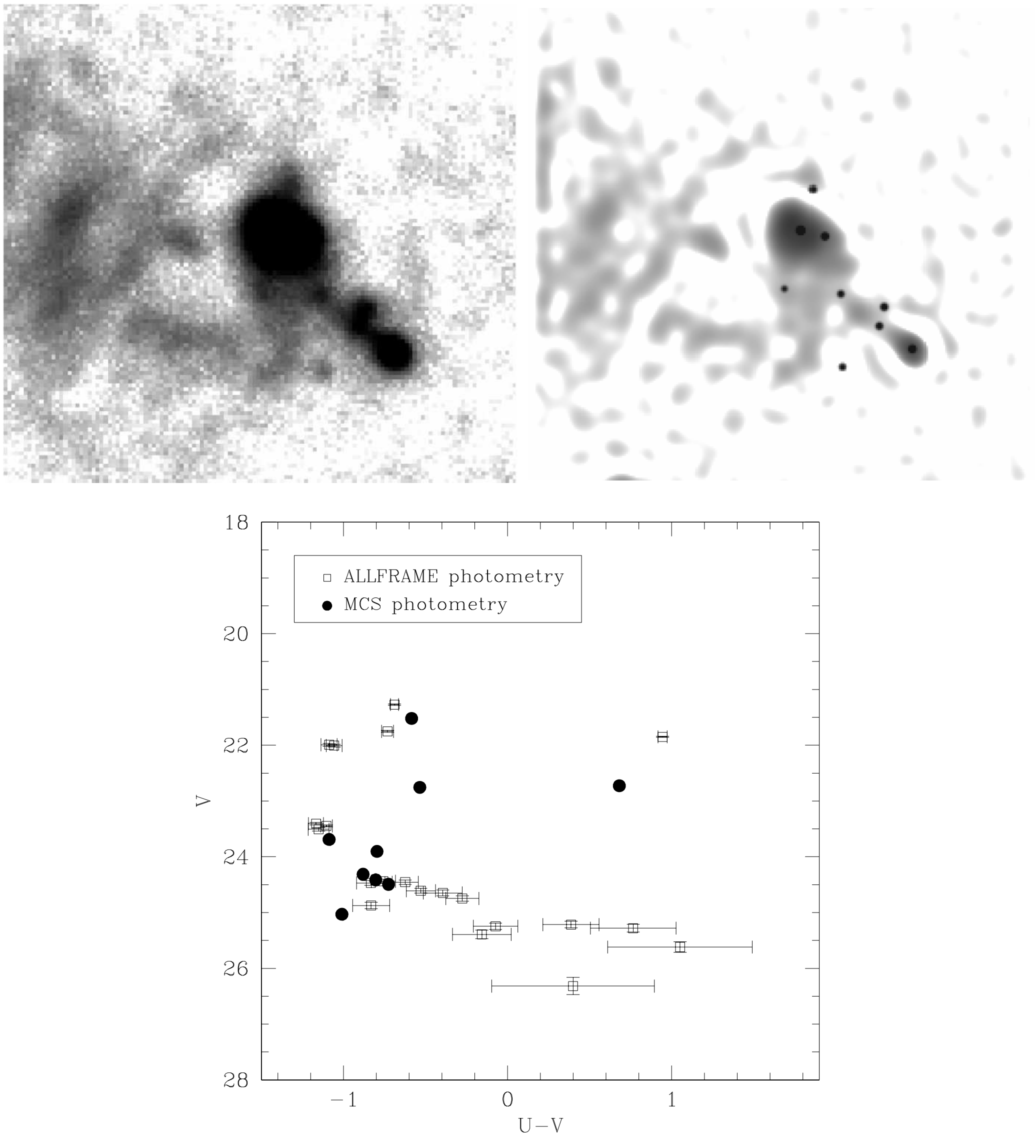

Figure 5.3: Top left: A detail of the inner filament field centered on knot A. This is the combined V-band stamp of $9'' \times 9''$. North is up and east to the left. Top right: The same image as on the left deconvolved with the MCS algorithm. In the CMD under the images the photometry obtained with ALLFRAME from the original frames is compared with the photometry measured on deconvolved images.

5.4 Knot A - image deconvolution

The photometry of knot A (Blanco et al. 1975), a possible compact star forming region in the jet, required particular care. It consists of a mixture of stellar like objects, extended nebular emission and an unresolved background of faint stars. In order to estimate the relative contribution of these components to our photometry, we deconvolved a small portion of the Magellan I image of 9×9 arcsec around the brightest hot spot using the MCS deconvolution algorithm (Magain et al. 1998). In this way we obtained a new image with improved spatial resolution (Fig. 5.3, top right) and a background map (or the "extended source channel") containing the extended sources. The final pixel scale on the deconvolved image is $0\farcs0345$ and the resolution of point sources is $0\farcs069$.

In the MCS algorithm, one has to give as an input, initial estimated positions and intensities for all suspected point sources. The program then iteratively changes them while trying to deconvolve the data. The difference between the data and the deconvolved image (reconvolved back with the PSF) in units of the noise, is used to check the quality of the process, a posteriori. This difference image or residual map should be flat and equal to 1 everywhere in the field in case of perfect deconvolution. Since introducing a higher number of point sources in the image will always produce a better result, we deliberately choose the minimum number of point sources required for the deconvolution process to yield acceptable residual maps. Some faint stars in the deconvolved image are therefore present in the "extended source channel" of the data and we "see" fewer stars with the deconvolution process than with ALLFRAME. However, the stars we see are decontaminated from the extended underlying nebular emission and we can infer their magnitudes and colors with no contribution from the emission of the surrounding gas. The comparison between these new measurements and the photometry obtained with ALLFRAME (Fig. 5.3) indicates that the magnitudes and colors of blue stars measured with ALLFRAME are not excessively contaminated by line emission from the surrounding gas. In particular we show that knot A is composed of at least two point sources embedded in a more extended envelope, possible nebular emission or a very compact and still unresolved cluster. Other objects in the field do not show such extended emission apart from the compact object ~ 3 arcsec SW of knot A. The residual flux of knot A after star subtraction is 9.4×10^{-17} erg/cm^2/sec/Å.

5.5 Discussion

Many high-redshift radio galaxies show optical images elongated in the same direction as their double radio sources, the so called alignment effect (McCarthy et al. 1987, Chambers et al. 1987, De Breuck et al. 1999). The alignment has often been explained with models of star formation induced by shocks associated with the passage of radio components (Rees 1989, Daly 1990, Best et al. 1996), but in some cases scattering of nuclear light by dust or electrons and line-emission excited by the continuum from the obscured active nucleus are dominating optical and UV light (di Serego Alighieri et al. 1989, Dickson et al. 1995, Vernet et al. 2001). In NGC 5128 we can observe in more detail physical processes that are acting in these more distant galaxies.

The direct observations of young blue supergiants associated with the outer filaments were recently reported by several authors (Fassett & Graham 2000, Mould et al. 2000, Rejkuba et al. 2001b, Chapter 4). Now for the first time we have resolved the young stars associated with the ionized filaments and knots in the inner part of the galaxy, and mapped these young stars over a large field along the radio jet. The remarkable alignment of the young stars and ionized gas over > 10 kpc is shown in Fig. 5.4 and 5.5. The red stars ($U - V > 2$) are evenly distributed in both fields as expected for foreground galactic stars, while almost all recently formed stars lie along the knots and filaments of ionized gas. The north-south (vertical) alignment in the outer field is along the eastern edge of the H I cloud that is associated with the stellar shells (Schiminovich et al. 1994).

We checked the locations of all of the blue stars and in particular of the most luminous ones. In the outer field they are evenly distributed along the star forming region, while the four brightest blue stars in the inner field lie within a very small region, known as knot A (Blanco et al. 1975). Graham & Price (1981) found that the spectrum of the knot A shows characteristics of a normal H II region and conclude that there must be hot stars embedded in that gas. We resolved here the brightest stars in that H II region. The northern extension of knot A is distinguished by a higher excitation and electron temperature similar to what is observed in other knots and filaments in the inner and outer halo (Graham & Price 1981, Morganti et al. 1991). The high excitation lines observed to be prominent

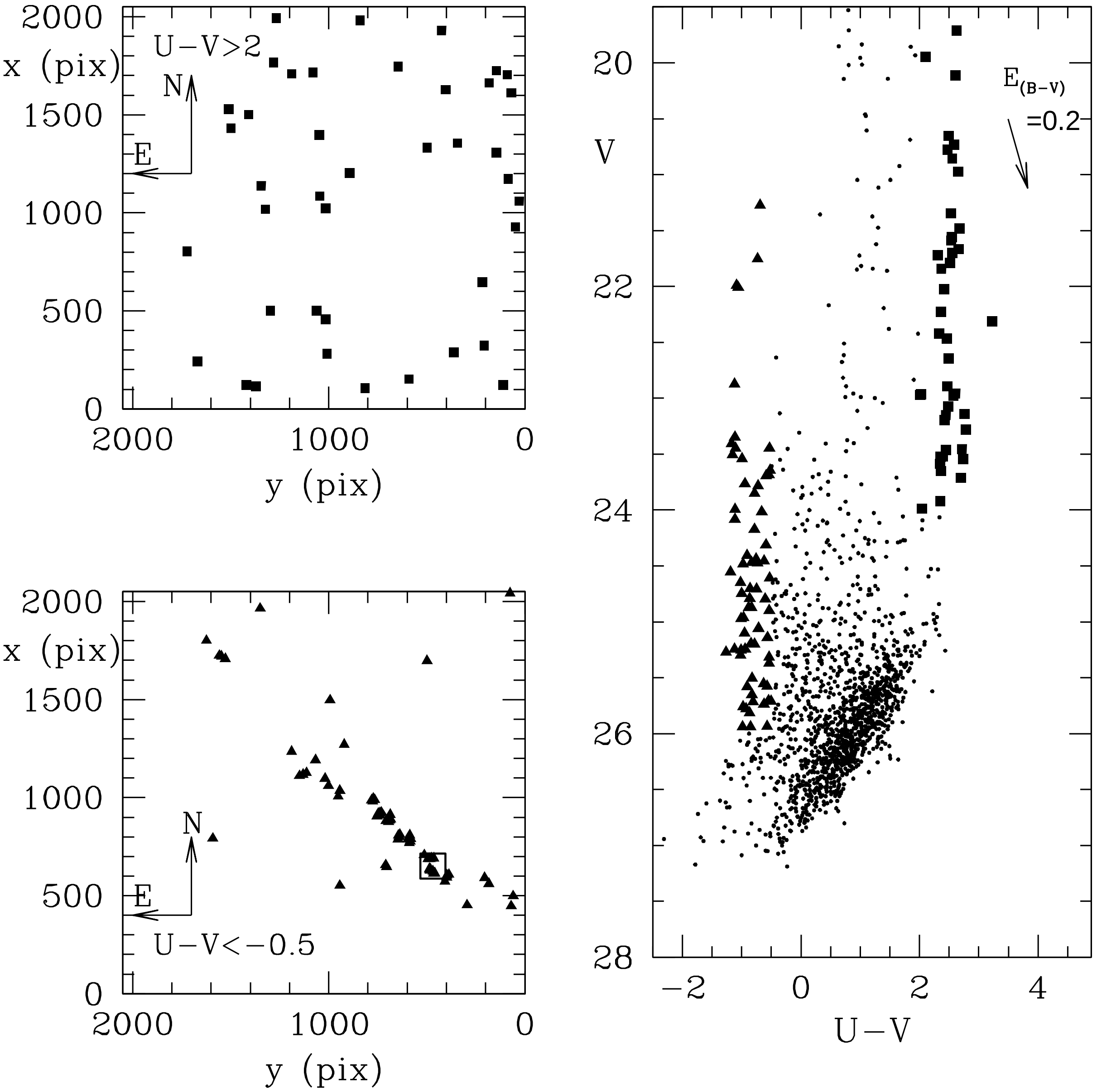

Figure 5.4: The spatial distribution of the bluest (U−V)< −0.75 (triangles) and the reddest (U−V)> 2 (squares) stars in the inner filament field for stars with magnitudes above the 50% completeness limit. The field of view is 2$'$.4 × 2$'$.4 and the scale 0$''$.069/pixel. The box indicates the location of knot A. The positions of the stars in the respective UV CMD are indicated on the right.

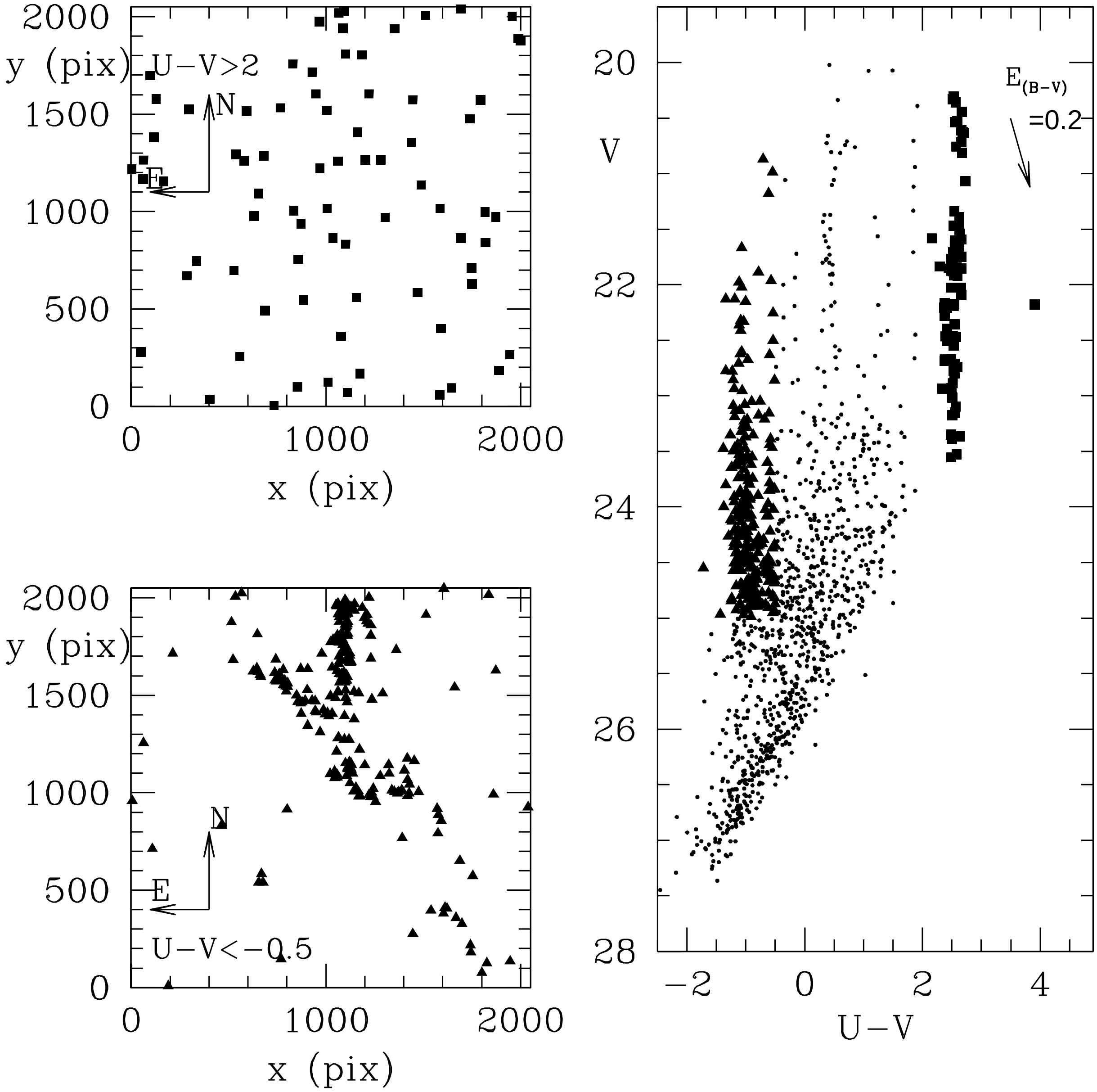

Figure 5.5: The spatial distribution of the bluest (U−V)< −0.75 (triangles) and the reddest (U−V)> 2 (squares) stars in the outer filament field for stars with magnitudes above the 50% completeness limit. The field of view is $6'.8 \times 6'.8$ and the scale $0''.2$/pixel. The positions of the stars in the respective UV CMD are indicated on the right.

in the filaments in the halo of NGC 5128 (e.g. HeII λ4686 and high ratio of [OIII] λ5007/[OII] λ3727> 1) show that the stars cannot be the only source of ionizing photons.

The complex velocity field of the filaments creates a puzzle. The spectroscopy of the ionized gas revealed a very wide range of velocities covering more than 550 km s^{-1} (Graham & Price 1981, Graham 1983, Morganti et al. 1991, Graham 1998) and varying significantly on scales of $\lesssim$ 100 pc. The mean velocity of the gas, around $\sim$ 300 km s^{-1}, is a few hundred km s^{-1} lower than the systemic velocity of the central region (Graham 1979, Morganti et al. 1991, Graham 1998), but is close to the measured velocity of the HI cloud that is located to the NW of the outer filaments (Schiminovich et al. 1994). If the stars shared the turbulent velocities of the gas, in 10^7 yr they would travel $\sim$ 3 kpc, which correspond to approx. $3'$ at the distance of NGC 5128 (note that the field of view of Magellan is less than $2\farcm5^2$ and that of VLT $\sim 6\farcm7^2$). If they had these velocities, the gas and the stars would have been dispersed in the halo of the galaxy.

The large amount of the HI and CO gas (Schiminovich et al. 1994, Charmandaris et al. 2000) and its association with the diffuse stellar shells in the halo can be interpreted with the dynamical scenario of phase-wrapping, following the merger of a spiral galaxy with NGC 5128 approximately 10^8 yr ago (Quinn 1984, Charmandaris et al. 2000). The similar mean velocity of the HI cloud and the ionized gas in the filaments indicates the common origin of the gas. We detect here for the first time the young stars associated with the inner filaments. Their strong alignment with the line emitting filaments and with the radio and x-ray jet coming from the AGN nucleus of NGC 5128 suggests a connection between them and poses interesting questions like "Did the jet trigger the star formation?" or "Are the jets seen because of the star formation?" and "Would we see the jet if there were no blue stars there?".

The answer to the first question is more complex and thus we address the others first. If we assume that the brightest stars have ages of $\sim$ 10 Myr and metallicities of Z=0.004, then they have temperatures of $\sim$ 15000 K. The high excitation lines observed in the spectra of the ionized gas require ionization temperatures of the order of 10^5 K. It is clear that an additional ionization mechanism is exciting the gas. The alignment of the ionized gas with the direction towards the nucleus of the galaxy and the fact that even though it is present, the gas in the other parts of the halo of NGC 5128 is not ionized, leaves as the most simple possibility either an interaction with the radio jet that leads to the shock excitation (Sutherland et al. 1993) or photoionization by the radiation field of a nuclear continuum source (Morganti et al. 1991, 1992). In any case, the "jet" of optical emission line features is not seen due to the star formation and it would most probably be visible even if the stars were not there.

The young stars formed after the collapse of the gas probably have the same origin as the HI and molecular clouds (Charmandaris et al. 2000). The presence of this cool gas, with $T \lesssim 10^4$ K, is the necessary ingredient in the jet induced star formation models. In the model described by Rees (1989) the prime effect of the radio outburst in a galaxy would be to heat the surrounding medium and evacuate the radio lobe of thermal gas. However, it would not disturb the cool-phase clouds, which would then be triggered to collapse in the overpressured medium. So, the jet could have induced the collapse and the star formation without transferring to the stars the high turbulent velocities that are observed today in the gas. The star formation process driven by the external pressure may not be dissimilar from the one observed in the classical stellar associations, such as Orion. This means that one needs to find an alternative mechanism in order to explain the velocities of the gas that have been observed. One possibility is that supernova explosions induced shocks into the surrounding medium. However, the problem with this scenario is that the first generation of supernovae would explode some 10^6 yr after the onset of the star formation. So, the gas would acquire the high velocities still $\sim 8-9$ million years ago and would have had plenty of time to disperse. It would have too low density and would probably not be visible any more. Thus either the first supernovae were not efficient enough to blow away all the gas or some new gas came from elsewhere. Also, the jet that triggered the star formation would have induced high velocities in the hot gas, which would then have plenty of time to disperse in the halo of the galaxy. The obvious source of the new gas is the close-by HI cloud that will continue to supply fresh material that can be ionized as long as it stays in the direction of the jet.

The inner and the outer filaments are not mutually aligned. Similarly the inner and the outer radio jets are misaligned. If we assume that the jet is precessing as suggested also by Haynes et al. (1983), it should have first hit the outer filament and precess in the eastward direction hitting later the inner filament field. The recent observations of the radio jet with VLBI (Tingay et al. 1998) and the x-ray jet with Chandra (Kraft et al. 2000) show close alignment with the inner filaments at the position angle of 55°. Stars in the inner and the outer filament have the same ages to within our precision, of the order of $\sim 1-2\times10^6$ yr. The distance between the inner and the outer filaments is $\sim 20^\circ$, implying the projected precession rate of the the order of 10^{-5} degrees per year. The presence of the large quantity of neutral gas towards the west of the outer filament implies that either the jet is precessing in a cone whose right edge does not pass the outer filaments on the west or that it is intermittent and started shining only few $\times 10^7$ yr ago.

Given the facts that the blue stars are aligned along the direction of the jet, that they have formed recently, that there is a lot of gas all over the halo of the galaxy (Schiminovich et al. 1994), but new stars are formed only where the jet passes across or close to that gas, we can conclude that the young stars observed in the filaments in the NE halo of NGC 5128 are result of the jet induced star formation. The optical emission from the gaseous filaments associated with those stars is mainly powered by the radiation field of the hidden nuclear continuum source (Morganti et al. 1991, 1992) or by the shock excitation due to the interaction of the radio jet with a dense cloud of material at the location of the filaments (Sutherland et al. 1993). If this cause-effect scenario is correct, we can put a lower limit to the age of the jet itself: it must have been acting for at least 10^7 yr in order to form the stars observed.

5.6 Conclusions

We have used the direct camera at the Magellan I and FORS1 at Antu VLT to measure the stellar photometry in two fields in the halo of the giant elliptical galaxy NGC 5128. The fields were located at the position of the inner and outer optical filaments (Blanco et al. 1975). We detected the chain of blue stars aligned with the line-emitting filaments and with the radio jet. The main conclusions from this work are:

1. We see young blue stars aligned with the jet over > 10 kpc.
2. The young stars have ages of 10^7 yr and their UV color-magnitude diagram is best fit with Padova isochrones (Bertelli et al. 1994) for abundance of Z=0.004.
3. The jet triggered star formation in the halo of NGC 5128, presumably when hitting dense clouds of neutral gas left in the halo by the previous accretion event (Schiminovich et al. 1994, Charmandaris et al. 2000).
4. The main excitation mechanism that ionizes the gas associated with the young stars is either beamed photoionization from the obscured AGN (Morganti et al. 1991, 1992) or shock ionization by the radio jet (Sutherland et al. 1993). The young stars with temperatures of the order of ~ 15000 K contribute only a smaller part of ionizing photons.
5. Our results support the alignment effect observed in high redshift radio galaxies, and suggest that radio galaxies should have higher than normal star formation rates.
6. There is evidence for the jet to be processing from the outer to inner filament field eastward in the sky.
7. We infer a lower limit for the age of the jet as 10^7 yr.

Chapter 6

Long Period Variables and distance to NGC 5128 [1,2]

Abstract

We have analyzed multi-epoch K-band photometry of two fields in the halo of NGC 5128 observed with ISAAC at VLT. A very deep K-band luminosity function was constructed and in the outer halo field a very clear tip of the red giant branch (RGB) is detected. This is a clear sign of a dominant old stellar population. Using an empirical calibration of the K-band RGB tip magnitude, assuming a mean metallicity of $[M/H] = -0.3$ dex and reddening of $E(B-V) = 0.11$, we have derived distance modulus of NGC 5128 of $(m-M)_0 = 27.97 \pm 0.10$. The second, inner halo field, presents much wider spread in metallicity and a larger number of blends. Thus the RGB tip feature is not as sharp.

The population of stars above the tip of the RGB amounts to 2286 stars in the outer halo field (Field 1) and 3973 stars in the inner halo field (Field 2). The large majority of these sources belong to the asymptotic giant branch (AGB) population in NGC 5128. Subtracting the foreground Galactic stars and probable blends, 26% and 62% of AGB stars are variable in Fields 1 and 2, respectively. While in old and metal-rich stellar populations most of the stars brighter than the RGB tip are variables, the detection of a large fraction of non-variable AGB stars and the maximum brightness achieved by them ($M_K = -8.8$ mag) is a sign of an intermediate-age population in the halo of NGC 5128. It is stronger in outer field, in which a diffuse stellar shell is detected, presumably containing stars from an accreted satellite.

The first variable star catalogue in a giant elliptical galaxy is presented. We have detected 528 and 1230 red variables in Field 1 and 2, respectively. The distribution of their amplitudes ranges from 0.3 to a few magnitudes in the K-band with a median value around 0.6 mag. Light curves were constructed for all the variables with 10 or more observations, and their periods were determined from a Fourier transform of the K-band light curve. Their amplitudes, mean magnitudes and periods indicate that the majority belongs to the class of long period variables with semiregular and Mira variables. The long period ($P \geq 200$ d) large amplitude ($\Delta K > 0.5$ mag) Mira variables were used to determine the distance of NGC 5128 from a period-luminosity relation calibrated using the Hipparcos parallaxes and LMC Mira period-luminosity relation. This is the first Mira period-luminosity relation outside the Local Group. We derive the distance modulus of 28.01 ± 0.07, adopting the LMC distance modulus of 18.50. The straight mean of the two methods yields distance modulus to NGC 5128 of 27.99 ± 0.12.

This work is still in progress as more data are going to be collected in the next few months.

6.1 Introduction

In a stellar population older than few hundred Myr the near-IR light is dominated by red giants. Among these, first ascent giants are the brightest among the metal-poor stars older than 1-2 Gyr. In a composite stellar population, like those found in galaxies the first ascent giants are mixed with asymptotic giant branch (AGB) stars. The red giants fainter than the tip of the first ascent giant branch are usually referred to as red giant branch (RGB)

[1] Based on observations collected at the European Southern Observatory, Paranal, Chile, within the Observing Programmes 63.N-0229, 65.N-0164, 67.N-503 and 68.B-0129.

[2] Rejkuba, M., Minniti, D., Silva, D.R., Bedding, T.R., in preparation

stars. In the following RGB is used to denote the first ascent giants, although it should be kept in mind that it is not possible to separate RGB and AGB stars that are fainter than the RGB tip. The tip of the RGB is a prominent feature in the color-magnitude diagrams (CMDs) for stellar populations older than about 1-2 Gyr. Its bolometric luminosity rises slowly with increasing metallicity of the population (Frogel et al. 1983, Salaris & Cassisi 1997, Salaris et al. 2002, Ferraro et al. 2000). In the I-band blanketing by metals compensates the increase in the luminosity and thus the magnitude of the RGB tip remains constant over a wide range of metallicities ($-2 \lesssim$ [M/H] $\lesssim -0.6$ dex; Da Costa & Armandroff 1990, Lee et al. 1993, Lee 1993). Thus the measurement of the I-band RGB tip magnitude is one of the secondary distance scale indicators and it has been widely used to measure distances to a number of nearby galaxies (e.g. Lee et al. 1993, Sakai et al. 1996, Minniti & Zijlstra 1997, Ferrarese et al. 2000, Jerjen & Rejkuba 2001). For stars with larger metallicities, the light emitted in the I-band starts to be dominated by metallic blanketing and the RGB tip luminosity decreases (e.g. Zoccali et al. 2002), while in the K-band it continues to brighten. The dependence of the luminosity of the RGB tip on the photometric band and on overall metallicity of the population bears important consequences to the use of this feature for distance determination.

In intermediate-age populations ($\sim 1-5$ Gyr old) numerous bright asymptotic giant branch (AGB) stars are located above the tip of the RGB. However, among old populations like Galactic globular clusters with [Fe/H] $\lesssim -1.0$ dex and in the Galactic bulge, bright stars have also been detected above the tip of the RGB (Frogel & Elias 1988, Guarnieri et al. 1997), implying the presence of bright AGB stars in metal-rich and old populations. All of the bright giants above the RGB tip in globular clusters seem to be long period variables (LPVs; Frogel & Elias 1988, Frogel & Whitelock 1998). The frequency of LPVs in old metal-rich globular clusters of the MW and in the Bulge has been studied by Frogel & Whitelock (1998). Old populations of lower metallicity are known not to have AGB stars brighter than the RGB tip. The presence or absence of these bright giants located above the tip of the first ascent giant branch has important implications for the magnitude of the surface brightness fluctuations specifically in the near-IR (e.g. Liu et al. 2002), a method used to determine distances to galaxies that are too distant to have their stellar content resolved, but that still present fluctuations due to the underlying light of giant stars (Tonry & Schneider 1988).

The properties of LPVs have been reviewed by Habing (1996). They are thermally pulsating asymptotic giant branch (TP-AGB) stars with main sequence masses between 1 and 6 $M_\odot$. They present variability with periods of 80 days or longer, and often longest period variables show variable or multiple periods. Two main classes of LPVs are Mira variables (Miras) and semiregular variables (SRs). SRs usually have smaller amplitudes as well as shorter and more irregular periods than Miras. SRs are sometimes also subdivided into subclasses (SRa, SRb) depending on the regularity and multiplicity of their periods and shape of their light curves. The separation between Miras and SRs is not always very clear (e.g. Kerschbaum & Hron 1992, 1994). The classical definition requires that Miras have V-band amplitudes larger than 2.5 mag and regular periods in the range of 80–1000 days (GCVS Kholopov 1985). Mean K-band amplitudes of Miras are ~ 0.6 mag (e.g. Feast et al. 1982, Wood et al. 1983).

Miras in the Large Magellanic Cloud (LMC), in the Galactic Bulge, in the Solar Neighbourhood and in the Galactic globular clusters follow a well-defined period-luminosity (PL) relation for both M_{bol} and M_K (Glass & Lloyd Evans 1981, Whitelock et al. 1991, Feast 1996, Bedding & Zijlstra 1998, Whitelock & Feast 2000, Feast et al. 2002). Being the most luminous giants, the tight PL relation makes them interesting for distance determination to other galaxies.

The brightest LPVs in old stellar populations like the Galactic globular clusters and the old disk in the Milky Way reach $M_K = -8$ (Mennessier et al. 2001, Feast et al. 2002). The higher mass (hence younger) LPVs in the LMC and in the disk of our galaxy can be more luminous, reaching $M_K = -9.4$ (Hughes & Wood 1990, Mennessier et al. 2001).

There exists a long standing debate about the presence of intermediate-age population in dwarf elliptical galaxies and spiral bulges. On the basis of the Wide Field Camera 1 (WFC1) HST data Holtzman et al. (1993) and Vallenari et al. (1996) concluded that the majority of stars in the Galactic bulge were of intermediate-age. Other studies indicated mainly old metal-rich population (e.g. Frogel et al. 1990, Tiede et al. 1995). Newer deep optical and near-IR CMDs suggest that the Bulge is old without even a trace of intermediate-age population (e.g. Ortolani et al. 1995, Feltzing & Gilmore 2000, Zoccali et al. 2002). In the M32 dwarf elliptical galaxy the situation might be different as the presence of an extended giant branch reaching $M_K = -8.7$ ($M_{bol} = -5.5$), indicative of an intermediate-age ($\sim$ 4 Gyr) population, has been revealed by near-IR photometry of Elston & Silva (1992) and Freedman (1992). However, it is of interest to note that in the deep optical VI photometry of M32 with HST no optically bright AGB stars have been found (Grillmair et al. 1996), which might be expected due to high bolometric corrections.

In the gE NGC 5128 Soria et al. (1996), based on VI HST CMD, and Marleau et al. (2000), based on JH NICMOS data, suggest a presence of up to 10% bright AGB stars belonging to an intermediate-age population. Harris et al. (1999, 2000) on the contrary do not find any bright AGB stars in their VI CMDs of two halo fields in NGC 5128. As mentioned above, V and I bands are not very sensitive indicators of these cool giants and thus some of them might have been confused with foreground stars and few stellar blends or stars with larger photometric errors. In our two fields observed in V and K-bands with VLT (Rejkuba et al. 2001b Chapter 4) a large number of bright AGB stars have been detected extending up to bolometric magnitude of –5. Most of these stars have been found to be variables in our long term monitoring programme with ISAAC@VLT.

In this chapter multi-epoch K-band photometry obtained with ISAAC@VLT is used to investigate the nature of the population of stars found above the RGB tip in two halo fields in NGC 5128. In the next section we briefly present the data and the reduction procedures. The technique used to detect the variable stars is described next. The light curves and periods of the long period variables are derived in section 6.4. The amplitude distribution and the luminosity function of variables as well as luminosity function of all K-band sources are presented in section 6.5. In section 6.6 the tip of the RGB and LPV K-band PL relation are used to determine the distance to NGC 5128. In the end we conclude and summarize the results.

6.2 The data

Part of the K-band data analyzed here were already described in Chapter 4. We have so far obtained a total of 14 epochs of K-band photometry in Field 1 and 17 epochs in Field 2 (see Chapter 4 for the location of fields in the halo of NGC 5128) in the time interval between April 1999 and February 2002. All of the data were obtained through the service mode observing with ISAAC@VLT, except one Field 2 epoch which was secured on an observing run in February 2000 at NTT. There are still 5 epochs to be observed in ESO period 69 (to be concluded by September 2002).

During the service observations of 2 epochs (E and F) of Field 2, the integration was interrupted before the end of the sequence due to changing weather conditions. Additional observations for these epochs were taken a few days after the original sequences. Thus we reduced them as separate epochs, yielding 17 data points for Field 2 and 14 for Field 1. The summary of the observations is given in table 6.1 where on the left we describe Field 1 observations an on the right Field 2 observations.

Data reduction followed the procedure described in Chapter 4. We first correct for the electronic ghost using the ESO supplied routine in the ECLIPSE package. Then we subtract the dark and divide with the sky flats provided from the service observing standard calibrations. The DIMSUM package (Stanford et al. 1995) in IRAF was used to subtract the sky in a double sky-subtraction run, the second time masking the objects detected in the registered and combined frames after the first sky subtraction. This double sky subtraction procedure is particularly important for these crowded images. We noticed that in a single sky subtraction pass, bright regions were often over-subtracted producing dark halos around the bright stars. Finally the sky-subtracted images were aligned with IMALIGN and combined with IMCOMBINE tasks in IRAF.

The PSF fitting photometry was done for each single epoch image individually. First we used DAOPHOT II and ALLSTAR (Stetson 1987) to create a PSF for each frame and to define the coordinate transformations between the frames. The complete star list was created from the median combined image that had only the best seeing epochs (i.e. those with FWHM stellar profiles measured < 3 pix). These included epochs 1A, 1B, 1D, 1E, 1G and 1J for Field 1 and epochs 2A, 2B, 2D, 2Fb, 2G, 2J, 2M and 2N for Field 2. We found that better results were obtained in this way instead of combining all the images. PSF fitting photometry using this star list and coordinate transformations was performed simultaneously on all images of a single field with the ALLFRAME programme (Stetson 1994). The final photometric catalogue contains 15324 stars in Field 1 and 17894 stars in Field 2, that have been detected on at least 3 frames.

Table 6.1: Near-IR multi-epoch photometry: on the left Field 1 observations and on the right Field 2 observations are described.

JD−2400000	Exposure (min)	Airmass	Seeing $''$	Epoch	JD−2400000	Exposure (min)	Airmass	Seeing $''$	Epoch
51277.1	60	1.15	0.41	1A	51277.2	60	1.05	0.36	2A
51306.1	60	1.05	0.40	1B	51306.1	60	1.10	0.39	2B
51327.1	60	1.14	0.51	1C	51328.0	60	1.06	0.44	2C
51650.1	65	1.09	0.35	1D	51594.4	45	1.04	0.55	2Sofi
51675.2	65	1.22	0.43	1E	51650.3	65	1.09	0.40	2D
51702.9	65	1.13	0.60	1F	51677.2	51	1.22	0.51	2Eb
51734.0	65	1.15	0.31	1G	51684.2	20	1.22	0.44	2Ec
52037.1	60	1.05	0.63	1H	51703.0	41	1.13	0.57	2Fa
52060.1	60	1.08	0.47	1I	51705.0	30	1.13	0.40	2Fb
52096.0	60	1.05	0.34	1J	51734.1	65	1.15	0.40	2G
52299.3	56	1.44	0.54	1K	52037.2	60	1.10	0.61	2H
52309.3	56	1.27	0.49	1L	52060.1	60	1.06	0.50	2I
52322.2	56	1.38	0.45	1M	52096.1	60	1.12	0.38	2J
52348.3	56	1.06	0.49	1N	52300.3	56	1.30	0.54	2K
					52315.3	56	1.10	0.47	2L
					52332.3	56	1.13	0.36	2M
					52348.3	54	1.10	0.37	2N

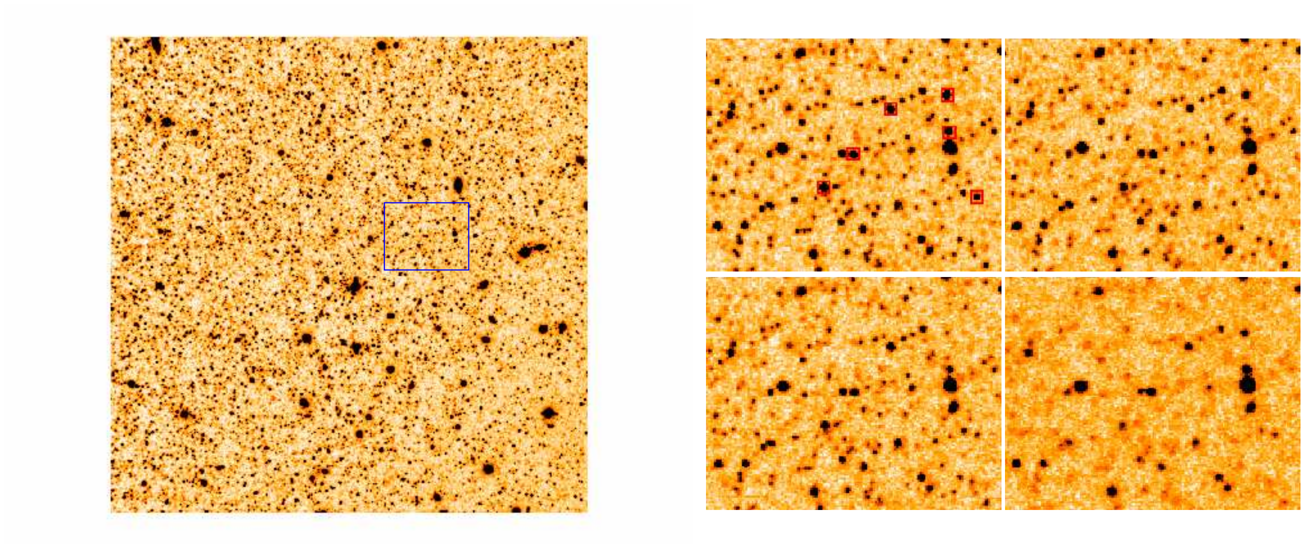

Figure 6.1: Left: A combined image of the 6 best seeing epochs (FWHM of stellar profiles measured on images < 3 pix) for Field 1. This field is located $\sim 14'$ north-east from the center of the galaxy, at the location of the diffuse stellar shell. The total exposure time of this image is 6.25 hours and the field of view $2'.07 \times 2'.07$. North is up and east to the left. Right: Zoom of a 150×120 pix region (indicated with a box on the left image) shown for 4 individual epochs: 1G, 1D, 1N and 1J (seeing $0''.31$, $0''.35$, $0''.49$ and $0''.34$, respectively), clockwise from upper left to lower left. Variable stars are indicated with boxes in 1G epoch.

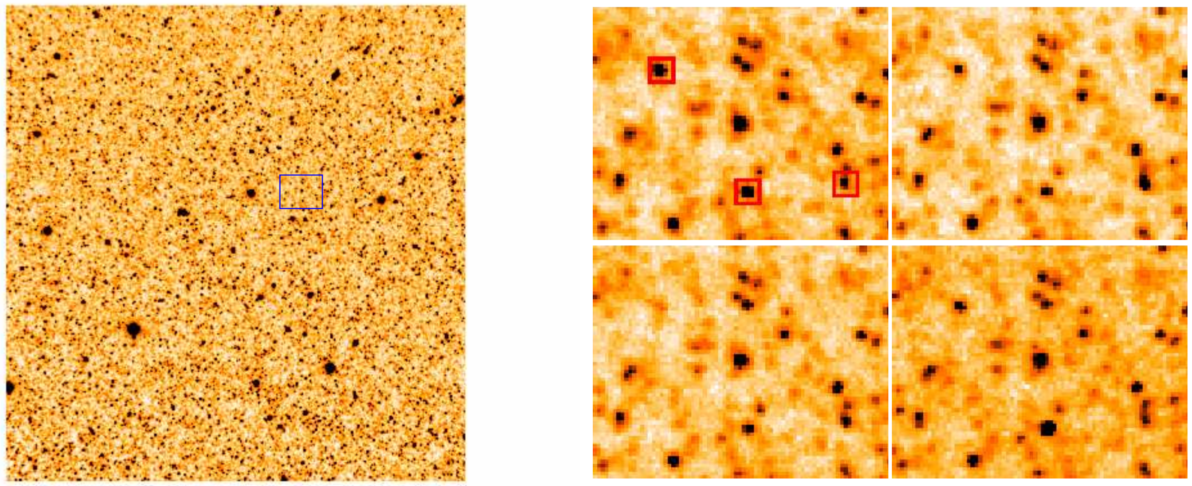

Figure 6.2: Left: A combined image of the 8 best seeing epochs (FWHM of stellar profiles measured on images < 3 pix) for Field 2. This field is located $\sim 9'$ south from the center of the galaxy and it coincides with the HST field studied by Soria et al. (1996) and Marleau et al. (2000). The total exposure time of this image is 7.5 hours and the field of view $2.'0 \times 2.'07$. North is up and east to the left. Right: Zoom of a 75×60 pix region (indicated with a box on the left image) shown for 4 individual epochs: 2G, 2D, 2N and 2J (seeing $0.''40$, $0.''40$, $0.''37$ and $0.''38$, respectively), clockwise from upper left to lower left. Variable stars are indicated with boxes in 2G epoch.

Combined images of the best seeing epochs for Field 1 and Field 2 are shown in figure 6.1 and figure 6.2, respectively. The total exposure time on these images are 6.25 and 7.5 hours. The fields of view correspond to the common area observed at different pointings for the best seeing epochs and they amount to $2.'07 \times 2.'07$ for Field 1 and $2.'0 \times 2.'07$ for Field 2. The areas covered with at least three pointings are slightly larger, $2.'27 \times 2.'28$ and $2.'23 \times 2.'29$, and the total exposure times are 14.07 and 14.98 hours, for fields 1 and 2, respectively. Incidentally these are the deepest near-IR images taken so far in an external galaxy halo.

Not all the epochs were observed in photometric conditions. The photometry was brought to the system of one of the photometric nights that had excellent seeing, the epoch 1G and 2G for fields 1 and 2, respectively, both observed on July 8, 2000. The zero point for that night has been derived from the observations of Persson et al. (1998) standards supplied by ESO service observing (Rejkuba et al. 2001b, Chapter 4).

The quality of the photometry can be assessed from figure 6.3 where we plot differences of individual epoch measurements vs. mean magnitudes. The mean magnitudes were calculated weighting the individual measurements with their photometric errors calculated by ALLFRAME:

$$\overline{K} = \frac{\sum_{i=1}^{n} \frac{K_i}{\sigma_i^2}}{\sum_{i=1}^{n} \frac{1}{\sigma_i^2}} \tag{6.1}$$

Only the stars with individual ALLFRAME σ uncertainty measurements smaller than 0.2 mag are plotted. The limiting accuracy of our photometry at the bright end is ± 0.05 mag and it gets worse at faintest magnitudes. The region around K=20 has more scattered measurements than the mean. This is where most variable stars are found.

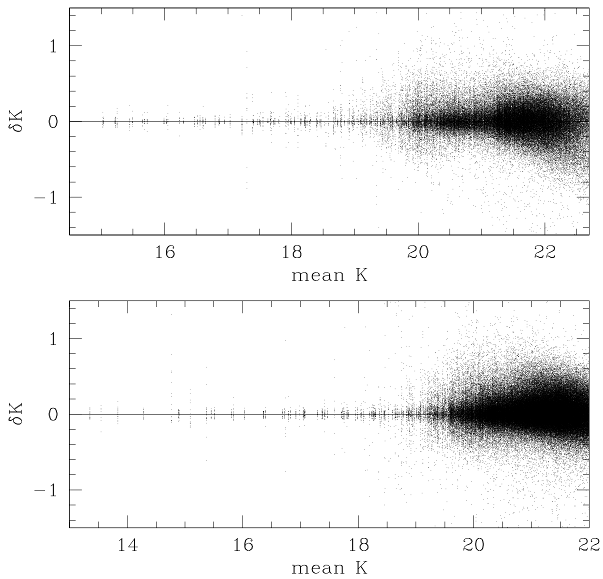

Figure 6.3: Photometric accuracy for the K-band data. Plotted are differences of individual epoch measurements with respect to their mean magnitudes. Only individual measurements with ALLFRAME σ error smaller than 0.2 are plotted. At the bright end the limiting accuracy of ± 0.05 mag can be seen. The variables are located where an excessive scatter with respect to the mean is present with both positive and negative excursions.

6.3 Search for variable stars

Variable stars were identified using a procedure similar to the one described by Welch & Stetson (1993) and Stetson (1996). First, we selected all the stars with mean of all photometric errors given by ALLFRAME, as measured on each individual epoch frame, smaller than 0.2 mag. We then required for each star to be detected on more than 5 frames and constructed variability indices J, K and L, following the prescriptions by Stetson (1996; equations 1–3). In particular the J index is used for single observations assuming $P_i = \delta_i^2 - 1$, where δ_i is a normalized residual of the measurement from the mean magnitude calculated as:

$$\delta = \sqrt{\frac{n}{n-1}} \frac{K_i - \overline{K}}{\sigma_i} \tag{6.2}$$

The mean magnitude is calculated using a weighting with inverse square of the measurement error (weight w_i) according to equation 6.1. The variability index J for each star is then:

$$J = \frac{\sum_{i=1}^{n} w_i \operatorname{sgn} P_i \sqrt{|P_i|}}{\sum_{i=1}^{n} w_i} \tag{6.3}$$

With this definition, J is a robust measure of the external repeatability relative to the internal precision. For single epoch observations containing only random noise its value tends to zero. For a physical variable it is a positive number.

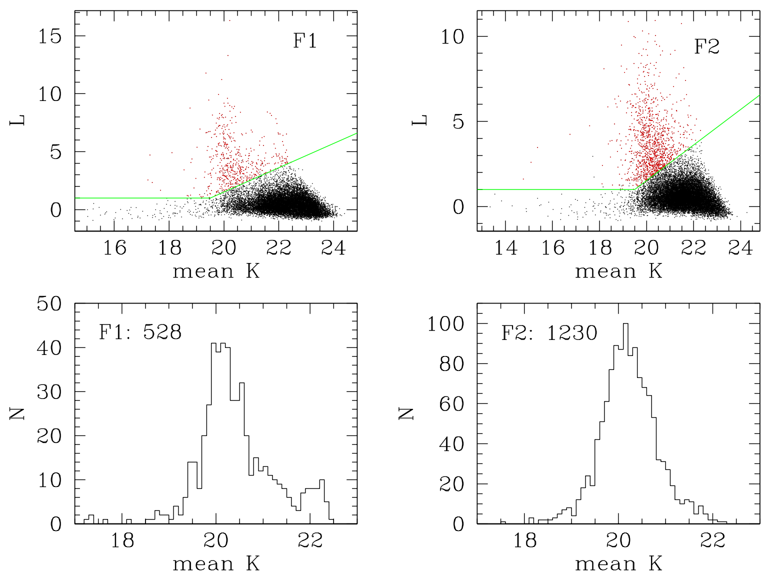

Figure 6.4: Variability index L vs. magnitude is plotted in the upper two panels for the Field 1 (left) and 2 (right). Variable stars are found above the red line and are plotted with red symbols. In the lower panels the magnitude distribution of variable stars is shown. The number of variables with at least 6 data points is displayed in lower panels.

The index K is defined by equation 2 in Stetson (1996) as:

$$K = \frac{\frac{1}{N}\sum_{i=1}^{n} |\delta_i|}{\sqrt{\frac{1}{N}\sum_{i=1}^{n} \delta_i^2}} \tag{6.4}$$

It is a robust measure of the kurtosis of the magnitude histogram. Stetson lists also the range of values for K for different shapes of light curves: for a hypothetical pure square-wave light curve K tends to 1.0; for a pure sinusoid $K \to \frac{\sqrt{8}}{\pi}$=0.900; for a sawtooth (uniform distribution of magnitude probabilities) $K \to \frac{\sqrt{12}}{4} = 0.866$; for a Gaussian magnitude distribution $K \to \frac{\sqrt{2}}{\pi}$=0.798; and for a single measurement blunder of size Δ it tends to 0 as $\frac{1}{\sqrt{N}}$ where N is the number of measurements. The gaussian limit is approached when random measurements errors dominate over the physical variation.

Including the information about the variability and the shape of the light curve, Stetson defined the final variability index L as:

$$L = \left(\frac{JK}{0.798}\right)\left(\frac{\sum w_i}{w_{all}}\right) \tag{6.5}$$

The second term in this expression assigns an additional weight to stars with the highest number of measurements.

Figure 6.4 is a plot of the variability index L for all the stars in Field 1 and 2 in the left and right panels, respectively. The stars above the line, plotted with red symbols were searched for periodic variations. In completeness simulations stars with constant magnitude light curves were added to the frames and their photometry and variability indices were measured in identical way as for the programme stars. A similar plot of the variability index *vs.* magnitude was used to decide on the separation line between the variable and non-variable stars. Further simulations are necessary to assess the completeness of the variable star search. This selection contains 528 stars in Field 1 and 1230 stars in Field 2. Of these 441 and 1148 had at least 10 measurements with individual errors smaller than 0.5 mag, and for them light curves were constructed.

6.4 Lightcurves and periods for LPVs

A Fourier analysis of the K-band light curves was used to search for the periodic signal in the data in the range of $30 < P < 1700$ days. Only individual measurements with ALLFRAME uncertainty smaller than 0.5 mag were used. First, an initial guess of the period was obtained using a routine "period" from Numerical Recipes (1992; Lomb 1976) that calculates spectral power as a function of angular frequency ($\omega = 2\pi f$):

$$P_N(\omega) = \frac{1}{2\sigma^2}\left\{\frac{[\sum_j (K_j - \overline{K})\cos\omega(t_j - \tau)]^2}{\sum_j \cos^2\omega(t_j - \tau)} + \frac{[\sum_j (K_j - \overline{K})\sin\omega(t_j - \tau)]^2}{\sum_j \sin^2\omega(t_j - \tau)}\right\} \tag{6.6}$$

where K_j and $\overline{K}$ are the individual and mean magnitudes, σ is the variance, t_j is the Julian Date (JD) of the measurement, and τ is defined as:

$$\tan(2\omega\tau) = \frac{\sum_j \sin 2\omega t_j}{\sum_j \cos 2\omega t_j} \tag{6.7}$$

The period obtained from the frequency with largest power corresponds to the most probable sinusoidal component. It was further improved with a non-linear least-square fitting of the function

$$K(t) = A\cos\left(2\pi\frac{(t - t_0)}{P}\right) + B\sin\left(2\pi\frac{(t - t_0)}{P}\right) + K_0 \tag{6.8}$$

From this, the best fitting period (P), amplitude ($2 \times \sqrt{A^2 + B^2}$), mean magnitude ($K_0$) and phase ($t_0$) were obtained.

In optical passbands Miras often have asymmetric light curves, usually steeply rising to the maximum and with a shallower decline. In near-IR the variations are more regular and nearly sinusoidal (e.g. Whitelock et al. 2000). Hence a sine-wave gives a reasonable approximation to most of the LPVs.

Our code that determines the best fitting period was tested on a subsample of data on Mira variables published by Whitelock et al. (2000). Their data are very similar to ours, with 10–15 data points per star and photometric errors of the order of 0.05 mag in K. In 8 out of 10 cases we obtain the same period as Whitelock et al. In two cases our periods were significantly different (in one case we derived 74 days period with respect to the published value of 185 days and in the second case our period is 422 days where Whitelock et al. got 327 days), but the light curves folded with these periods looked as good or even smoother than the published light curves. In some cases is possible to obtain more than one acceptable period when there are less than 15 data points. It is not clear however, if these stars really pulsate with two different periods as is the case for some Mira variables (Whitelock et al. 2000), or the insufficient data allow to derive such different periods due to aliases in the sampling of the data.

In figure 6.5 we show two examples of a periodogram, the original light curve in time domain and the light curves folded with the period obtained from the highest power frequency from the periodogram and by a sine curve fitting. Most of the times when a good period could be derived the two periods were similar, but sometimes they differed by more than 20-30 days and both light curves were of acceptable quality. This illustrates that the accuracy of the derived periods and amplitudes varies considerably from one star to the next, depending on the number of observations, their individual errors and the stability of the light curve over the sampling interval. A more quantitative accuracy of the periods, as well as the completeness of the detection of variables with a given period will be derived using Monte Carlo simulations, after all the data have been acquired.

For 33 stars in Field 1 and 264 in Field 2 no acceptable periods could be obtained because of the non-sinusoidal variations, large errors combined with small amplitudes, multiple periods or absence of period (e.g. microlensing, background AGN or SN). More data are necessary to determine the nature of these variables. The light curves for 408 variables in Field 1 and 884 in Field 2, that we could determine periods of, as well as the tables with the best

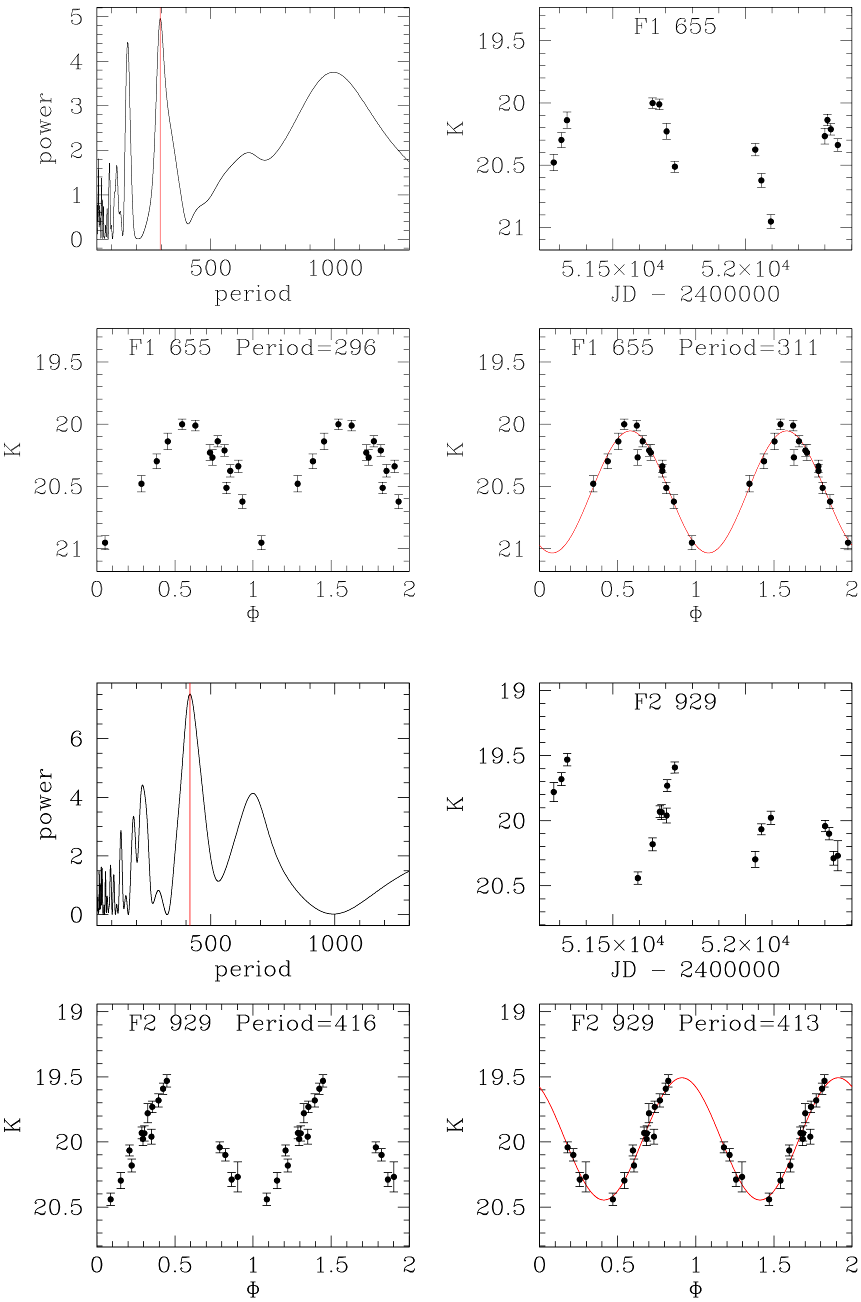

Figure 6.5: From left to right, top: periodogram and the original light curve in time domain; bottom: the light curve folded with the period obtained from the highest power frequency from the periodogram and the same light curve folded by the best period obtained from sine curve fitting. Each point in the phased ligth curves is plotted twice to emphasize the periodicity. Over the last light curve the fitting function is over-plotted. In top panels the four diagrams are plotted for star #655 in Field 1 and in bottom panels for star #929 in Field 2

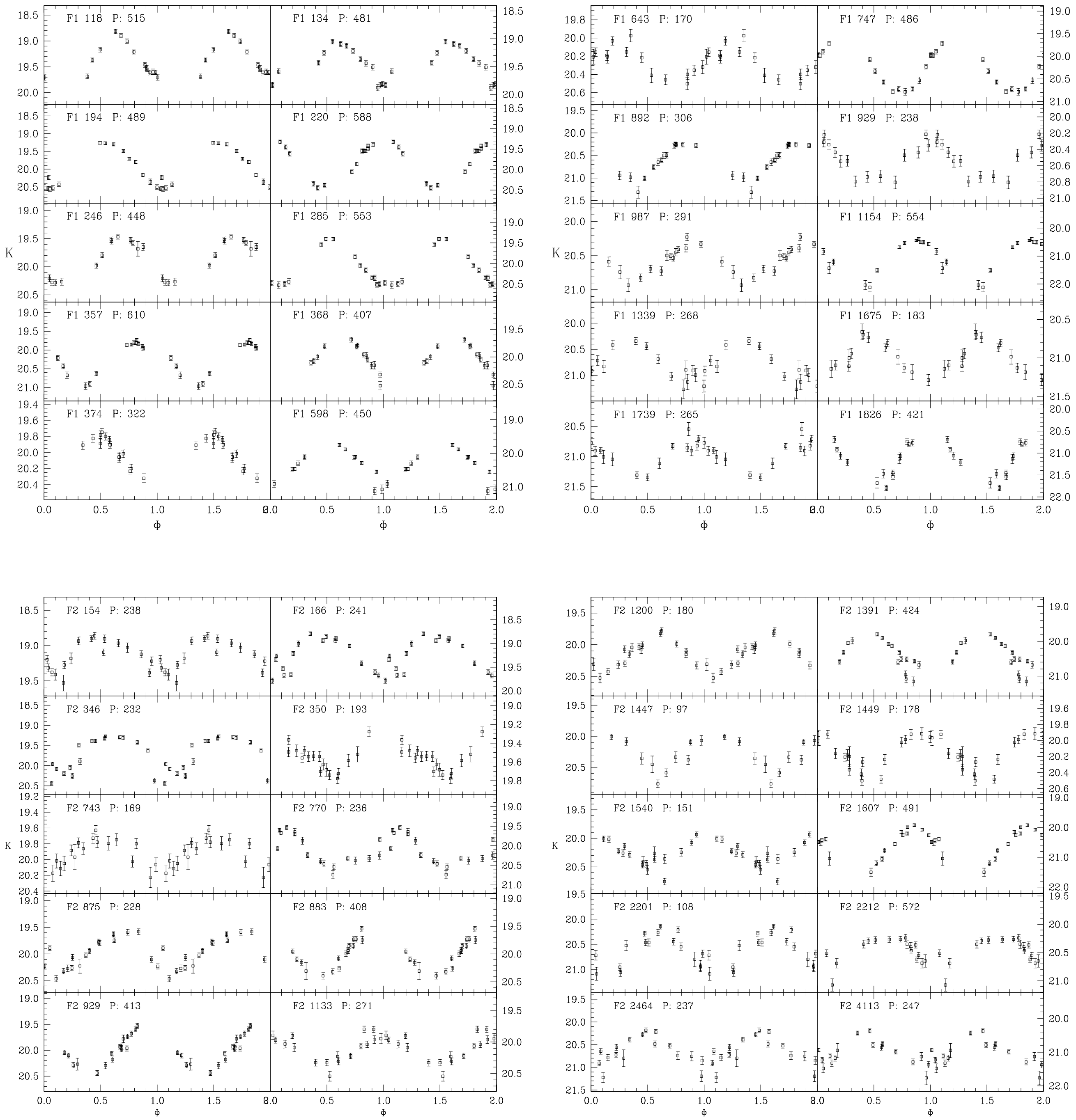

Figure 6.6: A sample of good phased K light curves. Each point is plotted twice to emphasize the variability.

Table 6.2: Data for a sample of variables with light curves plotted in figure 6.6. The columns from left to right list: star ID, x and y position with respect to epoch G, mean magnitude and the amplitude of variation from the sine wave fit, period from the best fitting sine wave, and reduced χ^2 of the fit.

#	x	y	N	$\overline{K}$	ΔK	P_{sin}	χ^2_r
F1 118	366.415	678.238	14	19.471	1.094	515	4.61
F1 134	241.710	710.162	14	19.475	0.720	481	7.53
F1 194	130.815	541.882	14	19.857	1.230	489	2.95
F1 220	314.725	367.313	14	19.866	1.236	588	1.73
F1 246	853.325	736.522	13	19.934	0.926	448	1.39
F1 285	480.504	569.929	14	19.988	1.142	553	0.80
F1 357	144.644	456.497	14	20.317	0.986	610	4.06
F1 368	400.918	355.989	14	20.092	0.936	407	0.85
F1 374	720.313	102.270	14	20.103	0.610	322	1.18
F1 598	844.513	709.324	13	20.224	1.088	450	4.91
F1 643	719.833	37.132	14	20.279	0.410	170	1.78
F1 747	83.867	591.335	14	20.156	1.326	486	1.18
F1 892	215.895	336.611	14	20.650	0.908	306	1.04
F1 929	262.042	271.020	14	20.558	0.544	238	1.85
F1 987	533.245	110.111	14	20.580	0.526	291	1.54
F1 1154	808.375	642.119	13	21.180	1.522	554	1.47
F1 1339	455.684	392.515	14	20.704	0.784	268	1.70
F1 1675	644.570	702.301	14	21.026	0.576	183	1.49
F1 1739	434.899	385.899	14	21.039	0.584	265	1.92
F1 1826	151.662	580.070	14	21.133	1.458	421	3.07
F2 154	834.503	691.920	17	19.112	0.408	238	4.28
F2 166	586.997	98.790	17	19.212	0.746	241	17.23
F2 346	553.117	180.719	17	19.670	0.954	232	17.65
F2 350	240.385	634.800	17	19.498	0.386	193	2.35
F2 743	234.896	556.086	17	19.895	0.398	169	1.50
F2 770	827.570	654.082	17	20.141	0.894	236	9.28
F2 875	219.659	848.026	17	19.927	0.646	228	8.59
F2 883	675.832	236.575	17	19.930	0.958	408	1.86
F2 929	683.390	648.248	17	19.977	0.938	413	1.97
F2 1133	626.091	102.723	17	20.112	0.494	271	3.96
F2 1200	691.089	27.208	17	20.140	0.596	180	1.78
F2 1391	174.522	430.641	17	20.352	0.308	424	36.94
F2 1447	388.567	870.014	10	20.259	0.698	97	4.67
F2 1449	232.357	42.350	17	20.149	0.556	178	2.21
F2 1540	711.909	559.909	17	20.226	0.544	151	4.65
F2 1607	541.512	536.064	17	20.800	1.578	491	3.91
F2 2201	409.422	459.009	17	20.615	0.802	108	4.92
F2 2212	50.671	369.979	17	20.457	0.486	572	3.44
F2 2464	377.048	64.826	17	20.596	0.674	237	4.59
F2 4113	167.085	449.518	17	20.905	0.748	247	8.19

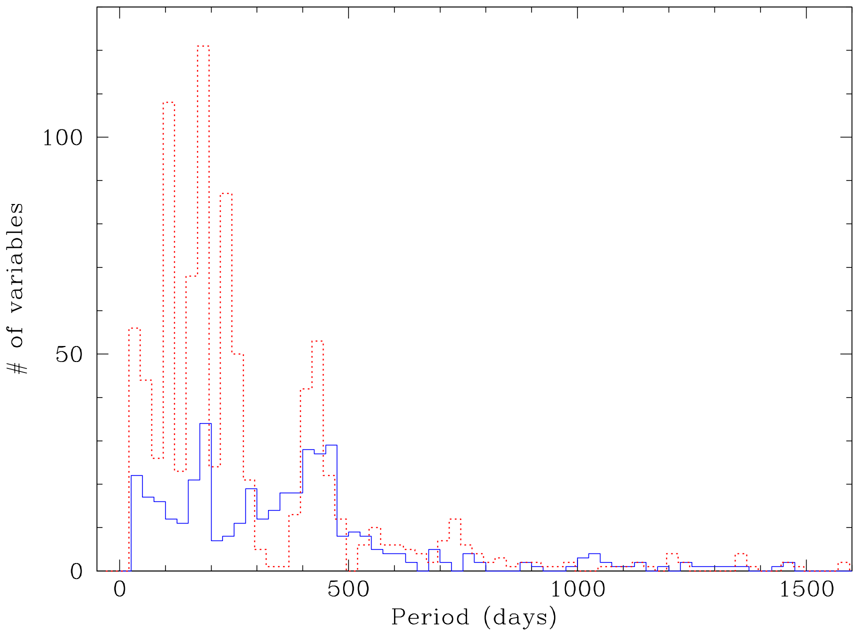

Figure 6.7: Histogram showing the period distribution of LPVs in Field 1 (solid line) and 2 (dotted line).

fitting parameters for these stars, are presented in the appendix. Here in figure 6.6 we show a sample of good light curves folded with the periods that are indicated in each panel. Table 6.2 lists for these stars: ID number, x and y positions with respect to the G-epoch frame, number of epochs with magnitude measurements with $\sigma < 0.5$, mean K magnitudes and amplitudes as obtained from sine-curve fitting, periods from sine-curve fitting and the reduced χ^2 of the last fits. Negative numbers for x and y positions mean that the star was out of the image of epoch G.

The distribution of periods for all the variables with at least 10 measurements for which we obtained periods with least square sine-wave fitting is shown in figure 6.7. About 13% of variables in Field 1 and 16% in Field 2 have periods shorter than 100 days. There are many stars with periods around 180 days. Some of them are genuine short period SR variables, but for some the short period may be result of aliasing in period sampling. Almost no variables with periods close to 365 days in Field 2 agrees with the previous statement about aliasing. The percentage of variables with periods longer than 700 days is 9% and 7% for Field 1 and 2, respectively.

These can be compared with periods of Mira variables in other stellar systems. In Galactic globular clusters Miras span a rather narrow range of periods $140 \lesssim P \lesssim 310$ (Feast et al. 2002). Analysis of Hipparcos data has shown that local Miras have periods ranging from $\sim$ 100 to $\sim$ 550 days (Whitelock et al. 2000). According to Whitelock et al. (1991) there are no Miras with periods longer than $\sim$ 750 days in the Galactic bulge. Their result is however in disagreement with Harmon & Gilmore (1988) and Blommaert et al. (1998). These last authors find some OH/IR variables with periods in excess of 2000 days in the Galactic bulge. In the LMC LPVs (including Mira and SR variables) span a range of periods from about 20 to $\sim$ 1000 days (e.g. Wood 2000, Alard et al. 2001).

It has been shown that longer periods correspond to higher masses of main sequence progenitors to LPVs (e.g. Jura & Kleinmann 1992a, 1992b, Kerschbaum & Hron 1992). Hence the distribution of periods provides an indication of the age of the population. The majority of the Miras have periods characteristic of low mass progenitors similar to those found in the globular clusters and the Galactic Bulge, but the tail towards longer periods indicates that there is also a substantial number of higher mass (hence intermediate-age) LPVs. However, periods longer than about 700 days need to be confirmed with data spanning a longer time-baseline, as our data span only 1071 days so far.

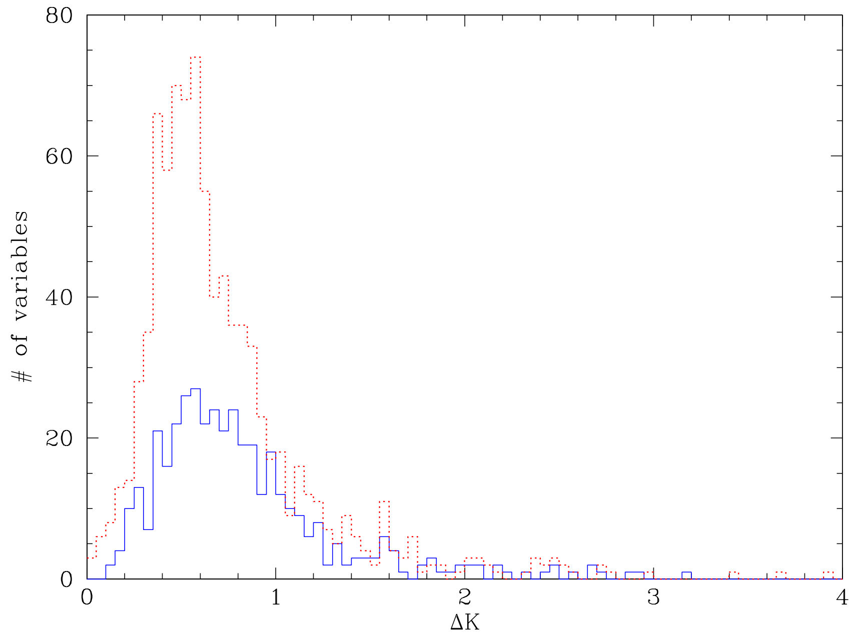

Figure 6.8: Histogram showing the amplitude distribution of LPVs in Field 1 (solid line) and 2 (dotted line).

6.5 Amplitude distribution and luminosity function of LPVs

6.5.1 Amplitudes

The amplitudes of the variables were calculated by fitting the sine wave to the data and measuring the separation between the two extreme magnitudes. These values are reported in table 6.2 and in the appendix.

For variables with 10 or more measurements for which we could determine periods we plot the histogram illustrating the amplitude frequency in figure 6.8. The majority of variables have K-band amplitudes of around 0.6 mag, with median values being 0.73 and 0.60 for Fields 1 and 2, respectively. The mean K-band amplitude for Miras in LMC (e.g. Wood et al. 1983) and in the MW (e.g. Whitelock et al. 2000) is around 0.6.

The dependence of the amplitudes on the mean magnitudes (also determined from the sine wave fit) and on the periods is shown in figures 6.9. The larger number of high amplitude variables at fainter magnitudes is a selection effect caused by increasing photometry errors.

As it was also found for Galactic Mira-like LPVs from the Hipparcos catalogue (Whitelock et al. 2000), there is only a very weak correlation in the sense that longer period variables tend to have larger amplitudes.

6.5.2 Luminosity functions

The luminosity functions for all the stars in Field 1 (left) and 2 (right) are shown in figure 6.10 as solid line histograms. These are not corrected for incompleteness nor for Galactic foreground contamination. The magnitude distribution of the blue stars (bluer than −(V−K)+25 line) is plotted as a dotted histogram. These stars are mostly foreground Galactic stars as well as young blue and red supergiants in Field 1 (see chapter 7). We also compare the luminosity functions with the magnitude distribution of variable stars (shaded red histogram). It is clear that majority of the variables have luminosities brighter than the RGB tip ($K < 21.3$) and are in the TP-AGB phase. In the lower panels the total luminosity functions are compared with the luminosity functions of the sums of the contributions of foreground stars and LPVs.

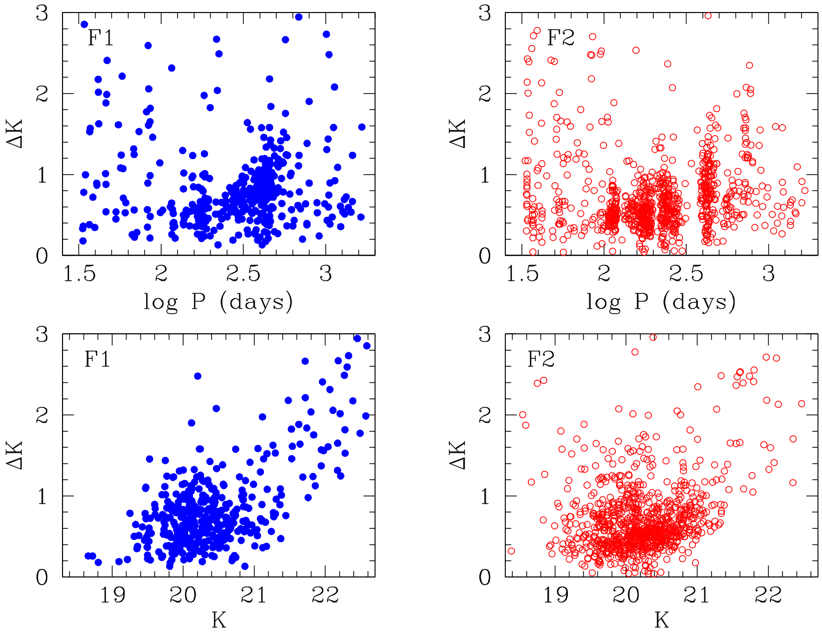

Figure 6.9: Amplitudes as a function of periods (top) and mean magnitudes (bottom) for Field 1 (left) and 2 (right).

As discussed in the Introduction, the maximum luminosity of the red giants is an indicator of the age of the stellar population. Brightest stars in old and high metallicity globular clusters are LPVs with K-band magnitudes as bright as $M_K = -8$ (Feast et al. 2002). The brightest variables in our fields have magnitudes of 17.75 and 15.1 in Fields 1 and 2, respectively. Very few if any of these brightest stars might be foreground eclipsing variables. From figure 6.9 most of the LPVs have magnitudes fainter than $K_0 \sim 19$. Assuming a distance modulus to NGC 5128 of 28.0 (see next section), the brightest LPVs in our fields reach similar magnitudes as LPVs in the LMC ($M_K = -8.8$), and are brighter than those found in metal-rich old populations like the MW bulge (e.g. Frogel & Whitford 1987, Zoccali et al. 2002).

While in old and metal-rich populations essentially all the stars above the RGB tip are variable, in the intermediate-age populations most of them are non-variable bright AGB giants. For example Groenewegen & de Jong (1994) estimate that only about 5-10% of oxygen-rich AGB stars are LPVs in the LMC. The reason is shorter lifetime of LPVs in the LMC of the order of few $\times 10^4$ yr (Groenewegen & de Jong 1994) compared to $\sim 2.5 \times 10^5$ yr in the Galaxy (Whitelock 1993, Renzini & Greggio 1990, Renzini 1993).

There are 2334 stars in Field 1 above the tip of the RGB ($K < 21.3$, see the next section). According to the VK CMD, 192 of these stars have color $V - K < -K + 25$. These blue stars either belong to the young population in Field 1 or to the Galactic foreground. Among the remaining 2142 stars 364 are LPVs (accounting for 89.2% variables in this field).

In Field 2 there are 6424 sources brighter than K=21.3. Of these 217 objects have colors bluer than $V - K < -K + 25$, and belong to the Galactic foreground contamination. Of the remaining 6207 stars in the AGB phase 847 are LPVs (accounting for 95.8% of variables in this field).

Some of the bright non-variable AGB giants could be blends of 2 RGB tip stars. Renzini (1998) provided the equations that enable the calculation of the expected number of stars in a given evolutionary phase (N_j) in an image in which the total sampled luminosity is L_T.

$$N_j = B(t) L_T t_j \tag{6.9}$$

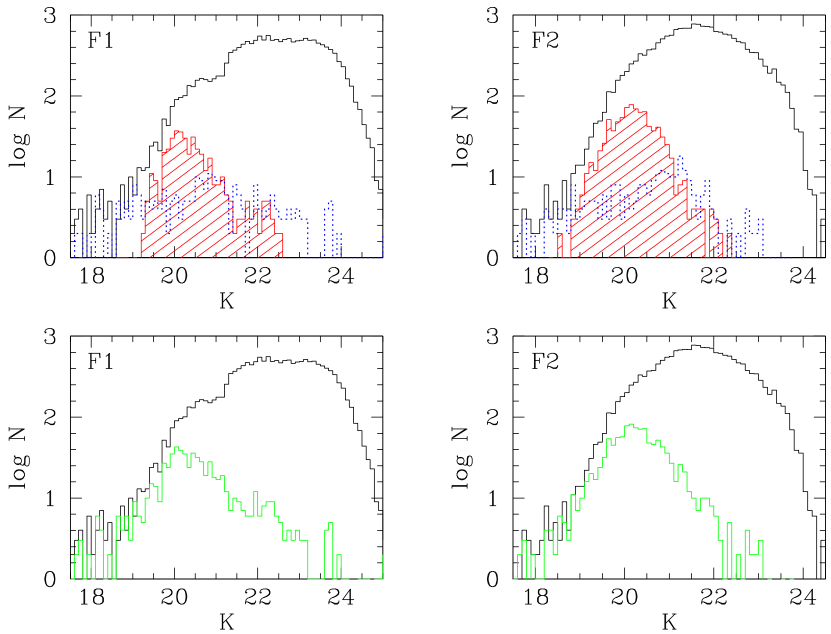

Figure 6.10: K-band luminosity function for all stars (solid black line) in Field 1 (left) and Field 2 (right). Top: dotted line histogram is for stars bluer than –(V–K)+25 line. Mostly they are foreground Galactic stars as well as young blue and red supergiants in Field 1 (see chapter 7). The variable star luminosity function (red shaded histogram) is also compared with the complete luminosity function. Bottom: A sum of the foreground and variable star luminosity function is compared to the total luminosity function of the two fields.

$B(t)$ is the specific evolutionary flux of the population or the number of stars entering or leaving any post main sequence evolutionary stage per year and per solar luminosity of the population. It is a very weak function of age and ranges from $\sim 0.5 \times 10^{-11}$ to $\sim 2.2 \times 10^{-11}$ stars $L_\odot^{-1}$ yr^{-1}, as age increases from 10 Myr to 15 Gyr. t_j is the duration of the evolutionary phase ($\sim 2.5 \times 10^5$ yr). For a solar-metallicity, 15 Gyr old population $L_T \simeq 0.36 L_K$. We can estimate the total sampled luminosity in the two fields by summing up the observed counts on the dark subtracted, flat-fielded, sky-subtracted and calibrated frames. Using the combined frames for epoch G, the total sampled luminosity is 5×10^7 L$_\odot$ and 7×10^7 L$_\odot$ for Field 1 and 2, respectively. From surface brightness profile of Dufour et al. (1979) the total luminosities are 5.9 and 28.7×10^7 L$_\odot$, while from that of Mathieu et al. (1996) they are 9.5 and 31×10^7 L$_\odot$. Our measured value for Field 1 is close to that of Dufour et al., but the measured luminosity of Field 2 is much lower.

From table 1 of Renzini (1998) the expected number of LPVs in an old near-solar metallicity population is $\sim 5/10^6$ L$_\odot$. The total sampled luminosity of Field 1 is 50-100 times higher, yielding 250-500 LPVs in agreement with the number of LPVs detected in that field. In Field 2 our measured luminosity would suggest ~ 350 LPVs, but the surface brightness measurements from the literature predict ~ 1500 LPVs. For comparison, we have detected and measured periods for 884 LPVs in Field 2.

The probability that a pixel contains two stars in phase j is $\sim N_j^2$ and the number of 2-star blends in a frame with a total number of pixels N^{pix} is:

$$N_{2j} = N_j^2 N^{pix} = [B(t) L_T t_j]^2 / N^{pix} \tag{6.10}$$

The resolution of ground based images is worse than 1 pixel and the sampled luminosity has to be divided by the available number of resolution elements. In our case each resolution element is of the order of 0.″4. Hence the

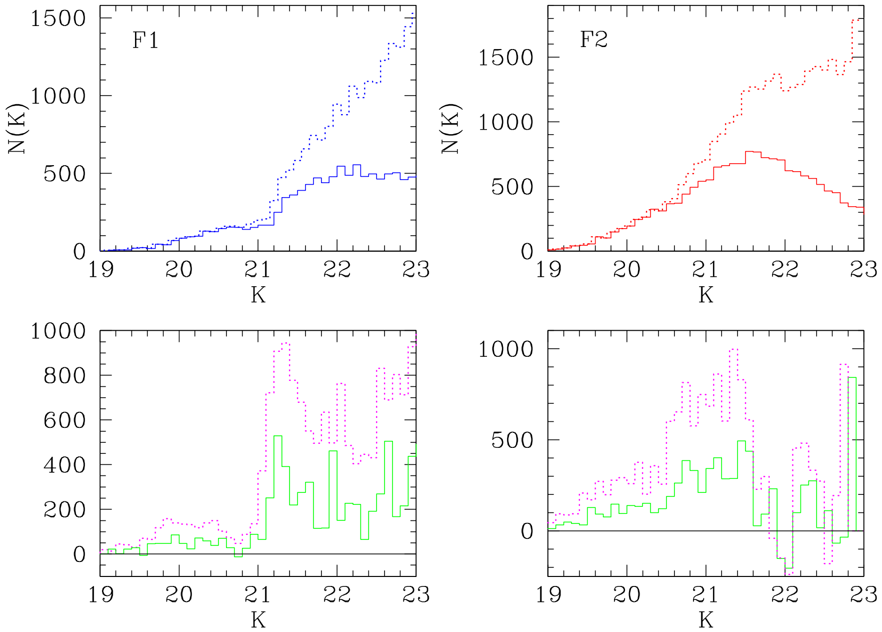

Figure 6.11: K-band luminosity functions for Field 1 (left) and Field 2 (right) are shown in the top panels. The contributions from the Galactic foreground and young blue stars were subtracted using the information from the VK CMDs. Dotted lines are used for the incompleteness-corrected luminosity functions. In the bottom panels the Sobel edge-detection filter response curves are shown for two different kernels (see text).

expected number of blends of two RGB tip giants in Field 1 is between 100 and 375 for the total sampled luminosity between 5 and 9.5×10^7 $L_\odot$. In Field 2 it is ~ 200 if the measured luminosity from the image is assumed, but it rises to 3990 for 31×10^7 $L_\odot$ from Mathieu et al. Taking the highest probable number of blends, there are at least 1400 non-variable bright AGB giants in Field 1 and 1370 in Field 2.

LPVs account for 26% and 62% of the extended giant branch population in both fields 1 and 2, respectively, and their high luminosity cut-off extends well beyond $M_K = -8$. The total number and the maximum brightness achieved by non-variable AGB stars is a clear evidence for the presence of an intermediate-age population. It is stronger in the outer field which contains the population of stars from an accreted satellite in the diffuse stellar shell (Malin et al. 1983).

6.6 NGC 5128 distance

In this section we measure the distance to NGC 5128 using two different methods: (i) the brightness of the RGB tip in K-band and (ii) the Mira PL relation.

6.6.1 RGB tip

The K-band luminosity functions of Field 1 and 2 are presented in figure 6.11. These are the deepest K-band luminosity functions for a stellar population belonging to a galaxy beyond the Local Group. The luminosity functions in the upper panels are binned with 0.1 bins and the contribution of the bright stars from Galactic foreground and fainter young blue stars has been subtracted using the information from the VK CMDs. Note that many of the stars in these luminosity functions are very red and thus too faint to be detected in optical. Only about half of the sources could be matched in the V-band. The dotted lines indicate luminosity functions corrected for incompleteness.

In the lower panels of figure 6.11 we show the luminosity functions convolved with the Sobel edge detection filter. The two response curves in each panel correspond to two different kernels, the solid (green) curve is for a $(-2, 0, +2)$ kernel (Lee et al. 1993) and the dotted (magenta) is for a $(-2, -1, 0, +1, +2)$ kernel. They are used as localized slope estimators with 2 and 4-point smoothing, respectively.

There is a very sharp peak in the Field 1 response function curve at 21.288 ± 0.029. It appears at the position where there is a strong change in the slope of the RGB luminosity function and it corresponds to the magnitude of the tip of the RGB. This feature is smoothed over few tenths of magnitude in Field 2. From the 2-point Sobel kernel there seem to be 3 peaks hidden in this broad distribution, corresponding to magnitudes 20.8, 21.1 and 21.3. However, the signal is very weak and it is not obvious that these three peaks are real. In the 4-point Sobel kernel the strongest of these three peaks corresponds to the RGB tip in Field 1 The broadening and smoothing of the peak is due to combination of larger photometric errors, contribution of blends, the presence of AGB giants and larger metallicity spread in this field.

The tip of the RGB in K-band is a function of metallicity. Its dependence has been measured empirically by Ferraro et al. (2000) using a set of Galactic globular clusters with a range of metallicities. They obtained the following relation:

$$\mathrm{M_K^{TRGB}} = -(0.64 \pm 0.12)[\mathrm{M/H}] - (6.93 \pm 0.14) \tag{6.11}$$

The peak metallicity for the stars in Field 1 has been inferred in Chapter 7 to be between Z=0.008 ([M/H]=–0.38) to Z=0.01 ([M/H]=–0.28). With these two estimates taken as extrema, and assuming a reddening of E(B–V)=0.11 (only foreground Galactic reddening; corresponding to $\mathrm{A_K} = 0.039$ Cardelli et al. 1989), we can use the empirical calibration of the RGB tip K-band magnitude to derive the distance to NGC 5128. The higher metallicity, yields lower distance modulus of 28.00, while for the lower metallicity distance modulus is 27.94. Higher reddening, e.g. E(B–V)=0.35, would result in shorter distances with distance moduli 27.92 and 27.85, for higher and lower Z values, respectively. As there is little evidence for high reddening values for the old populations, we prefer the lower reddening. Taking a straight mean for the metallicities, the distance modulus of NGC 5128 is 27.97 ± 0.10.

Recent distance determinations to NGC 5128 were obtained by surface brightness fluctuations from globular clusters yielding a distance modulus of 27.48 Tonry & Schechter (1990), later revised to 27.71 (Hui et al. 1993), and planetary nebula luminosity function that gave a distance modulus of 27.73 (Hui et al. 1993). Soria et al. (1996) and Harris et al. (1999) have used I-band tip of the RGB detection to determine the distance to NGC 5128. These last authors have revised the distance moduli derived by planetary nebula luminosity function and surface brightness fluctuations to 27.97 and 27.78, respectively, bringing them in agreement with the contemporary Local Group distance scale, $(\mathrm{m-M})_0(\mathrm{M31}) = 24.5$ (van den Bergh 1995, Harris 1999). Our result is within 2σ of 27.72 distance modulus of Soria et al. and almost identical to 27.98 of Harris et al. However, the result is based on photometric metallicities. An independent way of measuring the distance is given in the next section, using variable stars.

6.6.2 Mira PL relation

In figure 6.12 we plot the mean magnitudes *vs.* logarithm of periods for all the variables with 10 or more data points for which we derived periods (see light curves in the appendix). Field 1 variables are shown with filled symbols and Field 2 with open. There is a lot of scatter and Field 2 variables show evident signs of aliasing in their periods. Many of them lay around $\log \mathrm{P} = 2.26$ corresponding to a half a year period.

The mean magnitudes are corrected for extinction by subtracting $A_K = 0.039$ ($\mathrm{E(B-V)} = 0.11$). K_s-bandpass, used at ISAAC, is related to the standard K-band (Bessell & Brett 1988) through a zero point shift $K = K_s + 0.044 \pm 0.003$ (Grocholski & Sarajedini 2002). Most of the near-IR Mira PL studies have been published based on SAAO photometry which has the standard K passband (Carter 1990). In order to allow a more straight forward comparison with the published PL relations the 0.044 mag shift was applied to our data.

Restricting the selection only to the variables with best determined periods ($\chi^2 < 4$) two clear parallel sequences emerge in the PL diagram (figure 6.13). Multiple parallel sequences in the PL diagram of LPVs were reported by Wood & Sebo (1996), Wood (2000) and Cioni et al. (2001) in the Magellanic Clouds and by Bedding & Zijlstra

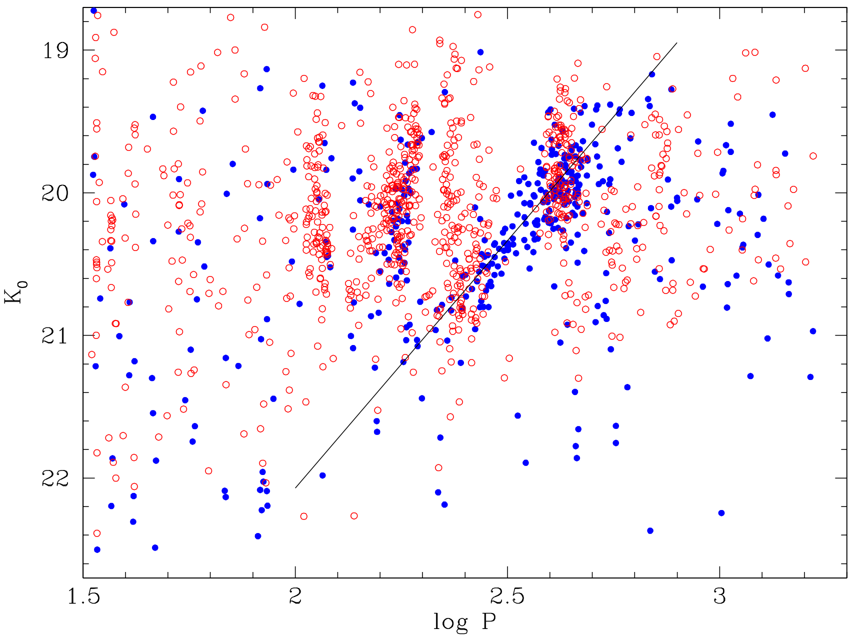

Figure 6.12: Period-luminosity diagram for all variables in NGC 5128 with 10 or more data points. Field 1 variables are plotted with filled and variables in Field 2 with open symbols. Note that the vertical sequences mainly outlined by open symbols are due to aliasing in period sampling.

(1998) in the Galaxy. The shorter period sequence corresponds to the sequence B of Wood (2000) and is the locus of short period SRa variables. The more populated sequence to the right is sequence C of Wood (2000) where Mira variables are found. Each of these period-luminosity relations corresponds to a pulsation in a certain mode. There is still some disagreement in the literature whether the pulsation mode of Mira variables is fundamental or first overtone (e.g. Wood & Sebo 1996, Bedding & Zijlstra 1998, Whitelock & Feast 2000, Wood 2000).

Our data are not sufficient to discriminate Mira from SR variables on the basis of the regularity of their light curves. Hence, to select most probable Miras we made additional selection on period ($2\,\mathrm{d} < \log \mathrm{P} < 2.6\,\mathrm{d}$) and on amplitude ($0.5\,\mathrm{mag} < \Delta K < 1.5\,\mathrm{mag}$). Mira variables, plotted with filled symbols in figure 6.13, are located where expected, along the main, more populated sequence in the PL diagram.

The Mira PL relation can be used as well to derive the distance to NGC 5128. Calibration of the PL relation lies on the LMC PL relation for Miras. Hughes & Wood (1990) fit to the LMC Mira PL relation is:

$$M_K = -3.85 \log P + 1.71 \tag{6.12}$$

Feast (1996) proposed shallower slope for the relation:

$$M_K = -3.47 \log P + \beta \tag{6.13}$$

The zero point of $\beta = 0.91$ has been derived by Feast (1996) using LMC Miras. More recently Whitelock et al. (2000) used Hipparcos parallaxes for Solar neighbourhood Miras to derive $\beta = 0.84 \pm 0.14$ and Feast et al. (2002) obtained $\beta = 0.93 \pm 0.14$ for globular cluster Miras with the cluster distances determined from subdwarf fitting with Hipparcos parallaxes of subdwarfs (Caretta et al. 2000). The straight mean of the two Hipparcos based zero points yields $\beta = 0.88 \pm 0.10$ and a Large Magellanic Cloud distance modulus of 18.60 ± 0.10.

Least square fit to the Mira sequence in figure 6.13, adopting the selection on period and amplitude and restricting the sample further to the central sequence with $\mathrm{K}_0 < -3.47 * \log \mathrm{P} + 29.43$ and $\mathrm{K}_0 < -3.47 * \log \mathrm{P} + 28.53$,

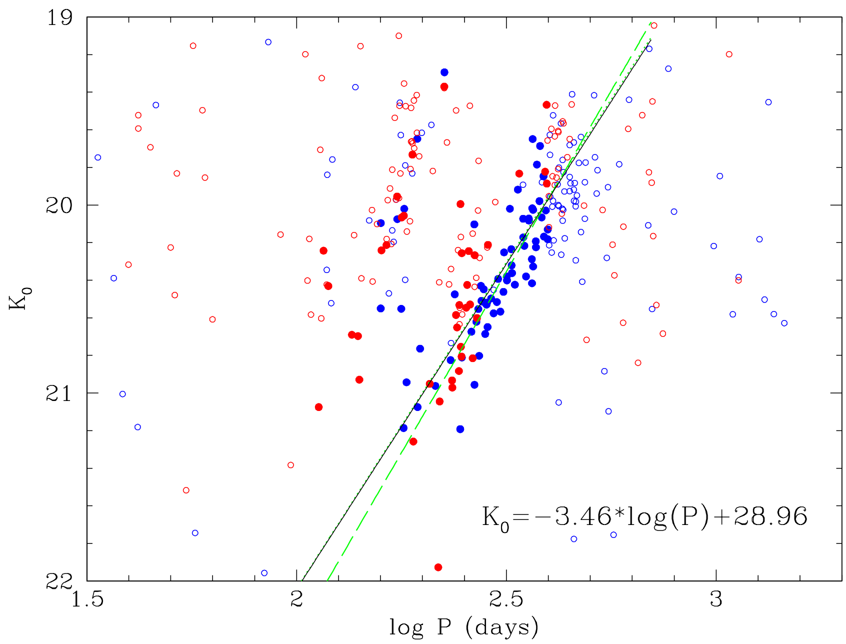

Figure 6.13: Mira PL relation in NGC 5128 for variables with best determined periods ($\chi^2 < 4$, open symbols). Long period ($2 < \log P < 2.6$) and large amplitude ($0.5 < \Delta K < 1.5$) Mira variables are plotted with filled symbols. The solid black line is our best fit to the Mira sequence. The dotted green line is Feast et al. (2002) relation and dashed line is from Hughes & Wood (1990).

results in an almost identical slope to that of Feast (1996):

$$\mathrm{K}_0 = -3.46(\pm 0.22) \log P + 28.96(\pm 0.56) \tag{6.14}$$

It is overplotted in figure 6.13 as a solid black line. The 1σ scatter around the fit is 0.18. Restricting the slope to -3.47, the best fitting zero point is 28.99 ± 0.6 (dotted green line in figure 6.13) with the same RMS of the fit. For comparison Hughes & Wood's relation is also shown as a dashed line.

Finally, the distance modulus to NGC 5128 is 28.11 ± 0.07, where only a statistical error is assumed. The systematic error includes the zero point calibration that relies on the LMC distance. The derived distance modulus corresponds to the LMC distance modulus of 18.60. If instead 18.5 is preferred (e.g. Freedman et al. 2001, Alves et al. 2002), the corresponding distance modulus to NGC 5128 would be 28.01 ± 0.07, in perfect agreement with that derived from the RGB tip.

6.7 Conclusions

The first variable star catalogue in a giant elliptical galaxy is presented. ISAAC multi-epoch K-band photometry of two fields in the halo of NGC 5128 was used to detect variable stars. 528 variables were detected in Field 1 and 1230 in Field 2. Among these 441 and 1148 had at least 10 measurements. We derived periods for these variables via Fourier analysis of the K-band light curves and sine-wave fitting. Their magnitudes indicate that they are in the AGB phase and their periods and amplitudes are consistent with being LPVs.

The tip of the RGB was detected in Field 1 at K=21.29, yielding a distance modulus of NGC 5128 of $(\mathrm{m}-\mathrm{M})_0 = 27.97 \pm 0.10$. The RGB tip in Field 2 is not a sharp feature due to larger metallicity spread, presence of blends and AGB stars.

A large population of stars above the tip of the RGB contains 2286 stars in the outer halo field (Field 1) and 3973 stars in the inner halo field (Field 2). Subtracting the foreground sources, detected LPVs, as well as 375 possible blends in Field 1 and 3990 in Field 2, there are 1400 and 1370 non-variable stars brighter than the first ascent giant branch tip in the two fields. LPVs account for 26% and 62% of the AGB population in fields 1 and 2, respectively. The large number of non-variable AGB stars and their high luminosity ($M_K \geq -8.8$) is a sign of an intermediate-age population. This signature is stronger in the outer shell field, where stars from an accreted satellite were found as well as a conspicuous recent star formation (Rejkuba et al. 2001b, 2002, Chapters 4 and 5).

The first Mira period-luminosity relation outside the Local Group is presented. The long period (P $\geq$ 200 d) large amplitude ($0.5\,\mathrm{mag} < \Delta\mathrm{K} < 1.5$ mag) Mira variables were used to determine the distance of NGC 5128 from a period-luminosity relation. We derive the distance modulus of 28.01 ± 0.07, adopting a LMC distance modulus of 18.50. The straight mean of the two methods yields distance to NGC 5128 of 27.99 ± 0.12, almost identical to 27.98 ± 0.14 measurement of Harris et al. (1999) and within 2σ of the distance modulus 27.72 ± 0.10 result of Soria et al. (1996).

Chapter 7

The star formation history of NGC 5128 with synthetic color-magnitude diagrams [1,2]

Abstract

We use simulated color-magnitude diagrams to investigate the star formation history of two fields in the NGC 5128 halo. It is the first time this technique has been used for a giant elliptical galaxy. The comparison of the simulations with the observed UV color-magnitude diagram for the field in the north-eastern shell, where recent star formation is present constrains the initial mass function (IMF) and the duration of the star formation episode. The star formation burst is still on going or at most has stopped some 2 Myr ago. The look-back time on the main sequence is set by the incompleteness of the U-band observations at V$\sim$26 and is of the order of $\sim$ 50 Myr. The post main sequence phases have look-back time up to 100 Myr, setting the maximum observable time for the star formation in this field. The comparison of the observed and simulated luminosity functions and the number of post main sequence vs. total number of stars favors models with active star formation in the last 100 Myr. The absence of gaps on the main sequence indicates that most probably no major fluctuations in the star formation rate have occurred over the sampled time interval. The data are best fitted by an IMF with Salpeter slope ($\alpha = 2.35$) and are also consistent with slopes in the range of $2 \lesssim \alpha \lesssim 2.6$. They exclude steeper IMF slopes. The mean star formation rate for a Salpeter IMF in the range of masses $0.6 \leq \mathrm{M} \leq 100\ \mathrm{M}_\odot$ within the last 100 Myr is $1.6 \times 10^{-4} \mathrm{M}_\odot\,\mathrm{yr}^{-1}\,\mathrm{kpc}^{-2}$.

The optical-near IR data are sensitive to the old and intermediate-age populations. Neglecting the contribution of the intermediate-age population, contributing bright AGB stars above the tip of the red giant branch (RGB), the simulations of the old RGB population were used to explore the metallicity spread sampled by the observations. They give the following results: (i) the observations are not consistent with a single metallicity broadened by photometric errors; (ii) there is a wide spread in metallicity ranging from Z=0.001 to Z=0.02 in Field 1 and from Z=0.0001 to Z=0.02 in Field 2; (iii) the closed box model cannot reproduce the observations because it produces too many metal-poor stars even when the chemical evolution starts with a pre-enriched gas with metallicity of Z=0.001 having a high nucleosynthetic yield of $y = 0.015$. The mis-match between simulated and observed luminosity functions for Field 1 need further investigations including the age spread in this field. The RGB of the Field 2 is instead better reproduced with the 10 Gyr old population. This difference is probably due to the presence of a large number of stars in Field 1 in the diffuse stellar shell which was presumably accreted during the last merging episode in this galaxy.

7.1 Introduction

The most powerful tool for studying the star formation history of nearby galaxies is through the construction of a color-magnitude diagram (CMD) for the stars in the galaxy. Containing stars that were born during the whole

[1] Based on observations collected at the European Southern Observatory, Paranal, Chile, within the Observing Programmes 63.N-0229 and 65.N-0164

[2] Rejkuba, M., Greggio, L., Zoccali, M., D. Silva and D. Minniti in preparation

life-time of the galaxy, CMDs represent snapshots of their star formation histories. Even the CMDs limited to the brightest stars are still very useful as there are number of indicators that can be used to constrain the star formation history. An example of a bright indicator of metallicity for old (age > several Gyr) populations is the color of the red giant branch (RGB). The presence of an extended asymptotic giant branch (AGB) with stars more luminous than the tip of the RGB is an indicator of an intermediate-age population or an old and very metal-rich population. The presence of the blue, luminous main sequence and core helium burning blue loop stars can be used to determine the age and metallicity of the young stellar population ($\lesssim 1$ Gyr).

The best way to analyze the distribution of stars in the CMD and to quantify the star formation history of the galaxy is through the comparison of the observed CMD with synthetic CMDs computed using stellar evolution models. This technique is based on the simulations of a large number of CMDs constructed assuming different star formation rate (SFR(t)), chemical enrichment law ($Z(t)$) and initial mass function (IMF). The photometric errors and the incompleteness of the data is also simulated. Each simulated CMD then depends on all the main parameters which determine the distribution of stars in a CMD. In this way it is best accounted for the evolutionary behaviour of stars, small number of stars and spread due to observational effects. The synthetic CMDs are then compared to the observed ones in order to determine the acceptable range of parameters and the best fitted models. This technique was first described by the Bologna group (Ferraro et al. 1989, Tosi et al. 1991), and later applied, with some variations in the details, to investigate different LMC stellar fields and clusters as well as dwarf galaxies by a number of groups (Bertelli et al. 1992, Tolstoy 1996, Gallart et al. 1996a, 1996b, Dolphin 1997, Greggio et al. 1998, Hurley-Keller, Mateo & Nemec 1998, Hernández, Valls-Gabaud & Gilmore 1998, Cole et al. 1999, Schulte-Ladbeck et al. 2000, Harris & Zaritsky 2001).

Here we apply this technique to investigate the star formation history of the halo of NGC 5128. The observations were taken with VLT using FORS1 and ISAAC in U, V and Ks bands. Their full description as well as data reduction and the resulting CMDs were presented in Chapter 4 (Rejkuba et al. 2001b).

This chapter starts with the description of the synthetic CMD simulator, including a detailed description of the algorithms used. In the next section the young stellar population in the north-eastern halo field is simulated. We test two different metallicities and a range of star formation histories. The initial mass function is also investigated. In the last section we apply the simulator to the old stellar populations observed in V and Ks-bands with VLT.

7.2 Description of the synthetic CMD simulator

The construction of the synthetic CMD goes through the following steps:

1. Random extraction of mass according to the initial mass function (IMF), age according to a chosen star formation rate (SFR) law and metallicity according to the chemical enrichment law ($Z(t)$).

2. Positioning of the extracted star(mass, age, metallicity) on the theoretical HR diagram ($\log(\mathrm{L}/\mathrm{L}_\odot)$, $\log(\mathrm{T_{eff}})$) interpolating within stellar evolutionary tracks.

3. Transformation of the theoretical position of the star in the HR diagram ($\log(\mathrm{L}/\mathrm{L}_\odot)$, $\log(\mathrm{T_{eff}})$) into the observational CMD assigning the bolometric corrections through interpolation within conversion tables.

4. Application of observational uncertainties: photometric errors and incompleteness according to the result of artificial star experiments on the real frame.

5. Repeat the procedure until a certain criterion (e.g. total number of stars generated, the total mass extracted, or the total number of stars in a certain region of the CMD simulated) is satisfied.

In the following subsections each of the above points is described in more detail.

7.2.1 Random extraction of a star with a given mass and age

We use a Monte Carlo algorithm to randomly select a mass and an age according to a given distribution. The mass is extracted according to a single slope (e.g. Salpeter IMF; Salpeter 1955),

$$dN = AM^{-\alpha}dM \tag{7.1}$$

or double slope initial mass function (e.g. Gould IMF; Gould et al. 1997) with slope α_1 within a mass range $M_1 \leq M \leq M_2$ and α_2 within $M_2 \leq M \leq M_3$. Here "A" is the normalisation factor that depends on the upper and lower mass limits used in the models. The choice of the slope is a free parameter.

The age distribution is adopted to be either flat, representing a constant star formation rate,

$$\Psi(t) = C \qquad \text{for} \qquad t_{min} \leq t \leq t_{max} \tag{7.2}$$

or exponentially decreasing,

$$\Psi(t) = Ce^{-t/\tau} \qquad \text{for} \qquad t_{min} \leq t \leq t_{max} \tag{7.3}$$

with given limits for the age of the oldest stars (t_{max}) and for the duration of the star formation episode ($\Delta t = t_{max} - t_{min}$).

We have used a single metallicity simulator to produce synthetic CMDs for the young stellar population. This is a good approximation, because the spread in ages of the young stars (few $\times$ 10 Myr) is too short for a significant metal enrichment to occur. However in the simulation of the optical-near IR CMDs that are dominated by the old and intermediate-age population, evolution of the metallicity has to be assumed. Thus in these simulations we also extract a random variable Z distributed according to a metal-enrichment law. The possible choices are a flat distribution between the minimum and maximum metallicity ($0.0001 \leq Z \leq 0.04$), a closed box, or a numerical distribution.

7.2.2 Interpolation of the stellar evolutionary models

We have adopted two different sets of models: Padova models (Fagotto et al. 1994) and models computed by Cassisi & Salaris (1997) and by Bono et al. (1997a, 1997b). For the simulations of single metallicity star formation histories used to compare with the youngest stars in NGC 5128, we use Padova models by Fagotto et al. (1994). These models have tracks for the stars with masses ranging from 0.6 to 120 $M_{\odot}$. The newer set of Padova models (Girardi et al. 2000) are not computed for stars with masses larger than 7 $M_{\odot}$ such as those that are observed in the north-eastern halo field of NGC 5128.

Given the extracted mass and age, the luminosity and temperature of the star were determined via the linear interpolation in a set of evolutionary tracks. Each track consists of a number of points (age, mass, $\log(L/L_{\odot})$, $\log(T_{\rm eff})$). We have divided each track into portions according to stellar evolutionary phase and interpolated linearly between the adjacent tracks within the same portion. Typically, the portions of the tracks are:

- Main sequence (MS) - ending either at core H exhaustion or at the start of the first runaway expansion
- Subgiant branch - ending at the base of the RGB
- RGB - ending at the tip of the RGB
- Horizontal branch - ending either at the core He exhaustion or at the base of the AGB
- Early AGB - ending at the first thermal pulse

For the high mass stars ($M \geq 20\,M_{\odot}$), whose evolution is affected by mass loss, we divide the evolution in two major phases (MS and post main sequence), and choose conveniently the description of the post main sequence (PMS) phase, inserting further trimming points when needed.

In most of the cases the log(L) and log(T_{eff}) of the extracted star are interpolated between the values of adjacent masses read at the same fractionary age in the appropriate evolutionary phase:

$$t_{ph} = (t - t_0)/(t_1 - t_0) \tag{7.4}$$

where t_0 and t_1 are respectively the ages at the beginning and at the end of the appropriate evolutionary phase and t is the age of the extracted object. In few evolutionary phases when luminosity and/or temperature presented a maximum or minimum at variable t_{ph}, we inserted a break $t_{ph}(t_{ph,br})$ and effectively divided that phase into two sub-phases. Log(L) and log(T_{eff}) of the extracted star at the extracted age are then found by interpolation at:

$$t_{ph}/t_{ph,br} \qquad \text{if age is such that} \qquad t_{ph} \leq t_{ph,br} \tag{7.5}$$

$$(t_{ph} - t_{ph,br})/(1 - t_{ph,br}) \qquad \text{if age is such that} \qquad t_{ph} \geq t_{ph,br} \tag{7.6}$$

When the interpolation has to be done also in metallicity, the simple linear interpolation algorithm described above is not enough. It is necessary to perform a bilinear interpolation, because the stars of the same mass, but different metallicity have different ages. Thus for each extracted mass one has to first interpolate in log(L) and log(T_{eff}) for a given age and then again for a given metallicity. In order to simplify the problem we adopted a set of isochrones as a starting point. Using the tabulated values of log(L) and log(T_{eff}) for stars of given mass in an isochrone we interpolate linearly within isochrones of the same age and different metallicities. The Padova models are not adequate for these simulations due to the very low number of points in each isochrone (approx. 30-55 points for each track). We prefer to use Cassisi models (Cassisi & Salaris 1997, Bono et al. 1997a, 1997b) which have much more detailed evolution with more than 600 points per track. Given a mass and metallicity, the luminosity and temperature of the star are determined through the linear interpolation in a set of isochrones. The interpolation in log(L) and log(T_{eff}) is made for the mass that has the same evolutionary phase of the extracted mass:

$$ph = m/m_1 \qquad \text{for objects on the main sequence} \tag{7.7}$$

$$ph = m_0 + (m - m_0)/(m_1 - m_0) \qquad \text{for later phases} \tag{7.8}$$

where m_0 and m_1 are the masses at the beginning and the end of the evolutionary phase. The evolutionary phases are as before: main sequence, subgiant branch, RGB, core-helium burning and AGB.

7.2.3 Bolometric corrections

In order to produce sensible synthetic CMDs that can be compared with the observed ones it is necessary to transform the theoretical quantities log(L) and log(T_{eff}) into observed magnitudes in the appropriate photometric passbands. An accurate knowledge of the photometric passbands is as important to synthetic photometry as the knowledge of the standard stars and the proper calibration procedure is to the observational photometry. The calibration of our data was described in detail in Rejkuba et al. (2001b, Chapter 4). We have derived a full set of calibration equations including the color term for the optical photometry, while only the zero point was derived for the near-IR photometry. Thus our photometric system consists of Landolt (1992) U- and V- and ISAAC K_s-bands (see ISAAC webpage for the filter transmission curve[1]).

Kurucz (1993) database of ATLAS9 synthetic spectra covers a large range in temperatures ($3500 \leq T_{eff} \leq 50,000$) and gravities ($0 \leq \log g \leq 5$). More recently Castelli et al. (1997) calculated improved ATLAS9 models without overshooting which present better agreement in T_{eff}–color relations with observations. We use these no-overshooting models available as "NOVER" files at http://cfaku5.harvard.edu/grids.html for metallicities [M/H] = $-2.0, -1.5, -1.0, -0.5, 0.0$ and $+0.5$ and microturbulent velocity $\xi = 2$ km s^{-1} to derive bolometric corrections as a function of gravity, effective temperature and metallicity. This is done by convolving the spectral energy

[1] http://www.eso.org/instruments/isaac/index.html

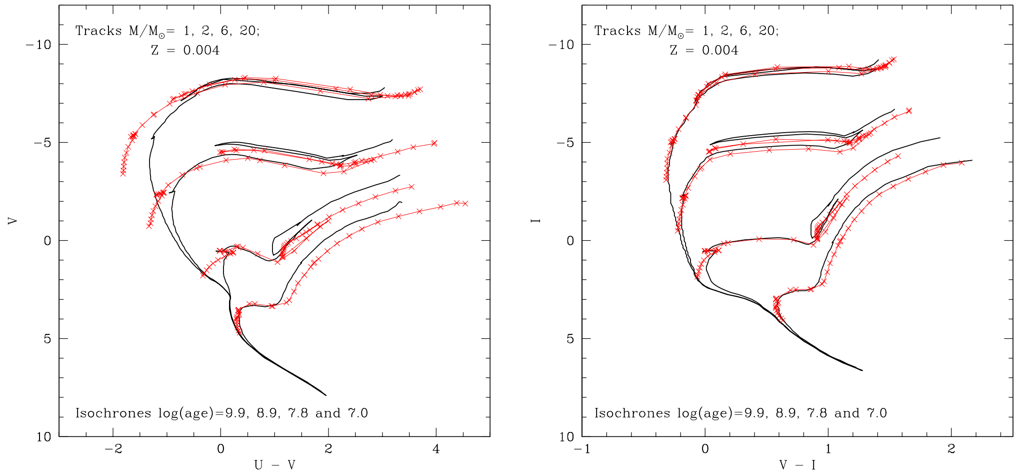

Figure 7.1: Left: Fagotto et al. (1994) tracks (red lines with crosses) for Z=0.004, transformed into V vs. U−V plane by applying bolometric corrections obtained by convolving spectral energy distributions of Kurucz stellar atmospheres (see text) with Landolt (1992) U and V filters, are compared with the Bertelli et al. (1994) isochrones for Z=0.004. The log(age) for isochrones and the masses of the tracks are indicated. Right: The same as on the left, but for I vs. V−I. V and I filter transmission curves used to derive BCs and color the tracks (red lines with crosses) are from Landolt (1992)

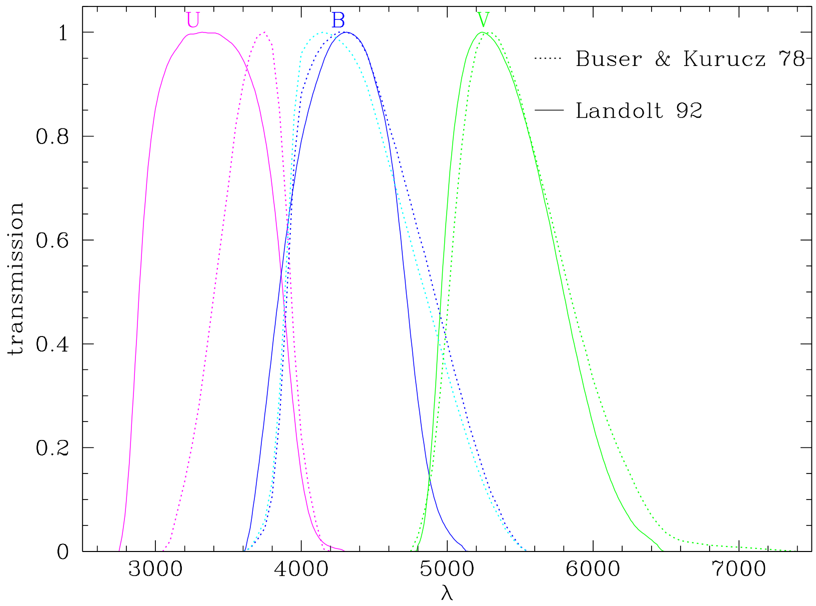

Figure 7.2: Comparison of the Landolt (1992; full lines) and Buser & Kurucz (1978; dotted lines) UBV passbands.

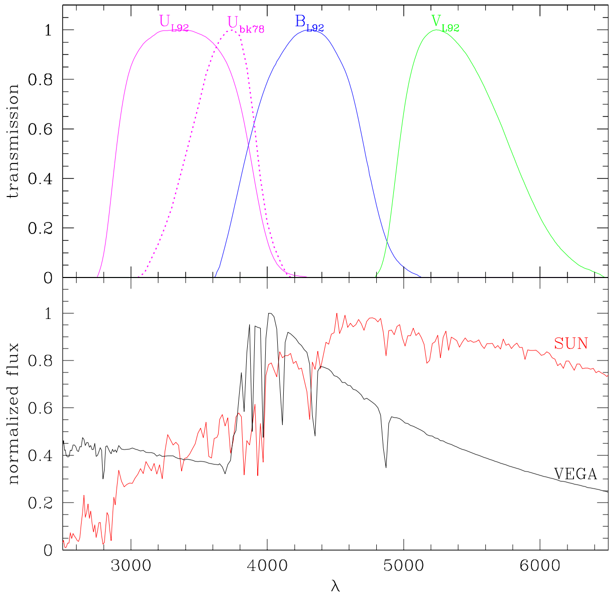

Figure 7.3: Sun and Vega spectral energy distributions are compared with the Landolt (1992) UBV passbands (full lines) and Buser & Kurucz (1978) U filter (dotted lines).

distributions from the Kurucz stellar library with filter transmission curves S^i_λ:

$$\langle F_i \rangle = \frac{\int_0^\infty F^i_\lambda S^i_\lambda \, d\lambda}{\int_0^\infty S^i_\lambda \, d\lambda} \tag{7.9}$$

The magnitude and the bolometric correction are then by definition:

$$f_i = -2.5 \log \langle F_i \rangle \tag{7.10}$$

$$BC_i = M_{bol} - M_i = -2.5 \log(\sigma T^4_{eff}) - f_i + ZP_i \tag{7.11}$$

$$\text{where} \quad \sigma T^4_{eff} = \int_0^\infty F_\lambda \, d\lambda \tag{7.12}$$

The calibration of the zero points in each band follows from the definition of the V-band bolometric correction of the Sun to be $\mathrm{BC}_V^\odot = -0.07$ and the colors of Vega $\mathrm{M}_V^{\alpha Lyr} - \mathrm{M}_i^{\alpha Lyr} = 0$. The spectral energy distributions of Sun and Vega were taken from the Kurucz library as well.

We calculate $\log g$ of the each simulated star with $(\log \mathrm{M}/\mathrm{M}_\odot, \log \mathrm{L}, \mathrm{T_{eff}})$ using the following set of equations:

$$L = 4\pi R^2 \sigma T^4_{\rm eff} \tag{7.13}$$

$$\log(g/g_\odot) = \log(M/M_\odot) - 2\log(R/R_\odot) \tag{7.14}$$

where $\log g_\odot = 4.437, \sigma = 5.6710^{-5}\mathrm{erg/cm^2/K^4}, \mathrm{L}_\odot = 3.82610^{33}\mathrm{erg/s}$ and $\mathrm{R}_\odot = 6.959910^{10}\mathrm{cm}$. The linearly interpolated bolometric correction $(\mathrm{T_{eff}}, \log g)$ is then applied to obtain magnitudes for the simulated stars.

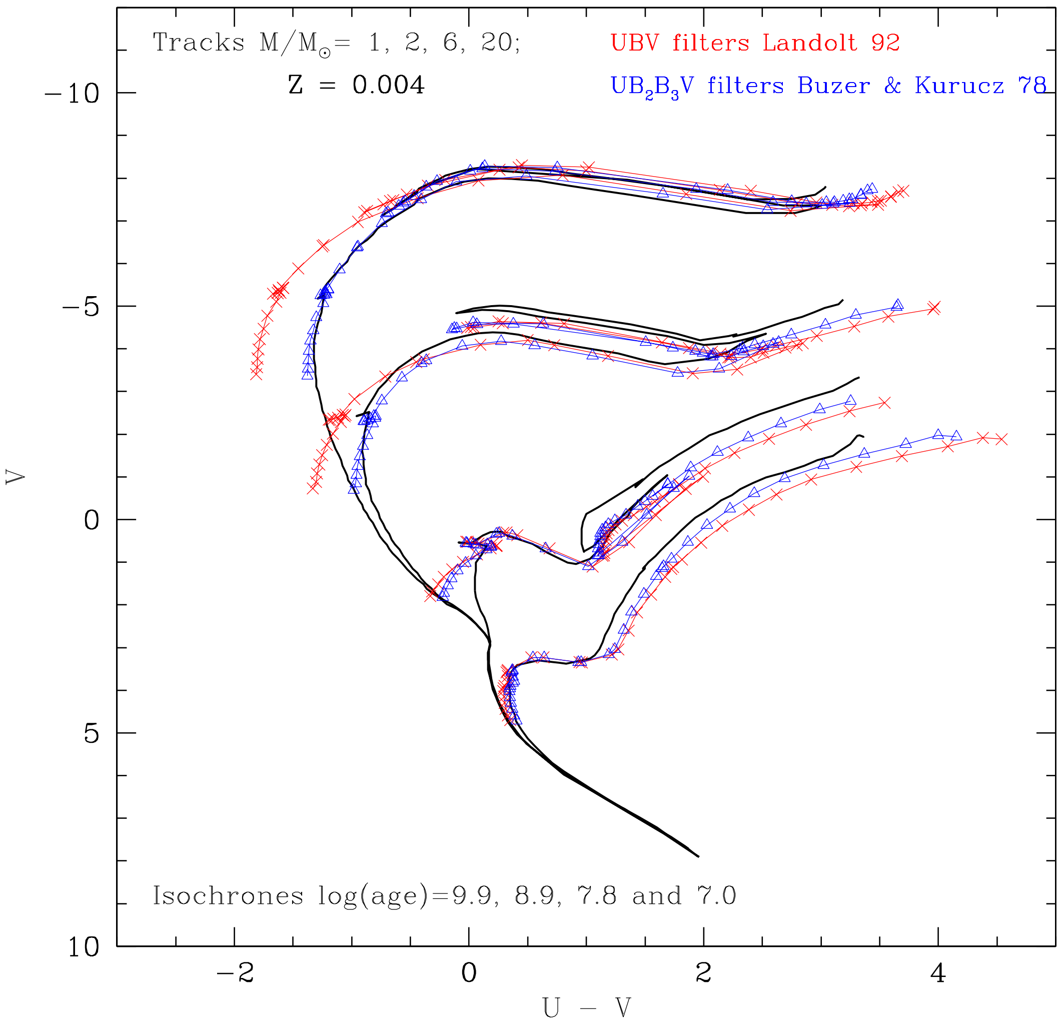

Figure 7.4: Fagotto et al. (1994) tracks (lines with crosses and triangles) for Z=0.004, transformed into V vs. U−V plane are compared with Bertelli et al. (1994) isochrones for Z=0.004 (thick lines). The tracks were colored by convolving spectral energy distributions of Kurucz stellar atmospheres (see text) with Landolt (1992) U and V filters (red lines with crosses). Overplotted are also the tracks colored using Buser & Kurucz (1978) UB_2B_3V passbands where (U−V) color is defined without zero points (equations 7.17; blue lines with triangles). The log(age) for isochrones and the masses of the tracks are indicated.

In Figure 7.1 we compare the evolutionary tracks of Fagotto et al. (1994) for Z=0.004 "colored" using the procedure described above with isochrones for Z=0.004 of the same group (Bertelli et al. 1994). In the right panel comparison of I vs. V−I shows an excellent agreement of the colors of tracks and isochrones, but in the left panel it is obvious that our bolometric corrections produce wider range of colors for the tracks in U−V. We investigated in detail the origin of this difference and here we show that it is entirely due to the different U-band filter used by Bertelli et al. (1994) in calculating the bolometric corrections.

The Padova group uses Buser & Kurucz (1978) UBV transmission curves, while our photometry has been calibrated to the Landolt (1992) system. The comparison of the two photometric systems is given in Figure 7.2. Note the huge difference in the U-passband wavelength coverage. U-band is known to be the most difficult to reproduce due to the presence of the atmospheric cut-off, the presence of the Balmer break within that band and strong blanketing by metals (see Fig. 7.3). The differences between B-band and V-band filters are much smaller. Buser & Kurucz (1978) UBV system has two B filters, B_2 and B_3. Both these systems claim to be based on Johnson & Morgan (1953) standard system with Buser & Kurucz U−B and B−V colors defined as follows:

$$(U-B)_{syn} = (U-B_2) - 1.093 \tag{7.15}$$
$$(B-V)_{syn} = (B_3-V) + 0.710 \tag{7.16}$$

We have calculated the bolometric corrections convolving the Kurucz stellar library with the UB_2B_3V filters of Buser & Kurucz (1978). There is an excellent agreement between the colored tracks and isochrones (Figure 7.4) if the following definition of U−V color is adopted:

$$(U-V)_{syn} = (U-B_2) + (B_3-V) \tag{7.17}$$

The difference in the zero point is due to different calibration of the zero point bolometric corrections adopted by Buser & Kurucz with respect to Padova isochrones (Girardi 2002, private communication). Padova group adopted the standard calibration of the synthetic photometry which is based on colors and magnitude of Vega, similar to our procedure.

This example shows how important it is to know precisely the transmission curves and the characteristics of the photometric system used. The calibration of the synthetic magnitude system has to be done in the same way as data are, convolving the spectral energy distributions from the stellar library with the same filters used for the real observations. As stated above, the photometric system we adopt is based on Landolt (1992) UBVRI filters and ISAAC K_s filter.

It is known that Kurucz (1993) spectral energy distributions are not very accurate for cool stars due to inadequate molecular opacities, non-LTE and sphericity related effects (e.g. Morossi et al. 1993). To extend our bolometric corrections to low temperatures ($T_{\rm eff} \lesssim 4200$K), we used the empirically determined temperatures and bolometric corrections from Montegriffo et al. (1998). Montegriffo et al. do not have fully developed metallicity classes, but they rather define metal-poor ([M/H] ≤ -1.0 dex) and metal-rich ([M/H] ≥ -1.0 dex) samples. The differences in bolometric corrections between the two groups span a wide range 0.05-0.4 mag/dex. Another point is that their bolometric corrections are determined only for giant stars. However, the last issue is not a problem, since the low temperature stars in our case are giants with photometry in V and K_s-bands. In the UV only bright, young stars are observed, the giants are too faint in the U-band.

7.2.4 Observational biases

The synthetic CMD needs to be "corrected" for observational biases before comparing it with the observed CMD. There are two main types of observational biases:

- *photometric error*: the magnitudes of stars are measured with some uncertainty
- *incompleteness*: some stars are lost due to crowding or high background

Blending is an additional bias that is important in crowded fields and that combines properties of photometric error and incompleteness.

Table 7.1: Fraction of stars in different parts of observed CMD – all stars, blue ($U - V < 0$), intermediate color ($0 < U - V < 1.5$), and red stars ($U - V > 1.5$) – that survive the error selection at maximum error of 0.1, 0.2 and 0.3 with respect to selection with $\sigma < 0.5$. Only the stars with U-band completeness limit larger than 50% are selected, corresponding to V-band magnitude smaller than 25.5.

σ cut	all stars	blue	intermediate	red
$\sigma < 0.3$	81 %	97%	70%	75%
$\sigma < 0.2$	66 %	87%	53%	55%
$\sigma < 0.1$	37 %	52%	29%	26%

We used the extensive artificial stars experiments (the full description can be found in Rejkuba et al. 2001b, Chapter 4) to assign the observational biases. In the artificial star experiment the input magnitude is given and the output magnitude measured at each position of the input magnitude. If the star was lost in the background noise or was completely blended with a much brighter object producing a magnitude difference between the input and measured magnitude of more than 0.75, we considered it to be non-detected. Observational biases are applied to magnitudes to which the appropriate distance modulus and extinction were added. Thus, when applying the observational biases we pick a random object from the output table of the artificial star experiments that has magnitude and color similar to the simulated star. The simulated star then receives a realistic photometric error (magnitude difference between the recovered and input magnitude in the artificial star experiment) and incompleteness (the star in the artificial star experiment was detected or not).

7.2.5 Comparing the simulations with the observations

The random extraction of synthetic stars, their interpolation in the theoretical HR diagram and transformation to the observational plane together with the application of photometric errors and incompleteness has been covered in the previous sections. The last step is to choose the right criterion with which different simulated CMDs are going to be ranked and the best fitting star formation history chosen. This criterion determines the number of stars in the simulated CMD. The possible criteria are:

- Compare the complete CMD and stop when the observed number of stars are simulated.
- Compare regions of CMD and stop simulation when the number of stars in a color-magnitude box matches the observations.
- Compare the number of thermally pulsating AGB stars and stop when it matches the observed number.
- Stop when a certain total mass has been extracted.

7.3 Young stellar populations in NGC 5128 observed with the VLT

The observations of the young stars in the north-eastern shell field of NGC 5128 are presented in Chapter 4 (Rejkuba et al. 2001b). The young blue sequence is present in the outer shell field and completely absent from the halo field (see Chapter 4). It dominates the blue part, while in the red most of the stars are Milky Way stars.

In figure 7.5 we display $U-V$ *vs.* V CMDs of the NGC 5128 shell field (Field 1) with different values of DAOPHOT errors in both U and V applied as a selection criterion. In the upper left panel the CMD shown in Chapter 4 with all stars that had $\sigma < 0.5$ is presented. Comparing it with the other panels it is evident that many of the red stars have large photometric errors. This is clearer in table 7.1 where we list fraction of stars that remain in the CMD when an error cut is applied at sigma of 0.3, 0.2 and 0.1. Even when only the stars with the smallest photometric errors are selected, more than 50% of the blue stars survive and the young blue sequence remains well populated. We shall use this feature to investigate the recent star formation history in this field.

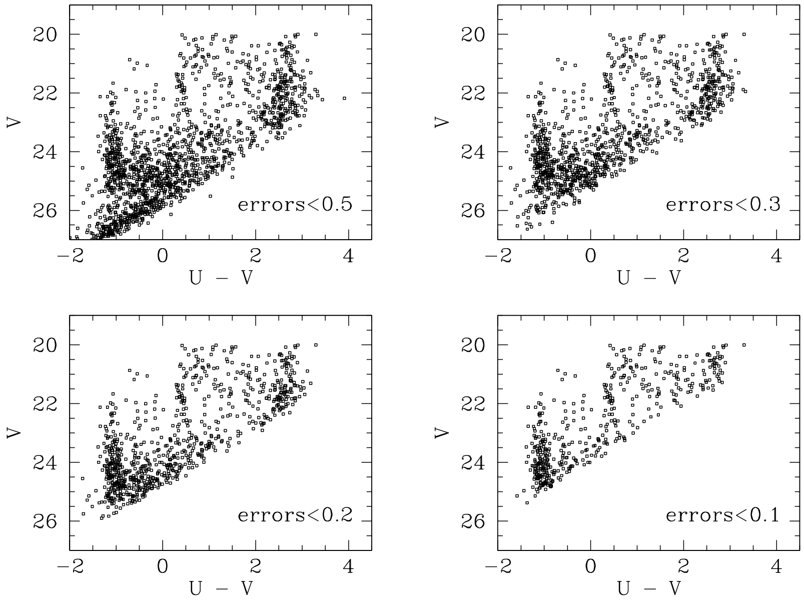

Figure 7.5: Color-magnitude diagrams of the young stellar populations in the shell field of NGC 5128 with different cuts applied on the size of the photometric errors in both bands U and V.

Table 7.2: Main sequence and total life-times of the stars with masses larger than 4 $M_\odot$ and metallicities Z=0.004 and Z=0.008 (Fagotto et al. 1994).

$M(M_\odot)$	τ_{MS}(Myr)	τ_{tot}(Myr)	τ_{MS}(Myr)	τ_{tot}(Myr)
	Z=0.004		Z=0.008	
5.0	101.89	112.09	104.91	116.05
6.0	70.98	76.74	71.63	77.71
7.0	52.58	56.39	52.40	56.26
9.0	33.07	35.25	32.42	34.52
12.0	20.20	21.48	19.85	21.08
15.0	14.35	15.27	14.03	14.93
20.0	9.805	10.48	9.44	10.10
30.0	6.37	6.86	6.18	6.66
40.0	5.01	5.44	4.89	5.31
60.0	3.85	4.20	3.84	4.23
100.0	3.11	3.38	3.12	3.44
120.0	2.98	3.24	3.01	3.33

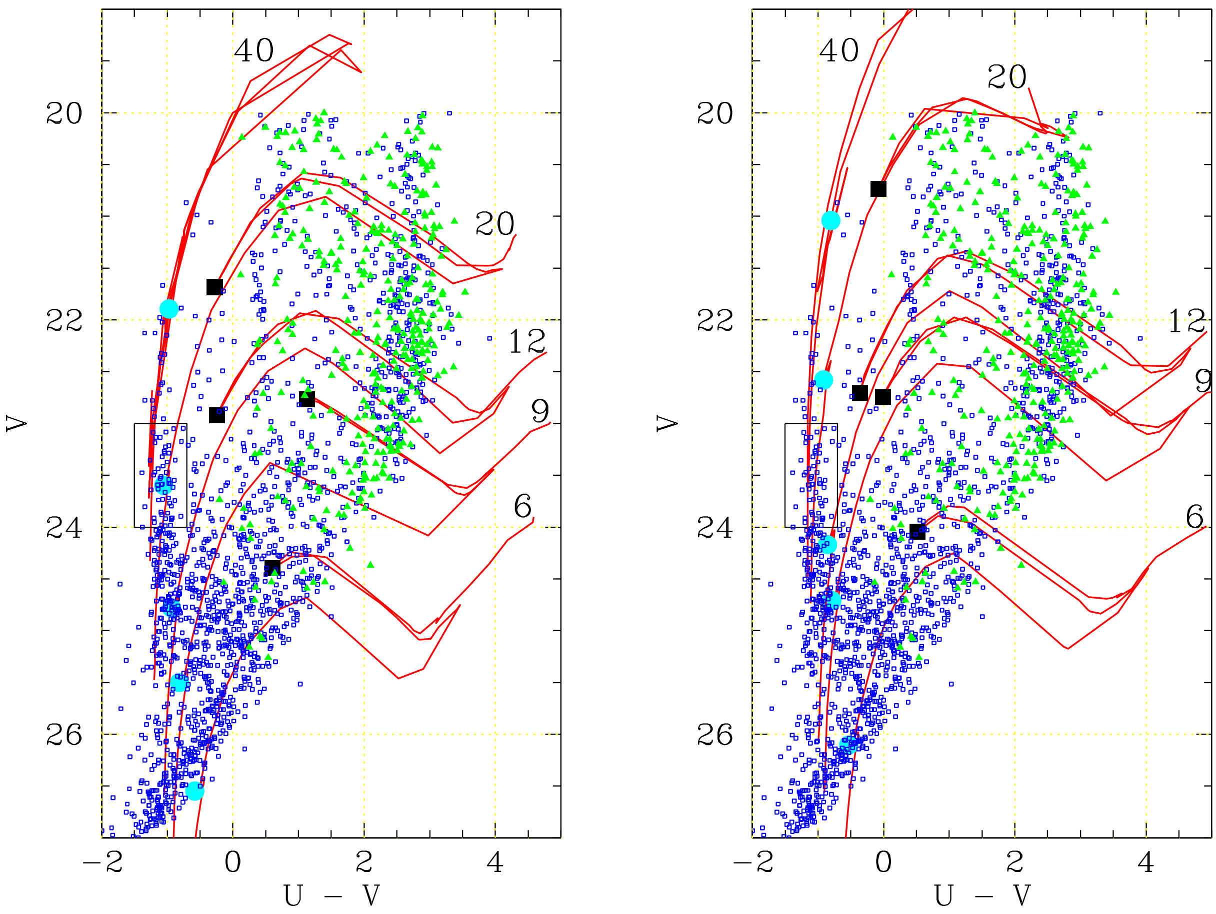

Figure 7.6: Comparison of the the UV CMD with stellar evolutionary tracks for Z=0.004 (left) and Z=0.008 (right panel) and masses of 6, 9, 12, 20 and 40 $M_{\odot}$. Overplotted are also the expected foreground stars (filled triangles) from the Besançon simulations (see Chapter 4). The big filled dots on the isochrones indicate the main sequence turn-off point the and big filled squares indicate the blue edge of the blue loops. Along the line connecting MS turn-offs (dots) and along the line connecting blue edges (squares) most of the stars are expected according to the models. A box on the main sequence between magnitudes 23 and 24 indicates the area used to constrain the simulations.

Before starting the simulations it is necessary to estimate the range of metallicities and ages, hence masses, of stars present in the observed CMD. The metallicity of the young stellar population of NGC 5128 has not yet been spectroscopically measured. Until now its only estimates come from our photometry. In Chapters 4 and 5 (Rejkuba et al. 2001b, 2002) we argued that the best fitting Padova isochrones, which could reproduce the position of the main sequence and the width of the blue loops, had metallicity of Z=0.004. In the previous section, however, we have shown that the U-band magnitudes of the Padova isochrones have been calculated using a different filter to ours. It is thus necessary to transform the evolutionary tracks or isochrones from the theoretical to the observational plane using a consistent set of bolometric corrections in order to compare them directly with the observations. This comparison is made in figure 7.6, where we overplot the Padova evolutionary tracks (Fagotto et al. 1994) for stars with metallicity of Z=0.004 (left) and Z=0.008 (right panel) and masses of 6, 9, 12, 20 and 40 $M_{\odot}$. The transformation of the tracks to the observational plane was described in previous sections. The corresponding life-times of the stars of these masses are given in table 7.2. Over the observed CMDs we have overplotted the Besançon simulations of the foreground Galactic stellar distribution (for more details see Chaper 4) as filled triangles. Essentially all the Galactic stars have $(U - V)$ color redder than 0 mag and they completely dominate in the red part of the CMDs accounting for the majority of stars there.

In order to fit the positions of the main sequence it was necessary to apply reddening of $E(U - V) = 0.62$, corresponding to $E(B - V) = 0.35$ (Cardelli et al. 1989). This value is higher than $E(B - V) = 0.15$ found by comparison with isochrones (Rejkuba et al. 2001b, Chapter 4). The difference derives from the filter mis-match. Unfortunately, as we show later, the width of the blue loops cannot be used to constrain the metallicity because of the strong foreground contamination and a small number of stars expected to be found in the red part of the CMD. Hence we have a degeneracy between metallicity, reddening and distance. In the following analysis we adopt distance modulus of 27.8 mag and reddening of $E(B-V) = 0.35$. The star formation history for two sets of tracks, for Z=0.004 and Z=0.008, is investigated in more detail.

Stellar evolution models reproduce very well the observed luminosities and temperatures of the massive stars along the main sequence. By looking at the positions of the main sequence turn-offs (cyan colored filled dots in fig. 7.6) we can estimate the approximate look-back time on the main sequence of $\sim 40 - 50$ Myr for the Z=0.004 and $\sim 50 - 65$ Myr for the Z=0.008 models. This means that using only the main sequence, we can say something about the star formation history up to this look-back time.

The look-back time for the evolved stars is somewhat larger ranging up to $\sim$ 80 Myr. Unfortunately, the evolution beyond the main sequence is not so well constrained. The evolution of the massive stars from the main sequence onwards is extremely sensitive to the input physics like the convection criteria or the mixing efficiency, the metallicity, the opacities at intermediate temperatures, the mass loss and the overshooting (Renzini et al. 1992, Ritossa 1996). At larger metallicities the thermal conductivity of the envelope is lower leading to a larger thermal imbalance of the stellar envelope and to a faster expansion to the red. The more metal-rich models have thus redder red giant minima. The models that adopt efficient mixing in the semiconvective region during the hydrogen shell burning spend most of the post main sequence life-times as blue supergiants, while the less efficient mixing drives the runaway expansion towards the red (Ritossa 1996). The convective core overshoot during the main sequence in combination with efficient mixing can, however, produce models with wider loops (e.g. Fagotto et al. 1994).

In the Padova models stars with masses $M < 3M_{\odot}$ burn helium in a clump. The first extended loop appears for the 3 $M_{\odot}$ stars and then the loops widen as the mass increases. The exception is the 9 $M_{\odot}$ model for Z=0.004 which has very short loop (see fig. 7.6). The blue excursion of this model is terminated at low temperatures. Padova models adopt the overshoot of the internal edge of the inner envelope in addition to the core overshoot in order to reproduce the loops width and bring stars across the instability strip where the Cepheids are found (Fagotto et al. 1994). The model for 20 $M_{\odot}$ is the last one to have the blue loops. The higher mass models have more erratic excursions in the post main sequence evolution.

The slowest evolutionary phases are the main sequence (indicated by large filled dots in fig. 7.6), the blue edge of the blue loops (large filled squares in fig. 7.6) and red giant minimum. The MS component is numerous in the observed CMD. It is not affected by the foreground contamination and is well understood on theoretical grounds. We take these stars as powerful diagnostic for our models.

PMS stars are composed of blue and red supergiants. Being the blue edge loop stars, the location of the blue supergiants depends critically on metallicity and overshooting, as well as their lifetimes. These are the quantities that translate directly the stellar counts into the astrated mass, hence also into the SF rate, at the appropriate age. The amplitude of the blue excursions is highly dependent on overshooting and opacity, which constrain $T_{\rm eff}$. Through the dependence of bolometric corrections on the effective temperature ($BC(T_{\rm eff})$) they produce the sharp edge in the observed CMD. Extremely short time for stars between the MS turn-off and blue edge leaves a "hole" in the CMD. On the other hand this area has stars in our observed CMD ($-0.5 \lesssim U-V \lesssim 0$ and $V \gtrsim 23$). The possible reasons include different metallicity, inadequate input physics (combination of overshooting and opacity parameters), differential reddening, bolometric corrections, photometric errors and blends of several lower mass stars. Thus we expect not to be able to reproduce well this zone.

At the location of red supergiants there is a too large contamination to interpret the counts here. However, one constraint on the number of contaminating stars comes from the Besançon Galaxy models and we can use those to compare the predicted PMS vs. total counts with the observations for a consistency check.

We have chosen a box on the main sequence between magnitudes 23 to 24, with color limit bluer than −1.7 mag (see fig. 7.6), that has 57 observed objects as a constraint for the simulations. Within the chosen box stars more massive than 14 and 15 $M_\odot$ for models with Z=0.008 and 0.004, respectively, are located. This means that simulations in which star formation stopped some 15 Myr ago will not be able to populate the box at all. When the number of simulated stars in that box reaches 57, the simulations are stopped. In order to select the best fitting model we compare the synthetic and observed CMDs directly as well as the luminosity function along the main sequence for the stars brighter than V=26, which are not affected critically by photometric errors and incompleteness. Comparing the simulations with the observed CMDs and luminosity functions along the main sequence in the next sections we address the following questions: "How old are the oldest and the youngest stars in the observed UV CMD?" and "What is the slope of the initial mass function?"

7.3.1 Age of the young stellar population in the NGC 5128 halo field

In all the simulations we adopted distance modulus of 27.8 and reddening $E(B-V) = 0.35$. The simulations were done for 2 metallicities, Z=0.004 and Z=0.008. We varied the parameters governing the beginning and the duration of the star formation and the IMF. The dependence on the IMF is discussed in the next section. Here we explore the age range of the stars in this field.

The range of models probed is listed in table 7.3.1. In the first column there is the model name, in columns 2, 3 and 4 the input parameters regarding the IMF and the duration of the star formation are given. The output total extracted mass in the range of 0.6 to 100 $M_\odot$, the mean SFR for the same mass range and the explored interval of the star formation ($\Delta\tau$), as well as the total number of stars above the 80% incompleteness limit in V-band ($V < 25.5$) and the number of simulated blue plume stars ($U-V < -0.7$ for $V < 25.5$) are listed in columns 6, 7, 8 and 9 for Z=0.004 and 10, 11, 12 and 13 for models using evolutionary tracks for metallicity Z=0.008, respectively. Due to small range of ages and to the smooth appearance of the main sequence, a constant star formation was considered. The mean SFR is thus equal to the actual SFR being the ratio of the total mass formed and the length of time for which the star formation has been taking place:

$$\langle \mathrm{SFR} \rangle = \frac{M_{star}}{\Delta\tau} \tag{7.18}$$

The synthetic CMDs with different star formation histories are shown for Z=0.004 and Z=0.008 assuming a Salpeter IMF ($\alpha = 2.35$) in figures 7.7 and 7.8. The duration of the star formation episode is indicated in each panel as the ending–starting time. The ending time of 0 Myr means that the star formation is on-going. The sharp blue edge of the blue loops is due to the theoretical form of the blue loops. In particular the early termination of the 9 $M_\odot$ model for Z=0.004 produces a bend in the simulated CMDs. This transition is much smoother for the Z=0.008 models.

As the star formation lasts longer it is possible to observe the excursions of the stars in post main sequence phases. The reddest parts of the CMD, however, remain very sparsely populated due to much shorter evolutionary timescales in the red with respect to the blue. Less massive ($M \lesssim 15 M_\odot$) red supergiants evolve less rapidly. Few of them are visible in the upper red part of the simulated CMDs in which star formation was not terminated. Also,

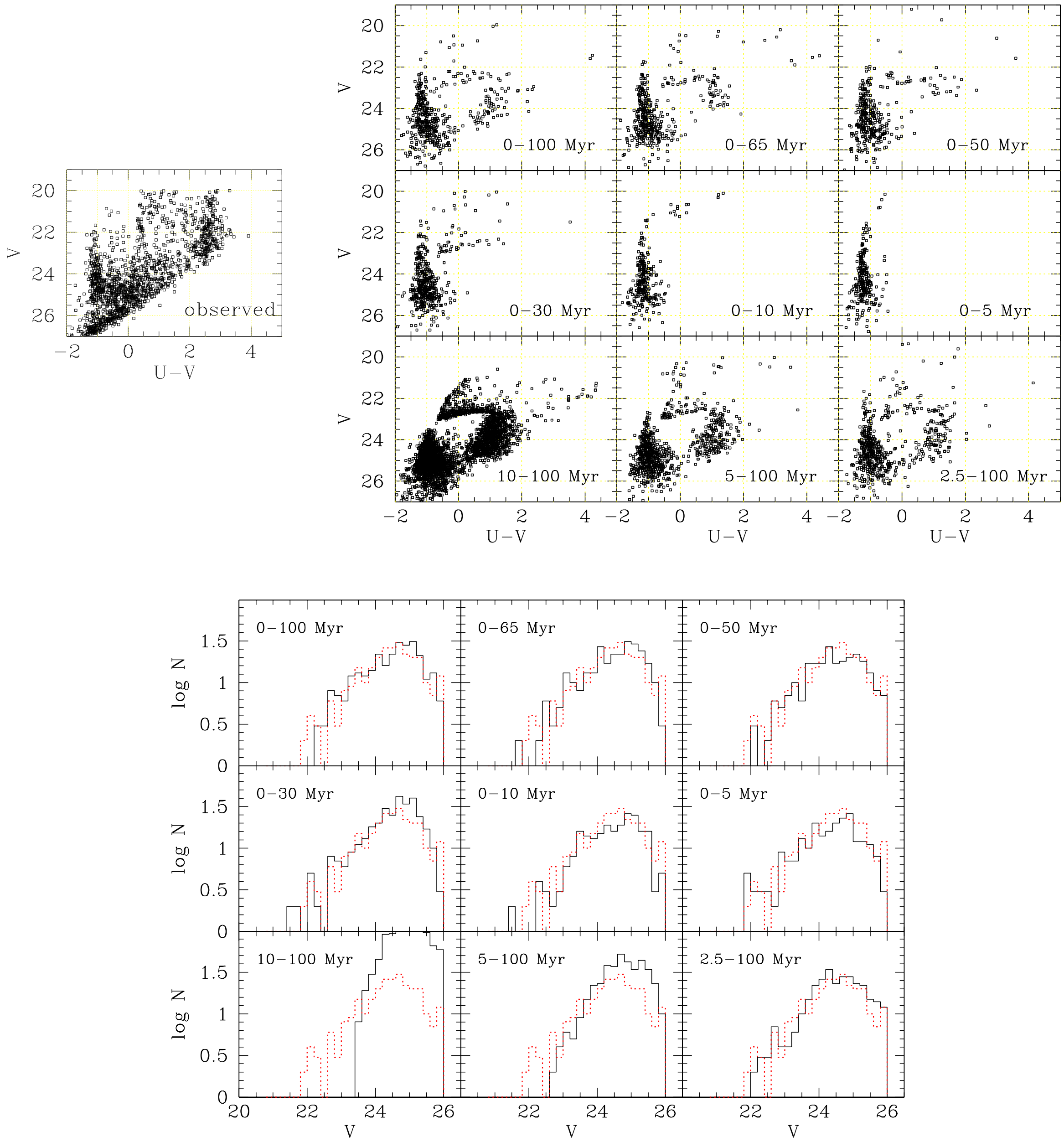

Figure 7.7: Synthetic CMDs for Z=0.004 using the Salpeter IMF ($\alpha = 2.35$), the appropriate distance and a constant SFR in the interval that is indicated in each panel (beginning-end of the burst). For comparison the observed CMD is also displayed. In the lower part simulated luminosity functions (solid lines) are compared with the observed luminosity function (dotted lines). In the observed and simulated luminosity functions the color and magnitude cuts are applied and only stars bluer than $\mathrm{U} - \mathrm{V} = -0.7$ and brighter than V=26 are compared.

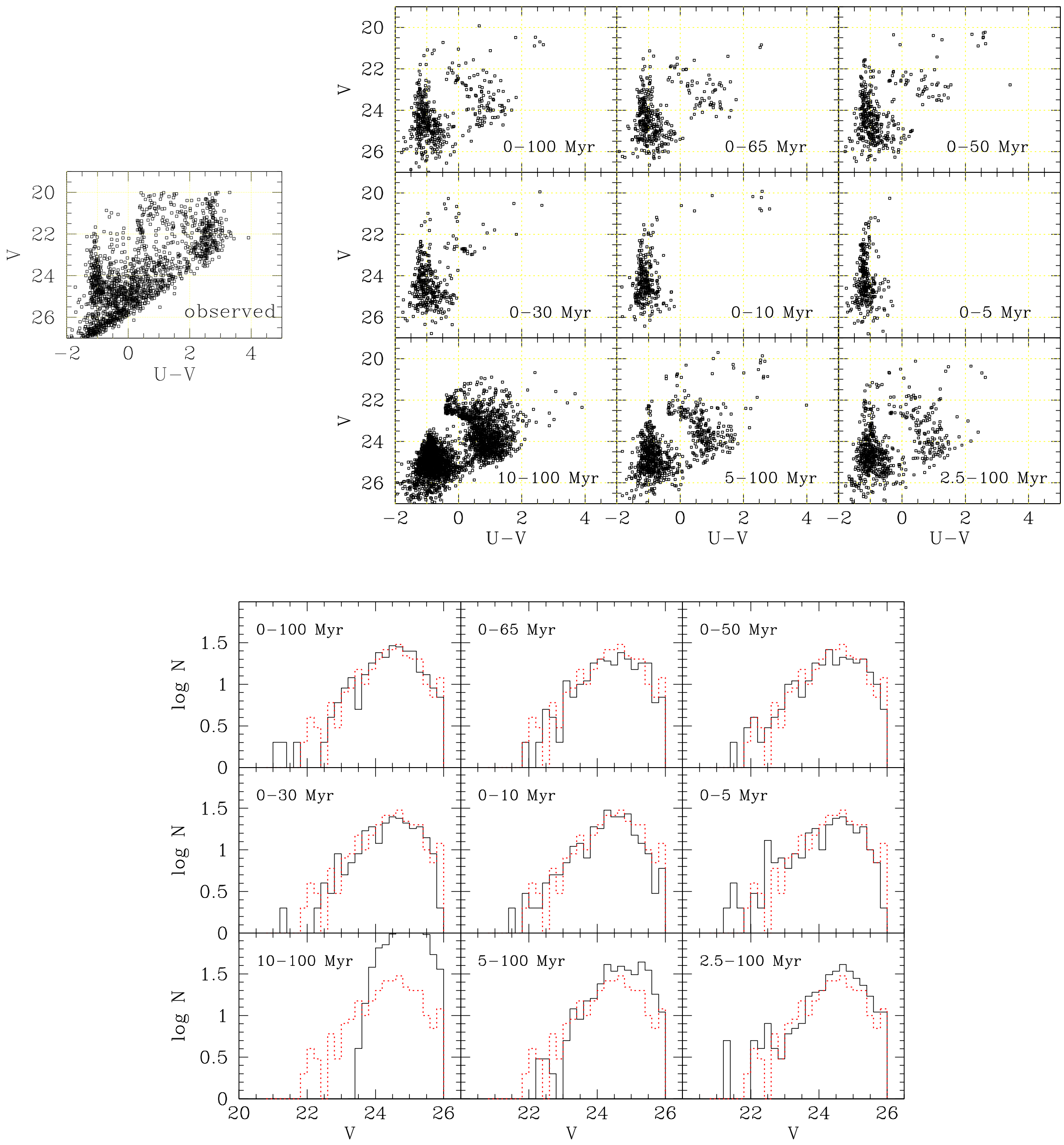

Figure 7.8: Synthetic CMDs for Z=0.008 using the Salpeter IMF ($\alpha = 2.35$), the appropriate distance and a constant SFR in the interval that is indicated in each panel (beginning-end of the burst). For comparison the observed CMD is also displayed on the left. In the lower panels the simulated luminosity functions (solid lines) are compared with the observed luminosity function (dotted lines). In the observed and simulated luminosity functions the color and magnitude cuts are applied and only stars bluer than $U - V = -0.7$ and brighter than V=26 are compared.

Table 7.3: Input parameters and results of the simulated star formation histories of young stellar populations. Columns 1 to 5 are identifier of the model, slope of the IMF, start and end of the star formation burst in Myr, respectively. In the next 8 columns extracted mass, mean star formation rate in the interval $\Delta\tau$, the total number (N_{tot}) and the number of blue plume stars (N_{blue}) in the simulated CMDs are given for Z=0.004 and Z=0.008

				Z=0.004				Z=0.008			
model ID	IMF α	τ_1 10^6 yr	τ_0 10^6 yr	mass 10^6 $M_\odot$	$\langle SFR\rangle$ $M_\odot$/yr	N_{tot}	N_{blue}	mass 10^6 $M_\odot$	$\langle SFR\rangle$ $M_\odot$/yr	N_{tot}	N_{blue}
salp01	2.35	1000	0	6.79	0.007	512	276	6.44	0.006	499	279
salp02	2.35	500	0	3.97	0.008	551	296	3.38	0.007	472	257
salp03	2.35	200	0	1.38	0.007	496	289	1.47	0.007	546	288
salp04	2.35	100	0	0.66	0.007	460	256	0.61	0.006	460	250
salp05	2.35	65	0	0.44	0.007	415	259	0.35	0.005	368	225
salp06	2.35	50	0	0.29	0.006	351	224	0.31	0.006	377	226
salp07	2.35	30	0	0.23	0.008	430	306	0.19	0.006	345	229
salp08	2.35	10	0	0.08	0.008	273	219	0.08	0.008	283	241
salp09	2.35	5	0	0.07	0.014	254	216	0.07	0.014	278	239
salp10	2.35	100	10	7.73	0.086	3080	887	6.43	0.071	2685	801
salp11	2.35	100	5	1.52	0.016	816	353	1.40	0.015	806	339
salp12	2.35	100	2.5	0.90	0.009	568	273	0.94	0.010	633	313
scal01	2.60	1000	0	12.8	0.013	591	288	9.95	0.010	478	257
scal02	2.60	500	0	6.65	0.013	641	291	5.38	0.011	548	261
scal03	2.60	200	0	2.30	0.011	610	301	2.12	0.011	526	254
scal04	2.60	100	0	1.65	0.017	719	337	1.19	0.012	600	296
scal05	2.60	65	0	0.96	0.015	619	349	0.96	0.015	704	372
scal06	2.60	50	0	0.65	0.013	512	289	0.57	0.011	492	296
scal07	2.60	30	0	0.32	0.011	406	267	0.32	0.011	418	267
scal08	2.60	10	0	0.14	0.014	253	206	0.10	0.010	191	160
scal09	2.60	5	0	0.15	0.030	291	257	0.12	0.025	257	217
scal10	2.60	100	10	12.1	0.134	3497	921	10.0	0.112	3030	777
scal11	2.60	100	5	1.95	0.020	789	314	2.09	0.022	787	309
scal12	2.60	100	2.5	2.43	0.025	984	442	1.49	0.015	669	289
imf301	3.00	1000	0	34.8	0.035	939	366	28.4	0.028	743	314
imf302	3.00	500	0	21.6	0.043	1038	419	18.4	0.037	819	344
imf303	3.00	200	0	6.93	0.035	819	312	7.54	0.038	891	378
imf304	3.00	100	0	4.41	0.044	991	426	3.62	0.036	792	319
imf305	3.00	65	0	2.51	0.039	693	340	1.82	0.028	573	278
imf306	3.00	50	0	2.63	0.053	869	464	1.87	0.037	738	361
imf307	3.00	30	0	1.29	0.043	601	363	0.95	0.032	503	309
imf308	3.00	10	0	0.49	0.049	304	238	0.55	0.055	362	278
imf309	3.00	5	0	0.50	0.101	331	277	0.39	0.078	287	237
imf310	3.00	100	10	31.8	0.353	5756	1333	19.7	0.219	3267	784
imf311	3.00	100	5	6.02	0.063	1118	379	5.39	0.057	1082	396
imf312	3.00	100	2.5	5.22	0.053	1057	387	4.54	0.047	927	359
imf201	2.00	1000	0	3.87	0.004	402	239	3.75	0.003	388	235
imf202	2.00	500	0	2.11	0.004	433	258	1.68	0.003	370	231
imf203	2.00	200	0	0.93	0.005	490	271	0.68	0.003	358	222
imf204	2.00	100	0	0.40	0.004	377	237	0.43	0.004	445	261
imf205	2.00	65	0	0.32	0.005	486	309	0.26	0.004	386	248
imf206	2.00	50	0	0.19	0.004	362	256	0.20	0.004	411	260
imf207	2.00	30	0	0.10	0.003	312	233	0.14	0.005	419	290
imf208	2.00	10	0	0.05	0.005	252	215	0.03	0.003	193	165
imf209	2.00	5	0	0.03	0.005	190	173	0.03	0.007	232	212
imf210	2.00	100	10	4.25	0.047	2127	699	3.05	0.034	1705	517
imf211	2.00	100	5	0.99	0.010	693	318	0.87	0.009	625	311
imf212	2.00	100	2.5	0.52	0.005	445	253	0.45	0.004	422	235

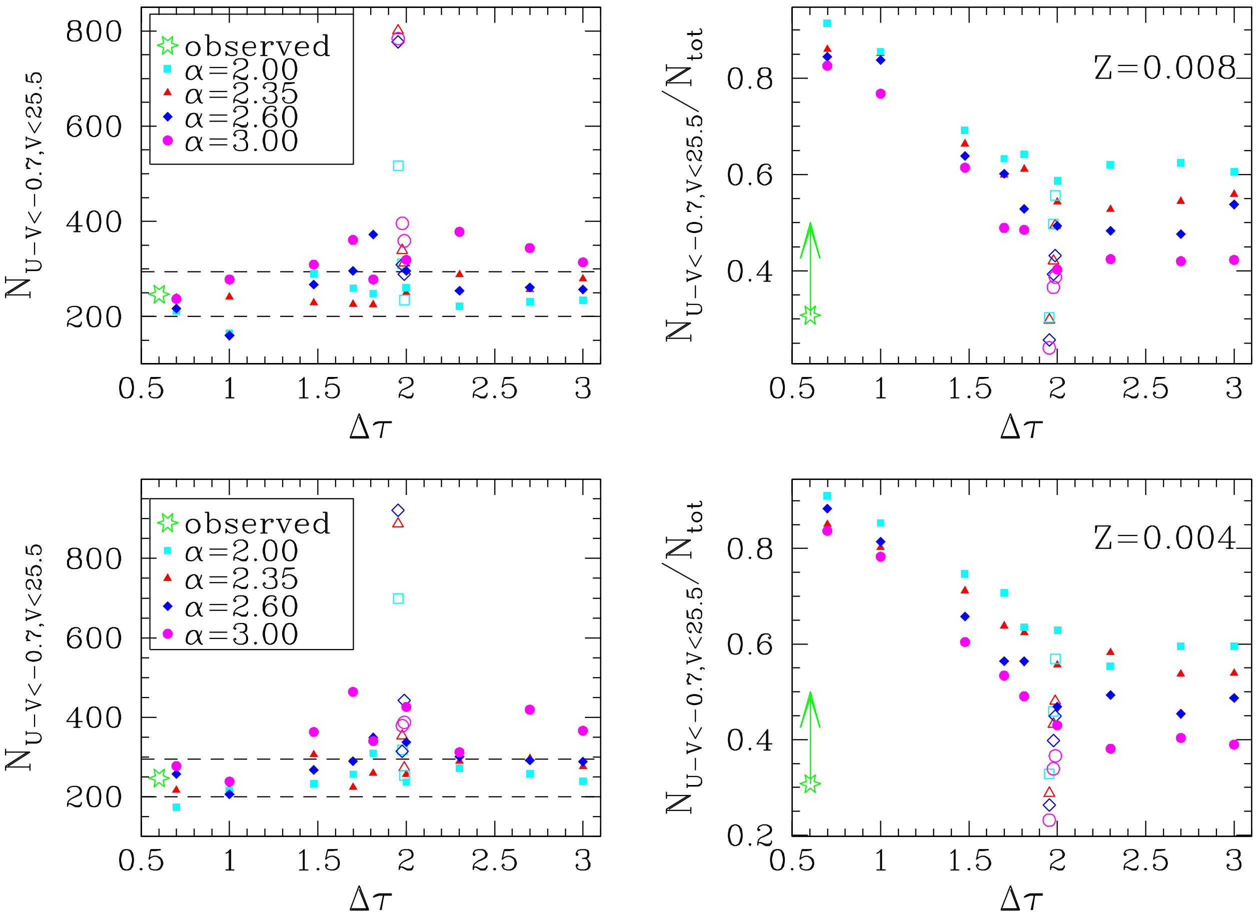

Figure 7.9: Number of stars in the blue plume ($U - V < -0.7$) for V brighter than 25.5 vs. logarithm of star formation duration is shown in left panels for the models with Z=0.008 (top) and Z=0.004 (bottom). The observed number of stars within the same limits is indicated with a green star. Dotted lines indicate 3 sigma Poissonian fluctuation limits in the number of observed stars. The length of star formation for the observed point is arbitrary. Different symbols are used for models with different IMF slopes as indicated in the legend. The models for which star formation was terminated 2.5, 5 and 10 Myr ago are plotted with open symbols and the models for which the star formation is still on-going have filled symbols. On the right the ratio of the blue plume vs. total number of simulated stars is shown. The observed point is only a lower limit due to a large uncertainty in foreground contamination.

as the star formation gets longer, the main sequence gets populated with stars of smaller masses, the total number of which is governed by the IMF.

In the direct comparison of the simulated and observed CMDs, and the corresponding luminosity functions (figures 7.7 and 7.8) it can be seen that all the simulations with on-going star formation fit the data equivalently well without regard of the maximum duration of the SF (τ_{max}) . The luminosity function peak is best fitted with models with longer star formation durations ($\tau_{max} \gtrsim 30-50$ Myr), but the differences between various models are within the Poissonian errors. Hence, using only MS stars ($\mathrm{U-V} < -0.7$) it is not possible to put a firm constraint on τ_{max}.

On the other hand, the simulations in which the star formation has stopped 5 or 10 million years ago have many more stars in the lower main sequence and around the blue edge of the loops than observed. In order to populate the box on the main sequence between magnitudes 23 and 24, which contained the youngest MS stars (younger than $14-15$ Myr) and thus the ones with the shortest evolutionary timescales, many more lower mass stars were produced in these simulations. Stopping the SF at 2.5 Myr produces a MS luminosity function in agreement with the observations. In figure 7.9 in left panels we plot the number of stars in the blue plume for all the models with Z=0.008 (top) and Z=0.004 (bottom). The observed value is shown as a green star. The dashed lines indicate 3σ Poissonian deviation from the observed value. The models outside of the dashed lines in this figure are ruled out. So, the total number of the MS stars and their luminosity function constrain the lower limit of the SF duration to be 2.5 Myr.

Although post main sequence stars cannot be used to select the best fitting model due to large uncertainties as discussed above, there are 17 bright ($21 < \mathrm{V} < 23$) and blue stars ($-0.7 < \mathrm{U-V} < 0$) most probably in the post main sequence phases in the observed CMD. They are found in the area of the CMD where there is no contamination by the foreground Galactic stars. The models that have active star formation only over the last 5-10 Myr, have 1 or no stars in this area of the CMD. So, the star formation in this field must have been going on for more than 10 Myr.

Better limits to the duration of the star formation can be obtained by comparison of the number of stars on the main sequence and in post main sequence phases. The ratio of the blue plume ($\mathrm{U-V} < -0.7$) and the total number of stars versus the duration of the star formation for the models described in table 7.3.1 is presented in the upper right panel of the figure 7.9 for Z=0.008 and lower right panel for Z=0.004 models. This ratio decreases with increasing τ_{max}, because the PMS phases become more populated. The observed ratio of the blue vs. total number of stars is indicated with a star in figure 7.9. The arrow shows that it is only a lower limit due to the large uncertainty in contamination which affects in particular the post main sequence phases. The number of stars in the observed CMD is much larger than in all the simulations which reproduce correctly the number of stars in the blue plume. Since this ratio is observed low, even after the foreground contamination subtraction, it points, independently from the evidence on number of MS stars, towards long τ_{max}.

The inflexion point in these diagrams corresponds to the maximum look-back time and hence the maximum age of the burst τ_{max}. It is ∼100 Myr for the models with Z=0.008 and ∼ 90 Myr for Z=0.004 models. Of course this value is the lower limit for the duration of the star formation. The older stars are not observed due to the incompleteness in U-band, hence the ratio of the blue vs. total number of stars becomes constant for longer star formation durations.

From the simulations with the above limits on the duration of the star formation episode ($\tau_{\mathrm{min}} = 0$ and $\tau_{\mathrm{max}} = 100$ Myr) the total extracted mass in stars in the range of masses $0.6 \leq \mathrm{M} \leq 100\ \mathrm{M}_{\odot}$ is ∼0.4, 0.7, 1.3 or $4.4 \times 10^{6}\ \mathrm{M}_{\odot}$, for IMF slopes of 2 and 2.35, 2.6 or 3, respectively. The SFR associated with these IMFs and mass limits are approximately 0.004, 0.007, 0.013 and 0.044 $\mathrm{M}_{\odot}\ \mathrm{yr}^{-1}$, for the four IMF slopes in the above order.

At the distance of 3.6 Mpc, the observed field surveys an area of approximately 45 kpc^2, so that the derived star formation rates range from $\sim 9 \times 10^{-5}$ to $\sim 1 \times 10^{-3}\ \mathrm{M}_{\odot}\ \mathrm{yr}^{-1}\ \mathrm{kpc}^{-2}$. This is lower than the typical SFR quoted for the solar neighbourhood ($4.2 \times 10^{-3}\ \mathrm{M}_{\odot}\ \mathrm{yr}^{-1}\ \mathrm{kpc}^{-2}$; Timmes et al. 1995) and is on the low side of the SFRs derived via theoretical simulations for dwarf irregular galaxies in the Local Group (ranging from approximately 10^{-4} to $10^{-2}\ \mathrm{M}_{\odot}\ \mathrm{yr}^{-1}\ \mathrm{kpc}^{-2}$; Marconi et al. 1995, Tolstoy 1996, Gallart et al. 1996a). For comparison, the star formation rate in WLM dIrr within the last million years was $1.3 \times 10^{-3}\ \mathrm{M}_{\odot}\ \mathrm{yr}^{-1}\ \mathrm{kpc}^{-2}$ (Dolphin 2000).

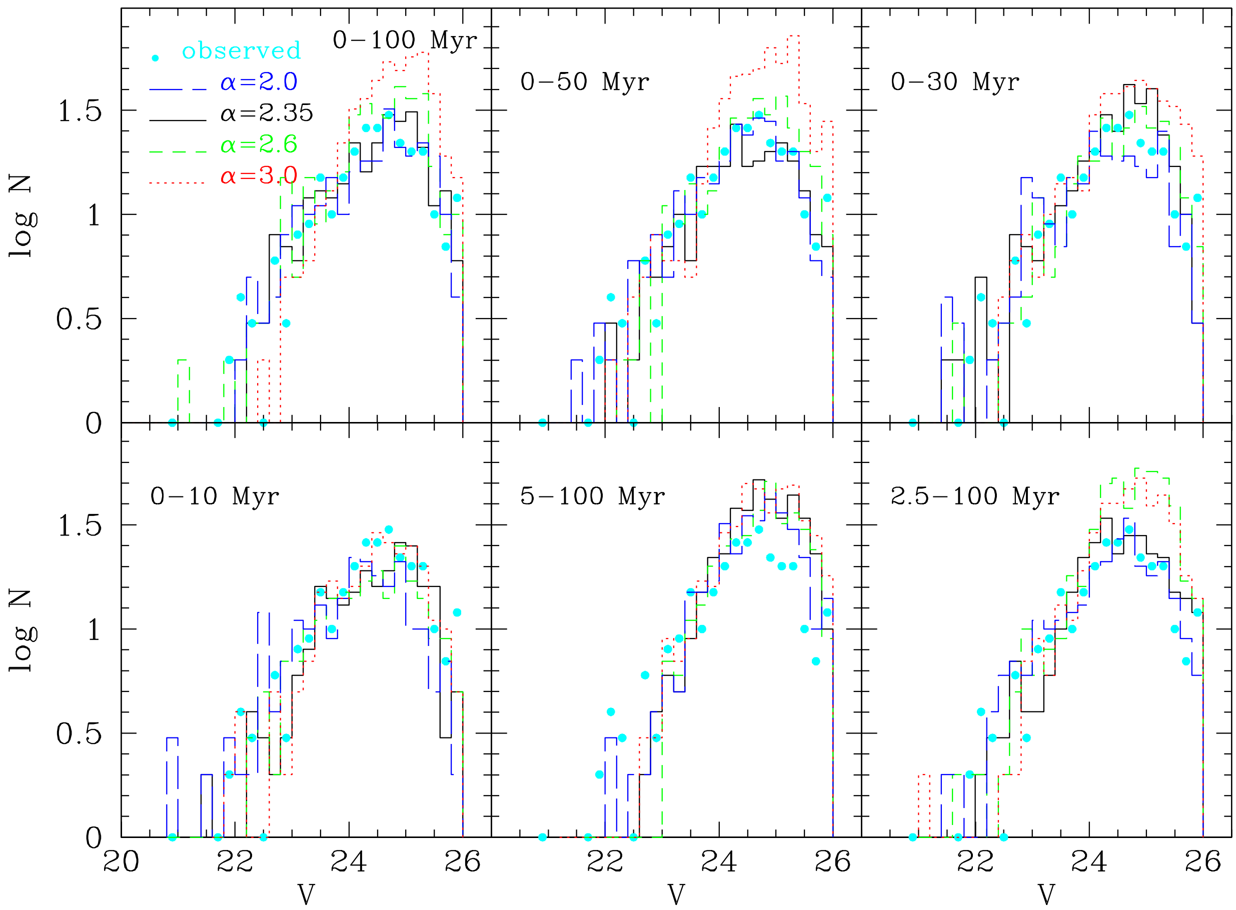

Figure 7.10: Observed MS luminosity function (cyan dots) is compared with synthetic luminosity functions for different SFHs for Z=0.004 and four different IMF slopes (α = 2.0, 2.35, 2.6, and 3.0) as indicated in the legend. Synthetic luminosity functions correspond to models calculated adopting the appropriate distance, reddening and a constant SFR in the interval that is indicated in each panel (beginning-end of the burst). In the observed and simulated luminosity functions the color and magnitude cuts are applied and only stars bluer than $U - V = -0.7$ and brighter than V=26 are compared.

7.3.2 The initial mass function

The observations of the young stars on the main sequence can be used to constrain the initial mass function for the range of masses observed, M $\gtrsim$ 5 $M_\odot$. Comparison of the simulated and observed luminosity functions along the main sequence is presented for a set of models with on-going SF lasting for 100, 50, 30 and 10 Myr as well as for two models in which the SF was stopped 5 and 2.5 Myr ago. Figure 7.11 compares observed luminosity function (dots) with the models for the Z=0.008 and four different IMF slopes: Salpeter IMF (slope $\alpha = 2.35$; solid black line), Scalo IMF (slope $\alpha = 2.6$ for M $\leq$ 3.5 $M_\odot$; Scalo 1986; green short dashed line), IMF with slope $\alpha = 2$ (blue long dashed line) and IMF with slope $\alpha = 3$ (red dotted line). Similar comparison for models with Z=0.004 is in figure 7.10.

The observed slope of the main sequence between 22.5 < V < 24.5 is $\Delta \log N/\Delta V = 0.47$ as derived by least square fitting of the observed luminosity function in this magnitude range. Results for the models with Z=0.004 and Z=0.008 are equivalent. The models with IMF slope $\alpha = 2.35$ provide the best fit of the luminosity function for both metallicities Z=0.004 and Z=0.008. Slightly shallower ($\alpha = 2$) and steeper ($\alpha = 2.6$) slopes for IMF are also acceptable, while the $\alpha = 3$ slope produces too many stars in the lower mass bins in all the simulations. Note that the models where SF has stopped 2.5 Myr ago are well fitted with Salpeter and shallower IMF and they would exclude Scalo IMF.

This result is also summarized in figure 7.9. In left panels the dashed lines exclude the models with IMF slope $\alpha = 3$, because the simulated number of blue plume stars is always larger than observed. In the right panels the above mentioned saturation value (or the inflexion point) of the number of PMS vs. total number of stars depends on the IMF slope. The steeper the IMF, the more favoured the PMS. The conclusion on the IMF is unfortunately hampered by the large contamination. The fact that the observed number of blue plume stars excludes the steepest IMF and at the same time the ratio of PMS vs. total number would favour the steepest IMF, implies that the contamination is indeed much larger than from the Besançon counts as already noted in Chapter 4. Additionally there may be few compact background galaxies contaminating the red part of the CMD.

Our simulations do not include the binary stars. The presence of binaries would increase the IMF slope by an amount that depends on the slope and the fraction of stellar mass in binary or multiple stellar systems. According to Sagar & Richtler (1991) if the fraction of binaries is more than 50% the IMF slope increases by 0.3 to 0.4. As the binary fraction in our field is not known, it is possible that the actual IMF slope is somewhat steeper than $\alpha = 2.35$.

7.3.3 Young stellar population in the V–K CMD

The VK optical–near IR CMD for this field has several dozens of stars in the bluest part of the diagram ($V - K < 2$) with respect to the control halo field (see Chapter 4, figure 4.12). They have very small photometric errors (90% has $\sigma < 0.2$) because they are bright in optical. Their colors are bluer than those for Galactic foreground stars (see Chapter 4 figure 4.7). To show that they belong to the star forming region in NGC 5128 we plot the spatial distribution of the blue ($V - K < 2$ and $K < 24$) and red ($V - K > 5$ and $19 < K < 21$) stars in the shell field (figure 7.12). While the reddest objects spread evenly over the field, the blue stars are strongly aligned in the direction of the jet just like in the optical CMDs.

Low number of young stars observed in the much smaller field of view of ISAAC prevents us from drawing strong conclusions from their observations. The comparison with the Padova stellar evolutionary tracks (in the upper panels of figure 7.12) for two different metallicities Z=0.004 (left) and Z=0.008, indicates again very small difference between the models.

7.3.4 Summary for the simulations of young population

In summary, the modelling of the young stellar populations in the north-eastern halo of NGC 5128 indicates that the star formation in this field is still on-going or at most has stopped some 2 Myr ago. Due to high foreground contamination and magitude limit of the U-band data, it is not possible to constrain the onset of the star formation. Most probably it has been lasting for at least 90-100 Myr, where the range depends on the adopted metallicity.

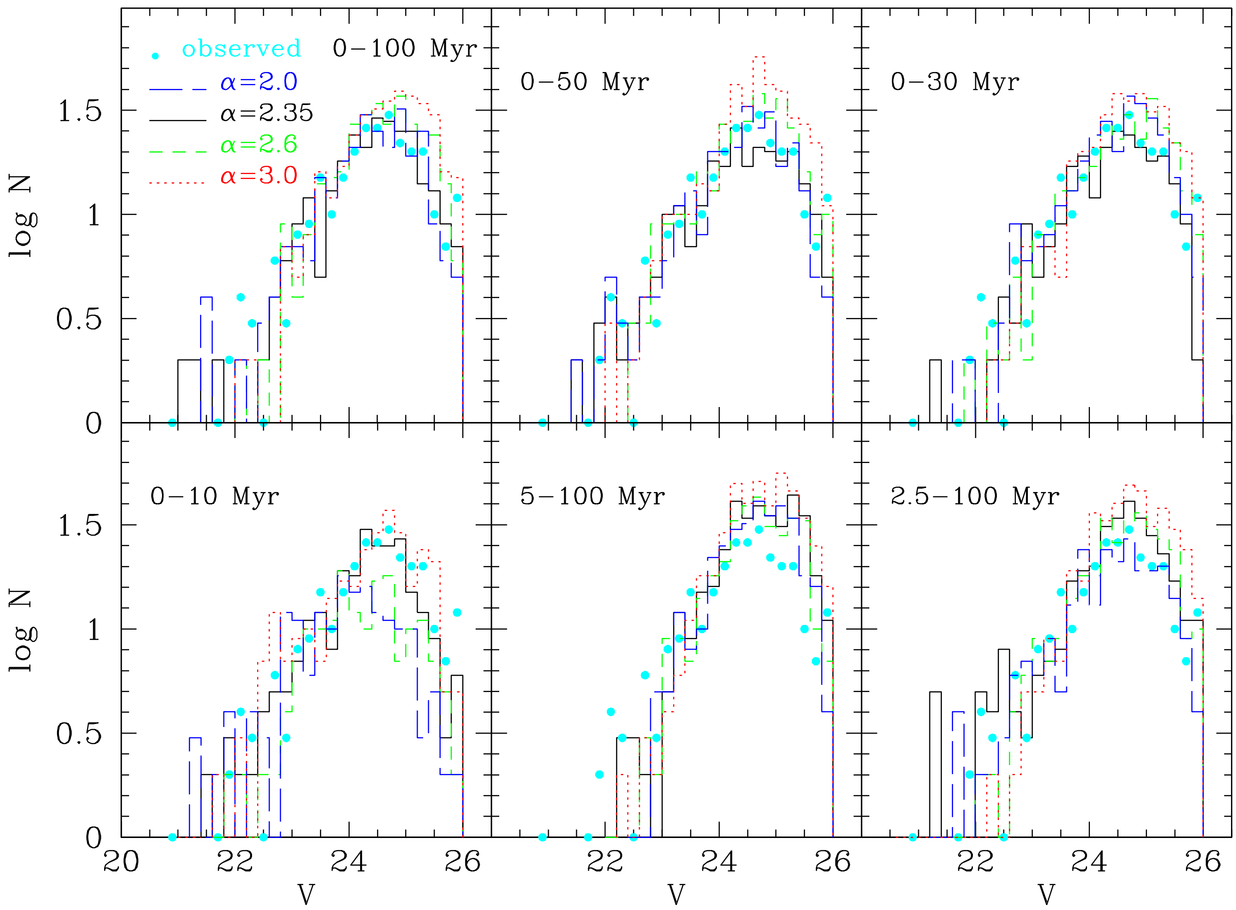

Figure 7.11: Observed MS luminosity function (cyan dots) is compared with synthetic luminosity functions for different SFHs for Z=0.008 and four different IMF slopes (α = 2.0, 2.35, 2.6, and 3.0) as indicated in the legend. Synthetic luminosity functions correspond to models calculated adopting the appropriate distance, reddening and a constant SFR in the interval that is indicated in each panel (beginning-end of the burst). In the observed and simulated luminosity functions the color and magnitude cuts are applied and only stars bluer than $U - V = -0.7$ and brighter than V=26 are compared.

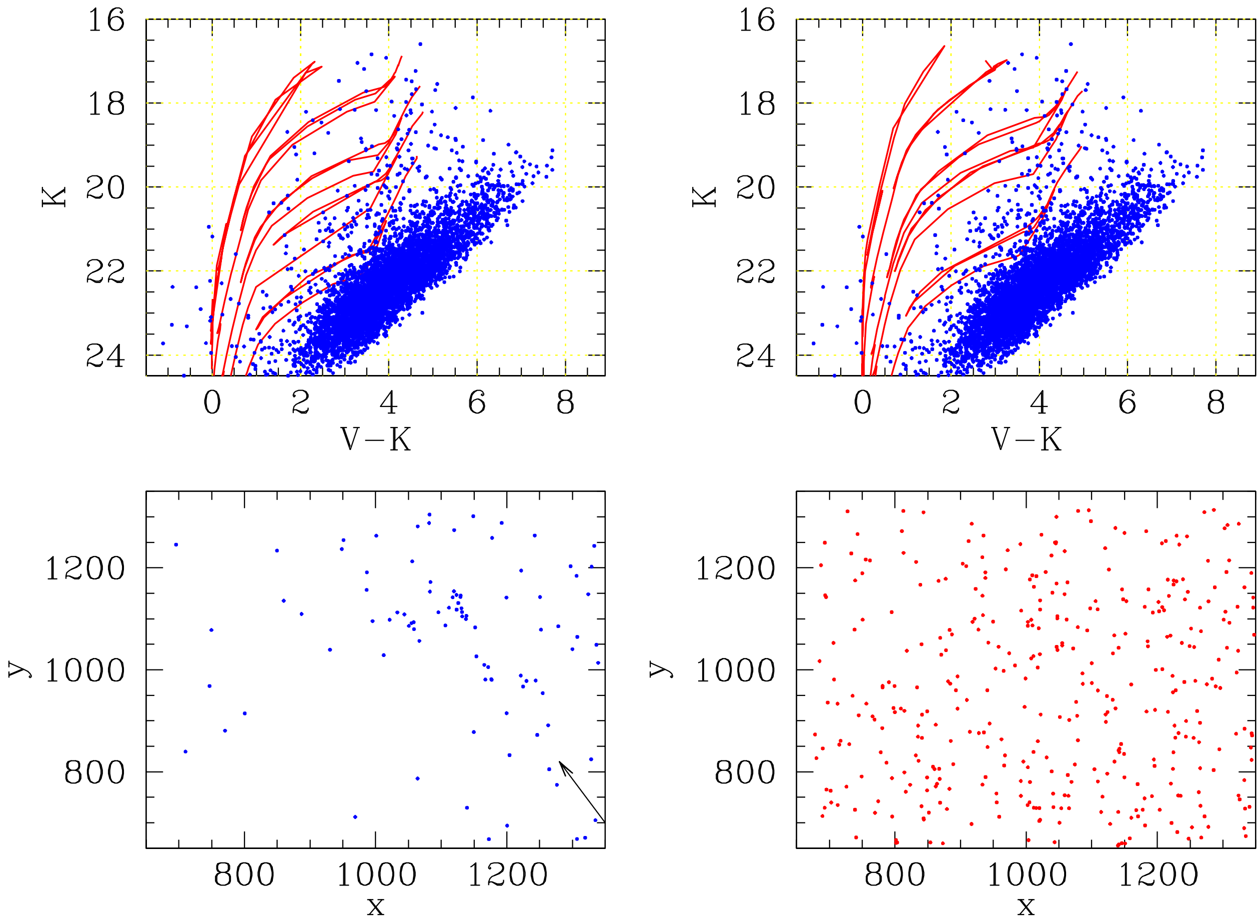

Figure 7.12: Comparison of the the VK CMD with stellar evolutionary tracks for Z=0.004 (upper left) and Z=0.008 (upper right panel) and masses of 6, 9, 12, 20 and 40 $M_{\odot}$. In the lower panels the spatial distribution of the blue ($V-K<2$ and $K<24$) stars on the left and red ($V-K>5$ and $19<K<21$) stars on the right is shown. Note the alignment of the blue stars along the direction of the radio jet indicated by the arrow in the lower right corner of the left panel.

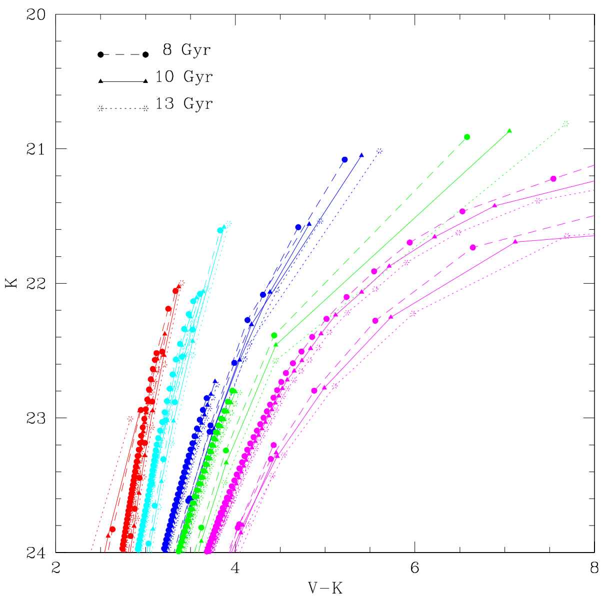

Figure 7.13: Comparison of the isochrones for 8 (dashed lines), 10 (solid lines) and 13 (dotted lines) Gyr old population computed by Cassisi & Salaris (1997) and by Bono et al. (1997a, 1997b) in the optical-near IR V–K CMD. The isochrones were brought to the distance of NGC 5128 (assuming 27.8 for the distance modulus) and reddened by $\mathrm{E(B-V)} = 0.1$. Each isochrone is plotted for 5 different metallicities: Z=0.0001, Z=0.001, Z=0.01, Z=0.02 and Z=0.04, from blue to red, respectively.

The SFR is consistent with a constant rate over that time and is of the order of 0.005-0.01 $\mathrm{M_\odot\ yr^{-1}}$ for models which reproduce the observations well. It depends only weakly on the IMF slope, but does not depend much on the adopted τ_{max}. The IMF slope steeper than $\alpha = 2.6$ overproduces the number of low mass stars in the MS luminosity function. The total extinction in this field corresponds to $\mathrm{E(B-V)} = 0.35$, implying a moderate internal extinction of $\mathrm{E(B-V)} = 0.25$. On the basis of the U- and V-band photometry alone it is not possible to constrain the metallicity of the stars due to reddening–distance–metallicity degeneracy of the models.

The fuel for this recent star formation is provided by the large HI gas cloud in the vicinity of the field (Schiminovich et al. 1994). Assuming the constant SFR and a 100% efficiency in converting gas to stars, we can estimate the gas depletion timescale as:

$$\tau_g = \frac{\mathrm{M_{HI}}}{\mathrm{SFR}} \tag{7.19}$$

In the northeastern shell very close to where the star formation is observed, 2.1×10^7 $\mathrm{M_\odot}$ of HI have been detected (Schiminovich et al. 1994) as well as 1.7×10^7 $\mathrm{M_\odot}$ of $\mathrm{H_2}$ (Charmandaris et al. 2000). At the constant star formation level of 0.006 $\mathrm{M_\odot\ yr^{-1}}$ it would take ∼100 Myr to use up all the molecular gas and ∼230 Myr to use all the hydrogen.

7.4 Old populations in NGC 5128 observed with the VLT

The observations of the old and intermediate-age population observed with FORS1 and ISAAC at VLT were described in Chapter 4. The two fields, shell or Field 1 and halo or Field 2, both present a wide RGB with a large number of stars brighter than the tip of the RGB. Among these bright AGB stars more than 1500 variables were detected (see Chapter 6). Here we investigate the old stellar populations in NGC 5128 with simulations.

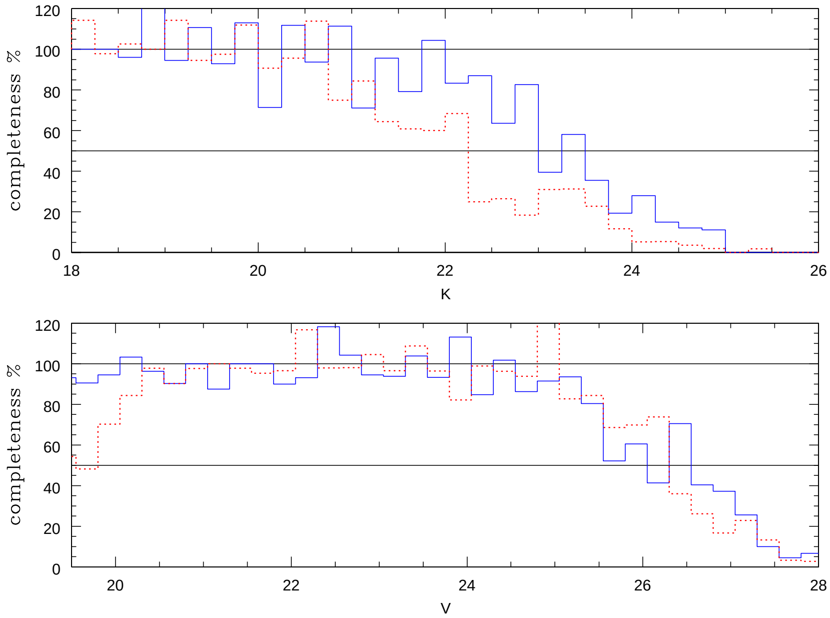

Figure 7.14: Magnitude vs. completeness for V (lower panel) and K-band (top panel). The histogram for Field 1 is coded with solid (blue) line and for Field 2 with dotted (red) line.

While the time resolution for age-dating of the young stellar populations permits investigations of star formation bursts lasting only few Myr, the older the stellar population the worse the time resolution. Stellar populations of only few tenths of Myr are characterized by the bright and blue high-mass stars. At a few hundred Myr the intermediate-mass stars on the early AGB or in the thermally pulsating AGB phase are detected as bright giants above the tip of the RGB. The RGB appears after an evolutionary timescale of about 1 Gyr (Sweigart et al. 1990, Bressan et al. 1994) independently of the initial metallicity of the population. In an older and relatively metal-poor (less than solar metallicity) stellar population AGB stars of much lower luminosity and mass are observed. The genuine indicators of stellar populations in excess of 10 Gyr are the old main sequence turnoff and horizontal branch stars. However, these stars are beyond the limits of present day large ground based telescopes. Thus actually the limit to the time resolution for NGC 5128 is of the order of 1-2 Gyr. The detection of a well-defined RGB is considered to be a necessary although not a sufficient condition to establish the presence of old ($\gtrsim$ 10 Gyr) stars (Da Costa 1994).

Figure 7.13 illustrates that. The stars on the RGB are fairly insensitive to age differences. For metal-poor populations ($Z < Z_\odot$) isochrones of different ages have almost identical V–K colors. The colors of the metal-rich populations start to be more age sensitive. The same figure also displays the high metallicity dependence of V–K color. Thus we do not expect to be able to derive precise ages for the old population in NGC 5128, but we can try to determine the metallicity range hidden in its RGB population.

Before starting the simulations for the old stellar populations observed in V and K-band we ran several more completeness tests in order to quantify the completeness and photometry errors. We found that the incompleteness derived in Chapter 4 (Rejkuba et al. 2001b) was overestimated especially in faint magnitude bins in K-band, mostly due to small number statistics in the faint bins of the recovered stars in the simulations and large fluctuations from one magnitude bin to the other due to larger blending. In figure 7.14 we plot magnitude vs. completeness for V (bottom panel) and K-bands (top panel) for Field 1 (solid blue line) and Field 2 (dotted red line). The 50% incompleteness level in the V-band sets in for both fields around magnitude 26.3, while in the K-band it is around 50% at $\sim$ 23.3 and $\sim$ 22.3 for Fields 1 and 2 respectively. Note the presence of large variations from bin to

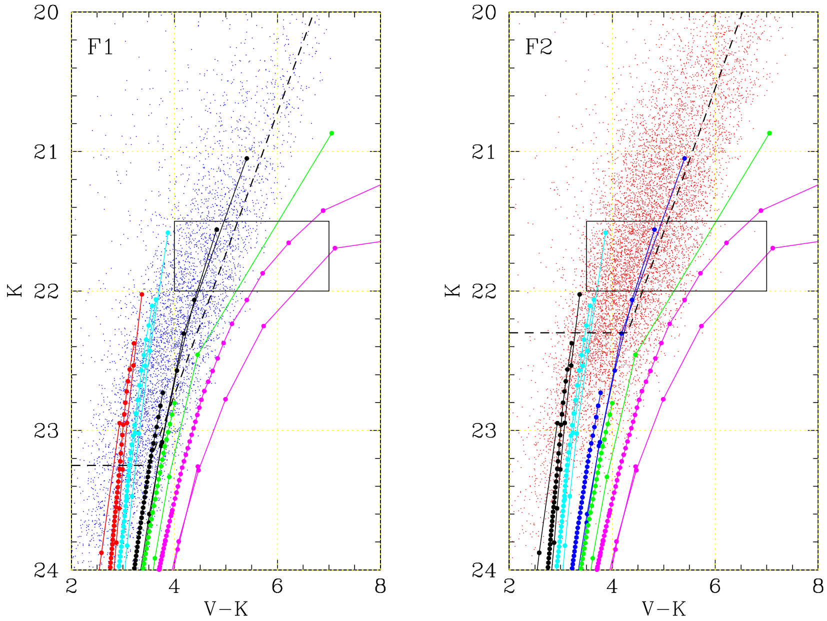

Figure 7.15: Comparison of the 10 Gyr isochrones for 5 different metallicities (Z=0.0001, 0.001, 0.01, 0.02 and 0.04) with the observed NGC 5128 CMDs of Field 1 (left) and 2 (right). The dashed line indicates 50% completeness level showing that the lack of red stars is an observational bias. The number of stars within the box (720 for Field 1 and 1977 for Field 2) is used as a constraint for the simulator.

bin which are mostly due to migration of stars in different bins caused by large photometric error and blending. The effect of blending is particularly evident in the K-band. In the simulations we include the blends of 2 stars (maximum difference between the added and measured star of 0.75), but especially at fainter magnitudes the blending is probably larger and hence inadequately described. This will result in a fewer number of stars in the faintest luminosity bins.

For the simulations of the old RGB stars in the two fields in NGC 5128 we have adopted the stellar evolutionary models calculated by Cassisi & Salaris (1997) and by Bono et al. (1997a, 1997b). The procedure for the interpolation in mass, temperature and metallicity is described above. In the next section we describe the results of the simulations using single age simulator with 10 Gyr. Also, for all the simulations we adopt distance modulus of 27.8 and reddening of $\mathrm{E(B-V)} = 0.1$.

For the young stars the derived reddening is larger ($\mathrm{E(B-V)} = 0.35$; see previous section) probably due to the presence of gas and dust in which these young stars are embedded. These young stars are found in Field 1, but it is plausible to suppose that the higher reddening is confined only to areas very close to the star forming regions. Older populations are typically less reddened. The difference in the adopted value makes very small changes due to low extinction in the K-band ($\mathrm{A_K} = 0.35\mathrm{E(B-V)}$; Cardelli et al. 1989). In $\mathrm{V-K}$ the difference may be of the order of few tenths of magnitude due to higher reddening dependence of this color ($\mathrm{E(V-K)} = 2.75\mathrm{E(B-V)}$; Cardelli et al. 1989).

The comparison of the 10 Gyr isochrones, colored using bolometric corrections described in section 7.2.3, with the observed CMDs is shown in figure 7.15. There is a considerable spread in metallicity on the RGB. However, just how much is very difficult to say due to large photometric errors combined with incompleteness. The lack of very metal-rich stars (if present in the fields) is due to incompleteness in V-band which drives the diagonal 50% incompleteness line in these diagrams.

A large number of stars above the RGB tip is observed in both fields. These AGB stars probably belong to an intermediate-age population. The thermally pulsating AGB (TP-AGB) phase is one of the least understood phases of the stellar evolution (e.g. Wagenhuber & Groenewegen 1998). Its physics is complicated by the fast changes in the stellar structure and the strong mass loss in the form of stellar winds and the current models do not reproduce very well the observed AGB stars in star clusters and galaxies (e.g. Blakeslee et al. 2001, Liu et al. 2002). Also the bolometric corrections for these stars are rather uncertain. Due to all these problems we did not include the intermediate-age in our models. This will lead to discrepancies in the bright end of the simulated and observed luminosity functions. This problem will be addressed in the future. Here we just address very simple questions about the old RGB population.

In order to be able to sample well the complete range of metallicities and not to be too affected by large photometric errors we chose the observed region between magnitudes 21.5 and 22 and redder than 3.5 for Field 2 and 4 for Field 1 as a constrain for the simulations. A redder box is chosen for Field 1 in order not to have contamination from the young population present in the field. These boxes are indicated in figure 7.15 and they contain 720 and 1977 stars in Field 1 and 2, respectively.

We adopted a Salpeter IMF for all the simulations. In this mass range (around 1 $M_{\odot}$) there are indications that the IMF slope is shallower with $\alpha = 1.33$ (in our notation), as found for the bulge of the Milky Way by Zoccali et al. (2000). However, the large photometric errors, the presence of blends, and, most importantly, the very small mass range sampled (from $\sim$0.9 to 1.1 $M_{\odot}$ along the RGB for a 10 Gyr old population), prevent us to explore the dependence on IMF. A few simulations were calculated with an IMF slope of 1.33 and they are essentially identical to the ones calculated with a Salpeter IMF.

7.4.1 Metallicity spread in the old population

The first simulation we show in figure 7.16 has been obtained without correction for photometric errors. Only incompleteness appropriate for Field 2 has been included in order to exclude the stars that are surely not present in our observed CMDs. The simulation was done with 10 Gyr model assuming a flat metallicity distribution ranging from Z=0.0001 to Z=0.04. There are several interesting points in this figure worth mentioning.

First of all it is obvious that in spite of the incompleteness in the most metal-rich part of the RGB, still some very metal-rich stars may be present (by the completeness arguments alone) in our sampled metallicity distribution function (MDF). In the right panel the stars with metallicities above solar are shown in cyan. Out of 9240 stars in the simulated CMD, there are 1990 stars with solar or higher metallicity. About 40% of these stars are in AGB phase which is bluer, hence favoured by incompleteness.

The tip of the RGB, the locus of the helium flash for the low-mass stars, is a clear signature in the old stellar population CMD. Its luminosity depends on the size of the He-core at the He-flash. Its I-band luminosity has been established as a good standard candle for stellar populations more metal-poor than -0.7 dex (Da Costa & Armandroff 1990, Lee et al. 1993). The bolometric magnitude of this feature is only slightly dependent on metallicity (e.g. Salaris et al. 2002, see also left panel of figure 7.16), while the dependence steepens for other photometric bands. In K-band there is a steep raise in the RGB tip magnitude, with more metal-rich stars being brighter, shown in figure 7.13 and in the right panel of figure 7.16.

In the left panel of figure 7.16 we show the simulated HR diagram with color coding according to evolutionary phase. The RGB stars are blue and the AGB stars are magenta. For a single metallicity stellar population the AGB stars lie to the blue of the RGB. However, in a population with a range of metallicities they are mixed with the giants on the RGB. Moreover, the populations with solar or higher metallicities have a very bright AGB population, overlapping in color and luminosity with more metal-poor RGB stars and partially also with younger and more metal-poor intermediate-mass AGB stars that are found above the RGB tip. Deriving the metallicity distribution function of such a mixed population with a strong high-metallicity tail directly by counting the stars on RGB has to be done with great care, because it may lead to an overestimation of red giants in the metallicity bins more metal-poor than the most metal-rich stars (e.g. Harris & Harris 2000).

Can the broad giant branch observed in NGC 5128 be consequence of large photometric errors and thus reproduced with the single metallicity model?

Simulations with a metallicity spread $\Delta Z < 0.001$ present much narrower red giant branch than observed. This is shown in figure 7.17 for Field 1 and 2. The simulations displayed there are for Z=0.01. The discrepancy in the

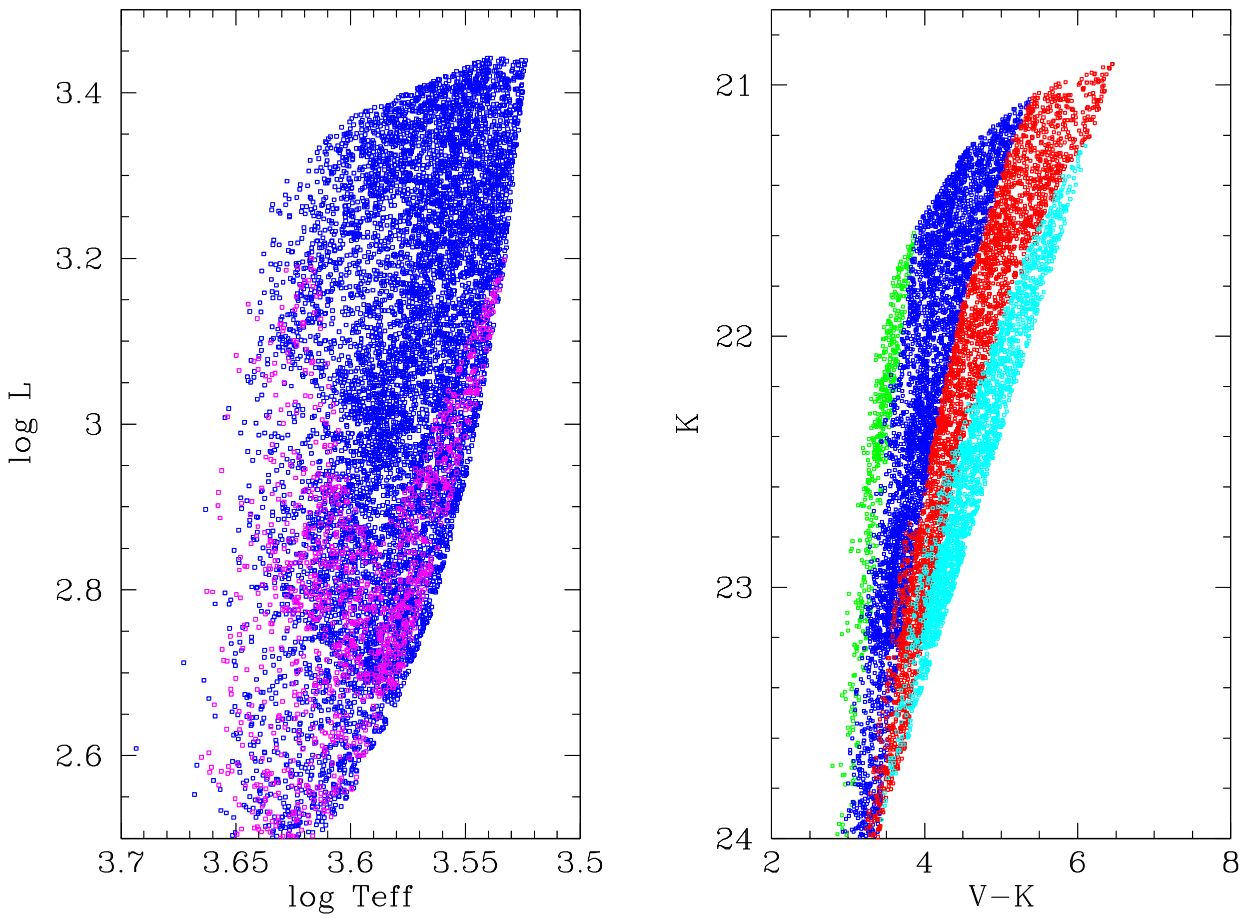

Figure 7.16: Left: simulated HR diagram for a 10 Gyr old population with a flat metallicity distribution ranging from Z=0.0001 to 0.04. Stars are color-coded according to the evolutionary phase: blue are red giants and magenta are AGB stars. In this simulation only the completeness information from the observed CMDs was used (for Field 2), but no photometric errors were applied. Right: VK CMD for the same simulation. Color coding reflects the metallicity distribution: green $0.0001 < Z < 0.001$, blue $0.001 < Z < 0.01$, red $0.01 < Z < 0.02$, cyan $Z > 0.02$.

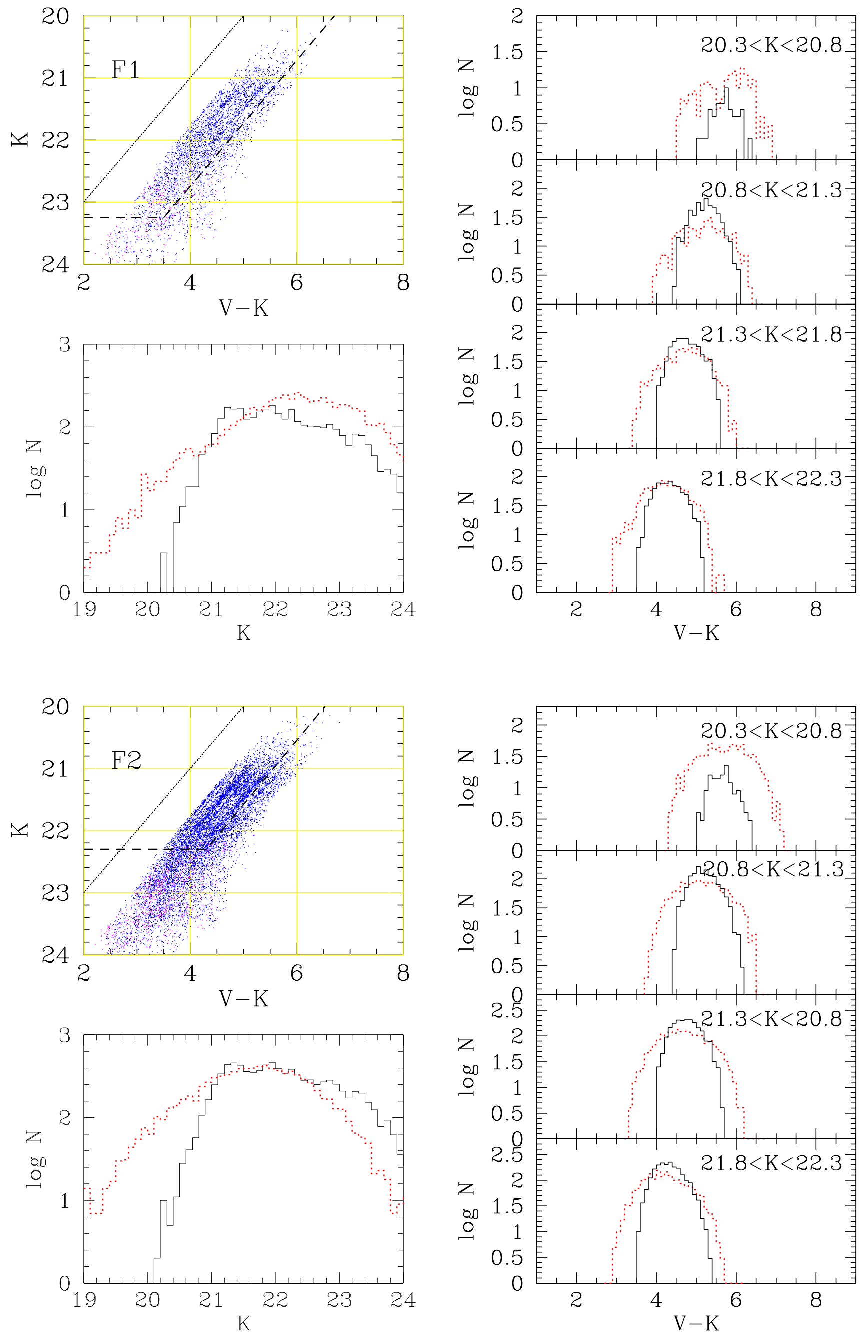

Figure 7.17: In the upper left panel the synthetic CMD for Field 1 (top) and Field 2 (bottom) is shown for a 10 Gyr old population with Z=0.01. Dashed lines indicate 50% completeness limits. Bluewards of the dotted line the stars present in the observed CMD are not used in comparison in the luminosity function (lower left panel) nor in the color distributions on the right. The color distribution of the observed CMD is given as dotted (red) histogram compared in 4 different magnitude bins with the simulated color distribution (solid black histogram). Also in the luminosity function comparisons observations are plotted as dotted red and simulations solid black histograms.

bright bin is expected, because given the single age simulator used we miss younger stars. So, as long as the RGB width is essentially speaking for the metallicity dispersion it is incompatible with a single metallicity.

All the figures which compare the synthetic color-magnitude diagram and the derived color and luminosity distributions with the observations are organized in the same way. The synthetic CMD is shown in the upper left, with the 50% completeness limits indicated with dashed lines. The dotted line on the left side of the RGB indicates the portion of the observed CMD that is not used in the comparison in other panels. Most of the foreground Galactic stars are found bluer than this line as well as young blue and red supergiants present in Field 1 (see fig. 7.12). Still there may be some minor contamination by the young population on the red side of the dotted line. Excluding more stars is dangerous as the metal-poor red giants may be scattered bluewards in the CMD due to photometric errors. The observed (always red dotted histograms) and synthetic (solid black histograms) luminosity functions are compared in the bottom left panel, while the color distribution in four magnitude bins are compared on the right. Magnitude bins were chosen so that in the first one there are mostly stars that are located above the tip of the first ascent giant branch, the second bin samples the tip of the RGB and the two successive bins are along the RGB above the 50% incompleteness level. The shift of the centroid of the color distribution follows the inclination of the RGB.

The color distribution along the RGB is principally driven by the MDF. So, a satisfying MDF must reproduce equally well the simulated and the observed color distributions in all magnitude bins fainter than the tip of the RGB. In figure 7.17 it is obvious that the color spread of the single metallicity simulation is much narrower than the observed spread. The peak of the simulated and the observed color distributions are very similar. In both fields majority of the observed stars have metallicity of Z=0.01 or $[\mathrm{m/H}] = -0.3$ dex where the conversion between the two scales is defined with:

$$[\mathrm{m/H}] = \log \frac{\mathrm{Z}}{\mathrm{Z}_{\odot}} \qquad \text{where} \quad \mathrm{Z}_{\odot} = 0.019 \quad \text{is the solar metallicity.} \tag{7.20}$$

The position of the peaks of the color distributions are also quite similar for the two fields and simulations if the simulations are run with Z=0.008, but it shifts significantly to the red for Z=0.02. The examples of the simulation for Field 1 with Z=0.008 and Field 2 with Z=0.02 are shown in figure 7.18.

The spread in metallicity was probed with simulations including flat metallicity distribution ranging in between the two extremes Z=0.0001 and Z=0.04. Simulations of 10 Gyr old population with flat $0.0001 < \mathrm{Z} < 0.04$ distribution for Field 1 and 2 are shown in figure 7.19. It is obvious that these simulations overproduce the number of stars in the most metal-rich bin (reddest color bin) in both fields. Much better agreement with the observed MDF is obtained with simulations with flat distribution ranging from Z=0.0001 to 0.02 (figure 7.20). Hence stars with abundances greater than solar are not present in our observations. We cannot say if this is because they are really not there or just because we cannot see them (they could be too faint in the V-band, having a huge bolometric correction due to strong blanketing by metals). To probe the limits of the highest metallicity bins it is necessary to obtain much deeper V-band images and sample well the red portion of the CMD.

What about the low metallicity tail of the distribution? If the lowest metallicity bin is left out, simulating only the stars between Z=0.001 and Z=0.02, the results are essentially the same for Field 1, but in Field 2 the number of simulated blue (metal-poor) stars is lower than observed in all three magnitude bins along the RGB (figure 7.21). However, here a greater care has to be put and a better investigation of the contribution of blends that scatter preferentially bluewards due to skewed photometric errors (they are larger in the red parts) is warranted.

In any case, we can conclude that the MDF of the halo of NGC 5128 is very large ranging from Z=0.001 for Field 1 and Z=0.0001 for Field 2 up to solar metallicities. Field 2 has probably more metal-rich stars because the best fitting simulation for that field with MDF $0.0001 < \mathrm{Z} < 0.02$ has too few metal-rich stars. In Field 1 the same simulation reproduces very well the metal-rich end.

While it was possible to find a relatively good fit between the color distributions of the observations and simulations, the luminosity function is not reproduced so well. The larger number of stars in magnitude bins above the tip of the RGB is due to foreground contamination (less than 100 stars according to Besançon simulations), presence of the young population in Field 1 and intermediate-age AGB stars with possible contribution of old and very metal-rich bright AGB stars. Among them 528 and 1230 long period variables were detected in Field 1 and 2, respectively. These variables are in a TP-AGB phase. As discussed above, TP-AGB phase is not well understood.

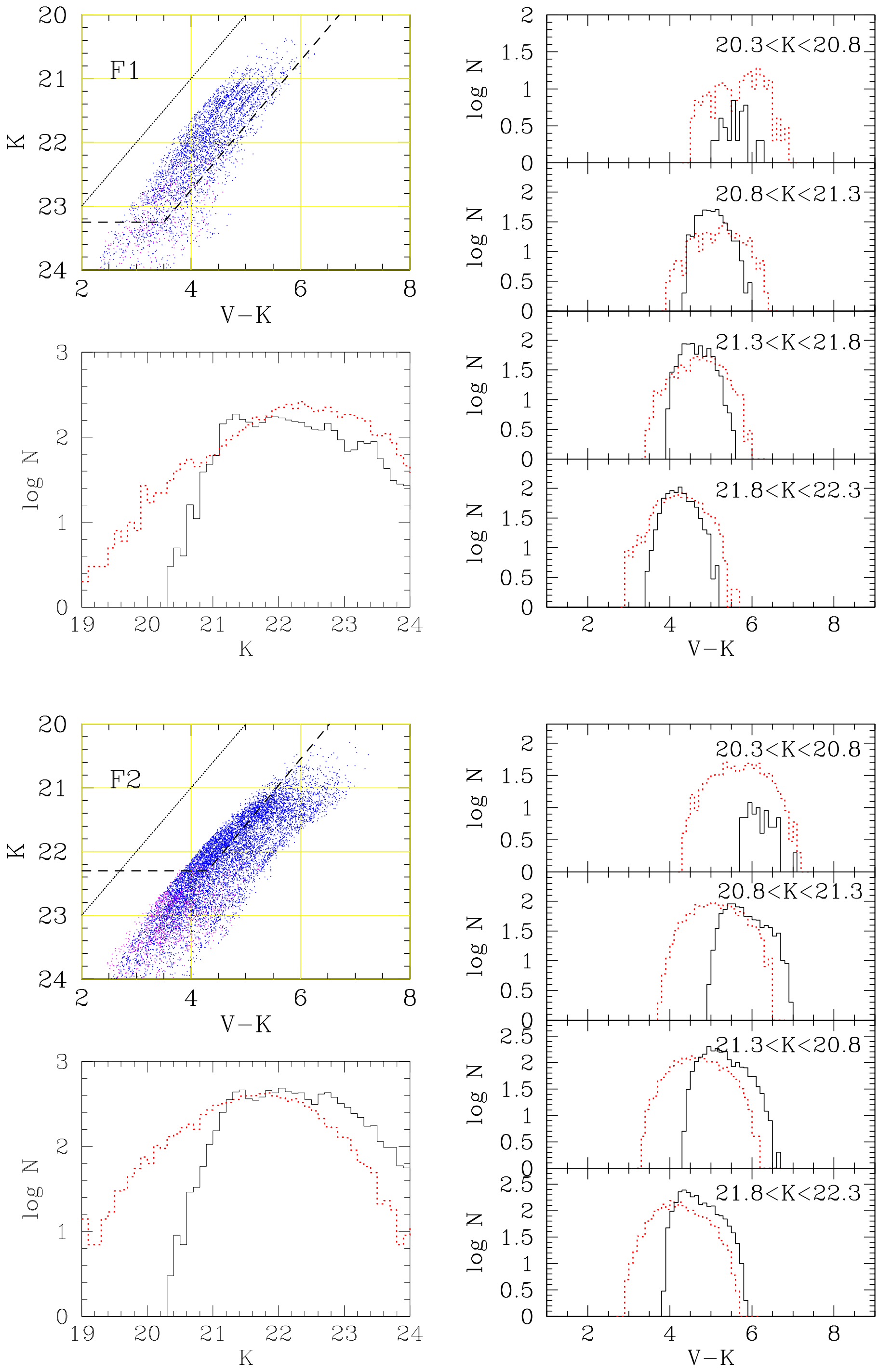

Figure 7.18: Comparison of the simulation of a 10 Gyr old population with Z=0.008 for Field 1 (top) and Z=0.02 for Field 2 (bottom) with observations. A detailed description of the different panels is given in the text and in figure 7.17.

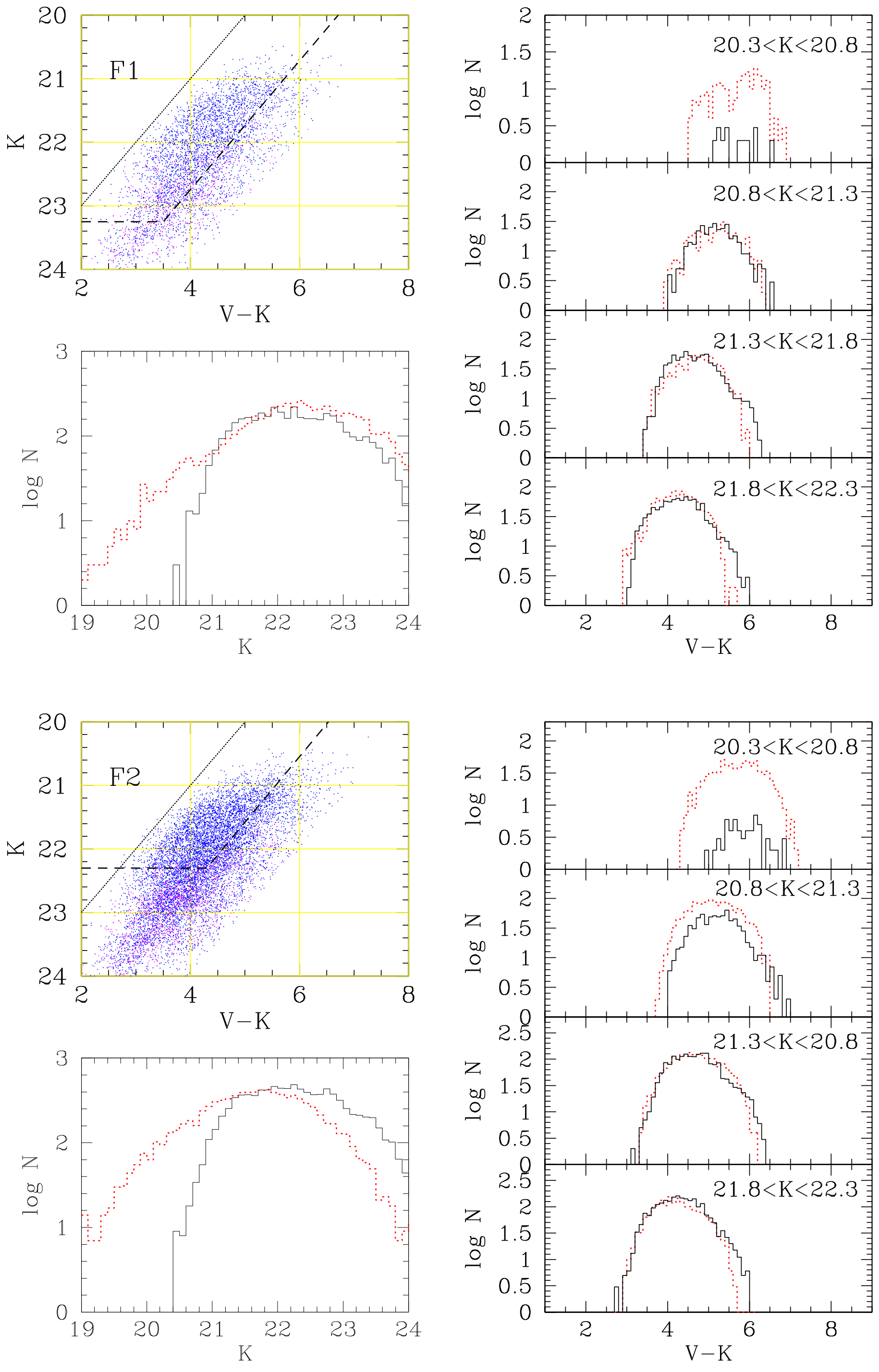

Figure 7.19: Comparison of the simulations of a 10 Gyr old population with $0.0001 < Z < 0.04$ for Field 1 (top) and 2 (bottom) with observations. A detailed description of the different panels is given in the text and in figure 7.17.

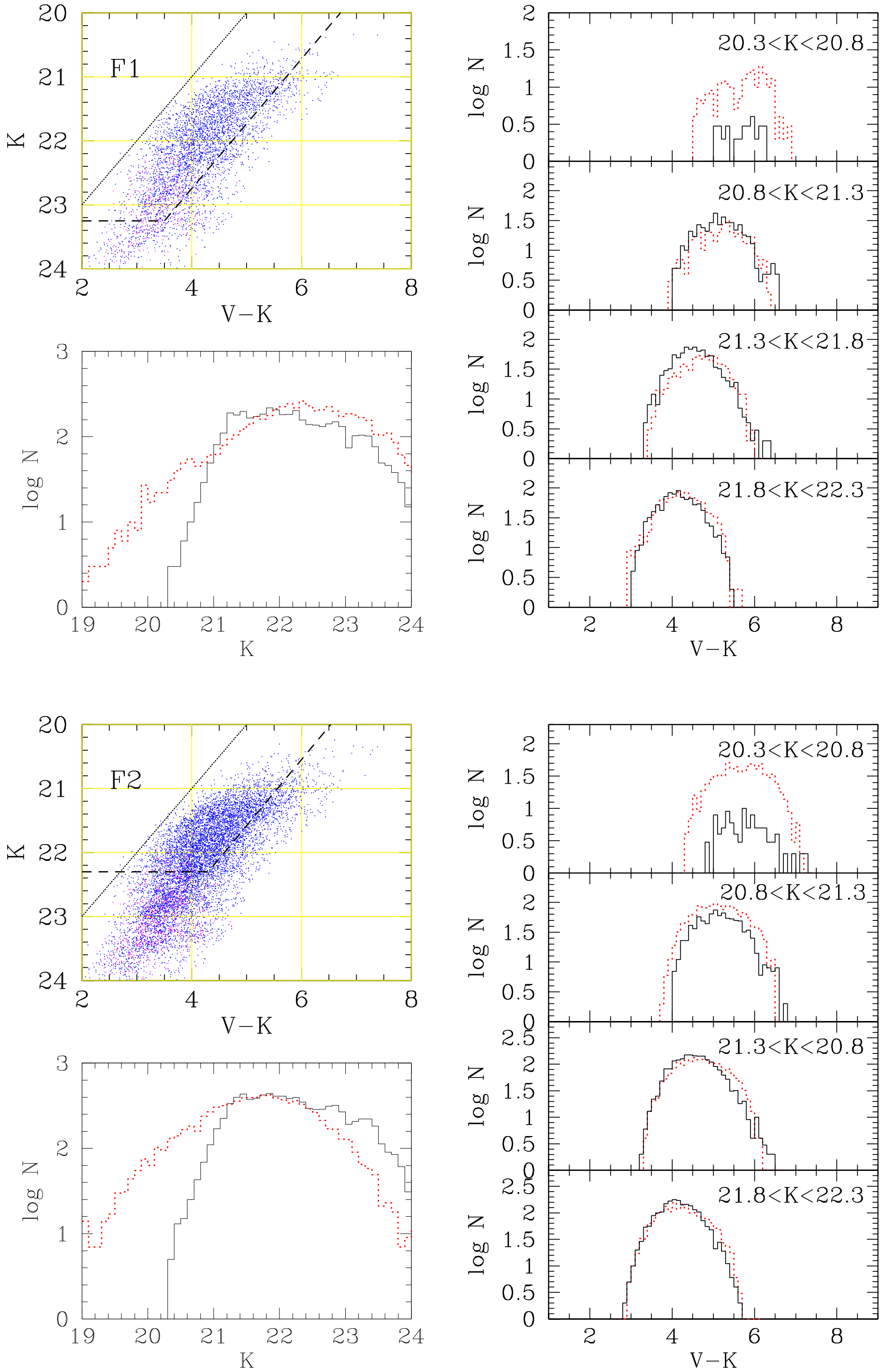

Figure 7.20: Comparison of the simulations of a 10 Gyr old population with $0.0001 < Z < 0.02$ for Field 1 (top) and 2 (bottom) with observations. A detailed description of the different panels is given in the text and in figure 7.17.

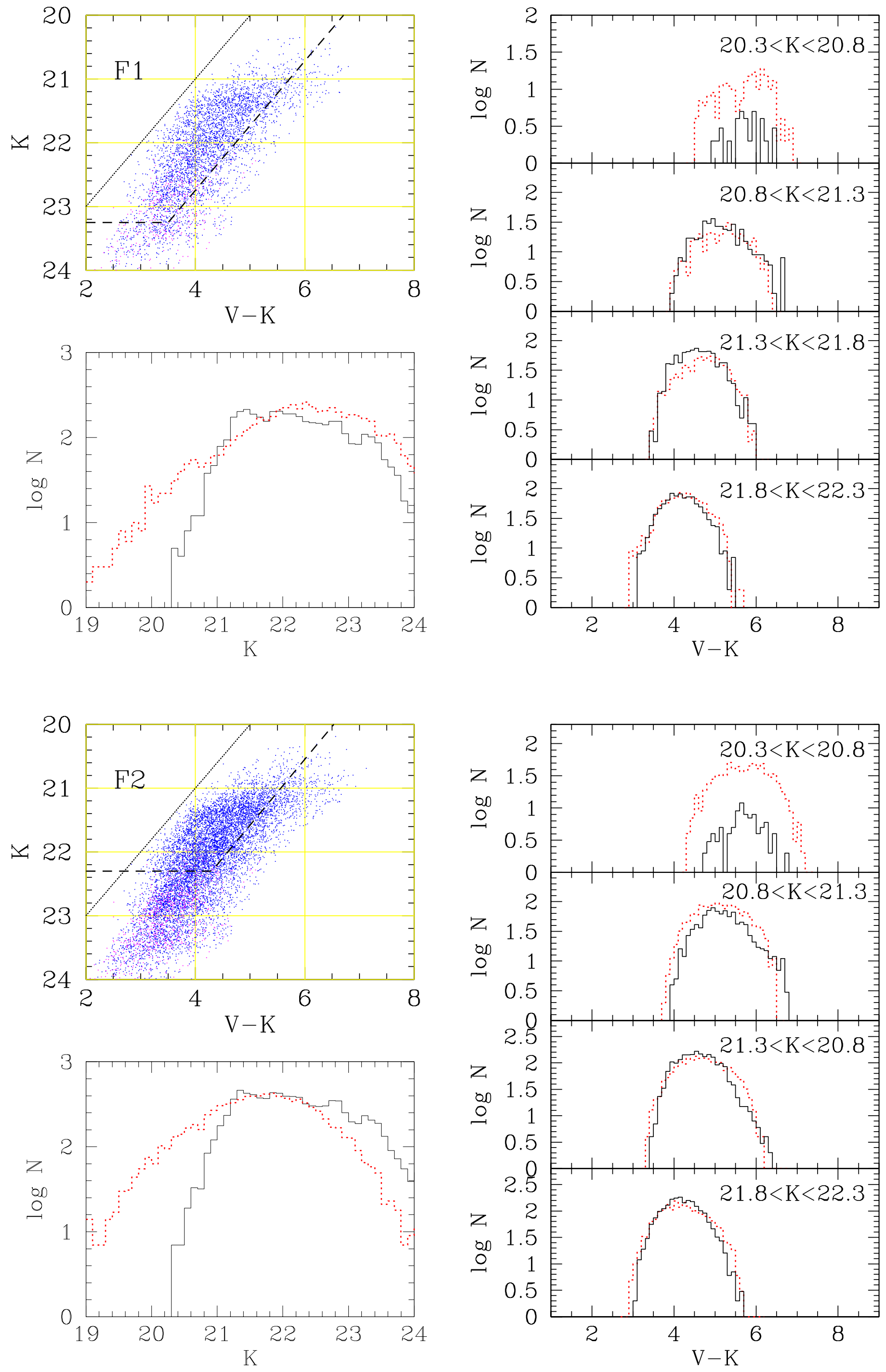

Figure 7.21: Comparison of the simulations of a 10 Gyr old population with $0.001 < Z < 0.02$ for Field 1 (top) and 2 (bottom) with observations. A detailed description of the different panels is given in the text and in figure 7.17.

Our simulations did not include the stellar evolution beyond the first thermal pulse, hence leading to discrepancies in the bright end of the simulated and observed luminosity function.

More disturbing is disagreement between the luminosity functions along the RGB of Field 1. Essentially in all the simulations for that field with respect to the observations there is an excess of stars around magnitude 21 (where the tip of the RGB is located) and lack of stars for lower magnitudes, which are still well above the photometric incompleteness. Whether this is due to a presence of an age spread in this field needs to be investigated with simulations that interpolate the models both in metallicity and in age. Fainter than 50% completeness level luminosity bins may have fewer stars because of an inadequate treatment of photometric errors, incompleteness and blends.

For Field 2 the observed and simulated red giant branch luminosity functions are in good agreement above the 50% incompleteness limit (K$\sim$22.3) for the models that give acceptable color distribution (e.g. figure 7.20). Below that magnitude there is an excess of simulated stars probably due to underestimated effect of blending in our simulations. In order to produce adequate number of stars in the selected box, out of which some might be blends of few fainter ones, more stars had to be extracted in the luminosity bin of the box, hence overpopulating the RGB at fainter levels.

7.4.2 Closed box model

The goal of deriving the metallicity distribution of the old stars in NGC 5128 is to put constraints on the formation and evolutionary history of the galaxy. Theoretical models and observations of giant elliptical galaxies suggest several possibilities for their formation and evolution. These include (i) an early formation in-situ with a following passive evolution; (ii) an early monolithic collapse of a gas cloud or an early hierarchical merging of gas clouds where dissipation plays a fundamental role (e.g. Larson 1974, Arimoto & Yoshii 1987, Matteucci & Tornambè 1987, Forbes et al. 1997, Cole et al. 2000) implying an early formation of the galaxy that however can still form several populations and produce a considerable metallicity spread, (iii) formation of elliptical galaxies in major mergers of previously formed large disk galaxies with a possible second population forming in the accompanying starburst (e.g. Ashman & Zepf 1992, Schweizer 1996) and (iv) later minor mergers and accretions of stellar fragments (e.g. Côté et al. 1998, 2000).

While it is obvious that Cen A has undergone at least one recent merger episode and hence did not evolve in isolation, it is instructive to see what the RGB would look like for a closed box model's metallicity distribution. The closed box distribution does not really refer to the age of the stars, but it rather implies a metallicity distribution of a system which self enriched with no communication to the outside.

The derived MDF has a high number of stars with high metal abundances, which must have formed out of a gas enriched by metals formed in a previous generation of lower metallicity stars. However, it is possible that additional gas was accreted through the infall of gas clouds in the early stages of the galaxy formation, suppressing the dilution effect and producing a smaller relative ratio of low to high metallicity stars with respect to closed box model.

Since it is reasonable to consider that majority of the observed stars (at least in Field 2) are from the giant elliptical and not from an accreted satellite it is reasonable to ask whether the observed MDF reflects the formation within a closed box, or by infall.

As a first step in modeling we simulated the closed box model of chemical evolution with assumed initial and final gas abundance (Z_1 and Z_2) and effective nucleosynthetic yield y. This model leads to a simple analytic form for the MDF:

$$\frac{dN}{dZ} \sim \exp^{-\frac{Z-Z_1}{y}} \tag{7.21}$$

In the first model we assumed a yield of y=0.006 and the lowest possible initial abundance for the gas (Z=0.0001 for our simulator). The high abundance limit was set to Z=0.04. The comparison of the simulations and observations for Field 1 and 2 are displayed in figure 7.22. The closed box model produces too many metal-poor stars and too few metal-rich stars. This means that some accretion of more metal-rich gas must have occured. Also possibly the nucleosynthetic yields are higher.

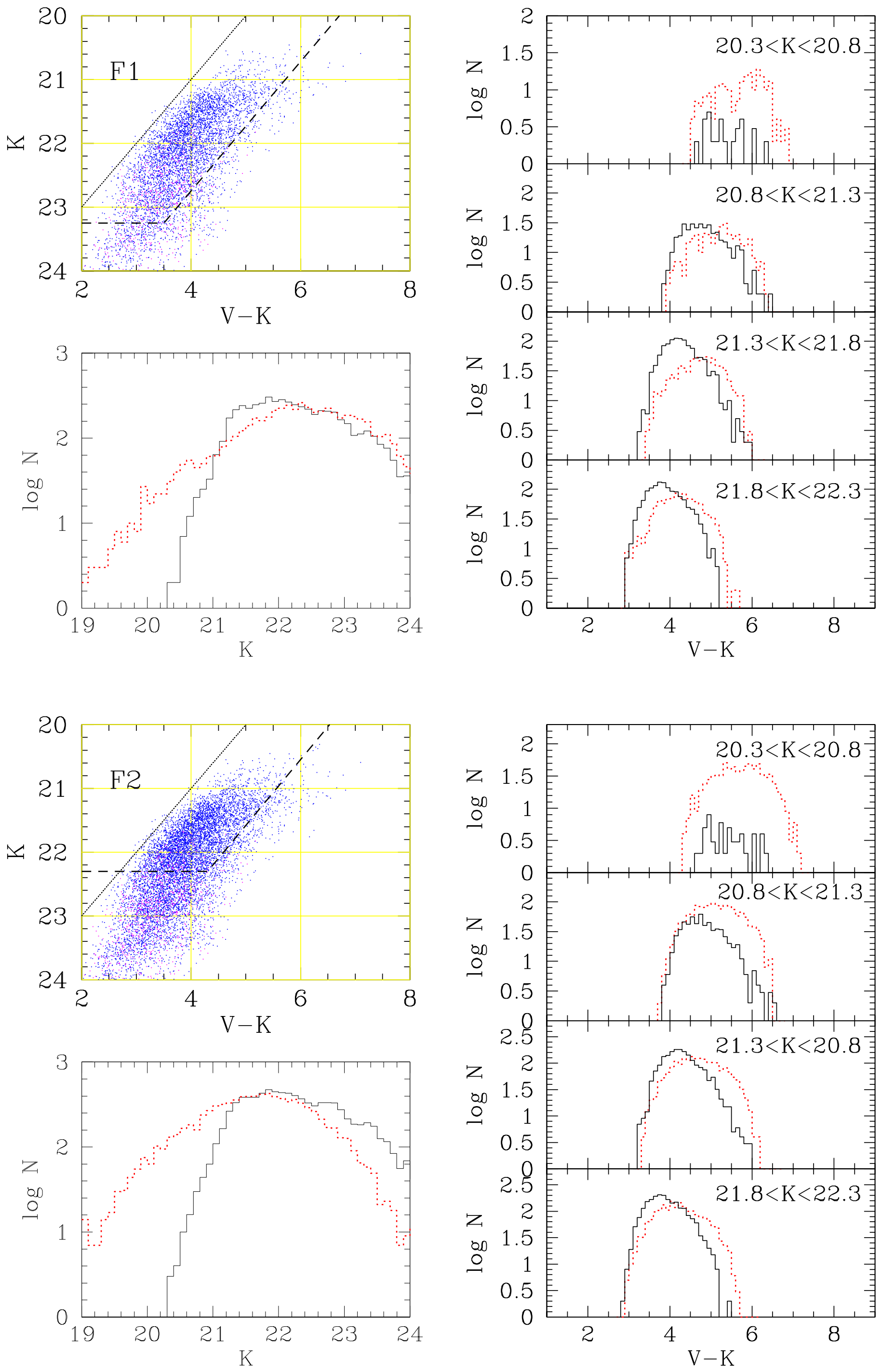

Figure 7.22: Comparison of the simulations of a closed box model with yield $y = 0.006$, initial abundance Z=0.0001 and final abundance Z=0.04, with observations. A detailed description of the different panels is given in the text and in figure 7.17.

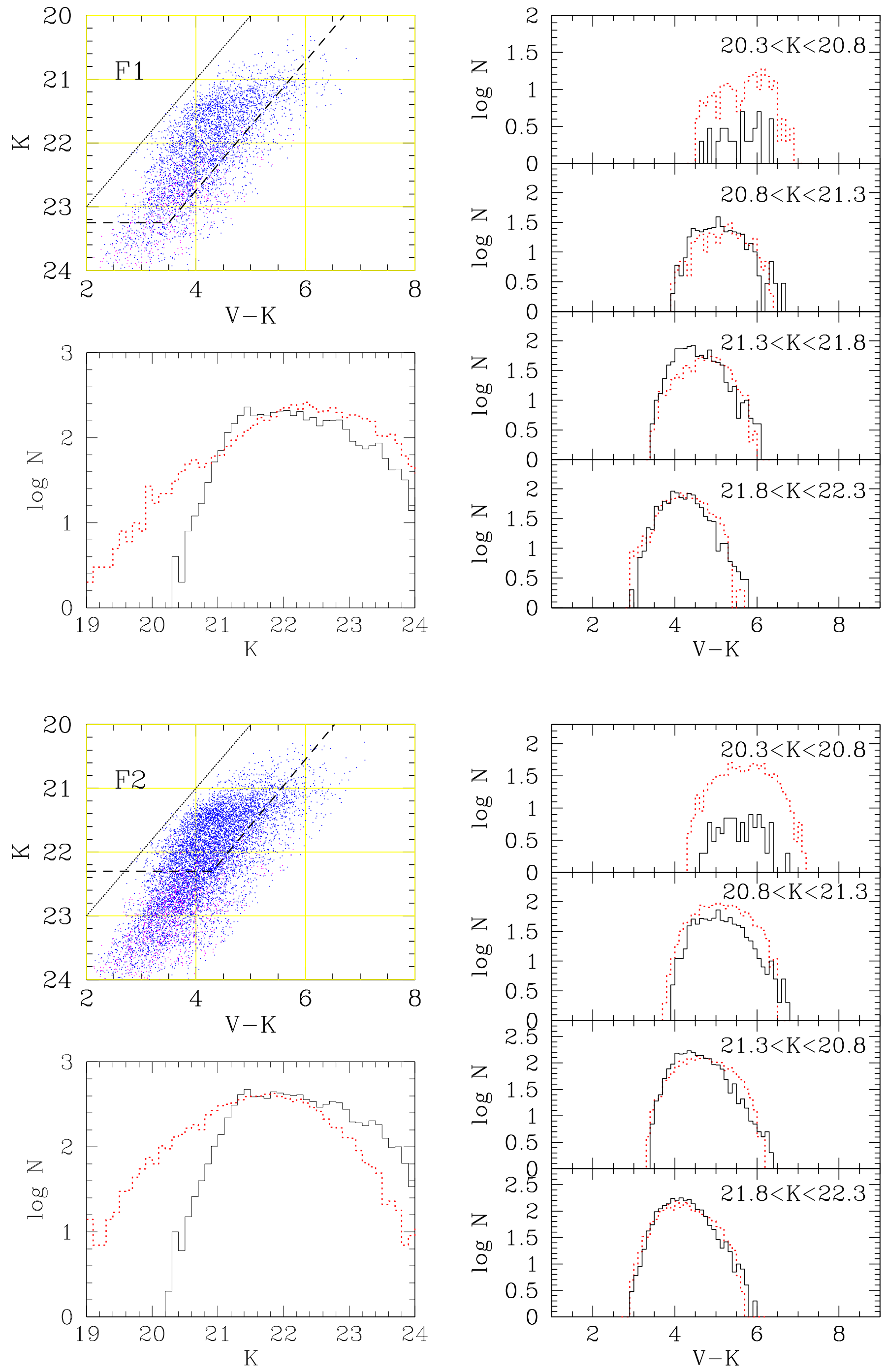

Figure 7.23: Comparison of the simulations of a closed box model with yield $y = 0.015$, initial abundance Z=0.001 and final abundance Z=0.04, with observations. A detailed description of the different panels is given in the text and in figure 7.17.

A second set of models with high yield ($y = 0.015$) and starting with enriched gas of Z=0.001, which corresponds to the lowest metallicity tail of the MDF established in the previous section, is displayed in figure 7.23. Although now the agreement at the metal-rich end is better there are still too many metal-poor stars.

In conclusion, closed box model overproduces metal-poor stars and does not appear to give a good fit to the observed MDF, at this first inspection. More sophisticated models (e.g. including gas accretion) need to be tested in future simulations.

7.5 Discussion and summary of the results

We have made synthetic CMDs for the stars in two halo fields of NGC 5128. The first, northeastern field (Field 1), which presents the recent star formation was modeled in UV and in VK plane and the second halo field (Field 2) was only studied in the VK plane.

In UV models with two different metallicities, Z=0.004 and Z=0.008, were created. However, the degeneracy between metallicity, reddening and distance and most importantly high contamination by the foreground Galactic stars in the red part of the CMD did not allow to determine the metallicity. The stellar evolution theory gives clear predictions for the number and luminosity function of young MS and PMS stars allowing us to obtain robust results from the comparison of the observations with models. The following results were obtained from the simulations of young stellar population in Field 1:

1. The comparison of the isochrones and the data has to be done with great care, using the correct filter transmission curves to compute a consistent set of bolometric corrections. The U-band is known to be the most difficult to reproduce due to the presence of the atmospheric cut-off, to the presence of the Balmer break within that band and to strong blanketing by metals.

2. The new reddening estimated by matching the locus of the observed MS in $\mathrm{U-V}$ plane with the models, using the corrected bolometric corrections for U passband and assuming the Galactic extinction law (Cardelli et al. 1989) is $\mathrm{E(B-V)} = 0.35$, significantly larger than previously obtained $\mathrm{E(B-V)} = 0.15$ (Rejkuba et al. 2001b, Chapter 4). Foreground reddening accounts for $\mathrm{E(B-V)} = 0.11$ (Schlegel et al. 1998).

3. The star formation duration was explored. It was found that the simulations that best fit the observations have either still active star formation or at most it has stopped some 2 Myr ago. Moreover, the star formation seems to have been lasting for at least 100 Myr, this lower limit to its duration being set by the maximum look-back time allowed by the shallower U-band photometry.

4. The MS luminosity function and the total number of stars in the blue plume constrain the IMF slope. It cannot be steeper than about 2.6, on a scale where Salpeter slope is $\alpha = 2.35$.

5. Total mass formed in stars over the last 100 Myr in the mass range from 0.6 to 100 Myr is $\sim 1 \times 10^6$ $\mathrm{M}_\odot$. It depends slightly on the IMF and ranges from 0.5 to 1.5×10^6 $\mathrm{M}_\odot$, for IMF slopes from 2 to 2.6.

6. The mean SFR is 0.004, 0.007 and 0.013 $\mathrm{M}_\odot \mathrm{yr}^{-1}$, for the four IMF slopes 2, 2.35 and 2.6, respectively. It is approximately one order of magnitude lower than the typical SFR quoted for the solar neighbourhood (Timmes et al. 1995) and is on the low side of the SFRs derived via theoretical simulations for dwarf irregular galaxies in the Local Group (e.g. Marconi et al. 1995, Tolstoy 1996, Gallart et al. 1996a). The mean SFR implied by the models that fit the data well are very close to each other, with small dependence on the IMF slope, but not much on the duration of the SF. Hence it is a robust result of our modeling.

7. On a more speculative side, it is possible to estimate the maximum duration of the future star formation. The fuel for this recent star formation is provided by the large HI gas cloud in the vicinity of the field (Schiminovich et al. 1994). Assuming the constant SFR and a 100% efficiency in converting gas to stars, the estimated gas depletion timescale is ~100 Myr. Adding the available molecular gas (Charmandaris et al. 2000 this timescale rises to ~230 Myr.

The simulations of the VK CMDs are more limited and a more detailed modeling is necessary in the future. For now, we neglected the contribution of the intermediate-age population, visible as the extended giant branch at luminosities brighter than the RGB tip. This results in disagreement in the bright end of the observed and simulated luminosity functions.

As the RGB color is mainly driven by the metallicity, we assumed a single age population 10 Gyr old to address the metallicity spread on the RGB. A younger, intermediate-age, RGB stars have bluer colors at a given metallicity. Hence, neglecting their contribution would result in the MDF that has more metal-poor stars than really present.

Furthermore, the uncertainties of the theoretical RGB models extensively discussed in a recent review by Salaris et al. (2002), which affect mostly the temperature of the RGB through the treatment of the low temperature opacities, convection, envelope equation of state and surface boundary conditions and even more importantly the adopted bolometric corrections, present limits to our results. We have used Cassisi models and calculated bolometric corrections using Castelli et al. (1997) ATLAS9 atmosphere models supplemented with empirically determined bolometric corrections for metal-rich giants by Montegriffo et al. (1998). The adopted models converted to the VK plane with these bolometric corrections reproduce well the location of the near-solar metallicity globular cluster NGC 6528.

Bearing these limitations in mind, the results of our simulations of the old RGB population in the two fields are the following:

- The observations are not consistent with a single metallicity broadened by photometric errors.
- There is a wide spread in metallicity ranging from Z=0.001 to Z=0.02 in Field 1 and from Z=0.0001 to Z=0.02 in Field 2.
- The observed mean metallicity of Field 1 is between Z=0.008 and Z=0.01, corresponding to [M/H] ~ -0.3 dex. The mean metallicity of Field 2 is also around Z=0.01, but it may be slightly higher, as there are more metal-rich stars in that field. Unfortunately, the V-band incompleteness, unables us to explore the reddest and thus most metal-rich end of the MDF.
- Since it is reasonable to consider that the majority of the observed stars (at least in Field 2) are from the giant elliptical and not from an accreted satellite, it is reasonable to ask whether the observed MDF reflects the formation within a closed box. In a first inspection, the simple closed box model is inconsistent with the data, overpopulating the metal-poor tail of the MDF.
- No single age old model can reproduce the luminosity function of Field 1, even neglecting the bright AGB stars. On the contrary, the RGB luminosity function of Field 2 is better fitted with a single age model with a large range of metallicities. This difference could be due to the presence of a large number of stars in Field 1 in the diffuse stellar shell which was presumably accreted during the last merging episode in this galaxy. Further modeling including the age spread is necessary to confirm this result.

Chapter 8

Conclusions and Future Directions

8.1 Conclusions and summary of the results

We have studied stellar populations in two nearby galaxies representative of two Hubble sequence extrema: WLM, a dwarf irregular galaxy, situated at the edge of the Local Group; and NGC 5128, the nearest giant elliptical and a recent merger. From the analysis of the color magnitude diagrams (CMDs) and the comparison of the present stellar content and simulations of star formation histories (through the construction of synthetic color-magnitude diagrams) the basic galaxy parameters are measured: distance, reddening, ages and metallicities of the stellar populations.

Using deep STIS CL and LP-band images taken with the Hubble Space Telescope, we have identified a horizontal branch population in WLM. An empirical calibration of the STIS non-standard photometric bands to the ground based Johnson-Cousins VI system has been derived. From the VI CMD we measured the distance to WLM obtaining a distance modulus of $(m-M)_0 = 24.95 \pm 0.13$ (D $= 978 \pm 60$) using the V-magnitude of the horizontal branch, and adopting $E(V-I) = 0.03$. The horizontal branch, extending blueward from the red giant clump, is an unambiguous signature of an old population. The implications of the presence of old horizontal branch stars in this dwarf galaxy are twofold. Firstly, WLM has formed stars at high redshift, implying that the star formation in this galaxy was not inhibited at early times by photoionization by UV sources such as QSOs and AGNs. This puts constraints to dwarf galaxy formation excluding scenarios where dwarf galaxies form recently (e.g. Babul & Rees 1992). Secondly, the old population found in the WLM halo is similar to that of the old and metal-poor halos of the spiral galaxies in the Local Group. Having remained isolated throughout its lifetime, WLM can be considered as a good example of a surviving protogalactic fragment, related to those that built up the Milky Way halo.

Can it be also considered a representative building block of a giant elliptical galaxy's halo? In order to answer this question it was necessary to study the stellar populations of the nearest giant elliptical NGC 5128 in detail. First, the results of our extensive photometric analysis and comparisons with simulations are presented.

We have resolved stars and detected 71 new globular clusters in NGC 5128 using the VLT with FORS1 and ISAAC. Very deep U and V-band globular cluster luminosity functions, spanning $-10.1 < M_V < -4.9$ and $-9.3 < M_U < -3.3$, have been constructed. These are the deepest globular cluster luminosity functions in an elliptical galaxy determined so far. Using the Kolmogorov-Smirnov statistical tests we have demonstrated the similarity of the globular cluster luminosity function belonging to the giant elliptical NGC 5128 and the spiral galaxies M31 and the MW. Their mutual similarity suggests that GCLF is unique and independent of Hubble type of its host galaxy. The $(U-V)_0$ color distribution of globular cluster system is bimodal with the metal-rich peak at [Fe/H]$= -0.6$ dex and the metal-poor peak at [Fe/H]$= -1.7$ dex.

Optical UV and optical-near-IR VK CMDs were used to investigate the stellar populations in two different halo fields (in the halo and in the north-eastern diffuse shell). In the outer, shell field, at ~ 14 kpc from the center of the galaxy, star formation is observed. Comparison with the synthetic CMDs suggests that this star formation started at least 100 Myr ago and is still on-going or at most has stopped some 2 Myr ago. The absence of gaps along the main sequence indicates that most probably no major fluctuations in the star formation rate have occurred over this time interval.

The fuel for the star formation is provided by the large HI gas cloud in the vicinity of the field (Schiminovich et al. 1994), most probably acquired during the last merger episode. While most of the gas from the accreted gas-rich galaxy settled in the central part of NGC 5128, some 2.1×10^7 $M_\odot$ of neutral hydrogen remains close to our field in the northeastern halo of the galaxy (Schiminovich et al. 1994). With it some 1.7×10^7 $M_\odot$ of H_2 molecular gas has been associated (Charmandaris et al. 2000). This gas fuels low level star formation in the halo (SFR$\sim$ 0.007 $M_\odot$ yr^{-1}). The most remarkable feature about this star formation is, however, its alignment with the radio and X-ray structure of the host galaxy.

Additional UV photometry was obtained with Magellan I telescope at Las Campanas Observatory in a field along the direction of the X-ray jet, at $\sim$ 8 kpc from the center of the galaxy, in order to study the alignment of the recently formed stars. Hot ionized gas is found to be associated with young stars and HII regions extending more than 10 kpc along the jet direction in the north-eastern halo of the galaxy. A vertical north-east alignment along the edge of the HI cloud is also present in the outer field. The highly collimated star formation present in the north-eastern halo of the galaxy, suggest the interaction of the jet with the gas clouds deposited during the last accretion event as the preferred triggering mechanism. The triggering of the star formation in the dense clouds in the halo of the galaxy by the jet supports the alignment effect observed in high redshift radio galaxies. It also suggests that radio galaxies should have higher than normal star formation rates.

The underlying stellar population of the halo of the giant elliptical is predominantly old with a broad metallicity distribution, and a peak around [M/H] = −0.3 dex. Using more than 14 hours of ISAAC observations very deep K-band luminosity functions were constructed for two halo fields. In the outer halo field a very clear tip of the red giant branch is detected. This is a sign of a dominant old stellar population. Using the empirical calibration of the K-band RGB tip magnitude, assuming a mean metallicity of [M/H] = −0.3 dex and reddening of $E(B-V) = 0.11$, we have derived distance modulus of NGC 5128 of $(m-M)_0 = 27.97 \pm 0.10$. The second, inner halo field, presents much wider spread in metallicity combined with larger number of blends. Thus its RGB tip feature is not as sharp.

The presence of an extended giant branch reaching $M_{\rm bol} = -5$ mag suggests the existence of a significant intermediate-age AGB population in the halo of this galaxy. There are 2286 stars in the outer halo field (Field 1) and 3973 stars in the inner halo field (Field 2). The large majority of these sources belong to the AGB population in NGC 5128. Subtracting the foreground Galactic stars and probable blends, 26% and 62% of the remaining AGB stars are variable in Fields 1 and 2, respectively.

The first variable star catalogue in a giant elliptical galaxy is presented. We have detected 528 and 1230 red variables in Field 1 and 2, respectively. Their amplitudes, mean magnitude distribution and periods indicate that the majority belongs to the class of long period variables with semiregular and Mira variables.

The long period ($P \geq 200$ d) large amplitude ($\Delta K > 0.5$ mag) Mira variables follow the same period-luminosity relation as Miras in the LMC and the Galactic bulge. This is the first Mira period-luminosity relation outside the Local Group. It was used to determine the distance of NGC 5128. We derive a distance modulus of 28.01 ± 0.07, adopting the LMC distance modulus of 18.50. The straight mean of RGB tip and LPV distances yields distance modulus to NGC 5128 of 27.99 ± 0.12 ($D = 3.96 \pm 0.22$ Mpc).

Some of the long period variables (LPVs) belong to the old population associated with the metal-rich RGB stars, but the large fraction of non-variable AGB stars and the maximum brightness achieved by them is a sign of an intermediate-age population in the halo of NGC 5128. The intermediate-age population is stronger in the outer field, in which a diffuse stellar shell is detected, presumably containing stars from an accreted satellite.

In conclusion, the stellar populations of NGC 5128 present a mix of ages and metallicities. There is a conspicuous intermediate-age population present in at least one of its fields. This field contains also younger generation of stars that have been forming over the last 100 Myr. Obviously this giant elliptical did not evolve in isolation. The stars and gas it has accreted in the last merger event mostly settled in the center of the galaxy, where a prominent dust lane is observed. Some of the gas has remained in the halo. The interaction of the jet from the active nucleus of the galaxy has triggered a low level of star formation strongly aligned along its direction. The total quantity of the gas in the halo and in the center of NGC 5128 is more reminiscent of a small gas rich spiral galaxy and is higher than the gas content of a typical dwarf irregular like WLM. The stellar content of the halo has been perturbed and there are signs of the recent star formation, but still the bulk of the halo must have formed in the early epochs from the gas that has been rapidly enriched to at least solar metallicities. The mean metallicity of halo stars is at least $[M/H] = -0.3$ dex, much higher than the mean metallicity of the Milky Way halo. This implies that while hierarchical accretion of small satellite galaxies has certainly contributed to the low metallicity tail of the halo population of NGC 5128, its main stellar content could not have been built by accretion of low metallicity protogalactic fragments like WLM.

8.2 Future directions

Strong scientific interest to study WLM and NGC 5128 presented in the introduction of this dissertation is confirmed by the number of most recent publications concerning the two galaxies. Still there is a lot more to learn about isolated dwarf galaxies like WLM and the nearest giant elliptical galaxy NGC 5128. Several new instruments are starting their operations or are soon coming on line at large ground based telescopes (e.g. FLAMES, VIMOS and NAOS-CONICA at VLT, MAGIC at Magellan) and at HST (Advanced Camera for Surveys). They offer possibilities for further study of stellar populations in these two galaxies as well in other nearby galaxies. Several projects aiming at better understanding of the stellar and globular cluster populations of dwarf and giant elliptical galaxies are described shortly.

8.2.1 Dwarf galaxies

The detection of the horizontal branch in WLM, as described in chapter 2, suggests the presence of RR Lyr variables in this galaxy. Using the best seeing observations available through the service mode observing at ESO it is possible to reach the horizontal branch magnitude with 8-m class telescopes and hence measure amplitudes, periods, mean magnitudes and frequency of these variables. Comparing these properties with those of RR Lyrae in the Milky Way globular clusters, Large and Small Magellanic Clouds and Fornax dwarf galaxy, the age of the old halo in WLM can be better determined, constraining the formation epoch of dwarf irregular galaxies. Also, the comparison between the properties of these oldest stars in dwarfs and giant spiral galaxies, offers important constraints to the theory of the formation of halos in giant galaxies through the accretion of many smaller dwarf systems (e.g. Searle & Zinn 1978).

Another way of probing the halos of dwarf galaxies is spectroscopically, through measurements of the kinematics of halo giant stars. The halo of the Milky Way and other large spirals contains old, metal-poor stars that are kinematically hot (i.e. with large velocity dispersion and negligible rotation). The growing evidence indicates the presence of old and metal-poor halos in dwarf irregular galaxies (e.g. Minniti & Zijlstra 1996, Rejkuba et al. 2000 in WLM, Minniti et al. 1999 in NGC 1309, Aparicio et al. 2000 in DDO187). However, the kinematics of the halo stars in dwarf irregular galaxies has yet to be measured. The finding of a halo in dwarf irregular galaxy argues for a generic mode of galaxy formation that requires a halo in the presence of a disk, regardless of galaxy size. This implies that formation mechanisms are similar along the spiral Hubble sequence, regardless of disk type or luminosity.

In recent years it became evident that the Local Group dwarf spheroidal galaxies show a considerable diversity of star formation histories (Mateo 1998). There is evidence that proximity to the Milky Way influenced the star formation histories of its companions, like Ursa Minor or Draco, that either lack intermediate-age populations or they make up only a minor component. On the contrary, the more distant systems, such as Fornax or Leo I have much more conspicuous intermediate-age populations.

To improve the understanding of the diversity of star formation histories seen in the Local Group dSphs, it is necessary to study dwarf galaxies in different environments. The Centaurus Group is the second nearest galaxy aggregate to our own at a distance of ~ 4 Mpc. This richest and densest galaxy aggregate in our neighbourhood is the home of many giant galaxies that show signs of strong interaction, a large number of dwarf irregular and a significant number of dwarf elliptical galaxies (Jerjen et al. 2000). It thus provides quite a different environment to that of the Local Group.

With the VLT+FORS imager it is possible to resolve individual stars at the distance of Centaurus Group (~ 4 Mpc) and thus to construct deep color-magnitude diagrams of the giant stars in dwarf galaxies in this nearby dense environment (e.g. Jerjen & Rejkuba 2001). Comparing the synthetic and observed color-magnitude diagrams will allow star formation histories to be derived. The comparison of the stellar populations and star formation histories of dwarf galaxies in Centaurus and Local Group will set constraints on influences of environment on evolution of the dwarf spheroidal galaxies.

8.2.2 The giant elliptical galaxy NGC 5128

The vicinity of the giant elliptical galaxy NGC 5128 provides a unique testing ground for stellar population models and for theories of giant galaxy formation. It is also the only giant elliptical galaxy in which a direct comparison between the age and metallicity distributions of stars and globular clusters can be made.

The large angular size of the galaxy and its GCS ($> 1°$ square) as well as the high contamination by the foreground Galactic stars, due to the low Galactic latitude, made the investigation of the complete GCS almost impossible before. Now, with the new large field imagers and spectrographs like VIMOS at the VLT, the globular cluster system of NGC 5128 can become the template globular cluster system for the study of other more distant systems. For the first time the complete globular cluster luminosity function in an elliptical galaxy can be constructed and calibrated with Cepheids that may be found in the young stellar population of NGC 5128.

With the large sample of about 500 globular clusters, it will be possible to determine whether or not the cluster system kinematics change with galactocentric distance and/or azimuth. It will be possible to investigate the kinematical differences in metal-rich and metal-poor cluster subsamples. In combination with the 400 planetary nebulae velocities of Hui et al. (1995) a dynamical analysis of the giant elliptical galaxy potential can be determined with an unprecedented accuracy.

The brightest and the most massive globular cluster in our Galaxy, ω Cen is peculiar in many ways: e.g. it is one of the most flattened Galactic globular clusters and it shows strong variations in nearly all element abundances (e.g. Pancino et al. 2002). G1, the brightest cluster in our neighbouring galaxy M31, shares many properties with ω Cen (Meylan et al. 2001).

Are the brightest globular clusters nuclei of accreted dwarf elliptical galaxies? How important is the accretion of smaller galaxies for the formation of the globular cluster system? Can the small accreted galaxies build the majority of the stellar halo of giant galaxies? The ongoing accretion of smaller galaxies has become an observational fact. For example our own Galaxy is undergoing a merger with the Sagittarius dwarf (Ibata et al. 1995) and NGC 5128 shows clear signs of a recent merger with a smaller galaxy.

Most recently, using the UVES echelle spectrograph at VLT we have obtained high dispersion spectra of the brightest globular clusters in NGC 5128. We are going to measure their central velocity dispersions and derive the masses and mass-to-luminosity ratios. The comparison of their masses and the mass-to-luminosity ratios with those of the nuclei of dwarf ellipticals in Centaurus Group will provide clues to the above questions.

With VLT and Magellan it was possible to resolve the stars in the halo of NGC 5128 (Chapters 4 and 5). We studied the young stellar population in the north-eastern halo using the U and V-band photometry, while V and K-bands were used to detect the old RGB stars. From the optical-near-IR CMDs we could see that there exists a large spread in metallicity in the halo of this giant elliptical. Also hints about the probable intermediate-age component were suggested by the presence of bright AGB stars above the tip of the RGB. But how much of the spread in ages is actually hidden in the wide RGB? The RGB stars provide a powerful tool for metallicity information, but they are very poor age discriminators. To gain additional leverage on both the metallicity distribution function and age distribution function, we need to reach more deeply into the CMD where features that are more sensitive to age are to be found. The brightest of these is the horizontal branch (core helium-burning stage), which has now been brought within reach of HST with the deployment of the Advanced Camera for Surveys (ACS) on HST.

To understand the complex formation and evolutionary history of NGC 5128 it is necessary to interpret the various clues coming from properties of its old and young stellar populations, globular clusters, interaction of jets and interstellar matter in a coherent picture. This giant elliptical galaxy can become a stepping stone for the investigations of more distant systems.

Appendix A

The light curves for all variables with at least 10 measurements for which a period could be obtained with the Fourier analysis of their K-band light curves. 408 variables in Field 1 and and 884 variables in Field 2 are presented. They have been folded with the periods obtained from sine-curve fitting and each point has been plotted twice to emphasize the variability. Note that the phase zero does not correspond to the minimum of the light curve.

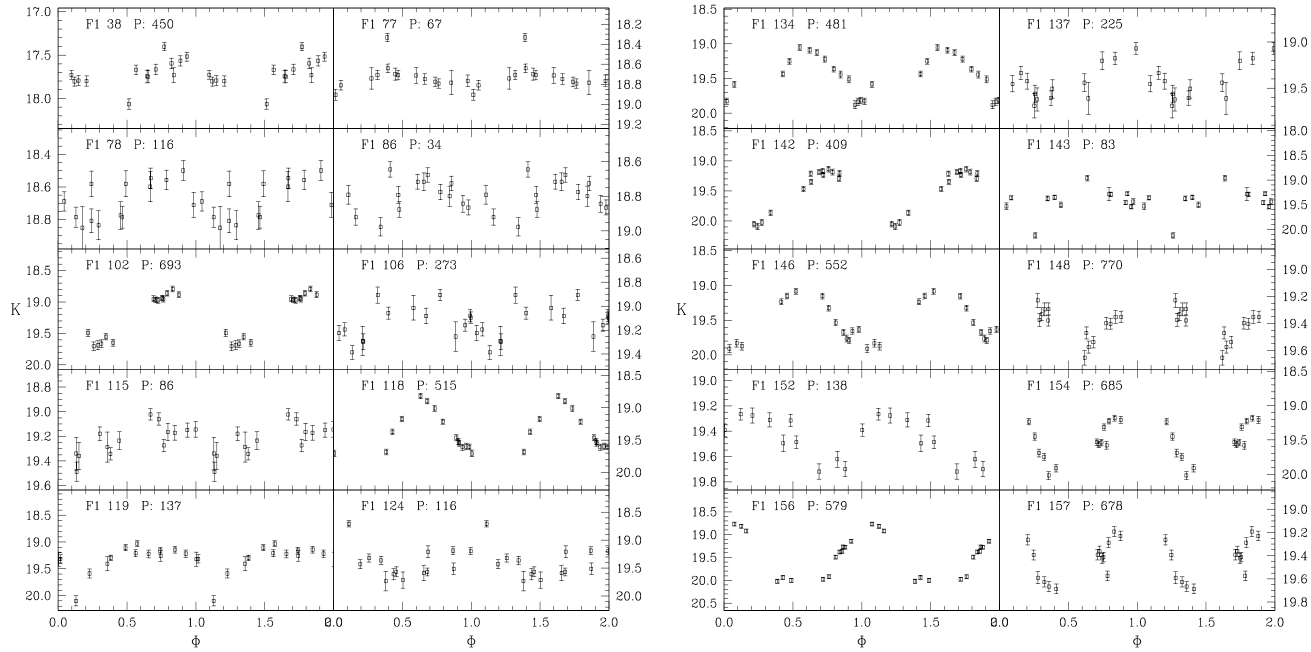

Figure 8.1: All the light curves from Field 1 and Field 2 folded with the periods obtained from sine-curve fitting. Each point has been plotted twice to emphasize the variability.

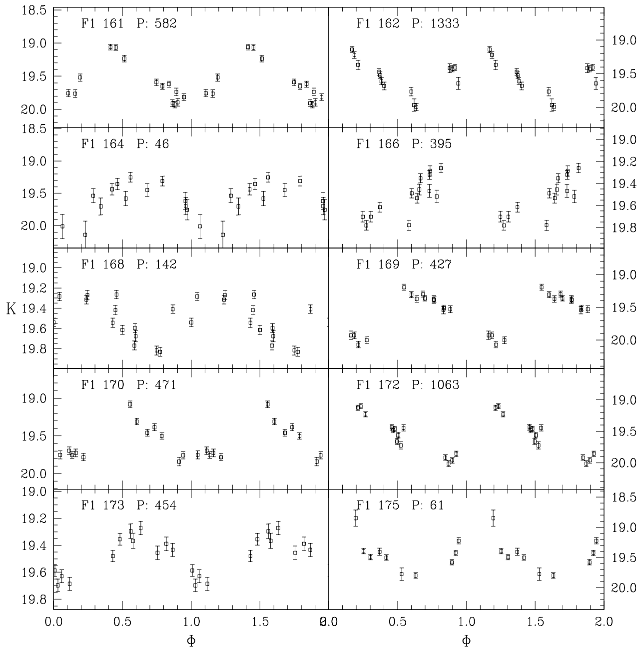
F1 161 P: 582
F1 162 P: 1333
F1 164 P: 46
F1 166 P: 395
F1 168 P: 142
F1 169 P: 427
F1 170 P: 471
F1 172 P: 1063
F1 173 P: 454
F1 175 P: 61
K
ϕ

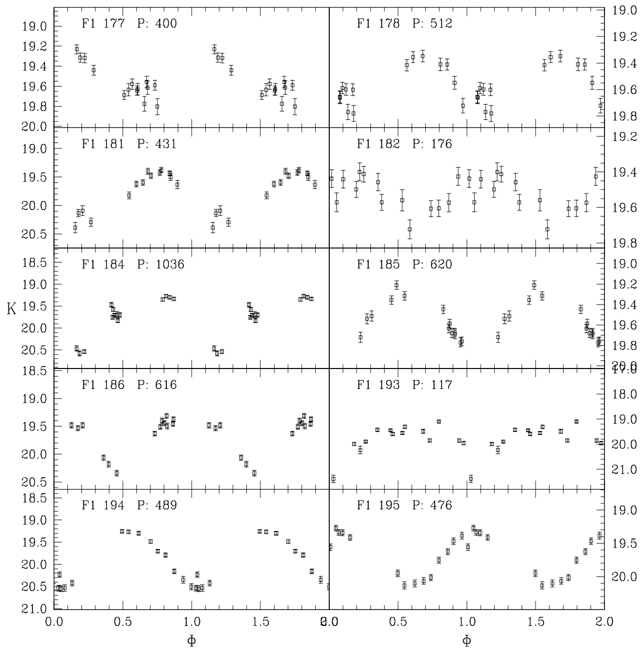
F1 177 P: 400
F1 178 P: 512
F1 181 P: 431
F1 182 P: 176
F1 184 P: 1036
F1 185 P: 620
F1 186 P: 616
F1 193 P: 117
F1 194 P: 489
F1 195 P: 476
K
ϕ

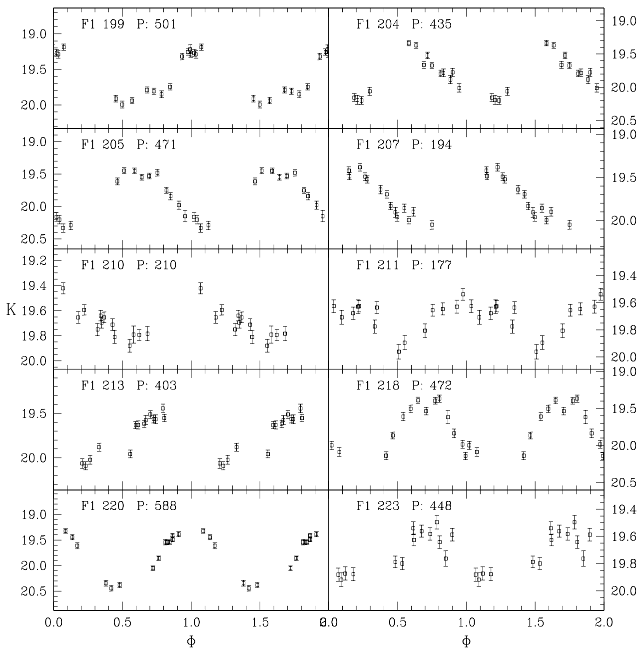
F1 199 P: 501
F1 204 P: 435
F1 205 P: 471
F1 207 P: 194
F1 210 P: 210
F1 211 P: 177
F1 213 P: 403
F1 218 P: 472
F1 220 P: 588
F1 223 P: 448
K
ϕ

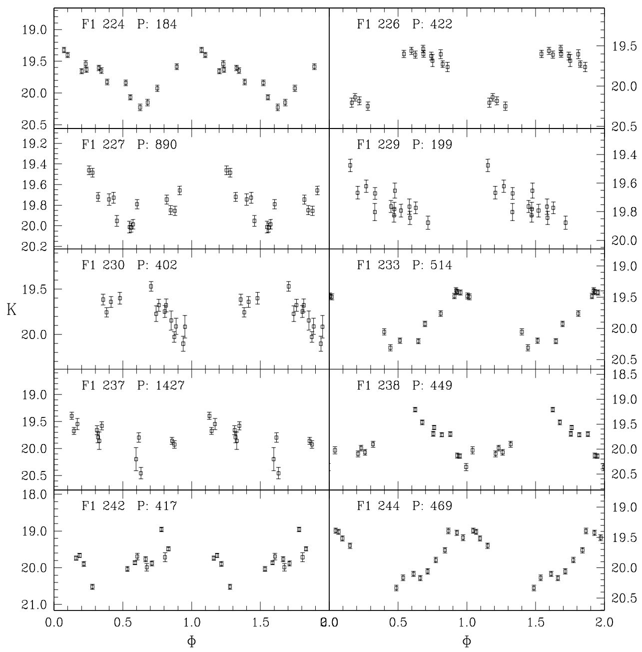
F1 224 P: 184
F1 226 P: 422
F1 227 P: 890
F1 229 P: 199
F1 230 P: 402
F1 233 P: 514
F1 237 P: 1427
F1 238 P: 449
F1 242 P: 417
F1 244 P: 469
K
ϕ

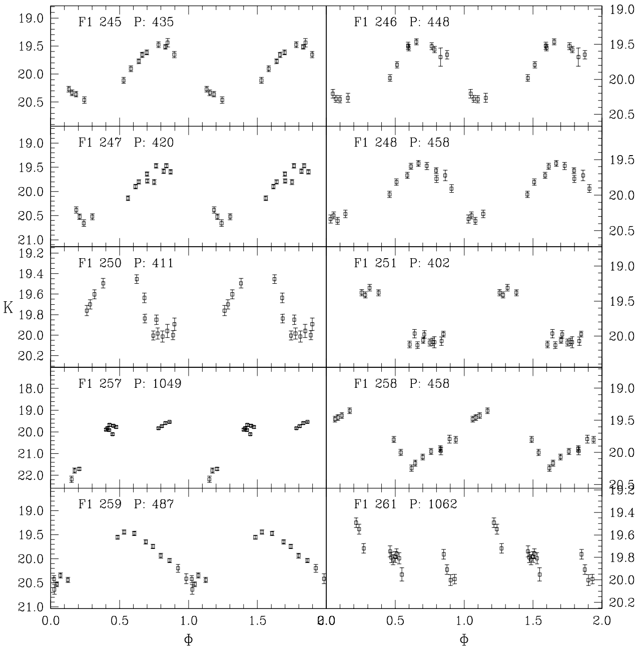
F1 245 P: 435
F1 246 P: 448
F1 247 P: 420
F1 248 P: 458
F1 250 P: 411
F1 251 P: 402
F1 257 P: 1049
F1 258 P: 458
F1 259 P: 487
F1 261 P: 1062
K
ϕ

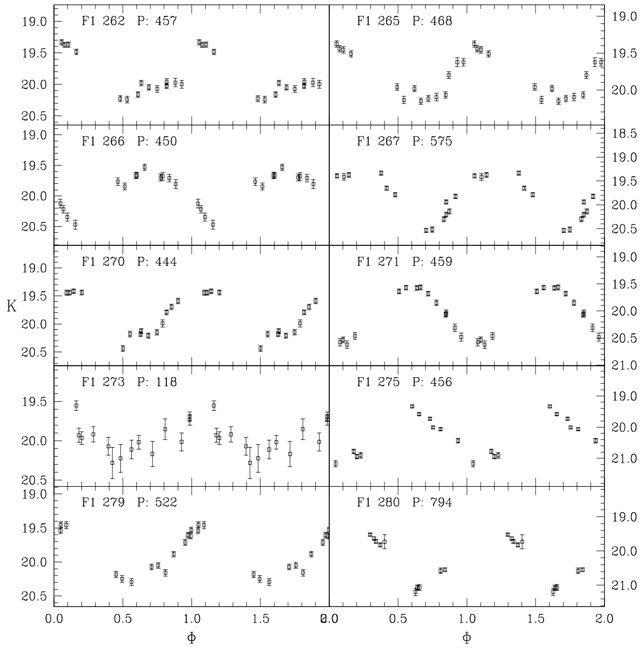
F1 262 P: 457
F1 265 P: 468
F1 266 P: 450
F1 267 P: 575
F1 270 P: 444
F1 271 P: 459
F1 273 P: 118
F1 275 P: 456
F1 279 P: 522
F1 280 P: 794
K
ϕ

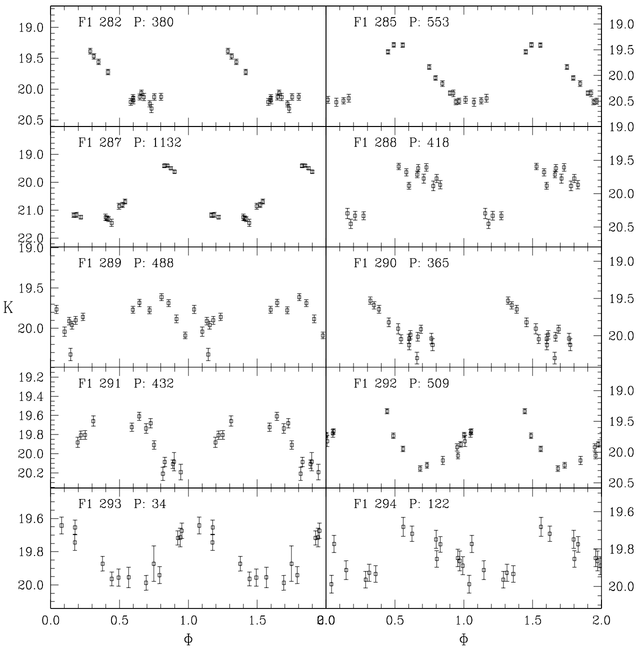
F1 282 P: 380
F1 285 P: 553
F1 287 P: 1132
F1 288 P: 418
F1 289 P: 488
F1 290 P: 365
F1 291 P: 432
F1 292 P: 509
F1 293 P: 34
F1 294 P: 122
K
ϕ

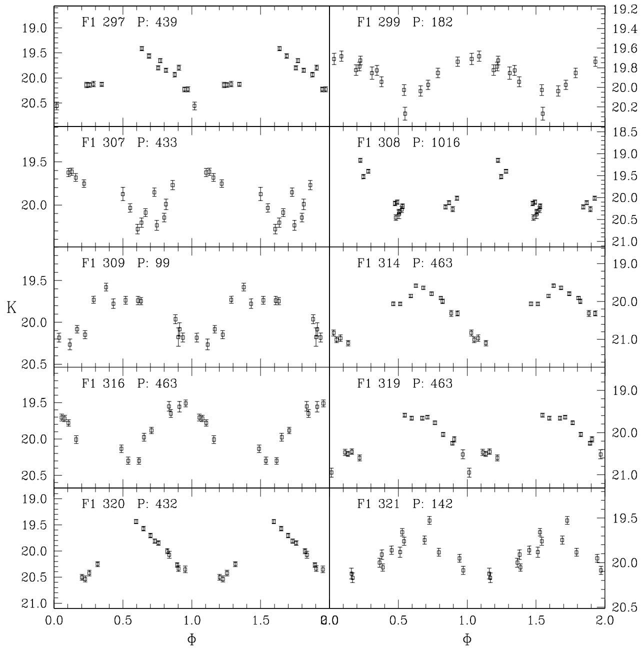
F1 297 P: 439
F1 299 P: 182
F1 307 P: 433
F1 308 P: 1016
F1 309 P: 99
F1 314 P: 463
F1 316 P: 463
F1 319 P: 463
F1 320 P: 432
F1 321 P: 142
K
ϕ

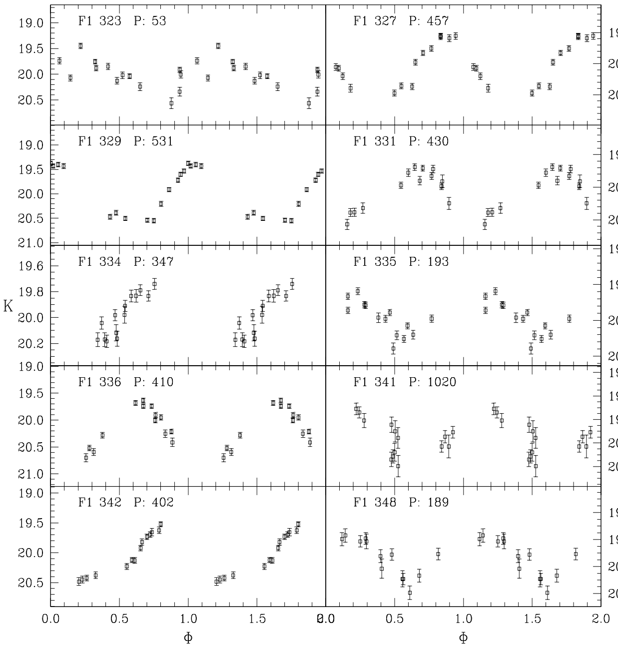

F1 323 P: 53
F1 327 P: 457
F1 329 P: 531
F1 331 P: 430
F1 334 P: 347
F1 335 P: 193
F1 336 P: 410
F1 341 P: 1020
F1 342 P: 402
F1 348 P: 189
K
ϕ

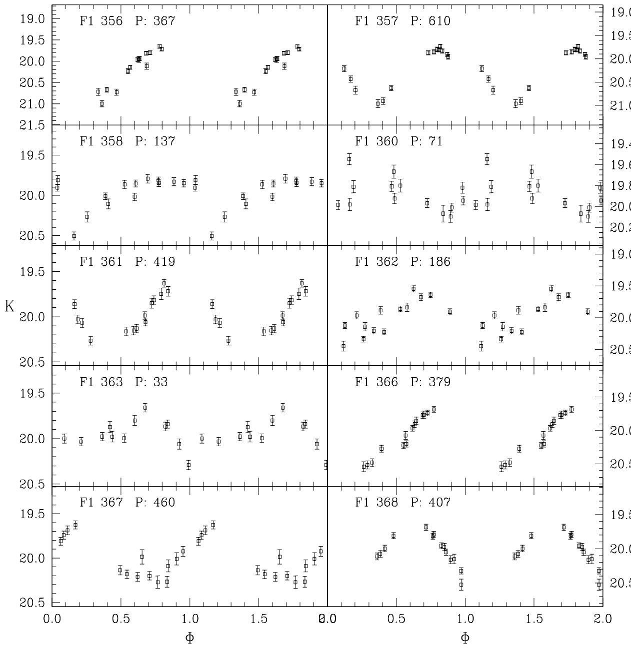

F1 356 P: 367
F1 357 P: 610
F1 358 P: 137
F1 360 P: 71
F1 361 P: 419
F1 362 P: 186
F1 363 P: 33
F1 366 P: 379
F1 367 P: 460
F1 368 P: 407
K
ϕ

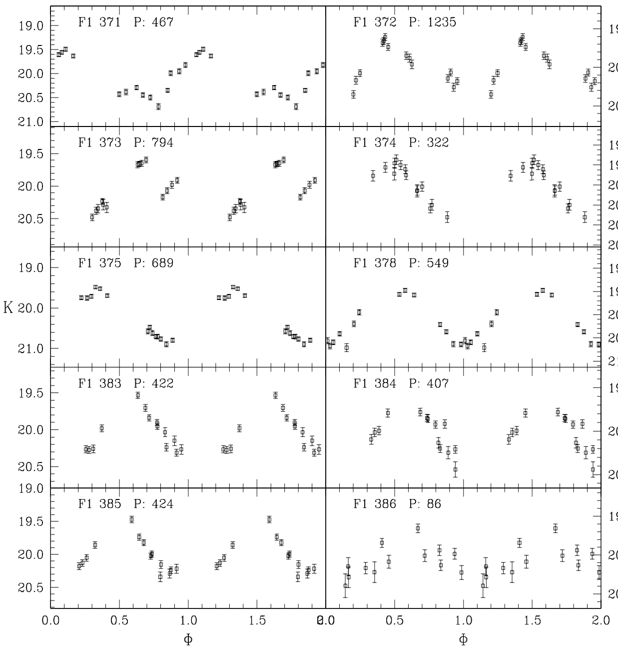

F1 371 P: 467
F1 372 P: 1235
F1 373 P: 794
F1 374 P: 322
F1 375 P: 689
F1 378 P: 549
F1 383 P: 422
F1 384 P: 407
F1 385 P: 424
F1 386 P: 86
K
ϕ

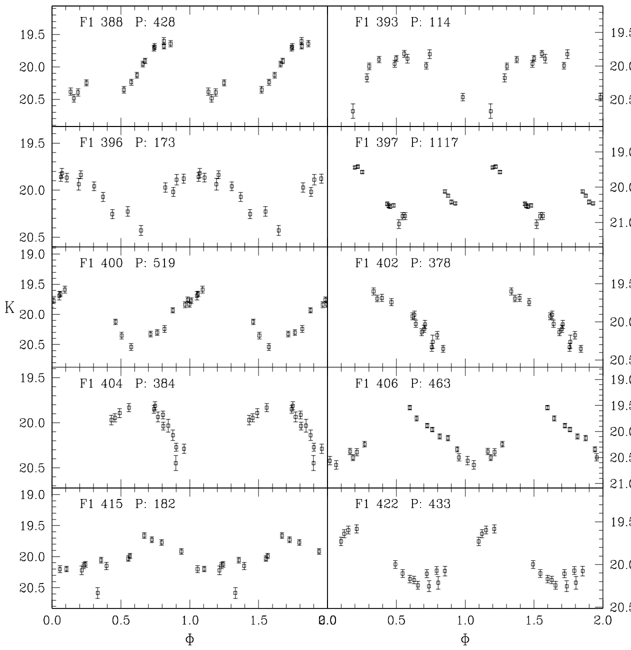

F1 388 P: 428
F1 393 P: 114
F1 396 P: 173
F1 397 P: 1117
F1 400 P: 519
F1 402 P: 378
F1 404 P: 384
F1 406 P: 463
F1 415 P: 182
F1 422 P: 433
K
ϕ

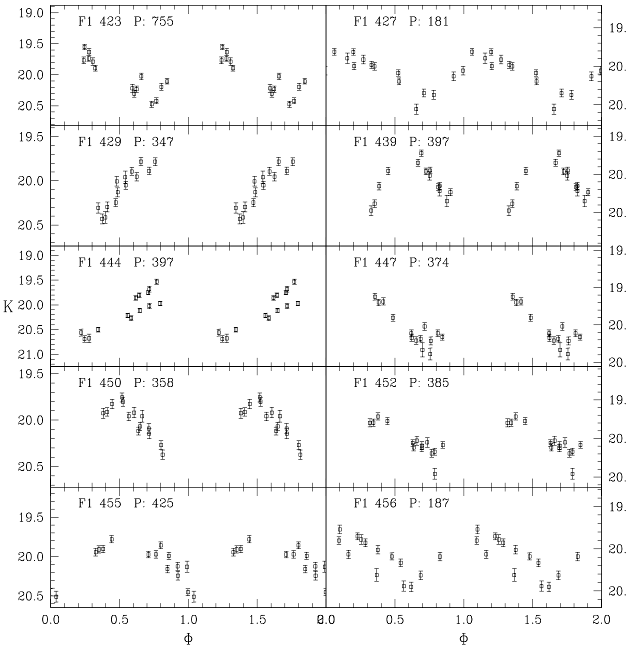
F1 423 P: 755
F1 427 P: 181
F1 429 P: 347
F1 439 P: 397
F1 444 P: 397
F1 447 P: 374
F1 450 P: 358
F1 452 P: 385
F1 455 P: 425
F1 456 P: 187
K
ϕ

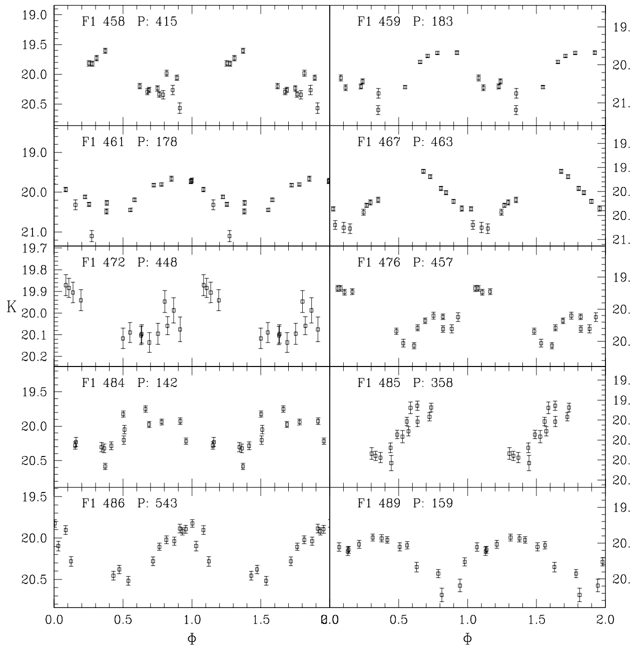
F1 458 P: 415
F1 459 P: 183
F1 461 P: 178
F1 467 P: 463
F1 472 P: 448
F1 476 P: 457
F1 484 P: 142
F1 485 P: 358
F1 486 P: 543
F1 489 P: 159
K
ϕ

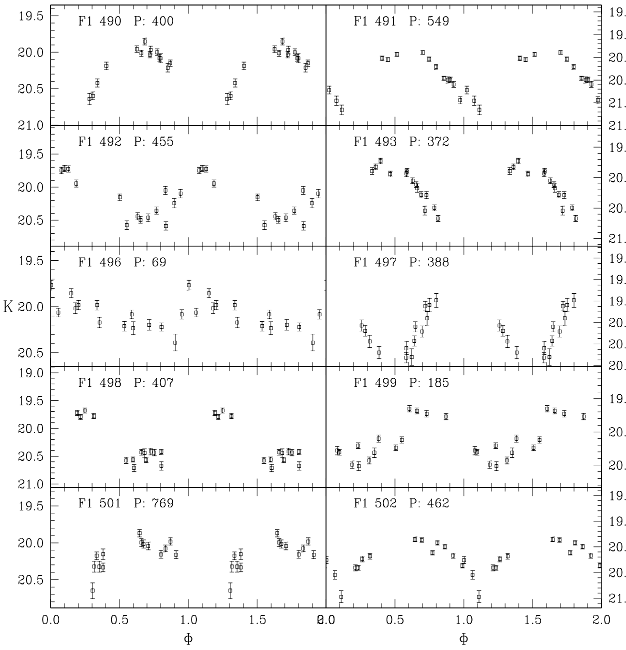
F1 490 P: 400
F1 491 P: 549
F1 492 P: 455
F1 493 P: 372
F1 496 P: 69
F1 497 P: 388
F1 498 P: 407
F1 499 P: 185
F1 501 P: 769
F1 502 P: 462
K
ϕ

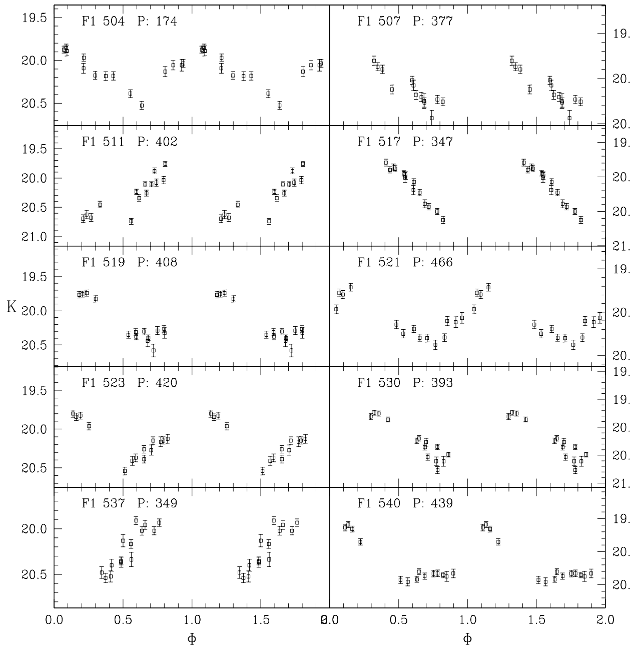
F1 504 P: 174
F1 507 P: 377
F1 511 P: 402
F1 517 P: 347
F1 519 P: 408
F1 521 P: 466
F1 523 P: 420
F1 530 P: 393
F1 537 P: 349
F1 540 P: 439
K
ϕ

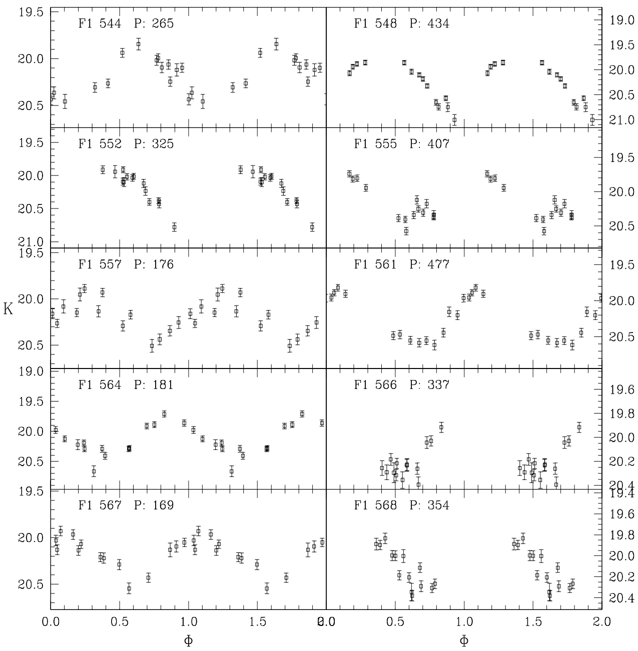
F1 544 P: 265
F1 548 P: 434
F1 552 P: 325
F1 555 P: 407
F1 557 P: 176
F1 561 P: 477
F1 564 P: 181
F1 566 P: 337
F1 567 P: 169
F1 568 P: 354
K
ϕ

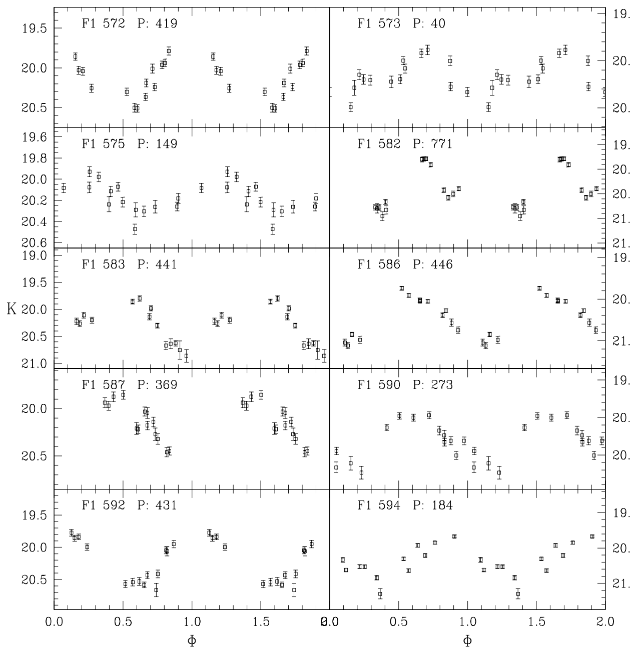
F1 572 P: 419
F1 573 P: 40
F1 575 P: 149
F1 582 P: 771
F1 583 P: 441
F1 586 P: 446
F1 587 P: 369
F1 590 P: 273
F1 592 P: 431
F1 594 P: 184
K
ϕ

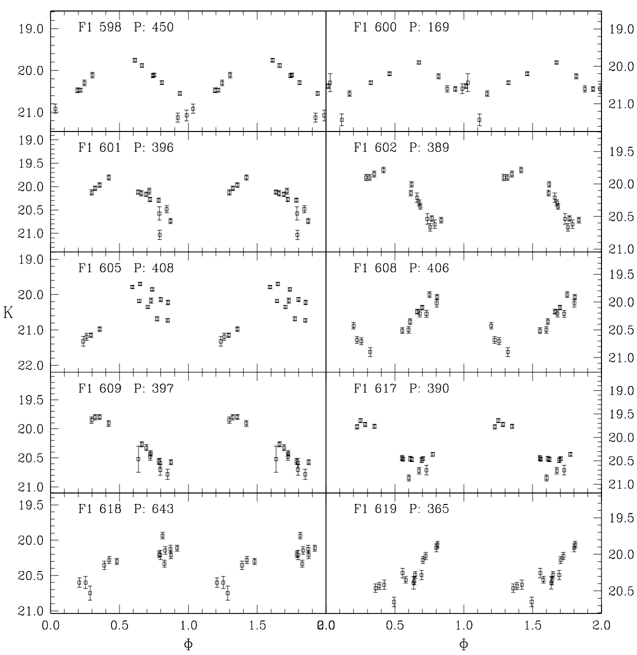
F1 598 P: 450
F1 600 P: 169
F1 601 P: 396
F1 602 P: 389
F1 605 P: 408
F1 608 P: 406
F1 609 P: 397
F1 617 P: 390
F1 618 P: 643
F1 619 P: 365
K
ϕ

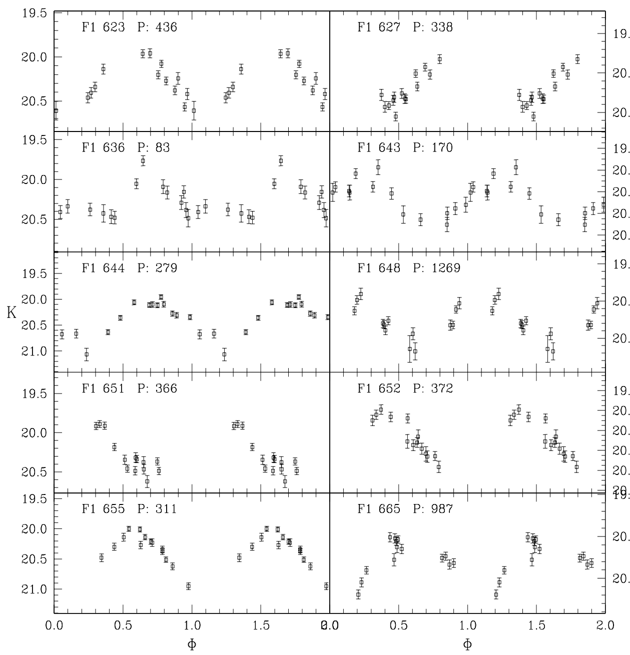
F1 623 P: 436
F1 627 P: 338
F1 636 P: 83
F1 643 P: 170
F1 644 P: 279
F1 648 P: 1269
F1 651 P: 366
F1 652 P: 372
F1 655 P: 311
F1 665 P: 987
K
ϕ

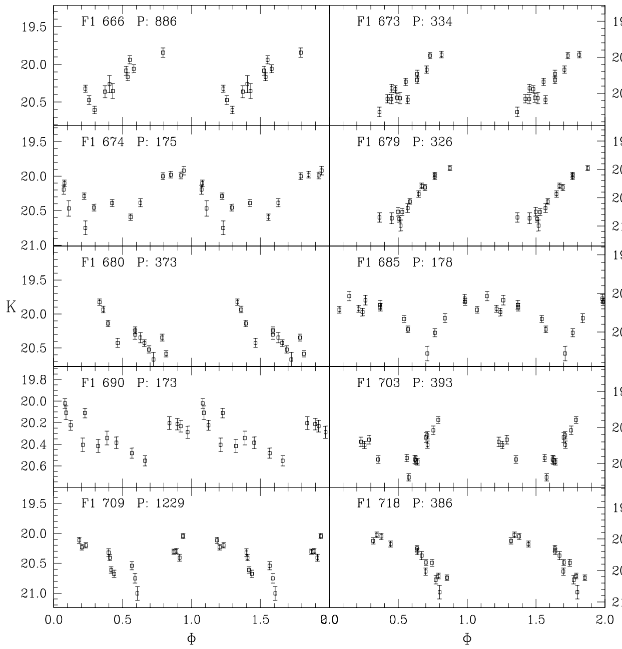
F1 666 P: 886
F1 673 P: 334
F1 674 P: 175
F1 679 P: 326
F1 680 P: 373
F1 685 P: 178
F1 690 P: 173
F1 703 P: 393
F1 709 P: 1229
F1 718 P: 386
K
ϕ

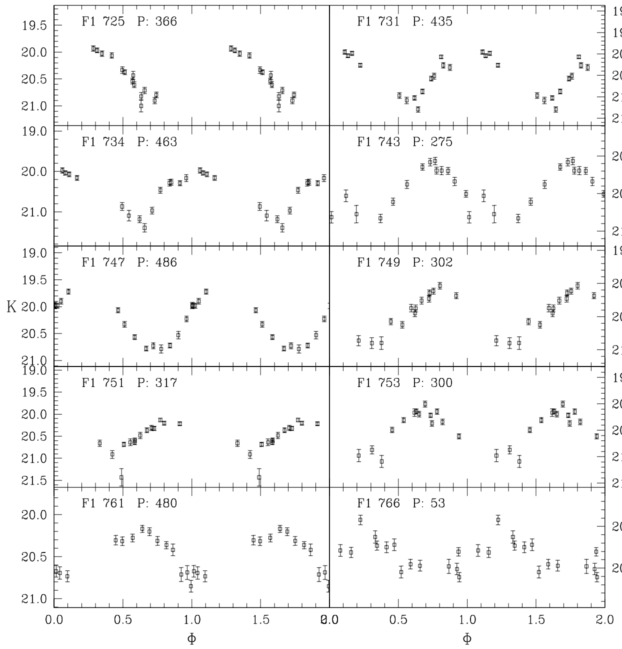
F1 725 P: 366
F1 731 P: 435
F1 734 P: 463
F1 743 P: 275
F1 747 P: 486
F1 749 P: 302
F1 751 P: 317
F1 753 P: 300
F1 761 P: 480
F1 766 P: 53
K
ϕ

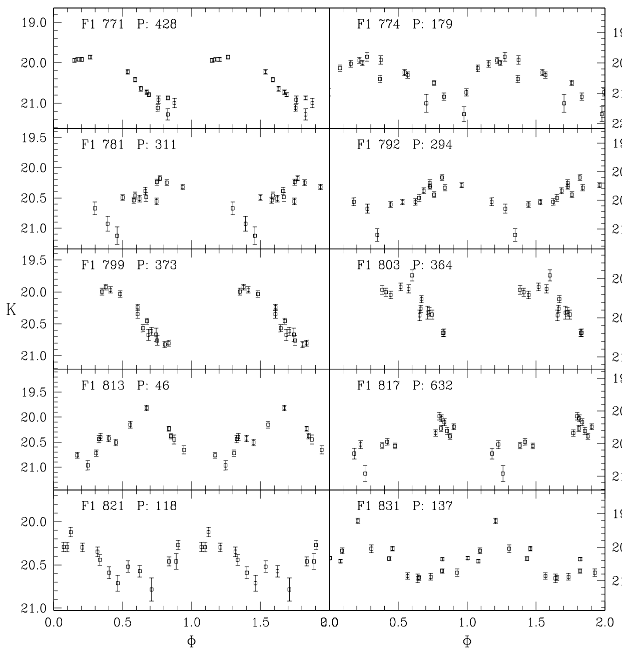
F1 771 P: 428
F1 774 P: 179
F1 781 P: 311
F1 792 P: 294
F1 799 P: 373
F1 803 P: 364
F1 813 P: 46
F1 817 P: 632
F1 821 P: 118
F1 831 P: 137
K
ϕ

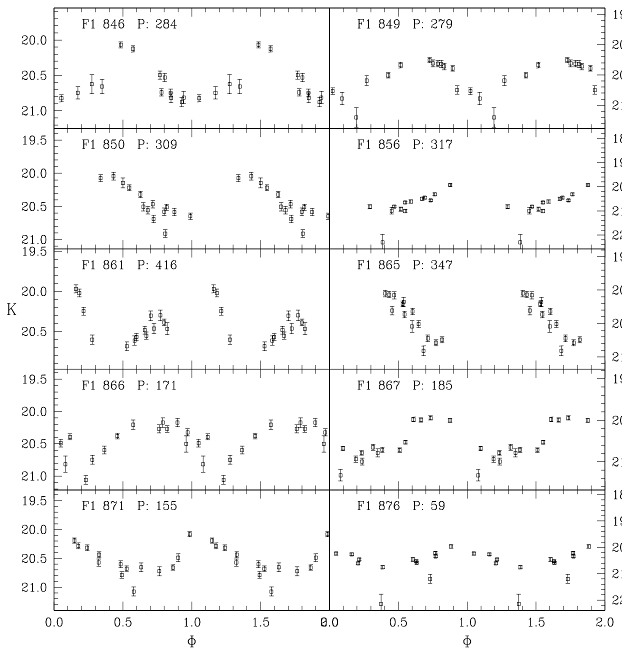
F1 846 P: 284
F1 849 P: 279
F1 850 P: 309
F1 856 P: 317
F1 861 P: 416
F1 865 P: 347
F1 866 P: 171
F1 867 P: 185
F1 871 P: 155
F1 876 P: 59
K
ϕ

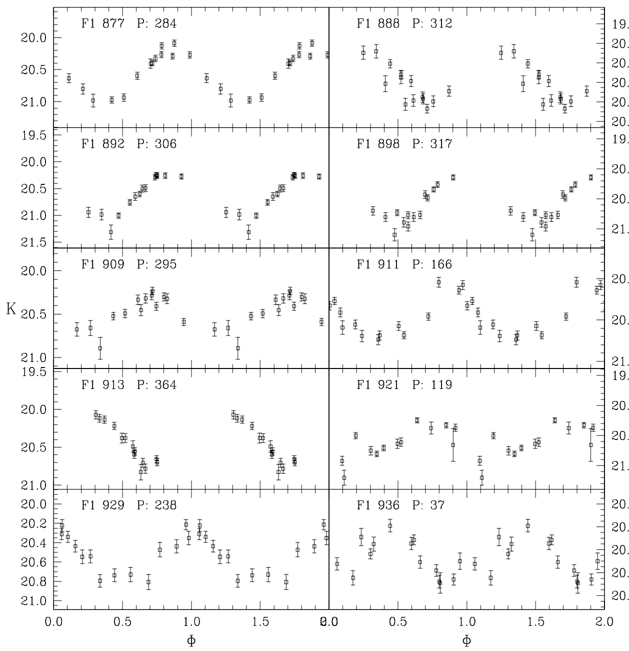
F1 877 P: 284
F1 888 P: 312
F1 892 P: 306
F1 898 P: 317
F1 909 P: 295
F1 911 P: 166
F1 913 P: 364
F1 921 P: 119
F1 929 P: 238
F1 936 P: 37
K
ϕ

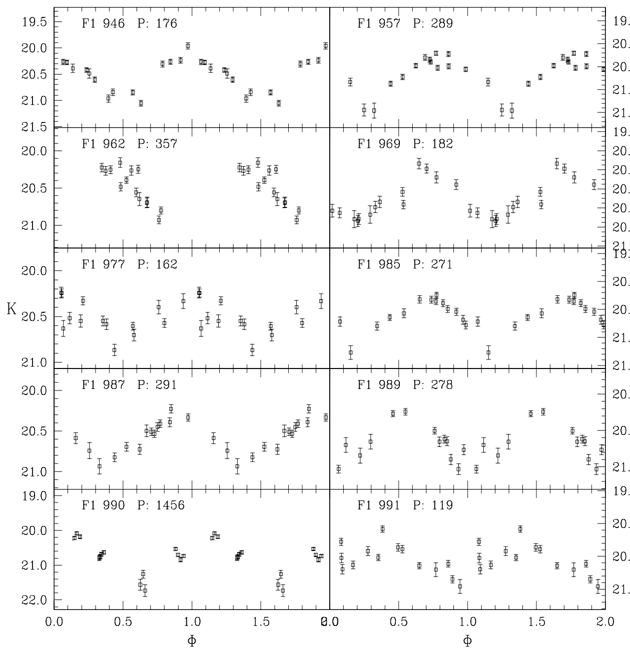
F1 946 P: 176
F1 957 P: 289
F1 962 P: 357
F1 969 P: 182
F1 977 P: 162
F1 985 P: 271
F1 987 P: 291
F1 989 P: 278
F1 990 P: 1456
F1 991 P: 119
K
ϕ

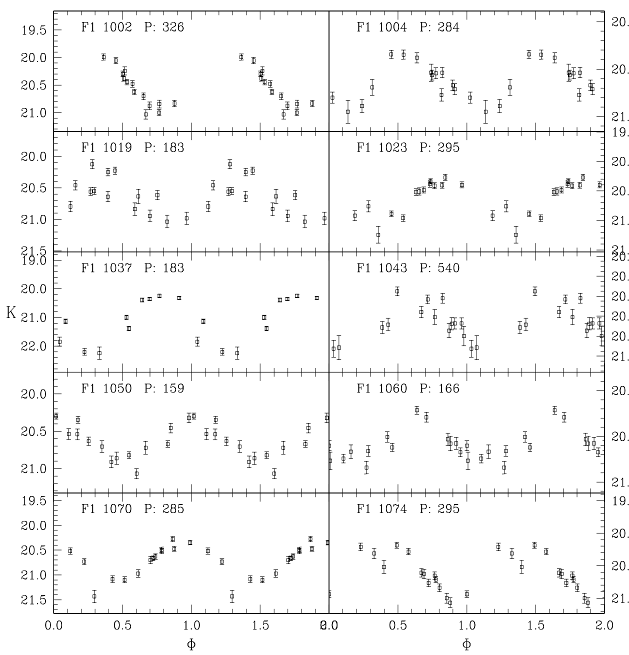
F1 1002 P: 326
F1 1004 P: 284
F1 1019 P: 183
F1 1023 P: 295
F1 1037 P: 183
F1 1043 P: 540
F1 1050 P: 159
F1 1060 P: 166
F1 1070 P: 285
F1 1074 P: 295
K
ϕ

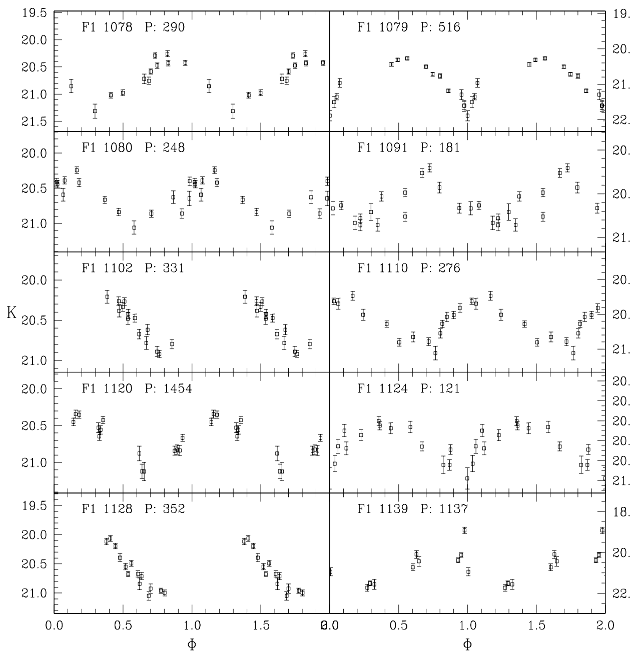
F1 1078 P: 290
F1 1079 P: 516
F1 1080 P: 248
F1 1091 P: 181
F1 1102 P: 331
F1 1110 P: 276
F1 1120 P: 1454
F1 1124 P: 121
F1 1128 P: 352
F1 1139 P: 1137
K
ϕ

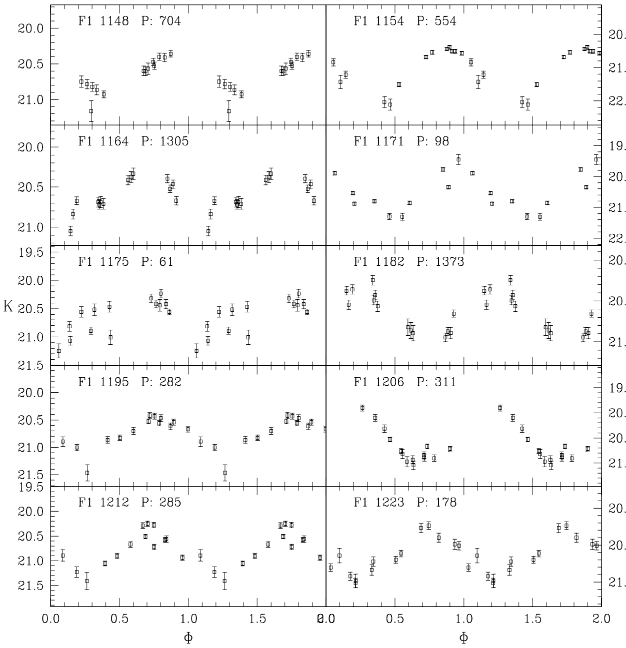
F1 1148 P: 704
F1 1154 P: 554
F1 1164 P: 1305
F1 1171 P: 98
F1 1175 P: 61
F1 1182 P: 1373
F1 1195 P: 282
F1 1206 P: 311
F1 1212 P: 285
F1 1223 P: 178
K
ϕ

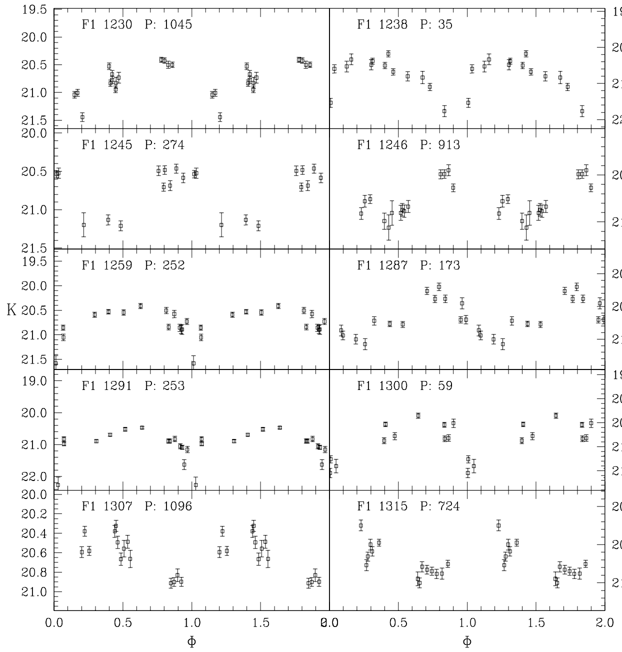
F1 1230 P: 1045
F1 1238 P: 35
F1 1245 P: 274
F1 1246 P: 913
F1 1259 P: 252
F1 1287 P: 173
F1 1291 P: 253
F1 1300 P: 59
F1 1307 P: 1096
F1 1315 P: 724
K
ϕ

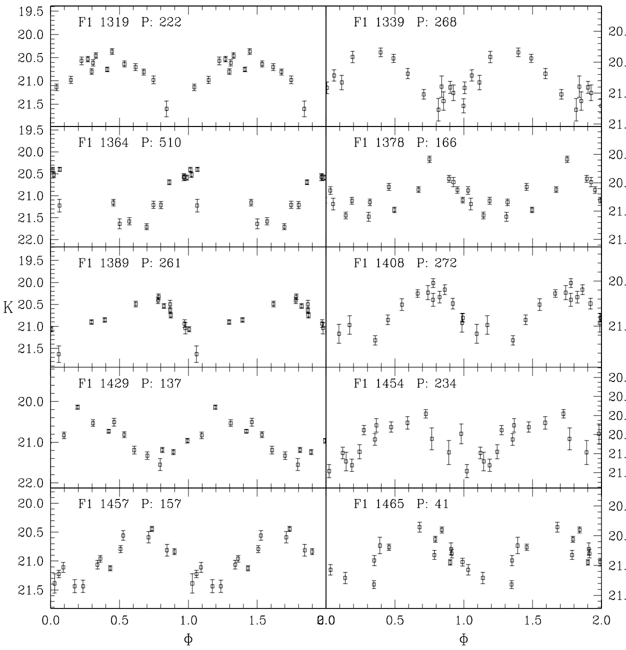
F1 1319 P: 222
F1 1339 P: 268
F1 1364 P: 510
F1 1378 P: 166
F1 1389 P: 261
F1 1408 P: 272
F1 1429 P: 137
F1 1454 P: 234
F1 1457 P: 157
F1 1465 P: 41
K
ϕ

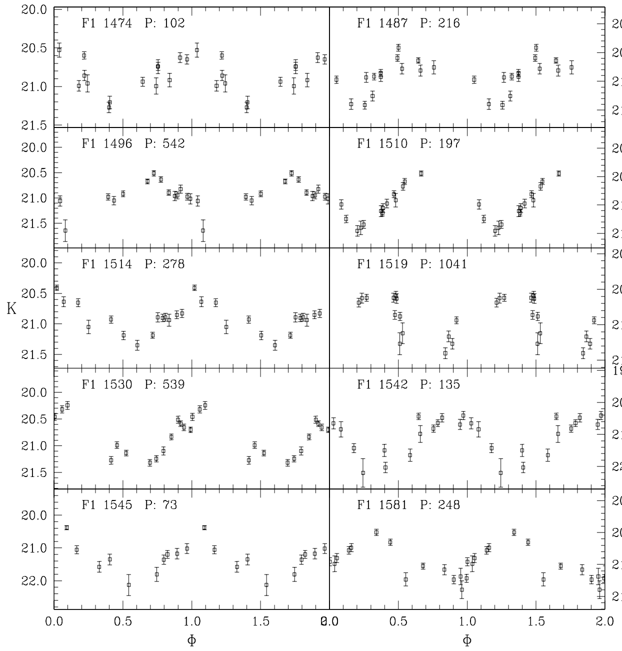
F1 1474 P: 102
F1 1487 P: 216
F1 1496 P: 542
F1 1510 P: 197
F1 1514 P: 278
F1 1519 P: 1041
F1 1530 P: 539
F1 1542 P: 135
F1 1545 P: 73
F1 1581 P: 248
K
ϕ

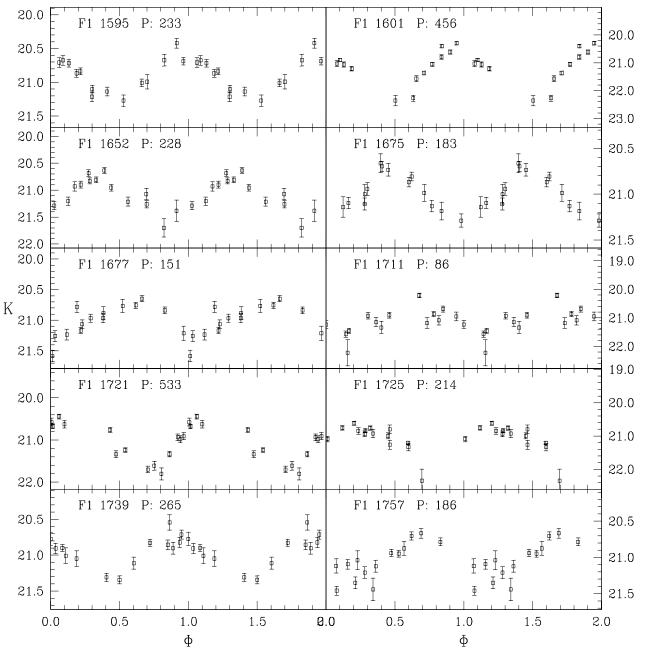
F1 1595 P: 233
F1 1601 P: 456
F1 1652 P: 228
F1 1675 P: 183
F1 1677 P: 151
F1 1711 P: 86
F1 1721 P: 533
F1 1725 P: 214
F1 1739 P: 265
F1 1757 P: 186
K
ϕ

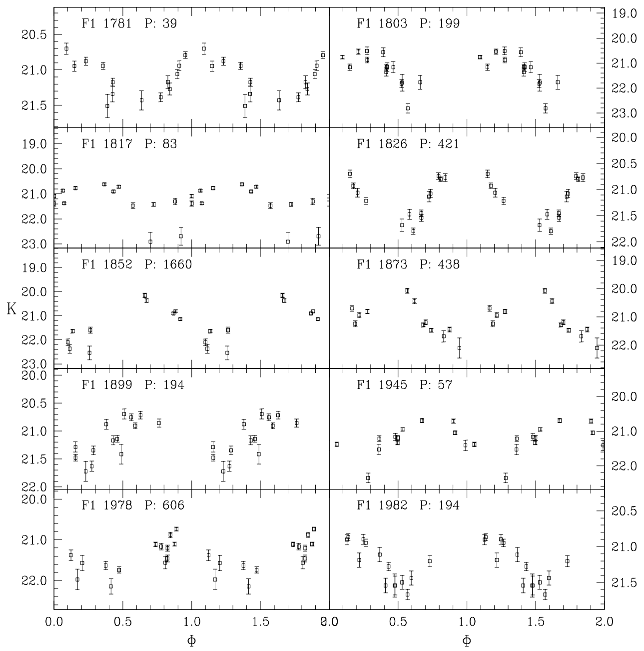
F1 1781 P: 39
F1 1803 P: 199
F1 1817 P: 83
F1 1826 P: 421
F1 1852 P: 1660
F1 1873 P: 438
F1 1899 P: 194
F1 1945 P: 57
F1 1978 P: 606
F1 1982 P: 194
K
ϕ

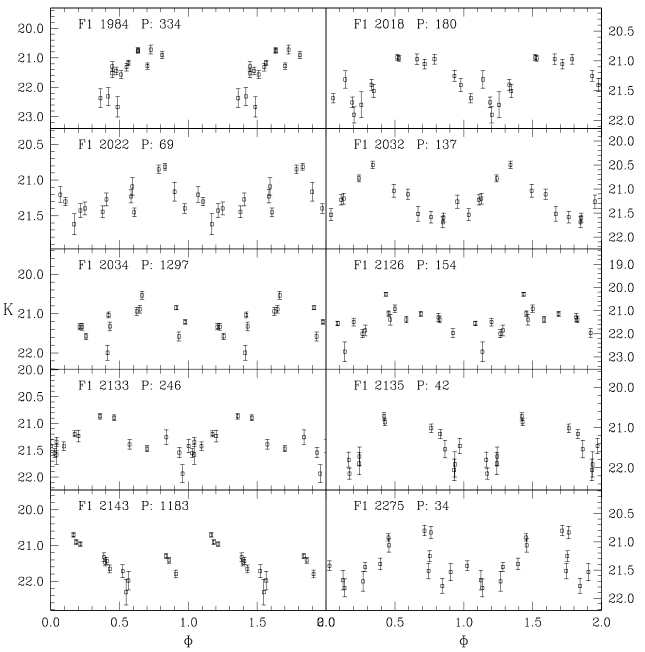
F1 1984 P: 334
F1 2018 P: 180
F1 2022 P: 69
F1 2032 P: 137
F1 2034 P: 1297
F1 2126 P: 154
F1 2133 P: 246
F1 2135 P: 42
F1 2143 P: 1183
F1 2275 P: 34
K
ϕ

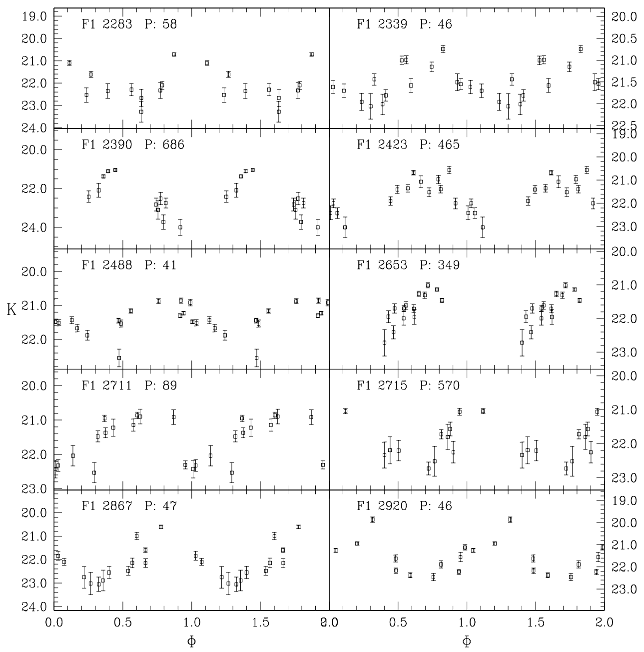
F1 2283 P: 58
F1 2339 P: 46
F1 2390 P: 686
F1 2423 P: 465
F1 2488 P: 41
F1 2653 P: 349
F1 2711 P: 89
F1 2715 P: 570
F1 2867 P: 47
F1 2920 P: 46
K
ϕ

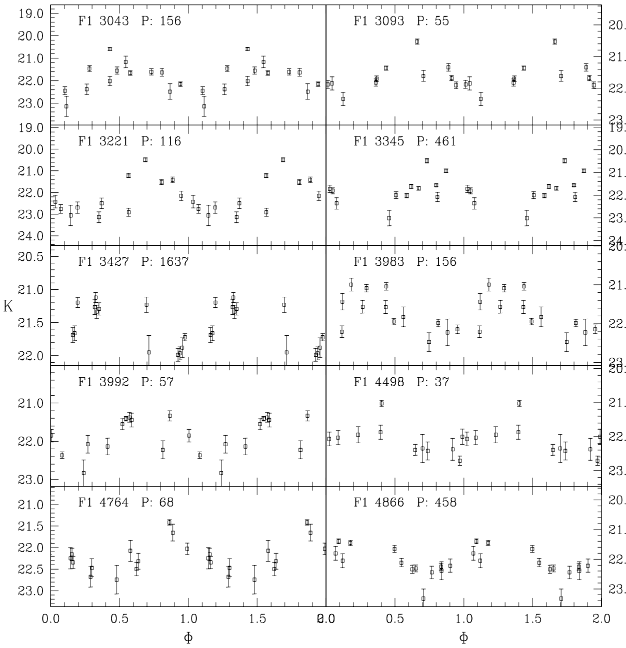

F1 3043 P: 156
F1 3093 P: 55
F1 3221 P: 116
F1 3345 P: 461
F1 3427 P: 1637
F1 3983 P: 156
F1 3992 P: 57
F1 4498 P: 37
F1 4764 P: 68
F1 4866 P: 458
K
ϕ

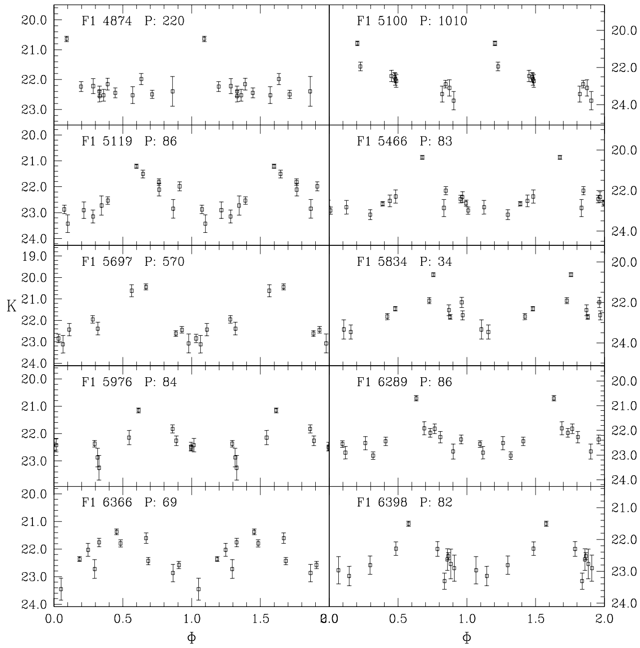

F1 4874 P: 220
F1 5100 P: 1010
F1 5119 P: 86
F1 5466 P: 83
F1 5697 P: 570
F1 5834 P: 34
F1 5976 P: 84
F1 6289 P: 86
F1 6366 P: 69
F1 6398 P: 82
K
ϕ

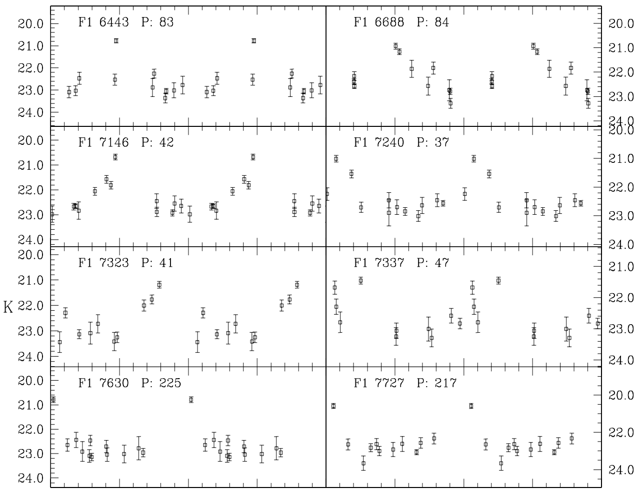

F1 6443 P: 83
F1 6688 P: 84
F1 7146 P: 42
F1 7240 P: 37
F1 7323 P: 41
F1 7337 P: 47
F1 7630 P: 225
F1 7727 P: 217
K

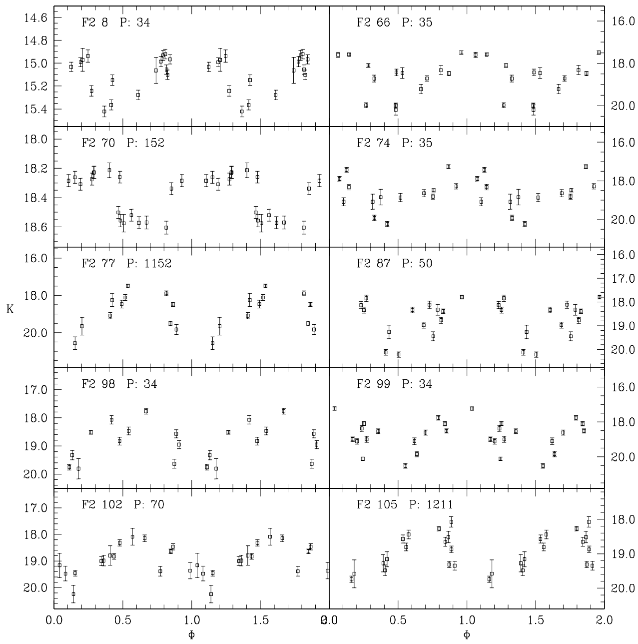

F2 8 P: 34
F2 66 P: 35
F2 70 P: 152
F2 74 P: 35
F2 77 P: 1152
F2 87 P: 50
F2 98 P: 34
F2 99 P: 34
F2 102 P: 70
F2 105 P: 1211
K
ϕ

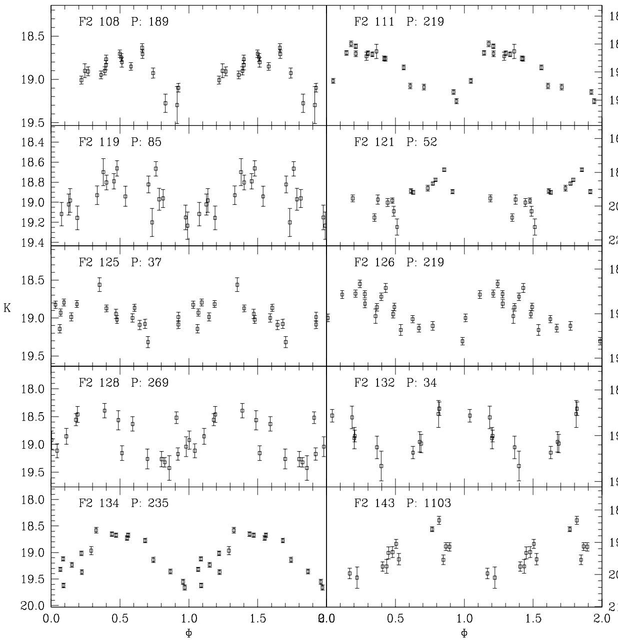
F2 108 P: 189
F2 111 P: 219
F2 119 P: 85
F2 121 P: 52
F2 125 P: 37
F2 126 P: 219
F2 128 P: 269
F2 132 P: 34
F2 134 P: 235
F2 143 P: 1103
K
ϕ
ϕ

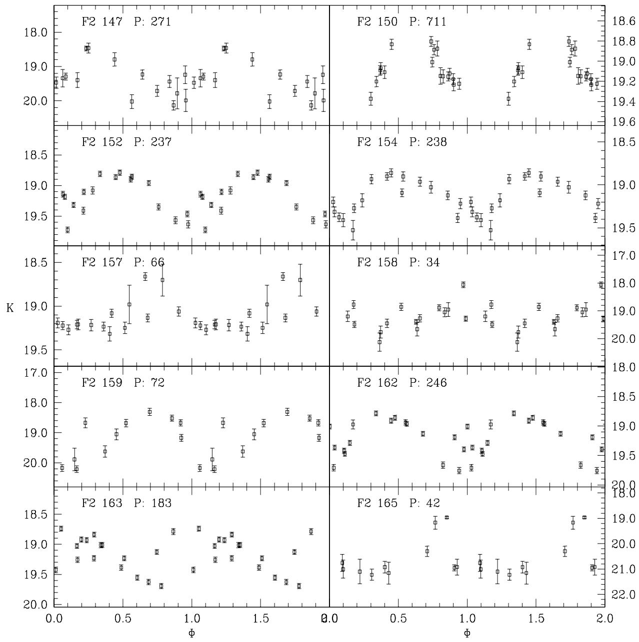
F2 147 P: 271
F2 150 P: 711
F2 152 P: 237
F2 154 P: 238
F2 157 P: 66
F2 158 P: 34
F2 159 P: 72
F2 162 P: 246
F2 163 P: 183
F2 165 P: 42
K
ϕ
ϕ

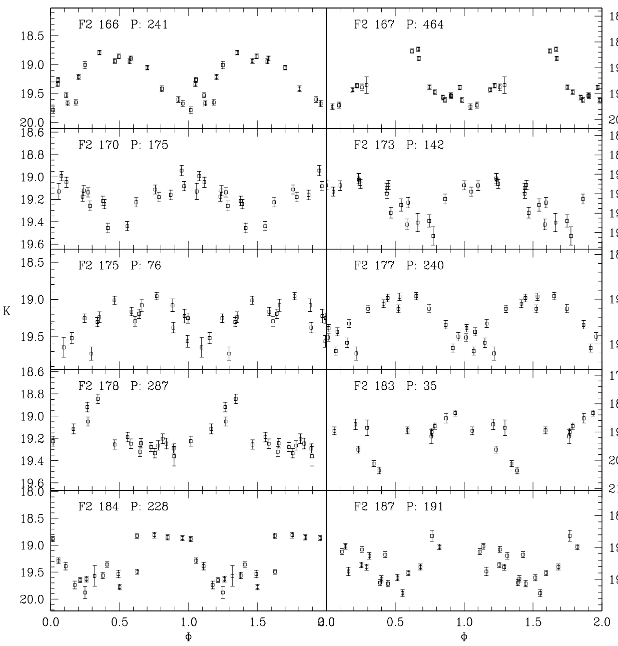
F2 166 P: 241
F2 167 P: 464
F2 170 P: 175
F2 173 P: 142
F2 175 P: 76
F2 177 P: 240
F2 178 P: 287
F2 183 P: 35
F2 184 P: 228
F2 187 P: 191
K
ϕ
ϕ

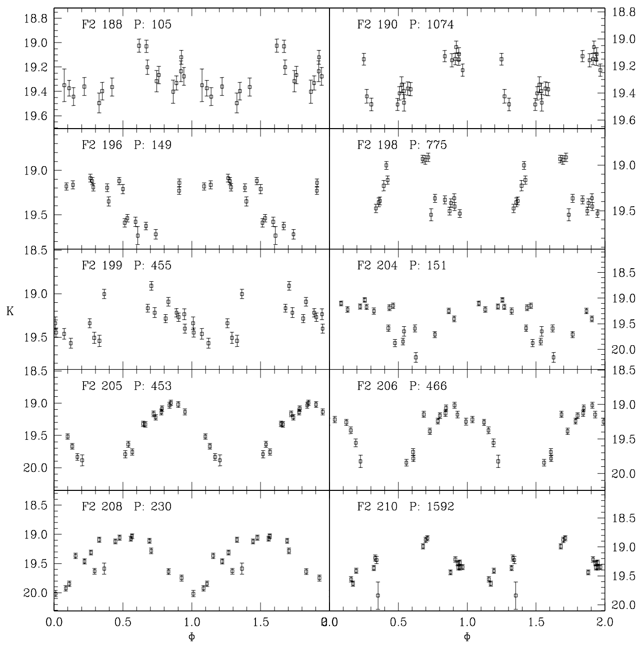
F2 188 P: 105
F2 190 P: 1074
F2 196 P: 149
F2 198 P: 775
F2 199 P: 455
F2 204 P: 151
F2 205 P: 453
F2 206 P: 466
F2 208 P: 230
F2 210 P: 1592
K
ϕ
ϕ

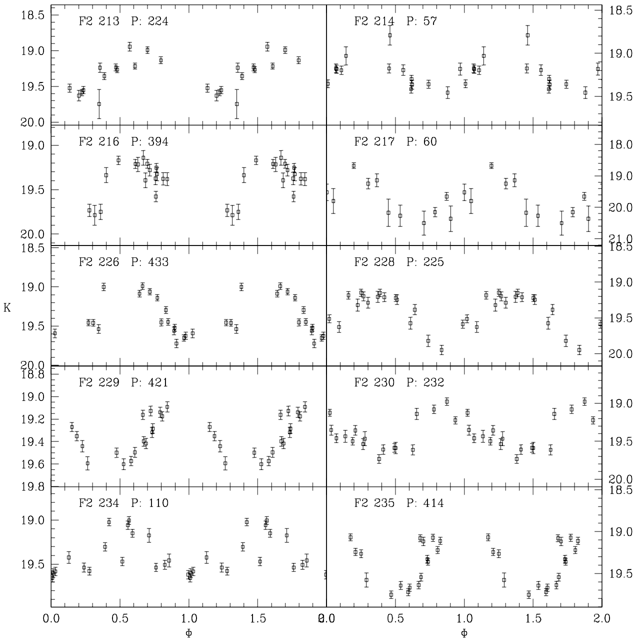
F2 213 P: 224
F2 214 P: 57
F2 216 P: 394
F2 217 P: 60
F2 226 P: 433
F2 228 P: 225
F2 229 P: 421
F2 230 P: 232
F2 234 P: 110
F2 235 P: 414
K
ϕ

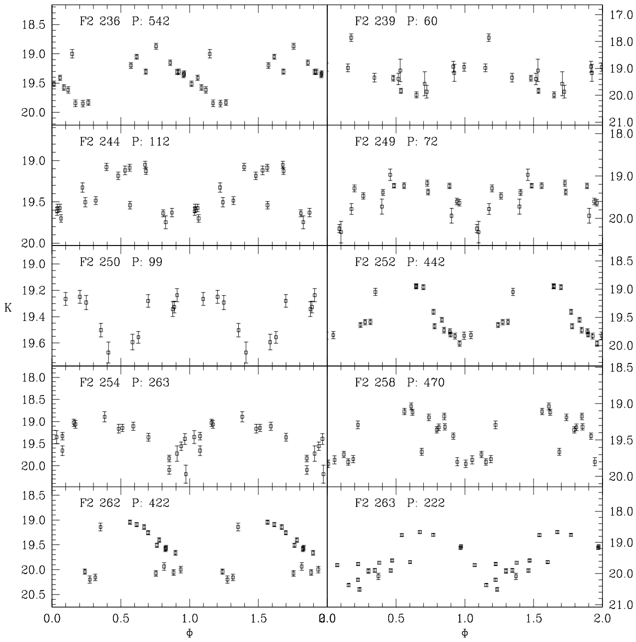
F2 236 P: 542
F2 239 P: 60
F2 244 P: 112
F2 249 P: 72
F2 250 P: 99
F2 252 P: 442
F2 254 P: 263
F2 258 P: 470
F2 262 P: 422
F2 263 P: 222
K
ϕ

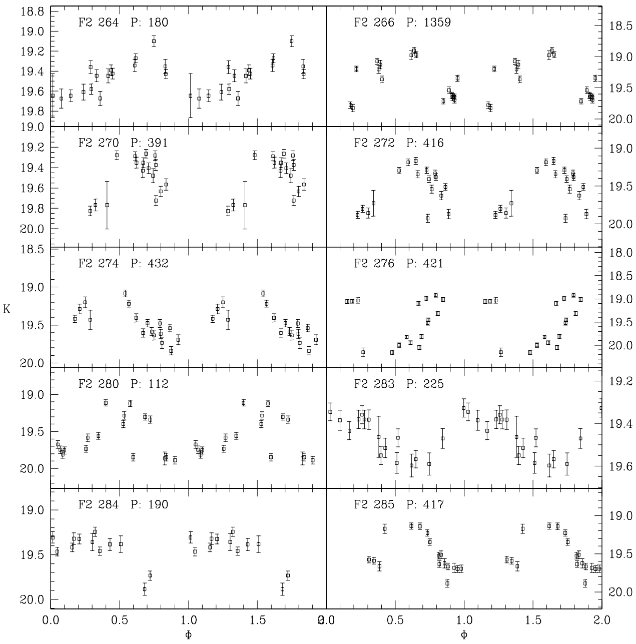
F2 264 P: 180
F2 266 P: 1359
F2 270 P: 391
F2 272 P: 416
F2 274 P: 432
F2 276 P: 421
F2 280 P: 112
F2 283 P: 225
F2 284 P: 190
F2 285 P: 417
K
ϕ

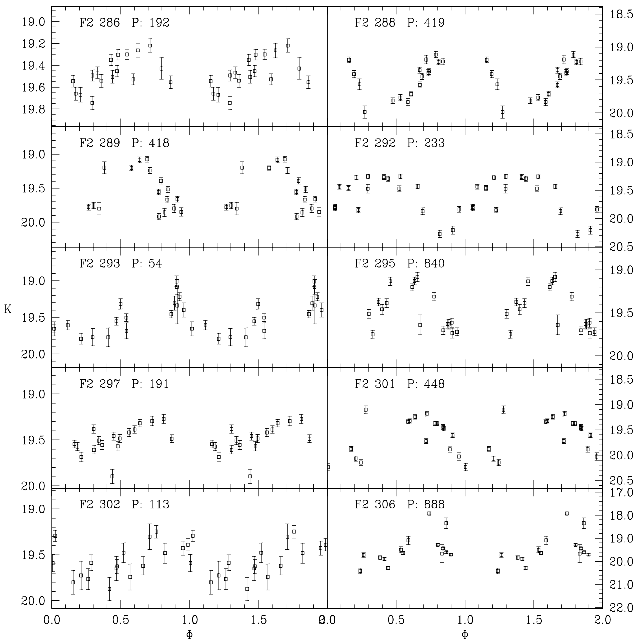
F2 286 P: 192
F2 288 P: 419
F2 289 P: 418
F2 292 P: 233
F2 293 P: 54
F2 295 P: 840
F2 297 P: 191
F2 301 P: 448
F2 302 P: 113
F2 306 P: 888
K
ϕ

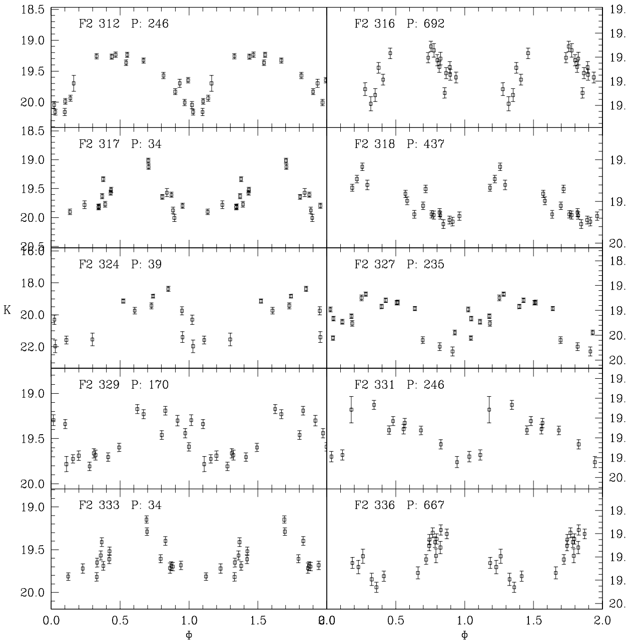
F2 312 P: 246
F2 316 P: 692
F2 317 P: 34
F2 318 P: 437
F2 324 P: 39
F2 327 P: 235
F2 329 P: 170
F2 331 P: 246
F2 333 P: 34
F2 336 P: 667
K
φ

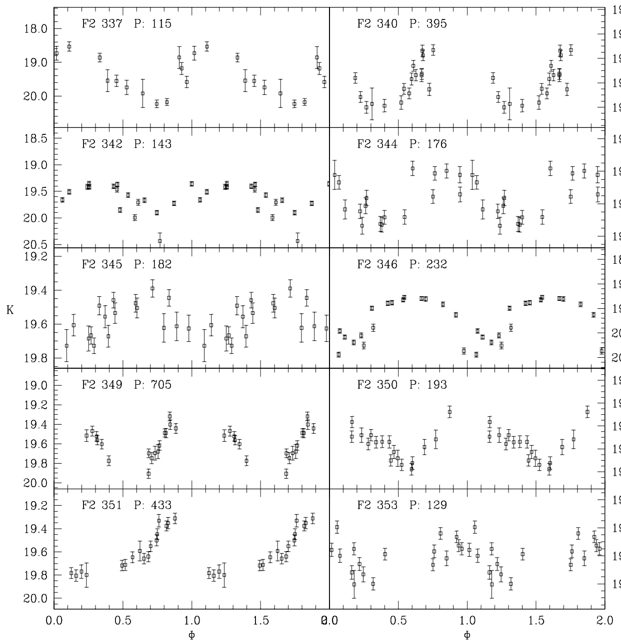
F2 337 P: 115
F2 340 P: 395
F2 342 P: 143
F2 344 P: 176
F2 345 P: 182
F2 346 P: 232
F2 349 P: 705
F2 350 P: 193
F2 351 P: 433
F2 353 P: 129
K
φ

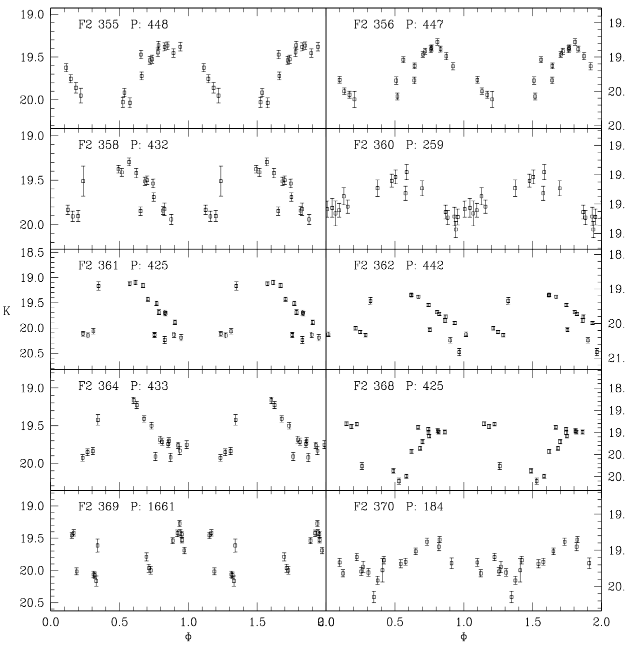
F2 355 P: 448
F2 356 P: 447
F2 358 P: 432
F2 360 P: 259
F2 361 P: 425
F2 362 P: 442
F2 364 P: 433
F2 368 P: 425
F2 369 P: 1661
F2 370 P: 184
K
φ

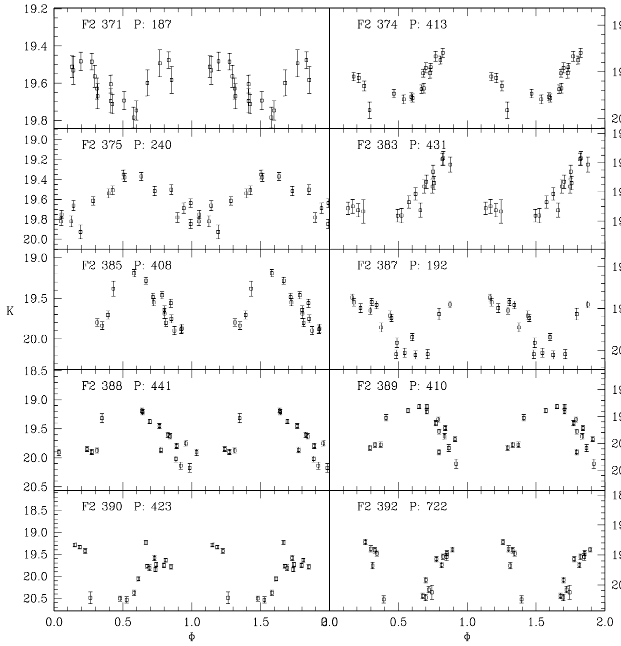
F2 371 P: 187
F2 374 P: 413
F2 375 P: 240
F2 383 P: 431
F2 385 P: 408
F2 387 P: 192
F2 388 P: 441
F2 389 P: 410
F2 390 P: 423
F2 392 P: 722
K
φ

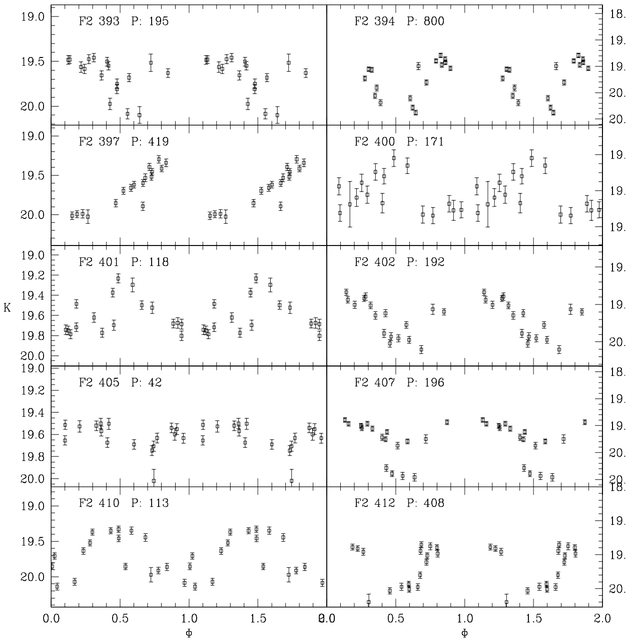
F2 393 P: 195
F2 394 P: 800
F2 397 P: 419
F2 400 P: 171
F2 401 P: 118
F2 402 P: 192
F2 405 P: 42
F2 407 P: 196
F2 410 P: 113
F2 412 P: 408
K
ϕ

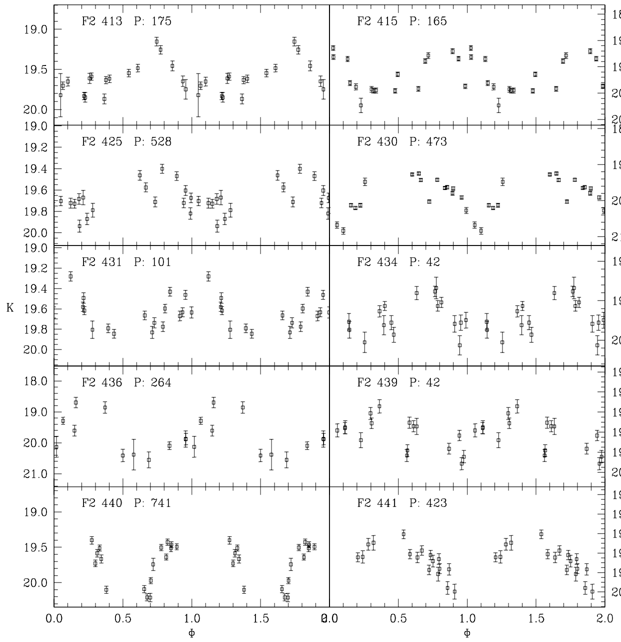
F2 413 P: 175
F2 415 P: 165
F2 425 P: 528
F2 430 P: 473
F2 431 P: 101
F2 434 P: 42
F2 436 P: 264
F2 439 P: 42
F2 440 P: 741
F2 441 P: 423
K
ϕ

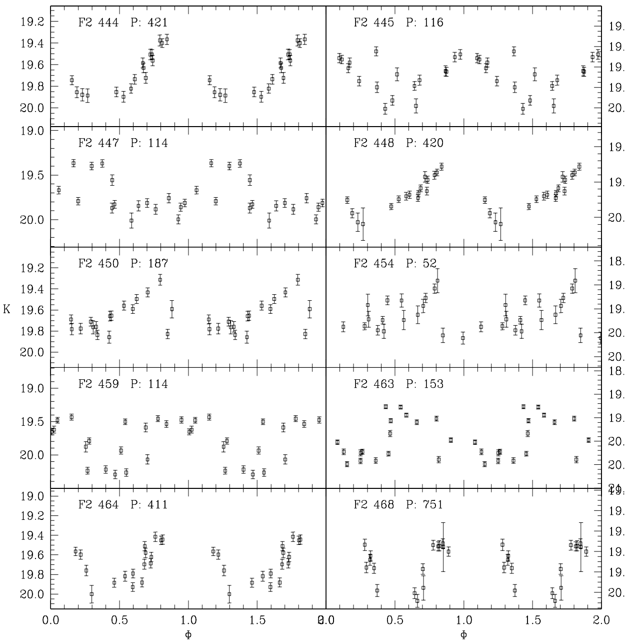
F2 444 P: 421
F2 445 P: 116
F2 447 P: 114
F2 448 P: 420
F2 450 P: 187
F2 454 P: 52
F2 459 P: 114
F2 463 P: 153
F2 464 P: 411
F2 468 P: 751
K
ϕ

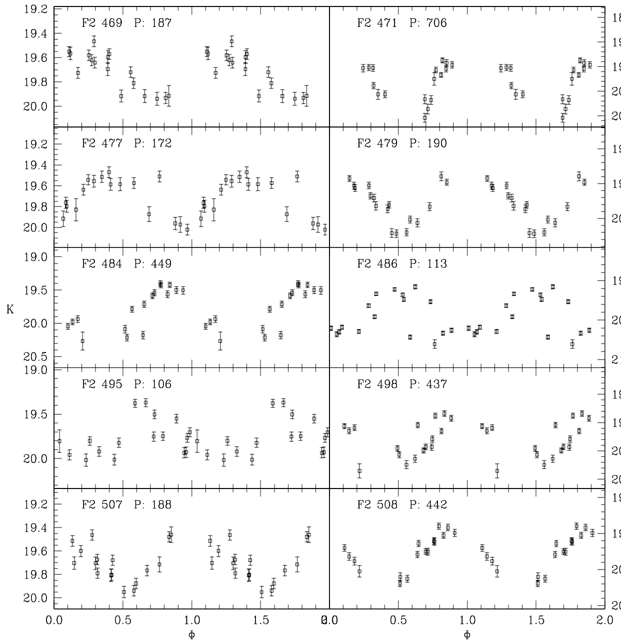
F2 469 P: 187
F2 471 P: 706
F2 477 P: 172
F2 479 P: 190
F2 484 P: 449
F2 486 P: 113
F2 495 P: 106
F2 498 P: 437
F2 507 P: 188
F2 508 P: 442
K
ϕ

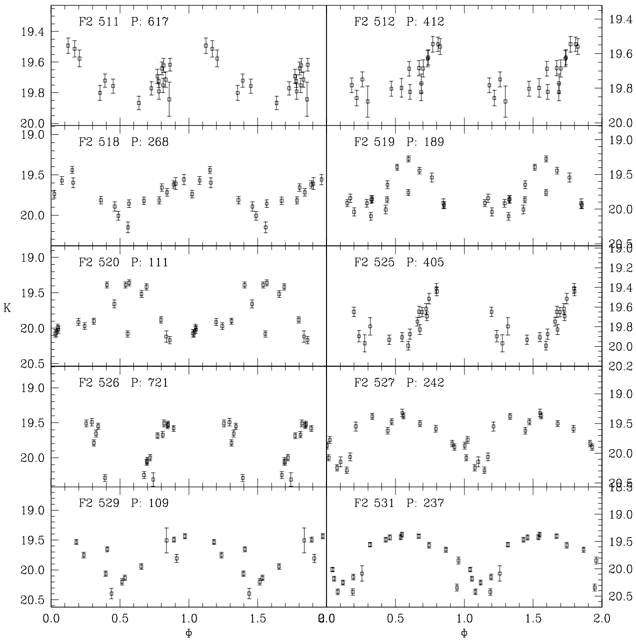

F2 511 P: 617
F2 512 P: 412
F2 518 P: 268
F2 519 P: 189
F2 520 P: 111
F2 525 P: 405
F2 526 P: 721
F2 527 P: 242
F2 529 P: 109
F2 531 P: 237
K
ϕ

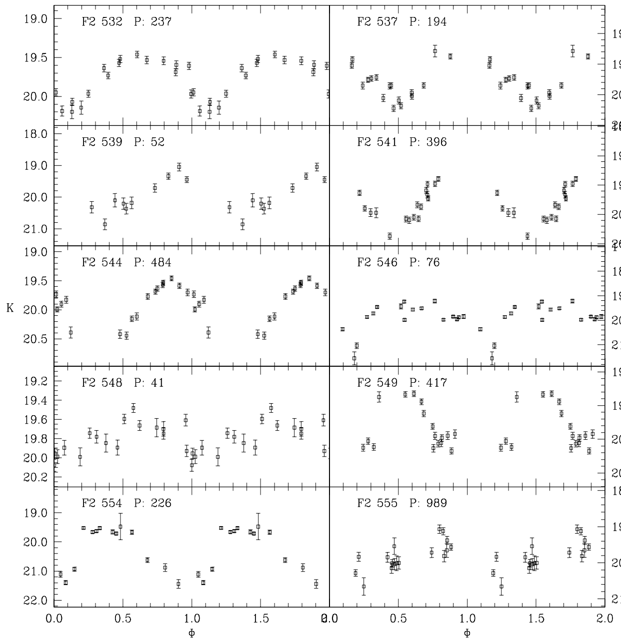

F2 532 P: 237
F2 537 P: 194
F2 539 P: 52
F2 541 P: 396
F2 544 P: 484
F2 546 P: 76
F2 548 P: 41
F2 549 P: 417
F2 554 P: 226
F2 555 P: 989
K
ϕ

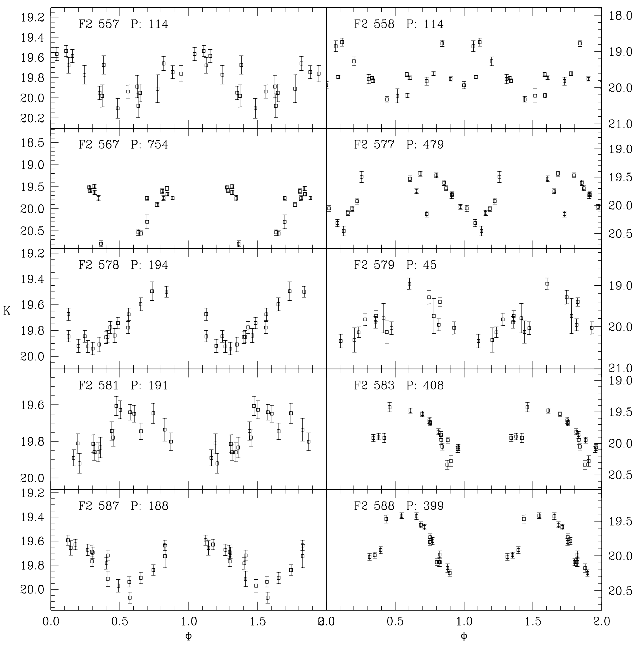

F2 557 P: 114
F2 558 P: 114
F2 567 P: 754
F2 577 P: 479
F2 578 P: 194
F2 579 P: 45
F2 581 P: 191
F2 583 P: 408
F2 587 P: 188
F2 588 P: 399
K
ϕ

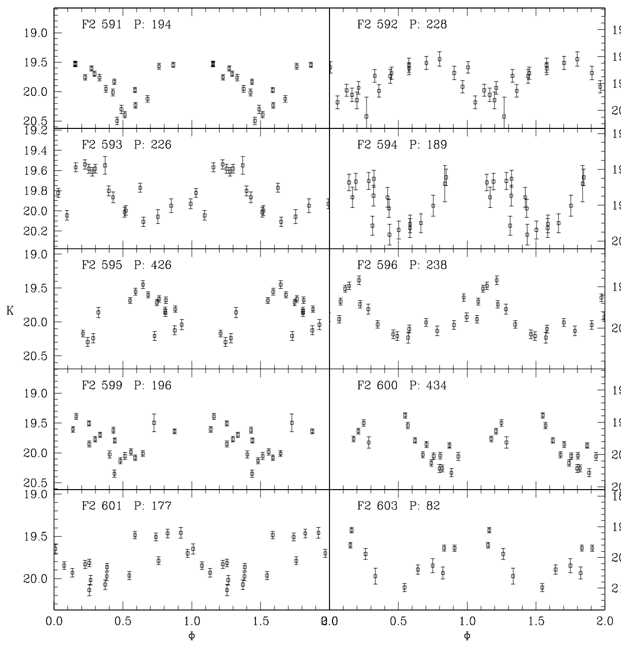

F2 591 P: 194
F2 592 P: 228
F2 593 P: 226
F2 594 P: 189
F2 595 P: 426
F2 596 P: 238
F2 599 P: 196
F2 600 P: 434
F2 601 P: 177
F2 603 P: 82
K
ϕ

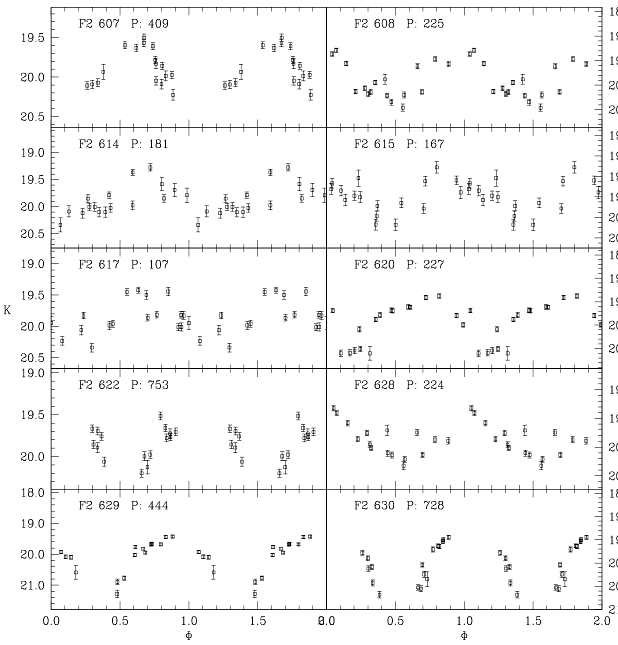
F2 607 P: 409
F2 608 P: 225
F2 614 P: 181
F2 615 P: 167
F2 617 P: 107
F2 620 P: 227
F2 622 P: 753
F2 628 P: 224
F2 629 P: 444
F2 630 P: 728
K
ϕ
ϕ

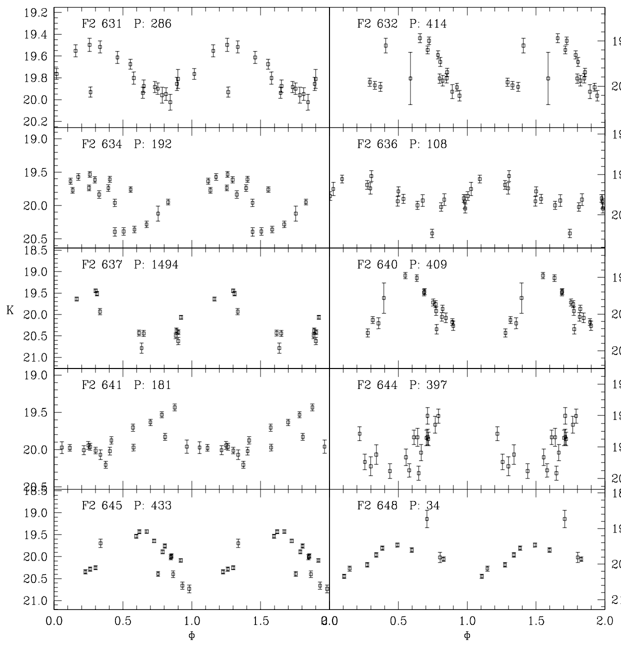
F2 631 P: 286
F2 632 P: 414
F2 634 P: 192
F2 636 P: 108
F2 637 P: 1494
F2 640 P: 409
F2 641 P: 181
F2 644 P: 397
F2 645 P: 433
F2 648 P: 34
K
ϕ
ϕ

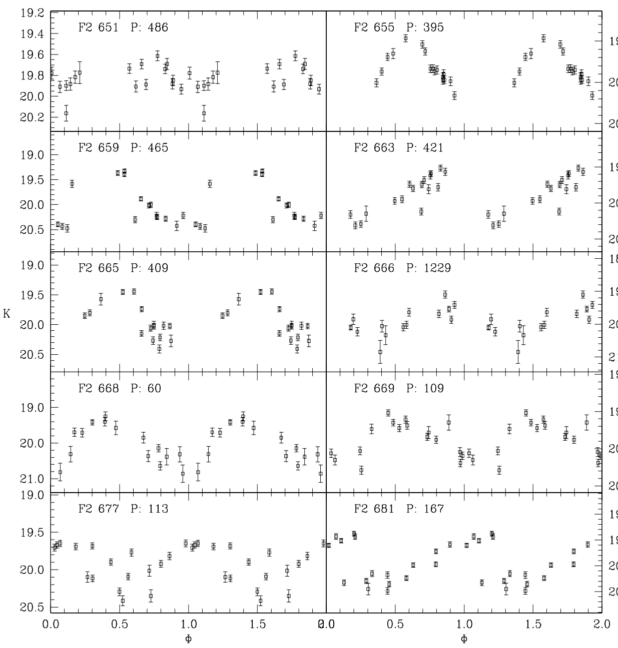
F2 651 P: 486
F2 655 P: 395
F2 659 P: 465
F2 663 P: 421
F2 665 P: 409
F2 666 P: 1229
F2 668 P: 60
F2 669 P: 109
F2 677 P: 113
F2 681 P: 167
K
ϕ
ϕ

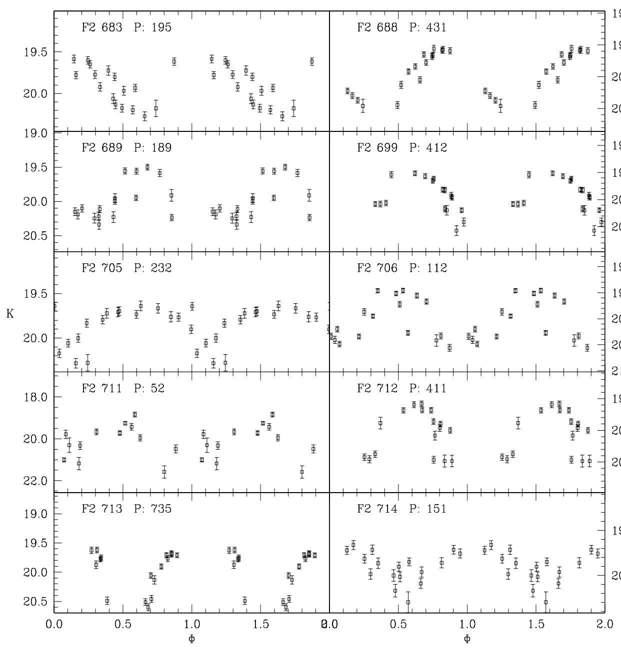
F2 683 P: 195
F2 688 P: 431
F2 689 P: 189
F2 699 P: 412
F2 705 P: 232
F2 706 P: 112
F2 711 P: 52
F2 712 P: 411
F2 713 P: 735
F2 714 P: 151
K
ϕ
ϕ

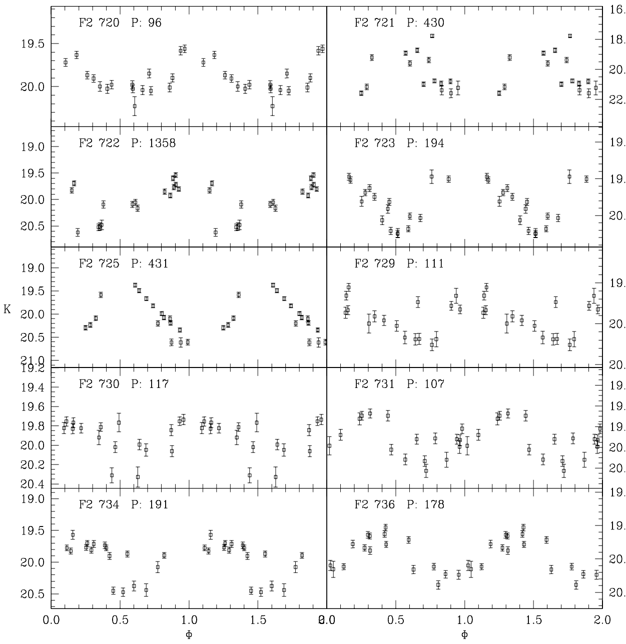
F2 720 P: 96
F2 721 P: 430
F2 722 P: 1358
F2 723 P: 194
F2 725 P: 431
F2 729 P: 111
F2 730 P: 117
F2 731 P: 107
F2 734 P: 191
F2 736 P: 178
K
ϕ

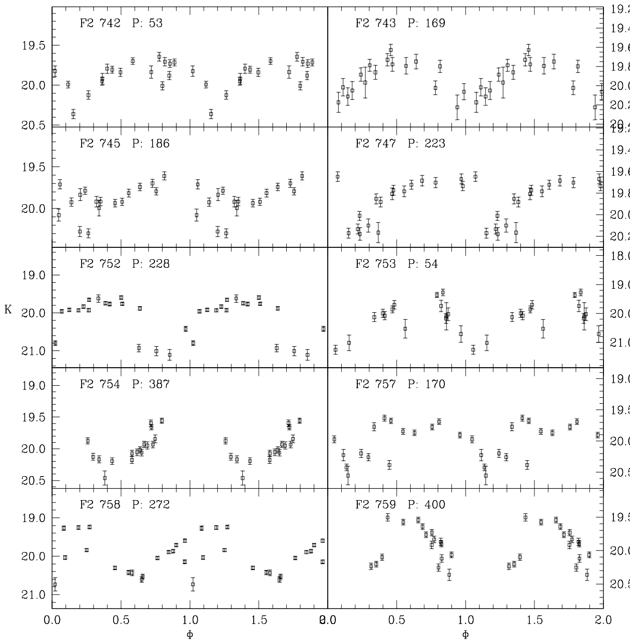
F2 742 P: 53
F2 743 P: 169
F2 745 P: 186
F2 747 P: 223
F2 752 P: 228
F2 753 P: 54
F2 754 P: 387
F2 757 P: 170
F2 758 P: 272
F2 759 P: 400
K
ϕ

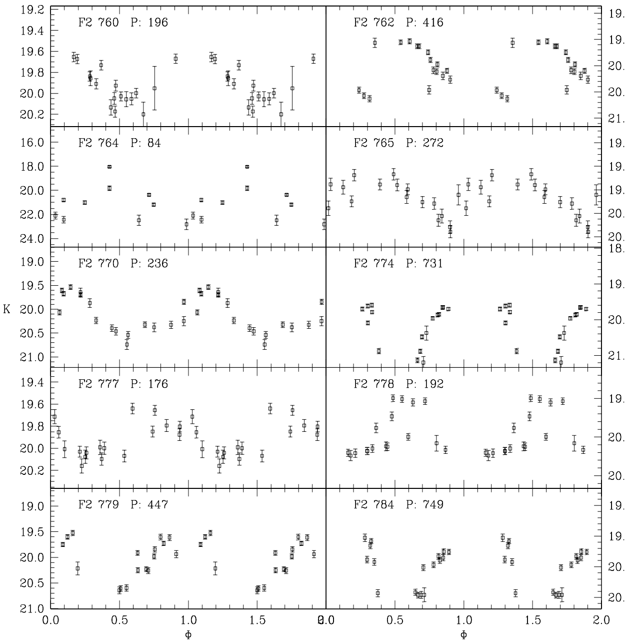
F2 760 P: 196
F2 762 P: 416
F2 764 P: 84
F2 765 P: 272
F2 770 P: 236
F2 774 P: 731
F2 777 P: 176
F2 778 P: 192
F2 779 P: 447
F2 784 P: 749
K
ϕ

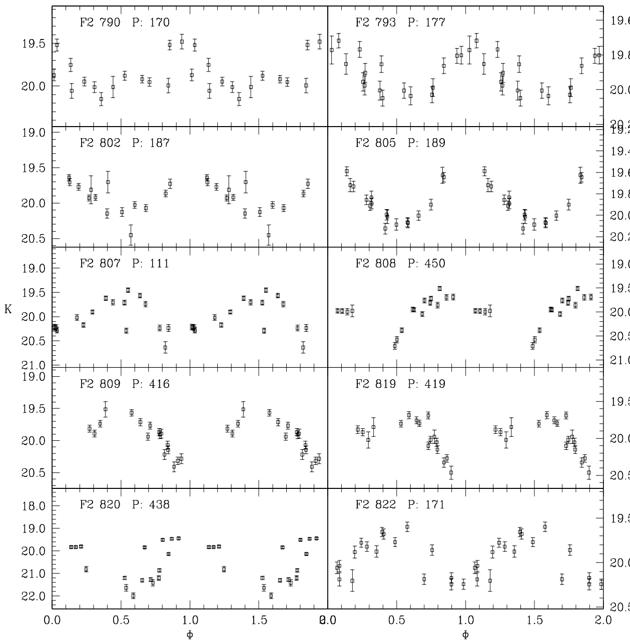
F2 790 P: 170
F2 793 P: 177
F2 802 P: 187
F2 805 P: 189
F2 807 P: 111
F2 808 P: 450
F2 809 P: 416
F2 819 P: 419
F2 820 P: 438
F2 822 P: 171
K
ϕ

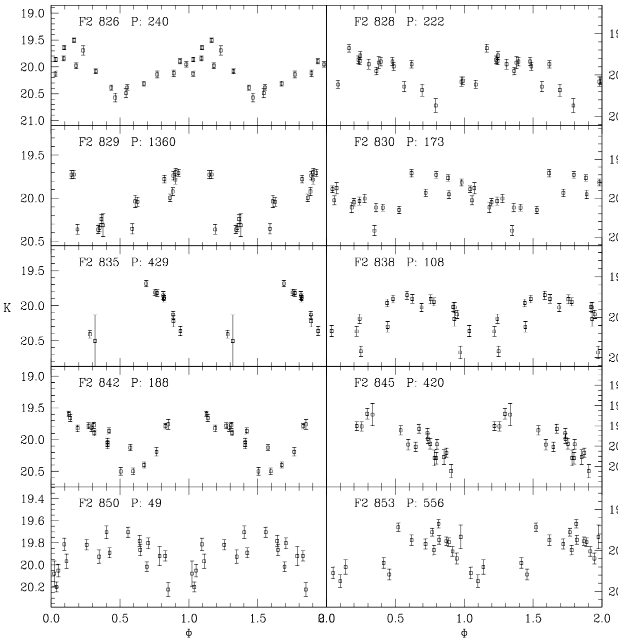
F2 826 P: 240
F2 828 P: 222
F2 829 P: 1360
F2 830 P: 173
F2 835 P: 429
F2 838 P: 108
F2 842 P: 188
F2 845 P: 420
F2 850 P: 49
F2 853 P: 556
K
ϕ

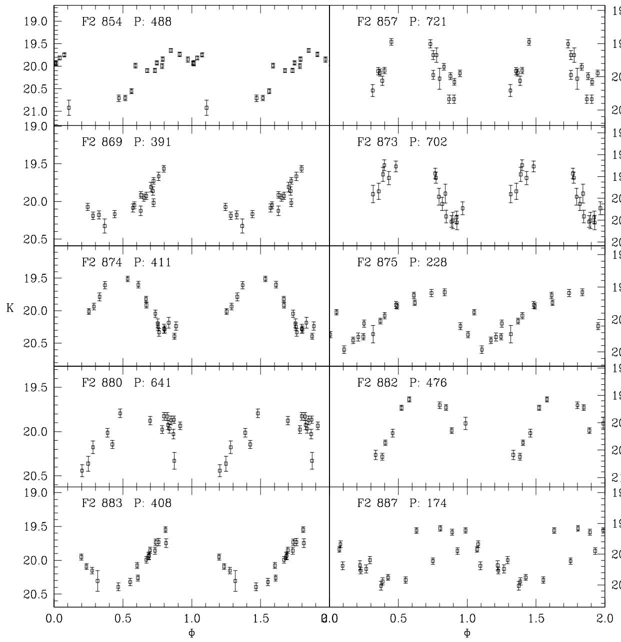
F2 854 P: 488
F2 857 P: 721
F2 869 P: 391
F2 873 P: 702
F2 874 P: 411
F2 875 P: 228
F2 880 P: 641
F2 882 P: 476
F2 883 P: 408
F2 887 P: 174
K
ϕ

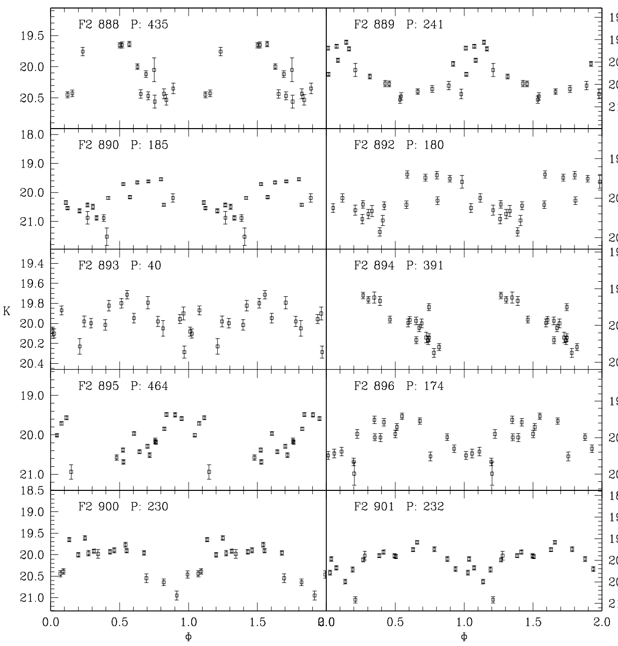
F2 888 P: 435
F2 889 P: 241
F2 890 P: 185
F2 892 P: 180
F2 893 P: 40
F2 894 P: 391
F2 895 P: 464
F2 896 P: 174
F2 900 P: 230
F2 901 P: 232
K
ϕ

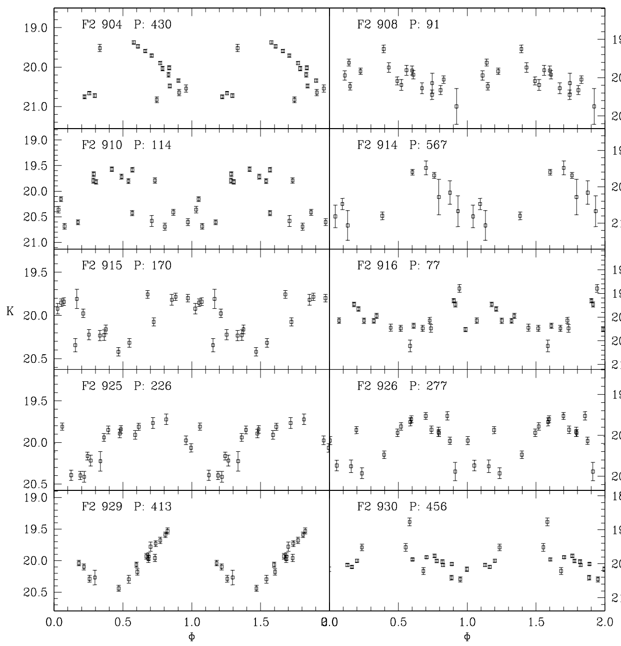
F2 904 P: 430
F2 908 P: 91
F2 910 P: 114
F2 914 P: 567
F2 915 P: 170
F2 916 P: 77
F2 925 P: 226
F2 926 P: 277
F2 929 P: 413
F2 930 P: 456
K
ϕ

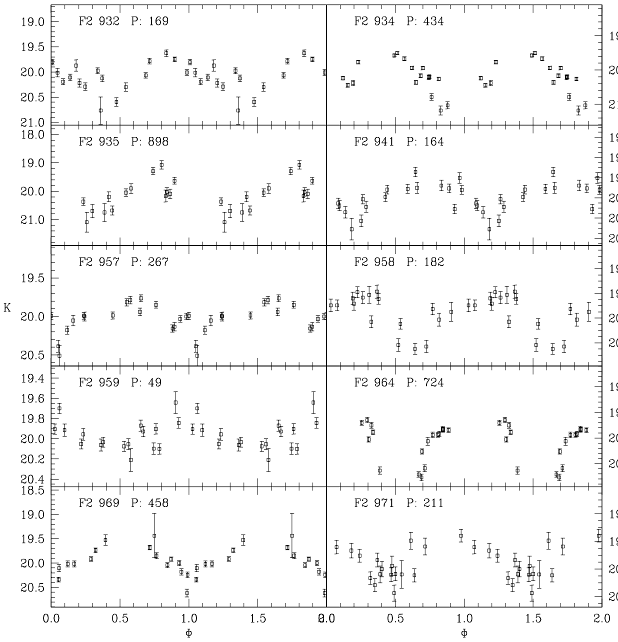
F2 932 P: 169
F2 934 P: 434
F2 935 P: 898
F2 941 P: 164
F2 957 P: 267
F2 958 P: 182
F2 959 P: 49
F2 964 P: 724
F2 969 P: 458
F2 971 P: 211
K
ϕ

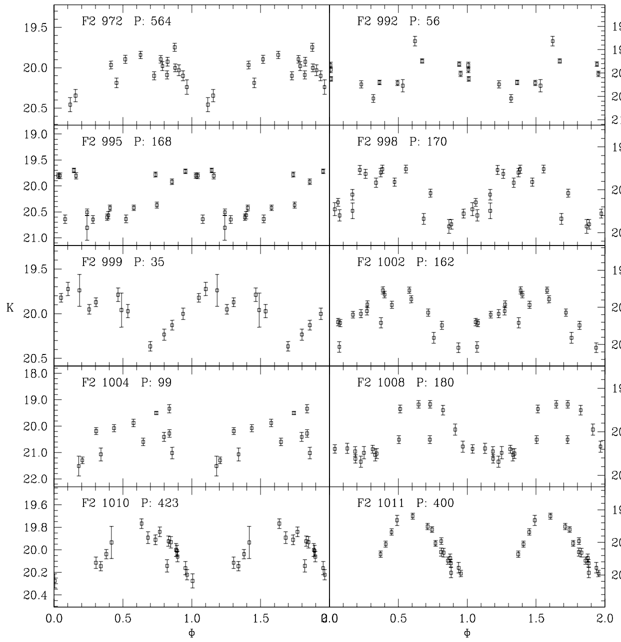
F2 972 P: 564
F2 992 P: 56
F2 995 P: 168
F2 998 P: 170
F2 999 P: 35
F2 1002 P: 162
F2 1004 P: 99
F2 1008 P: 180
F2 1010 P: 423
F2 1011 P: 400
K
ϕ

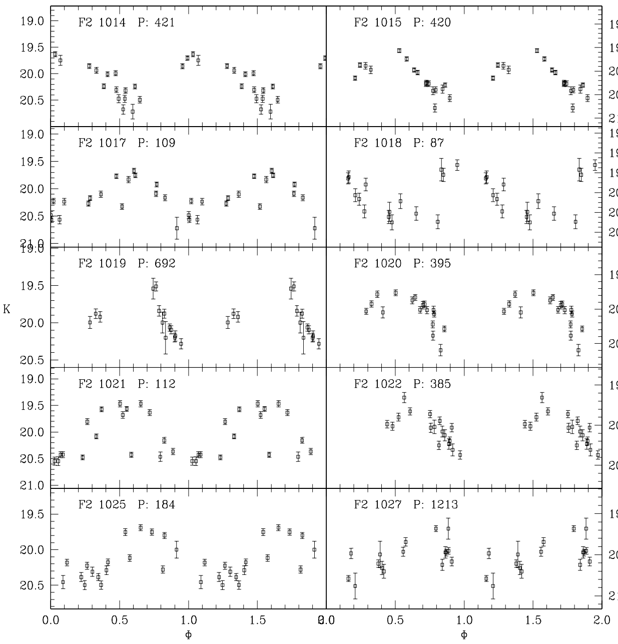
F2 1014 P: 421
F2 1015 P: 420
F2 1017 P: 109
F2 1018 P: 87
F2 1019 P: 692
F2 1020 P: 395
F2 1021 P: 112
F2 1022 P: 385
F2 1025 P: 184
F2 1027 P: 1213
K
ϕ

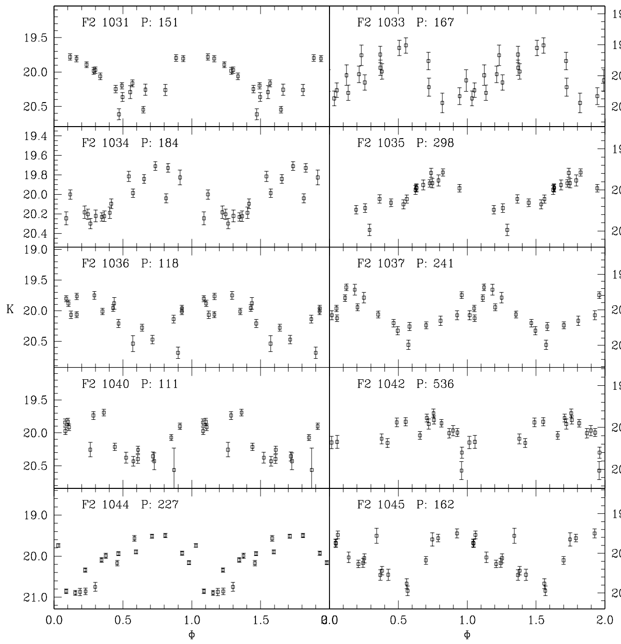
F2 1031 P: 151
F2 1033 P: 167
F2 1034 P: 184
F2 1035 P: 298
F2 1036 P: 118
F2 1037 P: 241
F2 1040 P: 111
F2 1042 P: 536
F2 1044 P: 227
F2 1045 P: 162
K
ϕ

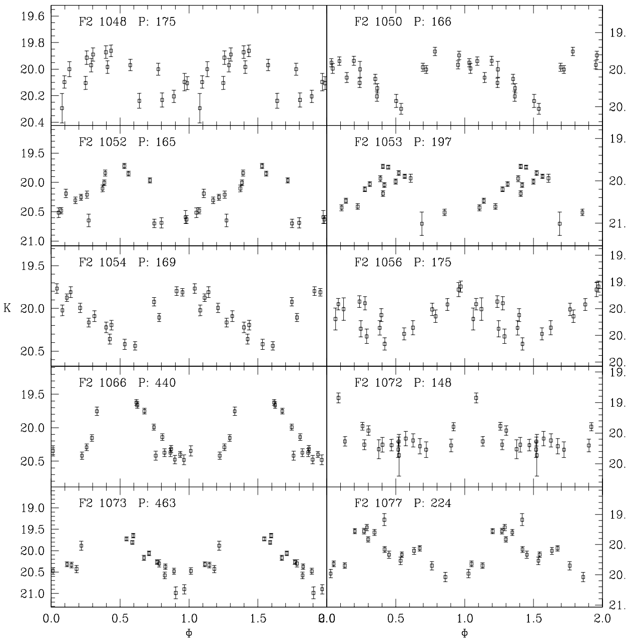

F2 1048 P: 175
F2 1050 P: 166
F2 1052 P: 165
F2 1053 P: 197
F2 1054 P: 169
F2 1056 P: 175
F2 1066 P: 440
F2 1072 P: 148
F2 1073 P: 463
F2 1077 P: 224
K
φ
φ

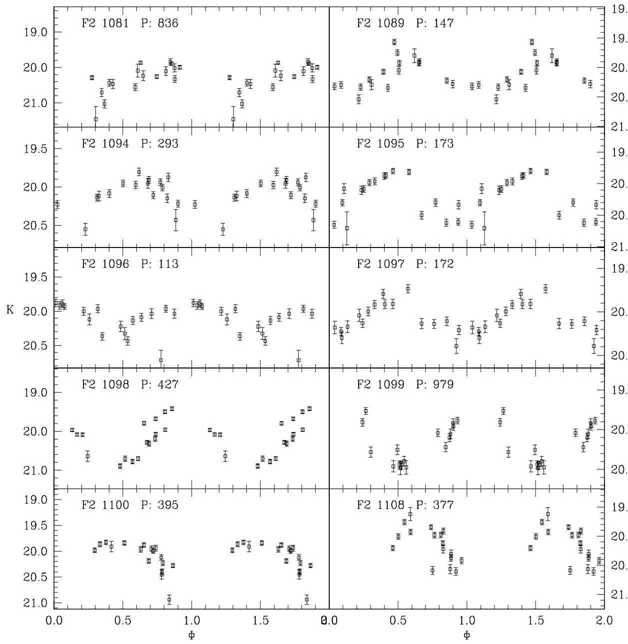

F2 1081 P: 836
F2 1089 P: 147
F2 1094 P: 293
F2 1095 P: 173
F2 1096 P: 113
F2 1097 P: 172
F2 1098 P: 427
F2 1099 P: 979
F2 1100 P: 395
F2 1108 P: 377
K
φ
φ

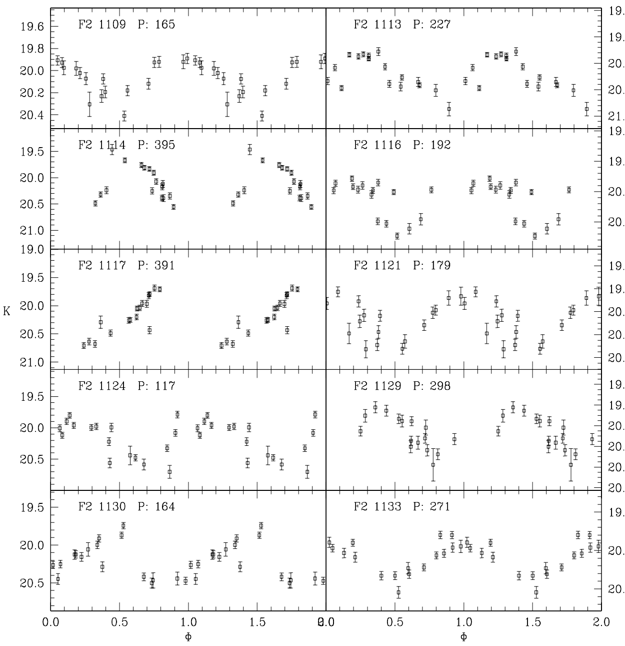

F2 1109 P: 165
F2 1113 P: 227
F2 1114 P: 395
F2 1116 P: 192
F2 1117 P: 391
F2 1121 P: 179
F2 1124 P: 117
F2 1129 P: 298
F2 1130 P: 164
F2 1133 P: 271
K
φ
φ

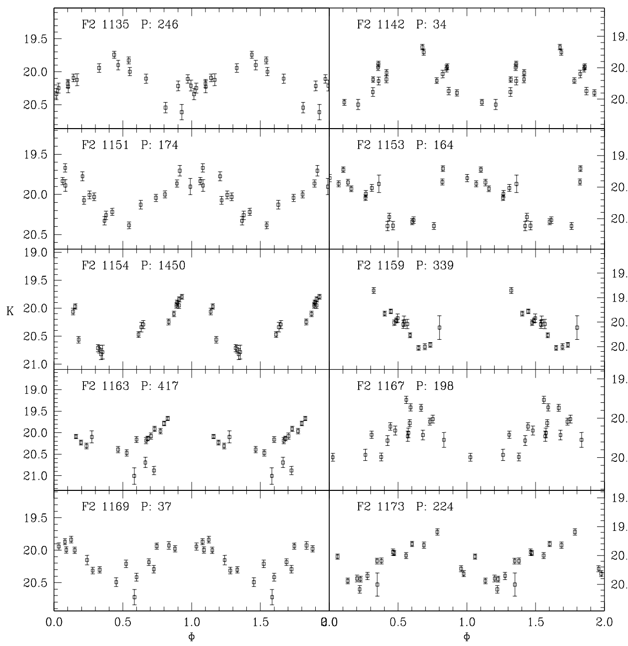

F2 1135 P: 246
F2 1142 P: 34
F2 1151 P: 174
F2 1153 P: 164
F2 1154 P: 1450
F2 1159 P: 339
F2 1163 P: 417
F2 1167 P: 198
F2 1169 P: 37
F2 1173 P: 224
K
φ
φ

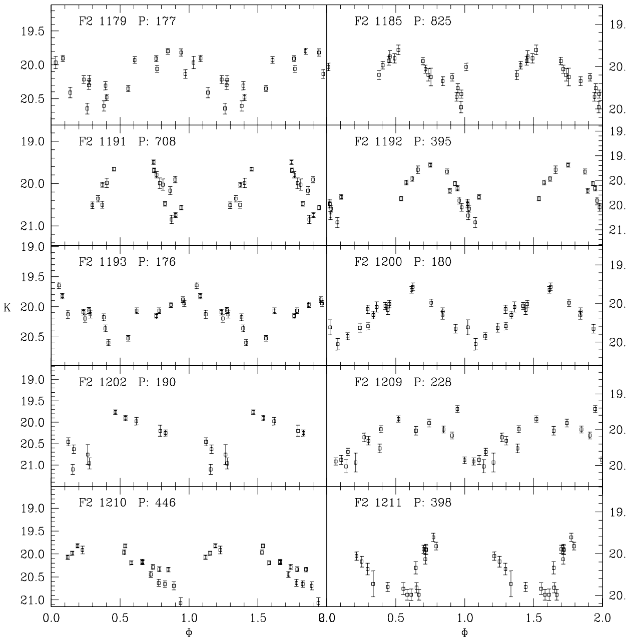
F2 1179 P: 177
F2 1185 P: 825
F2 1191 P: 708
F2 1192 P: 395
F2 1193 P: 176
F2 1200 P: 180
F2 1202 P: 190
F2 1209 P: 228
F2 1210 P: 446
F2 1211 P: 398
K
ϕ

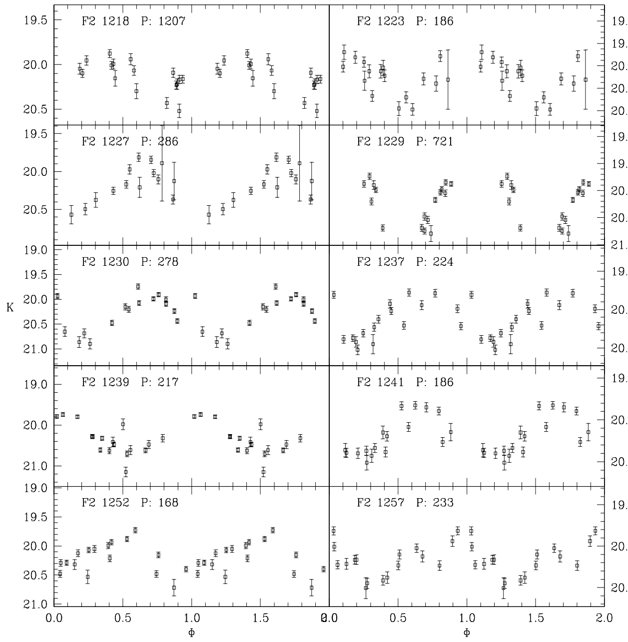
F2 1218 P: 1207
F2 1223 P: 186
F2 1227 P: 286
F2 1229 P: 721
F2 1230 P: 278
F2 1237 P: 224
F2 1239 P: 217
F2 1241 P: 186
F2 1252 P: 168
F2 1257 P: 233
K
ϕ

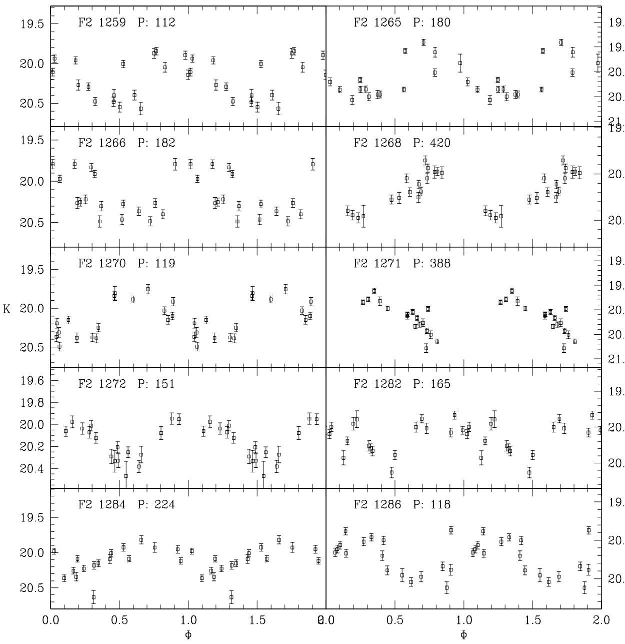
F2 1259 P: 112
F2 1265 P: 180
F2 1266 P: 182
F2 1268 P: 420
F2 1270 P: 119
F2 1271 P: 388
F2 1272 P: 151
F2 1282 P: 165
F2 1284 P: 224
F2 1286 P: 118
K
ϕ

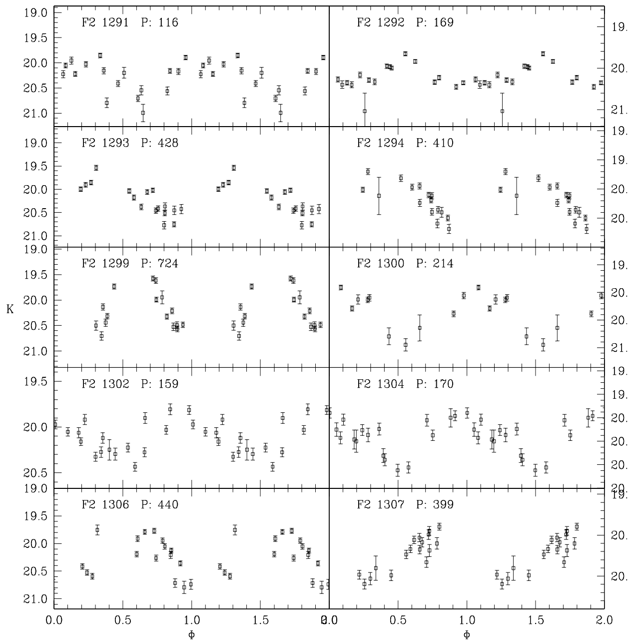
F2 1291 P: 116
F2 1292 P: 169
F2 1293 P: 428
F2 1294 P: 410
F2 1299 P: 724
F2 1300 P: 214
F2 1302 P: 159
F2 1304 P: 170
F2 1306 P: 440
F2 1307 P: 399
K
ϕ

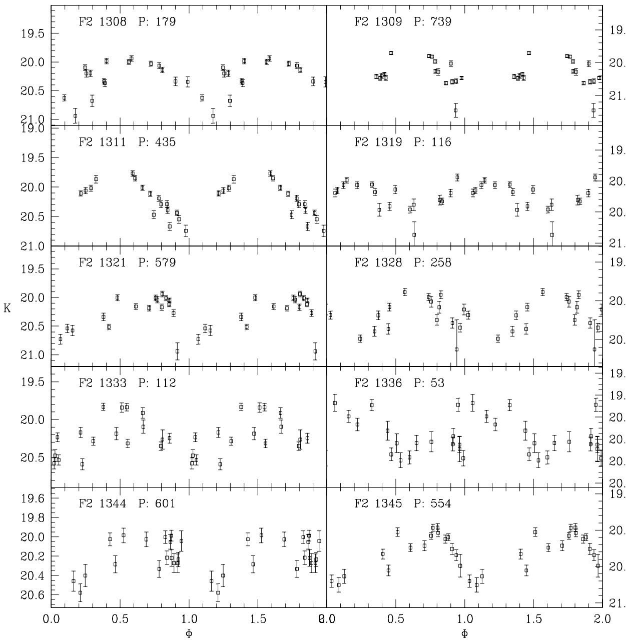
F2 1308 P: 179
F2 1309 P: 739
F2 1311 P: 435
F2 1319 P: 116
F2 1321 P: 579
F2 1328 P: 258
F2 1333 P: 112
F2 1336 P: 53
F2 1344 P: 601
F2 1345 P: 554
K
ϕ

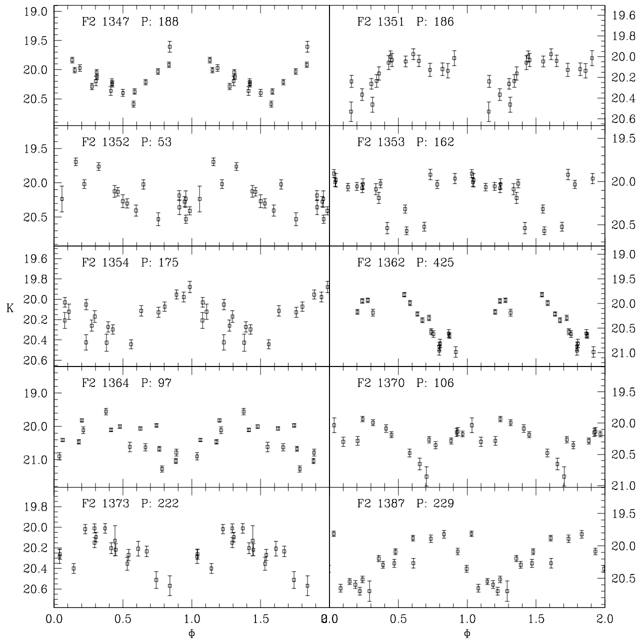
F2 1347 P: 188
F2 1351 P: 186
F2 1352 P: 53
F2 1353 P: 162
F2 1354 P: 175
F2 1362 P: 425
F2 1364 P: 97
F2 1370 P: 106
F2 1373 P: 222
F2 1387 P: 229
K
ϕ

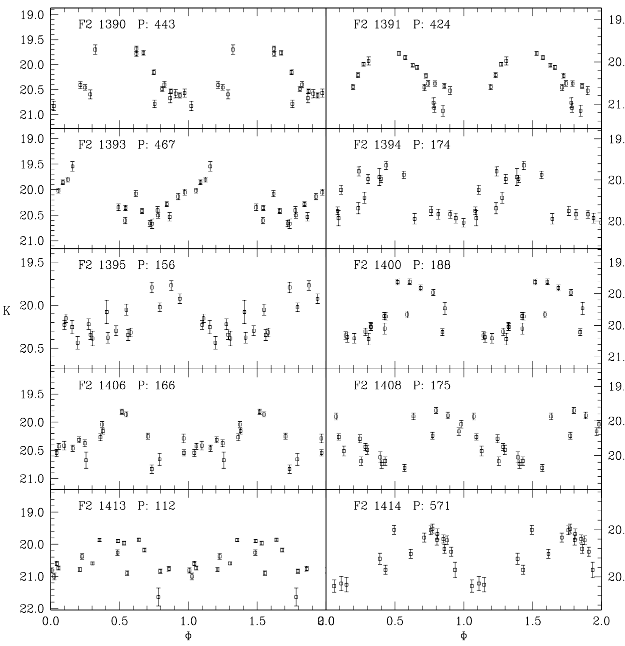
F2 1390 P: 443
F2 1391 P: 424
F2 1393 P: 467
F2 1394 P: 174
F2 1395 P: 156
F2 1400 P: 188
F2 1406 P: 166
F2 1408 P: 175
F2 1413 P: 112
F2 1414 P: 571
K
ϕ

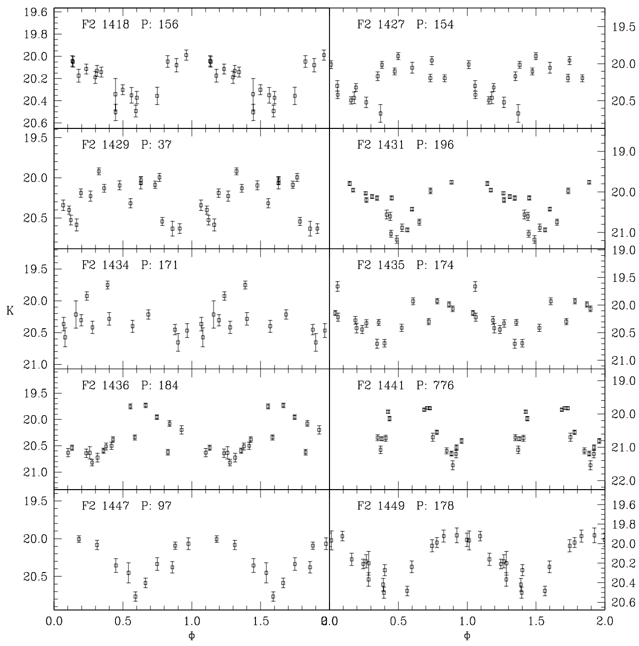
F2 1418 P: 156
F2 1427 P: 154
F2 1429 P: 37
F2 1431 P: 196
F2 1434 P: 171
F2 1435 P: 174
F2 1436 P: 184
F2 1441 P: 776
F2 1447 P: 97
F2 1449 P: 178
K
ϕ

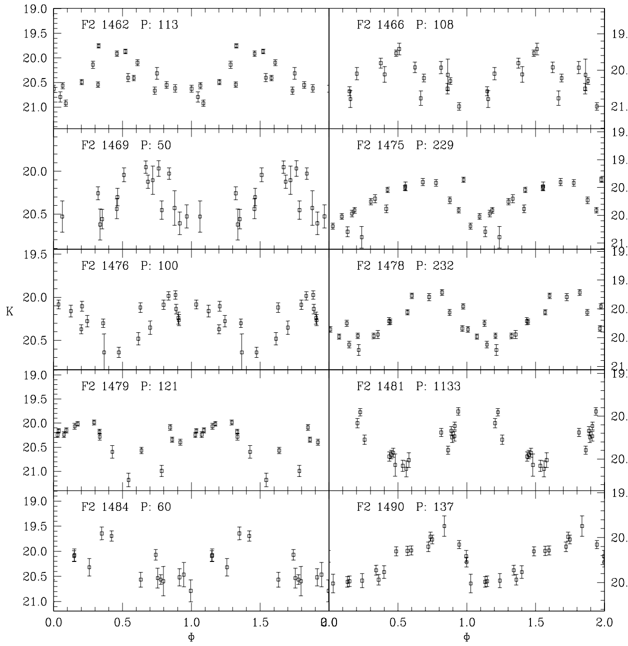
F2 1462 P: 113
F2 1466 P: 108
F2 1469 P: 50
F2 1475 P: 229
F2 1476 P: 100
F2 1478 P: 232
F2 1479 P: 121
F2 1481 P: 1133
F2 1484 P: 60
F2 1490 P: 137
K
ϕ

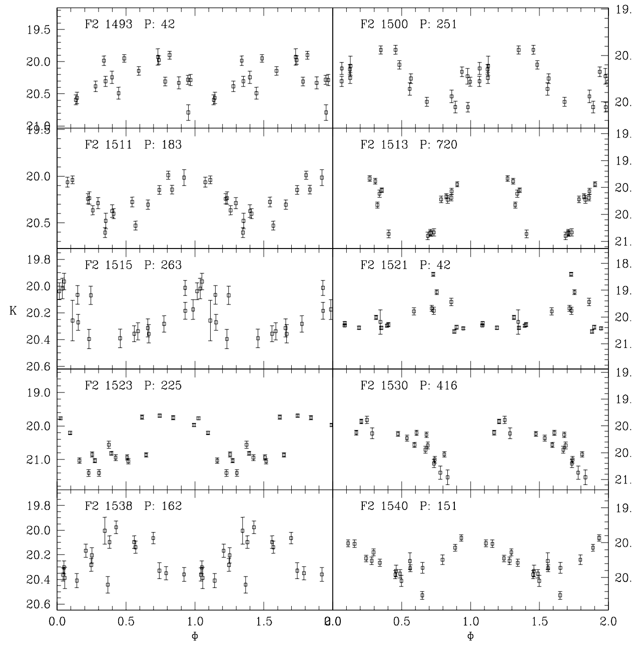
F2 1493 P: 42
F2 1500 P: 251
F2 1511 P: 183
F2 1513 P: 720
F2 1515 P: 263
F2 1521 P: 42
F2 1523 P: 225
F2 1530 P: 416
F2 1538 P: 162
F2 1540 P: 151
K
ϕ

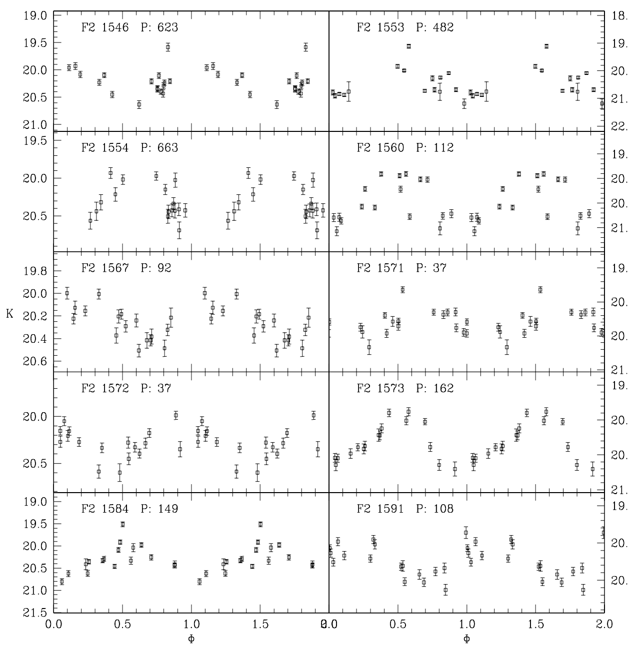
F2 1546 P: 623
F2 1553 P: 482
F2 1554 P: 663
F2 1560 P: 112
F2 1567 P: 92
F2 1571 P: 37
F2 1572 P: 37
F2 1573 P: 162
F2 1584 P: 149
F2 1591 P: 108
K
ϕ

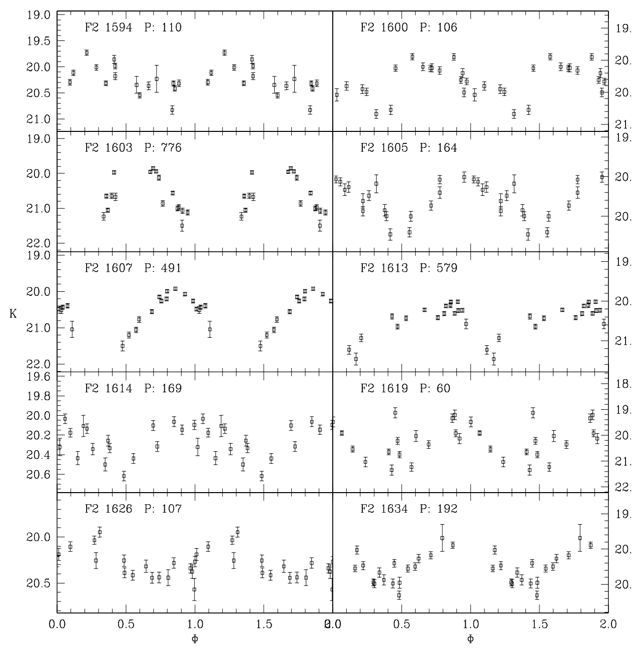
F2 1594 P: 110
F2 1600 P: 106
F2 1603 P: 776
F2 1605 P: 164
F2 1607 P: 491
F2 1613 P: 579
F2 1614 P: 169
F2 1619 P: 60
F2 1626 P: 107
F2 1634 P: 192
K
ϕ

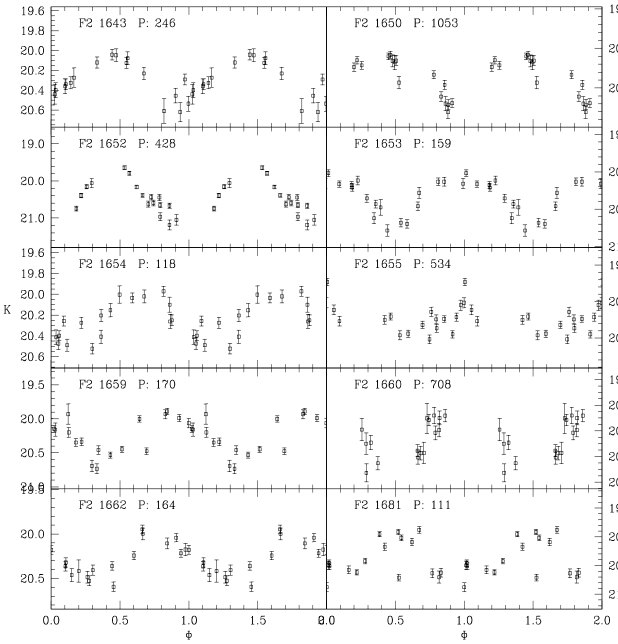
F2 1643 P: 246
F2 1650 P: 1053
F2 1652 P: 428
F2 1653 P: 159
F2 1654 P: 118
F2 1655 P: 534
F2 1659 P: 170
F2 1660 P: 708
F2 1662 P: 164
F2 1681 P: 111
K
ϕ

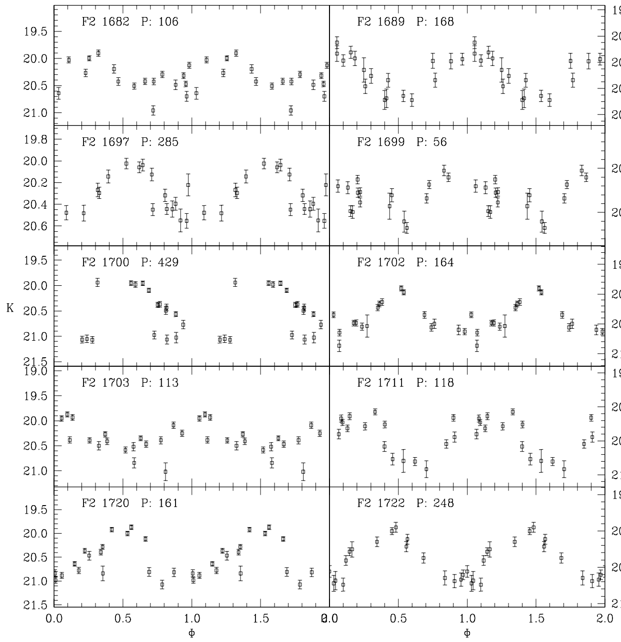
F2 1682 P: 106
F2 1689 P: 168
F2 1697 P: 285
F2 1699 P: 56
F2 1700 P: 429
F2 1702 P: 164
F2 1703 P: 113
F2 1711 P: 118
F2 1720 P: 161
F2 1722 P: 248
K
ϕ

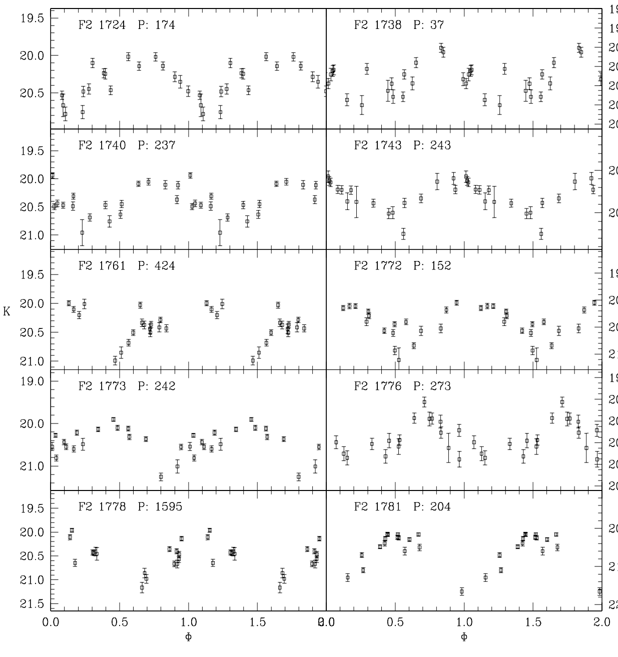
F2 1724 P: 174
F2 1738 P: 37
F2 1740 P: 237
F2 1743 P: 243
F2 1761 P: 424
F2 1772 P: 152
F2 1773 P: 242
F2 1776 P: 273
F2 1778 P: 1595
F2 1781 P: 204
K
ϕ

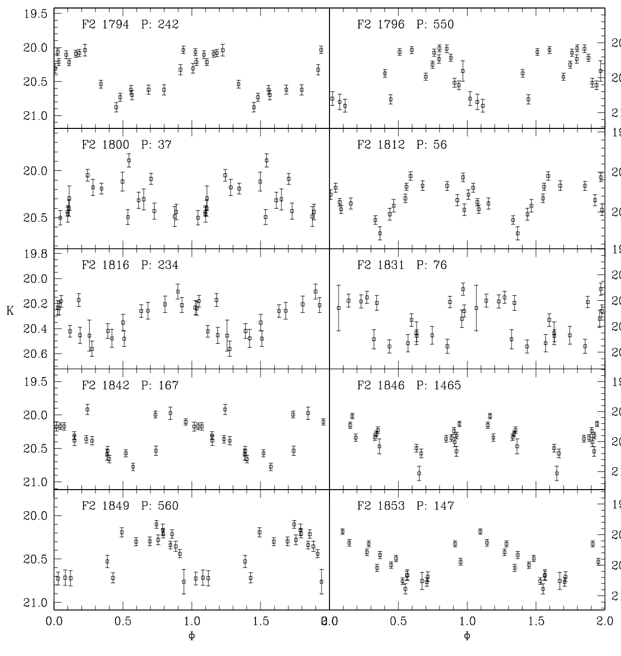
F2 1794 P: 242
F2 1796 P: 550
F2 1800 P: 37
F2 1812 P: 56
F2 1816 P: 234
F2 1831 P: 76
F2 1842 P: 167
F2 1846 P: 1465
F2 1849 P: 560
F2 1853 P: 147
K
ϕ

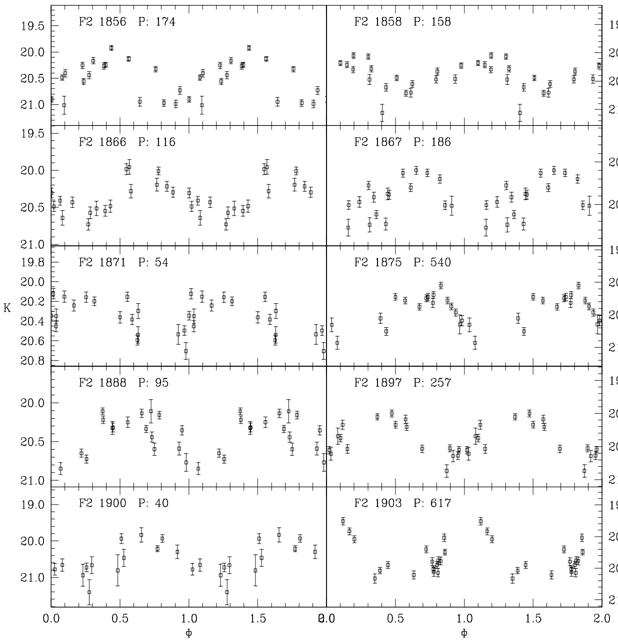
F2 1856 P: 174
F2 1858 P: 158
F2 1866 P: 116
F2 1867 P: 186
F2 1871 P: 54
F2 1875 P: 540
F2 1888 P: 95
F2 1897 P: 257
F2 1900 P: 40
F2 1903 P: 617
K
ϕ
ϕ

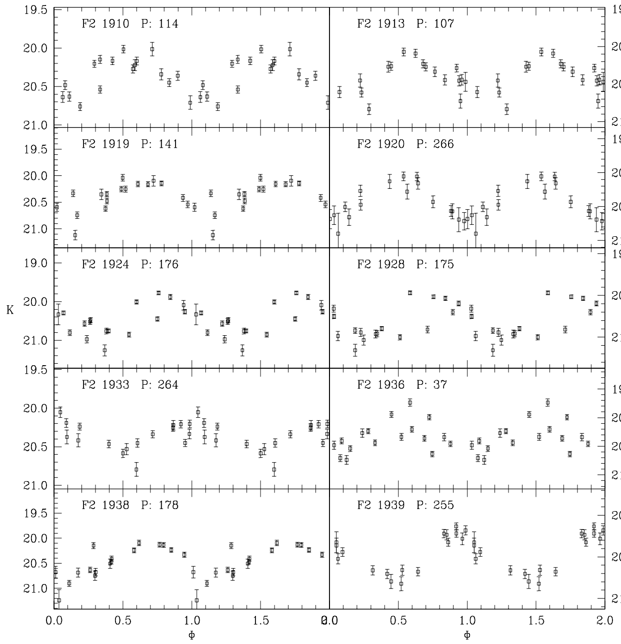
F2 1910 P: 114
F2 1913 P: 107
F2 1919 P: 141
F2 1920 P: 266
F2 1924 P: 176
F2 1928 P: 175
F2 1933 P: 264
F2 1936 P: 37
F2 1938 P: 178
F2 1939 P: 255
K
ϕ
ϕ

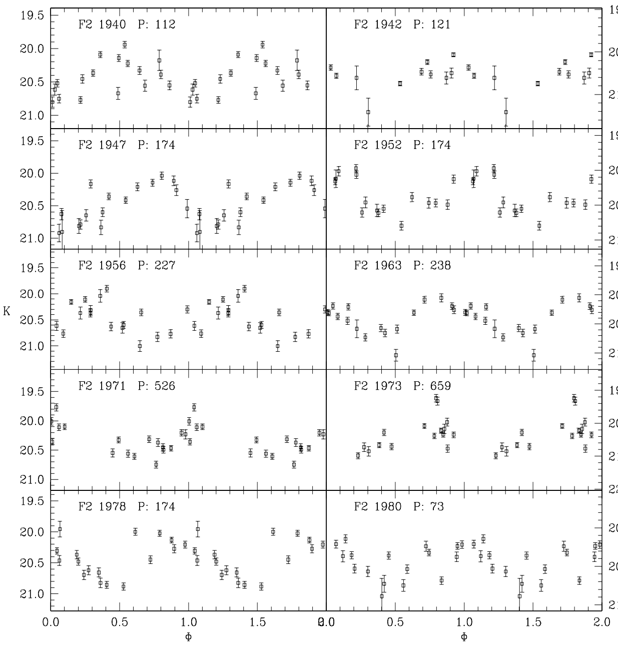
F2 1940 P: 112
F2 1942 P: 121
F2 1947 P: 174
F2 1952 P: 174
F2 1956 P: 227
F2 1963 P: 238
F2 1971 P: 526
F2 1973 P: 659
F2 1978 P: 174
F2 1980 P: 73
K
ϕ
ϕ

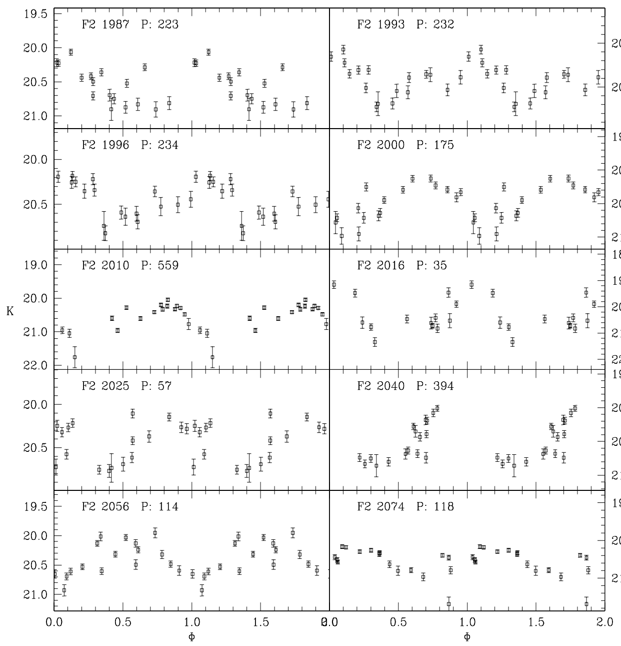
F2 1987 P: 223
F2 1993 P: 232
F2 1996 P: 234
F2 2000 P: 175
F2 2010 P: 559
F2 2016 P: 35
F2 2025 P: 57
F2 2040 P: 394
F2 2056 P: 114
F2 2074 P: 118
K
ϕ
ϕ

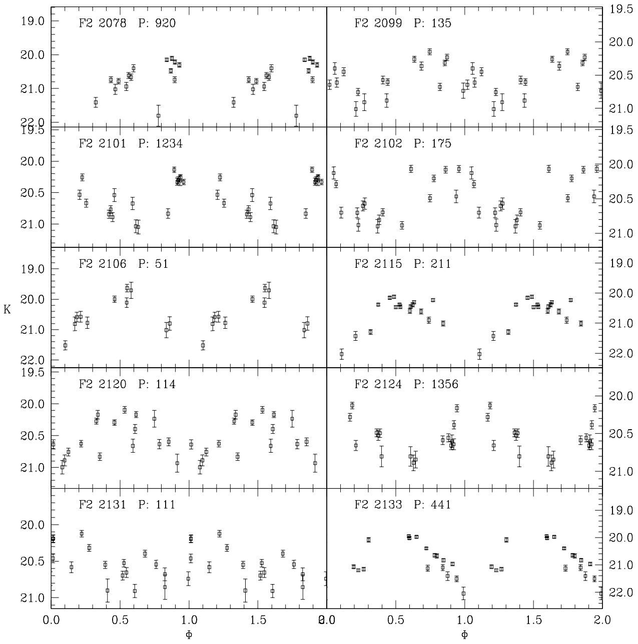
F2 2078 P: 920
F2 2099 P: 135
F2 2101 P: 1234
F2 2102 P: 175
F2 2106 P: 51
F2 2115 P: 211
F2 2120 P: 114
F2 2124 P: 1356
F2 2131 P: 111
F2 2133 P: 441
K
ϕ
ϕ

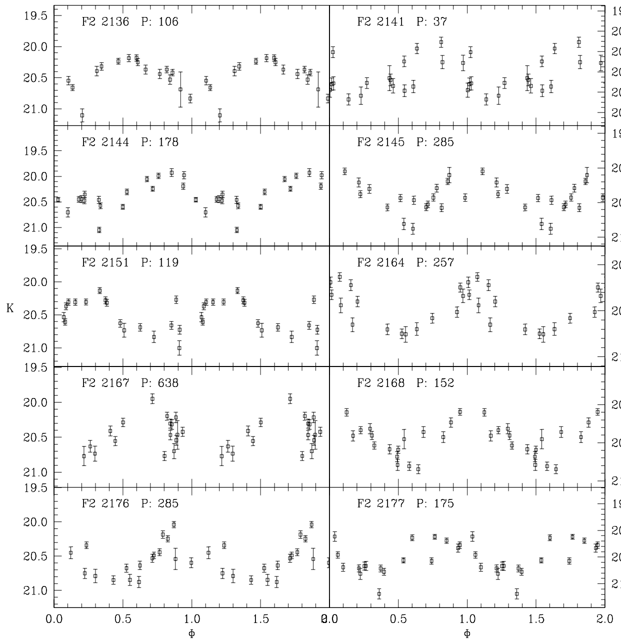
F2 2136 P: 106
F2 2141 P: 37
F2 2144 P: 178
F2 2145 P: 285
F2 2151 P: 119
F2 2164 P: 257
F2 2167 P: 638
F2 2168 P: 152
F2 2176 P: 285
F2 2177 P: 175
K
ϕ
ϕ

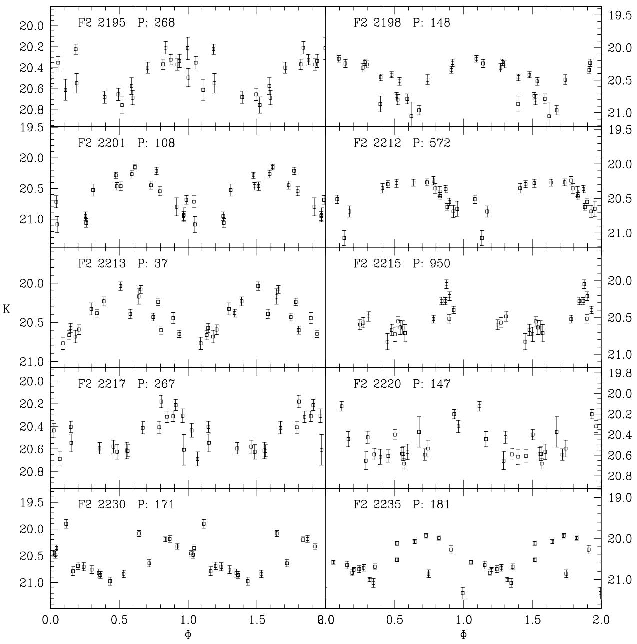
F2 2195 P: 268
F2 2198 P: 148
F2 2201 P: 108
F2 2212 P: 572
F2 2213 P: 37
F2 2215 P: 950
F2 2217 P: 267
F2 2220 P: 147
F2 2230 P: 171
F2 2235 P: 181
K
ϕ
ϕ

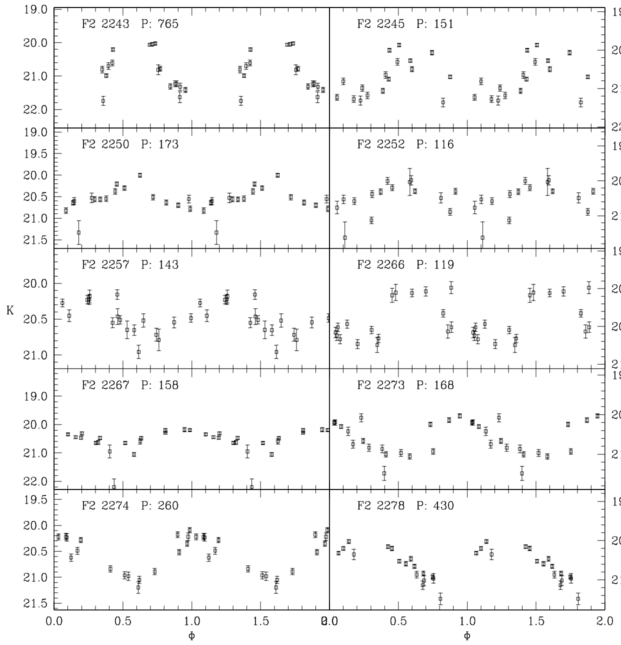
F2 2243 P: 765
F2 2245 P: 151
F2 2250 P: 173
F2 2252 P: 116
F2 2257 P: 143
F2 2266 P: 119
F2 2267 P: 158
F2 2273 P: 168
F2 2274 P: 260
F2 2278 P: 430
K
ϕ
ϕ

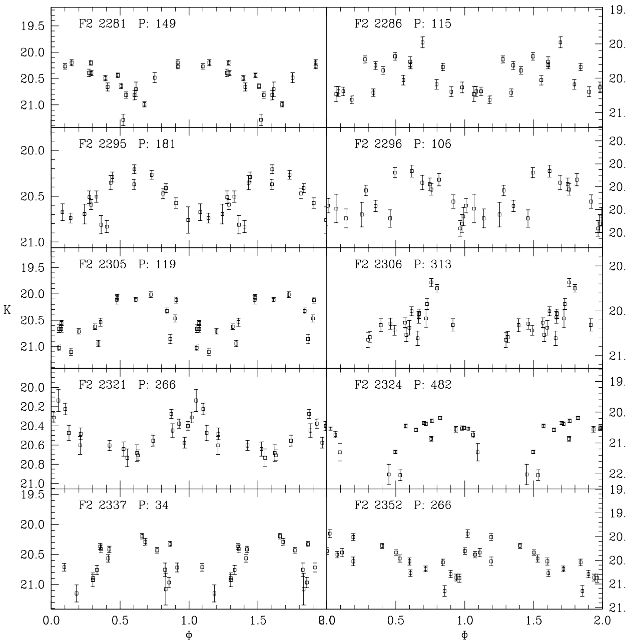
F2 2281 P: 149
F2 2286 P: 115
F2 2295 P: 181
F2 2296 P: 106
F2 2305 P: 119
F2 2306 P: 313
F2 2321 P: 266
F2 2324 P: 482
F2 2337 P: 34
F2 2352 P: 266
K
ϕ

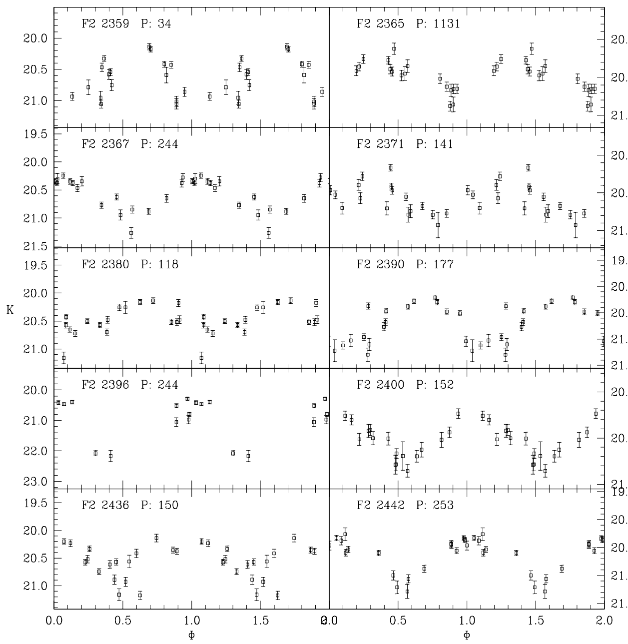
F2 2359 P: 34
F2 2365 P: 1131
F2 2367 P: 244
F2 2371 P: 141
F2 2380 P: 118
F2 2390 P: 177
F2 2396 P: 244
F2 2400 P: 152
F2 2436 P: 150
F2 2442 P: 253
K
ϕ

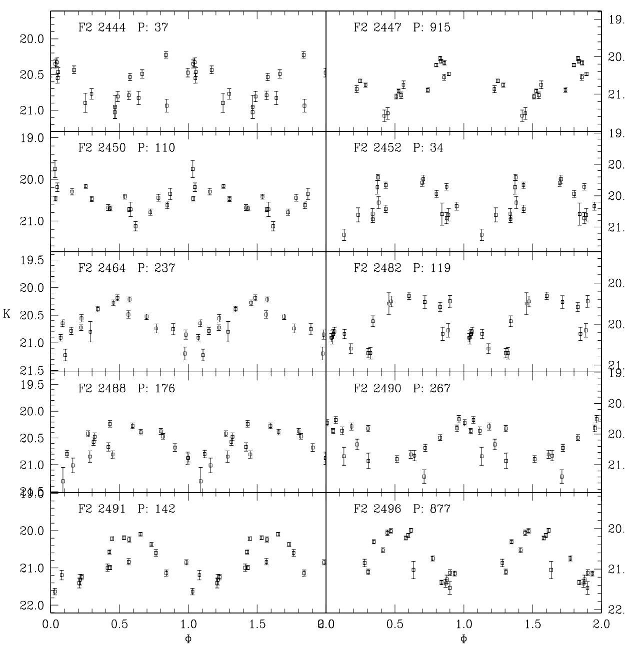
F2 2444 P: 37
F2 2447 P: 915
F2 2450 P: 110
F2 2452 P: 34
F2 2464 P: 237
F2 2482 P: 119
F2 2488 P: 176
F2 2490 P: 267
F2 2491 P: 142
F2 2496 P: 877
K
ϕ

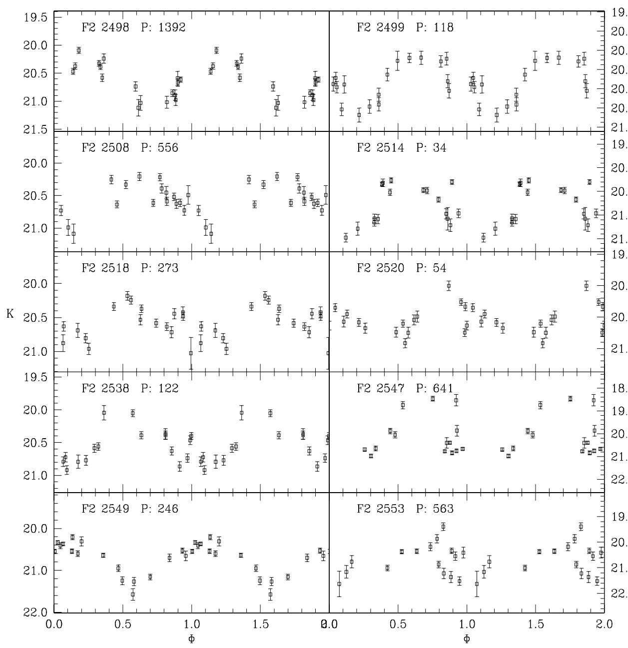
F2 2498 P: 1392
F2 2499 P: 118
F2 2508 P: 556
F2 2514 P: 34
F2 2518 P: 273
F2 2520 P: 54
F2 2538 P: 122
F2 2547 P: 641
F2 2549 P: 246
F2 2553 P: 563
K
ϕ

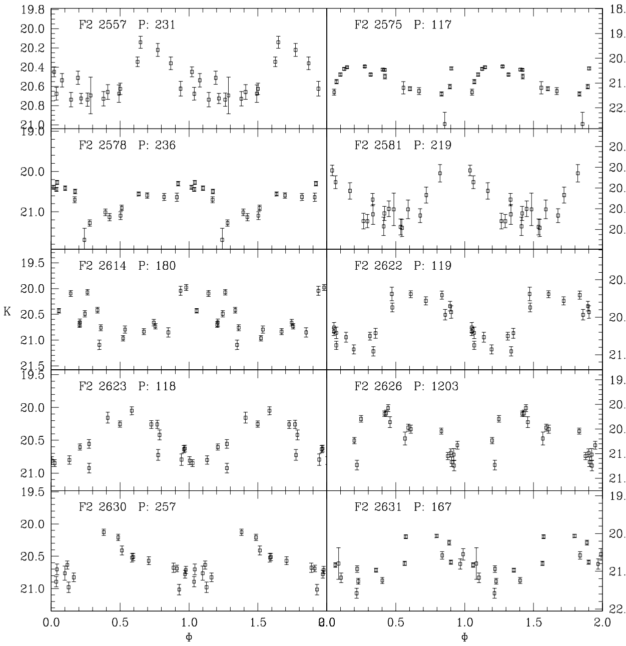
F2 2557 P: 231
F2 2575 P: 117
F2 2578 P: 236
F2 2581 P: 219
F2 2614 P: 180
F2 2622 P: 119
F2 2623 P: 118
F2 2626 P: 1203
F2 2630 P: 257
F2 2631 P: 167
K
ϕ

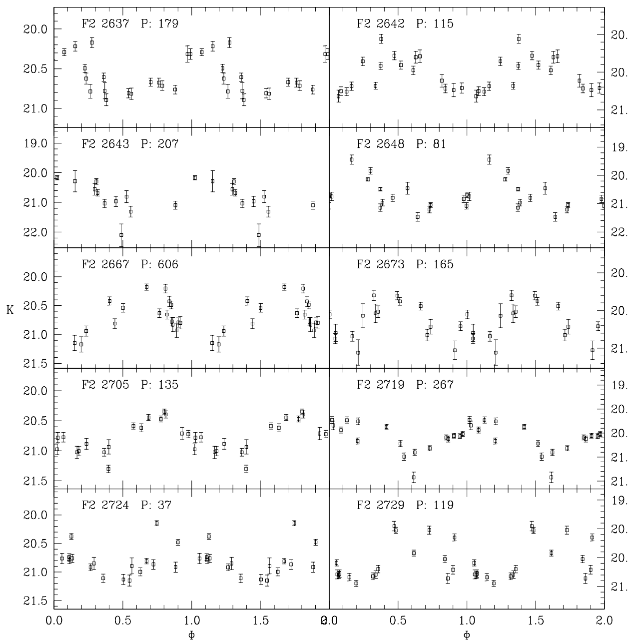
F2 2637 P: 179
F2 2642 P: 115
F2 2643 P: 207
F2 2648 P: 81
F2 2667 P: 606
F2 2673 P: 165
F2 2705 P: 135
F2 2719 P: 267
F2 2724 P: 37
F2 2729 P: 119
K
ϕ

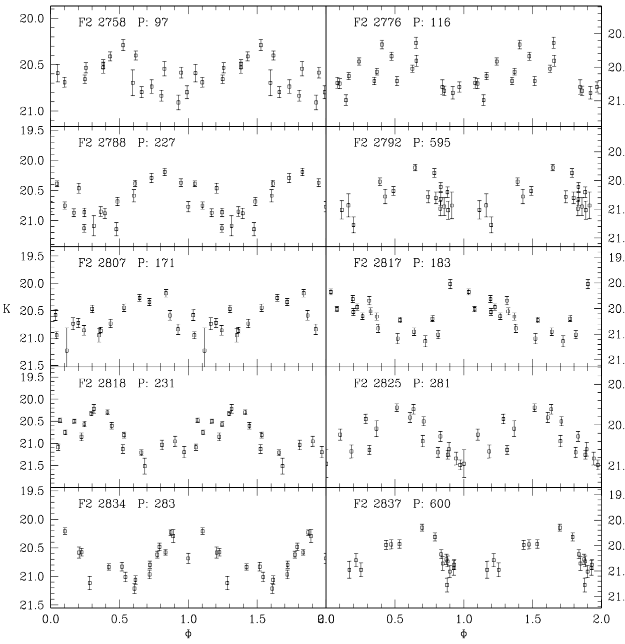
F2 2758 P: 97
F2 2776 P: 116
F2 2788 P: 227
F2 2792 P: 595
F2 2807 P: 171
F2 2817 P: 183
F2 2818 P: 231
F2 2825 P: 281
F2 2834 P: 283
F2 2837 P: 600
K
ϕ

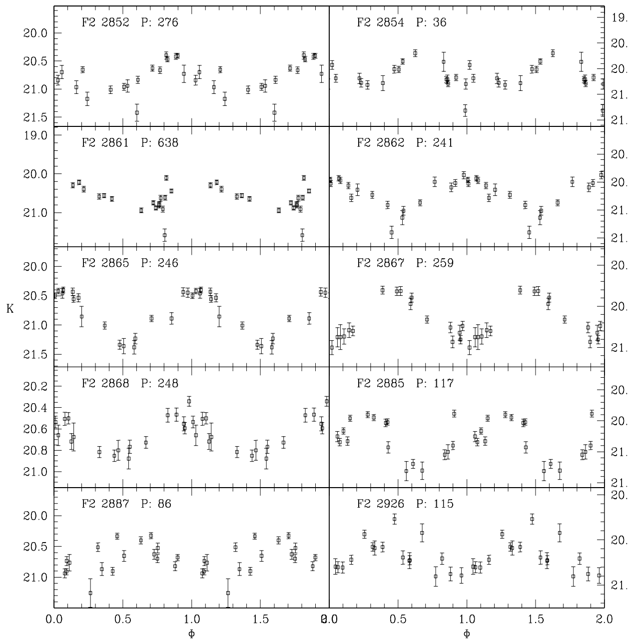
F2 2852 P: 276
F2 2854 P: 36
F2 2861 P: 638
F2 2862 P: 241
F2 2865 P: 246
F2 2867 P: 259
F2 2868 P: 248
F2 2885 P: 117
F2 2887 P: 86
F2 2926 P: 115
K
ϕ

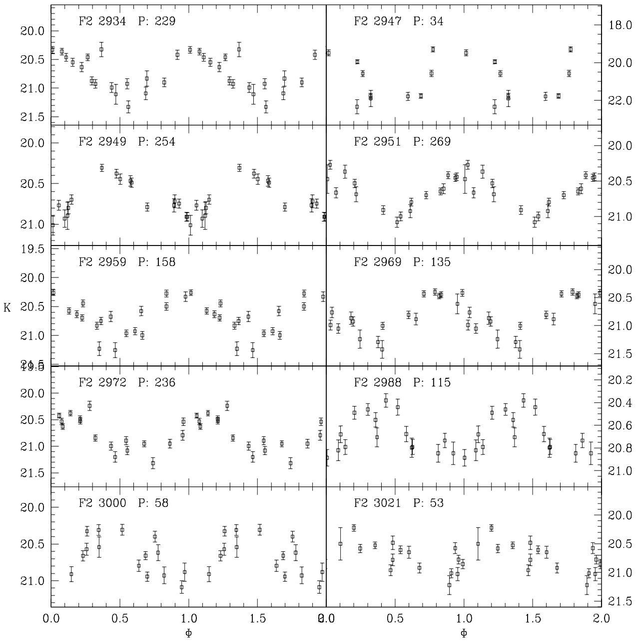
F2 2934 P: 229
F2 2947 P: 34
F2 2949 P: 254
F2 2951 P: 269
F2 2959 P: 158
F2 2969 P: 135
F2 2972 P: 236
F2 2988 P: 115
F2 3000 P: 58
F2 3021 P: 53
K
ϕ

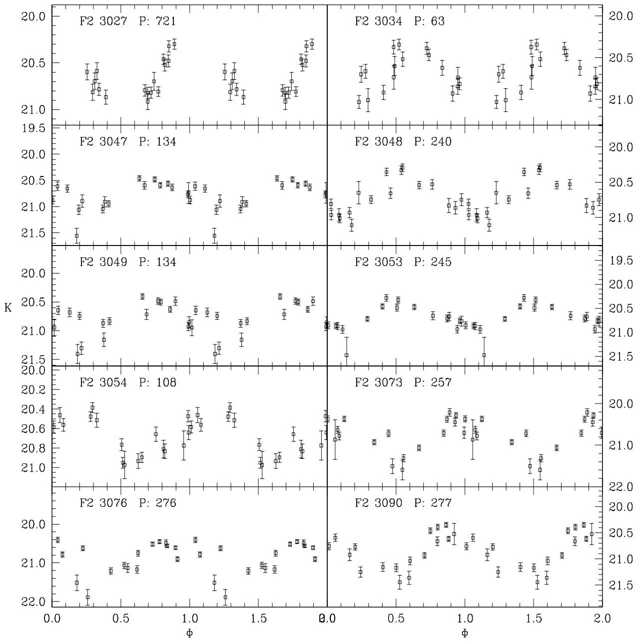
F2 3027 P: 721
F2 3034 P: 63
F2 3047 P: 134
F2 3048 P: 240
F2 3049 P: 134
F2 3053 P: 245
F2 3054 P: 108
F2 3073 P: 257
F2 3076 P: 276
F2 3090 P: 277
K
ϕ

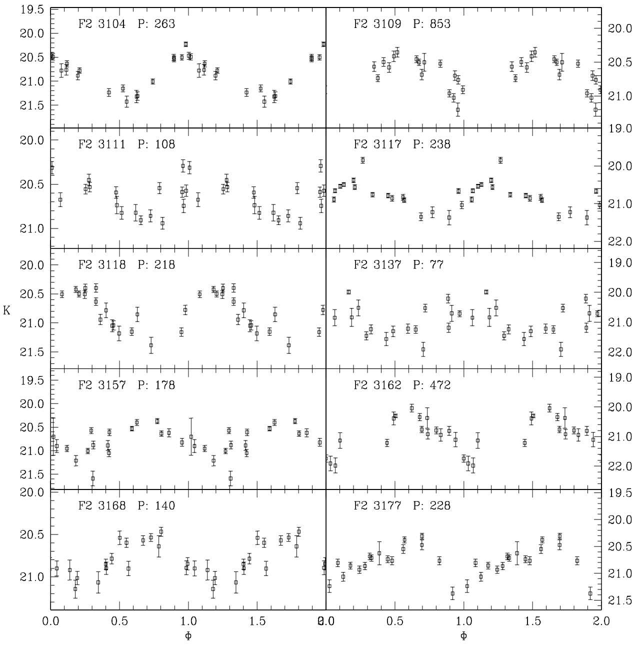
F2 3104 P: 263
F2 3109 P: 853
F2 3111 P: 108
F2 3117 P: 238
F2 3118 P: 218
F2 3137 P: 77
F2 3157 P: 178
F2 3162 P: 472
F2 3168 P: 140
F2 3177 P: 228
K
ϕ

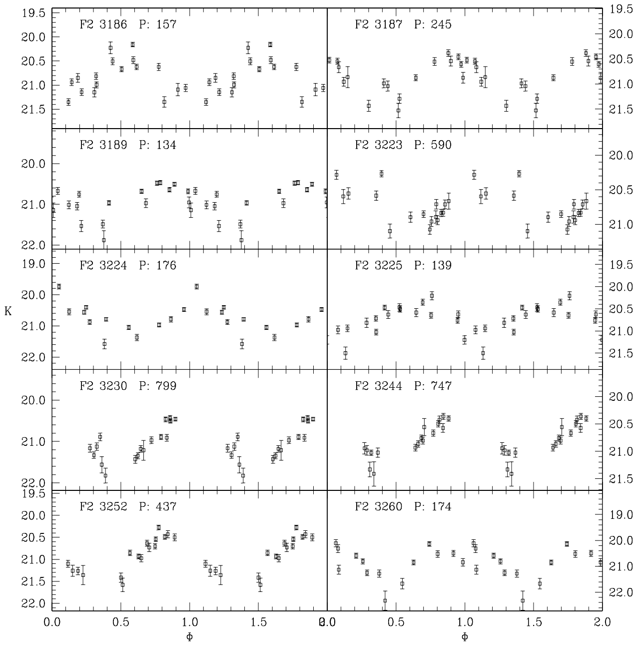
F2 3186 P: 157
F2 3187 P: 245
F2 3189 P: 134
F2 3223 P: 590
F2 3224 P: 176
F2 3225 P: 139
F2 3230 P: 799
F2 3244 P: 747
F2 3252 P: 437
F2 3260 P: 174
K
ϕ

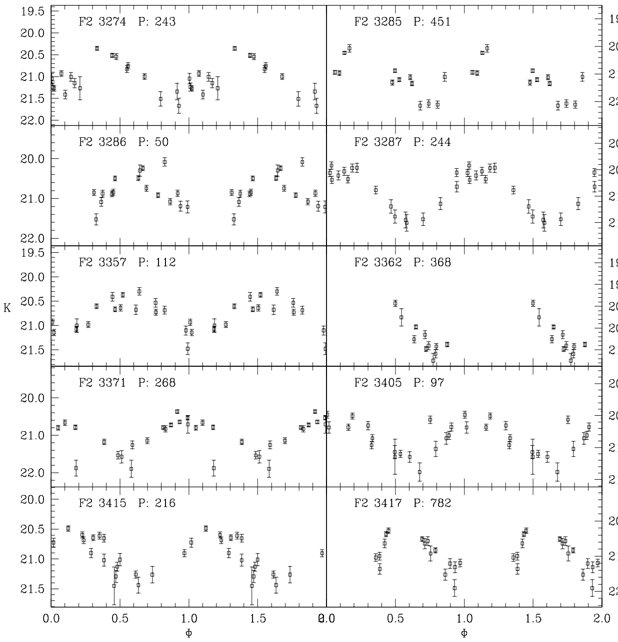
F2 3274 P: 243
F2 3285 P: 451
F2 3286 P: 50
F2 3287 P: 244
F2 3357 P: 112
F2 3362 P: 368
F2 3371 P: 268
F2 3405 P: 97
F2 3415 P: 216
F2 3417 P: 782
K
ϕ

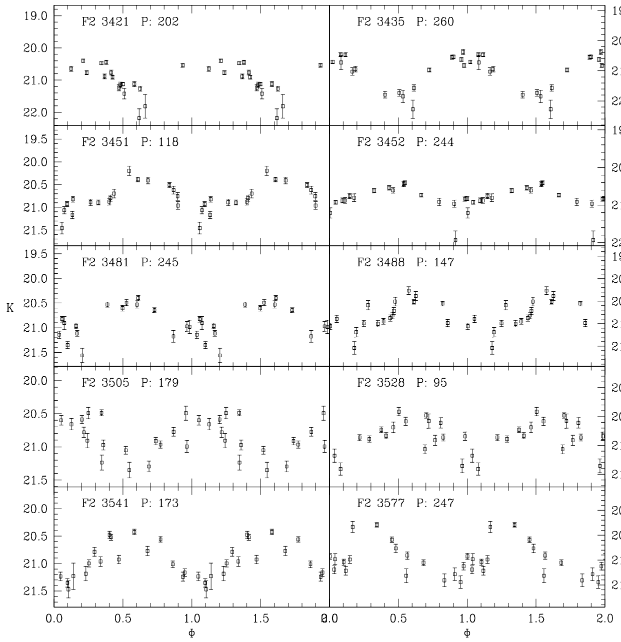
F2 3421 P: 202
F2 3435 P: 260
F2 3451 P: 118
F2 3452 P: 244
F2 3481 P: 245
F2 3488 P: 147
F2 3505 P: 179
F2 3528 P: 95
F2 3541 P: 173
F2 3577 P: 247
K
ϕ

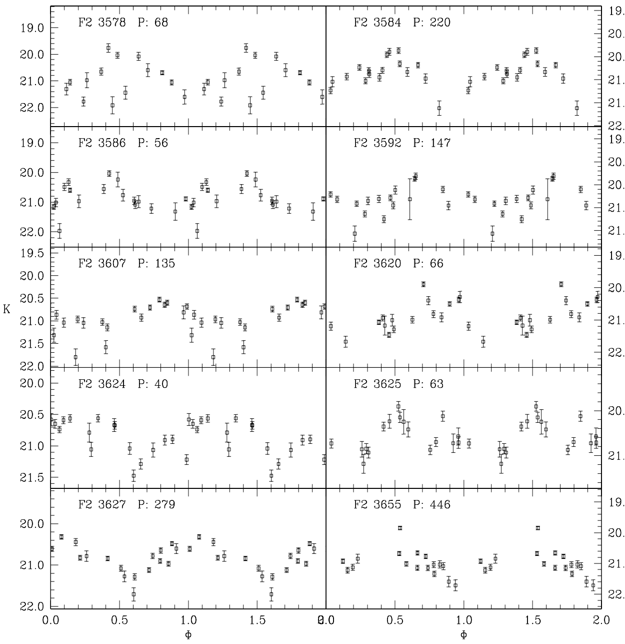
F2 3578 P: 68
F2 3584 P: 220
F2 3586 P: 56
F2 3592 P: 147
F2 3607 P: 135
F2 3620 P: 66
F2 3624 P: 40
F2 3625 P: 63
F2 3627 P: 279
F2 3655 P: 446
K
ϕ

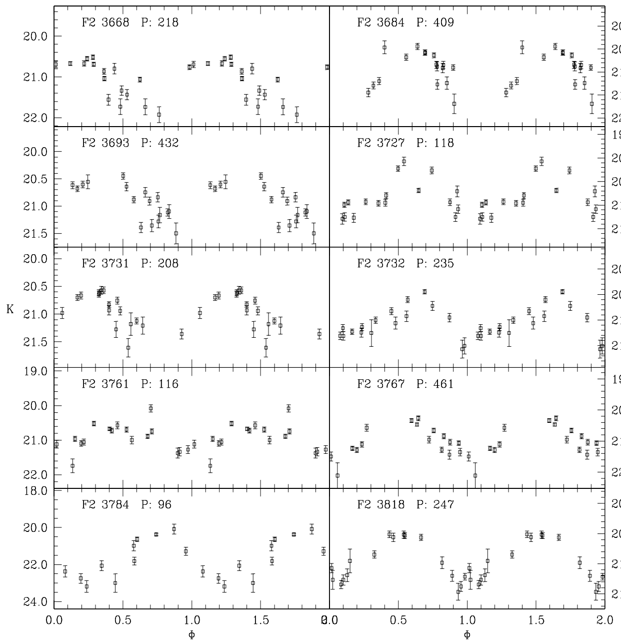
F2 3668 P: 218
F2 3684 P: 409
F2 3693 P: 432
F2 3727 P: 118
F2 3731 P: 208
F2 3732 P: 235
F2 3761 P: 116
F2 3767 P: 461
F2 3784 P: 96
F2 3818 P: 247
K
ϕ

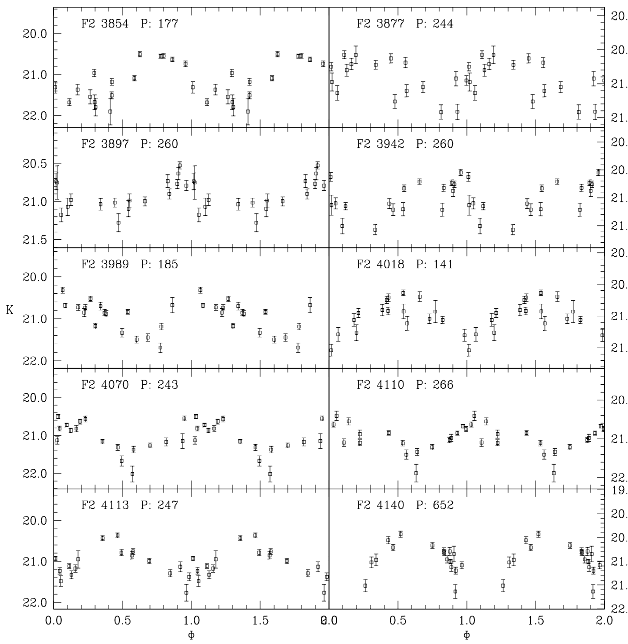
F2 3854 P: 177
F2 3877 P: 244
F2 3897 P: 260
F2 3942 P: 260
F2 3989 P: 185
F2 4018 P: 141
F2 4070 P: 243
F2 4110 P: 266
F2 4113 P: 247
F2 4140 P: 652
K
φ

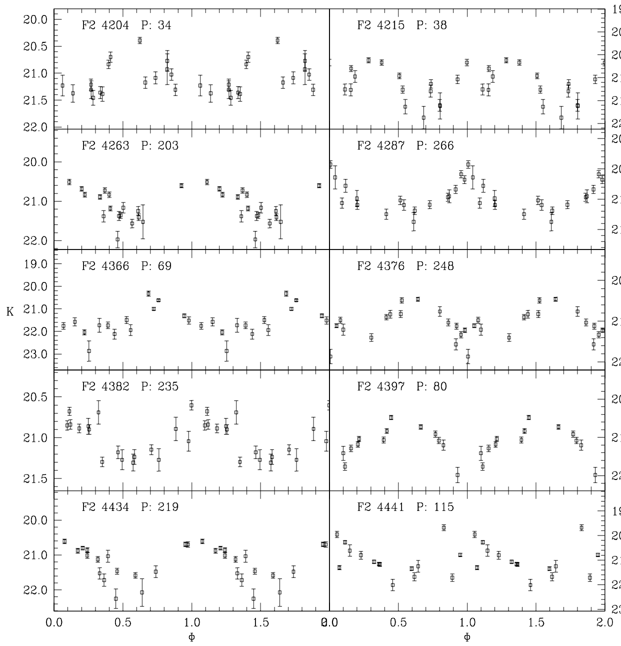
F2 4204 P: 34
F2 4215 P: 38
F2 4263 P: 203
F2 4287 P: 266
F2 4366 P: 69
F2 4376 P: 248
F2 4382 P: 235
F2 4397 P: 80
F2 4434 P: 219
F2 4441 P: 115
K
φ

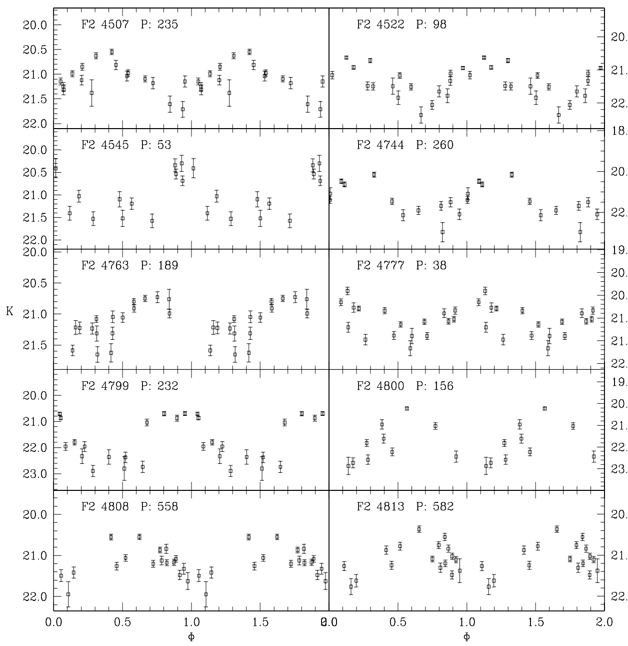
F2 4507 P: 235
F2 4522 P: 98
F2 4545 P: 53
F2 4744 P: 260
F2 4763 P: 189
F2 4777 P: 38
F2 4799 P: 232
F2 4800 P: 156
F2 4808 P: 558
F2 4813 P: 582
K
φ

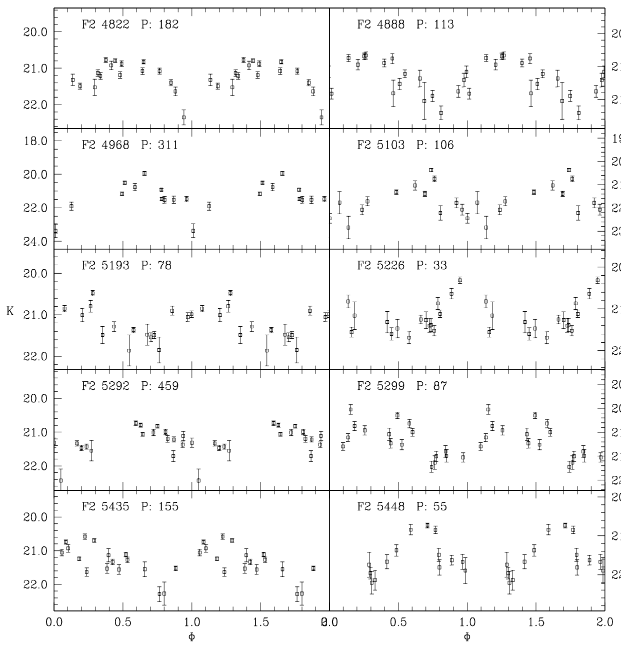
F2 4822 P: 182
F2 4888 P: 113
F2 4968 P: 311
F2 5103 P: 106
F2 5193 P: 78
F2 5226 P: 33
F2 5292 P: 459
F2 5299 P: 87
F2 5435 P: 155
F2 5448 P: 55
K
φ

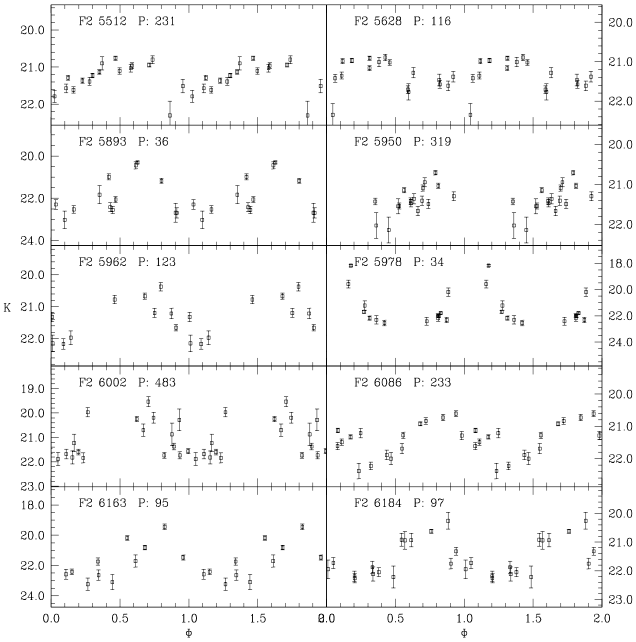
F2 5512 P: 231
F2 5628 P: 116
F2 5893 P: 36
F2 5950 P: 319
F2 5962 P: 123
F2 5978 P: 34
F2 6002 P: 483
F2 6086 P: 233
F2 6163 P: 95
F2 6184 P: 97
K
ϕ
ϕ

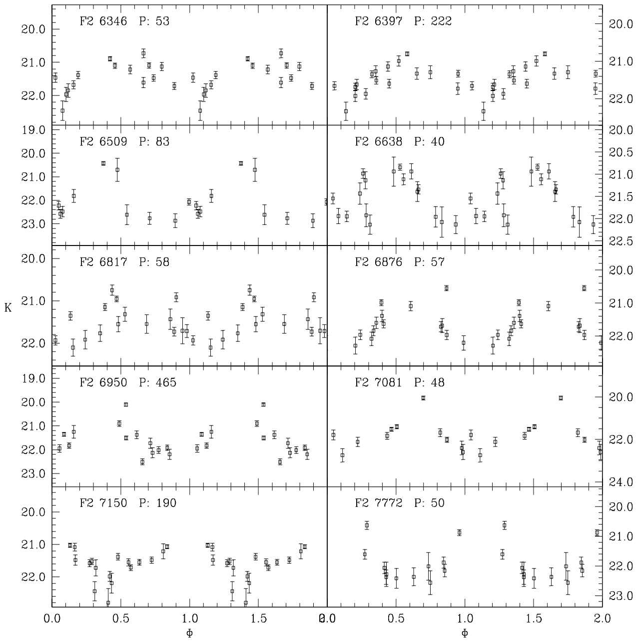
F2 6346 P: 53
F2 6397 P: 222
F2 6509 P: 83
F2 6638 P: 40
F2 6817 P: 58
F2 6876 P: 57
F2 6950 P: 465
F2 7081 P: 48
F2 7150 P: 190
F2 7772 P: 50
K
ϕ
ϕ

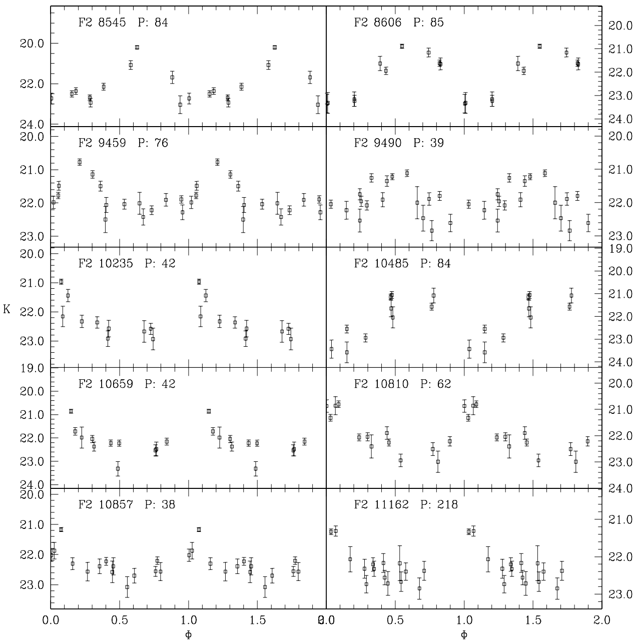
F2 8545 P: 84
F2 8606 P: 85
F2 9459 P: 76
F2 9490 P: 39
F2 10235 P: 42
F2 10485 P: 84
F2 10659 P: 42
F2 10810 P: 62
F2 10857 P: 38
F2 11162 P: 218
K
ϕ
ϕ

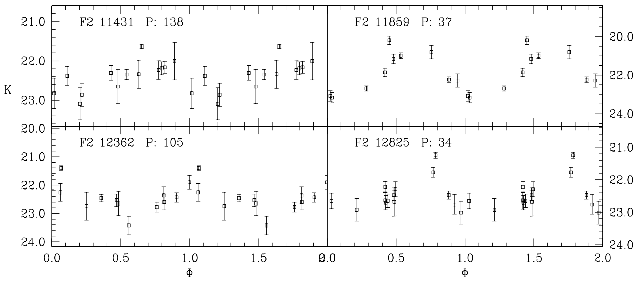
F2 11431 P: 138
F2 11859 P: 37
F2 12362 P: 105
F2 12825 P: 34
K
ϕ
ϕ

Appendix B

Information for all variables with at least 10 measurements for which a period could be obtained with the Fourier analysis of their K-band light curves. 408 variables in Field 1 and and 884 variables in Field 2 are presented. Lightcurves for these variables are in appendix A.

Table 8.1: Variable stars in Field 1. The data in columns are: stellar ID, x and y positions on the frame of epoch G, number of epochs with magnitude measurement for the variable, mean magnitude, amplitude and period from sine-wave fitting and the reduced χ^2 of the fit.

ID #	x	y	N	$\overline{K}$	A	P	χ_r^2
F1 38	107.3	831.7	14	17.751	0.460	450	4.37
F1 77	691.4	405.8	14	18.726	0.258	67	6.44
F1 78	107.8	828.6	14	18.664	0.260	116	1.68
F1 86	459.0	389.5	14	18.806	0.180	34	3.55
F1 102	469.2	296.3	14	19.252	0.786	693	1.45
F1 106	689.3	403.6	14	19.097	0.190	273	5.45
F1 115	690.0	408.0	14	19.216	0.216	86	3.37
F1 118	366.4	678.2	14	19.471	1.094	515	4.61
F1 119	788.1	473.2	14	19.311	0.502	137	6.55
F1 124	793.3	471.6	14	19.332	0.648	116	8.80
F1 134	241.7	710.1	14	19.475	0.720	481	7.53
F1 137	806.0	174.7	13	19.377	0.512	225	1.48
F1 142	63.6	662.8	14	19.606	0.846	409	2.04
F1 143	827.1	321.8	13	19.350	0.350	83	32.68
F1 146	681.4	593.4	14	19.465	0.784	552	4.68
F1 148	355.8	317.8	14	19.358	0.378	770	1.87
F1 152	110.2	846.5	10	19.456	0.454	138	3.29
F1 154	144.9	180.4	14	19.475	1.108	685	6.78
F1 156	450.3	778.6	14	19.527	1.456	579	5.92
F1 157	280.5	257.9	14	19.426	0.618	678	6.01
F1 161	281.8	543.0	14	19.499	0.366	582	26.16
F1 162	483.6	293.3	14	19.536	0.724	1333	3.20
F1 164	644.7	589.6	13	19.551	0.540	46	2.21
F1 166	387.5	211.6	14	19.519	0.440	395	6.76
F1 168	358.1	68.7	14	19.487	0.498	142	10.79
F1 169	794.7	177.1	14	19.649	0.728	427	3.52
F1 170	876.4	141.7	12	19.521	0.604	471	5.59
F1 172	645.7	675.4	14	19.599	0.896	1063	5.03
F1 173	679.1	-5.4	12	19.494	0.370	454	1.47
F1 175	901.018	25.961	10	19.508	0.528	61	8.19
F1 177	89.562	829.166	14	19.499	0.226	400	4.55
F1 178	70.636	767.242	14	19.499	0.270	512	3.41
F1 181	447.272	399.909	14	19.843	0.852	431	1.95
F1 182	97.568	801.391	14	19.539	0.210	176	1.98

ID #	x	y	N	$\overline{K}$	Amplitude	Period	reduced χ^2
F1 184	113.846	521.819	14	19.749	1.438	1036	14.19
F1 185	476.769	747.149	14	19.523	0.566	620	1.85
F1 186	129.657	501.290	14	19.701	1.016	616	6.08
F1 193	138.631	691.078	14	19.734	0.568	117	31.80
F1 194	130.815	541.882	14	19.857	1.230	489	2.95
F1 195	373.943	172.816	14	19.721	0.764	476	3.51
F1 199	383.250	278.848	14	19.605	0.770	501	4.64
F1 204	740.324	514.136	14	19.843	0.818	435	4.19
F1 205	550.022	697.229	14	19.859	0.828	471	1.82
F1 207	143.137	171.754	14	19.731	0.588	194	2.25
F1 210	858.911	407.739	13	19.657	0.310	210	2.43
F1 211	442.862	660.758	14	19.711	0.260	177	3.24
F1 213	377.689	736.660	14	19.779	0.516	403	4.93
F1 218	125.908	18.381	14	19.902	1.024	472	4.36
F1 220	314.725	367.313	14	19.866	1.236	588	1.73
F1 223	428.648	186.113	14	19.764	0.382	448	2.71
F1 224	344.881	770.512	14	19.745	0.640	184	8.06
F1 226	802.681	464.705	14	19.884	0.642	422	1.64
F1 227	348.997	58.363	14	19.723	0.528	890	5.83
F1 229	738.219	455.860	14	19.699	0.242	199	2.86
F1 230	158.332	173.202	14	19.816	0.734	402	2.39
F1 233	889.436	396.423	12	19.829	0.836	514	3.95
F1 237	394.492	-0.916	12	19.808	0.536	1427	5.61
F1 238	479.599	410.090	14	19.783	0.932	449	6.60
F1 242	862.781	628.232	13	19.753	1.016	417	19.22
F1 244	449.414	717.157	14	19.851	0.870	469	5.32
F1 245	825.421	606.259	13	20.011	1.018	435	0.57
F1 246	853.325	736.522	13	19.934	0.926	448	1.39
F1 247	574.025	475.744	14	20.078	1.064	420	4.39
F1 248	721.831	688.061	14	20.001	0.832	458	2.12
F1 250	31.886	419.345	14	19.811	0.132	411	35.94
F1 251	173.651	110.063	14	19.710	0.770	402	3.23
F1 257	636.699	523.014	14	20.205	2.480	1049	47.57
F1 258	672.811	492.077	14	19.750	0.742	458	2.57
F1 259	445.224	622.992	14	19.962	0.982	487	1.79
F1 261	139.732	474.167	14	19.796	0.388	1062	5.61
F1 262	182.282	335.691	14	19.828	0.490	457	20.70
F1 265	266.817	305.513	14	19.778	0.724	468	5.28
F1 266	815.309	176.499	13	19.967	0.776	450	1.82
F1 267	822.702	291.782	13	19.771	1.244	575	10.00
F1 270	575.939	702.256	14	19.827	0.892	444	5.05
F1 271	359.069	464.887	14	20.061	1.032	459	0.51
F1 273	766.562	466.815	14	19.922	0.344	118	3.86
F1 275	895.890	228.495	10	20.241	1.580	456	10.12
F1 279	506.822	159.277	14	19.898	0.794	522	3.62
F1 280	900.251	821.980	10	20.118	1.902	794	1.59
F1 282	589.038	492.812	14	19.769	0.852	380	2.48
F1 285	480.504	569.929	14	19.988	1.142	553	0.80
F1 287	87.871	792.263	14	20.466	2.080	1132	1.29

ID #	x	y	N	$\overline{K}$	Amplitude	Period	reduced χ^2
F1 288	30.993	245.427	14	20.025	0.716	418	4.63
F1 289	189.944	129.861	14	19.844	0.294	488	11.34
F1 290	187.036	76.634	14	19.732	0.680	365	2.80
F1 291	747.004	775.300	14	19.817	0.174	432	28.52
F1 292	871.750	142.673	13	19.742	1.116	509	4.54
F1 293	347.964	-3.862	13	19.830	0.362	34	0.75
F1 294	120.567	592.840	14	19.841	0.214	122	2.49
F1 297	124.564	330.037	14	19.938	0.856	439	8.03
F1 299	105.913	785.687	14	19.872	0.388	182	1.95
F1 307	489.546	400.984	14	19.888	0.476	433	7.60
F1 308	584.641	646.189	14	19.947	1.308	1016	8.69
F1 309	783.490	778.951	14	19.921	0.530	99	6.07
F1 314	147.258	308.849	14	20.377	1.426	463	3.32
F1 316	857.823	68.711	13	19.962	0.786	463	5.08
F1 319	52.024	187.931	14	20.086	1.000	463	4.37
F1 320	108.404	332.327	14	20.109	1.128	432	1.82
F1 321	263.266	697.749	14	19.933	0.516	142	4.80
F1 323	57.417	528.239	14	19.987	0.538	53	11.50
F1 327	624.606	728.766	14	20.160	1.172	457	4.16
F1 329	302.826	720.475	14	20.002	1.320	531	4.37
F1 331	119.309	1.587	14	20.103	0.684	430	3.15
F1 334	641.876	372.590	14	19.975	0.434	347	2.49
F1 335	279.241	67.309	14	19.915	0.458	193	7.81
F1 336	158.304	592.539	14	20.271	1.192	410	3.27
F1 341	191.284	56.941	14	19.929	0.434	1020	2.41
F1 342	382.215	561.723	14	20.039	1.022	402	2.62
F1 348	395.477	18.736	13	19.915	0.328	189	2.21
F1 356	341.669	462.948	14	20.292	1.180	367	4.12
F1 357	144.644	456.497	14	20.317	0.986	610	4.06
F1 358	100.829	143.386	14	19.983	0.404	137	10.89
F1 360	442.734	406.405	14	19.881	0.284	71	6.77
F1 361	340.625	307.708	14	19.973	0.738	419	1.96
F1 362	106.838	397.027	14	19.947	0.584	186	9.69
F1 363	882.544	214.530	12	19.957	0.332	33	7.69
F1 366	261.264	713.333	14	20.062	0.832	379	2.88
F1 367	86.899	788.009	14	19.966	0.568	460	2.46
F1 368	400.918	355.989	14	20.092	0.936	407	0.85
F1 371	107.750	247.290	14	20.025	0.968	467	9.34
F1 372	248.914	805.038	14	20.097	0.356	1235	32.32
F1 373	518.238	737.268	14	20.140	0.894	794	11.05
F1 374	720.313	102.270	14	20.103	0.610	322	1.18
F1 375	650.086	380.663	14	20.191	1.236	689	2.81
F1 378	506.208	698.170	14	20.023	1.154	549	4.61
F1 383	563.323	653.741	14	20.088	0.924	422	3.18
F1 384	267.606	522.319	14	20.058	0.684	407	4.70
F1 385	66.562	549.978	14	20.035	0.410	424	27.89
F1 386	862.001	625.312	13	20.021	0.482	86	4.35
F1 388	126.282	525.432	14	20.123	0.938	428	6.16
F1 393	738.632	-10.781	11	20.130	0.600	114	6.08

ID #	x	y	N	$\overline{K}$	Amplitude	Period	reduced χ^2
F1 396	414.630	108.821	14	20.054	0.484	173	2.60
F1 397	121.767	657.130	14	20.230	1.580	1117	17.18
F1 400	326.050	501.884	14	20.022	0.800	519	2.56
F1 402	310.265	220.159	14	19.919	0.318	378	25.64
F1 404	701.505	153.967	14	20.149	0.798	384	2.08
F1 406	169.968	226.729	14	20.090	0.912	463	2.58
F1 415	776.743	505.929	14	20.000	0.460	182	6.82
F1 422	364.774	570.456	14	19.908	0.586	433	1.39
F1 423	366.187	211.550	14	19.990	0.638	755	8.32
F1 427	399.155	565.095	14	20.102	0.482	181	4.87
F1 429	608.007	515.825	14	20.156	0.684	347	3.02
F1 439	394.374	672.036	14	20.265	0.952	397	3.66
F1 444	360.960	822.955	14	20.206	0.840	397	14.07
F1 447	233.535	541.966	14	19.868	0.676	374	2.88
F1 450	361.692	514.529	14	20.166	0.638	358	2.50
F1 452	266.170	53.287	14	19.962	0.424	385	3.39
F1 455	519.300	615.653	14	19.992	0.292	425	12.80
F1 456	434.887	18.082	14	20.085	0.422	187	7.13
F1 458	249.633	451.304	14	19.997	0.524	415	9.88
F1 459	757.567	-12.793	11	20.244	1.256	183	11.26
F1 461	87.164	36.914	14	20.060	0.806	178	7.34
F1 467	570.582	170.120	14	20.065	0.998	463	3.04
F1 472	273.519	621.851	14	20.009	0.212	448	1.09
F1 476	637.777	504.379	14	20.091	0.440	457	16.87
F1 484	461.099	786.446	14	20.136	0.560	142	12.39
F1 485	312.675	620.709	14	20.155	0.520	358	3.09
F1 486	564.319	580.317	14	20.217	0.488	543	5.75
F1 489	222.280	477.483	14	20.179	0.556	159	3.27
F1 490	557.916	724.311	14	20.297	0.712	400	2.45
F1 491	41.037	357.646	14	20.364	1.138	549	2.95
F1 492	58.903	617.084	14	20.112	0.718	455	8.46
F1 493	47.019	287.147	14	20.276	1.008	372	3.35
F1 496	506.523	285.499	14	20.090	0.226	69	6.83
F1 497	378.854	746.873	14	19.930	0.882	388	1.91
F1 498	78.927	286.745	14	20.128	0.878	407	5.58
F1 499	388.852	388.433	14	20.054	0.710	185	11.04
F1 501	442.040	601.497	14	20.180	0.396	769	4.26
F1 502	468.476	89.216	14	20.180	0.422	462	12.01
F1 504	526.030	793.064	14	20.158	0.526	174	2.88
F1 507	822.831	526.653	13	19.949	0.548	377	7.84
F1 511	308.444	660.666	14	20.280	0.930	402	10.90
F1 517	438.002	228.258	14	20.255	0.830	347	0.80
F1 519	752.580	36.630	14	20.061	0.648	408	1.44
F1 521	122.601	557.681	14	20.032	0.586	466	2.44
F1 523	445.208	779.237	14	20.083	0.670	420	2.37
F1 530	159.935	560.408	14	20.148	0.758	393	5.07
F1 537	108.975	250.088	14	20.300	0.706	349	3.77
F1 540	618.943	401.382	14	20.069	0.400	439	20.84
F1 544	143.315	386.305	14	20.186	0.538	265	3.67

ID #	x	y	N	$\overline{K}$	Amplitude	Period	reduced χ^2
F1 548	549.116	223.905	14	20.127	1.094	434	4.70
F1 552	694.332	800.683	14	20.318	0.750	325	3.15
F1 555	175.562	324.486	14	20.072	0.620	407	6.46
F1 557	34.958	649.837	14	20.196	0.426	176	4.38
F1 561	109.493	737.051	14	20.227	0.774	477	1.94
F1 564	101.464	95.763	14	20.103	0.628	181	3.61
F1 566	748.649	626.320	14	20.001	0.570	337	2.47
F1 567	147.233	746.686	14	20.218	0.434	169	2.43
F1 568	204.229	129.756	14	20.021	0.532	354	4.36
F1 572	69.070	385.061	14	20.104	0.818	419	5.75
F1 573	83.886	395.505	14	20.164	0.346	40	7.73
F1 575	687.311	541.670	14	20.165	0.366	149	3.73
F1 582	424.336	615.106	14	20.556	1.384	771	13.79
F1 583	99.952	4.551	14	20.144	0.280	441	43.79
F1 586	831.915	266.778	13	20.432	1.092	446	6.79
F1 587	214.408	198.625	14	20.306	0.274	369	33.87
F1 590	227.199	81.842	14	20.267	0.616	273	4.38
F1 592	765.924	33.867	14	20.166	0.870	431	2.65
F1 594	886.015	800.818	12	20.283	1.010	184	21.14
F1 598	844.513	709.324	13	20.224	1.088	450	4.91
F1 600	225.777	-14.811	11	20.359	0.842	169	6.50
F1 601	745.086	822.217	14	20.293	0.924	396	6.82
F1 602	380.163	672.583	14	20.251	0.924	389	2.72
F1 605	422.672	660.954	14	20.739	1.578	408	31.43
F1 608	682.081	17.056	14	20.336	0.954	406	3.30
F1 609	796.281	303.031	14	20.213	0.810	397	1.67
F1 617	656.804	627.713	14	20.082	0.864	390	8.11
F1 618	111.879	521.072	14	20.304	0.434	643	6.97
F1 619	90.483	126.503	14	20.100	0.792	365	3.00
F1 623	384.542	709.520	14	20.260	0.686	436	2.53
F1 627	120.639	235.847	14	20.087	0.266	338	21.56
F1 636	762.668	454.968	14	20.261	0.566	83	4.22
F1 643	719.833	37.132	14	20.279	0.410	170	1.78
F1 644	215.054	349.727	14	20.415	0.736	279	4.02
F1 648	677.780	585.627	14	20.265	0.542	1269	2.86
F1 651	761.620	384.550	14	20.109	0.730	366	3.45
F1 652	122.625	494.667	14	20.308	0.556	372	1.84
F1 655	705.338	239.886	14	20.545	0.980	311	2.05
F1 665	437.093	810.681	14	20.301	0.638	987	3.53
F1 666	153.497	-12.124	11	20.129	0.652	886	4.40
F1 673	502.753	296.039	14	20.235	0.316	334	18.53
F1 674	819.357	784.352	13	20.267	0.578	175	6.26
F1 679	323.420	229.955	14	20.445	0.962	326	1.32
F1 680	882.496	628.095	12	20.016	0.960	373	16.10
F1 685	198.146	560.677	14	20.281	0.356	178	5.41
F1 690	37.680	472.289	14	20.319	0.366	173	4.52
F1 703	188.181	504.835	14	20.112	1.058	393	3.65
F1 709	765.945	545.321	14	20.378	0.608	1229	6.00
F1 718	157.090	330.962	14	20.269	0.190	386	50.04

ID #	x	y	N	$\overline{K}$	Amplitude	Period	reduced χ^2
F1 725	508.814	516.046	14	20.410	0.936	366	1.99
F1 731	205.801	127.595	14	20.471	1.338	435	9.54
F1 734	606.435	349.075	14	20.573	1.130	463	4.41
F1 743	706.239	562.511	14	20.513	0.774	275	3.20
F1 747	83.867	591.335	14	20.156	1.326	486	1.18
F1 749	246.236	213.890	14	20.476	0.736	302	2.59
F1 751	139.885	121.791	14	20.484	0.664	317	3.02
F1 753	105.751	309.726	14	20.599	0.896	300	3.80
F1 761	536.448	380.161	14	20.491	0.588	480	1.56
F1 766	49.859	543.190	14	20.355	0.450	53	5.30
F1 771	71.030	715.031	14	20.347	1.196	428	2.70
F1 774	373.253	304.638	14	20.458	0.994	179	8.17
F1 781	628.546	761.208	14	20.489	0.450	311	6.12
F1 792	338.549	126.952	14	20.447	0.484	294	4.57
F1 799	680.376	528.445	14	20.404	0.264	373	39.61
F1 803	511.398	752.331	14	20.499	0.782	364	3.04
F1 813	58.785	532.753	13	20.422	0.878	46	6.35
F1 817	563.901	47.282	14	20.418	0.364	632	4.91
F1 821	161.413	767.053	14	20.428	0.396	118	2.36
F1 831	656.434	229.307	14	20.341	0.822	137	21.97
F1 846	808.138	688.998	13	20.520	0.796	284	4.49
F1 849	852.076	611.417	13	20.531	0.636	279	3.07
F1 850	337.806	155.369	14	20.362	0.620	309	6.33
F1 856	801.070	814.446	13	20.437	0.892	317	9.72
F1 861	654.389	370.155	14	20.329	0.622	416	7.39
F1 865	549.189	60.909	14	20.414	0.792	347	4.80
F1 866	96.883	45.766	14	20.414	0.520	171	8.25
F1 867	128.522	494.020	14	20.432	0.970	185	11.63
F1 871	395.327	403.646	14	20.505	0.630	155	7.48
F1 876	844.268	836.266	13	20.430	0.708	59	8.48
F1 877	266.539	225.026	14	20.602	0.850	284	2.01
F1 888	145.324	96.731	14	20.335	0.540	312	3.18
F1 892	215.895	336.611	14	20.650	0.908	306	1.04
F1 898	563.218	20.271	14	20.463	0.810	317	3.34
F1 909	331.425	714.265	14	20.534	0.438	295	2.43
F1 911	582.082	56.437	14	20.464	0.588	166	4.88
F1 913	230.521	829.521	14	20.371	0.688	364	1.33
F1 921	809.638	316.624	13	20.533	0.518	119	8.46
F1 929	262.042	271.020	14	20.558	0.544	238	1.85
F1 936	436.662	307.693	14	20.472	0.382	37	3.48
F1 946	725.718	704.182	14	20.538	0.822	176	6.16
F1 957	438.037	97.418	14	20.707	0.774	289	5.68
F1 962	83.774	289.084	14	20.614	0.730	357	6.14
F1 969	238.445	759.689	14	20.481	0.484	182	3.30
F1 977	178.646	82.596	14	20.506	0.356	162	6.31
F1 985	779.180	544.889	14	20.636	0.680	271	1.98
F1 987	533.245	110.111	14	20.580	0.526	291	1.54
F1 989	864.535	341.636	13	20.597	0.738	278	3.01
F1 990	369.765	611.713	14	20.793	1.236	1456	9.05

ID #	x	y	N	$\overline{K}$	Amplitude	Period	reduced χ^2
F1 991	88.962	80.155	14	20.525	0.408	119	11.50
F1 1002	175.542	762.959	14	20.404	1.086	326	2.35
F1 1004	157.864	314.575	14	20.613	0.530	284	2.55
F1 1019	425.962	500.182	14	20.697	0.238	183	35.20
F1 1023	594.146	346.409	14	20.659	0.688	295	3.16
F1 1037	490.482	400.801	10	21.116	1.976	183	13.14
F1 1043	135.379	811.358	14	20.646	0.478	540	4.24
F1 1050	737.961	479.961	14	20.633	0.570	159	3.99
F1 1060	671.707	132.313	14	20.553	0.484	166	3.16
F1 1070	455.042	37.280	14	20.732	0.810	285	2.75
F1 1074	793.096	281.763	14	20.437	0.252	295	33.38
F1 1078	854.655	771.621	12	20.737	0.762	290	5.27
F1 1079	252.816	598.500	14	20.877	1.190	516	4.45
F1 1080	677.517	807.216	14	20.671	0.614	248	4.38
F1 1091	347.264	344.193	14	20.575	0.456	181	7.76
F1 1102	87.923	336.983	14	20.507	0.764	331	1.98
F1 1110	140.816	632.920	14	20.593	0.660	276	2.30
F1 1120	108.479	540.308	14	20.711	0.666	1454	2.38
F1 1124	100.297	437.006	14	20.605	0.360	121	2.54
F1 1128	723.977	300.114	14	20.463	1.040	352	3.38
F1 1139	703.744	74.823	10	20.447	0.924	1137	102.01
F1 1148	75.084	169.177	14	20.636	0.576	704	0.76
F1 1154	808.375	642.119	13	21.180	1.522	554	1.47
F1 1164	288.410	801.134	14	20.586	0.512	1305	3.65
F1 1171	709.510	853.394	10	20.565	1.144	98	32.34
F1 1175	493.742	824.279	14	20.600	0.652	61	6.34
F1 1182	71.309	200.066	14	20.663	0.592	1373	3.49
F1 1195	290.474	132.379	14	20.769	0.564	282	2.14
F1 1206	58.176	315.065	14	20.435	0.970	311	5.46
F1 1212	593.077	698.148	14	20.884	0.864	285	8.59
F1 1223	409.172	469.670	14	20.635	0.638	178	3.15
F1 1230	308.707	748.899	14	20.723	0.746	1045	7.52
F1 1238	125.915	710.407	13	20.824	0.996	35	7.25
F1 1245	888.676	699.287	11	20.842	0.688	274	4.55
F1 1246	694.100	639.820	14	20.741	0.242	913	5.21
F1 1259	412.018	131.618	14	20.658	0.476	252	6.36
F1 1287	357.530	258.047	14	20.677	0.664	173	5.88
F1 1291	305.889	295.710	14	20.810	0.596	253	7.29
F1 1300	887.175	801.694	11	20.830	1.072	59	13.17
F1 1307	324.802	739.676	14	20.664	0.474	1096	3.46
F1 1315	176.569	702.595	14	20.688	0.202	724	7.21
F1 1319	325.052	77.076	14	20.869	0.132	222	33.76
F1 1339	455.684	392.515	14	20.704	0.784	268	1.70
F1 1364	172.226	215.972	14	20.990	1.144	510	8.83
F1 1378	275.828	724.737	14	20.721	0.264	166	22.76
F1 1389	858.230	664.260	13	20.757	0.838	261	3.91
F1 1408	298.711	687.962	14	20.885	0.596	272	1.40
F1 1429	24.204	798.272	12	20.852	1.018	137	8.65
F1 1454	573.773	841.072	14	20.817	0.452	234	3.81

ID #	x	y	N	$\overline{K}$	Amplitude	Period	reduced χ^2
F1 1457	705.604	752.704	14	20.924	0.848	157	4.68
F1 1465	62.319	65.772	14	20.850	0.868	41	8.64
F1 1474	89.667	146.113	14	20.862	0.560	102	6.61
F1 1487	123.231	499.940	14	20.905	0.660	216	8.69
F1 1496	252.483	92.674	14	20.967	0.642	542	3.11
F1 1510	281.043	309.651	14	20.847	0.952	197	1.21
F1 1514	252.601	54.567	14	20.883	0.698	278	5.07
F1 1519	500.873	277.497	14	20.888	0.598	1041	6.23
F1 1530	456.587	583.142	14	20.841	0.952	539	6.75
F1 1542	115.354	685.859	14	21.087	1.296	135	5.47
F1 1545	375.087	318.094	10	21.297	1.530	73	6.08
F1 1581	719.519	827.130	14	20.894	0.670	248	3.85
F1 1595	533.997	605.569	14	20.908	0.656	233	2.25
F1 1601	563.496	580.911	13	21.479	2.180	456	7.16
F1 1652	263.578	751.293	14	21.119	0.362	228	40.14
F1 1675	644.570	702.301	14	21.026	0.576	183	1.49
F1 1677	300.238	611.686	14	20.948	0.544	151	5.23
F1 1711	447.388	406.053	14	20.969	0.986	86	5.85
F1 1721	331.105	253.431	14	20.941	1.416	533	4.01
F1 1725	206.617	46.879	14	21.045	0.510	214	3.97
F1 1739	434.899	385.899	14	21.039	0.584	265	1.92
F1 1757	227.823	255.306	14	21.008	0.576	186	4.17
F1 1781	763.726	286.659	14	21.088	0.720	39	3.80
F1 1803	113.140	700.302	14	21.524	1.826	199	6.22
F1 1817	777.525	813.433	13	21.109	0.894	83	15.55
F1 1826	151.662	580.070	14	21.133	1.458	421	3.07
F1 1852	845.369	837.456	10	21.053	1.586	1660	7.45
F1 1873	357.561	318.432	12	21.008	0.384	438	59.68
F1 1899	101.305	455.335	14	21.115	0.696	194	5.63
F1 1945	865.928	292.753	12	21.183	1.082	57	10.35
F1 1978	251.690	690.096	14	21.446	0.758	606	11.82
F1 1982	644.152	327.912	14	21.158	0.676	194	3.42
F1 1984	115.763	409.411	14	21.645	1.640	334	5.71
F1 2018	722.446	633.771	14	21.269	0.794	180	2.14
F1 2022	652.073	471.000	14	21.241	0.562	69	7.77
F1 2032	58.853	531.237	12	21.172	0.378	137	20.46
F1 2034	814.468	833.050	12	21.104	0.692	1297	10.13
F1 2126	522.242	828.161	14	21.309	0.960	154	12.12
F1 2133	719.475	768.817	14	21.275	0.744	246	3.16
F1 2135	470.261	392.140	12	21.264	1.626	42	1.97
F1 2143	862.100	33.737	13	21.368	1.088	1183	5.40
F1 2275	107.870	410.505	14	21.299	0.780	34	6.32
F1 2283	574.370	666.573	10	21.719	2.214	58	9.53
F1 2339	167.625	179.256	14	21.382	1.010	46	5.64
F1 2390	721.918	721.724	11	22.452	2.944	686	2.13
F1 2423	691.223	72.451	14	21.740	1.840	465	6.69
F1 2488	386.985	826.644	14	21.362	0.892	41	8.13
F1 2653	206.921	513.449	14	21.976	1.560	349	4.86
F1 2711	109.566	697.835	13	21.527	1.460	89	6.06

ID #	x	y	N	$\overline{K}$	Amplitude	Period	reduced χ^2
F1 2715	388.643	309.138	11	21.837	1.754	570	3.05
F1 2867	500.532	818.748	13	21.961	2.408	47	8.44
F1 2920	813.429	333.363	11	21.628	1.884	46	22.21
F1 3043	513.762	821.123	13	21.684	1.234	156	16.12
F1 3093	856.089	772.283	11	21.537	1.614	55	6.65
F1 3221	522.384	821.774	12	22.065	2.314	116	17.13
F1 3345	802.021	815.415	12	21.943	1.372	461	24.84
F1 3427	565.446	841.859	13	21.374	0.474	1637	7.75
F1 3983	111.562	710.018	13	21.759	0.980	156	9.64
F1 3992	40.279	540.403	11	21.827	1.240	57	3.71
F1 4498	359.245	201.268	11	21.945	1.570	37	5.30
F1 4764	167.932	671.409	12	22.172	1.316	68	2.68
F1 4866	104.128	302.853	13	21.859	1.126	458	3.06
F1 4874	493.220	806.446	12	21.799	2.038	220	9.93
F1 5100	105.469	679.378	10	22.328	2.732	1010	5.69
F1 5119	346.642	200.370	12	22.277	1.818	86	4.36
F1 5466	508.023	803.181	12	22.166	3.170	83	6.39
F1 5697	298.518	847.718	10	21.717	2.664	570	4.11
F1 5834	567.784	639.835	10	22.585	2.854	34	23.24
F1 5976	845.554	630.436	10	22.040	1.608	84	3.85
F1 6289	354.961	325.515	12	22.174	1.652	86	13.02
F1 6366	368.167	354.632	11	22.216	1.248	69	5.18
F1 6398	216.080	87.636	11	22.490	1.774	82	3.35
F1 6443	526.515	817.824	11	22.308	2.592	83	9.04
F1 6688	442.111	401.463	11	22.108	2.058	84	3.10
F1 7146	583.823	678.273	13	22.209	2.016	42	6.94
F1 7240	532.097	813.360	12	22.279	1.528	37	9.21
F1 7323	578.432	642.435	10	22.389	2.174	41	4.01
F1 7337	153.049	659.043	10	22.571	1.988	47	5.09
F1 7630	398.598	296.655	12	22.269	2.490	225	7.24
F1 7727	857.958	534.606	11	22.183	2.670	217	7.86

Table 8.2: Variable stars in Field 2. The data in columns are: stellar ID, x and y positions on the frame of epoch G, number of epochs with magnitude measurement for the variable, mean magnitude, amplitude and period from sine-wave fitting and the reduced χ^2 of the fit.

ID #	x	y	N	$\overline{K}$	Amplitude	Period	reduced χ^2
F2 8	881.654	665.186	16	15.102	0.430	34	6.15
F2 66	34.592	166.338	14	18.545	2.004	35	38.42
F2 70	591.525	445.803	17	18.385	0.320	152	6.09
F2 74	44.767	180.579	14	18.750	2.392	35	18.20
F2 77	45.115	173.868	11	19.102	3.426	1152	16.89
F2 87	44.370	165.921	14	18.588	1.874	50	27.90
F2 98	268.239	284.448	11	18.667	1.172	34	22.59
F2 99	50.881	180.673	15	18.840	2.428	34	42.72
F2 102	256.321	277.168	15	18.854	1.268	70	4.54
F2 105	265.915	268.775	15	19.098	1.578	1211	9.38
F2 108	61.560	8.008	17	18.939	0.396	189	3.59
F2 111	875.215	67.259	16	19.037	0.910	219	8.75
F2 119	346.056	485.834	17	18.922	0.378	85	2.15
F2 121	269.261	265.635	14	19.307	1.704	52	10.31
F2 125	252.013	425.658	17	18.958	0.286	37	5.91
F2 126	736.177	751.101	17	19.013	0.454	219	8.04
F2 128	272.688	281.858	16	18.834	0.704	269	5.36
F2 132	261.900	263.343	11	18.994	0.632	34	0.94
F2 134	613.777	471.715	17	19.057	0.866	235	14.77
F2 143	276.128	276.658	13	19.411	1.592	1103	5.78
F2 147	273.012	272.684	15	19.221	0.744	271	15.34
F2 150	802.346	660.487	17	19.128	0.728	711	2.29
F2 152	744.566	648.633	17	19.146	0.678	237	14.83
F2 154	834.503	691.920	17	19.112	0.408	238	4.28
F2 157	890.629	579.198	15	19.099	0.344	66	7.83
F2 158	250.699	282.871	15	19.141	0.304	34	16.62
F2 159	52.714	173.113	11	19.082	1.802	72	15.86
F2 162	298.916	642.226	17	19.155	0.586	246	23.89
F2 163	206.569	721.164	17	19.187	0.424	183	45.90
F2 165	31.496	188.589	11	20.466	0.552	42	160.25
F2 166	586.997	98.790	17	19.212	0.746	241	17.23
F2 167	66.717	695.421	17	19.175	1.090	464	14.76
F2 170	637.464	70.001	17	19.183	0.332	175	3.72
F2 173	832.496	675.795	17	19.238	0.392	142	3.37
F2 175	236.416	677.689	17	19.249	0.350	76	7.01
F2 177	789.607	543.914	17	19.209	0.468	240	6.31
F2 178	789.312	224.550	17	19.201	0.220	287	12.83
F2 183	45.022	162.184	12	19.234	1.520	35	10.82
F2 184	89.453	42.888	17	19.256	0.900	228	17.95
F2 187	229.873	503.941	17	19.182	0.570	191	14.15
F2 188	332.896	138.761	17	19.281	0.298	105	2.94
F2 190	597.548	560.955	17	19.281	0.304	1074	3.24
F2 196	329.602	569.643	17	19.305	0.482	149	11.19
F2 198	538.040	121.277	17	19.354	0.800	775	11.05
F2 199	483.983	160.150	17	19.279	0.268	455	10.58

ID #	x	y	N	$\overline{K}$	Amplitude	Period	reduced χ^2
F2 204	118.156	302.614	17	19.387	0.632	151	14.06
F2 205	811.260	254.742	17	19.548	1.038	453	1.73
F2 206	614.961	263.825	17	19.493	0.874	466	7.57
F2 208	629.252	657.018	17	19.424	0.814	230	13.66
F2 210	43.283	736.169	17	19.210	0.652	1592	5.54
F2 213	7.416	183.856	13	19.321	0.472	224	4.37
F2 214	12.447	629.885	14	19.236	0.402	57	3.09
F2 216	850.262	87.974	17	19.550	0.748	394	3.80
F2 217	266.525	290.902	11	19.579	1.648	60	2.58
F2 226	563.207	365.031	17	19.353	0.772	433	7.11
F2 228	513.510	254.588	17	19.453	0.648	225	3.32
F2 229	767.634	146.581	17	19.342	0.546	421	4.84
F2 230	526.600	8.395	17	19.418	0.134	232	20.89
F2 234	792.017	662.189	17	19.401	0.486	110	10.42
F2 235	433.015	63.713	17	19.285	0.880	414	12.88
F2 236	479.495	204.686	17	19.339	0.356	542	30.13
F2 239	26.918	178.717	13	19.194	1.192	60	6.91
F2 244	691.165	210.113	17	19.406	0.502	112	14.55
F2 249	624.224	201.437	16	19.426	0.518	72	8.75
F2 250	468.253	867.895	11	19.384	0.334	99	4.49
F2 252	693.733	383.051	17	19.451	1.134	442	8.57
F2 254	610.524	199.065	16	19.303	0.940	263	4.58
F2 258	617.252	11.409	17	19.431	0.524	470	20.24
F2 262	528.192	34.947	17	19.714	1.178	422	25.12
F2 263	60.766	435.213	17	19.419	1.330	222	48.85
F2 264	18.739	61.782	16	19.437	0.368	180	3.23
F2 266	245.437	114.684	17	19.292	0.658	1359	18.02
F2 270	23.387	678.323	16	19.673	0.802	391	5.89
F2 272	65.495	671.802	17	19.623	0.724	416	13.36
F2 274	100.778	704.260	17	19.381	0.158	432	30.05
F2 276	596.120	808.672	17	19.369	1.334	421	45.61
F2 280	397.962	141.526	17	19.568	0.548	112	19.46
F2 283	421.796	676.846	17	19.461	0.222	225	1.32
F2 284	891.698	580.292	12	19.527	0.434	190	3.98
F2 285	829.039	545.463	17	19.544	0.780	417	7.16
F2 286	359.610	671.560	17	19.489	0.306	192	4.03
F2 288	78.147	117.525	17	19.426	0.850	419	5.71
F2 289	702.883	824.407	17	19.608	0.906	418	17.29
F2 292	843.922	426.940	17	19.593	0.718	233	20.33
F2 293	25.398	434.269	16	19.481	0.532	54	5.44
F2 295	679.976	778.065	17	19.537	0.790	840	6.10
F2 297	592.506	343.163	17	19.462	0.234	191	5.55
F2 301	753.522	17.613	17	19.631	0.710	448	23.54
F2 302	102.069	227.256	17	19.523	0.052	113	6.02
F2 306	21.578	164.711	15	19.806	1.550	888	49.68
F2 312	523.542	598.492	17	19.580	0.756	246	12.16
F2 316	504.315	13.527	17	19.557	0.504	692	4.11
F2 317	564.701	488.872	17	19.635	0.908	34	16.38
F2 318	217.893	526.155	17	19.439	0.420	437	6.36

ID #	x	y	N	$\overline{K}$	Amplitude	Period	reduced χ^2
F2 324	272.596	290.337	11	20.125	2.778	39	15.96
F2 327	428.782	781.850	17	19.628	0.732	235	18.82
F2 329	466.545	163.298	17	19.484	0.482	170	7.99
F2 331	300.097	861.288	11	19.593	0.378	246	6.40
F2 333	679.448	59.865	17	19.592	0.608	34	7.29
F2 336	725.303	96.766	17	19.605	0.458	667	2.70
F2 337	49.622	176.088	12	19.408	1.886	115	2.55
F2 340	191.638	365.719	17	19.545	0.494	395	4.81
F2 342	382.490	153.423	17	19.595	0.442	143	13.95
F2 344	504.683	611.143	17	19.555	0.254	176	3.75
F2 345	326.211	12.063	17	19.557	0.246	182	2.02
F2 346	553.117	180.719	17	19.670	0.954	232	17.65
F2 349	186.365	194.762	17	19.532	0.760	705	2.41
F2 350	240.385	634.800	17	19.498	0.386	193	2.35
F2 351	375.309	596.132	17	19.649	0.456	433	3.08
F2 353	223.914	234.600	17	19.612	0.192	129	4.82
F2 355	503.628	655.967	17	19.732	0.760	448	3.04
F2 356	266.794	166.535	17	19.788	0.790	447	7.73
F2 358	875.878	35.767	16	19.694	0.394	432	11.17
F2 360	409.186	322.188	17	19.555	0.256	259	1.01
F2 361	150.265	309.702	17	19.802	1.250	425	26.48
F2 362	654.272	480.812	17	19.840	1.232	442	25.61
F2 364	222.744	659.922	17	19.671	0.700	433	11.18
F2 368	335.325	155.853	17	19.639	1.220	425	34.33
F2 369	38.189	496.535	17	19.825	0.802	1661	13.20
F2 370	482.633	165.496	17	19.622	0.394	184	5.66
F2 371	164.686	651.700	17	19.566	0.292	187	1.37
F2 374	442.370	576.406	17	19.554	0.614	413	2.58
F2 375	405.761	554.161	17	19.580	0.412	240	3.56
F2 383	742.393	541.564	17	19.638	0.422	431	1.71
F2 385	241.829	410.707	17	19.742	0.874	408	5.44
F2 387	185.502	530.914	17	19.613	0.636	192	9.62
F2 388	765.472	395.909	17	19.668	0.836	441	13.66
F2 389	550.437	731.140	17	19.909	1.162	410	14.15
F2 390	541.059	317.736	17	19.609	0.770	423	46.31
F2 392	597.406	11.489	17	19.570	1.374	722	12.01
F2 393	126.656	70.833	17	19.637	0.288	195	9.35
F2 394	219.405	287.684	17	19.639	1.144	800	23.36
F2 397	376.195	655.217	17	19.739	0.630	419	6.27
F2 400	33.616	265.502	16	19.619	0.206	171	3.19
F2 401	623.489	122.809	17	19.591	0.318	118	9.67
F2 402	804.322	348.686	17	19.635	0.616	192	8.05
F2 405	301.115	527.190	17	19.605	0.164	42	3.27
F2 407	753.317	309.070	17	19.674	0.648	196	26.79
F2 410	557.126	429.554	17	19.699	0.574	113	20.08
F2 412	394.931	609.693	17	19.512	1.006	408	12.95
F2 413	107.375	14.261	17	19.553	0.416	175	5.44
F2 415	774.868	518.034	17	19.630	0.148	165	48.93
F2 425	624.870	681.515	17	19.638	0.178	528	10.11

ID #	x	y	N	$\overline{K}$	Amplitude	Period	reduced χ^2
F2 430	310.656	488.871	17	19.817	0.690	473	32.17
F2 431	308.432	327.350	17	19.656	0.356	101	7.51
F2 434	44.627	223.436	17	19.676	0.464	42	3.45
F2 436	250.318	270.851	11	19.748	1.462	264	5.54
F2 439	252.287	424.331	16	19.629	0.310	42	5.91
F2 440	559.649	843.515	17	19.616	1.204	741	11.47
F2 441	214.692	359.667	17	19.625	0.194	423	18.26
F2 444	791.055	118.389	17	19.695	0.606	421	1.59
F2 445	162.065	127.320	17	19.678	0.322	116	7.87
F2 447	862.014	481.224	16	19.728	0.430	114	13.82
F2 448	807.812	823.271	17	19.689	0.572	420	3.24
F2 450	328.239	403.949	17	19.657	0.274	187	6.90
F2 454	619.203	206.482	17	19.651	0.692	52	5.54
F2 459	854.503	430.508	17	19.725	0.286	114	43.62
F2 463	137.688	476.834	17	19.901	0.898	153	46.21
F2 464	487.021	630.997	17	19.623	0.626	411	4.65
F2 468	772.369	3.064	16	19.654	0.742	751	4.67
F2 469	225.507	184.807	17	19.746	0.352	187	3.92
F2 471	565.238	110.761	17	19.677	1.572	706	8.21
F2 477	353.398	442.544	17	19.696	0.412	172	4.50
F2 479	105.861	375.835	17	19.674	0.782	190	7.02
F2 484	446.777	197.518	17	19.894	0.884	449	10.01
F2 486	119.366	571.609	17	19.903	0.928	113	54.38
F2 495	443.911	118.337	17	19.754	0.434	106	10.28
F2 498	603.368	170.848	17	19.749	0.688	437	17.10
F2 507	817.607	95.649	17	19.653	0.414	188	5.52
F2 508	373.100	646.682	17	19.829	0.796	442	3.66
F2 511	679.423	336.171	17	19.678	0.352	617	1.52
F2 512	226.893	343.069	17	19.718	0.308	412	2.30
F2 518	880.901	305.086	16	19.742	0.388	268	4.61
F2 519	263.900	41.436	17	19.788	0.508	189	15.37
F2 520	788.009	400.450	17	19.810	0.568	111	24.44
F2 525	140.281	119.757	17	19.678	0.696	405	2.85
F2 526	260.172	752.257	17	19.677	1.208	721	12.54
F2 527	583.243	118.467	17	19.695	0.680	242	12.07
F2 529	891.495	765.524	12	19.759	0.642	109	16.57
F2 531	535.473	226.268	17	19.756	0.896	237	13.70
F2 532	200.618	102.860	17	19.713	0.614	237	6.30
F2 537	409.264	716.294	17	19.662	0.770	194	7.90
F2 539	611.119	213.197	10	19.915	1.250	52	2.86
F2 541	449.282	20.010	17	19.658	1.232	396	4.37
F2 544	779.790	44.413	17	20.086	1.134	484	3.69
F2 546	784.049	585.928	17	19.776	0.644	76	27.57
F2 548	359.524	421.189	17	19.764	0.350	41	4.47
F2 549	215.929	745.914	17	19.939	1.074	417	14.06
F2 554	442.430	-0.472	14	20.467	0.450	226	224.55
F2 555	608.614	220.032	17	19.799	0.836	989	4.35
F2 557	326.060	201.754	17	19.789	0.408	114	1.83
F2 558	602.318	223.793	17	19.693	0.452	114	26.53

ID #	x	y	N	$\overline{K}$	Amplitude	Period	reduced χ^2
F2 567	20.152	269.143	16	19.734	1.232	754	35.05
F2 577	217.406	544.318	17	19.853	0.438	479	23.94
F2 578	612.325	301.398	17	19.699	0.400	194	1.47
F2 579	615.943	211.941	15	19.776	0.984	45	3.84
F2 581	388.352	221.832	17	19.781	0.248	191	1.40
F2 583	217.589	43.446	17	19.914	0.846	408	5.46
F2 587	176.999	425.789	17	19.744	0.382	188	2.58
F2 588	141.468	398.022	17	20.036	1.264	399	3.35
F2 591	576.439	405.224	17	19.748	0.804	194	13.95
F2 592	61.060	594.157	17	19.750	0.234	228	1.91
F2 593	770.645	463.371	17	19.864	0.454	226	9.55
F2 594	367.401	203.554	17	19.755	0.288	189	2.72
F2 595	672.358	757.659	17	19.934	0.654	426	9.58
F2 596	231.990	714.727	17	19.872	0.464	238	9.63
F2 599	216.724	846.420	17	19.748	0.572	196	13.76
F2 600	489.305	607.938	17	19.741	0.314	434	63.11
F2 601	75.974	540.877	17	19.759	0.402	177	9.55
F2 603	893.390	672.102	10	20.026	1.586	82	8.05
F2 607	832.696	409.666	17	19.988	0.846	409	5.82
F2 608	288.621	647.857	17	19.816	0.926	225	19.02
F2 614	150.261	68.675	17	19.814	0.608	181	7.98
F2 615	729.079	572.044	17	19.797	0.334	167	4.72
F2 617	735.316	52.550	17	19.851	0.514	107	14.44
F2 620	612.817	108.314	17	19.827	0.892	227	20.28
F2 622	43.452	766.742	16	19.772	0.660	753	9.26
F2 628	29.277	391.389	16	19.833	0.694	224	12.35
F2 629	864.472	45.084	16	20.119	1.360	444	13.80
F2 630	376.486	391.720	17	19.891	1.676	728	8.28
F2 631	752.979	517.302	17	19.784	0.156	286	10.04
F2 632	621.444	185.186	17	19.889	0.820	414	4.26
F2 634	695.493	245.671	17	19.865	0.352	192	25.77
F2 636	392.851	681.028	17	19.773	0.422	108	4.18
F2 637	6.947	347.876	12	20.059	1.094	1494	10.65
F2 640	68.501	709.015	17	20.041	0.952	409	4.51
F2 641	388.722	379.745	17	19.837	0.420	181	8.83
F2 644	243.520	66.657	17	19.740	0.446	397	2.98
F2 645	437.661	95.481	17	20.030	1.100	433	19.80
F2 648	197.329	-4.632	10	19.827	0.758	34	6.14
F2 651	448.530	245.245	17	19.842	0.164	486	5.78
F2 655	250.784	727.529	17	19.969	0.862	395	2.23
F2 659	867.064	551.734	16	19.909	1.130	465	18.22
F2 663	442.655	159.750	17	19.960	0.622	421	9.51
F2 665	18.709	274.321	16	19.930	0.174	409	48.28
F2 666	612.906	216.769	14	19.887	0.786	1229	4.48
F2 668	612.212	220.155	15	19.937	1.246	60	2.73
F2 669	136.085	129.510	17	19.895	0.534	109	6.49
F2 677	593.410	604.341	17	19.887	0.424	113	15.41
F2 681	563.933	505.080	17	19.912	0.774	167	33.03
F2 683	764.890	387.731	17	19.835	0.506	195	10.56

ID #	x	y	N	$\overline{K}$	Amplitude	Period	reduced χ^2
F2 688	716.364	310.156	17	20.047	0.924	431	4.71
F2 689	823.332	255.810	17	19.981	0.608	189	17.26
F2 699	607.641	715.545	17	20.010	1.016	412	8.84
F2 705	192.530	554.659	17	19.803	0.362	232	11.08
F2 706	384.743	349.734	17	20.033	0.858	112	31.55
F2 711	874.861	660.243	13	20.099	1.558	52	13.44
F2 712	717.969	378.408	17	20.166	1.038	411	18.35
F2 713	127.901	596.158	17	19.813	1.396	735	13.08
F2 714	807.478	555.211	17	19.842	0.308	151	4.26
F2 720	386.494	661.383	17	19.867	0.410	96	5.60
F2 721	245.584	277.830	15	20.380	2.960	430	62.11
F2 722	51.848	373.793	17	19.926	0.372	1358	32.03
F2 723	227.945	389.660	17	19.729	0.766	194	8.43
F2 725	161.921	593.051	17	20.042	1.252	431	8.08
F2 729	143.320	67.834	17	19.906	0.410	111	6.51
F2 730	261.442	40.212	17	19.910	0.300	117	4.76
F2 731	825.938	275.266	17	19.895	0.372	107	5.06
F2 734	543.752	359.814	17	19.918	0.346	191	16.62
F2 736	168.675	199.799	17	19.971	0.080	178	27.31
F2 742	800.972	89.218	17	19.880	0.390	53	7.44
F2 743	234.896	556.086	17	19.895	0.398	169	1.50
F2 745	481.795	328.363	17	19.849	0.306	186	9.18
F2 747	586.991	469.608	17	19.827	0.374	223	8.59
F2 752	245.684	319.908	17	20.090	0.904	228	23.25
F2 753	606.024	212.791	15	20.096	2.014	54	4.90
F2 754	460.981	9.114	17	19.809	0.908	387	4.83
F2 757	870.467	38.636	15	19.930	0.460	170	19.74
F2 758	553.104	557.432	17	20.022	0.284	272	86.05
F2 759	327.221	294.324	17	20.097	1.048	400	11.18
F2 760	810.201	784.991	17	19.824	0.462	196	3.19
F2 762	738.338	482.237	17	20.175	1.178	416	14.95
F2 764	58.135	169.853	10	20.422	3.934	84	47.91
F2 765	802.887	303.445	17	19.848	0.342	272	3.88
F2 770	827.570	654.082	17	20.141	0.894	236	9.28
F2 774	39.219	632.946	17	19.897	2.076	731	25.29
F2 777	657.190	42.364	17	19.893	0.336	176	4.41
F2 778	684.780	31.183	17	19.993	0.660	192	19.46
F2 779	319.419	579.210	17	19.995	0.982	447	15.56
F2 784	384.951	361.454	17	19.843	1.210	749	13.97
F2 790	28.126	442.650	14	19.869	0.392	170	7.13
F2 793	228.087	349.669	17	19.915	0.278	177	2.15
F2 802	552.846	-1.377	14	19.892	0.488	187	2.37
F2 805	497.552	237.283	17	19.815	0.558	189	1.02
F2 807	761.662	134.908	17	19.986	0.598	111	20.70
F2 808	597.579	834.626	17	20.083	0.982	450	7.30
F2 809	331.061	213.319	17	19.937	0.796	416	3.00
F2 819	49.015	131.922	17	19.975	0.252	419	22.80
F2 820	549.074	166.580	17	20.274	1.730	438	87.21
F2 822	123.090	645.156	17	19.938	0.514	171	4.72

ID #	x	y	N	$\overline{K}$	Amplitude	Period	reduced χ^2
F2 826	276.182	581.523	17	20.134	0.610	240	13.69
F2 828	355.761	75.666	17	19.989	0.366	222	5.91
F2 829	470.711	678.068	17	19.956	0.420	1360	25.41
F2 830	638.559	168.191	17	19.951	0.382	173	7.21
F2 835	108.750	859.719	11	20.129	0.978	429	1.02
F2 838	350.029	761.700	17	19.970	0.456	108	6.89
F2 842	526.560	462.435	17	19.929	0.708	188	10.11
F2 845	405.286	296.480	17	19.892	0.252	420	3.82
F2 850	769.616	420.260	17	19.915	0.304	49	5.96
F2 853	798.510	34.801	17	20.062	0.572	556	5.84
F2 854	478.030	712.059	17	20.173	0.894	488	12.70
F2 857	254.098	28.469	17	19.959	0.880	721	10.92
F2 869	620.900	311.326	17	19.906	0.680	391	3.43
F2 873	455.271	724.789	17	19.964	0.672	702	2.62
F2 874	116.509	331.925	17	20.064	0.284	411	38.60
F2 875	219.659	848.026	17	19.927	0.646	228	8.59
F2 880	786.150	72.587	17	20.041	0.496	641	5.84
F2 882	894.163	151.042	10	20.227	1.610	476	8.32
F2 883	675.832	236.575	17	19.930	0.958	408	1.86
F2 887	599.395	44.994	17	20.023	0.694	174	18.42
F2 888	889.956	524.250	15	20.163	1.136	435	11.46
F2 889	490.560	232.415	17	20.331	1.004	241	21.53
F2 890	233.023	436.749	17	20.172	0.822	185	28.33
F2 892	700.070	428.177	17	19.991	0.444	180	9.83
F2 893	815.744	648.103	17	19.946	0.228	40	6.45
F2 894	164.053	165.687	17	19.898	0.492	391	10.64
F2 895	121.787	653.473	17	20.093	0.864	464	28.71
F2 896	287.056	201.611	17	20.012	0.432	174	8.04
F2 900	284.689	49.685	17	20.102	0.270	230	28.53
F2 901	74.941	149.611	17	19.973	0.574	232	16.14
F2 904	547.011	590.343	17	20.249	1.466	430	30.77
F2 908	66.194	34.928	17	19.990	0.116	91	8.78
F2 910	578.596	714.768	17	20.122	0.856	114	40.16
F2 914	622.372	213.120	10	20.294	1.450	567	3.23
F2 915	728.241	285.170	17	20.029	0.506	170	7.74
F2 916	265.342	15.246	17	20.019	0.402	77	18.11
F2 925	351.381	437.512	17	19.953	0.420	226	11.08
F2 926	195.610	278.901	17	20.039	0.386	277	11.15
F2 929	683.390	648.248	17	19.977	0.938	413	1.97
F2 930	237.840	279.704	17	19.864	0.526	456	14.60
F2 932	471.115	171.510	17	20.032	0.458	169	8.71
F2 934	224.999	57.006	17	20.105	1.122	434	17.99
F2 935	606.079	196.421	14	20.101	1.052	898	5.66
F2 941	637.036	413.435	17	19.962	0.284	164	4.06
F2 957	734.732	233.294	17	19.975	0.288	267	5.29
F2 958	210.934	361.345	17	19.971	0.266	182	5.50
F2 959	128.730	54.423	17	19.963	0.224	49	4.16
F2 964	690.056	79.860	17	19.942	1.448	724	15.06
F2 969	12.621	328.670	16	19.843	0.756	458	5.96

ID #	x	y	N	$\overline{K}$	Amplitude	Period	reduced χ^2
F2 971	764.590	373.904	17	19.902	0.294	211	2.58
F2 972	861.973	236.710	16	20.073	0.384	564	7.11
F2 992	480.878	-2.019	12	20.013	0.668	56	9.57
F2 995	773.795	71.255	17	20.157	0.838	168	22.93
F2 998	41.218	298.675	17	20.050	0.554	170	5.74
F2 999	5.277	232.155	12	20.010	0.450	35	4.82
F2 1002	442.816	243.972	17	20.097	0.532	162	7.33
F2 1004	868.299	667.284	12	20.336	1.360	99	19.70
F2 1008	548.965	372.200	17	20.038	0.510	180	8.07
F2 1010	356.240	158.061	17	20.050	0.360	423	4.37
F2 1011	302.653	543.326	17	20.201	1.140	400	1.95
F2 1014	234.731	350.057	17	20.022	0.718	421	8.42
F2 1015	815.230	569.734	17	20.080	0.192	420	50.32
F2 1017	710.976	410.799	17	20.122	0.588	109	13.12
F2 1018	869.544	231.404	15	20.029	0.472	87	4.95
F2 1019	730.048	856.760	14	19.909	1.252	692	1.81
F2 1020	354.587	206.357	17	20.100	0.710	395	5.24
F2 1021	86.566	427.416	17	20.085	0.808	112	37.76
F2 1022	480.089	231.833	17	20.141	0.642	385	4.44
F2 1025	631.387	109.552	17	20.104	0.548	184	14.18
F2 1027	873.230	654.912	16	20.058	0.904	1212	6.24
F2 1031	541.856	392.265	17	20.042	0.626	151	6.50
F2 1033	688.823	140.414	17	19.995	0.266	167	2.08
F2 1034	443.976	671.623	17	20.011	0.430	184	5.12
F2 1035	124.195	358.240	17	20.067	0.406	298	2.55
F2 1036	209.113	33.493	17	20.087	0.458	118	9.09
F2 1037	828.397	263.440	17	20.088	0.438	241	7.33
F2 1040	839.381	811.944	17	20.056	0.520	111	7.83
F2 1042	791.753	93.627	17	20.109	0.394	536	3.86
F2 1044	831.760	578.118	17	20.024	1.026	227	33.36
F2 1045	690.220	725.336	17	20.048	0.550	162	5.25
F2 1048	359.926	352.378	17	20.037	0.044	175	7.02
F2 1050	830.969	266.838	17	20.060	0.482	166	4.81
F2 1052	452.228	624.117	17	20.205	0.736	165	11.70
F2 1053	887.527	609.321	16	20.322	0.920	197	11.62
F2 1054	397.023	696.685	16	20.074	0.554	169	4.28
F2 1056	303.195	203.471	17	20.046	0.288	175	3.16
F2 1066	144.097	661.941	17	20.111	0.978	440	7.14
F2 1072	61.628	193.516	17	20.034	0.370	148	4.94
F2 1073	630.737	532.164	17	20.114	0.992	463	4.69
F2 1077	239.977	329.546	17	20.181	0.210	224	26.79
F2 1081	78.478	616.725	17	20.231	0.644	836	12.53
F2 1089	621.882	244.105	17	20.137	0.576	146	10.93
F2 1094	493.232	636.526	17	20.119	0.420	293	4.68
F2 1095	555.640	148.275	17	20.198	0.728	173	7.72
F2 1096	430.697	511.111	17	20.077	0.372	113	5.31
F2 1097	311.626	31.453	17	20.054	0.426	172	2.90
F2 1098	611.578	36.605	17	20.147	1.400	427	24.22
F2 1099	406.062	412.469	17	20.093	0.722	979	5.39

ID #	x	y	N	$\overline{K}$	Amplitude	Period	reduced χ^2
F2 1100	613.049	539.525	17	20.122	0.676	395	9.21
F2 1108	191.740	355.946	17	20.366	1.042	377	14.76
F2 1109	705.958	674.746	17	20.057	0.370	165	3.19
F2 1113	752.668	190.092	17	20.257	0.426	227	25.71
F2 1114	70.989	646.554	17	20.375	1.382	395	7.23
F2 1116	881.211	122.311	16	20.097	0.416	192	26.18
F2 1117	257.575	681.266	17	20.218	0.898	391	9.81
F2 1121	452.298	378.606	17	20.055	0.408	179	4.03
F2 1124	494.758	27.314	17	20.171	0.550	117	11.06
F2 1129	869.521	109.441	16	20.124	0.056	298	10.11
F2 1130	420.312	569.225	17	20.185	0.574	164	9.32
F2 1133	626.091	102.723	17	20.112	0.494	271	3.96
F2 1135	103.665	313.057	17	20.078	0.506	246	3.38
F2 1142	528.800	805.413	17	20.145	0.834	34	9.76
F2 1151	766.538	748.846	17	20.038	0.560	174	3.87
F2 1153	659.528	568.552	17	20.165	0.786	164	14.90
F2 1154	534.250	395.894	17	20.175	0.536	1450	27.99
F2 1159	863.423	656.039	14	19.916	1.136	339	3.51
F2 1163	144.625	757.718	17	20.136	0.830	417	11.54
F2 1167	628.352	442.214	17	20.258	0.562	198	10.09
F2 1169	300.295	735.626	17	20.137	0.564	37	5.03
F2 1173	319.612	816.077	17	20.063	0.622	224	9.05
F2 1179	604.349	485.236	17	20.129	0.568	177	9.35
F2 1185	696.621	801.326	17	20.082	0.346	825	5.77
F2 1191	72.539	20.002	17	20.246	1.758	708	17.59
F2 1192	496.543	370.730	17	20.275	0.482	395	49.23
F2 1193	666.308	727.835	17	20.125	0.578	176	8.94
F2 1200	691.089	27.208	17	20.140	0.596	180	1.78
F2 1202	337.801	-6.917	10	20.289	0.974	190	10.87
F2 1209	885.106	465.586	16	20.070	0.518	228	14.55
F2 1210	328.823	173.031	17	20.022	0.506	446	16.50
F2 1211	110.313	722.684	17	20.017	1.004	398	5.01
F2 1218	468.396	24.593	17	20.101	0.268	1207	4.91
F2 1223	45.103	731.205	17	20.069	0.382	186	4.91
F2 1227	134.532	3.389	14	20.295	0.682	286	3.98
F2 1229	450.789	258.261	17	20.061	1.544	721	9.77
F2 1230	592.238	113.580	16	20.302	0.672	278	16.20
F2 1237	294.412	571.850	17	20.061	0.506	224	13.10
F2 1239	815.917	748.280	17	20.235	0.952	217	7.61
F2 1241	721.044	644.476	17	20.177	0.570	186	5.37
F2 1252	818.698	625.949	17	20.156	0.494	168	9.28
F2 1257	741.930	653.471	17	20.107	0.126	233	12.14
F2 1259	109.548	261.771	17	20.143	0.192	112	22.35
F2 1265	91.833	2.784	15	20.060	0.740	180	20.97
F2 1266	541.680	448.695	17	20.172	0.480	182	16.62
F2 1268	193.148	727.941	17	20.232	0.478	420	4.07
F2 1270	387.904	598.761	17	20.099	0.556	119	6.61
F2 1271	169.984	493.087	17	20.125	0.704	388	12.18
F2 1272	652.908	748.377	17	20.110	0.362	151	1.98

ID #	x	y	N	$\overline{K}$	Amplitude	Period	reduced χ^2
F2 1282	149.951	55.768	17	20.132	0.114	165	10.62
F2 1284	414.069	729.691	17	20.064	0.336	224	6.88
F2 1286	685.462	290.946	17	20.219	0.468	118	11.59
F2 1291	127.416	26.245	17	20.239	0.518	116	15.17
F2 1292	61.944	796.044	17	20.163	0.556	169	6.64
F2 1293	692.435	94.442	17	20.131	0.794	428	11.73
F2 1294	14.523	722.495	16	20.110	0.846	410	6.04
F2 1299	25.280	214.197	16	20.312	1.576	724	12.18
F2 1300	894.812	436.832	10	20.427	0.826	214	10.98
F2 1302	791.868	392.279	17	20.104	0.416	159	7.04
F2 1304	327.642	811.622	17	20.160	0.340	170	4.58
F2 1306	342.231	598.418	17	20.246	0.700	440	17.89
F2 1307	571.828	6.316	17	20.268	0.548	399	4.00
F2 1308	869.119	267.048	16	20.211	0.492	179	10.41
F2 1309	570.299	356.375	17	20.349	1.248	739	18.64
F2 1311	763.361	172.866	17	20.127	0.806	435	4.01
F2 1319	220.334	30.493	17	20.219	0.368	116	4.59
F2 1321	613.402	357.207	17	20.306	0.600	579	8.40
F2 1328	32.195	36.679	16	20.184	0.498	258	5.85
F2 1333	583.340	658.698	17	20.210	0.480	112	11.43
F2 1336	572.340	115.394	17	20.167	0.390	53	5.71
F2 1344	154.003	298.912	17	20.198	0.446	601	3.66
F2 1345	424.520	645.717	17	20.355	0.702	554	5.05
F2 1347	314.047	818.495	17	20.076	0.622	188	5.92
F2 1351	503.841	149.953	17	20.169	0.354	186	2.77
F2 1352	38.498	63.594	17	20.172	0.624	53	8.21
F2 1353	529.284	819.818	17	20.151	0.442	162	10.33
F2 1354	135.922	532.683	17	20.155	0.372	175	4.05
F2 1362	655.207	418.430	17	20.233	0.262	425	61.21
F2 1364	869.840	39.475	16	20.273	0.146	97	45.58
F2 1370	685.490	498.934	16	20.198	0.380	106	5.86
F2 1373	241.224	575.524	17	20.279	0.136	222	10.58
F2 1387	781.282	221.812	17	20.155	0.684	229	17.40
F2 1390	176.400	28.126	17	20.242	1.138	443	11.93
F2 1391	174.522	430.641	17	20.352	0.308	424	36.94
F2 1393	235.369	370.898	17	20.146	0.698	467	8.90
F2 1394	590.227	348.678	17	20.208	0.556	174	7.21
F2 1395	851.894	53.944	17	20.142	0.492	156	4.56
F2 1400	414.635	114.282	17	20.376	0.846	188	13.35
F2 1406	359.891	637.725	17	20.278	0.584	166	11.47
F2 1408	99.981	253.539	17	20.245	0.592	175	13.84
F2 1413	673.478	23.449	17	20.434	0.868	112	30.98
F2 1414	541.370	443.695	17	20.303	0.572	571	4.94
F2 1418	600.699	98.443	17	20.184	0.380	156	2.64
F2 1427	885.197	241.056	16	20.175	0.386	154	9.87
F2 1429	679.749	105.190	17	20.241	0.502	37	13.11
F2 1431	373.289	462.314	17	20.127	1.028	196	21.35
F2 1434	9.538	625.078	13	20.263	0.076	171	13.40
F2 1435	32.767	281.422	16	20.223	0.480	174	9.80

ID #	x	y	N	$\overline{K}$	Amplitude	Period	reduced χ^2
F2 1436	249.162	142.140	17	20.350	0.782	184	20.02
F2 1441	297.542	737.609	17	20.718	2.050	776	22.35
F2 1447	388.567	870.014	10	20.259	0.698	97	4.67
F2 1449	232.357	42.350	17	20.149	0.556	178	2.21
F2 1462	93.196	244.998	17	20.392	0.788	113	19.94
F2 1466	872.320	666.382	15	20.195	1.036	108	6.10
F2 1469	269.270	1.797	16	20.309	0.560	50	3.85
F2 1475	848.554	389.541	17	20.184	0.578	229	15.87
F2 1476	404.768	183.555	17	20.244	0.370	100	6.59
F2 1478	370.264	103.553	17	20.164	0.766	232	8.23
F2 1479	96.316	669.143	16	20.326	0.508	121	9.02
F2 1481	706.733	203.528	17	20.265	0.608	1133	4.71
F2 1484	600.341	200.362	13	20.161	0.250	60	13.87
F2 1490	689.084	453.066	17	20.243	0.476	137	2.03
F2 1493	319.642	617.444	17	20.233	0.512	42	7.41
F2 1500	412.172	367.134	17	20.228	0.562	251	5.40
F2 1511	375.751	765.515	17	20.224	0.500	183	3.72
F2 1513	491.608	75.767	16	20.179	1.706	720	9.44
F2 1515	440.460	513.379	17	20.235	0.314	263	2.60
F2 1521	606.080	225.549	17	20.021	1.134	42	45.00
F2 1523	421.568	282.352	17	20.359	1.462	225	31.63
F2 1530	863.919	428.379	16	20.226	0.348	416	24.36
F2 1538	262.594	421.731	17	20.230	0.292	162	4.18
F2 1540	711.909	559.909	17	20.226	0.544	151	4.65
F2 1546	246.876	247.852	17	20.180	0.500	623	11.23
F2 1553	592.369	217.930	16	20.325	0.754	482	41.42
F2 1554	575.933	301.237	17	20.291	0.792	663	4.16
F2 1560	131.462	614.857	17	20.439	0.846	112	28.11
F2 1567	780.117	653.662	17	20.240	0.316	92	3.83
F2 1571	171.688	600.458	17	20.274	0.434	37	8.92
F2 1572	666.305	60.090	17	20.260	0.378	37	4.04
F2 1573	381.194	313.528	17	20.299	0.686	162	4.09
F2 1584	508.940	137.406	17	20.345	0.718	149	16.51
F2 1591	566.429	702.779	17	20.245	0.470	108	6.18
F2 1594	886.165	842.031	16	20.248	0.472	110	12.69
F2 1600	154.246	107.769	17	20.305	0.538	106	10.71
F2 1603	184.274	636.128	17	20.766	2.002	776	18.64
F2 1605	847.721	649.565	17	20.296	0.580	164	3.99
F2 1607	541.512	536.064	17	20.800	1.578	491	3.91
F2 1613	677.737	103.983	17	20.489	0.726	579	12.97
F2 1614	660.828	313.912	17	20.259	0.344	169	6.28
F2 1619	119.500	457.078	16	20.217	0.994	60	14.24
F2 1626	195.472	396.109	17	20.263	0.390	107	3.21
F2 1634	646.822	620.321	17	20.173	0.530	192	5.50
F2 1643	346.363	361.914	17	20.253	0.396	246	1.35
F2 1650	859.740	304.856	16	20.344	0.508	1053	4.71
F2 1652	71.731	566.204	17	20.408	0.368	428	35.42
F2 1653	598.688	641.240	17	20.324	0.602	159	3.62
F2 1654	113.037	406.123	17	20.214	0.438	118	4.39

ID #	x	y	N	$\overline{K}$	Amplitude	Period	reduced χ^2
F2 1655	407.416	579.852	17	20.206	0.396	534	10.57
F2 1659	849.509	740.469	17	20.267	0.218	170	16.59
F2 1660	869.722	250.832	16	20.248	0.506	708	2.55
F2 1662	575.474	194.851	17	20.264	0.496	164	3.37
F2 1681	826.847	327.655	17	20.360	0.554	111	22.05
F2 1682	70.395	424.610	17	20.288	0.488	106	10.64
F2 1689	202.682	585.188	17	20.290	0.346	168	1.76
F2 1697	153.804	74.109	17	20.309	0.486	285	3.42
F2 1699	843.073	828.160	16	20.296	0.422	56	6.72
F2 1700	293.221	671.382	17	20.576	1.176	429	22.76
F2 1702	640.327	69.991	17	20.347	0.596	164	7.44
F2 1703	99.701	328.759	17	20.288	0.494	113	9.40
F2 1711	740.244	45.226	16	20.416	0.508	118	10.37
F2 1720	694.866	817.787	17	20.464	0.986	161	11.34
F2 1722	672.016	536.987	17	20.339	0.664	248	1.89
F2 1724	622.433	620.684	17	20.292	0.512	174	5.70
F2 1738	142.721	474.944	17	20.313	0.044	37	12.48
F2 1740	834.209	238.470	17	20.337	0.112	237	20.61
F2 1743	817.019	740.809	17	20.323	0.362	243	2.54
F2 1761	77.649	340.107	17	20.257	0.464	424	14.33
F2 1772	643.389	672.885	17	20.336	0.600	152	7.80
F2 1773	108.715	335.933	17	20.357	0.646	242	12.43
F2 1776	212.002	72.663	17	20.364	0.376	273	3.29
F2 1778	50.521	354.260	17	20.568	0.914	1595	10.59
F2 1781	724.610	477.426	16	20.808	1.310	204	8.06
F2 1794	135.683	343.482	17	20.429	0.650	242	4.81
F2 1796	430.944	25.988	17	20.486	0.690	550	12.36
F2 1800	68.879	307.801	17	20.281	0.378	37	5.13
F2 1812	304.642	48.891	17	20.314	0.196	56	14.49
F2 1816	112.826	221.854	17	20.311	0.072	234	5.51
F2 1831	790.822	318.002	17	20.331	0.304	76	5.25
F2 1842	462.775	421.731	17	20.342	0.524	167	9.95
F2 1846	340.961	304.281	17	20.439	0.516	1465	5.32
F2 1849	296.290	208.560	17	20.491	0.628	560	4.35
F2 1853	664.953	396.472	17	20.385	0.668	147	6.73
F2 1856	406.821	782.045	17	20.420	0.560	174	19.46
F2 1858	152.762	576.541	17	20.376	0.454	158	6.89
F2 1866	101.056	391.058	17	20.326	0.554	116	3.25
F2 1867	200.921	249.848	17	20.382	0.376	186	9.40
F2 1871	65.500	262.035	17	20.336	0.388	54	6.71
F2 1875	370.507	152.146	17	20.500	0.632	540	6.16
F2 1888	40.390	627.762	17	20.417	0.526	95	10.27
F2 1897	739.885	55.878	17	20.328	0.598	257	3.79
F2 1900	601.155	203.366	13	20.400	0.866	40	2.42
F2 1903	802.802	165.107	17	20.300	0.802	617	9.24
F2 1910	165.815	722.616	17	20.364	0.490	114	8.73
F2 1913	461.821	103.826	17	20.394	0.476	107	4.80
F2 1919	832.798	178.952	17	20.390	0.572	141	7.18
F2 1920	70.627	821.115	17	20.350	0.598	266	1.13

ID #	x	y	N	$\overline{K}$	Amplitude	Period	reduced χ^2
F2 1924	49.254	103.296	17	20.393	0.732	176	19.95
F2 1928	421.450	429.998	17	20.512	0.868	175	21.16
F2 1933	691.069	7.807	17	20.376	0.294	264	4.76
F2 1936	754.744	98.622	17	20.341	0.500	37	17.05
F2 1938	213.129	364.442	17	20.386	0.564	178	8.65
F2 1939	683.722	606.478	17	20.508	0.548	255	2.83
F2 1940	768.250	550.948	17	20.425	0.544	112	10.67
F2 1942	894.795	468.305	11	20.586	0.802	121	6.91
F2 1947	104.445	64.046	17	20.373	0.488	174	8.21
F2 1952	24.292	491.294	16	20.390	0.608	174	8.91
F2 1956	166.310	219.654	17	20.464	0.564	227	13.49
F2 1963	741.724	440.168	17	20.398	0.154	238	22.53
F2 1971	154.966	109.619	17	20.303	0.548	526	9.10
F2 1973	97.513	635.774	16	20.465	0.904	659	15.10
F2 1978	332.235	207.477	17	20.440	0.280	174	19.21
F2 1980	716.636	540.446	17	20.406	0.248	73	10.02
F2 1987	816.792	195.108	17	20.428	0.446	223	12.51
F2 1993	495.125	239.634	17	20.384	0.390	232	6.79
F2 1996	771.532	230.141	17	20.423	0.412	234	3.94
F2 2000	403.396	508.050	17	20.408	0.526	175	6.56
F2 2010	414.357	218.193	17	20.590	0.716	559	11.75
F2 2016	117.177	442.823	13	20.425	1.732	35	11.61
F2 2025	404.237	72.160	17	20.395	0.040	57	18.40
F2 2040	289.744	806.128	17	20.457	0.844	394	8.53
F2 2056	708.756	734.812	17	20.399	0.502	114	10.46
F2 2074	125.023	494.075	17	20.496	0.448	118	10.93
F2 2078	508.247	852.293	15	20.617	0.604	920	10.13
F2 2099	799.351	510.020	17	20.507	0.456	135	8.83
F2 2101	430.969	423.969	17	20.553	0.594	1234	8.30
F2 2102	375.290	718.480	17	20.460	0.632	175	14.17
F2 2106	870.717	657.836	11	20.562	1.434	51	3.48
F2 2115	429.070	18.639	17	20.771	0.986	211	21.51
F2 2120	489.749	552.794	17	20.516	0.574	114	10.80
F2 2124	554.147	80.867	17	20.541	0.622	1356	7.74
F2 2131	207.782	519.520	17	20.443	0.350	111	10.34
F2 2133	565.263	368.951	17	20.713	1.572	441	14.69
F2 2136	860.155	34.103	16	20.442	0.494	106	4.13
F2 2141	674.006	41.738	17	20.422	0.406	37	6.68
F2 2144	137.874	178.084	17	20.357	0.608	178	12.64
F2 2145	706.220	436.092	17	20.384	0.426	285	8.03
F2 2151	330.195	797.894	17	20.503	0.464	119	9.52
F2 2164	679.973	51.079	15	20.546	0.446	257	6.37
F2 2167	110.363	30.990	17	20.475	0.536	638	8.72
F2 2168	397.574	301.951	17	20.405	0.594	152	4.83
F2 2176	395.139	623.700	17	20.498	0.636	285	8.89
F2 2177	602.886	254.866	17	20.480	0.582	175	8.93
F2 2195	235.667	781.083	17	20.470	0.364	268	3.98
F2 2198	538.254	244.317	17	20.422	0.568	148	5.95
F2 2201	409.422	459.009	17	20.615	0.802	108	4.92
F2 2212	50.671	369.979	17	20.457	0.486	572	3.44

ID #	x	y	N	$\overline{K}$	Amplitude	Period	reduced χ^2
F2 2213	669.383	466.229	17	20.418	0.562	37	5.27
F2 2215	668.567	785.199	17	20.480	0.372	950	4.75
F2 2217	275.274	130.638	17	20.489	0.058	267	11.75
F2 2220	691.721	394.763	17	20.417	0.386	147	4.18
F2 2230	698.048	398.035	17	20.521	0.598	171	12.46
F2 2235	786.669	606.920	17	20.449	0.808	181	15.90
F2 2243	219.631	704.722	17	21.008	2.348	765	13.70
F2 2245	629.667	131.195	17	20.682	1.124	151	31.09
F2 2250	447.955	58.204	17	20.503	0.578	173	6.07
F2 2252	99.512	452.048	15	20.455	0.556	116	9.57
F2 2257	416.898	483.976	17	20.473	0.498	143	3.78
F2 2266	651.253	824.263	17	20.378	0.572	119	7.22
F2 2267	501.531	825.158	17	20.465	0.554	158	7.47
F2 2273	133.887	116.298	17	20.583	0.934	168	10.23
F2 2274	194.215	762.477	17	20.632	0.816	260	6.40
F2 2278	203.951	493.390	17	20.448	1.034	430	4.36
F2 2281	647.818	43.058	17	20.453	0.640	149	9.94
F2 2286	79.968	365.162	17	20.468	0.434	115	10.49
F2 2295	309.837	113.632	17	20.502	0.456	181	4.97
F2 2296	543.187	34.379	17	20.485	0.358	106	3.69
F2 2305	847.244	472.570	17	20.437	0.782	119	15.70
F2 2306	403.362	452.989	17	20.566	0.458	313	6.57
F2 2321	247.590	626.912	17	20.518	0.330	266	3.49
F2 2324	870.716	395.501	16	20.812	1.134	482	15.06
F2 2337	740.726	381.769	17	20.553	0.632	34	10.29
F2 2352	503.912	145.871	17	20.443	0.696	266	10.65
F2 2359	596.037	699.708	17	20.608	0.946	34	12.91
F2 2365	579.012	77.705	17	20.484	0.400	1131	3.16
F2 2367	723.159	474.359	17	20.615	0.590	244	3.95
F2 2371	716.589	348.734	17	20.548	0.456	141	6.67
F2 2380	562.167	786.113	17	20.424	0.436	118	8.96
F2 2390	151.909	256.642	17	20.577	0.710	177	11.02
F2 2396	892.759	803.509	10	21.549	2.366	244	23.22
F2 2400	830.577	41.279	17	20.490	0.486	152	1.77
F2 2436	768.995	122.537	17	20.490	0.562	150	12.64
F2 2442	524.520	649.606	17	20.679	0.618	253	4.63
F2 2444	376.183	78.778	17	20.573	0.218	37	15.28
F2 2447	861.326	405.124	16	20.615	0.858	915	14.98
F2 2450	595.448	224.099	16	20.498	0.454	110	7.68
F2 2452	53.757	209.772	17	20.570	0.744	34	12.19
F2 2464	377.048	64.826	17	20.596	0.674	237	4.59
F2 2482	593.934	440.326	17	20.456	0.580	119	5.72
F2 2488	584.395	310.257	17	20.553	0.456	176	7.77
F2 2490	641.299	564.179	17	20.611	0.534	267	5.82
F2 2491	409.591	737.105	17	20.820	1.170	142	20.13
F2 2496	569.307	701.282	17	20.807	1.358	877	11.85
F2 2498	596.361	335.011	17	20.617	0.686	1392	4.55
F2 2499	613.394	242.969	17	20.506	0.490	118	3.62
F2 2508	76.846	565.401	17	20.569	0.488	556	6.66
F2 2514	232.180	4.586	17	20.684	0.858	34	22.22

ID #	x	y	N	$\overline{K}$	Amplitude	Period	reduced χ^2
F2 2518	801.989	306.649	17	20.544	0.396	273	6.54
F2 2520	509.901	346.994	16	20.555	0.430	54	8.50
F2 2538	573.770	101.091	17	20.474	0.528	122	9.09
F2 2547	19.899	169.654	15	20.313	1.996	641	40.77
F2 2549	112.273	590.721	17	20.783	0.834	246	4.97
F2 2553	483.122	512.774	16	20.746	1.020	563	12.79
F2 2557	583.361	95.208	17	20.505	0.468	231	3.36
F2 2575	696.355	337.361	17	20.763	0.744	117	19.38
F2 2578	819.433	304.720	17	20.650	0.332	236	27.14
F2 2581	767.309	373.897	17	20.494	0.470	219	2.11
F2 2614	542.987	765.523	17	20.577	0.668	180	19.99
F2 2622	307.942	427.546	17	20.514	0.720	119	3.78
F2 2623	878.771	393.940	16	20.478	0.644	118	5.97
F2 2626	226.342	182.649	17	20.700	0.488	1203	17.49
F2 2630	674.653	425.904	17	20.548	0.516	257	6.28
F2 2631	867.695	815.188	16	20.686	1.066	167	17.07
F2 2637	383.672	511.657	17	20.593	0.504	179	7.68
F2 2642	432.401	167.600	17	20.551	0.454	115	7.19
F2 2643	101.764	461.159	11	20.799	1.410	207	5.06
F2 2648	78.192	621.440	15	20.745	1.064	81	12.21
F2 2667	61.437	110.619	17	20.694	0.862	606	6.00
F2 2673	634.844	1.815	16	20.583	0.414	165	5.81
F2 2705	575.008	643.459	17	20.773	0.724	135	3.61
F2 2719	240.592	764.878	17	20.585	0.542	267	8.81
F2 2724	308.719	775.781	17	20.747	0.702	37	17.31
F2 2729	165.646	250.294	17	20.498	0.702	119	16.65
F2 2758	477.989	835.222	17	20.609	0.312	97	5.53
F2 2776	463.103	78.155	17	20.613	0.394	116	9.33
F2 2788	671.567	133.324	17	20.578	0.730	227	6.86
F2 2792	559.148	284.212	17	20.754	0.764	595	4.60
F2 2807	39.598	5.196	16	20.588	0.546	171	7.00
F2 2817	70.327	269.607	17	20.635	0.556	183	10.13
F2 2818	783.371	462.597	17	20.831	0.868	231	10.69
F2 2825	145.392	182.236	17	20.633	0.580	281	5.87
F2 2834	637.823	571.625	17	20.647	0.768	283	7.67
F2 2837	567.347	271.127	16	20.709	0.930	600	3.70
F2 2852	504.743	806.534	17	20.745	0.576	276	4.91
F2 2854	145.710	37.137	17	20.619	0.436	36	6.09
F2 2861	793.637	482.378	17	20.549	0.736	638	10.72
F2 2862	761.013	149.256	17	20.734	0.556	241	3.22
F2 2865	534.602	425.840	17	20.837	0.830	246	2.00
F2 2867	541.861	386.679	17	20.612	0.570	259	1.89
F2 2868	604.356	672.492	17	20.665	0.372	248	2.14
F2 2885	331.150	843.812	17	20.743	0.510	117	14.04
F2 2887	257.607	87.629	17	20.659	0.444	86	7.82
F2 2926	427.591	205.595	17	20.681	0.366	115	4.92
F2 2934	605.272	364.133	17	20.747	0.720	229	5.15
F2 2947	31.410	440.388	10	20.584	3.650	34	29.31
F2 2949	311.996	215.268	17	20.629	0.514	254	2.60
F2 2951	143.234	802.299	17	20.684	0.548	269	2.77

ID #	x	y	N	$\overline{K}$	Amplitude	Period	reduced χ^2
F2 2959	528.818	699.573	17	20.639	0.664	158	6.40
F2 2969	50.954	644.975	17	20.802	0.736	135	4.42
F2 2972	545.342	695.400	17	20.788	0.634	236	6.13
F2 2988	49.281	824.680	16	20.686	0.382	115	3.23
F2 3000	332.673	2.846	15	20.656	0.620	58	7.73
F2 3021	35.115	92.239	16	20.704	0.572	53	5.94
F2 3027	726.388	585.128	17	20.615	0.902	721	2.23
F2 3034	161.745	203.158	17	20.691	0.586	63	3.32
F2 3047	549.653	606.108	17	20.761	0.494	134	4.31
F2 3048	787.466	356.547	17	20.668	0.594	240	3.26
F2 3049	281.135	47.059	17	20.719	0.444	134	6.23
F2 3053	527.153	688.188	17	20.630	0.498	245	1.86
F2 3054	807.211	169.314	17	20.666	0.492	108	2.52
F2 3073	65.095	16.725	17	20.756	0.736	257	7.42
F2 3076	242.072	343.394	16	20.809	0.538	276	12.54
F2 3090	206.695	260.863	17	20.934	0.516	277	16.89
F2 3104	296.256	99.747	17	20.898	0.918	263	3.81
F2 3109	673.253	830.951	17	20.710	0.500	853	5.48
F2 3111	642.351	39.705	17	20.642	0.394	108	5.80
F2 3117	264.654	126.305	17	20.817	0.774	238	10.17
F2 3118	421.285	212.965	17	20.902	0.880	218	4.68
F2 3137	468.256	505.490	16	20.835	1.132	77	12.65
F2 3157	222.394	70.863	17	20.723	0.538	178	7.24
F2 3162	481.080	518.304	16	21.040	1.442	472	5.86
F2 3168	501.395	630.646	17	20.780	0.518	140	2.04
F2 3177	379.246	206.987	17	20.718	0.542	228	6.30
F2 3186	809.671	297.367	17	20.829	0.766	157	11.55
F2 3187	94.485	172.725	17	20.858	0.760	245	4.42
F2 3189	661.943	529.547	17	20.831	0.610	134	7.43
F2 3223	403.024	806.737	17	20.611	0.594	590	7.43
F2 3224	9.396	379.001	12	20.745	0.954	176	15.97
F2 3225	797.129	635.359	17	20.707	0.632	139	6.67
F2 3230	211.862	642.011	17	20.929	1.162	799	5.55
F2 3244	261.990	322.628	17	20.767	0.820	747	1.60
F2 3252	520.615	226.923	17	20.995	1.100	437	4.29
F2 3260	690.409	507.404	14	20.722	0.904	174	10.17
F2 3274	556.326	827.221	17	20.942	0.988	243	4.77
F2 3285	874.806	785.279	13	21.005	1.700	451	16.19
F2 3286	107.599	25.344	17	20.897	0.862	50	11.85
F2 3287	255.581	790.584	17	20.966	0.934	244	2.27
F2 3357	755.878	791.802	17	20.779	0.662	112	5.61
F2 3362	515.275	863.731	11	20.195	1.550	368	4.54
F2 3371	434.026	220.829	17	20.997	0.860	268	6.16
F2 3405	386.949	201.313	17	20.807	0.532	97	6.15
F2 3415	424.775	437.679	17	20.943	0.774	216	4.01
F2 3417	758.909	548.148	16	20.983	1.364	782	5.72
F2 3421	589.128	506.607	17	20.813	0.828	202	10.13
F2 3435	695.119	132.202	17	21.107	1.176	260	6.63
F2 3451	122.502	226.291	17	20.717	0.646	118	4.81
F2 3452	507.236	20.188	17	20.717	0.432	244	3.58

ID #	x	y	N	$\overline{K}$	Amplitude	Period	reduced χ^2
F2 3481	179.199	837.457	16	20.737	0.518	245	8.07
F2 3488	607.463	129.764	17	20.801	0.648	147	6.02
F2 3505	398.237	539.432	17	20.824	0.498	179	9.58
F2 3528	515.968	222.633	17	20.823	0.502	95	8.16
F2 3541	615.212	452.045	17	20.854	0.854	173	5.98
F2 3577	578.001	197.880	17	20.909	0.888	247	8.39
F2 3578	24.958	439.543	14	20.774	1.188	68	11.07
F2 3584	194.599	119.165	17	20.896	0.622	220	7.78
F2 3586	514.660	835.081	17	20.775	1.134	56	5.68
F2 3592	26.414	786.261	16	20.735	0.606	147	8.56
F2 3607	372.763	112.407	17	20.891	0.552	135	4.77
F2 3620	84.425	34.555	16	20.876	0.302	66	36.97
F2 3624	308.680	837.790	17	20.851	0.608	40	8.17
F2 3625	554.237	257.893	17	20.788	0.336	63	6.14
F2 3627	248.915	713.626	17	20.809	0.706	279	8.79
F2 3655	500.526	162.270	17	20.793	0.226	446	38.51
F2 3668	728.680	434.581	17	20.950	0.722	218	8.60
F2 3684	256.828	133.586	17	21.061	1.024	409	5.98
F2 3693	315.645	137.204	17	20.804	0.710	432	6.29
F2 3727	489.836	226.795	17	20.793	0.670	118	13.33
F2 3731	590.094	30.304	17	21.034	0.826	208	3.39
F2 3732	428.451	358.325	17	20.920	0.716	235	4.10
F2 3761	93.646	86.222	17	20.896	0.580	116	9.45
F2 3767	619.289	11.992	17	20.853	1.068	461	5.71
F2 3784	776.870	570.474	11	21.598	2.524	96	5.58
F2 3818	215.642	618.419	17	20.889	0.786	247	1.86
F2 3854	473.891	347.616	16	21.036	0.968	177	9.85
F2 3877	853.715	154.906	17	20.888	0.588	244	7.07
F2 3897	456.788	215.267	17	20.933	0.398	260	4.55
F2 3942	358.984	404.031	17	20.976	0.176	260	22.44
F2 3989	733.361	394.401	17	20.952	0.652	185	13.31
F2 4018	646.963	786.675	17	21.012	0.578	141	3.91
F2 4070	124.053	247.891	17	21.044	0.756	243	7.85
F2 4110	327.771	236.238	17	20.959	0.530	266	7.42
F2 4113	167.085	449.518	17	20.905	0.748	247	8.19
F2 4140	726.822	206.802	17	20.922	1.038	652	3.66
F2 4204	87.382	51.749	16	21.082	1.004	34	6.58
F2 4215	881.445	86.078	16	20.999	0.602	38	8.90
F2 4263	530.146	408.848	17	20.920	0.830	203	6.19
F2 4287	507.512	223.211	17	20.982	0.458	266	6.36
F2 4366	78.975	836.254	14	21.428	1.392	69	7.56
F2 4376	371.446	94.167	16	20.936	0.732	248	8.54
F2 4382	539.275	381.671	17	21.016	0.566	235	3.45
F2 4397	882.723	20.546	13	21.042	0.916	80	7.36
F2 4434	886.995	345.213	16	21.128	1.006	219	2.77
F2 4441	35.497	416.514	15	20.973	0.810	115	27.70
F2 4507	126.753	511.067	17	21.054	0.776	235	3.58
F2 4522	823.457	300.263	17	21.209	0.882	98	10.91
F2 4545	694.859	516.219	12	21.057	0.660	53	7.28
F2 4744	476.981	528.550	12	21.274	2.072	260	5.24

ID #	x	y	N	$\overline{K}$	Amplitude	Period	reduced χ^2
F2 4763	420.914	440.700	17	21.064	0.546	189	5.01
F2 4777	782.623	492.038	17	21.000	0.510	38	9.29
F2 4799	108.807	382.704	15	21.654	1.088	232	62.43
F2 4800	130.523	447.250	10	21.608	2.534	156	16.09
F2 4808	123.638	281.026	17	21.088	0.684	558	8.79
F2 4813	550.461	9.243	17	21.096	0.784	582	10.23
F2 4822	844.076	751.319	16	21.238	0.894	182	5.41
F2 4888	383.420	790.682	17	21.158	0.662	113	2.85
F2 4968	122.864	767.482	11	21.380	0.888	311	35.93
F2 5103	99.268	38.226	13	21.549	1.648	106	13.68
F2 5193	88.210	23.745	15	21.077	0.824	78	5.03
F2 5226	525.237	837.885	16	21.217	1.170	33	6.52
F2 5292	575.588	243.708	17	21.189	0.564	459	5.17
F2 5299	817.294	410.012	17	21.131	0.802	87	7.96
F2 5435	64.062	261.911	17	21.250	0.688	155	14.91
F2 5448	490.860	190.813	14	21.600	1.660	55	3.57
F2 5512	640.500	676.670	17	21.176	0.640	231	4.17
F2 5628	728.991	651.910	17	21.303	0.644	116	5.82
F2 5893	82.930	642.948	13	21.801	2.556	36	18.90
F2 5950	811.835	705.580	17	21.243	0.616	319	8.74
F2 5962	95.484	20.836	10	21.245	1.384	123	9.70
F2 5978	238.597	274.765	14	21.906	7.374	34	38.05
F2 6002	622.701	195.137	17	20.900	1.814	483	10.04
F2 6086	837.699	732.175	16	21.269	1.200	233	7.66
F2 6163	714.569	492.736	11	21.337	2.486	95	15.68
F2 6184	719.494	503.152	15	21.466	1.654	97	2.78
F2 6346	45.062	140.514	15	21.341	0.786	53	5.57
F2 6397	245.651	60.570	17	21.331	0.896	222	4.34
F2 6509	731.411	506.143	10	21.737	2.480	83	7.99
F2 6638	69.369	34.887	17	21.446	1.080	40	4.99
F2 6817	522.810	831.682	16	21.325	0.668	58	8.46
F2 6876	518.352	828.096	14	21.349	1.208	57	19.18
F2 6950	78.522	642.164	14	21.383	1.308	465	32.52
F2 7081	310.272	-0.351	11	21.795	2.412	48	17.63
F2 7150	599.040	257.448	17	21.341	0.814	190	3.78
F2 7772	94.594	37.474	12	21.646	2.396	50	5.35
F2 8545	87.682	457.815	10	21.564	2.472	84	9.31
F2 8606	501.359	849.302	10	22.116	2.702	85	1.25
F2 9459	657.711	174.768	15	21.773	1.252	76	5.32
F2 9490	240.161	21.155	17	21.785	1.048	39	4.85
F2 10235	758.675	600.665	10	22.142	2.132	42	5.09
F2 10485	723.815	509.328	10	21.979	2.182	84	5.59
F2 10659	519.167	131.829	11	21.939	1.634	42	9.36
F2 10810	689.888	490.925	13	22.032	1.596	62	7.09
F2 10857	576.562	311.475	14	22.083	1.412	38	5.58
F2 11162	536.093	846.281	15	22.010	1.328	218	1.78
F2 11431	807.050	508.914	13	22.348	1.164	138	3.73
F2 11859	29.644	411.668	10	21.972	2.714	37	6.26
F2 12362	253.225	381.791	12	22.351	1.706	105	3.05
F2 12825	541.490	839.272	14	22.470	2.140	34	5.07

Bibliography

References

Ables, H.D. & Ables, P.G., 1977, ApJS, 34, 245

Alard, C., Blommaert, J.A.D.L., Cesarsky, C., et al., 2001, ApJ, 552, 289

Alonso, M.V. & Minniti D., 1997, ApJS, 109, 397

Alves, D.R., Rejkuba, M., Minniti, D. & Cook, K.H., ApJ, 573, L51

Aparicio, A., 1998, in: "IAU Symposium 192 - The Stellar Content of Local Group Galaxies", P. Whitelock & R. Cannon eds., p. 20.

Aparicio, A., et al. 2000, AJ, 119, 177

Arimoto, N. & Yoshii, Y., 1987, A&A, 173, 23

Ashman, K.M. & Zepf, S.E., 1992, ApJ, 384, 50

Ashman, K.M., Conti, A. & Zepf, S.E., 1995, AJ, 110, 1164

Baade, W., 1944, ApJ, 100, 137

Baade, W. & Minkowski, R., 1954, ApJ, 119, 215

Babul, A., & Rees, M., 1992, MNRAS, 255, 346

Barrientos, L.F., 2000, private communication

Barmby, P. & Huchra, J.P., 2000, ApJ, 531, L29

Barmby, P., Huchra, J.P., Brodie, J.P. et al., 2000, AJ, 119, 727

Bedding, T.R. & Zijlstra, A.A., 1998, ApJ, 506, L47

Begelman, M.C. & Cioffi, D.F., 1989, APJ, 345, L21

Bell, R.A., 1992, MNRAS, 257, 423

Bertelli, G., Mateo, M., Chiosi, C. & Bressan, A., 1992, ApJ, 388, 400

Bertelli, G., Bressan, A., Chiosi, C., Fagotto, F. & Nasi, E., 1994, A&AS, 106, 275

Bertin, E. & Arnouts, S., 1996, A&AS, 117, 393

Bessell, M.S., 1995, PASP, 107, 672

Bessell, M.S. & Brett, 1988, PASP, 100, 1134

Bessell, M.S. & Wood, P.R., 1984, PASP, 96, 247

Bessell, M.S., Castelli, F. & Plez, B., 1998, A&A, 333, 231

Best, P.N., Longair, M.S. & Röttgering, 1996, H.J.A., MNRAS, 280, L9

Bica, E. 1988, A&A, 195, 76

Blakeslee, J.P., Vazdekis, A. & Ajhar, E.A., 2001, MNRAS, 320, 193

Blanco, V.M., Graham, J.A., Lasker, B.M. & Osmer, P.S., 1975, ApJ, 198, L63

Blommaert, J.A.D.L., van der Veen, W.E.C.J, Van Langevelde, H.J., Habing, H.J. & Sjouwerman, L.O., A&A, 329, 991

Bolton, J.G., Stanley, G.J. & Slee, O.B., 1949, Nature, 164, 101

Bono, G., Caputo, F., Cassisi, S., Castellani, V. & Marconi, M., 1997, ApJ, 489, 822

Bono, G., Caputo, F., Cassisi, S., Castellani, V. & Marconi, M., 1997, ApJ, 479, 279

Bressan, A., Chiosi, C. & Fagotto, F., 1994, ApJS, 94, 63

Broadhurst, T.J., Ellis, R.S. & Shanks, T., 1988, MNRAS, 235, 827

Bruzual, A.G. & Charlot, S., 1993, ApJ, 405, 538

Bruzual, A.G. & Charlot, S., 2001, private communication

Burstein, D. & Heiles, C., 1982, AJ, 87, 1165

Buser, R. & Kurucz, R.L., 1978, A&A, 70, 555

Buzzoni, A., 1995, ApJS, 98, 69

Cardelli, J.A., Clayton, G.C. & Mathis, J.S., 1989, ApJ, 345, 245

Caretta, E., Gratton, R.G., Clementini, G. & Fusi Pecci, F, 2000, ApJ, 533, 215

Carroll, S. M., Press, W. H. & Turner, E. L., 1992, ARA&A 30, 499

Carter, B.S., 1990, MNRAS, 242, 1

Cassisi, S. & Salaris, M., 1997, MNRAS, 285, 593

Cassisi, S., Castellani, V., degl'Innocenti, S, Salaris, M. & Weiss, A., 1999, A&AS, 134, 103

Castellani, V., Giannone, P. & Renzini, A., 1969, Ap&SS, 3, 518

Castellani, V., degl'Innocenti, S. & Marconi, M., 1999, MNRAS, 303, 265

Castelli, F., Gratton, R.G. & Kurucz, R.L, 1997, A&A, 318, 841

Chaboyer, B., Demarque, P. & Pinsonneault, M.H., 1995, ApJ, 441, 876

Chambers, K.C., Miley, G.K. & van Breugel, W., 1987, Nature, 329, 604

Charmandaris, V., Combes, F. & van der Hulst, J.M., 2000, A&A, 356, L1

Chiosi, C., Bertelli, G. & Bressan, A. 1992, ARA&A, 30, 235

Cioni, M.-R.L., Marquette, J.-B., Loup, C., et al., 2001, A&A, 377, 945

Clarke, D.A., Burns, J.O. & Norman, M.L., 1992, ApJ, 395, 444

Cooper, B.F.C., Price, R.M. & Cole, D.J., 1965, Aust.J.Phys., 18, 589

Cole, A.A., Tolstoy, E., Gallagher III, J.S., et al., 1999, AJ, 118, 1657

Cole, S., Lacey, C.G., Baugh, C.M. & Frenk, C.S., 2000, MNRAS, 319, 168

Côté, P., Marzke, R.O. & West, M.J., 1998, ApJ, 501, 554

Côté, P., Marzke, R.O., West, M.J. & Minniti, D., 2000, ApJ, 553, 869

Da Costa, G., 1994, in "The Local Group: Comparative & Global Properties", eds. A. Layden & J. Storm (ESO: Garching), p. 101

Da Costa, G. S., & Armandroff, T. E., 1990, AJ, 100, 162

Daly, R.A., 1990, ApJ, 355, 416

Davidge, T.J. & van den Bergh, S., 2001, ApJ, 553, L133

de Boer, K. S. 1999, in ASP Conf. on "Harmonizing the Cosmic Distance Scale in the Post Hipparcos Era", eds. D. Egret & A. Heck (ASP: San Francisco), p. 167

De Breuck, C., van Breugel, W., Minniti, D. et al., 1999, A&A, 352, L51

Dekel, A., & Silk, J., 1986, ApJ, 303, 39

Demarque, P. & Gisler, G.R., 1975, A&AS, 20, 237

di Serego Alighieri, S., Fosbury, R.A.E., Tadhunter, C.N. & Quinn, P.J., 1989, Nature, 341, 307

Dickson, R., Tadhunter, C., Shaw, M., Clark, N., & Morganti, R., 1995, MNRAS, 273, L29

Dolphin, A., 1997, New Astronomy, 2 (5), 397

Dolphin, A.E., 2000, ApJ, 531, 804

Dreyer, J.L.E., 1888, Mem. Roy. Astron. Soc., 49, 1, "The original NGC Catalog"

Dreyer, J.L.E., 1895, Mem. Roy. Astron. Soc., 51, 185, "First supplement to the NGC, the IC "

Dreyer, J.L.E., 1908, Mem. Roy. Astron. Soc., 59, 105, "Second supplement to the NGC, the IC continued"

Dufour, R.J. & van den Bergh, S., 1978, ApJ, 226, L73

Dufour, R.J., van den Bergh, S., Harvel, C.A., et al., 1979, AJ, 84, 284

Dunlop, J., 1828, Philosophical Transactions of the Royal Society, 118, 113

Ebneter, K. & Balick, B., 1983, PASP, 95, 675

Efstathiou, G., 2000, MNRAS, 317, 697

Eggen, O.J., Lynden-Bell, D. & Sandage, A.R., 1962, ApJ, 136, 748

Elston, R. & Silva, D.R., 1992, AJ, 104, 1360

Fagotto, F., Bressan, A., Bertelli, G. & Chiosi, C., 1994, A&AS, 105, 29

Fassett, C.I. & Graham, J.A., 2000, ApJ, 538, 594

Feast, M.W., 1996, MNRAS, 278, 11

Feast, M.W. & Walker, A.R., 1987, ARA&A, 25, 345

Feast, M., Whitelock, P. & Menzies, J., 2002, MNRAS, 329, L7

Feast, M.W., Robertson, B.S.C., Catchpole, R.M., et al., 1982, MNRAS, 201, 439

Feigelson, E.D., Schreier, E.J., Delvaille, J.P., Giacconi, R., Grindlay, J.E. & Lightman, A.P., 1981, ApJ, 251, 31

Feltzing, S. & Gilmore, G., 2000, A&A, 355, 949

Ferrarese, L., Ford, H.C., Huchra, J., et al., 2000, ApJS, 128

Ferraro, F.R., Fusi Pecci, F., Tosi, M. & Buonanno, R., 1989, MNRAS, 241, 433

Ferraro, F.R., Montegriffo, P., Origlia, L. & Fusi Pecci, F., 2000, AJ, 119, 1282

Ferguson, H.C., 1989, AJ, 98, 367

Fleming, D.E.B., Harris, W.E., Pritchet, C.J. & Hanes, D.A., 1995, AJ, 109, 1044

Forbes, D.A., Brodie, J.P., Grillmair, C.J., 1997, AJ, 113, 1652

Freedman, W.L., 1992, AJ, 104, 1349

Freedman, W.L., Madore, B.F., Gibson, B.K., et al., ApJ, 553, 47

Frogel, J.A., 1984, ApJ, 278, 119

Frogel, J.A., 1980, ApJ, 241, 41

Frogel, J.A. & Whitford, A.E., 1987, ApJ, 320, 199

Frogel, J.A. & Elias, J.H., 1988, ApJ, 324, 823

Frogel, J.A. & Whitelock, P.A., 1998, AJ, 116, 754

Frogel, J.A., Cohen, J.G. & Persson, S.E., ApJ, 275, 773

Frogel, J.A., Terndrup, D.M., Blanco, V.M. & Whitford, A.E., 1990, ApJ, 353, 494

Gallart, C., 1998, ApJ, 495, L43

Gallart, C., Aparicio, A., Bertelli, G. & Chiosi, C., 1996a, AJ, 112, 1950

Gallart, C., Aparicio, A., Bertelli, G. & Chiosi, C., 1996b, AJ, 112, 2596

Gallart, C., Freedman, W.L., Mateo, M., et al., 1999, ApJ, 514, 665

Gardner, J. P., Baum, S. A., Brown, T. M.,et al., 2000, AJ, 119, 486

Gardner, J. P., Hill, R. S., Baum, S. A., et al., 1998, ApJ, 492, L99

Gavazzi, G., Boselli, A., Vílchez, J.M., Iglesias-Paramo, J. & Bonfanti, C., 2000, A&A, 361, 1

Gebhardt, K. & Kissler-Patig, M., 1999, AJ, 118, 1526

Gilliland, R. L., Goudfrooij, P., & Kimble, R. A., 1999, PASP 111, 1009

Girardi, L., Bressan, A., Bertelli, G., & Chiosi, C., 2000, A&AS, 141, 1

Glass, I.S. & Loyd Evans, T., 1981, Nature, 291, 303

Gonzalez, J.J., & Gorgas, J. 1995, ASP Conf. 86 on "Fresh Views on Elliptical galaxies", p. 225

Gould, A., Bahcall, J.N. & Flynn, C., 1997, ApJ, 482, 913

Graham, J.A., 1983, ApJ, 269, 440

Graham, J.A., 1979, ApJ, 232, 60

Graham, J.A., 1998, ApJ, 502, 245

Graham, J.A. & Phillips, M.M., 1980, ApJ, 239, L97

Graham, J.A. & Price, R.M., ApJ, 247, 813

Grebel, E., 1998, in IAU Symp. 192 on "The Stellar Content of Local Group Galaxies", eds. P. Whitelock & R. Cannon, (ASP: San Francisco), p. 1

Grebel, E.K., 2000, in: "The Evolution of Galaxies. I.Observational Clues", J.M. Vilchez, G. Stasinska & E. Perez eds., Kluwer, Dordrecht

Gregg, M. D., & Minniti, D., 1997, PASP, 109, 1062

Greggio, L., Tosi, M., Clampin, M., De Marchi, G., Leitherer, C., Nota, A. & Sirianni, M., 1998, ApJ, 504, 725

Grillmair, C.J., Lauer, T.R., Worthey, G., et al., 1996, AJ, 112, 1975

Groenewegen, M.A.T. & de Jong, T., 1994, A&A, 288, 782

Grocholski, A.J. & Sarajedini, A., 2002, AJ, 123, 1603

Guarnieri, M.D., Renzini, A. & Ortolani, S., 1997, ApJ, 477, L21

Habing, H.J., 1996, A&A Rev., 7, 97

Harmon, R.T. & Gilmore, G., 1988, MNRAS, 235, 1025

Harris, G.L.H. & Harris, W.E., 2000, AJ, 120, 2423

Harris, G.L.H., Geisler, D., Harris, H.C. & Hesser, J.E, 1992, AJ, 104, 613

Harris, G.L.H., Harris, W.E. & Poole, G.B., 1999, AJ, 117, 855

Harris, H.C., Harris, G.L.H., Hesser, J.E. & MacGillivray, H.T., 1984, ApJ, 287, 185

Harris, J. & Zaritsky, D., 2001, ApJS, 136, 25

Harris, W.E., 1991, ARA&A, 29, 543

Harris, W.E., 1996, AJ, 112, 1487 (http://physun.physics.mcmaster.ca/Globular.html)

Harris, W.E., 1999, in Star Clusters, ed. L. Labhardt & B. Binggeli (28th Saas-Fee Advanced Course), Berlin, Springer

Harris, W.E., 2000, "Globular Cluster Systems", Lectures for the 1998 Saas-Fee Advanced School on Star Clusters, Springer

Harris, W.E. & van den Bergh, S., 1981, AJ, 86, 1627

Haynes, R.F., Cannon, R.D. & Ekers, R.D., 1983, PASAu, 5, 241

Held, E.V., Saviane, I., Momany, Y. & Carraro, G., 2000, ApJ, 530, L85

Hernández, X., Valls-Gabaud D. & Gilmore G., 1998, MNRAS, 304, 705

Hernquist, L. & Spergel, D.N., 1992, ApJ, 399, L117

Hernquist, L. & Quinn, P.S., 1989, ApJ, 342, 1

Herschel, W., 1785, Phil. Trans., 75, 213

Hesser, J.E., Harris, H.C., van den Bergh, S. & Harris, G.L.H., 1984, ApJ, 276, 491

Hesser, J.E., Harris, H.C. & Harris, G.L.H., 1986, ApJ, 303, L51

Hodge, P. 1989, ARA&A, 27, 139

Hodge, P. W., Dolphin, A. E., Smith, T. R., & Mateo, M., 1999, ApJ, 521, 577

Holland, S., Côté, P. & Hesser, J.E., 1999, A&A, 348, 418

Holtzman, J.A., Light, R.M., Baum, W.A., et al., 1993, AJ, 106, 1826

Hubble, E., 1925, ApJ, 62, 409

Hubble, E., 1926, ApJ, 64, 321

Hughes, S.M.G. & Wood, P.R., 1990, AJ, 99, 784

Hui, X., Holland, C.F., Freeman, K.C. & Dopita, M.A., 1995, ApJ, 449, 592

Hui, X., Holland, C.F., Freeman, K.C. & Dopita, M.A., 1995, ApJ, 449, 592

Humason, M.L., Mayall, N.U. & Sandage, A.R., 1956, AJ, 61, 97

Hurley-Keller, D., Mateo, M. & Nemec, J., 1998, AJ, 115, 1840

Ibata, R.A., Gilmore, G. & Irwin, M.J., 1995, MNRAS, 277, 781

Iben, I.Jr., 1967, ARA&A, 5, 571

Iben, I.Jr., 1974, ARA&A, 12, 215

Iben, I.Jr., 1982, ApJ, 260, 821

Iben, I.Jr. & Renzini, A., 1983, ARA&A, 21, 271

Iben, I.Jr. & Renzini, A., 1984, Phys. Rep., 105, 329

Israel, F.P., 1998, A&AR 8, 237

Izotov, Y.I. & Thuan, T.X., 1999, ApJ, 511, 639

Jablonka, P., Bica, E., Pelat, D. & Alloin, D., 1996, A&A, 307, 385

Jacoby, G.H., Branch, D., Ciardullo, R., et al., 1992, PASP, 104, 599

Jerjen, H. & Rejkuba, M., 2001, A&A, 371, 487

Jerjen, H., Freeman, K.C. & Binggeli, B., 2000, AJ, 119, 166

Johnson, H.M., 1963, AJ, 68, 76

Johnson, J. A., & Bolte, M., 1998, ApJ, 115, 639

Johnson, H.L., Morgan, W.W., 1953, ApJ, 117, 313

Jura, M. & Kleinmann, S.G., 1992, ApJS, 79, 105

Jura, M. & Kleinmann, S.G., 1992, ApJS, 83, 329

Kauffmann, G., 1996, MNRAS, 281, 475

Kauffmann, G. & Charlot, S., 1998, MNRAS, 294, 705

Kauffmann, G., Guideroni, B. & White, S.D.M., 1994, MNRAS, 267, 981

Kapteyn, J.C., ApJ, 55, 302

Kennicutt, R. C., 1998, ARA&A 36, 189

Kerschbaum, F. & Hron, J., 1992, A&A, 263, 97

Kerschbaum, F. & Hron, J., 1994, A&AS, 106, 397

Kholopov, P.N. et al., 1985, General Catalogue of Variable Stars 4th edn., Nauka Publishing House, Moscow (GCVS)

Kissler-Patig, M., 2000, Reviews in Modern Astronomy, Vol. 13, p. 13

Kissler-Patig, M., Forbes, D.A. & Minniti, D., 1998, MNRAS, 298, 1123

Kraft, R.P., Forman, W, Jones, C., Kenter, A.T., et al., 2000, ApJ, 531, L9

Kundu, A., 1999, PhD thesis, U. of Maryland

Kurth, O.M., Fritze-v. Alvensleben, U. & Fricke, K.J., 1999, A&AS, 138, 19

Kurucz, R.L., 1993, IAU Symposium 149: "The Stellar Populations of Galaxies", B. Barbuy, A. Renzini, eds., Dordrecht, Kluwer, p. 225

Kurucz, R.L., 1998, IAU Symposium 189, T.R. Bedding, A.J. Booth & J. Davis eds., Kluwer, Dordrecht, p. 217

Lomb, N.R., 1976, Ap&SS, 39, 447

Landolt, A.U., 1992, AJ, 104, 340

Langer, N. & Maeder, A., 1995, A&A, 295, 685

Larsen, S.S. & Richtler, T., 1999, A&A, 345, 59

Larson, R.B., 1974, MNRAS, 169, 229

Lazareff, B, Castets, A., Kim D.-W. & Jura, M., 1989, ApJ, 336, L13

Lee, M. G., 1993, ApJ, 408, 409

Lee, M.G., Freedman, W.L. & Madore, B.F., 1993, ApJ, 417, 553

Liu, M.C., Graham, J.R. & Charlot, S., 2002, ApJ, 564, 216

Maeder, A., 2001, ApSSS, 277, 291

Maeder, A. & Meynet, G., 2001, A&A, 373, 555

Magain, P., Courbin, F. & Sohy, S., 1998 ApJ 494, 472

Malin, D.F., Quinn, P.J. & Graham, J.A., 1983, ApJ 272, L5

Maraston, C., 1998, MNRAS, 300, 872

Maraston, C., 2001, private communication

Marconi, A., Capetti, A., Axon, D., Koekemoer, A., Macchetto, D. & Schreier, E.J., 2001, ApJ, 549, 915

Marconi, G., Tosi, M., Greggio, L. & Focardi, P., 1995, AJ, 109, 173

Marleau, F.R., Graham, J.R., Liu, M.C. & Charlot, S., 2000, AJ, 120, 1779

Mateo, M., 1998, ARA&A, 36, 435

Mathieu, A., Dejonghe, H. & Hui, X., 1996, A&A, 903, 30

Matteucci, F. & Tornambè, A., 1987, A&A, 185, 51

McCarthy, P.J., van Breugel, W., Spinrad, H. & Djorgovski, S., 1987, ApJ, 321, L29

McWilliam, A. & Rich, R.M., 1994, ApJS, 91, 749

Melotte, P.J., 1926, MNRAS, 86, 636

Mennessier, M.O., Mowlavi, N., Alvarez, R. & Luri, X., 2001, A&A, 374, 968

Meylan, G., Sarajedini, A., Jablonka, P., et al., 2001, AJ, 122, 830

Minniti, D., 1993, PhD thesis, The Univ. of Arizona

Minniti, D., & Zijlstra, A. A., 1996, ApJ, 467, L13

Minniti, D., & Zijlstra, A. A., 1997, AJ, 114, 147

Minniti, D., Alonso, M.V., Goudfrooij P. et al. 1996, ApJ, 467, 221

Minniti, D., Zijlstra, A.A. & Alonso, M.V., 1999, AJ, 117, 881

Mirabel, I.F., Laurent, O., Sanders, D.B., Sauvage, M., Tagger, M., Charmandaris, V., Vigroux, L., Gallais, P., Cesarsky, C. & Block, D.L., 1999, A&A, 341, 667

Montegriffo, P., Ferraro, F.R., Origlia, L., Fusi Pecci, F., 1998, MNRAS, 297, 872

Morganti, R., Robinson, A., Fosbury, R.A.E., di Serego Alighieri, S., Tadhunter, C.N. & Malin, D.F., 1991, MNRAS, 249, 91

Morganti, R., Fosbury, R.A.E., Hook, R.N., Robinson, A. & Tsvetanov, Z., 1992, MNRAS, 256, 1P

Morganti, R., Killeen, N.E.B., Ekers, R.D. & Oosterloo, T.A., 1999, MNRAS, 307, 750

Morossi, C., Franchini, M., Malagnini, M.L., Kurucz, R.L. & Buser, R., 1993, A&A, 277, 173

Mould, J., & Kristian, J., 1986, ApJ, 305, 591

Mould, J.R., Ridgewell, A., Gallagher, J.S. III et al., 2000, ApJ, 536, 266

Olszewski, E. W., 1994, in IAU Symp. 164 "Stellar Populations", eds. G. Gilmore & P. van der Kruit (Kluwer: Dordrecht), p. 181

Oort, J.H., 1926, Groningen Pub., 40

Ortolani, S., Renzini, A., Gilmozzi, R., et al., 1995, Nature, 377, 701

Ostriker, J.P. & Gnedin, O.Y., 1997, ApJ, 487, 667

Pancino, E., Pasquini, L., Hill, V., Ferraro, F.R. & Bellazzini, M., 2002, ApJ 568, L101

Peebles, P.J.E., 1995, ApJ, 449, 52

Pelló, R., Kneib, J. P., & Bruzual, G., 1998, Ap&SS, 263, 55

Persson, S.E., Murphy, D.C., Krzeminski, W., Roth, M. & Rieke, M.J., 1998, AJ, 116, 2475

Peterson, B.A, Dickens, R.J. & Cannon, R.D., 1975, Proc. Astron. Soc. Aust., 2, p. 366

Press, W.H., Teukolsky, S.A., Vetterling, W.T. & Flannery, B.P., Numerical Recipes in Fortran 77, 2. edition, 1992, Cambridge Press

Quinn, P.J., 1984, ApJ, 279, 596

Rees, M.J., 1989, MNRAS, 239, 1P

Rieke, M.J. & Lebofsky, M.J., 1985, ApJ, 288, 618

Rejkuba, M., 2001, A&A, 369, 812 (Chapter 3)

Rejkuba, M., Minniti, D., Gregg, M.D., Zijlstra, A.A., Alonso, M.V. & Goudfrooij, P., 2000, AJ, 120, 801 (Chapter 2)

Rejkuba, M., Minniti, D., Bedding, T. & Silva, D.R., 2001, in: "Galaxy Disks and Disk Galaxies", J.G. Funes S.J. & E.M. Corsini eds., ASP Conf. Series

Rejkuba, M., Minniti, D., Bedding, T. & Silva, D.R., 2001, A&A, 379, 781 (Chapter 4)

Rejkuba, M., Minniti, D., Courbin, F. & Silva, D.R., 2002, ApJ, 564, 688 (Chapter 5)

Renzini, A., 1993, in: "Galactic Bulges", DeJonghe, H., Habing, H.J. (eds.), Kluwer, Dordrecht, p. 151

Renzini, A., 1994, A&A, 285, L5

Renzini, A., 1998, AJ, 115, 2459

Renzini, G. & Greggio, L., 1990, in: "Bulges of Galaxies", Jarvis, B.J. & Terndrup, D.M. (eds.), ESO, p. 47

Renzini, A. & Fusi Pecci, F., 1988, ARA&A, 26, 199

Renzini, A., Greggio, L., Ritossa, C. & Ferrario, L., 1992, ApJ, 400, 280

Rich, R.M. & Mould, J.R., 1991, AJ, 101, 1268

Ritossa, C., 1996, MNRAS, 281, 970

Robin, A. & Creze, M., 1986, A&A, 157, 71

Robin, A.C., Haywood, M., Creze, M., Ojha, D.K. & Bienayme, O., 1996, A&A, 305, 125

Rodighiero, G., Granato, G.L., Franceschini, A., Fasano, G. & Silva, L., 2000, A&A, 364, 517

Sabra, B.M., Shields, J.C. & Filippenko, A.V., 2000, ApJ, 545, 157

Sagar, R. & Richtler, T., 1991, A&A, 250, 324

Sakai, S., Madore, B. & Freedman, W.L., ApJ, 461, 713

Salaris, M. & Cassisi, S., 1997, MNRAS, 289, 406

Salaris, M., Cassisi, S. & Weiss, A., 2002, PASP, 114, 375

Salpeter, E.E., 1955, ApJ, 121, 161

Salzer, J.J., di Serego Alighieri, S., Matteucci, F., Giovanelli, R. & Haynes, M.P., 1991, AJ, 101, 1258

Sandage, A., 1986, A&A, 161, 89

Sandage, A. & Binggeli, B., 1984, AJ, 89, 919

Sandage, A., & Carlson, G., 1985, AJ, 90, 1464

Sandquist, E. L., Bolte, M., Stetson, P. B., & Hesser, J. E., 1996, ApJ 470, 910

Saracco, P., Giallongo, E., Cristiani, S., et al., 2001, A&A, 375, 1

Scalo, J.M., 1986, in: "Fundamentals of Cosmic Physics", vol. 11, p. 1

Schiminovich, D.; van Gorkom, J.H., van der Hulst, J.M. & Kasow, S., 1994, ApJ 423, L101

Schlegel, D.J., Finkbeiner, D.P. & Davis, M., 1998, ApJ, 500, 525

Schreier, E.J., Burns, J.O. & Feigelson, E.D., 1981, ApJ, 251, 523

Schulte-Ladbeck, R.E., Hopp, U., Greggio, L. & Crone, M.M., 2000, AJ, 120, 1713

Schweizer, F., 1996, AJ, 111, 109

Schweizer, F., 1997, in ASP Conf. Ser. 116, The Nature of Elliptical Galaxies, ed. M. Arnaboldi, G.S. Da Costa & P. Saha (Sand Francisco: ASP), 447

Searle, L. & Sargent, W.L.W., 1972, ApJ, 173, 25

Searle, L. & Zinn, R., 1978, ApJ, 225, 357

Shapley, H., 1919, ApJ, 49, 311

Silverman, B.W., 1986, "Density estimation for statistics and data analysis", London: Chapman and Hall

Soria, R., Mould, J.R., Watson, A.M., et al., 1996, ApJ 465, 79

Stanford, S.A., Eisenhardt, P.R.M. & Dickinson, M., 1995, ApJ, 450, 512

Stetson, P. B., 1987, PASP, 99, 191

Stetson, P.B., 1994, PASP, 106, 250

Stetson, P.B., 1996, PASP, 108, 851

Stetson, P.B., 2000, PASP, 112, 925

Sutherland, R.S., Bicknell, G.V. & Dopita M.A., 1993, ApJ, 414, 510

Sweigart, A.V., Greggio, L. & Renzini, A., 1990, ApJ, 364, 527

Thomson, R.C. & Wright, A.E., 1990, MNRAS, 247, 122

Tiede, G.P., Glenn, P., Frogel, J.A. & Terndrup, D.M., 1995, AJ, 110, 2788

Timmes, F.X., Woosley,S.E. & Weaver, T.A., 1995, ApJS, 98, 617

Tingay, S.J., Jauncey, D.L., Reynolds, J.E. et al., 1998, AJ, 115, 960

Tolstoy, E., 1996, ApJ, 462, 684

Tolstoy, E., 1999, in proceeding of XVIIIth Moriond Astrophysics Meeting "Dwarf Galaxies & Cosmology", eds. T. X. Thuan, C. Balkowski, V. Cayatte, J. Tran Thanh Van

Tonry, J.L., 1991, ApJ, 373, L1

Tonry, J. & Schneider, D.P., 1988, AJ, 96, 807

Tonry, J.L. & Schechter, P.L., 1990, AJ, 100, 1794

Toomre, A. & Toomre, J., 1972, ApJ, 178, 623

Tosi, M., Greggio, L., Marconi, G. & Focardi, P., 1991, AJ, 102, 951

Trimble, V., 1995, PASP, 107, 1133

Tyson, J. A., 1988, AJ, 96, 1

Unger, S.J., Clegg, P.E., Stacey, G.J., et al., 2000, A&A, 355, 885

Vallenari, A., Chiosi, C., Bertelli, G. & NG, Y.K., 1996, in: "The Galactic Centre", Gredel R. (ed.), ASP Conf. Ser, 102, p. 320

Vandenberg, D.A. & Bell, R.A., 1985, ApJS, 58, 561

van den Bergh, S. 1976, ApJ, 208, 637

van den Bergh, S., 1994, AJ, 107, 1328

van den Bergh, S., 1995, ApJ, 446, 39

van den Bergh, S., 1999, A&ARv, 9, 273

van den Bergh, S.,2000, PASP, 112, 932

van den Bergh, S., 2000, "The Galaxies of the Local Group", Cambridge University Press van den Bergh, S., Hesser, J.E. & Harris, G.L.H., 1981, AJ, 86, 24

Vazdekis, A. & Arimoto, N. 1999, ApJ, 525, 144

Vazdekis, A., Salaris, M., Arimoto, N. & Rose, J.A., 2001, ApJ, 549, 274

Vesperini, E., 2000, MNRAS, 318, 841

Vernet, J., Fosbury, R.A.E., Villar-Martín, M. et al., 2001, A&A, 366, 7

Wagenhuber, J. & Groenewegen, M.A.T., 1998, A&A, 340, 183

Walsh, J.R., Walton, N.A., Jacoby, G.H. & Peletier, R.F., 1999, A&A, 346, 753

Welch, D.L. & Stetson, P.B., 1993, AJ, 105, 1813

White, S.D.M. & Rees, M.J., 1978, MNRAS, 183, 341

White, R.E & Shawl, S.J., 1987, ApJ, 317, 246

Whitelock, P.A., 1993, in: "Galactic Bulges", DeJonghe H., Habing H.J. (eds.), Kluwer, Dordrecht, p. 39

Whitelock, P. & Feast, M., 2000, MNRAS, 319, 759

Whitelock, P., Feast, M. & Catchpole, R., 1991, MNRAS, 248, 276

Whitelock, P., Marang, F. & Feast, M., 2000, MNRAS, 319, 728

Whiting, A. B., Hau, G. K. T., & Irwin, M. J., 1999, AJ 118, 2767

Whitmore, B.C., Zhang, Q., Leitherer, C., Fall, S.M., Schweizer, F. & Miller, B.W., 1999, AJ, 118, 1551

Wild, W. & Eckart, A., 2000, A&A, 359, 483

Wolf, M., 1909, Astron. Nachr., 183, 187

Wood, P.R., 2000, PASA, 17, 18

Wood, P.R. & Sebo, K.M., 1996, MNRAS, 282, 958

Wood, P.R., Bessell, M.S. & Fox, M.W., 1983, ApJ, 272, 99

Worthey, G., 1994, ApJs, 95, 107

Zepf, S.E. & Ashman, K.M., 1993, MNRAS, 264, 611

Zijlstra, A. A., Minniti, D., & Brewer, J., 1997, The Messenger, 90, 19

Zinn, R., & West, M. J., 1984, ApJS, 55, 45

Zoccali, M., Cassisi, S., Frogel, J.A., et al., 2000, ApJ, 530, 418

Zoccali, M., Renzini, A., Ortolani, S., et al., 2002, A&A, in preparation